DOE/BES Materials Chemistry Program Principal Investigators' Meeting

Virtual Meeting *July 20-22, 2021*

Program and Abstracts

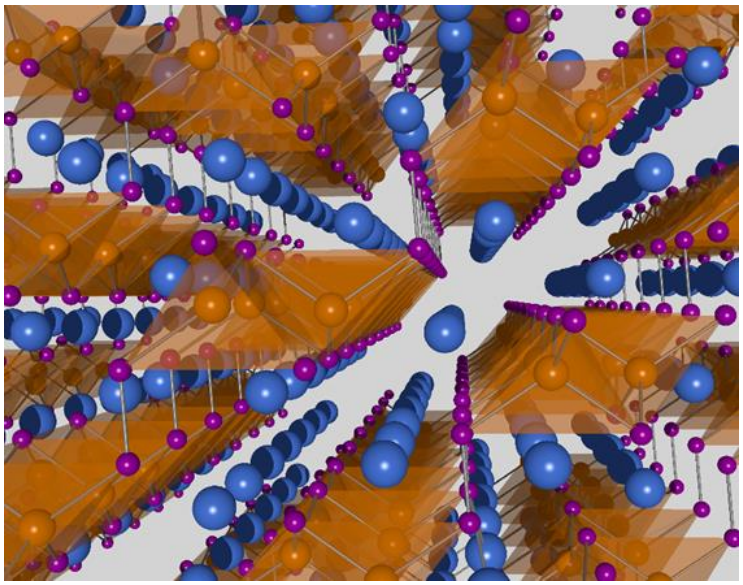

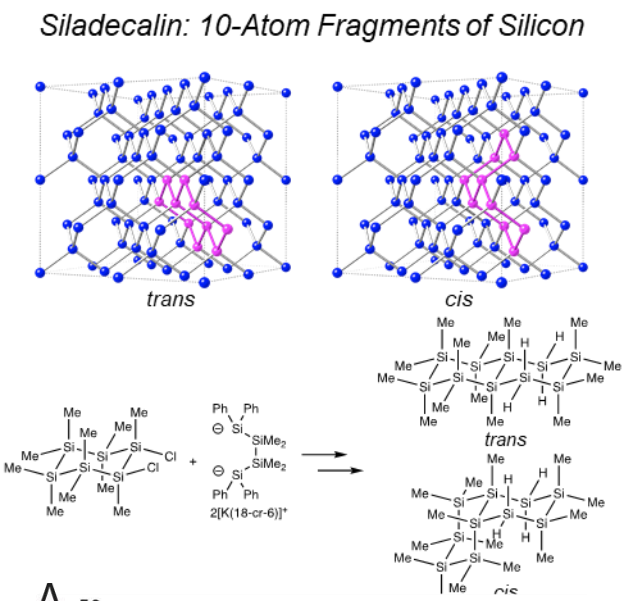

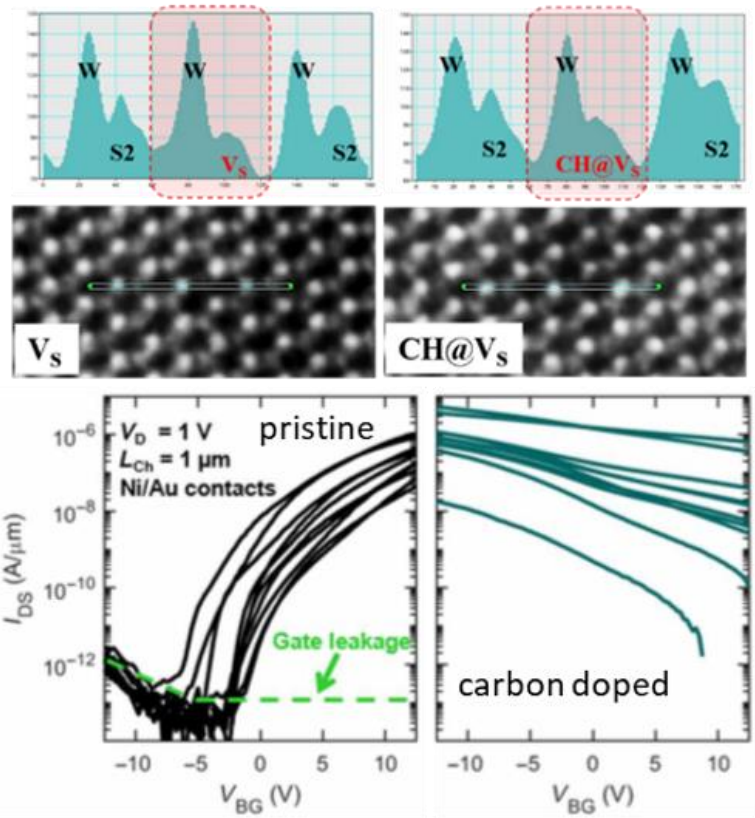

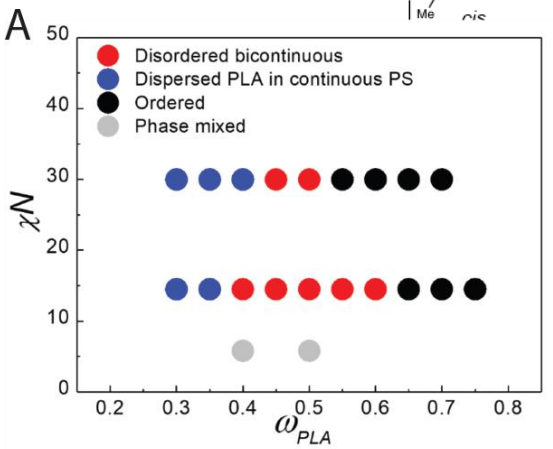

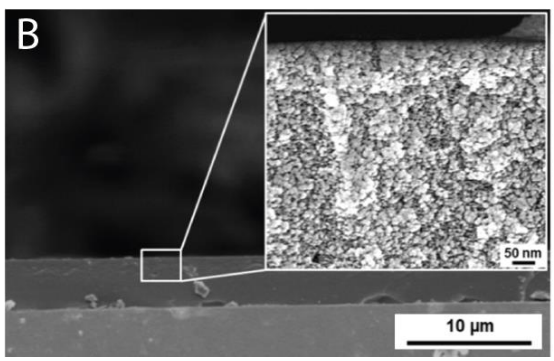

U.S. DEPARTMENT OF ENERGY

Office of Basic Energy Sciences

Materials Sciences and Engineering Division

On the Cover

Top Left: The structure of novel Zintl Phase $Ba_3Cd_2P_4$ semiconductor shows an intricate bonding pattern. There are Cd atoms (orange) at the center of tetrahedra of phosphorus atoms (magenta), which are arranged in infinite double-chains. They are interlinked by covalent P-P bonds, forming an overall structure with a layered appearance. Potential applications include thermoelectric energy conversion.
Svilen Bobev, University of Delaware

Top Right: ***Top***: Crystalline silicon lattice highlighting 10-atom fragments.
Bottom: Chemical synthesis of *cis*- and *trans-siladecalins*. This work expands the range of available building blocks for silicon-based semiconductors and optical materials.
Rebekka Klausen, Johns Hopkins University

Bottom Left: A plasma-assisted method introduces CH units into monolayer WS_2, showing reduction of the optical band gap and p-type transport. Atomic resolution TEM image and back-gated FET transport characteristics of pristine WS_2 monolayers before and after carbon-hydrogen groups incorporation within sulfur monovacancies of WS_2.
Mauricio Terrones, Pennsylvania State University

Bottom Right: A phase diagram (A) showing the formation of disordered cocontinuous phases across a wide-range of composition in linear multiblock copolymers, enabling the formation of spin-coated nanoporous films, as characterized by electron microscopy (B). Cocontinuous nanostructures are of interest for applications including membranes for water purification, batteries, and catalysis.
Ryan Hayward, University of Colorado, Boulder

This document was produced under contract number DE-SC0014664 between the U.S. Department of Energy and Oak Ridge Associated Universities.

The research grants and contracts described in this document are supported by the U.S. DOE Office of Science, Office of Basic Energy Sciences, Materials Sciences and Engineering Division.

Table of Contents

University Grant Projects

Foreword

This document is a collection of abstracts of the presentations made at the Principal Investigators' Meeting of the Materials Chemistry program, sponsored by the Materials Sciences and Engineering (MSE) division in the Office of Basic Energy Sciences (BES) of the U.S. Department of Energy (DOE). The meeting took place July 20–22, 2021 as a virtual event conducted entirely over the internet. The use of virtual meetings rather than the traditional in-person gatherings is due to the COVID-19 pandemic, which also is responsible for the postponement of the meeting from the originally scheduled dates in 2020.

This is one of a series of Principal Investigators' Meetings organized regularly by BES. The purpose of the meeting is to bring together all the Principal Investigators with currently active projects in the Materials Chemistry program for the multiple purposes of raising awareness among PIs of the overall program content and of each other's research, encouraging exchange of ideas, promoting collaboration and stimulating innovation. The meeting also provides an opportunity for the Program Managers and MSE/BES management to get a comprehensive overview of the program on a periodic basis, which provides opportunities to identify program needs and potential new research directions.

The Materials Chemistry program supports basic research in the discovery, design and synthesis of materials with an emphasis on elucidating the complex relationships between a material's functional properties and its composition, atomic and molecular structure and higher-order morphology. Major focus areas of the program include the discovery, synthesis and characterization of new materials and the manipulation of materials' structure across a range of length scales using chemistry.

We would like to thank all of the meeting attendees, for their active participation and for sharing their ideas and new research results. Sincere thanks also go to Teresa Crockett of BES/MSE and Linda Severs and her colleagues at the Oak Ridge Institute for Science and Education (ORISE) for their excellent work providing all the logistical support for the meeting.

Michael Sennett
Craig Henderson
Program Managers, Materials Chemistry
Materials Sciences and Engineering Division
Office of Basic Energy Sciences
U.S. Department of Energy

2021 DOE BES Materials Chemistry
Virtual Principal Investigators' Meeting

Meeting Chairs: **Craig Henderson and Michael Sennett, Program Managers, DOE/BES**

All times are Eastern Time

Day 1 - Tuesday, July 20, 2021

10:45 – 11:00	**Zoom** *Log in*
11:00 – 11:15	Welcome and Materials Sciences and Engineering Division Update **Andrew Schwartz**, Acting Division Director, *MSED, DOE-BES*
11:15 – 11:30	Introductory Remarks from **Michael Sennett and Craig Henderson**, Program Managers, *BES Materials Chemistry*
Session 1	**Energy Storage, Transport and Conversion Materials**
11:30 – 11:45	**Paul Braun**, University of Illinois, Urbana-Champaign *New Paradigms for Controlling Molecular and Ion Transport in Precise, Tight and Reconfigurable Polymer Networks*
11:45 – 12:00	**Christine Luscombe**, University of Washington *Unraveling the Links between Molecular Structure, Microstructure, Delocalization and Charge Transport in New High-Performance Semiconducting Polymers*
12:00 – 12:15	**Michael Aziz,** Harvard University *Understanding Flow Cell Porous Electrodes as Active Materials for Electrochemical Transformations*
12:15 – 12:30	**Ö. Özgür Çapraz,** University of Oklahoma *Elucidating the Link between Alkali Metal Ions and Reaction-Transport Mechanisms in Cathode Electrodes for Alkali-Ion Batteries*
12:30 – 1:00	**BREAK**
1:00 – 1:15	**Ram Manthiram**, University of Texas, Austin *Materials and Interfacial Chemistry for Sustainable Sodium-Based Batteries*
1:15 – 1:30	**Claire Xiong**, Boise State University *Understanding Interfacial Chemistry and Cation Order-Disorder in Mixed-Phase Complex Sodium Metal Oxide Cathodes for Sodium Ion Batteries*
1:30 – 1:45	**Xiaowei Teng**, University of New Hampshire *Understanding the Interplay between Nanostructured Electrode and Aqueous Electrolyte for Na-ion Energy Storage*

1:45 – 2:00 **Gary Rubloff**, University of Maryland
Thin Film Platforms to Advance Scientific Frontiers in Solid State Energy Storage

2:00 – 2:15 **Sarah Tolbert,** University of California, Los Angeles
Using Nanoporous Materials to Understand Kinetic Constraints in Pseudocapacitive Energy Storage

2:15 – 2:30 **Song Jin,** University of Wisconsin
Fundamental Studies of Charge Transfer in Nanoscale Heterostructures of Earth-Abundant Semiconductors for Solar Energy Conversion

2:30 – 2:45 **David Mitzi**, Duke University
Design and Validation of Defect-Resistant Multinary Chalcogenide Semiconductors for Energy Conversion

2:45 – 3:15 **BREAK**

3:15 – 3:30 **Thuc-Quyen Nguyen**, University of California, Santa Barbara
Understanding Novel Lewis Acid Doping Mechanisms in Organic Semiconductors

3:30 – 3:45 **Jodie Lutkenhaus**, Texas A&M University
Diffusion and Kinetics in Organic Radical Polymers

3:45 – 4:00 **J.D. Tovar**, University of Maryland
Exploration of Radial Conjugation Pathways in Pi-Electron Materials

4:00 – 4:15 **Siddhartha Das**, University of Maryland
Polyelectrolyte-Grafted Nanochannels for Enhanced Electrochemomechanical Energy Conversion

4:15 – 4:30 **Rachel Segalman**, University of California, Santa Barbara
Energy Flow in Polymers with Mixed Conduction Pathways

4:30 – 4:45 **Samuel Thomas**, Tufts University
Controlling Solid-State Conjugated Materials with Aromatic Interactions of Side Chains

Session 2 Novel Materials, Characterization, Physical Properties

4:45 – 5:00 **Paul Nealey**, Argonne National Laboratory
Precision Synthesis and Assembly of Ionic and Liquid Crystalline Polymers

5:00 – 5:15 **Aaron Rossini**, Ames Laboratory
Solid State NMR Spectroscopy for Advanced Energy Materials

5:15 – 5:30 **Jeffrey Reimer**, University of California, Berkeley
Metal-Organic Frameworks: Structure, Function and Design via Hyperpolarized NMR Spectroscopy

5:30 **Adjourn Day 1**

Day 2 - Wednesday, July 21, 2021

10:45 – 10:55 **Zoom** *Log In*

10:55 – 11:00 **Welcome to Day 2 (BES Staff)**

11:00 – 11:15 **Timo Thonhauser**, Wake Forest University
Understanding and Tailoring Diffusion and Co-Adsorption Inside the Confined Pores of Metal-Organic Frameworks

11:15 – 11:30 **Adam Matzger**, University of Michigan
Dynamic Properties of Nanostructured Porous Materials

11:30 – 11:45 **Pingyun Feng**, University of California, Riverside
Pore Space Engineering and Functionalization in Porous Metal-Organic Framework Materials

11:45 – 12:00 **Rebekka Klausen**, Johns Hopkins University
Multi-length Scale Synthesis of Silicon Materials

12:00 – 12:15 **Mauricio Terrones**, Pennsylvania State University
2D-EFICACY: Control of Metastable 2D Carbide-Chalcogenide Heterolayers: Strain and Moiré Engineering

12:15 – 12:30 **Howard Katz**, Johns Hopkins University
Electroactive Subunits in Insulating Polymer Heterostructures

12:30 – 1:00 **BREAK**

Session 3 Energy Materials – Organic and Hybrid

1:00 – 1:15 **Marc Baldo**, Massachusetts Institute of Technology
Bimolecular Interactions in Organic Semiconductors: Hot Charge, Hot Excitons, Efficiency Droop, and Instability

1:15 – 1:30 **Kenneth Graham**, University of Kentucky
Surface Ligand Effects on Energetics, Charge Transfer, and Stability at Interfaces between Metal Halide Perovskites and Organic Semiconductors

1:30 – 1:45 **James Neilson**, Colorado State University
Informed Materials Design Principles from Local Structures and Dynamics in Hybrid Inorganic-Organic Perovskite Halides

1:45 – 2:00 **Ram Seshadri**, University of California, Santa Barbara
Hybrid Metal Halides: Advancing Optoelectronic Materials

2:00 – 2:15 **Gregory Grason**, University of Massachusetts, Amherst
Shaping Symmetry and Molding Morphology of Triply-Periodic Network Assemblies via Molecular Design of Block Copolymers

2:15 – 2:30 **Arthi Jayaraman**, University of Delaware
Predictive Coarse-Grained Modeling of Morphologies in Polymer Nanocomposites with Specific and Directional Intermolecular Interactions

2:30 – 2:45 **Lei Zhu**, Case Western Reserve University
An Integrated Theoretical and Experimental Approach to Achieve Highly Polarizable Relaxor Ferroelectric Liquid Crystalline Polymers

2:45 – 3:00 **Ryan Hayward**, University of Colorado, Boulder
Self-Assembly of Co-continuous Nanostructured Copolymer Templates with Compositional and Architectural Dispersity

3:00 – 3:15 **Thomas Epps**, University of Delaware
Modulating Phase Separation and Constituent Density Profiles in Nanostructured Polymer Electrolytes – Joint Experiment and Theory Effort in Tunable Hierarchical Assembly

3:15 – 3:45 **BREAK**

Session 4 Energy Materials – Inorganic and Organometallic

3:45 – 4:00 **Yury Gogotsi**, Drexel University
Compositional Control of Fundamental Electronic and Magnetic Properties of Ordered Layered Multielemental MXenes

4:00 – 4:15 **Joseph Kolis**, Clemson University
Crystal Growth and Quantum Phases of Frustrated Rare Earth Oxides

4:15 – 4:30 **Jing Kong**, Massachusetts Institute of Technology
Novel 2D Materials and Structures via Janus Manipulation

4:30 – 4:45 **Pierre Ferdinand Poudeu**, University of Michigan
Hierarchical Hybrid Multifunctional Materials through Interface Engineering

4:45 – 5:00 **Richard Brutchey**, University of Southern California
Unravelling the Mechanisms of Phase Determination in Metastable Multinary Chalcogenides

5:00 – 5:15 **Yi Cui**, SLAC National Accelerator Laboratory
Two-Dimensional Chalcogenide Nanomaterials

5:15 – 5:30 **Robert Fleming**, Arkansas State University
Fundamental Studies of Soiling and Cementation of PV Cover Glass Materials: Addressing Reliability with Advanced X-ray Scattering/Spectroscopy and First Principles Modeling

5:30 **Adjourn Day 2**

Day 3 - Thursday, July 22, 2021

10:45 – 10:55 **Zoom** *Log In*

10:55 – 11:00 **Welcome to Day 3 (BES Staff)**

Session 5 **New Materials Synthesis**

11:00 – 11:15 **May Nyman**, Oregon State University
Hydrolysis, Self-Assembly and Supramolecular Assembly of Early Transition Metal-oxo Clusters: MOF Nodes and Aqueous Reaction Pathways

11:15 – 11:30 **Mercouri Kanatzidis**, Argonne National Laboratory
Rational Synthesis of Superconductors

11:30 – 11:45 **Ashkan Salamat**, University of Nevada, Las Vegas
The Synthesis of Metal Superhydrides through Extreme Temperature/Pressure Conditions: Towards Room Temperature Superconductivity

11:45 – 12:00 **Timothy Strobel**, Carnegie Institution of Washington, D.C.
Carbon-Based Clathrates as a New Class of sp^3-Bonded Framework Materials

12:00 – 12:15 **Adam Veige**, University of Florida
Expanding iClick to Link Metal Ions in Multidimensional Metallopolymers and Materials Synthesis

12:15 – 12:30 **Daniel Fredrickson**, University of Wisconsin
Intermetallic Reactivity: From Frustrated Bonding to Mechanisms for Intergrowth and Modular Functionality in Metals and Alloys

12:30 – 1:00 **BREAK**

1:00 – 1:15 **Jarad Mason**, Harvard University
Converting Metal–Organic Liquids into Microporous Glasses via Non-Equilibrium Syntheses

1:15 – 1:30 **Nicola Perry**, University of Illinois, Urbana-Champaign
Chemo-Mechanically Driven In-Situ Hierarchical Structure Formation in Mixed Conductors

1:30 – 1:45	**Bayram Saparov**, University of Oklahoma *Additive-Assisted Preparation of Multinary Halides*
1:45 – 2:00	**Svilen Bobev**, University of Delaware *Solid-State Chemistry of Novel Pnictides with Complex Structures*
2:00 – 2:15	**Gregory McKenna**, Texas Tech University *Polymer Macrocycles: A Novel Topology to Control Dynamics of Rubbery Materials*
2:15 – 2:30	**Miquel Salmeron**, Lawrence Berkeley National Laboratory *Structure and Dynamics of Materials Interfaces*
2:30 – 2:45	**Ting Xu**, Lawrence Berkeley National Laboratory *Diversifying Composition Leads to Design Flexibility and Structural Fidelity in Hierarchical Composites*
2:45 – 3:00	**Andriy Zakutayev**, National Renewable Energy Laboratory *Kinetically Controlled Synthesis of Metastable Nitride Materials*
3:00 – 3:30	**BREAK**
3:30 – 3:45	**Vinayak Dravid,** Northwestern University *Design of Next Generation Thermoelectrics*
3:45 – 4:00	**Emmanuel Theodorakis**, University of California, San Diego *MOF-polymer Hybrids for Energy Science*
4:00 – 4:15	**Danna Freedman**, Massachusetts Institute of Technology *Permanent Magnets Featuring Heavy Main Group Elements for Magnetic Anisotropy*
4:15 – 4:30	**Philip Power**, University of California, Davis *Activation of Hydrogen under Ambient Conditions and Unusual Element Hydride Reactivity by Main Group Molecules*
4:30 – 4:45	**Hans-Conrad zur Loye**, University of South Carolina *Directed Synthesis of New Actinide Containing Oxides, Fluorides and Chalcogenides*
4:45 – 5:00	**Hong Wang**, University of North Texas *Pi-Extended Porphyrins Fused with Five- and Six-Membered Rings: Synthesis, Characterization and Property Studies*
5:00 – 5:15	**Jeramy Zimmerman**, Colorado School of Mines *Understanding and Controlling Aggregation Processes in Mixed-Molecular Solids*

5:15 – 5:30	**Bob Cava**, Princeton University *Looking for Superconductors among Tungsten-Bronze-Related Oxides*
5:30 – 5:45	**Closing Remarks** – BES Staff
5:45	**Adjourn PI Meeting**

LABORATORY PROJECTS

Physical Chemistry of Inorganic Nanostructures

A. Paul Alivisatos, Department of Chemistry, UC Berkeley; Materials Sciences Division, Lawrence Berkeley National Laboratory

Peidong Yang, Department of Chemistry, UC Berkeley; Materials Sciences Division, Lawrence Berkeley National Laboratory

Stephen R. Leone, Department of Chemistry, UC Berkeley; Materials Sciences Division, Lawrence Berkeley National Laboratory

Eran Rabani, Department of Chemistry, UC Berkeley; Materials Sciences Division, Lawrence Berkeley National Laboratory

David T. Limmer, Department of Chemistry, UC Berkeley; Materials Sciences Division, Lawrence Berkeley National Laboratory

Program Scope

The properties of inorganic nanostructures depend critically on the structures of individual nanoscale building blocks as well as their assembled superstructures. The controlled synthesis, advanced structural characterization, and theoretical modeling of optical and electronic properties of inorganic semiconductor nanostructures will enable the design and control of nanoscale energy conversion systems with great precision. Herein, our program focuses on three interconnecting themes: 1) rationalized synthesis and assembly of colloidal nanoscale building blocks, 2) *in situ* observation of structural dynamics and transformations, and 3) excited state dynamics of inorganic nanostructures and the development of new spectroscopic methods. With the three efforts combined, we aim to develop a holistic understanding that both imparts fundamental knowledge of inorganic nanostructures and guides the design of their advanced applications.

Recent Progress

1. Rationalized Synthesis and Assembly of Nanoscale Building Blocks: Rationalized synthesis and assembly of nanoscale building blocks are key to tailoring nanomaterials for applications. High-throughput synthesis offers a unique opportunity for understanding the reaction networks using a data-driven approach with the aim of achieving rationalized synthesis of nanocrystals. We explored the synthesis space of cesium lead bromide perovskite species using a robotic high-throughput synthesis and characterization platform. Machine learning algorithm was deployed to de-convolute the absorption spectra of multiple lead-containing species and obtain their relative concentrations. This combined approach has allowed us to create a map of the cesium lead bromide perovskite synthesis space (Figure 1), which elucidates the interconversion between various distinct species.[1] By parameterizing a chemical model to reproduce this map using machine-learning algorithms, we can reveal the best routes for reaching synthesis targets.

In addition to the synthesis of building blocks, we aim to understand and engineer the interactions between nanoparticles and rationalize the design of nanocrystal assemblies. Using *in situ* TEM, we illuminated the annealing and defects removal pathways of assembled CdSe QDs.[2] Knowledge of such pathways has allowed us to design and synthesize atomically attached QD superlattices with precise control of crystallographic alignment and long-range translational order, opening the door to a new dimension of control in engineering the properties of nanoscale materials.[3] The synthetic diversity and flexible assembly of perovskite building blocks have brought new opportunities and challenges on the nanoscale control and manipulation of colloidal nanocrystals. We have harnessed the synthetic control of $CsPbBr_3$ to produce uniform size distribution of 0D QDs, 1D nanowires,[4] and 2D nanoplates.[5] Their self-assembly processes were probed in situ with optical spectroscopy and synchrotron small-angle x-ray scattering technique.

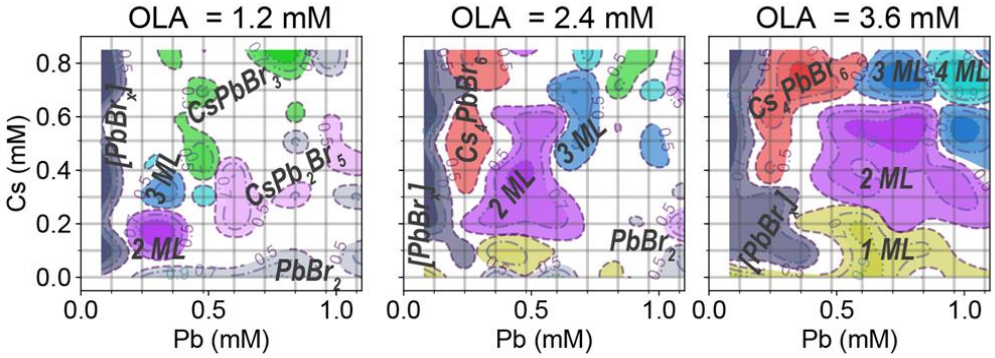

Figure 1. Example maps for the synthesis space of cesium lead bromide perovskite species.

2. <u>*In situ* Observation of Nanoscale Structural Transformation:</u> Observing the structural transformation and dynamics of semiconductors under different environmental conditions can greatly enhance our prediction and control of their physical behaviors. In this program, *in situ* techniques were utilized to tackle the structural transformation with not only high spatial resolution, but also high time resolution.

The halide perovskite materials with soft ionic lattices have a library of structural polymorphs. However, the transformation kinetics and mechanism among different species are difficult to probe directly by electron microscopy due to the fragility of perovskite under electron bombardment. Recently, direct, non-invasive imaging techniques such as photoluminescence (PL) microscopy,[6] cathodoluminescence (CL) microscopy, and high-pressure Raman spectroscopy were utilized to probe the structural transformation of halide perovskite nanostructures. In particular, through *in situ* dynamic CL imaging and multiscale modeling of the LT-$CsPbIBr_2$ to HT-$CsPbIBr_2$ structural phase transition, we have uncovered the mechanism in which liquid-like interface mediates structural transformation in cesium lead halides (Figure 2).[7] The liquid-like dynamics arise from the low cohesive energy of their ionic bonds, in sharp contrast to traditional covalent semiconductors such as CdSe. The phase transition of charge-ordered halide perovskite $Cs_2In(I)In(III)Cl_6$ was another demonstration of the importance of the reconfigurable halide

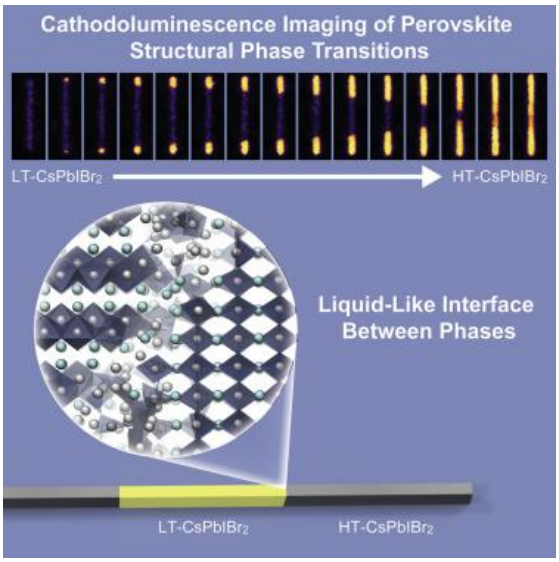

Figure 2. Phase transition modulated by the liquid-like interface between halide perovskite lattices.

perovskite nanostructures.[8] This charge disproportioned material is a semiconductor at ambient condition, but behaves like metal under high pressure. The In-based charge-ordered structure may provide a platform for future discovery of exotic electronic phenomena such as high-TC superconductivity in halide perovskite compounds.

With the advancement of liquid-cell transmission electron microscopy (TEM) technique, we are probing the structural and chemical dynamics of colloidal nanocrystals with high spatial resolution. We have developed new methods to introduce user-defined chemical potentials in graphene liquid cells with redox additives. This approach has allowed us to regulate the etching dynamics of noble metals. Furthermore, we have recently crossed the threshold of investigating the etching dynamics of semiconductor colloidal nanocrystals such as PbSe and CdSe QDs. Preliminary results revealed that the etching trajectories depend on the faceting conditions of these nanocrystals. Extensive studies of structure-property relationships in II-VI semiconducting nanostructures conducted within this program can inform the identification of the most suitable candidates for single particle in situ etching studies, which often yield valuable insights into the inverse process of growth. In addition to the graphene encapsulation, carbon nanotubes as a reaction tube were also utilized in TEM experiments to visualize the structural dynamics of halide perovskite with atomic spatial resolution and high temporal resolution.

3. <u>Excited State Dynamics of Inorganic Nanostructures:</u> Thin film and nanoscale junctions have driven recent progress across the photovoltaic and photoelectrochemical fields. However, the transport in nanoscale junctions is still measured as a bulk-averaged quantity by measuring the transport or kinetics across an entire junction. In this program, we developed a transient extreme ultraviolet (XUV) technique for measuring the layer-specific carrier transport simultaneously in each layer of a junction. We first developed a theoretical model which extracts detailed carrier and lattice dynamics from the Si $L_{2,3}$ edge.[9] The carrier population and temperature, as well as the excited state lattice deformations (optical and acoustic phonons), are obtained in a single measurement, and their scattering processes are compared over time following excitation into different valleys in the Si band structure.[10] The insight gained from these studies allowed us

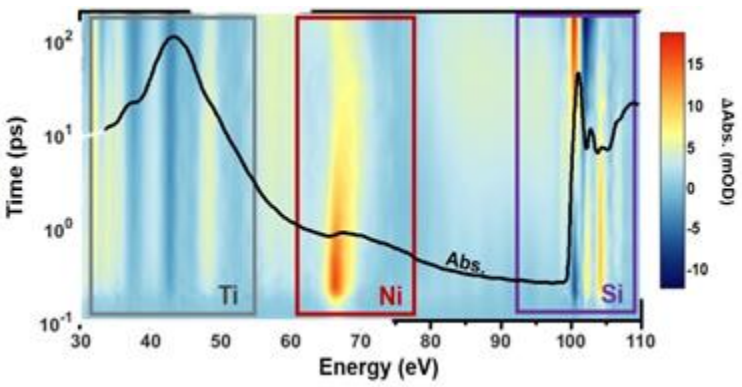

Figure 3. The XUV ground state spectrum (black line) and the transient XUV spectrum (colormap) of the Si-TiO_2-Ni junction, with the energy region of each elemental edge labeled. The transient spectrum is shown in a logarithmic time axis for visual clarity.

to address the debated case of how hole transport occurs in the amorphous oxide layer of a metal-oxide-semiconductor junction (Figure 3).[11] The photoexcited holes on Si are measured to tunnel rapidly through the TiO_2 to the Ni while the photoexcited electrons on Si do not transport. Our findings represent the first element-specific, all-optical, ultrafast quantification of the hole dynamics in a multi-layer nanoscale junction, advancing the element-specific technique of XUV spectroscopy.

The excitonic and charge transfer dynamics of semiconductor nanostructures were also investigated using a combination of visible wavelength transient absorption (TA) spectroscopy, classical simulation and quantum dynamical theory. We have achieved the transfer of multiple holes (~3) from multi-excitonic II-VI QDs to customized molecular acceptors.[12] A broad photo-induced absorption feature, assigned based on atomistic modeling to surface trapped holes,[13] revealed stark differences between the surface trap states on native QDs and those on QDs modified with molecular acceptors. Modeling of the TA data shows that a reservoir of long-lived trapped holes on surface-modified QDs may continue to transfer to molecular acceptors over a timescale significantly beyond the Auger recombination lifetime, increasing the transfer efficiency. In a related study, TA was used to characterize the phonon dephasing process in Ruddlesden-Popper layered lead halide perovskites, which couples strongly to excitonic dynamics and hence influences charge carrier lifetimes. It was found that the choice of organic cation to separate the lead halide sheets has a strong effect on dephasing rates: flexible alkyl-amines give faster dephasing than aryl amines, with a smaller temperature dependence. Atomistic classical simulations of the two materials suggest that dephasing is driven largely by anharmonic coupling of optical modes in the ligand and lead halide layers, particularly significant for flexible alkyl groups with high dynamic disorder. This work lays the foundations for a more detailed study of exciton-phonon coupling in Ruddlesden-Popper phases, leading ultimately to design principles for optoelectronic devices. The two studies above highlight the important impacts of molecular components on the excited state dynamics of inorganic semiconductor nanostructures.

Future Plans

In the future, we will continue to advance the rationalized synthesis of new colloidal nanoscale building blocks and their assemblies. Such efforts will leverage on the large datasets of automated synthesis and advanced machine learning methods. Furthermore, machine learning algorithms are being developed to enable new structural analysis methods using data such as electron microscopy images; this will accelerate the feedback loop to inform precise synthesis. Single particle optical microscopies as well as *in situ* electron microscopies will continue to be developed and applied to yield powerful insights on the structural transformation and reactivity of inorganic nanostructures. In addition, measurements of lead halide perovskite nanostructures using advanced time-resolved spectroscopic methods such as the XUV spectroscopy are underway, along with the development of theoretical tools for modeling the observed excited state dynamics.

References

1. JC Dahl, WT Osowiecki, Y Cai, JK Swabeck, Y Bekenstein, M Asta, EM Chan, and **AP Alivisatos**. "Probing the Stability and Band Gaps of $Cs_2AgInCl_6$ and $Cs_2AgSbCl_6$ Lead-Free Double Perovskite Nanocrystals", *Chem. Mater.,* 2019, 31, 3134–3143.

2. JC Ondry, JP Philbin, M Lostica, **E Rabani,** and **AP Alivisatos**. "Resilient Pathways to Atomic Attachment of Quantum Dot Dimers and Artificial Solids from Faceted CdSe Quantum Dot Building Blocks," *ACS Nano*, 2019, 13, 12322-12344.
3. JC Ondry, JP Philbin, M Lostica, **E Rabani,** and **AP Alivisatos**. "Colloidal Synthesis Path to 2D Crystalline Quantum Dot Superlattices", *ACS Nano*, 2020, DOI: 10.1021/acsnano.0c07202.
4. M Gao, H Liu, S Yu, S Louisia, Y Zhang, DP Nenon, **AP Alivisatos** and **P Yang**. "Scaling Laws of Exciton Recombination Kinetics in Low Dimensional Halide Perovskite Nanostructures", *J. Am. Chem. Soc*., 2020, 142, 8871-8879.
5. Y Liu, M Siron, D Lu, J Yang, R Reis, F Cui, M Gao, M Lai, J Lin, Q Kong, T Lei, J Kang, J Jin, J Ciston, and **P Yang**. "Self-Assembly of Two-Dimensional Perovskite Nanosheet Building Blocks into Ordered Ruddlesden–Popper Perovskite Phase," *J. Am. Chem. Soc.*, 2019, 141, 13028-13032.
6. Y Zhang, D Lu, M Gao, M Lai, J Lin, T Lei, Z Lin, L Quan, and **P Yang**. "Quantitative imaging of anion exchange kinetics in halide perovskites," *Proc. Natl. Acad. Sci. USA*, 2019, 116, 12648–12653.
7. CG Bischak, M Lai, Z Fan, D Lu, P David, D Dong, H Chen, AS Etman, T Lei, J Sun, M Grünwald, **DT Limmer, P Yang**, and NS Ginsberg. "Liquid-like Interfaces Mediate Structural Phase Transitions in Lead Halide Perovskites", *Matter*, 2020, 3, 534-545.
8. J Lin, H Chen, Y Gao, Y Cai, J Jin, AS Etman, J Kang, T Lei, Z Lin, MC Folgueras, LN Quan, Q Kong, M Sherburne, M Asta, J Sun, MF Toney, J Wu and **P Yang**. "Pressure Induced Semiconductor to Metal Phase Transition of a Charge-Ordered Indium Halide Perovskite", *Proc. Natl. Acad. Sci. USA*, 2019, 116, 23404-23409.
9. SK Cushing, M Zurch, PM Kraus, LM Carneiro, A Lee, HT Chang, CJ Kaplan, and **SR Leone**. "Hot phonon and carrier relaxation in Si(100) determined by transient extreme ultraviolet spectroscopy," *Struct. Dyn.*, 2018 5, 054302.
10. SK Cushing, A Lee, IJ Porter, LM Carneiro, HT Chang, M Zuerch, and **SR Leone**. "Differentiating Photoexcited Carrier and Phonon Dynamics in the D, L, and G Valleys of Si(100) with Transient Extreme Ultraviolet Spectroscopy," *J. Phys. Chem. C*, 2019, 123, 3343–3352.
11. SK Cushing, IJ Porter, BR de Roulet, A Lee, BM Marsh, S Szoke, ME Vaida, and **SR Leone**. "Layer-Resolved Ultrafast Extreme Ultraviolet Measurement of Hole Transport in a Ni-TiO2-Si Photoanode," *Sci. Adv.*, 2020, 6(14), eaay6650.
12. C Yan, D Weinberg, D Jasrasaria, MA Kolaczkowski, Z Liu, JP Philbin, AD Balan, Y Liu, AM Schwartzberg, **E Rabani,** and **AP Alivisatos**. "Uncovering the Role of Hole Traps in Promoting Hole Transfer from Multiexcitonic Quantum Dots to Molecular Acceptors", *ACS Nano*, 2020, DOI: 10.1021/acsnano.0c08158.
13. D Jasrasaria, JP Philbin, C Yan, D Weinberg, **AP Alivisatos,** and **E Rabani**. "Sub-Bandgap Photoinduced Transient Absorption Features in CdSe Nanostructures: The Role of Trapped Holes", *J. Phys. Chem. C*, 2020, 124, 17372–17378.

Publications

A. Publications primarily funded and intellectually led by this FWP

1. MR Hauwiller, LB Frechette, MR Jones, JC Ondry, GM Rotskoff, P Geissler, and **AP Alivisatos**. "Unravelling Kinetically-Driven Mechanisms of Gold Nanocrystal Shape Transformations using Graphene Liquid Cell Electron Microscopy," *Nano Lett.,* 2018, 18 (9), 5731-5737.

2. SK Cushing, M Zurch, PM Kraus, LM Carneiro, A Lee, HT Chang, CJ Kaplan, and **SR Leone**. "Hot phonon and carrier relaxation in Si(100) determined by transient extreme ultraviolet spectroscopy," *Struct. Dyn.,* 2018, 5, 054302.

3. D Lu, Y Zhang, M Lai, A Lee, C Xie, J Lin, T Lei, Z Lin, CS Kley, J Huang, **E Rabani**, and **P Yang**. "Giant Light-Emission Enhancement in Lead Halide Perovskites by Surface Oxygen Passivation," *Nano Lett.,* 2018, 18, 6967-6973.

4. M Lai, A Obliger, D Lu, CS Kley, CG Bischak, Q Kong, T Lei, L Dou, NS Ginsberg, **DT Limmer**, and **P Yang**. "Intrinsic anion diffusivity in lead halide perovskites is facilitated by a soft lattice," *Proc. Natl. Acad. Sci. USA*, 2018, 115, 11929-11934.

5. DP Nenon, K Pressler, J Kang, BA Koscher, JH Olshansky, WT Osowiecki, MA Koc, LW Wang, and **AP Alivisatos**. "Design Principles for Trap-Free $CsPbX_3$ Nanocrystals: Enumerating and Eliminating Surface Halide Vacancies with Softer Lewis Bases," *J. Am. Chem. Soc.,* 2018, 140, 17660-17772.

6. SK Cushing, A Lee, IJ Porter, LM Carneiro, HT Chang, M Zuerch, and **SR Leone**. "Differentiating Photoexcited Carrier and Phonon Dynamics in the D, L, and G Valleys of Si(100) with Transient Extreme Ultraviolet Spectroscopy," *J. Phys. Chem. C,* 2019, 123, 3343–3352.

7. MR Hauwiller, JC Ondry, CM Chan, P Khandekar, J Yu, and **AP Alivisatos**. "Gold Nanocrystal Etching as a Means of Probing the Dynamic Chemical Environment in Graphene Liquid Cell Electron Microscopy," *J. Am. Chem. Soc.,* 141, 4428-4437 (2019).

8. J Gao, L Kidon, **E Rabani**, and **AP Alivisatos**. "Ultrahigh Hot Carrier Transient Photocurrent in Nanocrystal Arrays by Auger Recombination," *Nano Lett.,* 2019, 19, 4804-4810.

9. Y Zhang, D Lu, M Gao, M Lai, J Lin, T Lei, Z Lin, L Quan, and **P Yang**. "Quantitative imaging of anion exchange kinetics in halide perovskites," *Proc. Natl. Acad. Sci. USA*, 2019, 116, 12648–12653.

10. Y Liu, M Siron, D Lu, J Yang, R Reis, F Cui, M Gao, M Lai, J Lin, Q Kong, T Lei, J Kang, J Jin, J Ciston, and **P Yang**. "Self-Assembly of Two-Dimensional Perovskite Nanosheet Building Blocks into Ordered Ruddlesden–Popper Perovskite Phase," *J. Am. Chem. Soc.,* 2019, 141, 13028-13032.

11. J Lin, H Chen, J Kang, L Quan, Z Lin, Q Kong, M Lai, S Yu, L Wang, LW Wang, M Toney, and **P Yang**. "Copper(I) Based Highly Emissive All-Inorganic Rare-Earth Halide Clusters," *Matter*, 2019, 1, 180-191.

12. A Levy, W Dou, **E Rabani** and **DT Limmer**. A complete quasiclassical map for the dynamics of interacting fermions. *J. Chem. Phys.*, 2019, 150, 234112.

13. A Levy, L Kidon, J Bätge, J Okamato, M Thoss, **DT Limmer**, and **E Rabani**. Absence of Coulomb blockade in the Anderson impurity model at the symmetric point. *J. Phys. Chem. C,* 2019, 123, 13538-13544.

14. JC Ondry, JP Philbin, M Lostica, **E Rabani**, and **AP Alivisatos**. "Resilient Pathways to Atomic Attachment of Quantum Dot Dimers and Artificial Solids from Faceted CdSe Quantum Dot Building Blocks," *ACS Nano,* 2019, 13, 12322-12344.

15. JC Dahl, WT Osowiecki, Y Cai, JK Swabeck, Y Bekenstein, M Asta, EM Chan, and **AP Alivisatos**. "Probing the Stability and Band Gaps of $Cs_2AgInCl_6$ and $Cs_2AgSbCl_6$ Lead-Free Double Perovskite Nanocrystals", *Chem. Mater.*, 2019, 31, 3134–3143.

16. LN Quan, J Kang, CZ Ning, and **P Yang**. "Nanowires for Photonics", *Chem. Rev.*, 2019, 119, 9153-9169.

17. BA Koscher, Z Nett, and **AP Alivisatos**. "The Underlying Chemical Mechanism of Selective Chemical Etching in $CsPbBr_3$ Nanocrystals for Reliably Accessing Near-Unity Emitters", *ACS Nano,* 2019, 13, 11825–11833.

18. AD Balan, JH Olshansky, Y Horowitz, HL Han, EA O'Brien, L Tang, GA Somorjai, and **AP Alivisatos**. "Unsaturated Ligands Seed an Order to Disorder Transition in Mixed Ligand Shells of CdSe/CdS Quantum Dots", *ACS Nano,* 2019, 13, 13784–13796.

19. J Lin, H Chen, Y Gao, Y Cai, J Jin, AS Etman, J Kang, T Lei, Z Lin, MC Folgueras, LN Quan, Q Kong, M Sherburne, M Asta, J Sun, MF Toney, J Wu and **P Yang**. "Pressure Induced Semiconductor to Metal Phase Transition of a Charge-Ordered Indium Halide Perovskite", *Proc. Natl. Acad. Sci. USA*, 2019, 116, 23404-23409.

20. H Chen, J Lin, J Kang, Q Kong, D Lu, J Kang, M Lai, LN Quan, Z Lin, J Jin, LW Wang, MF Toney and **P Yang**. "Structural and Spectral Dynamics of Single-Crystalline Ruddlesden-Popper Phase Halide Perovskite Blue Light-Emitting Diodes", *Sci. Adv.*, 2020, 6, eaay4045.

21. CK Lin, Q Zhao, Y Zhang, S Cestellos-Blanco, Q Kong, M Lai, J Kang, and **P Yang**. "Two-Step Patterning of Scalable All-Inorganic Halide Perovskite Arrays", *ACS Nano*, 2020, 14, 3500-3508.

22. SK Cushing, IJ Porter, BR de Roulet, A Lee, BM Marsh, S Szoke, ME Vaida, and **SR Leone**. "Layer-Resolved Ultrafast Extreme Ultraviolet Measurement of Hole Transport in a Ni-TiO_2-Si Photoanode", *Sci. Adv.*, 2020, 6, eaay6650.

23. H Liu, M Siron, M Gao, D Lu, Y Bekenstein, D Zhang, L Dou, **AP Alivisatos**, and **P Yang**. "Lead Halide Perovskite Nanowires Stabilized by Block Copolymers for Langmuir-Blodgett Assembly", *Nano Res.*, 2020, 5, 5404.

24. M Gao, H Liu, S Yu, S Louisia, Y Zhang, DP Nenon, **AP Alivisatos** and **P Yang**. "Scaling Laws of Exciton Recombination Kinetics in Low Dimensional Halide Perovskite Nanostructures", *J. Am. Chem. Soc.*, 2020, 142, 8871-8879.

25. V Jamali, F Niroui, LW Taylor, OS Dewey, BA Koscher, M Pasquali, and **AP Alivisatos**. "Perovskite-Carbon Nanotube Light-Emitting Fibers", *Nano Lett.*, 2020, 20(5), 3178–3184.

26. GA Kamat, C Yan, WT Osowiecki, IA Moreno-Hernandez, M Ledendecker, and **AP Alivisatos**. "Self-Limiting Shell Formation in Cu@Ag Core–Shell Nanocrystals during Galvanic Replacement", *J. Phys. Chem. Lett.*, 2020, 11(13), 5318–5323.

27. JC Dahl, X Wang, X Huang, EM Chan, and **AP Alivisatos**. "Elucidating the Weakly Reversible Cs–Pb–Br Perovskite Nanocrystal Reaction Network with High-Throughput Maps and Transformations", *J. Am. Chem. Soc.*, 2020, 142, 11915–11926.

28. **DT Limmer**, NS Ginsberg. "Photoinduced phase separation in the lead halides is a polaronic effect", *J. Chem. Phys*., 2020, 152, 230901.

29. D Jasrasaria, JP Philbin, C Yan, D Weinberg, **AP Alivisatos**, and **E Rabani**. "Sub-Bandgap Photoinduced Transient Absorption Features in CdSe Nanostructures: The Role of Trapped Holes", *J. Phys. Chem. C*, 2020, 124, 17372–17378.

30. CG Bischak, M Lai, Z Fan, D Lu, P David, D Dong, H Chen, AS Etman, T Lei, J Sun, M Grünwald, **DT Limmer**, and **P Yang**, and NS Ginsberg. "Liquid-like Interfaces Mediate Structural Phase Transitions in Lead Halide Perovskites", *Matter*, 2020, 3, 534-545.

31. Q Chen, JM Yuk, MR Hauwiller, J Park, KS Dae, JS Kim, and **AP Alivisatos**. "Nucleation, Growth, and Superlattice Formation of Nanocrystals Observed in Liquid Cell Transmission Electron Microscopy", *MRS Bull.*, 2020, 45, 713–726.

32. Q Kong, A Obliger, M Lai, M Gao, **DT Limmer**, **P Yang**, "Solid-State Ionic Rectification in Perovskite Nanowire Heterostructures", *Nano Letters* 2020, 20, 8151–8156.

33. JA Steele, M Lai, Y Zhang, Z Lin, J Hofkens, MB Roeffaers, **P Yang**, "Phase Transitions and Anion Exchange in All-Inorganic Halide Perovskites", *Acc. Mater. Res.* **2020**, 1, 3–15.

34. M Lai, T Lei, Y Zhang, J Jin, JA Steele, **P Yang**, "Phase Transition Dynamics in One-Dimensional Halide Perovskite Crystals", *MRS Bull.* 2021, 46, 310–316.

35. C Yan, D Weinberg, D Jasrasaria, MA Kolaczkowski, Z Liu, JP Philbin, AD Balan, Y Liu, AM Schwartzberg, **E Rabani**, and **AP Alivisatos**. "Uncovering the Role of Hole Traps in Promoting Hole Transfer from Multiexcitonic Quantum Dots to Molecular Acceptors", *ACS Nano*, 2021, 15, 2281–2291.

36. JC Ondry, JP Philbin, M Lostica, **E Rabani**, and **AP Alivisatos**. "Colloidal Synthesis Path to 2D Crystalline Quantum Dot Superlattices", *ACS Nano*, 2021, 15, 2251–2262.

37. J Ondry, and **AP Alivisatos**. "Application of Dislocation Theory to Minimize Defects in Artificial Solids Built with Nanocrystal Building Blocks", *Acc. Chem. Res.*, 2021, 54, 1419–1429.

38. JJ Calvin, TM Kaufman, AB Sedlak, MF Crook and **AP Alivisatos**, "Observation of ordered organic capping ligands on semiconducting quantum dots via powder X-ray diffraction", *Nat. Comm.*, 2021, 12, 2663.

39. IJ Porter, A Lee, SK Cushing, H Chang, JC Ondry, **AP Alivisatos**, and **SR Leone,** "Characterization of Carrier Cooling Bottleneck in Silicon Nanoparticles by Extreme Ultraviolet (XUV) Transient Absorption Spectroscopy", *J. Phys. Chem. C*, 2021, 125, 9319-9329.

40. LN Quan; Y Park, P Guo, M Gao, J Jin, J Huang, JK Copper, A Schwartzberg, R Schaller, **DT Limmer, P Yang**, "Vibrational Relaxation Dynamics in Layered Perovskite Quantum Wells", *Proc. Natl. Acad. Sci. USA*, 2021, 118, e2104425118.

41. Z Lin, Y Zhang, M Gao, JA Steele, S Louisia, S Yu, LN Quan, C-K Lin, **DT Limmer**, **P Yang**. "Kinetics of Moisture-Induced Phase Transformation in Inorganic Halide Perovskite", *Matter*, 2021, DOI: 10.1016/j.matt.2021.04.023.

42. A Dey, *et al*., LN Quan, M Gao, **P Yang**, *et al*., "State of the Art and Prospects for Halide Perovskite Nanocrystals", *ACS Nano*, 2021, DOI: 10.1021/acsnano.0c08903.

43. H-T Chang, A Guggenmos, SK Cushing, Y Cui, NU Din, SR Acharya, IJ Porter, U Kleineberg, V Turkowski, TS Rahman, *et al.*, DM Neumark, **SR Leone**, "Electron Thermalization and Relaxation in Laser-Heated Nickel by Few-Femtosecond Core-Level Transient Absorption Spectroscopy", *Phys. Rev. B*, 2021, 103, 064305.

B. Collaborative publications

1. MD Fabian, B Shapiro, **E Rabani**, D Neuhauser and R Baer. Stochastic density functional theory. WIREs Computational Molecular Science 2019, e1412.

2. L Kidon, H Wang, M Thoss and **E Rabani.** "On the memory kernel and the reduced system propagator," *J. Chem. Phys.*, 2018, 149, 104105.

3. J Deng, Y Su, D Liu, **P Yang**, B Liu, and C Liu. "Nanowire Photoelectrochemistry", *Chem. Rev.*, 2019, 119, 9221-9259.

4. MH Oh, MG Cho, DY Chung, I Park, YP Kwon, C Ophus, D Kim, MG Kim, B Jeong, XW Gu, J Jo, JM Yoo, J Hong, S McMains, K Kang, YE Sung, **AP Alivisatos**, and T Hyeon. "Design and Synthesis of Multigrain Nanocrystal via Geometric Misfit Strain", *Nature*, 2020, 577, 359-363.

5. BD Folie, JA Tan, J Huang, PC Sercel, M Delor, M Lai, JL Lyons, N Bernstein, A Efros, **P Yang**, NS Ginsberg. "Effect of Anisotropic Confinement on Electronic Structure and Dynamics

of Band Edge Excitons in Inorganic Perovskite Nanowires", *J. Phys. Chem. A*, 2020, 124, 1867-1876.

6. BH Kim, J Heo, S Kim, CF Reboul, H Chun, D Kang, H Bae, H Hyun, J Lim, H Lee, B Han, T Hyeon, **AP Alivisatos**, P Ercius, H Elmlund, and J Park "Critical Differences in 3D Atomic Structure of Individual Ligand-Protected Nanocrystals in Solution", *Science,* 2020, 368, 60-67.

7. E Shi, B Yuan, SB Shiring, Y Gao, Akriti, Y Guo, C Su, M Lai, **P Yang**, J Kong, BM Savoie, Y Yu, L Dou. "Two-Dimensional Halide Perovskite Lateral Epitaxial Heterostructures", *Nature*, 2020, 580, 614-620.

8. S Toso, D Baranov, D Altamura, F Scattarella, J Dahl, X Wang, S Marras, **AP Alivisatos**, A. Singer, C. Giannini, and L. Manna, "Multilayer Diffraction Reveals That Colloidal Superlattices Approach the Structural Perfection of Single Crystals", *ACS Nano*, 2021, 15, 6243-6256.

Two-Dimensional Chalcogenide Nanomaterials

Yi Cui[1,2], Harold Y. Hwang[1,3]

1. **Stanford Institute for Materials and Energy Sciences, SLAC National Accelerator Laboratory, Menlo Park, CA, USA**
2. **Department of Materials Science and Engineering, Stanford University, Stanford, CA, USA**
3. **Department of Applied Physics, Stanford University, Stanford, CA, USA**

Program Scope

Our long-term vision is a cutting-edge research program developing an exciting class of two-dimensional (2D) nanomaterials including metal chalcogenides (O, S, Se, Te), which can generate high impact on a wide range of DoE BES priorities in materials design and control. Our central focus is understanding and utilizing the modification of the physical and chemical properties of these materials by their heterogeneous ionic environment. Here this ionic environment is realized through synthesis of heterostructured interfaces, electric double layer gating, electrochemical intercalation, deintercalation, and chemical doping. These studies underlie the development of advanced quantum materials, as well as address the fundamental need to understand and improve catalysts, energy storage and conversion materials. Cui and Hwang integrate an expert team to explore an exciting territory of 2D nanomaterials discovery, design, synthesis, and exploration of novel properties.

Recent Progress

In the past 3 years, we have built an integrated effort utilizing the synthesis and fabrication techniques, and materials, benefitting from the expertise and perspectives of chemistry from Cui and physics from Hwang. Major progress was made in three aspects: 1) alkali ion intercalation of 2D materials; 2) the nucleation behavior of polysulfide ions on the surfaces 2D materials to form supercooled sulfur microdroplets; 3) deintercalation of oxygen to form infinite-layer nickelate superconductors.

- We demonstrated, for the first time, an electrochemical intercalation technique where the alkali ions intercalate through the top surface of the 2D materials instead of the edge.[1] This technique not only proves to be more reversible and stable compared to the conventional intercalation method but also expands the understanding of the intercalation process. Electrochemical intercalation of ions into the van der Waals gap of 2D layered materials like molybdenum disulfide (MoS_2) is a promising low-temperature synthesis strategy to tune their physical and chemical properties. It is widely believed that ions prefer intercalation into the van der Waals gap through the edges of the 2D flake, which generally

causes wrinkling and distortion of the flake.[1] In a sealed-edge configuration, we show that intercalation may also take place through the top surface. Density function theory calculations show that this intercalation is enabled by the existence of natural defects in exfoliated MoS_2 flakes. We show fully reversible changes in the optical properties of MoS_2, as well as a drastic reduction in the resistivity upon intercalation of Na^+ ions. These findings pave the way for designing more stable and reliable energy storage devices, as well as highly tunable 2D-material-based optoelectronic and nanoelectronic devices. Furthermore, we demonstrate that few-layer MoS_2 with sealed edges allows intercalation of small alkali metal ions (e.g., Li^+ and Na^+) and rejects large ions (e.g., K^+). The capability of tuning the ion selectivity through subtle electrochemical control implies potential applications in developing advanced devices for ionic sieving, water desalination and ion exchange channels.

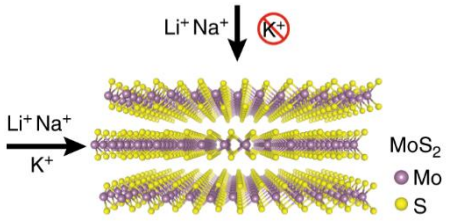

Fig. 1. Schematic representation of Li^+, Na^+, and K^+ intercalation into MoS_2 through top and edge channels.

- We discovered the distinct growth behavior of sulfur on 2D materials surfaces and studied its effect on the areal capacity in lithium sulfur (Li-S) batteries by in situ observation of electrochemical sulfur generation. Li-S batteries are attractive candidates for energy storage in electric vehicles and grid-scale storage due to the high energy density and low-cost.[2] We recently found that sulfur, a solid material in its elementary form S_8, can stay in the supercooled state as liquid sulfur in an electrochemical cell.[3] In this work, we further established that this newly discovered state could have implications for lithium–sulfur batteries. We found that on the basal plane of 2D materials, only liquid sulfur accumulates; by contrast, at the edge sites, liquid sulfur accumulates if the thickness of the two-dimensional material is small, whereas solid sulfur nucleates if the thickness is large (tens of nanometers). Moreover, we found that liquid sulfur provides a much higher areal capacity than the solid in the same charging period. Based on our understanding of the edge-induced sulfur crystallization, we can control the sulfur state (liquid or solid) and achieve much higher areal capacities with the liquid sulfur for use in Li-S batteries. This work correlates the sulfur states with their respective areal capacities, as well as controlling the growth of sulfur on two-dimensional materials, which could provide insights for the design of future Li-S batteries. Additionally, we also achieved the control of electrowetting and merging of sulfur droplets with potentiostatic conditions and the selective design of sulfiphilic/sulfiphobic substrates. The manipulation of liquids with tunable shape and optical functionalities in real time is

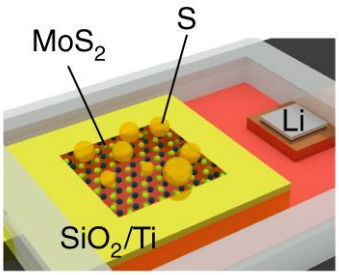

Fig. 2. Electrochemical generation of liquid sulfur on the surface of MoS_2.

important for electroactive flow devices and optoelectronic devices, but remains a great challenge.[4] We employed the electrowetting phenomena to create a microlens based on the liquid sulfur microdroplets with real-time tunable characteristics by changing the shape of the liquid microdroplets in a fast, repeatable, and controlled manner.

- We observed superconductivity in the infinite-layer nickelate. The infinite-layer nickelate (e.g., $LaNiO_2$) is isostructural to infinite-layer copper oxides.[5] The infinite layer nickelates are interesting 2D materials in part due to the fact that they are electronically analogous to the parent compound of cuprate superconductors, with a d^9 electronic configuration for Ni^{1+}.[6] We synthesize these materials by starting from thin films of perovskite $LaNiO_3$, and then using soft chemistry reduction to deintercalate one oxygen from each unit cell. The perovskite substrate gives a template that preserves the single crystalline structure of the reduced nickelate. X-ray scattering and spectroscopy experiments demonstrate that indeed the d^9 electronic configuration is found, but with unusual tendencies to hybridize with the La states rather than the oxygen ligands. By moving to $NdNiO_2$ (increasing the electronic bandwidth), and chemically hole doping the system by Sr substitution, we have discovered superconductivity for the first time in a nickel oxide system. We then have systematically investigated the effects of the growth and reduction parameters on the crystallinity of the resultant superconducting $Nd_{0.8}Sr_{0.2}NiO_2$ films, and identified narrow stability windows in both parameter spaces. To this end, superconducting single-phase and single-crystalline $Nd_{0.8}Sr_{0.2}NiO_2$ epitaxial thin films up to ~ 10 nm have been stabilized and the wide sample-to-sample variation in Tc (superconducting transition temperature) initially reported has been reproducibly narrowed. Recently, we can systematically probe the strain dependence of superconductivity and normal state properties in $Nd_{1-x}Sr_xNiO_2$ by stabilizing this material in substrates with varying lattice constants. We have successfully stabilized $Nd_{0.8}Sr_{0.2}NiO_2$ on three different substrates: $SrTiO_3$, $(LaAlO_3)_{0.3}(Sr_2TaAlO_6)_{0.7}$, and $NdGaO_3$. In contrast with hole-doped cuprates which show enhanced superconductivity as a function of compressive strain, our data suggest that superconductivity is instead suppressed as a function of compressive strain in hole-doped nickelates. Our results suggest that, despite the structural and electronic similarities between the hole-doped cuprates and nickelates, the multi-band nature of the hole-doped nickelates introduces significant differences to this system in comparison with the cuprates.

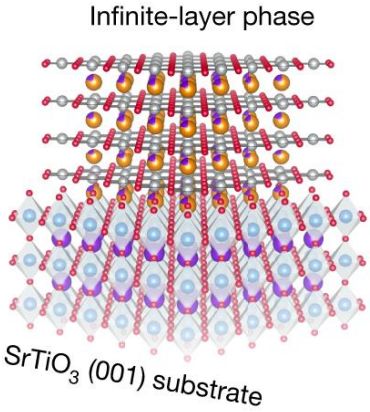

Fig. 3. Schematic crystal structures of $Nd_{0.8}Sr_{0.2}NiO_2$ thin films on the TiO_2-terminated single-crystal $SrTiO_3$ (001) substrate.

Future Plans

We will continue our strong synergy between Cui and Hwang to further investigate the interaction of guest species and layered materials. Our future research plan will follow our current achievements to further study the ionic tuning of 2D chalcogenide nanomaterials.

- We will continue to study the intercalation and deintercalation techniques, besides atoms and ions, we will also focus on the intercalation of organic molecules. The relatively large size of organic molecules can expand the interlayer spacing of 2D materials over 2 times. The change of interlayer distance will strongly modulate the interlayer coupling of 2D materials, which will result in novel behaviors in 2D magnetotransport and 2D thermal transport.
- The superconducting infinite-layer nickelates have shown distinctive strain responses. More growth optimization and stuctural measurements will be conducted to eliminate the extrinsic crystallinity effects and further probe the intrinsic response of this system under epitaxial strain. The opportunities of deintercalation chemistry will be expanded to other transition metal oxides systems.
- Advanced microscopic characterizations (e.g., cryogenic electron microscopy) will be used to characterize the modifications of chalcogenide nanomaterials by the heterogeneous ionic environment to understand the physics and chemistry behind the tuning process.

References

1. F. Xiong, H. Wang, X. Liu, H. Sun, M. Brongersma. E. Pop, Y. Cui, "Li intercalation in MoS_2: in situ observation of its dynamics and tuning optical and electrical properties", *Nano. Lett.*, 15, 6777–6784 (2015).
2. A. Manthiram, Y. Fu, S. H. Chung, C. Zu, Y. S. Su, "Rechargeable lithium–sulfur batteries", *Chem. Rev.*, 114, 23 11751-11787 (2014).
3. N. Liu, G. Zhou, A. Yang, X. Yu, F. Shi, J. Sun, J. Zhang, B. Liu, C.-L. Wu, X. Tao, Y. Sun, Y. Cui, S. Chu, "Direct electrochemical generation of supercooled sulfur microdroplets well below their melting temperature", *Proc. Natl. Acad. Sci. U. S. A.*, 116, 3 765-770 (2019).
4. S.-Y. Teh, R. Lin, L.-H. Hung, A. P. Lee, "Droplet microfluidics", *Lab Chip*, 8, 198–220 (2008).
5. T. Siegrist, S. M. Zahurak, D. W. Murphy, R. S. Roth, "The parent structure of the layered high-temperature superconductors", *Nature* 334, 231-232 (1988).
6. V. I. Anisimov, D. Bukhvalov, T. M. Rice, "Electronic structure of possible nickelate analogs to the cuprates", *Phys. Rev. B* 59, 7901–7906 (1999).

Publications

1. J. Zhang, A. Yang, X. Wu, J. van de Groep, P. Tang, B. Liu, F. Shi, J. Wan, Q. Li, Y. Sun, Z. Lu, G. Zhou, J. Li, S.-C. Zhang, M. L. Brongersma, Y. Cui, "Reversible and

Selective Ion Intercalation through Top Surface of Few-Layer MoS_2", *Nat. Comm.*, 9, 5289 (2018).

2. Z. Y. Chen, A. G. Swartz, H. Yoon, H. Inoue, T. A. Merz, D. Lu, Y. W. Xie, H. T. Yuan, Y. Hikita, S. Raghu, and H. Y. Hwang, "Carrier Density and Disorder Tuned Superconductor-Metal Transition in a Two-Dimensional Electron System," *Nat. Comm.* 9, 4008 (2018).
3. P. Singh, A. G. Swartz, D. Lu, S. S. Hong, K. Lee, K. Nishio, Y. Hikita, and H. Y. Hwang, "Large-Area Crystalline $BaSnO_3$ Membranes with High Electron Mobilities", *ACS Appl. Electron. Mater.*, 1, 1269-1274 (2019).
4. D. Li, K. Lee, B. Y. Wang, M. Osada, S. Crossley, H. R. Lee, Y. Cui, Y. Hikita, and H. Y. Hwang, "Superconductivity in an Infinite-Layer Nickelate", *Nature*, 572, 624-627 (2019).
5. N. Liu, G. Zhou, A. Yang, X. Yu, F. Shi, J. Sun, J. Zhang, B. Liu, C.-L. Wu, X. Tao, Y. Sun, Y. Cui, S. Chu, "Direct electrochemical generation of supercooled sulfur microdroplets well below their melting temperature," *Proc. Natl. Acad. Sci. U. S. A.*, 116, 765 (2019)
6. A. Sood, F. Xiong, S. Chen, R. Cheaito, F. Lian, M. Asheghi, Y. Cui, D. Donadio, K. E. Goodson, E. Pop, "Quasi-Ballistic Thermal Transport Across MoS_2 Thin Films," *Nano Lett.*, 19, 2434 (2019)
7. D. Lu, S. Crossley, R. Xu, Y. Hikita, and H. Y. Hwang, "Freestanding Oxide Ferroelectric Tunnel Junction Memories Transferred onto Silicon," *Nano Lett.*, 19, 3999 (2019).
8. Z. Y. Chen, B. Y. Wang, B. H. Goodge, D. Lu, S. S. Hong, D. F. Li, L. F. Kourkoutis, Y. Hikita, and H. Y. Hwang, "Freestanding Crystalline $YBa_2Cu_3O_{7-x}$ Heterostructure Membranes," *Phys. Rev. Mater.*, 3, 060801 (2019). (Rapid Communications)
9. Y. Li, K. Wang, W. Zhou, Y. Li, R. Vila, W. Huang, H. Wang, G. Chen, G.-H. Wu, Y. Tsao, H. Wang, R. Sinclair, W. Chiu, Y. Cui, "Cryo-EM Structures of Atomic Surfaces and Host-Guest Chemistry in Metal-Organic Frameworks," *Matter*, 1, 1 (2019).
10. H. Wang, Z. Liang, M. Tang, G. Chen, Y. Li, W. Chen, D. Lin, Z. Zhang, G. Zhou, J. Li, Z. Lu, K. Chan, T. Tan, Y. Cui, "Self-Selective Catalyst Synthesis for CO_2 Reduction," *Joule*, 3, 1927 (2019).
11. A. Yang, G. Zhou, C. Su, Y. Wu, A. Pei, C.-L. Wu, R. A. Vila, X. Yu, B. Liu, H. Chen, Y. Chen, D. Chen, Y. Li, H. Y. Hwang, J. Li, S. Chu, Y. Cui, "Electrochemical generation of liquid and solid sulfur on two-dimensional layered materials with distinct areal capacity", *Nat. Nanotechnol.*, 15, 231-237 (2020).
12. G. Zhou, A. Yang, Y. Wang, G. Gao, A. Pei, X. Yu, Y. Zhu, L. Zong, B. Liu, J. Xu, N. Liu, J. Zhang, Y. Li, L.-W. Wang, H. Y. Hwang, M. L. Brongersma, S. Chu, Y. Cui, "Electrotunable liquid sulfur microdroplets", *Nat., Comm.*, 11, 606 (2020).
13. K. Lee, B. H. Goodge, D. Li, M. Osada, B. Y. Wang, Y. Cui, L. F. Kourkoutis, H. Y. Hwang, "Aspects of the Synthesis of Thin Film Superconducting Infinite-Layer Nickelates", *APL Mater.*, 8, 041107 (2020). (Editor's Pick)

14. M. Osada, B. Y. Wang, B. H. Goodge, K. Lee, H. Yoon, K. Sakuma, D. F. Li, M. Miura, L. F. Kourkoutis, and H. Y. Hwang, "A Superconducting Praseodymium Nickelate with Infinite-Layer Structure," *Nano Lett.*, 20, 5735-5740 (2020).
15. M. Hepting, D. Li, C. J. Jia, H. Lu, E. Paris, Y. Tseng, X. Feng, M. Osada, E. Been, Y. Hikita, Y.-D. Chuang, Z. Hussain, K. J. Zhou, A. Nag, M. Garcia-Fernandez, M. Rossi, H. Y. Huang, D. J. Huang, Z. X. Shen, T. Schmitt, H. Y. Hwang, B. Moritz, J. Zaanen, T. P. Devereaux, and W. S. Lee, "Electronic Structure of the Parent Compound of Superconducting Infinite-Layer Nickelates," *Nat. Mater.*, 19, 381-385 (2020).
16. D. Li, B. Y. Wang, K. Lee, S. P. Harvey, M. Osada, B. H. Goodge, L. F. Kourkoutis, and H. Y. Hwang, "Superconducting Dome in $Nd_{1-x}Sr_xNiO_2$ Infinite Layer Films," *Phys. Rev. Lett.*, 125, 027001:1-6 (2020).
17. Phase Diagram of Infinite-Layer Praseodymium Nickelate $Pr_{1-x}Sr_xNiO_2$ Thin Films. M. Osada, B. Y. Wang, K. Lee, D. F. Li, and H. Y. Hwang, *Phys. Rev. Mater.*, 4, 121801 (2020). (Rapid Communications)
18. M. Osada, K. Nishio, K. Lee, M. Colletta, B. H. Goodge, W. J. Kim, L. F. Kourkoutis, H. Y. Hwang, Y. Hikita, "Highly Efficient Surface Charge Transfer in Fe_2TiO_5 Epitaxial Thin Film Photoanodes", *ACS Appl. Energy Mater.*, 4, 3 2098 (2021).
19. Stabilization of $Sr_3Al_2O_6$ Growth Templates for Ex Situ Synthesis of Freestanding Crystalline Oxide Membranes. Li, D. F., Adamo, C., Wang, B. Y., Yoon, H., Chen, Z. Y., Hong, S. S., Lu, D., Cui, Y., Hikita, Y., & Hwang, H. Y. *Nano Lett.*, 21, 10 4454 (2021).
20. K. Lee, R. A. Flores, Y. Liu, B. Y. Wang, M. Bajdich, Y. Hikita, R. Sinclair, M. Bajdich, and H. Y. Hwang, "Epitaxial Stabilization and Oxygen Evolution Reaction Activity of Metastable Columbite Iridium Oxide", *ACS Appl. Energy Mater.*, 4 3074 (2021).
21. B. H. Goodge, D. Li, K. Lee, M. Osada, B. Y. Wang, G. A. Sawatzky, H. Y. Hwang, and L. F. Kourkoutis, "Doping Evolution of the Mott–Hubbard Landscape in Infinite-Layer Nickelates", *Proc. Natl. Acad. Sci. U. S. A.*, 118, e2007683118 (2021).
22. E. Been, W. -S. Lee, H. Y. Hwang, Y. Cui, J. Zaanen, T. Devereaux, B. Moritz, and C. Jia, "Electronic Structure Trends Across the Rare-Earth Series in Superconducting Infinite-Layer Nickelates", *Phys. Rev. X*, 11, 011050 (2021).
23. F. Xiong, E. Yalon, C. J. McClellan, J. Zhang, O. B. Aslan, A. Sood, J. Sun, C. M. Andolina, W. A. Saidi, K. E. Goodson, T. F. Heinz, Y. Cui, E. Pop, "Tuning electrical and interfacial thermal properties of bilayer MoS_2 via electrochemical intercalation", *Nanotechnology*, 32, 265202 (2021).

Rational Synthesis of Superconductors

Mercouri G. Kanatzidis, Materials Science Division, Argonne National Laboratory
Duck Young Chung, Materials Science Division, Argonne National Laboratory

Program Scope

We create and investigate materials that can exhibit competing ground states and tune them in a controlled way using chemical modification. The goals of this FWP are: a) to design, synthesize and tune the electronic and magnetic properties of new low-dimensional materials that display density-wave instabilities and b) to induce superconductivity in these materials through external doping. Our strategies focus on designing a diverse set of two-dimensional materials with well-defined characteristics such as square sheets and complex heterostructures with intergrown layers. For example, the critical superconducting transition temperature (T_c) of $[LaO_{1-x}F_x][FeAs]$ (x = 0.05-0.12) is 26 K, but neither FeAs nor [LaO][FeAs] are superconductors. Similarly, FeSe a homo-layered material with superconducting T_c below 8 K, but upon forming heterolayered structures such as $[Li_{1-x}Fe_xOH][FeSe]$ the T_c increases to 43 K. Moreover, the long-range magnetic ordering in the $[Li_{1-x}Fe_xOH]$ layer makes the $[Li_{1-x}Fe_xOH][FeSe]$ a rare example of a magnetic superconductor. It is also predicted that pnictide(chalcogenide)-cuprate heterostructures such as $Ba_2CuO_2Fe_2As_2$ and $K_2CuO_2Fe_2Se_2$ are predicted to be high T_c superconductors. However, one of the greatest challenges in stabilizing heterolayered compounds is posed by thermodynamics, where they cannot easily form by heating direct mixtures of precursors because of phase separation to simpler and more stable phases. Hence, in order to achieve the goal of rational synthesis of heterolayered superconductors, we have developed a new synthetic process to achieve them.

Recent Progress

- *Rational Synthesis of Heterolayered Structures by New Synthetic Approach*
  - We established formulation of a new tunable flux using the mixed hydroxide/halide which can form oxide metal complexes with the more oxophilic metal ions (harder Lewis acids) while at the same time in-situ form chalcogenide (pnictide) anions that can complex the chalcophilic metal ions (softer Lewis acids). This new approach allows us to find and select the correct synthesis path to the heterolayered class of compounds in a very general way to create new class of compounds.
  - Using the mixed flux of LiOH/LiCl or NaOH/NaI in the method shown in Figure 1, we demonstrate a compelling general approach which achieves for the first time the crystal growth of a large series of heterolayered

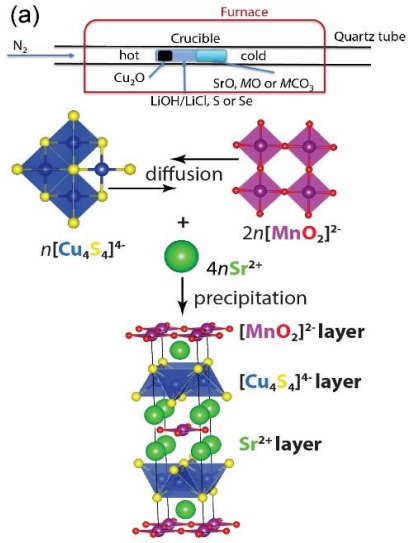

Figure 1. Synthesis of heterolayers using mixed hydroxide/halides

$[AE_xM_yO_z][M'_2Q_2]$ (*AE* = Sr or Ba, *M* = Mn, Fe, Co, Ni, Cu and Zn; *M*'=Cu, Ag, Li) and $[LaO][M'_2Q_2]$.[1-4] Among these, $[Sr_2M_{1-x}O_2][(Cu_{1-y}Li_y)_2Q_2]$ (*M* = Mn and Ni), $[Sr_2Mn_{1-x}O_2][(Cu_{1-y}Li_y)_{2n}S_{n+1}]$ (*n* = 2-4), $[Sr_2Cu_{0.7}O_2][Cu_2Se_2]$, $[Ba_2Co_{0.54}O_2][Cu_2Se_2]$, [LaO][Ag*Q*] (*Q* = Se and Te), $[AE_2M_{1-x}O_2][(Ag_{1-y}Li_y)_2Se_2]$ and $[Ba_3Fe_2O_5][Ag_2Se_2]$ are new compounds. This work was submitted for publication in *Nature*.

- We found correlation of basicity of mixed flux *AOH/A'X* (*A. A'* = alkali metal; *X* = Cl, I) and temperature in controlling solubility of reactants, oxidation states, local geometry, and stability of kinetic phases. For the ternary K-Ni-*Q* (*Q* = S and Se) systems, using mixed LiOH/KOH, in addition to all known ternaries of the K-Ni-S systems, α-$K_2Ni_3S_4$[5] and KNi_2S_2[6] (Figure 2a,b) new ternaries of β-$K_2Ni_3S_4$, KNi_4S_2 (Figure 3c) and $K_4Ni_9S_{11}$ were obtained. Moreover, we discovered a correlation between the oxidation state of Ni (+2, +1.5 and +1-0.75) and the basicity ([KOH]). Increasing [KOH] leads to lower Ni oxidation state in K-Ni-S ternaries. We have also stabilized a new heterolayer compound, $[Sr_2Fe_2O_6][Sr_{0.8}Se_2]$, which features the Ruddlesden-Popper type $Sr_3Fe_2O_7$ and CsCl-type $SrSe_2$ layers. With the kinetic stabilization of these completely new structure types, it shows great potential for our strategy with rational synthesis of heterolayers. Submitted to *JACS*.

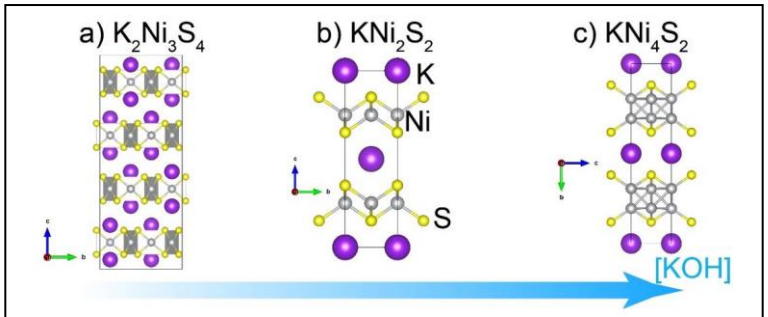

Figure 2. Crystal structures of a) $K_2Ni_3S_4$, b) KNi_2S_2 and c) KNi_4S_2.

- *Exploratory Synthesis of Superconductors and Novel Electronic/Magnetic Materials*
  - We discovered uncommon ferroelectric-like transition from nonpolar semiconducting to polar metallic state induced by pressure in defect antiperovskite $Hg_3Te_2X_2$ (X = Cl, Br) was discovered by X-ray diffraction and theoretical calculations. This study presents evidence of rare but unambiguous ferroelectric-like transition in perovskites promoted by hydrostatic pressure. It points to a new avenue for exploring the interplay between pressure-induced electronic transitions and ferroelectric/multiferroic properties. The work was published in *Nature Communications*.

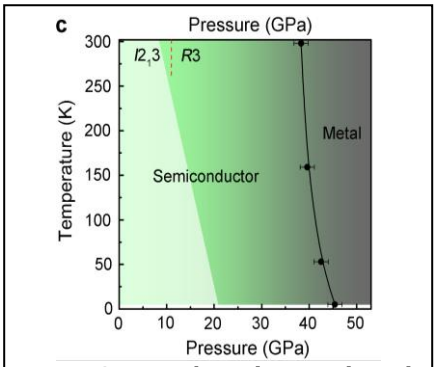

Figure 3. P–T phase diagram derived from resistance measurements. solid line: semiconductor–metal phase boundary.

  - We discovered a wide bandgap semiconductor (E_g ~ 1.89 eV) $Cu_2Br_2Se_6$ with unique Cu/Br helical chain and Se_6 cyclohexane-like ring that emerges superconductivity under pressure (T_c ~ 4.0 – 6.7 K at 21 - 40 GPa) and studied the structure-property relationship.
  - We studied the $RbEuFe_4As_4$ superconductor and Ni doping on Fe site with transport, heat capacity and magnetism indicating a decoupling of the Eu magnetism from superconductivity and essentially no influence of Ni doping on the Eu magnetism.

- We discovered a new polymorph LuRuGe, which exhibits Pauli paramagnetism as the ground state with no local magnetic moments from either the Ru or Lu sites. This polymorph can convert into another centrosymmetric one (TiNiSi-type structure) at high temperatures. We studied electrical transport, magnetization and specific heat measurements on this new phase.
- Studied magnetic flux behavior on the magnetic superconductor $RbEuFe_4As_4$ using magneto-optical imaging and magnetization measurements. The study indicates that the interplay of magnetic susceptibility amplifying the magnetic induction and vortex pinning attenuating the magnetic-flux entry results in a field- and temperature-dependent critical state that emulates a paramagnetic Meissner effect.
- Discovered a new mixed-anion 2D semiconductor $BaFMn_{0.5}Te$ (E_g 1.76 eV) and investigated the formation pathway using in-situ synchrotron X-ray diffraction, characterized crystal, magnetic and electronic structures with transport properties, heat capacity, and revealed antiferromagnetism (AFM) and strong red photoluminescence (PL) associated with its unique $[Mn_{0.5}Te]^-$ sublattice.

▪ *Exploration of New Topological Materials*

- We discovered a new Dirac semimetal candidate Ir_2In_8S and investigated Shubnikov-de Haas oscillations for Fermi surface and its topological behavior.
- We synthesized the subchalcogenides Ir_2In_8Q (Q = Se, Te) and studied commensurately modulated low-temperature phase transitions with re-entrant behavior of supercell structure, suggesting competing structural and electronic interactions dictate the overall structure.

▪ *New Compounds with Novel Properties*

- Superionic conductors (SICs) possess liquid-like ionic diffusivity in the solid state, finding wide applicability from electrolytes in energy storage to materials for thermoelectric energy conversion. During our investigations of looking for superconductivity in two-dimensional KAg_3Se_2 we discovered the materials is Type-I SIC which is defined by a first-order transition to the superionic state and has so far been found exclusively in three-dimensional crystal structures. We demonstrate that the phase transition temperature can be controlled by chemical substitution of the alkali metal ions that comprise the immobile charge-balancing layers. The work was published in *Nature Materials*.
- We studied $CsPbBr_3$ crystal with inelastic neutron scattering, X-ray diffraction and first-principles simulations to track the evolution of the spatial and temporal atomic correlations across the structural transitions of the perovskite crystal. We revealed the two-dimensional sheets of correlated dynamic rotations of $PbBr_6$ octahedra directly modulate the optoelectronic properties. This discovery provides a new route to design materials with partially liquid-like atomic motions in a crystalline lattice for possible applications in energy harvesting. The work was published in *Nature Materials*.

Future Plans

1. Using our new approach for heterolayers utilizing hydroxide/halide flux, we will explore the combination of cuprate layers with insulating layers such as CsCl-type $[SrSe_2]$, $[Cu_2Q_2]$,

[Ag_2Q_2], etc. We will use our knowledge with oxidation state control in the hydroxide flux to control the Cu oxidation state in the cuprate layer and study how it can affect the superconductivity.

2. We will also explore the combinations of CuO_2 or NiO_2 with other superconducting FeSe or FeAs layers. Both CuO_2 and FeSe or FeAs exhibit square-net structures. Therefore, it is possible to form commensurate crystalline structures due to high lattice stability, but such compounds have proven difficult to synthesize using conventional methods. Using our new approach by a slow diffusion process in a flux, we will separate CuO at one end and FeAs, FeSe, or $K_{1-x}Fe_{2-y}Se_2$ at the opposite end of a flux containing boat as shown in Figure 1, which can avoid the oxidation of Fe^{2+}, As^{3-} or Se^{2-} by Cu^{2+} by direct mixing. Similar to co-precipitation of CuO_2 layer and Cu_2Se_2 layer in the synthesis of $Sr_2CuO_2Cu_2Se_2$, when these precursors diffuse to the center of the reaction boat, they can precipitate into the target heterolayered compounds interleaved by either K^+ or Ba^{2+} ions.

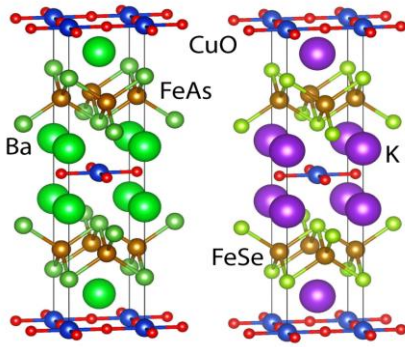

Figure 4. Structural models for the intergrown layers of CuO/FeSe (left) and CuO/FeAs (right).

3. We will also perform isoelectronic P doping for $RbEuFe_4(As_{1-x}P_x)_4$ to tune T_c vs T_N and study interplay of superconductivity and magnetism and of topological surface state by a collaborative work with other programs in Materials Science Division.
4. We will explore new multinary heavy pnictides by new approaches using alkali (A) and alkaline earth (AE) metals and their pnictide fluxes including heavy pnictide (Sb/Bi) and investigate doping effect on normal or superconducting states in new compounds.

References

1. Zhu, W. J., et al. Unusual Layered Transition-Metal Oxysulfides: $Sr_2Cu_2MO_2S_2$ (M = Mn, Zn). *J. Solid State Chem.* **1997**, *130*, 319.
2. Gál, Z. A., et. al. Structural Chemistry and Metamagnetism of an Homologous Series of Layered Manganese Oxysulfides. *J. Amer. Chem. Soc.* **2006**, *128*, 8530.
3. Adamson, P., et. al. Competing Magnetic Structures and the Evolution of Copper Ion/Vacancy Ordering with Composition in the Manganite Oxide Chalcogenides $Sr_2MnO_2Cu_{1.5}(S_{1-x}Se_x)_2$. *Chem. Mater.* **2012**, *24*, 2802.
4. Jin, S., et. al. $Sr_2Mn_3Sb_2O_2$ Type Oxyselenides: Structures, Magnetism, and Electronic Properties of $Sr_2AO_2M_2Se_2$ (A = Co, Mn; M = Cu, Ag). *Inorg. Chem.* **2012**, *51*, 10185.
5. Bronger, W., et. al. Schichtstrukturen ternärer Chalkogenide $A_2M_3X_4$ (A = K, Rb, Cs; M = Ni, Pd, Pt; X = S, Se). *Z. Anorg. Alleg. Chem.* **1991**, *597*, 27.
6. Neilson, J. R., et. al. Density Wave Fluctuations, Heavy Electrons, and Superconductivity in KNi_2S_2. *Phys. Rev. B* **2013**, *87*, 045124.

Publications

1. Alexander J. E. Rettie, Jingxuan Ding, Christos D. Malliakas, Naresh Osti, Duck Young Chung, Raymond Osborn, Olivier Delaire, Stephan Rosenkranz, Mercouri G. Kanatzidis "*Discovery of a Two-Dimensional Type I Superionic Conductor*" *Nature Materials* **2021**, accepted.
2. Jin-Ke Bao, Daniel E. Bugaris, Huihuo Zheng, Duck Young Chung, Mercouri G. Kanatzidis "*A Non-centrosymmetric Polymorph of LuRuGe*" *Inorg. Chem.* **2021**, accepted.
3. Bao, Jin-Ke; Malliakas, Christos; Zhang, Chi; Cai, Songting; Chen, Haijie; Rettie, Alexander; Fisher, Brandon; Chung, Duck Young; Dravid, Vinayak; Kanatzidis, Mercouri "*Quasi-two-dimensional heterostructures $KM_{1-x}Te(LaTe_3)$ (M = Mn, Zn) with charge density waves*" *Chem. Mater.* **2021**, *33*, 2155–2164.
4. Jin-Ke Bao, Daniel E. Bugaris, Huihuo Zheng, Duck Young Chung, Mercouri G. Kanatzidis "*A Non-centrosymmetric Polymorph of LuRuGe*" *Inorg. Chem.* **2021**, accepted.
5. D. Collomb, S. J. Bending, A. E. Koshelev, M. P. Smylie, L. Farrar, J.-K. Bao, D. Y. Chung, M. G. Kanatzidis, W.-K. Kwok, and U. Welp "*Observing the suppression of superconductivity in $RbEuFe_4As_4$ by correlated magnetic fluctuations*" *Phys. Rev. Lett.,* **2021**, *126*, 157001-1-7.
6. Guo, Zhongnan; Sun, Fan; Puggioni, Danilo; Luo, Yubo; Li, Xiaotong; Zhou, Xiuquan; Chung, Duck Young; Cheng, Erjian; Li, Shiyan; Rondinelli, James; Yuan, Wenxia; Kanatzidis, Mercouri "*Local distortions and metal-semiconductor-metal transition in quasi-one-dimensional nanowire compounds $AV_3Q_3O_\delta$ (A=K, Rb, Cs and Q=Se, Te)*" *Chem. Mater.* **2021**, *33*, 2611–2623.
7. T. Lanigan-Atkinsy, X. Hey, M. J. Krogstad, D. M. Pajerowski, D. L. Abernathy, Guangyong NMN Xu, Zhijun Xu, D.-Y. Chung, M. G. Kanatzidis, S. Rosenkranz, R. Osborn, and O. Delaire "*Two-dimensional overdamped Fluctuations of soft perovskite lattice in $CsPbBr_3$*" *Nature Materials* **2021**, 1059.
8. Weizhao Cai, *Jiangang He, Hao Li, Rong Zhang, Dongzhou Zhang, Duck Young Chung, Christopher Wolverton,* Mercouri G. Kanatzidis, Shanti Deemyad "*Pressure-Induced Ferroelectric-Like Transition Creates a Polar Metal in Defect Antiperovskites $Hg_3Te_2X_2$ (X = Cl, Br)" Nature Comm.* **2021**, 12, 1509-1-10.
9. Weihua Ning, Jinke Bao, Yuttapoom Puttisong, Fabrizo Moro, Libor Kobera, Seiya Shimono, Linqin Wang, Fuxiang Ji, Maria Cuartero, Shogo Kawaguchi, Sabina Abbrent, Hiroki Ishibashi, Roland De Marco, Irina A. Bouianova, Gaston A. Crespo, Yoshiki Kubota, Jiri Brus, Duck Young Chung, Licheng Sun, Weimin M. Chen, Mercouri Kanatzidis, Feng Gao *"Magnetizing Lead-Free Halide Double Perovskites" Sci. Adv.* **2020**, 6 : eabb5381-1-8.
10. Nigel Becknell, Pietro P. Lopes, Toru Hatsukade, Xiuquan Zhou, Yuzi Liu, Brandon Fisher, Duck Young Chung, Mercouri G. Kanatzidis, Nenad M. Markovic, Sanja Tepavcevic, Vojislav R. Stamenkovic "*Employing the dynamics of the electrochemical interface at aqueous zinc-ion battery cathode" Adv. Func. Mater.* **2021**,
11. Khoury, Jason; Rettie, Alexander; Robredo, Iñigo; Krogstad, Matthew; Malliakas, Christos; Bergara, Aitor; Vergniory, Maia; Osborn, Raymond; Rosenkranz, Stephan; Chung, Duck Young; Kanatzidis, Mercouri "The subchalcogenides Ir_2In_8Q (Q = S, Se, Te): Dirac semimetal candidates with re-entrant structural modulation" *J. Amer. Chem. Soc.* **2020**, *142*, 6312-6323.
12. Tyler J. Slade, Koushik Pal, Jann A. Grovogui, Trevor P. Bailey, James Male, Jason F. Khoury, Xiuquan Zhou, Duck Young Chung, G. Jeffrey Snyder, Ctirad Uher, Vinayak P. Dravid,

Christopher Wolverton, Mercouri G. Kanatzidis *"Contrasting SnTe–$NaSbTe_2$ and SnTe–$NaBiTe_2$ thermoelectric alloys: high performance facilitated by increased cation vacancies and lattice softening" J. Amer. Chem. Chem.* **2020**, *142*, 12524-12535.

13. V. K. Vlasko-Vlasov, U. Welp, A. E. Koshelev, M. Smylie, J.-K. Bao, D. Y. Chung, M. G. Kanatzidis, and W.-K. Kwok "*Cooperative response of magnetism and superconductivity in the magnetic superconductor $RbEuFe_4As_4$*" *Phy. Rev. B* **2020**, *101*, 1045040-1-14.
14. K. Willa, M. P. Smylie, Y. Simsek, J.-K. Bao, D. Y. Chung, M. Kanatzidis, W.- K. Kwok, and U. Welp *"Magnetic and superconducting anisotropy in Ni-doped $RbEuFe_4As_4$ single crystals" Phy. Rev. B* **2020**, *101*, 064508-1-10.
15. Jie Chen, Hai L. Feng, Yoshitaka Matsushita, Alexei A. Belik, Yoshihiro Tsujimoto, Yoshio Katsuya, Masahiko Tanaka, Duck Young Chung, Kazunari Yamaura "*Study of polycrystalline bulk Sr_3OsO_6 double-perovskite insulator: comparison with 1000 K ferromagnetic epitaxial films*" *Inorg. Chem*. **2020**, *59*, 4049-4057.
16. D. Koumoulis, L. Fang, D. Y. Chung, M.G. Kanatzidis, L.-S. Bouchard "*Evolution of non-trivial Fermi Surface Features in the Band Structures of Homologous Members $Pb_5Bi_6Se_{14}$ and $Pb_5Bi_{12}Se_{23}$*" *Phy. Rev. B* **2020**, *101*, 115309-1-11.
17. Weizhao Cai, Wenwen Lin, Yan Yan, Katerina P. Hilleke, Jared Coles, Jin-Ke Bao, Jingui Xu, Dongzhou Zhang, Duck Young Chung, Mercouri G. Kanatzidis, Eva Zurek, Shanti Deemyad "*Pressure-induced superconductivity in the wide band gap semiconductor $Cu_2Br_2Se_6$ with a robust framework*" *Chem. Mater.* **2020**, *32*, 6237-6246.
18. Yang-Yang Lyu, Fei Han, Zhi-Li Xiao, Jing Xu, Yong-Lei Wang, Hua-Bing Wang, Jin-Ke Bao, Duck Young Chung, Mingda Li, Ivar Martin, Ulrich Welp, Mercouri G. Kanatzidis, and Wai-Kwong Kwok, "Magnetization-governed magnetoresistance anisotropy in the topological semimetal CeBi," Physical Review B **2019**, *100* (18), 180407.
19. Jason F. Khoury, Alexander J. E. Rettie, Mojammel A. Khan, Nirmal J. Ghimire, Iñigo Robredo, Jonathan E. Pfluger, Matthew J. Krogstad, Raymond Osborn, Stephan Rosenkranz, Chris Wolverton, Aitor Bergara, Jidong S. Jiang, Maia G. Vergniory, John F. Mitchell, Duck Young Chung, and Mercouri G .Kanatzidis "A new three-dimensional subsulfide Ir_2In_8S with Dirac semimetal behavior" *J. Amer. Chem. Soc.* **2019**, *141* (48), 19130-19137.
20. Haijie Chen, Rebecca McClain, Jiangang He, Chi Zhang, Jack N. Olding, Roberto dos Reis, Jin-Ke Bao, Ido Hadar, Ioannis Spanopoulos, Christos D. Malliakas, Yihui He, Duck Young Chung, Wai-Kwong Kwok, Emily A. Weiss, Vinayak P. Dravid, Christopher Wolverton, and Mercouri G. Kanatzidis, "Antiferromagnetic semiconductor $BaFMn_{0.5}Te$ with unique Mn ordering and red photoluminescence," *J. Amer. Chem. Soc.* **2019***, 141* (43), 17421–17430.
21. Weizhao Cai, Wenwen Lin, Long-Hua Li, Christos D. Malliakas, Rong Zhang, Matthew, Groesbeck, Jin-Ke Bao, Dongzhou Zhang, Eran Sterer, Mercouri G. Kanatzidis, and Shanti Deemyad "*Pressure-induced Superconductivity and Flattened Se_6 Rings in the Wide Bandgap Semiconductor $Cu_2I_2Se_6$*" *J. Amer. Chem. Soc.* **2019**, *141*, 15174-15182.
22. Hee Joon Jung, Jin-Ke Bao, Duck Young Chung, Mercouri Kanatzidis, Vinayak Dravid "*Unconventional Defects in a Quasi-One-Dimension KMn_6Bi_5*" *Nano Lett.* **2019,** *19,* 7476-7486.
23. Fei Han, Yongping Du, Christos D. Malliakas, Mihai Sturza, Jin-Ke Bao, Duck Young Chung, Xiangang Wan, and Mercouri G. Kanatzidis "*Enormous Electron-Electron Scattering in the Filled-Cage Cubic Compound $Ba_{10}Ti_{24}Bi_{39}$*" *Phys. Rev. M* **2019**, *3,* 105001-1-8.

24. A. E. Koshelev, K. Willa, M. Smylie, R. Willa, J.-K. Bao, D. Y. Chung, M. G. Kanatzidis, W.-K. Kwok, and U. Welp "*Melting of vortex lattice in magnetic superconductor* $RbEuFe_4As_4$" *Phy. Rev. B* **2019**, *100*, 094518-1-8.
25. M. P. Smylie, A. E. Koshelev, K. Willa, W.-K. Kwok, J.-K. Bao, D. Y. Chung, M. G. Kanatzidis, J. Singleton, F. F. Balakirev, P. Niraula, E. Bokari, A. Kayani, and U. Welp *"Anisotropic upper critical field of pristine and proton-irradiated single crystals of the magnetically ordered superconductor* $RbEuFe_4As_4$" *Phys. Rev. B* **2019**, *100*, 054507-1-10.
26. Rettie, Alexander; Malliakas, Christos; Botana, Antia; Bao, Jin-Ke; Chung, Duck Young; Kanatzidis, Mercouri "*KCu_7P_3: A Two-Dimensional Noncentrosymmetric Metallic Pnictide*" *Inorg. Chem.* **2019**, 58, 10201−10208.
27. Jing Xu, Fengcheng Wu, Jinke Bao, Fei Han, Zhi-Li Xiao, Ivar Martin, Yang-Yang Lyu, Yong-Lei Wang, Duck Young Chung, Mingda Li, Wei Zhang, John E. Pearson, Jidong S. Jiang, Mercouri G. Kanatzidis, and Wai-Kwong Kwok *"Orbital Flop in Rare Earth Monopnictide CeSb" (*arXiv preprint arXiv:1905.08682*) Nature Comm.* **2019**, 10, 2875-1-8.
28. K. Willa, R. Willa, J.-K. Bao, A. E. Koshelev, D. Y. Chung, M. Kanatzidis, W.- K. Kwok, and U. Welp *"Strongly fluctuating moments in the high-temperature magnetic superconductor* $RbEuFe_4As_4$*"* (arXiv:1811.00480v1, 1 Nov 2018) *Phys. Rev. B.* **2019**, 99, 180502-1-7.
29. Haijie Chen, Jiangang He, Christos D. Malliakas, Constantinos C. Stoumpos, Alexander J. E. Rettie, Jin-Ke Bao, Duck Young Chung, Wai-Kwong Kwok, Christopher Wolverton, and Mercouri G. Kanatzidis "*A Natural 2D Heterostructure* $[Pb_{3.1}Sb_{0.9}S_4][Au_xTe_{2-x}]$ *with Large Transverse Non-saturating Negative Magnetoresistance and High Electron Mobility*" *J. Amer. Chem. Soc.* **2019**, *141*, 7544–7553. (April 11, 2019) (**DOI:** 10.1021/jacs.9b02599)
30. Li Xiang, Sergey L. Bud'ko, Jin-Ke Bao, Duck Young Chung, Mercouri G. Kanatzidis, and Paul C. Canfield *"Pressure-temperature phase diagram of* $EuRbFe_4As_4$ *superconductor" Phys. Rev. B.* **2019**, 99, 144509-1-6.
31. Riley Hanus, Matthias Agne, Alexander J. E. Rettie, Zhiwei Chen, Gangjian Tan, Duck Young Chung, Mercouri G. Kanatzidis, Yanzhong Pei, Peter W. Voorhees, and G. Jeff Snyder "*Lattice softening significantly reduces thermal conductivity and leads to high thermoelectric efficiency PbTe*" *Adv. Mat.* **2019,** 1900108-1-10.
32. V. K. Vlasko-Vlasov, A. E. Koshelev, M. Smylie, J.-K. Bao, D. Y. Chung, M. Kanatzidis, U. Welp, and W.- K. Kwok *"Self-induced Magnetic Flux Structure in the Magnetic Superconductor* $RbEuFe_4As_4$*" Phys. Rev. B.* **2019**, *99*, 134503-1-6.
33. Jin-Ke Bao, Daniel E. Bugaris, Kristin Willa, Ulrich Welp, Duck Young Chung, Mercouri G. Kanatzidis *"Superconductivity in* $Y_7Ru_4InGe_{12}$*" Phys. Rev. M* **2019**, *3*, 024802-1-9.
34. Haijie Chen, João N. B. Rodrigues, Alexander J. E. Rettie, Tze-Bin Song, Daniel G. Chica, Xianli Su, Jin-Ke Bao, Duck Young Chung, Lucas K. Wagner, Wai-Kwong Kwok, and Mercouri G. Kanatzidis *"High Hole Mobility and Nonsaturating Giant Magnetoresistance in the New 2D Metal* $NaCu_4Se_4$ *Synthesized by a Unique Pathway" J. Amer. Chem. Soc.* **2019**, *141*, 635–642
35. Matthias T. Agne, Kazuki Imasato, Shashwat Anand, Kathleen Lee, Sabah Bux, Alex Zevalkink, Alexander Rettie, Duck Young Chung, Mercouri G. Kanatzidis, G. Jeffrey Snyder, "*Heat capacity of* Mg_3Sb_2, Mg_3Bi_2 *and their alloys at high temperature*" *Materials Today Physics* **2018**, 6, 83-88. (Nov. 3, 2018)

36. Y. Yang, H. Yao, Z. Yu, S.M. Islam, H. He, M. Yuan, Y. Yue, K. Xu, W. Hao, G. Sun, H. Li, S. Ma, P Zapol, M G Kanatzidis "*Hierarchical Nanoassembly of $MoS_2/Co_9S_8/Ni_3S_2/Ni$ as a Highly Efficient Electrocatalyst for Overall Water Splitting in a Wide pH Range*" *J. Am. Chem. Soc.*, **2019**, *141*, 10417-10430.
37. M. P. Smylie, K. Willa, J.-K. Bao, K. Ryan, Z. Islam, H. Claus, Y. Simsek, Z. Diao, A. Rydh, A. E. Koshelev, W.-K. Kwok, D. Y. Chung, M. G. Kanatzidis, and U. Welp "*Anisotropic superconductivity and magnetism in single-crystal $RbEuFe_4As_4$*" *Phys. Rev. B* **2018**, 98, 104503-1-10.
38. Rettie, Alexander; Malliakas, Christos; Botana, Antia; Hodges, James; Han, Fei; Huang, Ruiyun; Chung, Duck Young; Kanatzidis, Mercouri "*Ag_2Se to KAg_3Se_2: Suppressing order-disorder transitions via reduced dimensionality*" *J. Am. Chem. Soc.* **2018**, 140, 9193−9202.
39. Chen, Haijie; Claus, Helmut; Bao, Jin-Ke; Stoumpos, Constantinos; Chung, Duck Young; Kwok, Wai-Kwong; Kanatzidis, Mercouri *"Superconductivity and Structural Conversion with Na and K doping of the Narrow-gap Semiconductor $CsBi_4Te_6$" Chem. Mater.* **2018**, 30, 5293−5304.
40. Saiful M. Islam, Lintao Peng, Li Zeng, Christos D. Malliakas, Duck Young Chung, *D. Bruce Buchholz*, Thomas Chasapis, Ran Li, Konstantinos Chrissafis, *Julia* E. *Medvedeva*, G*iancarlo G. Trimarchi*, Mathew Grayson, Tobin J. Marks, Michael J. Bedzyk, Robert P. H. Chang, Vinayak P. Dravid, Mercouri G. Kanatzidis "*Multi-States and Polymorphism in Phase Change $K_2Sb_8Se_{13}$*" *J. Amer. Chem. Soc.* **2018**, 140, 9261−9268.

FWP PRJ1000089 Precision synthesis and assembly of ionic and liquid crystalline polymers

Paul Nealey (PI), Materials Science Division, Argonne National Laboratory
Juan de Pablo (co-PI), Materials Science Division, Argonne National Laboratory
Matthew Tirrell (co-PI), Materials Science Division, Argonne National Laboratory

Program Scope

Molecular self-assembly is arguably the most promising strategy for imparting structure and function to materials at the molecular, meso-, and macro-scale and for developing high-performance soft and biomolecular materials for energy related applications. The challenge is to encode information into the building blocks of materials systems through precision synthesis, thereby introducing specific and controllable intra- and intermolecular interactions to drive assembly with hierarchical structure. A key aspect of our functional self-assembling materials design is avoiding or overcoming undesirable states through pathway engineering. Defects and disorder can be mitigated or controlled, for example, by relying on external fields or templates to direct assembly (in conjunction with self-assembly), leading to a better understanding of fundamental behavior. We note that the basic tenets of molecular self- assembly and directed self-assembly are derived from biology, but that synthetic organic material scientists have not yet systematically deployed the full range of molecular interactions used in biology to create functional soft materials, nor are they limited to the toolsets of biology resulting from evolution. Our activities are organized into three interrelated thrusts of increasing complexity, from the self-assembly of sequence-specific homopolymers in solution in Thrust 1: "Physics and materials science of hetero-charged polymers from A to Z (Polyampholytes to Polyzwitterions)," to the directed self-assembly and intrinsic ion-conducting properties of (A-block-(B-random-C) architectures in Thrust 2: "Fundamental investigation of physical and electrochemical properties of block copolymer electrolytes," to the most complex materials incorporating liquid crystallinity and charge in fully three-dimensional assemblies in Thrust 3: "Directed self-assembly of blue phase liquid crystals- fundamentals and functionality." The themes that connect our activities include manipulating sequence, charges, and liquid crystallinity to control structure and achieve function, and cross-cutting synthetic strategies, characterization techniques, and theoretical and computational methods.

Recent Progress

Physics and materials science of hetero-charged polymers. Work on hetero-charged polymers has concentrated on expanding the range of zwitterionic polymers that can be studied, with the ultimate goal of determining quantitatively how this class of polymers interacts with water, which is likely the key to their unique properties of biocompatibility and anti-biofouling. We are specifically exploring polyether backbones, incorporating poly(allyl glycidyl ether) (PAGE), which give us a pendant side chain that can be

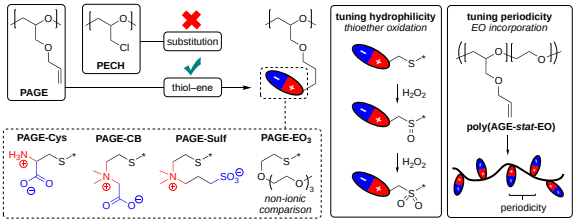

Figure 1. High throughput synthesis of a library of zwitterionic polymers.

functionalized in a variety of ways (see Figure 1). These polymers, and other zwitterionic polymers, can be made in soluble or grafted brush form, the latter providing a unique experimental platform to examine the conformational aspects of these polymers under different solution conditions.[1]

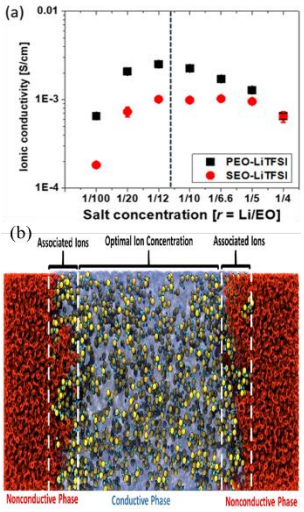

Figure 2. (a) Salt concentration dependence of Li^+ conductivity in PEO and SEO at 100 C; (b) Li^+ distribution in SEO at r = 0.2.

Ion Transport Behavior in Ethylene Oxide (EO)-Based Block Copolymer Electrolytes (BCEs). Many fundamental aspects of the ionic transport behavior in salt-blended BCEs are still not fully understood. Recent experiments have shown differences on the dependence of ionic conductivity on salt concentration between polystyrene-*b*-poly(ethylene oxide) (SEO)-LiTFSI BCEs and PEO-LiTFSI homopolymers, but no clear description of the actual changes in terms of ionic solvation properties had been given. Through experimental and simulation methods, we showed that these differences can be explained by changes in ionic solvation, association, and distribution at the molecular level. Comparison of conductivities as function of r = [Li]/[EO] showed similar behavior for both systems up to the maximum in conductivity at a concentration of r = 1/12, where about half of the available solvation sites in the system are filled (see Figure 2a). Above this regime, the conductivity of the homopolymer drops while conductivity of the BCEs remains constant up to r = 1/4. Vibrational spectroscopy measurements and atomistic MD simulations showed that in the second regime, no additional EO units in BCEs participate in cation coordination but instead clusters or partial clusters of ions segregate to the interfacial mixing layer, keeping the solvated ion concentration close to the optimal value for maximum conductivity in the conducting BCE domains as shown in Figure 2b.[2]

Ion Transport Behavior in Ethylene Oxide-Based Side-chain Polymer Electrolytes. Incorporation of EO side-chain units to polymers is a common strategy to impart and improve – through lowering of the glass transition temperature (T_g) – their ionic conductivity, but low T_g alone is not necessarily a good predictor of this property. We synthesized a series of EO side-chain polymers and used impedance and vibrational spectroscopies, as well as atomistic MD simulations to understand how chain architecture, polymer composition and side-chain length affect ion solvation, ionic conductivity and segmental dynamics of these electrolytes at the molecular level. We observed that the ionic conductivity varies by an order of magnitude in poly[(oligo(ethylene oxide)) methyl ether methacrylate] (POEM) materials of different side-chain lengths, and that this effect is not well explained by differences in T_g or ionic dissociation (see Figure

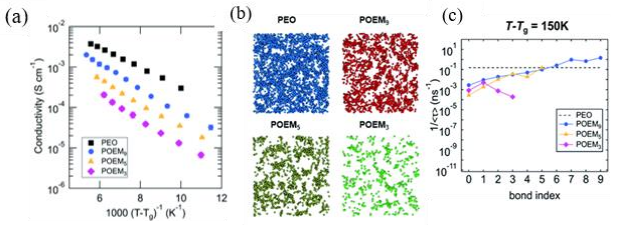

Figure 3. (a) Experimental conductivity corrected by T_g; (b) visualization of solvation site network in PEO and $POEM_x$ from MD simulations; (c) inverse mean relaxation time ($1/\langle\tau\rangle$) of bonds along polymer chains. $1/\langle\tau\rangle$ serves here as an indicator of local segmental.

3a). By introducing solvation site edge density, solvation site connectivity and local relaxation times of EO segments as additional metrics to the analysis, we were able to fully capture the transport behavior in side-chain polyethers (see Figure 3b and 3c), and most importantly, to identify local segmental mobility of EO side chains to be the most critical parameter in determining ion conductivity rather than overall ether oxygen content.[3,4]

Correlation Length in the Directed Self-Assembly of Blue Phase Liquid Crystals (BPLCs). The correlation length dictates the length-scale over which templated order can be maintained. Lithographically defined chemical patterns with alternating homeotropic and planar regions, and with pitches equal to the blue-phase unit cell size, can be used to nucleate and grow single crystals of BPLCs. To determine the correlation length, we patterned alternating regions of chemical patterns to direct the assembly of BPLCs and unpatterned interspatial regions with separation distances from 2 to 20 μm. As shown in Figure 4, if the distance between patterned and unpatterned regions was shorter than the correlation length, single BPLCs extended over both the templating and non-templating regions, whereas for distances greater than the correlation length, a polycrystalline morphology resulted. In a separate set of experiments, the correlation length was determined from the minimum size of the patterned region to observe directed self-assembly. Both sets of experiments indicate the correlation length to be ~10 μm. The experimentally observed correlation length is consistent with our theoretical estimate derived from continuum free energy simulations. Our work demonstrates that blue-phases can serve as model systems to test theories of nucleation and establishes a new strategy to maximize the size of blue-phase single crystals.[5]

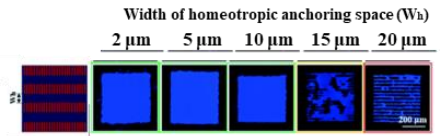

Figure 4. Directed self-assembly of BPLC on chemical patterns was used to extract a correlation length.

Active Liquid Crystals. Our efforts about active liquid crystals have established that topological defects can be confined by introducing gradients of activity. In particular, we have studied the dynamical behavior of two defects confined by a sharp gradient of activity that separates an active circular region and a surrounding passive nematic material. Using continuum simulations, we have explained how the interplay between energy injection into the system, hydrodynamic interactions, and frictional forces governs the dynamics of topological self-propelling defects. Our findings have been rationalized in terms of a phase diagram for the dynamical response of defects in terms of activity and frictional damping strength. Different regions of the underlying phase diagram correspond to distinct dynamical modes, namely immobile defects, steady rotation of defects, bouncing defects, bouncing-cruising defects, dancing defects, and multiple defects with irregular dynamics. These dynamic states raise the prospect of generating synchronized defect arrays for microfluidic applications.[6]

Future Plans

For synthesis and self-assembly of heterocharged polymers, our efforts in the next year will produce systematic variations in polyzwitterionic structures leading to a database of information

on polymer configurational properties in different solution conditions that can be mined to ascertain the dominant, controlling, structural features of their hydration and interactions with water. Tools to be applied are SAXS, light scattering, IR spectroscopy, and surface forces measurement. For ion conducting BCEs, we will: 1) elucidate the role that intermixing of conducting and nonconducting components plays on ionic mobility by comparing the ionic conductivity of polymer blends and block copolymers of differing interaction strength; 2) extend to side-chain polyether-based BCE our previous hypothesis on χ being the main factor dictating the ionic conductivity rather than T_g differences at the domain interface; 3) understand the ion transport mechanism in polyether-polycarbonate copolymers, where multiple solvation site forming moieties may compete. In our research on 3D liquid crystals, we will: 1) use single crystalline blue phase gels to prepare isoporous membranes by washing out the non-polymerizable mesogens; 2) render the assemblies conductive by refilling washed out blue-phases gels with electrolytes to probe the influence of lattice orientation and grain boundaries on ion-transport; and 3) use sequential infiltration synthesis on washed out gels to prepare inorganic membranes templated by the disclination network of blue-phases. In our inter FWP research with the Snezhko group active liquid crystal design, we will seek to validate the predictions of our active liquid crystal design simulations in experiments. An important new direction will be to combine and integrate different active region designs, with the goal of creating active systems that can perform logic operations.

References

1. Dinic, J.; Marciel, A. B.; **Tirrell, M. V.** Polyampholyte Physics: Liquid-Liquid Phase Separation and Biological Condensates. *Curr. Opin. Colloid Interface Sci.* **2021**, 101457.
2. Sharon, D.; Bennington, P.; Webb, M. A.; Deng, C.; **de Pablo, J. J.**; Patel, S. N.; **Nealey, P. F.** Molecular Level Differences in Ionic Solvation and Transport Behavior in Ethylene Oxide-Based Homopolymer and Block Copolymer Electrolytes. *J. Am. Chem. Soc.* **2021**, *143*, 3180–3190.
3. Deng, C.; Webb, M. A.; Bennington, P.; Sharon, D.; **Nealey, P. F.**; Patel, S. N.; **de Pablo, J. J.** Role of Molecular Architecture on Ion Transport in Ethylene Oxide-Based Polymer Electrolytes. *Macromolecules* **2021**, *54*, 2266–2276.
4. Bennington, P.; Deng, C.; Sharon, D.; Webb, M. A.; **de Pablo, J. J.**; **Nealey, P. F.**; Patel, S. N. Role of Solvation Site Segmental Dynamics on Ion Transport in Ethylene-Oxide Based Side-Chain Polymer Electrolytes. *J. Mater. Chem. A* **2021**, *9*, 9937–9951.
5. Li, X.; Martínez-González, J. A.; Guzmán, O.; Ma, X.; Park, K.; Zhou, C.; Kambe, Y.; Jin, H. M.; Dolan, J. A.; **Nealey, P. F.**; **de Pablo, J. J.** Sculpted Grain Boundaries in Soft Crystals. *Science Advances* **2019**, *5*, eaax9112
6. Mozaffari, A.; Zhang, R.; Atzin, N.; **de Pablo, J. J.** Defect Spirograph: Dynamical Behavior of Defects in Spatially Patterned Active Nematics. *Phys. Rev. Lett.* **2021**, *126*, 227801.

Publications (Reverse chronological order since October 1, 2018)

Primary

1. Zhang, R.; Mozaffari, A.; **de Pablo, J. J.** Autonomous Materials Systems from Active Liquid Crystals. *Nature Reviews Materials* **2021**, 1–17. https://doi.org/10.1038/s41578-020-00272-x.
2. Sharon, D.; Bennington, P.; Webb, M. A.; Deng, C.; **de Pablo, J. J.**; Patel, S. N.; **Nealey, P. F.** Molecular Level Differences in Ionic Solvation and Transport Behavior in Ethylene Oxide-Based Homopolymer and Block Copolymer Electrolytes. *J. Am. Chem. Soc.* **2021**, *143*, 3180–3190. https://doi.org/10.1021/jacs.0c12538.
3. Rumyantsev, A. M.; Jackson, N. E.; Johner, A.; **de Pablo, J. J.** Scaling Theory of Neutral Sequence-Specific Polyampholytes. *Macromolecules* **2021**, *54*, 3232–3246. https://doi.org/10.1021/acs.macromol.0c02515.
4. Rumyantsev, A. M.; Jackson, N. E.; **de Pablo, J. J.** Polyelectrolyte Complex Coacervates: Recent Developments and New Frontiers. *Annu. Rev. Condens. Matter Phys.* **2021**, *12*, 155–176. https://doi.org/10.1146/annurev-conmatphys-042020-113457.
5. Mozaffari, A.; Zhang, R.; Atzin, N.; **de Pablo, J. J.** Defect Spirograph: Dynamical Behavior of Defects in Spatially Patterned Active Nematics. *Phys. Rev. Lett.* **2021**, *126*, 227801. https://doi.org/10.1103/PhysRevLett.126.227801.
6. Huang, H.-H.; Ma, Z.; Strzalka, J.; Ren, Y.; Lin, K.-F.; Wang, L.; Zhou, H.; Jiang, Z.; Chen, W. Mild Water Intake Orients Crystal Formation Imparting High Tolerance on Unencapsulated Halide Perovskite Solar Cells. *Cell Reports Physical Science* **2021**, *2*, 100395. https://doi.org/10.1016/j.xcrp.2021.100395.
7. Dolan, J. A.; Cai, H.; Delalande, L.; Li, X.; Martinson, A. B. F.; **de Pablo, J. J.**; López, D.; Nealey, P. F. Broadband Liquid Crystal Tunable Metasurfaces in the Visible: Liquid Crystal Inhomogeneities Across the Metasurface Parameter Space. *ACS Photonics* **2021**, *8*, 567–575. https://doi.org/10.1021/acsphotonics.0c01599.
8. Dinic, J.; Marciel, A. B.; **Tirrell, M. V.** Polyampholyte Physics: Liquid-Liquid Phase Separation and Biological Condensates. *Current Opinion in Colloid & Interface Science* **2021**, 101457. https://doi.org/10.1016/j.cocis.2021.101457.
9. Deng, C.; Webb, M. A.; Bennington, P.; Sharon, D.; **Nealey, P. F.**; Patel, S. N.; **de Pablo, J. J.** Role of Molecular Architecture on Ion Transport in Ethylene Oxide-Based Polymer Electrolytes. *Macromolecules* **2021**, *54*, 2266–2276. https://doi.org/10.1021/acs.macromol.0c02424.
10. Cohen, A. E.; Jackson, N. E.; **de Pablo, J. J.** Anisotropic Coarse-Grained Model for Conjugated Polymers: Investigations into Solution Morphologies. *Macromolecules* **2021**, *54*, 3780–3789. https://doi.org/10.1021/acs.macromol.1c00302.
11. Bennington, P.; Deng, C.; Sharon, D.; Webb, M. A.; **de Pablo, J. J.**; **Nealey, P. F.**; Patel, S. N. Role of Solvation Site Segmental Dynamics on Ion Transport in Ethylene-Oxide Based Side-Chain Polymer Electrolytes. *J. Mater. Chem. A* **2021**, *9*, 9937–9951. https://doi.org/10.1039/D1TA00899D.
12. Webb, M. A.; Jackson, N. E.; Gil, P. S.; **de Pablo, J. J.** Targeted Sequence Design within the Coarse-Grained Polymer Genome. *Sci. Adv.* **2020**, *6*, eabc6216. https://doi.org/10.1126/sciadv.abc6216.

13. Bezik, C. T.; **de Pablo, J. J.** Formation, Stability, and Annihilation of the Stitched Morphology in Block Copolymer Thin Films. *Macromolecules* **2020**, *53*, 10446–10456. https://doi.org/10.1021/acs.macromol.0c01777.
14. Yu, J.; Mao, J.; Nagao, M.; Bu, W.; Lin, B.; Hong, K.; Jiang, Z.; Liu, Y.; Qian, S.; **Tirrell, M.**; Chen, W. Structure and Dynamics of Lipid Membranes Interacting with Antivirulence End-Phosphorylated Polyethylene Glycol Block Copolymers. *Soft Matter* **2020**, *16*, 983–989. https://doi.org/10.1039/C9SM01642B.
15. Yu, B.; Rauscher, P. M.; Jackson, N. E.; Rumyantsev, A. M.; **de Pablo, J. J.** Crossover from Rouse to Reptation Dynamics in Salt-Free Polyelectrolyte Complex Coacervates. *ACS Macro Lett.* **2020**, *9*, 1318–1324. https://doi.org/10.1021/acsmacrolett.0c00522.
16. Sharon, D.; Bennington, P.; Patel, S. N.; **Nealey, P. F.** Stabilizing Dendritic Electrodeposition by Limiting Spatial Dimensions in Nanostructured Electrolytes. *ACS Energy Lett.* **2020**, *5*, 2889–2896. https://doi.org/10.1021/acsenergylett.0c01543.
17. Sharon, D.; Bennington, P.; Dolejsi, M.; Webb, M. A.; Dong, B. X.; **de Pablo, J. J.**; **Nealey, P. F.;** Patel, S. N. Intrinsic Ion Transport Properties of Block Copolymer Electrolytes. *ACS Nano* **2020**, *14*, 8902–8914. https://doi.org/10.1021/acsnano.0c03713.
18. Sadati, M.; Martinez-Gonzalez, J. A.; Zhou, Y.; Qazvini, N. T.; Kurtenbach, K.; Li, X.; Bukusoglu, E.; Zhang, R.; Abbott, N. L.; Hernandez-Ortiz, J. P.; **de Pablo, J. J.** Prolate and Oblate Chiral Liquid Crystal Spheroids. *Science Advances* **2020**, *6*, eaba6728. https://doi.org/10.1126/sciadv.aba6728.
19. Rumyantsev, A. M.; **de Pablo, J. J.** Microphase Separation in Polyelectrolyte Blends: Weak Segregation Theory and Relation to Nuclear "Pasta." *Macromolecules* **2020**, *53*, 1281–1292. https://doi.org/10.1021/acs.macromol.9b02466.
20. Ren, J.; Segal-Peretz, T.; Zhou, C.; Craig, G. S. W.; **Nealey, P. F.** Three-Dimensional Superlattice Engineering with Block Copolymer Epitaxy. *Science Advances* **2020**, *6*, eaaz0002. https://doi.org/10.1126/sciadv.aaz0002.
21. Rauscher, P. M.; Rowan, S. J.; **de Pablo, J. J.** Hydrodynamic Interactions in Topologically Linked Ring Polymers. *Phys. Rev. E* **2020**, *102*, 032502. https://doi.org/10.1103/PhysRevE.102.032502.
22. Qiao, Y.; Zhou, H.; Jiang, Z.; He, Q.; Gan, S.; Wang, H.; Wen, S.; **de Pablo, J. J.**; Liu, Y.; **Tirrell, M. V.**; Chen, W. An in Situ Shearing X-Ray Measurement System for Exploring Structures and Dynamics at the Solid–Liquid Interface. *Review of Scientific Instruments* **2020**, *91*, 013908. https://doi.org/10.1063/1.5129819.
23. Palacio-Betancur, V.; Armas-Pérez, J. C.; Villada-Gil, S.; Abbott, N. L.; Hernández-Ortiz, J. P.; **de Pablo, J. J.** Cuboidal Liquid Crystal Phases under Multiaxial Geometrical Frustration. *Soft Matter* **2020**, *16*, 870–880. https://doi.org/10.1039/C9SM02021G.
24. Menéndez, C. A.; Byléhn, F.; Perez-Lemus, G. R.; Alvarado, W.; **de Pablo, J. J.** Molecular Characterization of Ebselen Binding Activity to SARS-CoV-2 Main Protease. *Science Advances* **2020**, *6*, eabd0345. https://doi.org/10.1126/sciadv.abd0345.
25. Jin, H. M.; Li, X.; Dolan, J. A.; Kline, R. J.; Martínez-González, J. A.; Ren, J.; Zhou, C.; **de Pablo, J. J.**; **Nealey, P. F.** Soft Crystal Martensites: An in Situ Resonant Soft x-Ray Scattering Study of a Liquid Crystal Martensitic Transformation. *Science Advances* **2020**, *6*, eaay5986. https://doi.org/10.1126/sciadv.aay5986.
26. Jackson, N. E.; Bowen, A. S.; **de Pablo, J. J.** Efficient Multiscale Optoelectronic Prediction for Conjugated Polymers. *Macromolecules* **2020**, *53*, 482–490. https://doi.org/10.1021/acs.macromol.9b02020.

27. Li, X.; Martínez-González, J. A.; Guzmán, O.; Ma, X.; Park, K.; Zhou, C.; Kambe, Y.; Jin, H. M.; Dolan, J. A.; **Nealey, P. F.**; **de Pablo, J. J.** Sculpted Grain Boundaries in Soft Crystals. *Science Advances* **2019**, *5*, eaax9112. https://doi.org/10.1126/sciadv.aax9112.
28. Zhou, Y.; Senyuk, B.; Zhang, R.; Smalyukh, I. I.; **de Pablo, J. J.** Degenerate Conic Anchoring and Colloidal Elastic Dipole-Hexadecapole Transformations. *Nat Commun* **2019**, *10*, 1000. https://doi.org/10.1038/s41467-019-08645-9.
29. Xu, X.; Mastropietro, D.; Ruths, M.; **Tirrell, M.**; Yu, J. Ion-Specific Effects of Divalent Ions on the Structure of Polyelectrolyte Brushes. *Langmuir* **2019**, *35*, 15564–15572. https://doi.org/10.1021/acs.langmuir.9b01984.
30. Webb, M. A.; Delannoy, J.-Y.; **de Pablo, J. J.** Graph-Based Approach to Systematic Molecular Coarse-Graining. *J. Chem. Theory Comput.* **2019**, *15*, 1199–1208. https://doi.org/10.1021/acs.jctc.8b00920.
31. Wang, X.; Zhou, Y.; Kim, Y.-K.; Tsuei, M.; Yang, Y.; **de Pablo, J. J.**; Abbott, N. L. Thermally Reconfigurable Janus Droplets with Nematic Liquid Crystalline and Isotropic Perfluorocarbon Oil Compartments. *Soft Matter* **2019**, *15*, 2580–2590. https://doi.org/10.1039/C8SM02600A.
32. Rumyantsev, A. M.; Jackson, N. E.; Yu, B.; Ting, J. M.; Chen, W.; **Tirrell, M. V.**; **de Pablo, J. J.** Controlling Complex Coacervation via Random Polyelectrolyte Sequences. *ACS Macro Lett.* **2019**, *8*, 1296–1302. https://doi.org/10.1021/acsmacrolett.9b00494.
33. Rumyantsev, A. M.; **de Pablo, J. J.** Liquid Crystalline and Isotropic Coacervates of Semiflexible Polyanions and Flexible Polycations. *Macromolecules* **2019**, *52*, 5140–5156. https://doi.org/10.1021/acs.macromol.9b00797.
34. Qu, J.; Zhao, Q.; Zhou, J.; Lai, H.; Liu, T.; Li, D.; Chen, W.; Xie, Z.; He, F. Multiple Fused Ring-Based Near-Infrared Nonfullerene Acceptors with an Interpenetrated Charge-Transfer Network. *Chem. Mater.* **2019**, *31*, 1664–1671. https://doi.org/10.1021/acs.chemmater.8b05047.
35. Molina, J.; **Pablo, J. J. de**; Hernández-Ortiz, J. P. Structure and Proton Conduction in Sulfonated Poly(Ether Ether Ketone) Semi-Permeable Membranes: A Multi-Scale Computational Approach. *Phys. Chem. Chem. Phys.* **2019**, *21*, 9362–9375. https://doi.org/10.1039/C9CP00598F.
36. Li, X.; Martínez-González, J. A.; Park, K.; Yu, C.; Zhou, Y.; **de Pablo, J. J.**; **Nealey, P. F.** Perfection in Nucleation and Growth of Blue-Phase Single Crystals: Small Free-Energy Required to Self-Assemble at Specific Lattice Orientation. *ACS Appl. Mater. Interfaces* **2019**, *11*, 9487–9495. https://doi.org/10.1021/acsami.8b18078.
37. Li, J.; Deng, T.-S.; Liu, X.; Dolan, J. A.; Scherer, N. F.; **Nealey, P. F.** Hierarchical Assembly of Plasmonic Nanoparticle Heterodimer Arrays with Tunable Sub-5 Nm Nanogaps. *Nano Lett.* **2019**, *19*, 4314–4320. https://doi.org/10.1021/acs.nanolett.9b00792.
38. Kambe, Y.; Arges, C. G.; Czaplewski, D. A.; Dolejsi, M.; Krishnan, S.; Stoykovich, M. P.; **de Pablo, J. J.**; **Nealey, P. F.** Role of Defects in Ion Transport in Block Copolymer Electrolytes. *Nano Lett.* **2019**, *19*, 4684–4691. https://doi.org/10.1021/acs.nanolett.9b01758.
39. Jackson, N. E.; Bowen, A. S.; Antony, L. W.; Webb, M. A.; Vishwanath, V.; **de Pablo, J. J.** Electronic Structure at Coarse-Grained Resolutions from Supervised Machine Learning. *Science Advances* **2019**, *5*, eaav1190. https://doi.org/10.1126/sciadv.aav1190.
40. Jackson, N. E.; Webb, M. A.; **de Pablo, J. J.** Recent Advances in Machine Learning towards Multiscale Soft Materials Design. *Current Opinion in Chemical Engineering* **2019**, *23*, 106–114. https://doi.org/10.1016/j.coche.2019.03.005.

41. Ediger, M. D.; **de Pablo, J. J.**; Yu, L. Anisotropic Vapor-Deposited Glasses: Hybrid Organic Solids. *Acc. Chem. Res.* **2019**, *52*, 407–414. https://doi.org/10.1021/acs.accounts.8b00513.
42. Dong, B. X.; Bennington, P.; Kambe, Y.; Sharon, D.; Dolejsi, M.; Strzalka, J.; Burnett, V. F.; **Nealey, P. F.**; Patel, S. N. Nanothin Film Conductivity Measurements Reveal Interfacial Influence on Ion Transport in Polymer Electrolytes. *Mol. Syst. Des. Eng.* **2019**, *4*, 597–608. https://doi.org/10.1039/C9ME00011A.
43. Doise, J.; Bezik, C.; Hori, M.; **de Pablo, J. J.**; Gronheid, R. Influence of Homopolymer Addition in Templated Assembly of Cylindrical Block Copolymers. *ACS Nano* **2019**, *13*, 4073–4082. https://doi.org/10.1021/acsnano.8b08382.
44. Colón, Y. J.; Guo, A. Z.; Antony, L. W.; Hoffmann, K. Q.; **de Pablo, J. J.** Free Energy of Metal-Organic Framework Self-Assembly. *J. Chem. Phys.* **2019**, *150*, 104502. https://doi.org/10.1063/1.5063588.
45. Arges, C. G.; Li, K.; Zhang, L.; Kambe, Y.; Wu, G.-P.; Lwoya, B.; Albert, J. N. L.; **Nealey, P. F.**; Kumar, R. Ionic Conductivity and Counterion Condensation in Nanoconfined Polycation and Polyanion Brushes Prepared from Block Copolymer Templates. *Mol. Syst. Des. Eng.* **2019**, *4*, 365–378. https://doi.org/10.1039/C8ME00081F.
46. Sharon, D.; Bennington, P.; Liu, C.; Kambe, Y.; Dong, B. X.; Burnett, V. F.; Dolejsi, M.; Grocke, G.; Patel, S. N.; **Nealey, P. F.** Interrogation of Electrochemical Properties of Polymer Electrolyte Thin Films with Interdigitated Electrodes. *J. Electrochem. Soc.* **2018**, *165*, H1028–H1039. https://doi.org/10.1149/2.0291816jes.
47. Sevgen, E.; Dolejsi, M.; **Nealey, P. F.**; Hubbell, J. A.; **de Pablo, J. J.** Nanocrystalline Oligo(Ethylene Sulfide)- *b* -Poly(Ethylene Glycol) Micelles: Structure and Stability. *Macromolecules* **2018**, *51*, 9538–9546. https://doi.org/10.1021/acs.macromol.8b01812.
48. Qiu, Y.; Antony, L. W.; Torkelson, J. M.; **de Pablo, J. J.**; Ediger, M. D. Tenfold Increase in the Photostability of an Azobenzene Guest in Vapor-Deposited Glass Mixtures. *J. Chem. Phys.* **2018**, *149*, 204503. https://doi.org/10.1063/1.5052003.
49. Lueckheide, M.; Vieregg, J. R.; Bologna, A. J.; Leon, L.; **Tirrell, M. V.** Structure–Property Relationships of Oligonucleotide Polyelectrolyte Complex Micelles. *Nano Lett.* **2018**, *18*, 7111–7117. https://doi.org/10.1021/acs.nanolett.8b03132.
50. Liu, Z.; Gao, Y.; Dong, J.; Yang, M.; Liu, M.; Zhang, Y.; Wen, J.; Ma, H.; Gao, X.; Chen, W.; Shao, M. Chlorinated Wide-Bandgap Donor Polymer Enabling Annealing Free Nonfullerene Solar Cells with the Efficiency of 11.5%. *J. Phys. Chem. Lett.* **2018**, *9*, 6955–6962. https://doi.org/10.1021/acs.jpclett.8b03247.
51. Bowen, A. S.; Jackson, N. E.; Reid, D. R.; **de Pablo, J. J.** Structural Correlations and Percolation in Twisted Perylene Diimides Using a Simple Anisotropic Coarse-Grained Model. *J. Chem. Theory Comput.* **2018**, *14*, 6495–6504. https://doi.org/10.1021/acs.jctc.8b00742.

Collaborative Publications

1. Yanagimachi, T.; Li, X.; **Nealey, P. F.**; Kurihara, K. Surface Anchoring of Nematic Liquid Crystal on Swollen Polymer Brush Studied by Surface Forces Measurement. *Advances in Colloid and Interface Science* **2019**, *272*, 101997. https://doi.org/10.1016/j.cis.2019.101997.
2. Fukami, M.; Yale, C. G.; Andrich, P.; Liu, X.; Heremans, F. J.; **Nealey, P. F.**; Awschalom, D. D. All-Optical Cryogenic Thermometry Based on Nitrogen-Vacancy Centers in Nanodiamonds. *Phys. Rev. Applied* **2019**, *12*, 014042. https://doi.org/10.1103/PhysRevApplied.12.014042.

3. Bagchi, K.; Jackson, N. E.; Gujral, A.; Huang, C.; Toney, M. F.; Yu, L.; **de Pablo, J. J.**; Ediger, M. D. Origin of Anisotropic Molecular Packing in Vapor-Deposited Alq3 Glasses. *J. Phys. Chem. Lett.* **2019**, *10*, 164–170. https://doi.org/10.1021/acs.jpclett.8b03582.
4. Liu, L.; Chen, H.; Chen, W.; He, F. From Binary to Quaternary: High-Tolerance of Multi-Acceptors Enables Development of Efficient Polymer Solar Cells. *J. Mater. Chem. A* **2019**, *7*, 7815–7822. https://doi.org/10.1039/C9TA00948E.
5. Chen, H.; Qu, J.; Liu, L.; Chen, W.; He, F. Carrier Dynamics and Morphology Regulated by 1,8-Diiodooctane in Chlorinated Nonfullerene Polymer Solar Cells. *J. Phys. Chem. Lett.* **2019**, *10*, 936–942. https://doi.org/10.1021/acs.jpclett.9b00063.
6. Hsieh, H.-C.; Hsiow, C.-Y.; Su, Y.-A.; Liu, Y.-C.; Chen, W.; Chiu, W.-Y.; Shih, Y.-C.; Lin, K.-F.; Wang, L. Two-Dimensional Polythiophene Homopolymer as Promising Hole Transport Material for High-Performance Perovskite Solar Cells. *Journal of Power Sources* **2019**, *426*, 55–60. https://doi.org/10.1016/j.jpowsour.2019.04.008.
7. Wang, J.-Y.; Chen, W.; Nagao, M.; Shelat, P.; Hammer, B. A. G.; Tietjen, G. T.; Cao, K. D.; Henderson, J. M.; He, L.; Lin, B.; Akgun, B.; Meron, M.; Qian, S.; Ward, S.; Marks, J. D.; Emrick, T.; Lee, K. Y. C. Tailoring Biomimetic Phosphorylcholine-Containing Block Copolymers as Membrane-Targeting Cellular Rescue Agents. *Biomacromolecules* **2019**, *20*, 3385–3391. https://doi.org/10.1021/acs.biomac.9b00621.
8. Sokolov, A.; Mozaffari, A.; Zhang, R.; **de Pablo, J. J.**; Snezhko, A. Emergence of Radial Tree of Bend Stripes in Active Nematics. *Phys. Rev. X* **2019**, *9*, 031014. https://doi.org/10.1103/PhysRevX.9.031014.

Solid State NMR Spectroscopy for Advanced Energy Materials

Aaron J. Rossini, Frederic A. Perras, Takeshi Kobayashi, Javier Vela, Wenyu Huang, Rana Biswas

Division of Materials Science and Engineering, US DOE Ames Laboratory, Ames, Iowa, USA

Program Scope

The overarching goal of our research program is to advance the science of nanomaterials by using solid state NMR (SSNMR) spectroscopy to reveal the interplays between material properties and the structures of their bulk, interfaces and defects. Nanomaterials will fulfill current and future societal needs related to optoelectronic devices, energy storage and conversion, quantum information, sensing, and separations/purifications. In order to advance the science and applications of nanomaterials, analytical techniques capable of probing surfaces, defects, and atomic scale disorder are required. To address this problem, we develop SSNMR methods that exploit dynamic nuclear polarization (DNP) or fast magic angle spinning (MAS) to enhance sensitivity and spectral resolution. These techniques are used to determine the relationships between the surface structure of semiconductor nanoparticle (NP) and their optical properties. We also use these approaches to elucidate the bulk structure, edge terminations and intra-sheet defects of continuous and porous 2D materials. DFT calculations are used to model materials structure and properties.

Recent Progress

Sensitivity-Enhanced SSNMR Spectroscopy. In the past decade, (indirect) proton detection enabled by fast MAS has been established as widespread method to obtain order of magnitude gains in the sensitivity of solid-state NMR experiments with ubiquitous, but insensitive spin-½ nuclei such as ^{13}C, ^{15}N and ^{29}Si. Our team has developed a variety of SSNMR methods for ^{1}H detection of exotic and unreceptive isotopes found in materials including high-*Z* spin-½ nuclei such as ^{113}Cd, ^{195}Pt, ^{207}Pb, etc. with large chemical shift anisotropy (CSA), low-γ spin-1/2, (^{89}Y, ^{109}Ag, ^{183}W), and half-integer quadrupolar nuclei (^{11}B, ^{17}O, ^{27}Al, ^{71}Ga, etc.). These experiments have subsequently been applied to study the structure of semiconductor nanoparticles and 2D materials.

We have also developed protocols to enable MAS DNP experiments on a variety of inorganic materials. We showed that gamma irradiation or doping with Gd or Mn ions could be used to enable DNP in inorganic glasses and other bulk solids. It was previously shown that DNP could be performed on semiconductor NP by trapping them in mesoporous silica with an exogenous polarizing agent solution. We demonstrated much better NMR sensitivity is obtained if hexagonal boron nitride (*h*-BN) is used to disperse the NP instead of silica and if the NP are precipitated from solution and mixed with the *h*-BN to maximize NP concentration. We have

used this method to study a variety of NP and these results are foundational for our future work. Finally, we have developed a fully *ab initio* theoretical framework of DNP that enabled the calculation of enhancement factors in spin systems containing >1000 spins, providing insight into the fundamental mechanisms underlying DNP.

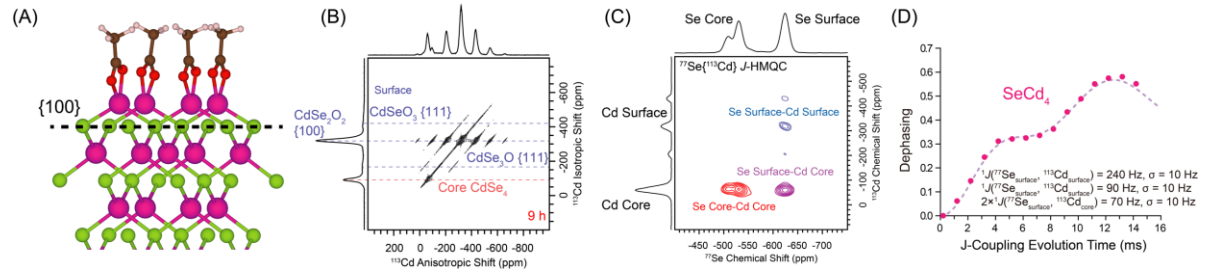

Figure 1. (A) Model of {100} surfaces of a CdSe NP. DNP-enhanced (B) ^{113}Cd 2D magic angle turning (MAT) spectrum, (C) ^{77}Se{^{113}Cd} 2D *J*-HMQC spectrum and (D) ^{77}Se{^{113}Cd} *J*-resolved dephasing curve for surface Se atoms. The DNP SSNMR experiments confirm that the surfaces of CdSe are primarily terminated by {100} facets featuring surface $SeCd_4$ atoms capped by $CdSe_2O_2$ fragments.[1]

Probing the Surface Structure of Semiconductor Nanoparticles. Semiconductor NP possess tunable optical and electronic properties. Due to their typically small diameters of a few nanometers, a large fraction of each semiconductor NP is made up of surface atoms. However, the disordered and irregular nature of NP surfaces make them difficult to directly probe experimentally. We have developed and applied surface-selective, sensitivity-enhanced SSNMR spectroscopy experiments to study NP surface structures. The types of NP we have studied (and collaborators) include CdS, and CdSe (Vela group – team member), silicon (Neale group - NREL), Cd_3P_2, InP (Cossairt Group - University of Washington), $CsPbBr_3$ (Brutchey Group - University of Southern California). Recently, we used DNP to enable homonuclear ^{77}Se, ^{113}Cd and ^{77}Se{^{113}Cd} heteronuclear scalar-correlation SSNMR experiments on archetypal spheroidal and platelet zinc blende CdSe NP.[1] A ^{113}Cd magic angle turning (MAT) spectrum spherical shows distinct Cd signals from core $CdSe_4$ and surface $CdSe_3O$, $CdSe_2O_2$, and $CdSeO_3$ fragments (**Figure 1B**). The variation in the number of Se and O atoms occurs because surface Cd atoms are present on {100} and {111} facets. Comparison of the NMR data for the CdSe NP with spheroidal and atomically-flat platelet morphology confirms that the predominant surfaces are {100} facets capped with $CdSe_2O_2$ units (**Figure 1A**). ^{77}Se{^{113}Cd} *J*-HMQC spectra illustrate the one-bond connections between surface Se and core and surface Cd atoms (**Figure 1C**). ^{77}Se{^{113}Cd} *J*-resolved experiments confirmed that the surface Se atoms predominantly have a $SeCd_4$ tetrahedral coordination (**Figure 1D**). In summary, our prior studies of NPs demonstrate we have the tools to create detailed models of surfaces, including direct determination of the stoichiometry of surface fragments, and identification of specific crystalline facets. The proposed research describes the applications of these strategies to address a number of fundamental problems related to the surface structures, properties and functions of semiconductor NPs.

Structural Characterization of 2D Materials. Two-dimensional (2D) materials have potential applications in optoelectronics, electrocatalysis and quantum information. Since the synthesis of graphene in 2004, 2D materials such as hexagonal boron nitride (*h*-BN), carbon

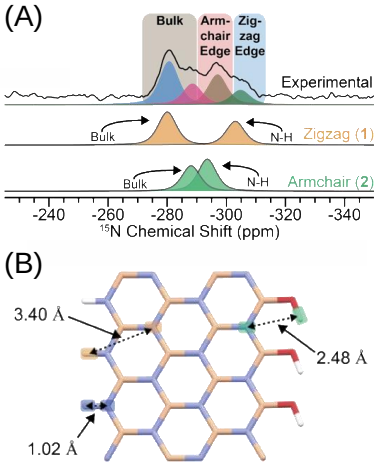

Figure 2. (A) DNP-enhanced $^{1}H \rightarrow ^{15}N$ CPMAS spectrum of *h*-BN nanosheets. The DFT predicted ^{15}N chemical shifts are shown for zigzag and armchair edges. (B) Planewave DFT model of zigzag edges.[2]

nitride, transition metal dichalcogenide (TMDC), phosphorane, silicane, germanane, and transition metal carbides/nitrides (MXenes) have also emerged. The design and development of 2D materials requires an understanding of molecular structure. Microscopy and diffraction techniques are the current gold-standard to characterize 2D material structure. However, many 2D materials lack long-range order, making determination of their bulk structure challenging. We used $^{1}H \rightarrow ^{29}Si$ INEPT SSNMR experiments to prove that the 2D material silicane primarily consists of sheets of sp^3 hybridized silicon atoms with $SiHSi_3$ local structure. We have also probed the structure of edges and/or defect sites with SSNMR spectroscopy. ^{11}B, ^{14}N and ^{15}N SSNMR spectroscopy was used to determine the molecular structure of the edges *h*-BN nanosheets. DNP allowed us to obtain surface-selective ^{11}B and ^{15}N SSNMR spectra, the latter of which could be accurately reproduced by DFT-calculated models of zigzag and armchair edge terminations (**Figure 2**).[2] Many 2D materials can also be prepared in a porous form, with the structures of atoms making up the pores often being unknown. In forthcoming work, we have used a combination of ultra-high field 35.2 T ^{11}B homonuclear and ^{1}H-^{11}B, ^{1}H-$^{14}N/^{15}N$ and ^{11}B-^{15}N heteronuclear correlation SSNMR spectroscopy techniques, in conjunction with plane-wave DFT calculations, to determine that the pores of mesoporous *h*-BN consist of oxygen rich terminations.

Future Plans

Sensitivity-Enhanced SSNMR Spectroscopy.

We are currently developing new SSNMR methods that use both ^{1}H-detection and/or DNP to enhance sensitivity and resolution. In particular we are developing pulse sequences that enable precise measurements of inter-nuclear distances, or rapid acquisition of 2D correlation NMR spectra. These methods are targeted towards high-*Z* spin-1/2 (e.g., ^{77}Se, ^{113}Cd, ^{195}Pt, ^{207}Pb, etc) and quadrupolar spins (^{11}B, ^{14}N, ^{17}O, ^{35}Cl, ^{93}Ge, etc.) found in the materials under study in our program. For instance, we have used our recently described TONE D-HMQC pulse sequence[3] to obtain a surface-selective $^{1}H\{^{207}Pb\}$ SSNMR spectrum of PbS NP (**Figure 3**). This spectrum shows extremely broad

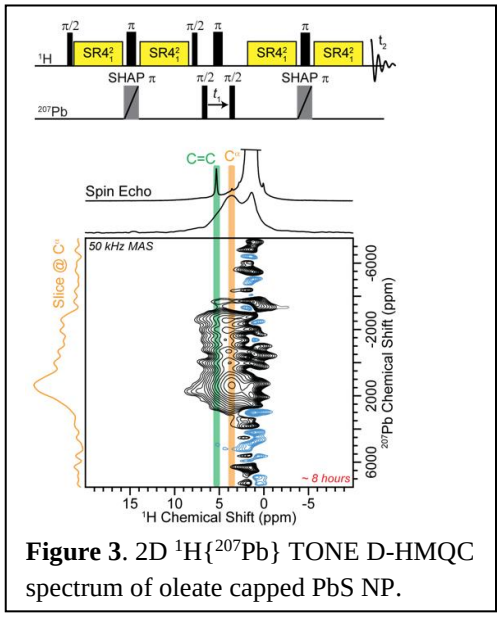

Figure 3. 2D $^{1}H\{^{207}Pb\}$ TONE D-HMQC spectrum of oleate capped PbS NP.

NMR signals and is at odds with currently accepted structural models of PbS surfaces which predict regular {100} facets.[4] We are also investigating alternative types of radicals to facilitate DNP on materials; we have found that ball milling can create millimolar concentrations of stable free radicals in inorganic and organic network solids. Finally, we are developing new theories of DNP to predict spin dynamics and use them as structural probes in nanomaterials.

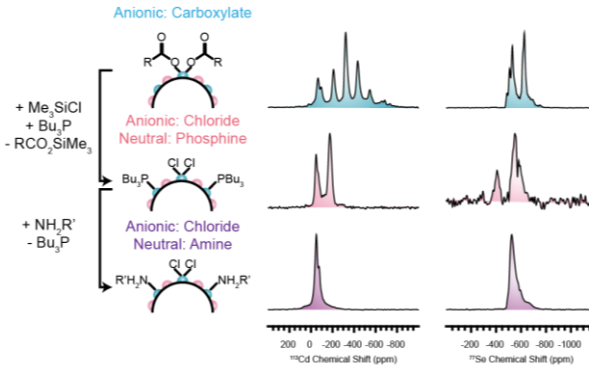

Figure 4. (left) Accepted scheme of ligand exchange experiments. (right) DNP-enhanced ^{113}Cd and ^{77}Se SSNMR spectra of CdSe nanocrystals with carboxylate, phosphine, amine and chloride ligands.

Probing the Surface Structure of Semiconductor Nanoparticles. Our goal is to understand the connection between the surface structure of semiconductor nanoparticles and their optoelectronic properties. Based on our prior studies of CdSe NP (**Figure 1**) we are positioned to use SSNMR to determine how ligand exchange and other surface treatments change the surface structure of NP, and correlate these atomic level changes to optoelectronic and chemical properties. To this end, we are pursuing NMR studies of CdSe magic sized clusters and NP with unique exposed facets to record the NMR signatures of different exposed surface facets and defects. Importantly, sensitivity gains provided by fast MAS in combination with DNP will enable us to observe minor surface facets and defects. We have obtained preliminary ^{113}Cd and ^{77}Se SSNMR spectra of CdSe nanoparticles after exchange of native carboxylate ligands for phosphines and amines (**Figure 4**). The SSNMR spectra illustrate that there are clear changes in surface structure induced by ligand exchange. Relativistic DFT calculations are being used to create molecular models of surfaces and predict NMR observables.

Structural Characterization of 2D Materials. We are using SSNMR spectroscopy to determine the structure of silicane, borophane, germanane, TMDC, carbon nitride, and porous organic materials. Experimental structural models are lacking for many emerging 2D materials. For example, ^{1}H and ^{11}B SSNMR spectroscopy in conjunction with DFT modeling is being used to determine the bulk structure of borophane. We are also observing the distribution of selenides in mixed TMDC produced by mechanochemical routes. The structures of edges and defect sites are often unknown in 2D materials despite their critical importance for the optical, electronic and chemical properties. We are currently studying the structure of chloride and hydroxide defects native to silicane materials produced by topotactic hydrogenation of calcium silicide. Finally, ^{11}B and ^{17}O SSNMR is being used to detect defect sites in porous covalent organic thin films and relate them to their capacity to uptake heavy metal ions and other guest molecules/ions.

References

[1] Y. Chen, et al., *J. Am. Chem. Soc.*, **2021**, 143, 8747-8760. [2] R. Dorn, et al., *Chem. Mat.*, **2020**, *32*, 3109-3121. [3] A. Venkatesh, et al., *J. Magn. Reson.*, **2021**, *327*, 106983. [4] Zherebetskyy D., et al., *Science*, **2014**, *344*, 1380-1384.

Publications

"A" Publications

[A22] T. Kobayashi, F.A. Perras., Y. Nishiyam, "Determination of the chemical shift tensor anisotropy and asymmetry of strongly dipolar coupled protons under fast MAS," *Solid State Nuclear Magnetic Resonance,* **114**, (2021), 101743.

[A21] Y. Chen, R.W Dorn., M.P. Hanrahan, L. Wei, R. Blome-Fernández, A.M. Medina-Gonzalez, M.A.S. Adamson, A.H. Flintgruber, J. Vela, A.J. Rossini, "Revealing the Surface Structure of CdSe Nanocrystals by Dynamic Nuclear Polarization-Enhanced ^{77}Se and ^{113}Cd Solid-State NMR Spectroscopy," *Journal of the American Chemical Society,* **143**, (2021), 8747-8760.

[A20] T. Kobayashi, M. Pruski, "Indirectly Detected DNP-Enhanced ^{17}O NMR Spectroscopy: Observation of Non-Protonated Near-Surface Oxygen at Naturally Abundant Silica and Silica-Alumina," *ChemPhysChem,* **In Press**, (2021), https://doi.org/10.1002/cphc.202100290.

[A19] A. Venkatesh, F.A. Perras, A.J. Rossini, "Proton-Detected Solid-State NMR Spectroscopy of High-CSA Spin-1/2 Nuclei", *J. Magn. Reson.*, **327**, 106983 (2021).

[A18] B. Zhang, T.W. Goh, T. Kobayashi, D. Jing, X. Wu, M. Chen, W. Huang, "Structure evolution ofsingle-site Pt in a metal–organic framework," *Journal of Chemical Physics,* **154**, 094710 (2021).

[A17] M.P. Hanrahan, J.L. Stein, N. Park, B.M. Cossairt, A.J. Rossini, "Elucidating the location of Cd^{2+} inpost-synthetically treated InP quantum dots using dynamic nuclear polarization ^{31}P and ^{113}Cd solid-state NMR spectroscopy," *Journal of Physical Chemistry C,* **125(5)**, 2956–2965 (2021).

[A16] A.L. Paterson, F.A. Perras, M.F. Besser, M. Pruski, "Dynamic nuclear polarization of metal-dopedoxide glasses: A Test of the generality of paramagnetic metal polarizing agents," *Journal of Physical Chemistry C,* **124(42)**, 23126-23133 (2020).

[A15] A. Venkatesh, X. Luan, F.A. Perras, I. Hung, W. Huang, A.J. Rossini, "t_1-Noise eliminated dipolar heteronuclear multiple-quantum coherence solid-state NMR spectroscopy," *Physical Chemistry ChemicalPhysics,* **36**, 20815-20828 (2020).

[A14] F.A. Perras, M. Raju, S.L. Carnahan, D. Akbarian, A.C.T. van Duin, A.J. Rossini, M. Pruski, "Full- scale ab initio simulation of magic-angle-spinning dynamic nuclear polarization," *The Journal of PhysicalChemistry Letters,* **11(14)**, 5655-5660 (2020).

[A13] R.W. Dorn, M.J. Ryan, T.H. Kim, T.W. Goh, A. Venkatesh, P.M. Heintz, L. Zhou, W. Huang, A.J.Rossini, "Identifying the molecular edge termination of exfoliated hexagonal boron nitride nanosheets with solid-state NMR spectroscopy and plane-wave DFT calculations," *Chemistry of Materials,* **32(7)**, 3109-3121 (2020).

[A12] F.A. Perras, S. Hwang, Y. Wang, E.C. Self, P. Liu, R. Biswas, S. Nagarajan, V.H. Pham, Y. Xu, J.A. Boscoboinik, D. Su, J. Nanda, M. Pruski, D. Mitlin, "Site-specific sodiation mechanisms of seleniumin microporous carbon host," *Nano Letters,* **20**, 918-928 (2020).

[A11] Y. Chen, S.R. Smock, A.H. Flintgruber, F.A. Perras, R.L. Brutchey, A.J. Rossini, "Surface termination of $CsPbBr_3$ perovskite quantum dots determined by solid-state

NMR spectroscopy," *Journalof the American Chemical Society*, **142(13)**, 6117-6127 (2020).
[A10] R.W. Dorn, E.A. Marro, M.P. Hanrahan, R.S. Klausen, A.J. Rossini, "Investigating the microstructure of poly(cyclosilane) by ^{29}Si solid-state NMR spectroscopy and DFT calculations," *Chemistry of Materials,* **31(21)**, 9168-9178 (2019).
[A9] M.P. Hanrahan, Y. Chen, R. Blome-Fernández, J.L. Stein, G.F. Pach, M.A.S. Adamson, N.R. Neale, B.M. Cossairt, J. Vela, A.J. Rossini, "Probing the surface structure of semiconductor nanoparticlesby DNP SENS with dielectric support materials," *Journal of the American Chemical Society,* **141(39)**, 15532-15546 (2019).
[A8] A. Venkatesh, I. Hung, K.C. Boteju, A.D. Sadow, P.L. Gor'kov, Z. Gan, A.J. Rossini, "Suppressing^{1}H spin diffusion in fast MAS proton detected heteronuclear correlation solid-state NMR experiments," *Solid State Nuclear Magnetic Resonance*, **105**, 101636 (2019).
[A7] F.A. Perras, T.W. Goh, L.-L. Wang, W. Huang, M. Pruski, "Enhanced ^{1}H-X D-HMQC performance through improved ^{1}H homonuclear decoupling," *Solid State Nuclear Magnetic Resonance*,**98**, 12-18 (2019).
[A6] S.L. Carnahan, A. Venkatesh, F.A. Perras, J.F. Wishart, A.J. Rossini, "High-field magic anglespinning dynamic nuclear polarization using radicals created by γ-Irradiation," *Journal of Physical Chemistry Letters*, **10(17)**, 4770-4776 (2019).
[A5] F.A. Perras, M. Pruski, "Linear-scaling ab initio simulations of spin diffusion in rotating solids," *The Journal of Chemical Physics*, **151**, 034110 (2019).
[A4] F.A. Perras, M. Pruski, "Reducing t_1 noise through rapid scanning," *Journal of MagneticResonance*, **298**, 31-34 (2019).
[A3] F.A. Perras, M. Pruski, "Large-scale ab initio simulations of MAS DNP enhancements using aMonte Carlo optimization strategy," *Journal of Chemical Physics*, **149(15)**, 154202 (2018).
[A2] M.P. Hanrahan, L. Men, B.A. Rosales, J. Vela, A.J. Rossini, "Sensitivity-enhanced ^{207}Pb solid-stateNMR spectroscopy for the rapid, non-destructive characterization of organolead halide perovskites," *Chemistry of Materials,* **30(20)**, 7005-7015 (2018).
[A1] A. Venkatesh. M.J. Ryan, A. Biswas, K.C.Boteju, A.D. Sadow, A.J. Rossini, "Enhancing the Sensitivity of Solid-State NMR Experiments with Very Low-Gyromagnetic Ratio Nuclei with Fast MASand Proton Detection,"*Journal of Physical Chemistry A*, **122**, 5635–5643 (2018).

Select "B" Publications

[B21] S.R. Smock, Y. Chen, A.J. Rossini, R.L. Brutchey, "The Surface chemistry and structure of colloidallead halide perovskite nanocrystals," *Accounts of Chemical Research*, **54(3)**, 707-718.
[B20] G. Bhaskar, V. Gvozdetskyi, M. Batuk, K.M. Wiaderek, Y. Sun, R. Wang, C. Zhang, S.L. Carnahan, X. Wu, R.A. Ribeiro, S.L. Bud'ko, P.C. Canfield, W. Huang, A.J. Rossini, C.-Z. Wang, K.-M. Ho, J. Hadermann, J.V. Zaikina, "Topochemical deintercalation of Li from layered LiNiB: toward 2D MBene,"*Journal of the American Chemical Society,* **143(11)**, 4213–4223 (2021).
[B19] S. Lee, S.L. Carnahan, G. Akopov, P. Yox, L.-L. Wang, A.J. Rossini, K. Wu, K.

Kovnir, “Noncentrosymmetric tetrel pnictides $RuSi_4P_4$ and $IrSi_3P_3$: Nonlinear optical materials with outstandinglaser damage threshold,” *Advanced Functional Materials*, Early View 2010293 (2021).
[B18] K.W. Mitra, C.H. Chang, M.P. Hanrahan, J. Yang, D. Tofan, W.M. Holden, N. Govind, G. Seidler, A.J. Rossini, A. Velian, “Surface functionalization of black phosphorus with nitrenes: Identification ofP=N bonds using isotopic labeling,” *Angewandte Chemie-International Edition*, **60(16)**, 9127-9134 (2020).
[B17] Z. Wang, M.P. Hanrahan, T. Kobayashi, F.A. Perras, Y. Chen, F. Engelke, C. Reiter, A. Purea, A.J.Rossini, M. Pruski, “Combining fast magic angle spinning dynamic nuclear polarization with indirect detection to further enhance the sensitivity of solid-state NMR spectroscopy,” *Solid State Nuclear Magnetic Resonance*, **109**, 101685 (2020).
[B16] V. Gvozdetskyi, Y. Sun, X. Zhao, G. Bhaskar, S.L. Carnahan, C.P. Harmer, F. Zhang, R. Ribeiro, P.Canfield, A.J. Rossini, C.Z. Wang, K.M. Ho, J.V. Zaikina, “Lithium nickel borides: Evolution of [NiB] layers driven by Li pressure,” *Inorganic Chemistry Frontiers*, **8**, 1675-1685 (2020).
[B15] O. Dolotko, I.Z. Hlova, A.K. Pathak, Y. Mudryk, V.K. Pecharsky, P. Singh, D.D. Johnson, B.W. Boote, J. Li, E.A. Smith, S.L. Carnahan, A.J. Rossini, L. Zhou, E.M. Eastman, V.P. Balema, “Unprecedented generation of 3D heterostructures by mechanochemical disassembly and re-ordering ofincommensurate metal chalcogenides,” *Nature Communications*, **11(1)**, 3005 (2020).
[B14] K. Liu, S.S. Tan, J. Moon, C.J. Jafta, C. Li, T. Kobayashi, H. Lyu, C.A. Bridges, S. Men, W. Guo, Y.F. Sun, J.L. Zhang, M.P. Paranthaman, X.G. Sun, S. Dai, “Insights into the enhanced cycle and rateperformances of the F-substituted P2-type oxide cathodes for sodium-ion batteries,” *Advanced EnergyMaterials*, **10(19)**, 2000135 (2020).
[B13] C.L. Daniels, M. Knobeloch, P. Yox, M.A.S. Adamson, Y. Chen, R.W. Dorn, H. Wu, G. Zhou, H.Fan, A.J. Rossini, J. Vela, “Intermetallic nanocatalysts from heterobimetallic Group 10–14 pyridine-2- thiolate precursors,” *Organometallics*, **39(7)**, 1092-1104 (2020).
[B12] B.S. Chang, A. Martin, B. Thomas, A. Li, R.W. Dorn, J. Gong, A.J. Rossini, M.M. Thuo, “Synthesis of interface-driven tunable bandgap metal oxides,” *ACS Materials Letters*, **2(9)**, 1211-1217(2020).
[B11] B.J. Ryan, M.P. Hanrahan, Y. Wang, U. Ramesh, C.K.A. Nyamekye, R.D. Nelson, Z. Liu, C. Huang, B. Whitehead, J. Wang, L.T. Roling, E.A. Smith, A.J. Rossini, M.G. Panthani, “Silicene, siloxene, or silicane? Revealing the structure and optical properties of silicon nanosheets derived fromcalcium disilicide,” *Chemistry of Materials*, **32(2)**, 795-804 (2019).
[B10] A.M. Love, M.C. Cendejas, M.P. Hanrahan, S.L. Carnahan, P. Uchupalanun, A.J. Rossini, I. Hermans, “Understanding the synthesis of supported vanadium oxide catalysts using chemical grafting,”*Chemistry: A European Journal*, **26(5)**, 1052-1063 (2019).
[B9] V. Gvozdetskyi, M.P. Hanrahan, R.A. Ribeiro, T.-H. Kim, L. Zhou, A.J. Rossini, P.C. Canfield, J.V. Zaikina, “A Hydride route to ternary alkali metal borides: A Case study of lithium nickel borides,” *Chemistry - A European Journal*, **25(16)**, 4123-4135 (2019).
[B8] B.S. Chang, B. Thomas, J.H. Chen, I.D. Tevis, P. Karanja, S. Cinar, A. Venkatesh, A.J. Rossini, M.M. Thuo, “Ambient synthesis of nanomaterials by in situ heterogeneous metal/ligand reactions,” *Nanoscale*, **11(29)**, 14060-14069 (2019).

[B7] J. Mark, M.P. Hanrahan, K.E. Woo, S. Lee, A.J. Rossini, K. Kovnir, “Chemical and electrochemical lithiation of van der Waals tetrel-arsenides,” *Chemistry - A European Journal*, **25(25)**,6392-6401 (2019).
[B6] T. Kobayashi, Z. Wang, M. Pruski, “Homonuclear dipolar recoupling of arbitrary pairs in multi- spin systems under magic angle spinning: A double-frequency-selective ZQ-SEASHORE experiment,” *Solid State Nuclear Magnetic Resonance*, **101**, 76-81 (2019).
[B5] A.M. Love, B. Thomas, S.E. Specht, M.P. Hanrahan, J.M. Venegas, S.P. Burt, J.T. Grant, M.C.Cendejas, W.P. McDermott, A.J. Rossini, I. Hermans, “Probing the transformation of boron nitride catalysts under oxidative dehydrogenation conditions,” *Journal of the American Chemical Society*, **141(1)**, 182-190 (2019).
[B4] A. Yadav, P. Agarwal, R. Biswas, “Quantum size effects and tunable visible photoluminescence ina-Si: H/nc-Si: H superlattices,” *Journal of Materials Science: Materials in Electronics*, **30(5)**, 4696-4704(2019).
[B3] X.M. Huang, F.A. Perras, J.S. Manzano, I.I. Slowing, A. McNabb, M. Pruski, “The anomaloussolidification of concrete grindings from acid treatment,” *Cement and Concrete Research*, **116**, 65-69(2019).
[B2] M.A. White, K.J. Baumler, Y.H. Chen, A. Venkatesh, A.M. Medina-Gonzalez, A.J. Rossini, J.V. Zaikina, E.M. Chan, and J. Vela, "Expanding the I-II-V Phase Space: Soft Synthesis of Polytypic Ternary and Binary Zinc Antimonides," *Chemistry of Materials*, **30**, 6173 (2018).
[B1] J.L. Stein, W.M. Holden, A. Venkatesh, M.E. Mundy, A.J. Rossini, G.T. Seidler, and B.M. Cossairt, “Probing Surface Defects of InP Quantum Dots Using Phosphorus K alpha and K beta X-Ray Emission Spectroscopy," *Chemistry of Materials*, **30**, 6377 (2018).

Structure and Dynamics of Materials Interfaces FWP KC31SM

Miquel Salmeron, Materials Science Division, Lawrence Berkeley National Laboratory

Peidong Yang, Materials Science Division, Lawrence Berkeley National Laboratory

Gabor Somorjai, Materials Science Division, Lawrence Berkeley National Laboratory

David Prendergast, Materials Science Division, Lawrence Berkeley National Laboratory

Program Scope

This program aims to obtain a fundamental understanding of the structure and dynamics of materials interfaces with gas and liquid environments. Interfaces are defined here to include regions extending nanometers to micrometers away from the ideal sharp interface. It focuses on three main thrust areas:

a) materials interfaces (single crystals, films, and nanoparticles) with gas environments at ambient pressure and temperature, and with liquid electrolytes as a function of pH and electrical potential. Special focus is on corrosion and its inhibition by adsorbed molecules;

b) development of new instrumentation and methods that make possible surface sensitive microscopy and spectroscopy studies of interfaces in realistic environments, expanding the science of surfaces beyond from the high vacuum environments of traditional surface science;

c) development of theoretical models for Density Functional Theory calculations, ab-initio Molecular Dynamics simulations, and continuum thermodynamics to determine chemical speciation, solvation, and distribution as a function of distance from the electrode, and their spectroscopic signatures to allow for comparison with experimental results using XPS, XAS, IR and other spectroscopies.

Recent Progress

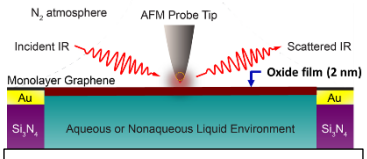

Schematic of liquid cell with an oxide membrane 2 nm thick on graphene for tip-enhanced FTIR, XPS, AFM and NEXAFS

-Ultrathin suspended membranes, 2-4 nm thick, were developed that can withstand pressure differentials of several atmospheres in gases and liquids. The membranes, which close a reaction cell, are transparent to electrons and photons allowing for the use of many spectroscopies (XPS, NEXAFS, IR, Raman, AFM, etc) to interrogate the interfaces and the reactions occurring inside the cell. To date membranes include pure metals, such as Pt, oxides Al2O3, SiO2, CoOx, TiO2 and others. They can act as supports of nanoparticles, and organic films for studies of gas or electrochemical reactions. First results include determination of the structure of the electrical double layer structure and composition of TiO2 and Al2O3 with various electrolytes, and measurement of concentration of solutes near the oxide electrode as a function of bias.

-Using AFM with the tip on the air or vacuum side of the membrane, and using the KPFM mode we measured surface potentials arising from the adsorption of anions and cations located on the solution side of oxides and on graphene membranes enclosing electrochemical cells. In the case of graphene, simultaneous Raman spectroscopy allowed us to separate charges in the graphene from doping, for the ionic charges in the cell, whose electric field is felt by the AFM tip outside

- We synthesized Pt-Co rombo-dodecahedra with two segregated phases, a Pt-rich phase concentrated on the edges and a Co-rich phase inside the particle. We etched away the Co-rich phase by nitric acid corrosion to prepare Pt-Co nanoframe structures with open surface and a hollow interior. The Pt-Co NF exhibited remarkable behavior for both Oxygen reduction and Methanol Oxidation reaction in acid/alkali solutions, outperforming those of commercial Pt/C. The outstanding structural stability after various electrocatalysis cycles is due to the negligible electrochemical dissolution of Co.

-We performed fundamental studies of corrosion of copper in saline solutions using sum frequency vibrational spectroscopy (SFVS), atomic force microscopy (AFM), Kelvin probe force microscopy (KPFM), and X-ray photoelectron spectroscopy (XPS). We determined the structure and composition of the copper surface in equilibrium with aqueous solutions of benzotriazole (BTAH) and NaCl as a function of concentration and bias during cyclic voltammetry (CV). The protection provided by BTAH films is effective for negative bias below the open circuit potential (OCP). By measuring the Gibbs adsorption energy of BTAH and Cl- we found that a particularly stable Cl- structures are formed around the OCP, suggesting that electronegative additives could move the OCP to higher negative values and improve BTAH protection, which we confirmed by addition of sodium dodecyl sulfate (SDS) surfactant.

Future Plans

-Expand our fundamental studies on the structure of the electrical double layer in solid-liquid interfaces, using graphene, oxides, and pure metal membranes. We will move on to studies of de-alloying in various electrolytes, with emphasis on the structure of ion solvation shells as they approach the interface as a function of bias and concentration.

-We plan to study in more detail new and unexpected properties of the new class of ultrathin suspended materials developed in the past year (oxides, metals, and next polymer materials). These include mechanical properties, already manifested in the extreme mechanical strength found, with Young Moduli exceeding 200 GPa in the case of TiO2. We started testing the drum-like vibration of the membranes suspended, when covered with thin nm-films of polymers, and when in contact with electrolytes.

Publications

Yi-Hsien Lu, Carlos Morales, Xiao Zhao, Matthijs A. van Spronsen, Artem Baskin, David Prendergast, Peidong Yang, Hans A. Bechtel, Edward S. Barnard, D. Frank Ogletree, Virginia

Altoe, Leonardo Soriano, Adam M. Schwartzberg, and Miquel Salmeron. *Ultrathin Free-Standing Oxide Membranes for Electron and Photon Spectroscopy Studies of Solid−Gas and Solid−Liquid Interfaces.* NanoLetters. **2020**, 20, 6364-6371.

Shouping Chen, Xiao-Yuan Liu, Jianbo Jin, Mengyu Gao, Chubai Chen, Qiao Kong, Zhe Ji, Gabor A. Somorjai, Omar M. Yaghi, and Peidong Yang. Individually Encapsulated Frame-in-Frame Structure. ACS Mater. Lett., 2, 685-690. (2020).

Ano, Taishi; Kishimoto, Fuminao; Tsubaki, Shuntaro; Lu, Yi-Hsien; Hohman, J.; Maitani, Masato; Salmeron, Miquel; Wada, Yuji. Controlling the Schottky Barrier at the Pt/TiO2 Interface by Intercalation of Self-Assembled Monolayer with Oriented Dipole Moment". Journal of Physical Chemistry, 2021. Accepted. Manuscript ID: jp-2021-00993h.R4

Shanshan Yang, Xiao Zhao, Zhiyuan Qi, Yi-Hsien Lu, Gabor Somorjai, Peidong Yang, Artem Baskin, David Prendergast, Miquel Salmeron. Operando Spectroscopy study of the Chloride Assisted Corrosion of Copper and Protection by Benzotriazole. Corrosion Science. Under review. Manuscript, CORSCI_2020_1942

Peng-Cheng Chen, Mengyu Gao, Sunmoon Yu, Jianbo Jin, Miquel Salmeron, Mary C. Scott, Peidong Yang, Nano Lett. Revealing the Phase Separation Behavior of Thermodynamically Immiscible Elements in a Nanoparticle. Manuscript 20210525. Nano Letters 2021.

Mufan Li, Bei Zhang, Tao Cheng, Sunmoon Yu, Sheena Louisia, Chubai Chen, Shouping Chen, Stefano Cestellos-Blanco, Miquel B. Salmeron, William A. Goddard III, Peidong Yang. Sulfur-doped Graphene Anchoring of Ultrafine Au Nanoclusters for Electrocatalysis. Nano Research. 2021

Monica Luna, Mariam Barawi, Yi-Hsien Lu, Ravi Chintala, Patricia Reñones, Laura Collado, Virginia Altoe, Lidia Martínez, Yves Huttel, Seiji Kawasaki, Alexander Weber-Bargioni, Victor A. de la Peña O´Shea, Paul D. Ashby, Peidong Yang, Miquel Salmeron. Photoinduced Charge Transfer and Trapping on Single Gold Metal Nanoparticles on TiO2. ACS Nano. Manuscript nn-2020-03925v. Under Review. 2021.

Dynamics in Multicomponent Polymeric Materials

Alexei P. Sokolov, Oak Ridge National Laboratory

Program Scope

The overarching goal of the proposed research is to develop a fundamental and predictive understanding of the structure, dynamics and macroscopic properties in polymer nanocomposites (PNCs). This will provide the foundation for the rational design of new materials with superior properties for energy relevant applications. The pervasive presence of interfaces between different phases or species in multicomponent systems is the unifying aspect of our research. We address the following fundamental issues: How do the nanoparticle-polymer interactions and nanoparticle size and softness affect structural relaxation and dynamics of the composite materials, including the emergence of nonequilibrium states? How do confinement and interactions affect polymer and nanoparticles diffusion? How are bulk viscoelastic and mechanical properties of nanocomposites affected by nanoparticle size, surface chemistry, softness and shape fluctuations? We pursue a comprehensive interdisciplinary approach that integrates advanced theory and simulations, precise synthesis and state-of-the-art characterization. The proposed research connects well to the priority research directions formulated in the BESAC report on Mesoscale Science, Challenges at the Frontier of Matter and Energy, and the DOE report on Computational Materials Science and Chemistry. The fundamental knowledge developed in this program will contribute to the scientific foundation for the rational design of multicomponent polymer-based materials with superior properties and functionality that can address many DOE challenges.

Recent Progress

Our studies of several model PNCs revealed many interesting phenomena and underlying mechanisms, and led to several discoveries. We continued studies of structure and properties of the polymer interfacial layer formed around nanoparticles [1-3]. Combined SAXS and SANS studies using partially deuterated polymers revealed a surprising decrease in density of the interfacial layer relative to the density of the bulk polymer in case when the interparticle surface distance becoming smaller than two radius of gyration of a polymer, Rg [1]. We ascribed this effect to frustration of chain packing due to confinement. We also discovered that this frustration in chain packing leads to a decrease of the mechanical reinforcement effect in PNCs [2]. Following the developed ideas, we demonstrated that adding short chains to PNC based on long chains can significantly improve the mechanical properties [3]. The developed approach revealed a simple way to tune mechanical properties in PNCs.

Detailed theoretical and experimental studies also revealed formation of polymer bridging mediated organization of nanoparticles in PNCs [4]. Strong polymer-nanoparticles attractions leads to polymer bridging of nanoparticles and their clustering. The latter leads to significant enhancement of mechanical properties in PNCs. Developed theory provides direct quantitative estimates of the polymer bridging based on analysis of SAXS data [4].

Analysis of the interfacial layer thickness and its temperature dependence in various PNCs revealed a direct relationship to the dynamic heterogeneity length scale [5]. Moreover, the performed analysis revealed that the temperature variations in the thickness of the interfacial layer is actually encoded in the temperature variations of segmental relaxation in a bulk polymer [5]. Furthermore, we discovered that the amplitude of segmental fluctuations in the interfacial layer is strongly reduced relative to that in a bulk polymer [6]. Surprisingly, the amplitude of segmental relaxation in the interfacial layer is always suppressed, regardless of whether segmental dynamics in the interfacial layer is getting slower or faster than in the bulk [6]. Majority of the PNCs studies never paid attention to the amplitude of segmental fluctuations. The current discovery reveals that the changes in amplitude and in characteristic time scales of segmental relaxation in the interfacial layer are decoupled, and this might explain many controversies in current PNC studies.

We also continued studies of nanoparticles diffusion in PNCs [7-10]. Results of X-PCS studies revealed that the temperature dependence of collective nanoparticles diffusion is much weaker than the temperature dependence of viscosity [7]. Understanding of these results remains a puzzle. Our combined theoretical and experimental study elucidated the mechanism of diffusion by soft polymeric nanoparticles [8-10]. Neutron reflectivity results combined with a simple and predictive statistical mechanical model explains the observed rich behavior by invoking the threading of linear polymer chains through the loops that exist near the crosslinked SNP surface. Our combined experimental and theoretical insights may also be relevant to understanding diffusive motion in other soft materials such as dense microgel and nanogel suspensions, and linear/ring polymer blends.

Future Plans

We plan to finalize our studies of nanoparticles diffusion, and also the role of PNCs preparation in trapping them in a non-equilibrium state. Our preliminary results revealed that details of the PNC samples preparation might affect significantly their macroscopic properties. And the difference in properties cannot be erased with even extremely long annealing. This opens new ways in tuning macroscopic properties of PNCs. We also plan to develop comprehensive understanding of microscopic mechanisms controlling mechanical properties of PNCs.

References

1. A.C. Genix, et al., **ACS Applied Materials & Interfaces 10**, 33601-33610 (2018).

2. A.C. Genix, et al., **ACS Applied Materials & Interfaces 11**, 17863-17871 (2019).
3. Vera Bocharova, et al., **ACS Appl. Nano Materials 3**, 3427-3438 (2020).
4. Yuxing Zhou, et al., **Macromolecules 53**, 6984-6994 (2020).
5. S. Cheng, A.P. Sokolov, **J. Chem. Phys. 152**, 094904/1-6 (2020).
6. I. Popov, et al., **Macromolecules 53**, 4126-4135 (2020).
7. B. M. Yavitt, et al., **ACS Nano** (2021, in print).
8. S. Rostom and M. D. Dadmun, **J. Appl. Phys. 127,** 074303 (2020).
9. U. M. Shrestha, et al., **Macromolecules 53**, 7580 (2020).
10. S. Rostom, et al., **J. Phys. Chem. C 124**, 18834 (2020).

Publications (FY2018-FY2021):

1. Halie J. Martin, B. Tyler White, Guangcui Yuan, Tomonori Saito, Mark D. Dadmun, *Relative Size of the Polymer and Nanoparticle Controls Polymer Diffusion in All-Polymer Nanocomposites*, **Macromolecules 52**, 2843 (2019).
2. A. Kisliuk, V. Bocharova, I. Popov, C. Gainaru, A. P. Sokolov, *Fundamental parameters governing ion conductivity in polymer electrolytes*, **Electrochimica Acta 299**, 191 (2019).
3. A.C. Genix, V. Bocharova, B. Carroll, M. Lehman, T. Saito, S. Krueger, L. He, P. Dieudonne-George, A. P. Sokolov, J. Oberdisse, *Understanding the Static Interfacial Polymer Layer by Exploring the Dispersion States of Nanocomposites*, **ACS APPLIED MATERIALS & INTERFACES 11,** 17863 (2019).
4. Y.Zhou and K.S.Schweizer, *Local Structure, Thermodynamics and Phase Behavior of Asymmetric Particle Mixtures: Comparison between Integral Equation Theories and Simulation*, **J.Chemical Physics 150**, 214902 (2019).
5. F. Wieland, V. Bocharova, P. Munzner, W. Hiller, R. Sakrowski, C. Sternemann, R. Bohmer, A. P. Sokolov, C. Gainaru, *Structure and dynamics of short-chain polymerized ionic liquids*, **J. Chem. Phys. 151**, 034903 (2019).
6. Kunyue Xing, Martin Tress, Peng-Fei Cao, Fei Fan, Shiwang Cheng, Tomonori Saito, Alexei P. Sokolov, *The Role of Chain-End Association Lifetime in Segmental and Chain Dynamics of Telechelic Polymers*, **Macromolecules 51**, 8561 (2018).
7. D. Bhowmik, P. Ganesh, B.G. Sumpter, M. Goswami, *Dynamical disparity between hydration shell water and RNA in a hydrated RNA system*, **Phys. Rev. E. 98**, 062407 (2018).
8. Piaoran Ye, Peng-Fei Cao, Qiyi Chen, and Rigoberto Advincula, *Continuous Flow Fabrication of Block Copolymer–Grafted Silica Micro-Particles in Environmentally Friendly Water/Ethanol Media*, **Macromol. Mater. Eng. 304**, 1800451 (2019).

9. E. W. Stacy, C.P. Gainaru, M. Gobet, Z. Wojnarowska, V. Bocharova, S. G. Greenbaum, A. P. Sokolov, *Fundamental limitations of ionic conductivity in polymerized ionic liquids*, **Macromolecules 51**, 8637 (2018).

10. Peng-Fei Cao, Guang Yang, Bingrui Li, Yiman Zhang, Sheng Zhao, Shuo Zhang, Andrew Erwin, Zhengcheng Zhang, Alexei P. Sokolov, Jagjit Nanda, and Tomonori Saito, *Rational Design of a Multifunctional Binder for High-Capacity Silicon-Based Anodes*, **ACS Energy Lett. 4**, 1171 (2019).

11. Yiyang Pan, Shilun Gao, Feiyuan Sun, Huabin Yang, Peng-Fei Cao, *Polymer Binders Constructed through Dynamic Noncovalent Bonds for High-Capacity Silicon-Based Anodes*, **Chem. Eur. J. 25**, 1 (2019).

12. Dmitry N. Voylov, Vera Bocharova, Nickolay V. Lavrik, Ivan Vlassiouk, Georgios Polizos, Alexei Volodin, Yury M. Shulga, Alexander Kisliuk, Thirumagal Thiyagarajan, Duane D. Miller, Ramesh Narayanan, Bobby G. Sumpter, Alexei P. Sokolov, *Noncontact tip-enhanced Raman spectroscopy for nanomaterials and biomedical applications*, **Nanoscale Advances 1**, 3392 (2019).

13. Michelle L. Lehmann, Guang Yang, Dustin Gilmer, Kee Sung Han, Ethan C. Self, Rose E. Ruther, Sirui Ge, Bingrui Li, Vijayakumar Murugesan, Alexei P. Sokolov, Frank M. Delnick, Jagjit Nanda, Tomonori Saito, *Tailored Crosslinking of Poly(Ethylene Oxide) Enables Mechanical Robustness and Improved Sodium-Ion Conductivity*, **Energy Storage Materials 21**, 85 (2019).

14. Benjamin Doughty, Anne-Caroline Genix, Ivan Popov, Bingrui Li, Sheng Zhao, Tomonori Saito, Daniel A. Lutterman, Robert L. Sacci, Bobby G. Sumpter, Zaneta Wojnarowska, Vera Bocharova, *Structural correlations tailor conductive properties in polymerized ionic liquids*, **Phys. Chem. Chem. Phys. 21**, 14775 (2019).

15. Qiyi Chen, Jiayu Zhao, Jingbo Ren, Lihan Rong, Peng-Fei Cao, Rigoberto C Advincula, *3D Printed Multifunctional, Hyperelastic Silicone Rubber Foam*, **Advanced Functional Materials 29**, 1900469 (2019).

16. Yun-Hui Yan, Li-Han Rong, Jin Ge, Brylee David B Tiu, Peng-Fei Cao, Rigoberto C Advincula, *Mussel-Inspired Hydrogel Composite with Multi-Stimuli Responsive Behavior*, **Macromolecular Materials and Engineering 304**, 1800720 (2019).

17. A. J. Erwin, H. Lee, S. Ge, S. Zhao, V. F. Korolovych, H. He, K. Matyjaszewski, A. P. Sokolov, V. V. Tsukruk, *Viscoelastic properties and ion dynamics in star-shaped polymeric ionic liquids*, **Eur. Polymer J. 109**, 326 (2018).

18. V. Bocharova, A. C. Genix, J.-M. Y. Carrillo, R. Kumar, B. Carroll, A. Erwin, D. Voylov, A. Kisliuk, Y. Wang, B. G. Sumpter, and A. P. Sokolov, Addition of short polymer chains mechanically reinforces glassy poly(2-vinylpyridine)-silica nanoparticle nanocomposites, *ACS Appl. Nano Mater*. **3**, 3427 (2020).

19. K. S. Schweizer and D. S. Simmons, *Progress towards a phenomenological picture and theoretical understanding of glassy dynamics and vitrification near interfaces and under confinement*, **J. Chem. Phys. 151**, 240901 (2019). **Invited Perspective Article**

20. S. Cheng and A.P. Sokolov, *Correlation between the temperature evolution of the interfacial region and the growing dynamic cooperativity length scale*, **J. Chem. Phys. 152**, 094904 (2020). **Cover Page**.

21. S.-J. Xie and K. S. Schweizer, *A collective elastic fluctuation mechanism for decoupling and stretched relaxation in glassy colloidal and molecular liquids***, J. Chemical Physics 152**, 034502 (2020).

22. A. Phan and K. S. Schweizer, *Theory of spatial gradients of relaxation, vitrification and fragility of glass-forming polymer liquids near solid substrates*, **ACS Macro Letters 9**, 448 (2020).

23. S. Rostom and M. D. Dadmun, *The Impact of Nanoparticle Softness on Its Tracer Diffusion Coefficient in All Polymer Nanocomposites*, **J. Appl. Phys. 127,** 074303 (2020). **Invited.**

24. V. Bocharova and A. P. Sokolov; *Perspectives for polymer electrolytes: A view from fundamentals of ionic conductivity*, **Macromolecules 53**, 4141 (2020). **Invited Perspective Article. Cover Page**

25. P.-F. Cao, B. Li, G. Yang, S. Zhao, J. Townsend, K. Xing, Z. Qiang, K. D. Vogiatzis, A. P. Sokolov, J. Nanda, and T. Saito, *Elastic single-ion conducting polymer electrolytes: Toward a versatile approach for intrinsically stretchable functional polymers*, **Macromolecules 53**, 3591 (2020).

26. I. Popov, B. Carroll, V. Bocharova**,** A.-C. Genix, S. Cheng, A. Khamzin, A. Kisliuk, and A. P. Sokolov, *Strong reduction in amplitude of the interfacial segmental dynamics in polymer nanocomposites*, **Macromolecules 53**, 4126 (2020).

27. Y. Zhou, B. Mei, and K. S. Schweizer, *Integral equation theory of thermodynamics, pair structure, and growing static length scale in metastable hard sphere and WCA fluids*, **Phys. Rev. E 101**, 042121 (2020).

28. S. J. Xie and K. S. Schweizer, *Collective elasticity activated physics as origin of decoupling of segmental relaxation & chain dynamics in supercooled polymer melts*, **Macromolecules 53**, 5350 (2020).

29. B. Mei, Y. Zhou, and K. S. Schweizer, *Structure-thermodynamics-dynamics correlations and nonuniversal effects in elastically collective activated hopping theory of glass-forming liquids*, **J. Physical Chemistry B 124**, 6121 (2020).

30. U. M. Shrestha, K. M. Vailonis, D. M. Jenkins, and M. D. Dadmun, *Investigating the co-polymerization of ligands into metal-organic nanotubes using small angle neutron scattering*, **ACS Appl. Nano Mater. 3**, 5605-5611 (2020).

31. U. M. Shrestha, L. Han, T. Saito, K. S. Schweizer, and M. D. Dadmun, *The mechanism of soft nanoparticle diffusion in entangled polymer melts*, **Macromolecules 53**, 7580 (2020).

32. S. Rostom, B. T. White, G. Yuan, T. Saito, and M. D. Dadmun, *Competing effects in polymer chain diffusion in all-polymer nanocomposites: Confinement vs. chain acceleration*, **J. Phys. Chem. C 124**, 18834 (2020).

33. L. Han, M. L. Lehmann, J. Zhu, T. Liu, Z. Zhou, X. Tang, C.-T. Hsieh, A. P. Sokolov, P. Cao, X. Chen, and T. Saito, *Recent developments and challenges in hybrid solid electrolytes for lithium-ion batteries*, **Front. Energy Res. 8**, 202 (2020).

34. Y. Zhou, B. M. Yavitt, Z. Zhou, V. Bocharova, D. Salatto, M. K. Endoh, A. E. Ribbe, A. P. Sokolov, T. Koga, and K. S. Schweizer, *Bridging-controlled network microstructure and long-wavelength fluctuations in silica-poly(2-vinylpyridine) nanocomposites: Experimental results and theoretical analysis*, **Macromolecules 53**, 6984 (2020).

35. Y. Zhou and K. S. Schweizer, *Theory of microstructure-dependent glassy shear elasticity and dynamic localization in melt polymer nanocomposites*, **J. Chem. Phys. 153**, 114901 (2020). **Editors Pick**.

36. S. Gao, D. Yang, Y. Pan, L. Geng, S. Li, X. Li, P.-F. Cao, and H. Yang, *From natural material to high-performance silicon based anode: Towards cost-efficient silicon based electrodes in high-performance Li-ion batteries*, **Electrochimica Acta 327**, 135058 (2019).

37. M. Tress, K. Xing, S. Ge, P. Cao, T. Saito, and A. P. Sokolov, *What dielectric spectroscopy can tell us about supramolecular networks*, **Euro. Phys. J. E 42**, 133 (2019).

38. S. Ge, M. Tress, K. Xing, P.-F. Cao, T. Saito, and A. P. Sokolov, *Viscoelasticity in associating oligomers and polymers: experimental test of the bond lifetime renormalization model*, **Soft Matter 16**, 390 (2020).

39. A. U. Chowdhury, G. J. Taylor, V. Bocharova, R. L. Sacci, Y. Luo, W. T. McClintic, Y.-Z. Ma, S. A. Sarles, K. Hong, P. C. Collier, and B. *Doughty, Insight into the mechanisms driving the self-assembly of functional interfaces: Moving from lipids to charged amphiphilic oligomers*, **JACS 142**, 290 (2020).

40. S. J. Rinehart, G. Yuan, and M.D. Dadmun, *The interplay of thermodynamics and kinetics: Imparting hierarchical control over film formation of self-stratified blends*, **Soft Matter 16**, 1287 (2020).

41. L. Geng, D. Yang, S. Gao, Z. Zhang, F. Sun, Y. Pan, S. Li, X. Li, P.-F. Cao, and H. Yang, *Facile fabrication of porous Si microspheres from low-cost precursors for high-capacity electrode*, **Adv. Mater. Interfaces**, 1901726 (2020).

42. Y. Pan, S. Ge, Z. Rashid, S. Gao, A. J. Erwin, V. V. Tsukruk, K. D. Vogiatzis, A. P Sokolov, H. Yang, and P.-F. Cao, *Adhesive polymers as efficient binders for high-capacity silicon electrodes*, **ACS Appl. Ener. Mater. 3**, 3387 (2020).

43. R. Kumar, J. P. Mahalik, K. S. Silmore, Z. Wojnarowska, A. Erwin, J. F. Ankner, A. P. Sokolov, B. G. Sumpter, and V. Bocharova, *Capacitance of thin films containing polymerized ionic liquids*, **Sci. Adv. 6**, eaba7952 (2020).

44. S. J. Rinehart, B. N. Nguyen, R. P. Viggiano, M. A. B. Meador, and M. D. Dadmun, *Quantitative evaluation of the hierarchical porosity in polyimide aerogels and corresponding solvated gels*, **ACS Applied Mat. & Interfaces 12**, 30457 (2020)

45. R. C. Chapleski Jr, A. U. Chowdhury, A. K. Wanhala, V. Bocharova, S. Roy, P. C. Keller, D. Everly, S. Jansone-Popova, A. Kisliuk, R. L. Sacci, A. G. Stack, C. G.

Anderson, B. Doughty, and V. S Bryantsev, *A molecular-scale approach to rare earth beneficiation: Thinking small to avoid large losses*, **iScience 23**(9), 25 (2020).

46. V. Bocharova, N. Jayakody, J. Yang, R. L. Sacci, W. Yang, S. Cheng, B. Doughty, S. Greenbaum, S. P. Jeong, I. Popov, S. Zhao, C. Gainaru, and Z. Wojnarowska, *Modulation of cation diffusion by reversible supramolecular assemblies in ionic liquid-based nanocomposites,* **ACS Appl. Mater. Interfaces 12**, 31842 (2020).
47. S. Gao, F. Sun, A. Brady, Y. Pan, A. Erwin, D. Yang, V. Tsukruk, A. G. Stack, T. Saito, H. Yang, and P.-F. Cao, *Ultra-efficient polymer binder for silicon anode in high-capacity lithium-ion batteries,* **Nano Ener. 73**, 104804 (2020).
48. B. P. Thapaliya, I. Popov, and S. Dai, *Layer-by-layer assembly strategy for reinforcing the mechanical strength of an ionogel electrolyte without affecting ionic conductivity*, **ACS Appl. Ener. Mater. 3**, 1265 (2019).
49. Vera Bocharova, Anne-Caroline Genix, Alexander Kisliuk, Gabriele Sala, Naresh C. Osti, Eugene Mamontov, Alexei P. Sokolov, *Role of Fast Dynamics in Conductivity of Polymerized Ionic Liquids,* **J. Phys. Chem. B 124**, 46, 10539–10545 (2020).
50. Y.Zhou and K.S.Schweizer, *PRISM Theory of Local Structure and Phase Behavior of Polymer Nanocomposites, New Closure Approximation and Comparison to Simulation*, **Macromolecules 53**, 9962 (2020).
51. Anjali N. Preman, Hyocheol Lee, Jungwoo Yoo, Il Tae Kim*, Tomonori Saito*, Suk-kyun Ahn, *Progress of 3D Network Binders in Silicon Anodes for Lithium Ion Batteries*, **J. Mater. Chem. A 8**, 25548-25570 (2020).
52. Guang Yang, Michelle L. Lehmann , Sheng Zhao , Bingrui Li , Sirui Ge , Peng-Fei Cao, Frank M. Delnick , Alexei P. Sokolov , Tomonori Saito, Jagjit Nanda, *Anomalously high elastic modulus of a poly(ethylene oxide)-based composite electrolyte*, **Energy Storage Materials 35**, 431–442 (2021).
53. Sheng Zhao, Yiman Zhang, Hoang Pham, Jan-Michael Y. Carrillo, Bobby G. Sumpter, Jagjit Nanda, Nancy J. Dudney, Tomonori Saito, Alexei P. Sokolov**,** Peng-Fei Cao**,** *Improved Single-Ion Conductivity of Polymer Electrolyte via Accelerated Segmental Dynamics,* **ACS Applied Energy Materials 3**, 12540-12548 (2020).
54. Shilun Gao, Feiyuan Sun, Nian Liu, Huabin Yang, and Peng-Fei Cao, *Ionic conductive polymers as artificial solid electrolyte interphase films in Li metal batteries* – A review, **Materials Today 40**, 140-159 (2020).
55. Li, B.; Zhao, S.; Zhu, J.; Ge, S.; Xing, K.; Sokolov, A.P; Saito, T.; Cao, P. *Rational Polymer Design of Stretchable Poly(ionic liquid)s Membranes for Dual Applications*. **Macromolecules 54,** 896−905 (2021).
56. Totsch T.R., Popov I., Stanford V.L., Lucius A.L., Foulger S.H., Gray G.M., *Polyphosphonates as ionic conducting polymers*, **J. Polymer Science**, 1–7 (2020).
57. Tress, M.; Ge, S.; Xing, K.; Cao, P.; Saito, T.; Genix, A.; Sokolov, A.P. *Turning Rubber into a Glass: Mechanical Reinforcement by Microphase Separation*, **ACS Macro Letters 10**, 197–202 (2021).

58. Yang, G.; Li, X.; Cheng, Y.; Wang, M.; Ma, D.; Sokolov, A.P.; Kalinin, S.V.; Veith, G.M.; Nanda, J. *Distilling Nanoscale Heterogeneity of Amorphous Silicon using Tip-enhanced Raman Spectroscopy (TERS) via Multiresolution Manifold Learning*, **Nature Communications 12,** 578 (2021).

59. Yang, G,; Lehmann, M; Zhao, S.; Li, B.; Ge, S.; Cao, P.F.; Delnick, F.M.; Sokolov, A.P.; Saito, T.; Nanda, J. *Anomalously high elastic modulus of a poly(ethylene oxide)-based composite electrolyte*, **Energy Storage Materials 35**, 359431-4420 (2021)

60. Lubnin A., Kisliuk A., Sokolov A.P., *The puzzling role of symmetry: a tool for macromolecular engineering*, In: **Macromolecular Engineering**, pp. 3-19, Elsevier 2021.

61. Dadmun, M.D. *X-Ray and Neutron Scattering of Polymers* **In: Molecular Characterization of Polymers A Fundamental Guide,** 561-585 (2021).

62. Ge, Sirui; Samanta, Subarna; Tress, Martin; Li, Bingrui; Xing, Kunyue; Dieudonne-George, Philippe; Genix, Anne-Caroline; Cao, Peng-Fei; Dadmun, Mark; Sokolov, Alexei, *The critical role of the interfacial layer in associating polymers with microphase separation*, **Macromolecules 54**, 4246-4256 (2021).

63. I. Popov, S. Cheng, A. P. Sokolov, *Broadband Dielectric Spectroscopy and Its Application in Polymeric Materials*, In: **Macromolecular Engineering: From Precise Synthesis to Macroscopic Materials and Applications,** Eds. Matyjaszewski, Hadjichristidis (in print, 2021).

64. Jeong, Seung Pyo; Kumar, Rajeev; Genix, Anne-Caroline; Popov, Ivan; Li, Congyi ; Hu, Xunxiang ; Bras, Wim; Popovs, Ilja; Sokolov, Alexei; Bocharova, Vera, *Improving gas selectivity in membranes based on polymer grafted nanoparticles by modulating nanoscale structure*, **ASC Appl. Nano Materials** (2021, in print).

65. B. M. Yavitt, D. Salatto, Y. Zhu, Z. Huang, M. Endoh, L. Wiegart, V. Bocharova, A. E. Ribbe, A. P. Sokolov, K. S. Schweizer, T. Koga, *Collective Nanoparticle Dynamics Associated with Bridging Network Formation in Model Polymer Nanocomposites*, **ACS Nano** (2021, in print).

FWP 58601 - Energy and fuels from multifunctional electrochemical interfaces

Dusan Strmcnik, Materials Science Division, Argonne National Laboratory

Program Scope

Electrochemical energy technologies require the application of novel concepts that are derived from a variety of fields including chemistry, materials science and physics. A multidisciplinary effort is pursued to develop active, stable, selective and conductive solid-aqueous, solid-organic and solid-solid electrochemical interfaces that is capable to address challenging obstacles in electrochemical energy conversion and storage. This research work is aimed to discover physicochemical parameters of electrified interfaces that are ultimately used in the design of novel materials. Along the way, the established fundamental framework links synthesis, characterization and functional properties of materials that goes beyond interfacial boundaries towards the real-world applications. A strategy that assumes insight at atomic/molecular levels has been found to be effective in defining the potential-controlled bond-making and breaking events. These processes are simultaneously controlled by a synergy between electron and ion mobility across electrochemical interfaces, the structure and nature of surface atoms, and organization of the electrolyte components that operates in the double layer, including reactive species, spectators and impurities. The range of materials and electrolytes includes metals, metal/metal-oxides, pure oxides, S-/N-/C-based materials as well as aqueous electrolytes with a wide pH range, organic solvents, and single crystal solid electrolytes. The tools in resolving complexities of interfacial properties ranges from ex-situ and in situ spectro-electrochemical methods to microscopy-based structural probes to synchrotron-based techniques and traditional electrochemical screening and computational evaluations.

Recent Progress

Understanding the effects of conductivity on the performance of electrochemical interfaces

1. Poorly Conductive Electrochemical Interfaces

While many factors can influence the activity of the electrochemical interface at atomic and molecular levels, the electron and ion transport have a big impact on the overall electrochemical performance. Although there is ample evidence how electrical conductivity can affect the electrochemical performance in the battery field where one commonly encounters poorly conductive active materials, a more in-depth analysis for electrocatalytic reactions utilizing poorly conducting materials is needed to adequately evaluate and understand the link between their fundamental and functional properties. We conducted a systematical analysis to reveal how the electronic conductivity of the electrode material affects its electrocatalytic performance using the

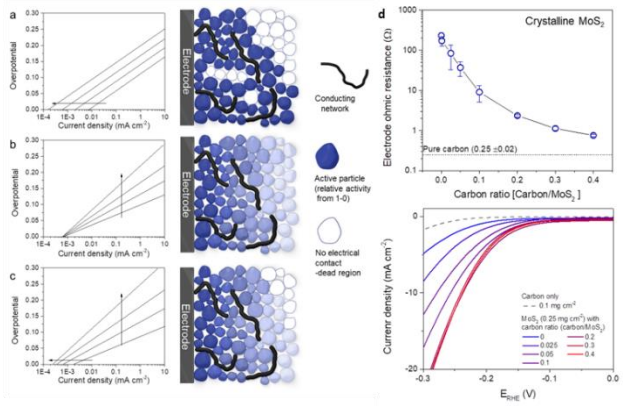

Figure 1: Three typical models for electrochemical activity changes depending on the resistance of electrode. The arrow indicates the deviation as increasing electrode ohmic resistance scheme of each scenario. (a) difference of number of active site (particle), (b) potential variation model due to ohmic loss of applied potential, (c) mixture of model (a) and (b). (d) Electrode ohmic resistance measured by 4-point probe method depending on carbon additive ratio for crystalline MoS_2 and I-E plot of hydrogen evolution reaction (HER) activity for same material[1].

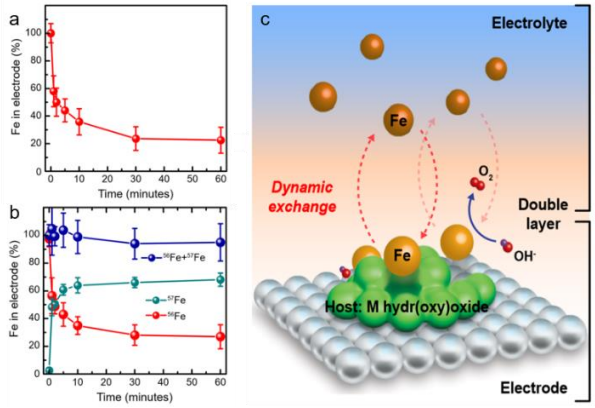

Figure 2: Total amount of Fe in electrode (a and b) during chronoamperometry measurements at 1.7 V in (a) 'Fe free' electrolyte and (b) 0.1 ppm of ^{57}Fe containing electrolyte reveals the Fe dynamic exchange (dissolution and redeposition) at the interface during OER catalysis[2], as the quick dissolution of ^{56}Fe from the electrode is followed by immediate ^{57}Fe redeposition from the electrolyte. (c) Schematic diagram of "dynamically stable" active site/host pair in electrode/electrolyte interface highlighting the role of M-hydr(oxy)oxide as a suitable host for Fe species.

hydrogen evolution reaction as a model reaction. Molybdenum disulfide (MoS_2) was chosen as the active material because of its poor conductivity and significant relevance in HER electrocatalysis as a durable and active candidate for replacing Pt. We clearly demonstrated the effect of poor electronic conductivity of MoS_2 on the electrochemical performance, as both values of the exchange current density i_0 as well as the Tafel slope depend on the level of utilization of the active material and the ohmic losses[1], stressing the importance of the experimental conditions and good control of electrode/electrolyte system for the proper evaluation and comparison of materials' kinetic parameters.

Understanding the stability of electrode materials and its effects on the performance of electrochemical interfaces

1. Dynamic stability of oxygen evolution

Progress in the fundamental understanding of electrochemical interfaces, encompassing electrode materials (catalysts) and hydrated (solvated) ions in the double layer, has begun to revolutionize the development of alternative energy systems as a viable replacement to fossil fuel technology. At the core of this transition lies the oxygen evolution reaction (OER), an important electrochemical process in hydrogen production in water electrolysers, corrosion, metal/air batteries and the synthesis of new chemicals from CO_2 reduction. Recently, it has been found that many OER active materials suffer severe dissolution during the reaction. However, the fact that dissolution occurs indicates that the surface atoms are dynamic, which is inconsistent with the

common view of the electrochemical interface as a static environment. By studying activity-stability trends for the OER on conductive $M^1O_xH_y$, Fe-$M^1O_xH_y$ and Fe-$M^1M^2O_xH_y$ hydr(oxy)oxide clusters (M^1= Ni, Co, Fe; M^2= Mn, Co, Cu), we show that balancing the rates of Fe dissolution and redeposition over a MO_xH_y host establishes dynamically stable Fe active sites (Figure 2). Together with tuning the Fe content of the electrolyte, the strong interaction of Fe with the MOxHy host is the key to control the average number of Fe active sites present at the solid-liquid interface[2]. We suggest that the Fe-M adsorption energy can therefore serve as a reaction descriptor that unifies OER catalysis on 3d transition metal hydr(oxy)oxides in alkaline media. Thus, introduction of dynamically stable active sites extends the design rules for making active and stable interfaces.

2. <u>Eliminating Dissolution at the Atomic Scale</u>

The current picture of catalyst degradation comes from observing metal dissolution, particle-size changes and carbon support corrosion during or after an accelerated stress test, which typically induces a decrease in the electrochemically active surface area (ECSA) that is particularly exaggerated for small particles (< 3 nm). These changes are often rationalized thermodynamically

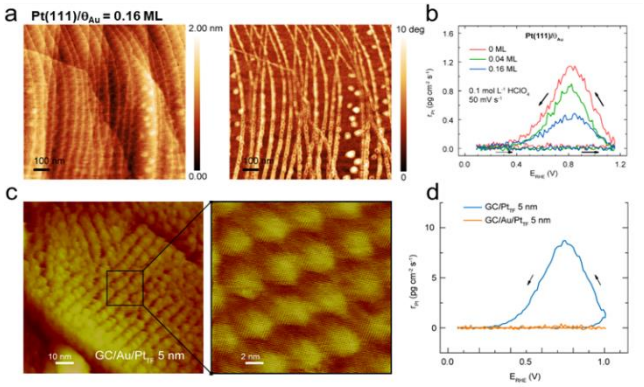

Figure 3: (a) Pt(111) surface covered by Au atoms positioned at the step-edge sites and (b) the consequent decrease in dissolution rate. (c) sputtered Pt thin-film tuned to 3 nm nanograins deposited over Au thin film exhibits surface texturing towards a (111) structure, which is the least susceptible to dissolution, and (d) the in situ Pt dissolution rate demonstrating elimination of Pt dissolution in case of subsurface Au presence[3].

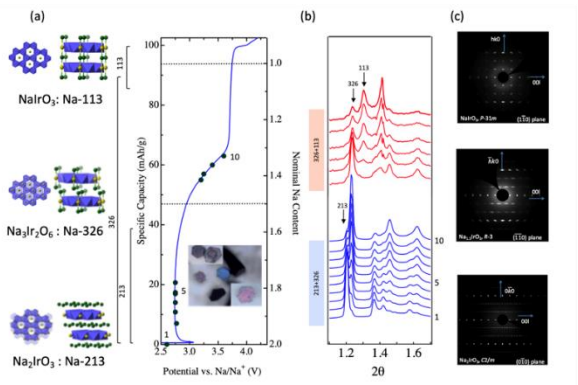

Figure 4: Structural and chemical evolution of Na2-xIrO3 during electrochemical charging. Crystal structures (a) determined by in situ diffraction at points along the capacity-voltage curve (b). Single crystals are robust to the charging process, as evidenced by sharp diffraction patterns (c) that could be used to refine crystal structure models shown in (a)[4].

by Ostwald ripening and Gibbs–Thompson effects, but provide little to no insight into the key physicochemical parameters and the processes that govern atomic-scale dissolution-redeposition mechanism on real-world Pt nanoscale catalysts. Thus, the establishment of such a functional link is needed to aid the development of viable mitigation strategies. A newly defined metric, intrinsic dissolution, is essential to understanding the correlation between the measured Pt loss, surface structure, size and ratio of Pt-nanoparticles in carbon support. It was found that utilization of Au underlayer promotes ordering of Pt surface atoms towards (111)-structure, while Au on the surface

selectively protects low-coordinated Pt sites (Figure 3). This mitigation strategy was applied towards 3 nm Pt_3Au/C nanoparticles, resulting in elimination of Pt dissolution in liquid electrolyte[3].

3. A Single Crystal Oxide Battery

Electrochemically driven chemical transformations play a key role in controlling storage of energy in chemical bonds and subsequent conversion to power electric vehicles and consumer electronics. The promise of coupling anionic oxygen redox with cationic redox to achieve substantial increase in capacities has inspired research in a wide range of electrode materials. A key challenge is that these studies have focused on polycrystalline materials, where it is hard to perform precise structural determinations, especially related to the location of light atoms. We utilized a different approach and harnessed a highly ordered single crystal, $Na_{2-x}IrO_3$, to explore the role of defects and structural transformations in layered transition metal oxide materials on redox-activity, capacity, reversibility and stability[4]. Within a combined experimental and theoretical framework, we demonstrate that (1) it is possible to cycle $Na_{2-x}IrO_3$, offering proof of principle for single-crystal based batteries (2) structural phase transitions coincide with Ir^{4+}/Ir^{5+} redox couple with no evident contribution from anionic redox, and (3) strong irreversibility and capacity fade observed during cycling correlates with the Na^+ migration between layers in the structure, resulting in progressive growth of an electrochemically inert $NaIrO_3$ endmember phase (Figure 4).

Future Plans

This project will be discontinued at the end of FY 2021.

References

1. Dong Young Chung, Subin Park, Pietro P. Lopes, Vojislav R. Stamenkovic, Yung-Eun Sung, Nenad M. Markovic, Dusan Strmcnik, *ACS Catal.* 10 (**2020**) 4990−4996

2. Dong Young Chung, Pietro P. Lopes, Pedro Farinazzo Bergamo Dias Martins, Haiying He, Tomoya Kawaguchi, Peter Zapol, Hoydoo You, Dusan Tripkovic, Dusan Strmcnik, Yisi Zhu, Soenke Seifert, Sungsik Lee, Vojislav R. Stamenkovic, Nenad M. Markovic, *Nat. Energy*, 5 (**2020**) 222-230

3. Pietro P Lopes, Dongguo Li, Haifeng Lv, Chao Wang, Dusan Tripkovic, Yisi Zhu, Roberto Schimmenti, Hideo Daimon, Yijin Kang, Joshua Snyder, Nigel Becknell, Karren L More, Dusan Strmcnik, Nenad M Markovic, Manos Mavrikakis, Vojislav R Stamenkovic *Nat. Mater.* 19 (**2020**) 1207-1214

4. Sanja Tepavcevic, Hong Zheng, David G. Hinks, Baris Key, Logan Ward, Zhi Lu, Costas Stoumpos, Yang Ren, John W. Freeland, Christopher Wolverton, Patrick Phillips, Robert Klie, John F. Mitchell, Nenad M. Markovic, *Adv. Energy Mater*. 10 (**2020**) 1903128

Publications

1. Nigel Becknell, Pietro Lopes, Toru Hatsukade, Xiuquan Zhou, Yuzi Liu, Brandon Fisher, Duck Young Chung, Mercouri Kanatzidis, Nenad Markovic, Sanja Tepavcevic, Vojislav Stamenkovic "Employing the dynamics of the electrochemical interface at aqueous zinc-ion battery cathode" *Accepted in Adv. Funct. Mater.*

2. Milena Zorko, Pedro Farinazzo Bergamo Dias Martins, Justin G Connell, Pietro Papa Lopes, Nenad M Markovic, Vojislav R Stamenkovic, Dusan Strmcnik "Improved Rate for the Oxygen Reduction Reaction in a Sulfuric Acid Electrolyte using a Pt (111) Surface Modified with Melamine" *ACS Appl. Mater. Interfaces* 13 (**2021**) 3369-3376

3. Pietro P Lopes, Dong Young Chung, Xue Rui, Hong Zheng, Haiying He, Pedro Farinazzo Bergamo Dias Martins, Dusan Strmcnik, Vojislav R Stamenkovic, Peter Zapol, JF Mitchell, Robert F Klie, Nenad M Markovic "Dynamically Stable Active Sites from Surface Evolution of Perovskite Materials during the Oxygen Evolution Reaction" *J. Am. Chem. Soc*. 143 (**2021**) 2741-2750

4. Nannan Shan, Paul C. Redfern, Anh T. Ngo, Peter Zapol, Nenad Markovic and Larry A. Curtiss "Theoretical evidence of water serving as a promoter for lithium superoxide disproportionation in Li–O_2 batteries" *Phys. Chem. Chem. Phys.* 23, (**2021**) 10440

5. Pietro P Lopes, Dongguo Li, Haifeng Lv, Chao Wang, Dusan Tripkovic, Yisi Zhu, Roberto Schimmenti, Hideo Daimon, Yijin Kang, Joshua Snyder, Nigel Becknell, Karren L More, Dusan Strmcnik, Nenad M Markovic, Manos Mavrikakis, Vojislav R Stamenkovic "Eliminating dissolution of platinum-based electrocatalysts at the atomic scale" *Nat. Mater.* 19 (**2020**) 1207-1214

6. Jéssica A Nogueira, Pietro P Lopes, Nenad M Markovic, Hamilton Varela "Active electrochemical interfaces stabilized through self-organized potential oscillations" *Electrochem. Comm.* 121 (**2020**) 106853

7. Justin G. Connell, Milena Zorko, Garvit Agarwal, Mengxi Yang, Chen Liao, Rajeev S. Assary, Dusan Strmcnik, Nenad M. Markovic "Anion Association Strength as a Unifying Descriptor for the Reversibility of Divalent Metal Deposition in Nonaqueous Electrolytes" *ACS Appl. Mater. Interfaces* 12, (**2020**) 36137−36147

8. Dong Young Chung, Subin Park, Pietro P. Lopes, Vojislav R. Stamenkovic, Yung-Eun Sung, Nenad M. Markovic, Dusan Strmcnik "Electrokinetic Analysis of Poorly Conductive Electrocatalytic Materials" *ACS Catal.* 10, (**2020**) 4990−4996

9. Dong Young Chung, Pietro P. Lopes, Pedro Farinazzo Bergamo Dias Martins, Haiying He, Tomoya Kawaguchi, Peter Zapol, Hoydoo You, Dusan Tripkovic, Dusan Strmcnik, Yisi Zhu, Soenke Seifert, Sungsik Lee, Vojislav R. Stamenkovic, Nenad M. Markovic, "Dynamic stability of active sites in hydr(oxy)oxides for the oxygen evolution reaction" *Nat. Energy*, 5 (**2020**) 222-230

10. Ivano E. Castelli, Milena Zorko, Thomas M. Østergaard, Pedro F. B. D. Martins, Pietro P. Lopes, Byron K. Antonopoulos, Filippo Maglia, Nenad M. Markovic, Dusan Strmcnik and Jan Rossmeisl, "The role of an interface in stabilizing reaction intermediates for hydrogen evolution in aprotic electrolytes" *Chem. Sci*., 11, (**2020**) 3914

11. Rongyue Wang, Dongguo Li, Sandip Maurya, Yu Seung Kim, Yimin Wu, Yuzi Liu, Dusan Strmcnik, Nenad Markovic, Vojislav Stamenkovic "Ultrafine Pt Cluster and RuO_2 Heterojunction Anode Catalysts Designed for Ultra-low Pt-Loading Anion Exchange Membrane Fuel Cells" *Nanoscale Horiz*. 5 (**2020**) 316-324

12. Sanja Tepavcevic, Hong Zheng, David G. Hinks, Baris Key, Logan Ward, Zhi Lu, Costas Stoumpos, Yang Ren, John W. Freeland, Christopher Wolverton, Patrick Phillips, Robert Klie, John F. Mitchell, and Nenad M. Markovic "Fundamental Insights from a Single-Crystal Sodium Iridate Battery" Adv. Energy Mater. 10 (**2020**) 1903128

13. Bostjan Genorio, Katharine L. Harrison, Justin G. Connell, Goran Dražić, Kevin R. Zavadil, Nenad M. Markovic, and Dusan Strmcnik "Tuning the Selectivity and Activity of Electrochemical Interfaces with Defective Graphene Oxide and Reduced Graphene Oxide" *ACS Appl. Mater. Interfaces* 11 (**2019**) 34517−34525

14. P. Martins, P. P. Lopes, E. Ticinelli, V. R. Stamenkovic, N. M. Markovic and D. Strmcnik "Hydrogen evolution reaction on copper: promoting water dissociation by tuning the surface oxophilicity" *Electrochem. Comm.*, 100 (**2019**) 30-33

15. D. Tripkovic, K. Popovic, V. Jovanovic, J. Nogueira, H. Varela, P. P. Lopes, D. Strmcnik, V. R. Stamenkovic and N. M. Markovic "Tuning catalytic properties for electrooxidation of small organic molecules on Pt-based thin films via controlled thermal treatment" *J. of Catal.*, 96 (**2019**) 96-105

16. Y. Zhu, J. G. Connell, S.Tepavcevic, P. Zapol, A. Sharafi, N. Taylor, J. Sakamoto, L. A. Curtiss, D. D. Fong, J. W. Freeland, Nenad M. Markovic "Dopant-Dependent Stability of Garnet Solid Electrolyte Interfaces with Lithium Metal", *Adv. Energy Mater.*, 9 (**2019**) 1803440

17. Y. Yang, H. Yao, Z. Yu, S.M. Islam, H. He, M. Yuan, Y. Yue, K. Xu, W. Hao, G. Sun, H. Li, S. Ma, P. Zapol, M. G. Kanatzidis "Hierarchical Nanoassembly of

MoS2/Co9S8/Ni3S2/Ni as a Highly Efficient Electrocatalyst for Overall Water Splitting in a Wide pH Range" *J. Am. Chem. Soc.* 141 (**2019**) 10417-10430.

18. M. Asadi, M. H. Motevaselian, T. V. Sun, C. Liu, A. Moradzadeh, R. Bose, P. Abbasi, P. Zapol, A. P. Khodadoust, L. A. Curtiss, N. R. Aluru, A. Salehi-Khojin "Highly Efficient Solar-driven Carbon Dioxide Reduction on Molybdenum Disulfide Catalyst using Choline Chloride based Electrolyte", *Advanced Materials*, 9, (**2019**) 1803536

19. H. He, C. Morrissey, L. A. Curtiss and P. Zapol "Graphene Supported Monometallic and Bimetallic Dimers for Electrochemical CO_2 Reduction" *J. Phys. Chem. C*, 122, (**2018**) 28629-28636

Conductive ink with circular life cycle for printed electronics

PI: Ting Xu,

Co-PI: Paul Alivisatos, Yi Liu, Robert Ritchie, Miquel Salmeron, Lin-wang Wang, Jie Yao

Materials Science Division, Lawrence Berkeley National Laboratory

University of California at Berkeley

Program Scope

3D printed electronics provide flexible and precise circuit architectures, but their recyclability and impact on the sustainability haven't been integrated as critical design criteria. In fact, due to the inherent rarity and toxicity of heavy metal elements, the energetic costs and environmental burdens of electronic waste have been more significant and long-term important, than those of the plastic waste. Given ever-increasing demands in microelectronic devices for the information age, future devices have to simultaneously satisfy functional needs and long-term environmental sustainability. As the initial attempt toward this goal, we aim to develop conductive composite inks for 3D printing of circuits with full recovery of fillers without compromising device performance. In pursuit of this goal, we focus on two milestones:

I. Program polyester degradation with near completion
II. Develop conductive composites with programmable degradation

Recent Progress

We envy nature's ability to program complex processes to achieve system-wide, long-term sustainability. The key bottleneck is molecularly interfacing catalytically reactive elements with synthetic counterparts and, for enzyme-based plastic modification/degradation, how to manipulate catalysis with macromolecules being both the reaction substrates and host matrices. In semi-crystalline polymers, which represent the majority of plastics, substrate accessibility can be rate-limiting due to the reduced mobilities of the confined catalysts and polymer matrix. By nanoscopically confining enzymes in semi-crystalline polyesters and exploiting enzyme-active-site features

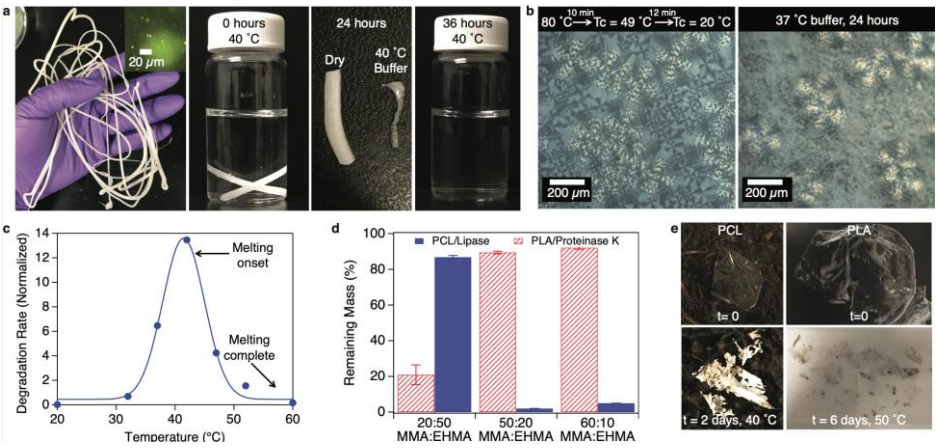

Figure 1. Programmable degradation of polyesters.

and enzyme-protectant interactions, we show that processive depolymerization can be enabled as the primary degradation pathway with expanded substrate selectivity. Nanoscopic dispersion of a trace amount of enzyme, e.g., ~0.02 wt.% lipase (<2 wt.% total additives) in poly(caprolactone), PCL, or ~1.5 wt.% proteinase K (<5 wt.% total additives) in poly(lactic acid), PLA, leads to near-complete conversion to small molecules, eliminating microplastics in a few days using household tap water and standard soil composts. The programmable degradation overcomes their incompatibility with industrial compost operations, making them viable polyolefin substitutes. Analysis on the effects of polymer conformation and segmental cooperativity guide the thermal treatment of the polyester to spatially and temporally program degradation, while maintaining latency during processing and storage. The protectants are designed to regulate biocatalysis and stabilize enzymes during common plastic processing.

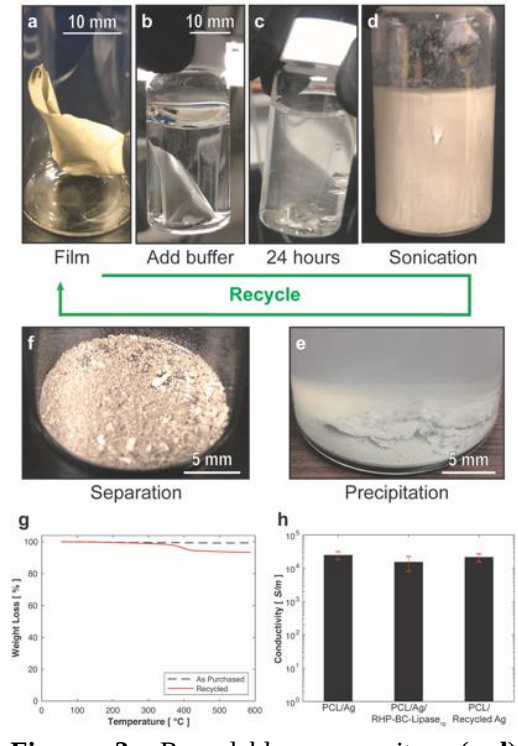

Figure 2. Recyclable composites (**a-d**) degradation of conductive composites (**e**) Ag flakes are precipitated in aqeuous solution and (**f**) recollected and dried. (**g**) Thermogravimetric analysis of the recycled and as purchased Ag flakes. (**h**) The electrical conductivity comparisons.

Electronic-waste (e-waste) containing toxic chemicals and precious components is one of the most pressing concerns[3] as current waste management strategies have failed to keep up with the rapid turnover rate of new electronics. Consequently, developing degradable and transient electronic to achieve circular life cycle is desirable, but remains challenges since recyclability has been rarely included as a design criterion in current design. Instead, many devices are often over engineered given increasing rapid pace of upgrades. Composites with nanoscopically embedded catalysts can enable simple and low-cost recycling with reduced secondary contamination and higher purity of metal fillers. The composite inks are formulated with biodegradable polymer, *i.e.* polycaprolactone, enzyme/protector nanoclusters and conductive fillers such as silver flake and carbon black. Circuits can be readily printed by either in solution or melt with good mechanical flexibility (breaking strains ε_{Break} ~ 80%), and electrical conductivity (~1.3×10^4 S/m) and subsequently disintegrated by immersing in warm water. The conductive fillers can be readily separated, recycled and reused with no deleterious effects. With enzymes being dispersed as nanoclusters, their presence didn't compromise the conductivity of printed circuits. The electrical current doesn't degrade enzyme either after one month of continuous operation under electrical voltage of 3 V. Practically, conductive inks can be readily formulated using commercially available enzymes without purification and the printed circuits remain functional after 7-month storage on the counter at room

temperature. Their disintegration can also be programmed by thermal treatment based on demand. Thus, present studies demonstrate feasibility to realize recyclability in the future design of wearable electronics, biosensors, and soft robotics while facilitating environmentally clean disposal at end-of-life.

Future Plans

We aim to develop molecular insights in programmable disassembly of nanocomposites such that each building blocks, especially nanoparticles, can be readily collected and reused. Such knowledge will fundamentally change how we design, synthesis and manufacture composite materials. This ambitious goal also raised significant challenge in our basic understanding in modulating and synergizing different chemical processes. In the case of controlled degradation of polymeric components inside of composites, , the polymer chain conformation contributes to the entropic gain thermodynamically, and thus, the global driving force of depolymerization. Kinetically, local polymer chain packing affects the segmental mobility and substrate binding to initiate and continue processive depolymerization. Protectants used to disperse the catalytic species, should be it be enzymes or molecular catalysts, may compete for substrate binding and/or transiently modify the active sites, offering opportunities to regulate catalytic latency.

Publications

[1] J. Kwon, K. Evans, L. Ma, D. Arnold, M. E. Yildizdag, T. Zohdi, R. O. Ritchie, and T. Xu, "Scalable Electrically Conductive Spray Coating Based on Block Copolymer Nanocomposites," ACS Appl. Mater. Interfaces, 12, 8687-8694, 2020.

[2] C. DelRe, Y. Jiang, P. Kang, J. Kwon, A. Hall, I. Jayapurna, Z. Ruan, L. Ma, K. Zolkin, T. Li, C. D. Scown, R. O. Ritchie, T. P. Russell, T. Xu, Near-complete depolymerization of polyesters with nano-dispersed enzymes. Nature, 2021, 592, 558.

Diversifying Composition Leads to Design Flexibility and Structural Fidelity in Hierarchical Composites

PI: Ting Xu,

Co-PI: Paul Alivisatos, Yi Liu, Robert Ritchie, Miquel Salmeron, Lin-wang Wang, Jie Yao

Materials Science Division, Lawrence Berkeley National Laboratory

University of California at Berkeley

Program Scope

Periodic structures spanning multiple length scales can produce exceptional mechanics, as found in spider silk, and beautiful optics, as seen in the photonic wings of many birds and insects [1, 2]. While human-engineered materials will likely never match the diversity and complexity of natural materials, similar hierarchies of hard and soft materials have been achieved using a self-assembling polymer nanocomposite system [3-10]. The system is a blend of polymers, organic small molecules, and inorganic nanoparticles (Figure 1A). The co-assembly of the soft and hard components generate structures never seen before, which could provide excellent optical, mechanical, and magnetic properties. We aim to develop this system as a framework for a new family of hybrid materials. In pursuit of this goal, we have identified the following milestones:

I. Structural control of organic and inorganic building blocks over multiple length scales, with high precision, and without constraint of filler size
II. Fabrication of nanocomposites in arbitrary patterns with controlled macroscopic alignment to modulate macroscopic properties
III. Understanding of nanocomposite structure-property relationships, taking advantage of the multi-scale architecture

Recent Progress

We have achieved hierarchical assemblies with ordered nanostructure and tunable microstructure by using complex blends containing small molecules, block copolymer-based supramolecules, and nanoparticles/colloidal particles (Figure 1). The mixing entropy in complex blends diversifies the composition of each phase, leads to reduced interfacial interactions and enhanced inter-phase miscibility, and enables long-range cooperativity (Figure 1C). This approach releases multiple long-standing constraints in composite design, such as filler size, specific composition, and strict chemistry requirements. We resolved a long-standing roadblock to incorporate large fillers in the structured polymer matrix. Also, well-defined, uniform assemblies were achieved while accommodating various formulation variables, such as nanoparticle size, small molecule type, small molecule amount, and supramolecule type. This formulation flexibility indicates that increasing a blend's complexity enables it to self-regulate the distribution of each component to accommodate compositional variations without compromising the predictability and fidelity of its self-assemblies. Kinetically, the lack of preferential intermolecular interactions

minimizes diffusion barriers crossing chemically heterogeneous domains, enabling the blends to access tunable microstructures without compromising the order of the nanostructure, expanding the window in which microstructures can be designed and manipulated (Figure 1D).

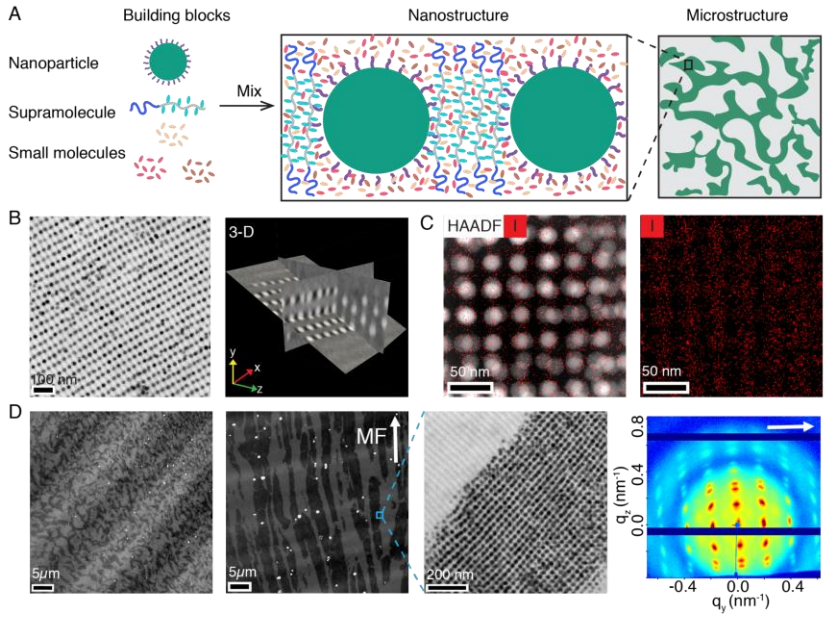

Figure 1. A, Schematic of hierarchical assembly in the complex blends: molecular assembly, ordered nanostructure, and phase-separated microstructure. B, The 3-D ordered nanostructures formed in the complex blends. C, Energy dispersive X-ray spectroscopy (EDS) maps of the element distribution in blends. The high-angle annular dark-field (HAADF) image shows the overall nanostructure. The I map indicates the distribution of iodine-labelled small molecules (red). D, Transmission electron microscopy (TEM) images and 2D small-angle X-ray scattering (SAXS) pattern of the complex blends. The blends can access tunable microstructures without compromising the order of the nanostructure. The arrows indicate the magnetic field (MF) direction.

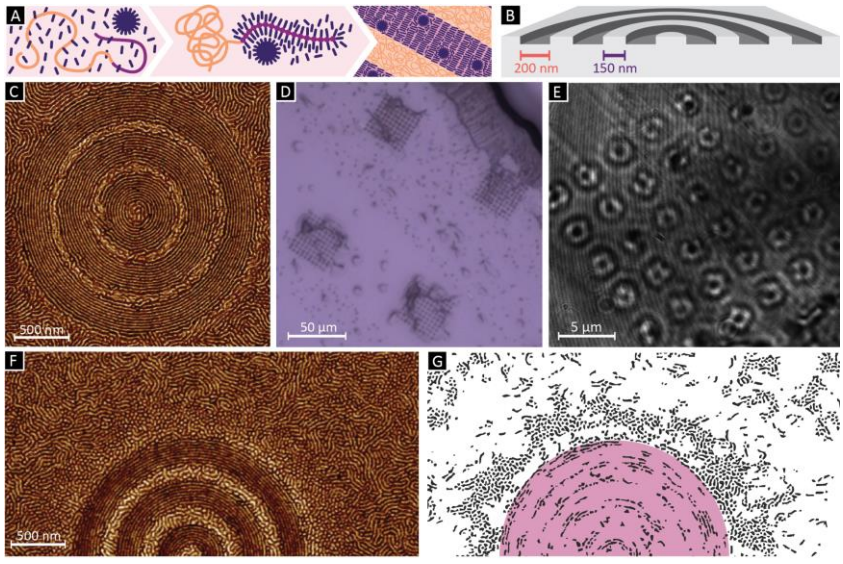

Figure 2. A, Schematic of the polymer, small molecule, and nanoparticle blend. The components first form a supramolecular repeat unit, then the supramolecules line up into cylindrical microdomains. B, Schematic of the lithographically-patterned ring template used for directed self-assembly. C, Representative atomic force microscopy (AFM) micrograph, showing very good alignment of the microdomains with the underlying pattern. D, Optical microscope image of four 10x10 ring arrays produced in parallel. E, Image captured using a charge-coupled device (CCD) demonstrates high-quality OAM generation. F, Lower-magnification AFM image shows that the effect of the template on the thin film extends outward. G, The cylinders-to-spheres morphological transition (spheres colored black) shows that small molecule self-regulation occurs across micron-scale distances, up to 500 nm from the template itself (colored pink).

The same nanocomposite can also be fabricated as a functional thin film coating. Using the principle of directed self-assembly (DSA), wherein the composite's nanoscale features are guided

by a coarse template, we produced concentric rings of nanoparticles with radii spanning 150-1150 nm and ring widths spanning 30-60 nm (Figure 2). When plasmonic nanoparticles were used, ring nanodevice arrays can be fabricated in a single ~10-minute step. As a proof of concept, we successfully fabricated orbital angular momentum (OAM) devices, suitable for applications in communication, particle manipulation, astronomy, imaging, and quantum optics (Figure 2E). Nanocomposite DSA simplifies and streamlines nanofabrication by producing metal structures without etching or deposition steps; it also introduces inter-particle coupling as a new design axis. Detailed analysis of the nanoparticle ring assemblies confirms that the supramolecular system self-regulates the spatial distribution of its components, as described above (Figure 2F-G), and thus exhibits a degree of flexibility absent in simpler blends.

Future Plans

The current studies show the important role of small molecules on self-regulating assembly of organic/inorganic nanocomposites. To further understand the assembly process from the molecular level, we propose using nanoscale Fourier transform infrared spectroscopy (nano-FTIR) to map the small molecule distribution. This technique will also allow us to study the small molecules' interactions with the other components in the blends. Nano-FTIR will enable us to get both the mapping and chemical information with nanoscale spatial resolution [11].

The complex blends show the potential to release current constraints in the composite design and to navigate uncertainties during structure formation over multiple length scales. The biological composites that inspire this work—spider silk, beetle shells, bird feathers, bone, and nacre, among others—all inherit properties from micro- and meso-scale structures. Looking forward, we will push the organic/inorganic nanocomposites to larger length-scales and explore the new functionalities that become available with larger feature sizes. We will also use this extension of our work to establish connections between ordered structures and properties across multiple scales. We plan to access the larger feature sizes by using high molecular weight supramolecules with periodicities of 100s of nm, or incorporating colloidal particles with sizes within the same range. Proof-of-concept studies suggest that the system will comfortably form features within the target size range.

References

[1] J. Kao, P. Bai, V. P. Chuang, Z. Jiang, P. Ercius, and T. Xu, "Nanoparticle Assemblies in Thin Films of Supramolecular Nanocomposites," Nano Lett., 12, 2610–2618, 2012.

[2] J. Kao, K. Thorkelsson, P. Bai, Z. Zhang, C. Sun, and T. Xu, "Rapid Fabrication of Hierarchically Structured Supramolecular Nanocomposite Thin Films in One Minute," Nat. Commun., 5, 1-8, 2014.

[3] J. Kao, S. J. Jeong, Z. Jiang, D. H. Lee, K. Aissou, C. A. Ross, T. P. Russell, T. Xu, T. "Direct 3-D Nanoparticle Assemblies in Thin Films via Topographically Patterned Surfaces. Adv. Mater., 26, 2777–2781, 2014.

[4] J. Kao and T. Xu, "Nanoparticle Assemblies in Supramolecular Nanocomposite Thin Films: Concentration Dependence," J. Am. Chem. Soc.,137, 6356–6365, 2015.

[5] B. Rancatore, B. Kim, C. Mauldin, J. Frechet, T. Xu, "Organic Semiconductor-Containing Supramolecules: Effect of Small Molecule Crystallization and Molecular Packing. Macromolecules, 49, 833-843, 2016.

[6] J. Huang, Y. Xiao, and T. Xu, "Achieving 3-D Nanoparticle Assembly in Nanocomposite Thin Films via Kinetic Control," Macromolecules, 50, 2183–2188, 2017.

[7] K. Evans and T. Xu, "Self-Assembly of Supramolecular Thin Films: Role of Small Molecule and Solvent Vapor Annealing," Macromolecules, 52, 639–648, 2018.

[8] J. Huang, X. Chen, P. Bai, R. Hai, C. Sun, and T. Xu, "45% Periodicity Reduction in Nanocomposite Thin Films via Rapid Solvent Removal," Macromolecules, 52, 1803–1809, 2019.

[9] J. Huang, Y. Qian, K. Evans, and T. Xu, "Diffusion-Dependent Nanoparticle Assembly in Thin Films of Supramolecular Nanocomposites: Effects of Particle Size and Supramolecular Morphology," Macromolecules, 52, 5801-5810, 2019.

[10] H. McNally et al. "Self-assembly of Micro-and Nano-Scale Particles Using Bio-Inspired Events,"Appl. Surf. Sci., 214, 1-4, 2003.

[11] F. Huth, A. Govyadinov, S. Amarie, W. Nuansing, F. Keilmann, and R. Hillenbrand, "Nano-FTIR Absorption Spectroscopy of Molecular Fingerprints at 20 nm Spatial Resolution," Nano Lett., 12, 3973-3978, 2012.

Publications

[1] K. Evans and T. Xu, "Self-Assembly of Supramolecular Thin Films: Role of Small Molecule and Solvent Vapor Annealing," Macromolecules, 52, 639–648, 2018.

[2] J. Huang, X. Chen, P. Bai, R. Hai, C. Sun, and T. Xu, "45% Periodicity Reduction in Nanocomposite Thin Films via Rapid Solvent Removal," Macromolecules, 52, 1803–1809, 2019.

[3] J. Huang, Y. Qian, K. Evans, and T. Xu, "Diffusion-Dependent Nanoparticle Assembly in Thin Films of Supramolecular Nanocomposites: Effects of Particle Size and Supramolecular Morphology," Macromolecules, 52, 5801-5810, 2019.

[4] S. Hsu, and T. Xu. "Tailoring Co-assembly of Nanodiscs and Block Copolymer-Based Supramolecules by Manipulating Interparticle Interactions," Macromolecules, 52, 2833-2842, 2019.

[5] B. S. Chang, L. Ma, M. He, and T. Xu, "NMR Studies of Block Copolymer-Based Supramolecules in Solution," ACS Macro Lett., 9, 1060-1066, 2020.

[6] J. Kwon, K. Evans, L. Ma, D. Arnold, M. E. Yildizdag, T. Zohdi, R. O. Ritchie, and T. Xu, "Scalable Electrically Conductive Spray Coating Based on Block Copolymer Nanocomposites," ACS Appl. Mater. Interfaces, 12, 8687-8694, 2020.

[7] J. Huang, A. Hall, I. Jayapurna, S. Algharbi, V. Ginzburg, and T. Xu, "Nanocomposites Based on Coil-Comb Diblock Copolymers," Macromolecules, 54, 1006-1016, 2021.

[8] E. Vargo, K. Evans, Q. Wang, A. Sattler, Y. Qian, J. Yao, and T. Xu, "Orbital Angular Momentum from Self-Assembled Concentric Nanoparticle Rings," Adv. Mater., in revision.

[9] L. Ma, H. Huang, E. Vargo, J. Huang, C. Anderson, T. Chen, I. Kuzmenko, J. Ilavsky, C.Wang, Y. Liu, P. Ercius, A. Alexander-Katz, and T. Xu, "Diversifying Composition Leads to Hierarchical Composites with Design Flexibility and Structural Fidelity," ACS Nano, submitted.

2D and 3D crystallization of nanoparticles

PI: Ting Xu,

Co-PI: Paul Alivisatos, Yi Liu, Robert Ritchie, Miquel Salmeron, Lin-wang Wang, Jie Yao

Materials Science Division, Lawrence Berkeley National Laboratory

University of California at Berkeley

Program Scope

Controlled crystallization of nanoparticles (NPs) can lead to a new class of functional materials to meet energy needs. Extensive efforts have been devoted to understanding and manipulating assemblies of NPs in 1, 2, and 3-dimensions by chemically modifying ligand chemistry and using external templates. There are still knowledge gap in the initial nucleation process, kinetic control over the crystal growth and hierarchical control over crystal registry from individual atom to macroscopic material. Despite ongoing debates over crystallization pathways, developing a clearer picture of nucleation may help determine the optimal conditions for the effective organization of NPs or lead to new strategies that can accelerate the rate of nucleation and as a result avoid the formation of undesired amorphous forms and obtain the final product in a timely and reproducible manner. Using NPs with alkyl ligands and grafted polymers, we aim to understand the key effects of NP shape, size, and surface modification on the effective interactions and structures of NPs and kinetically control the formation and growth pathway of NP crystals.

Recent Progress

1. Crystallization of nanoparticles induced by precipitation of trace polymeric additives

While the initial stages of the nucleation process are still open to debate, it is commonly accepted that the critical nucleus size depends on the balance between the NP/solvent interfacial interactions and the NP/NP cohesive energy stored within the nucleus. Nuclei are energetically stable at elevated NP concentrations and/or with strong ligand interactions. To achieve highly-ordered NP crystals, adequate system mobility must be maintained during the assembly process. The NP mobility scales inversely with the NP concentration and the strength of the ligand pair interactions. Precipitating agents have been used to drive and accelerate the crystallization of small molecules and proteins and may lead to control over the assembly kinetics and pathway. We hypothesize that by introducing polymers with poor solubility, NP surfaces may be the preferred precipitating sites and the adsorbed polymers gradually change the NP surface chemistry. To minimize non-favorable NP-solvent interactions, NPs form small clusters, which subsequently act as nuclei to initiate NP crystallization within a dilute solution (**Fig. 1a**). Given sufficient NP mobility, rapid NP crystallization is realized, and the more attractive ligand-ligand interactions lead to desorption of the polymer precipitates to achieve a high degree of crystalline order.

We test this hypothesis and experimentally realize polymer precipitation-induced crystallization of polymer-grafted nanoparticles (PGNPs). 3-D PGNP clusters can be obtained rapidly (in a few to tens of minutes) using a range of polymers, including impurities from plastic containers. The polymeric precipitants indeed lead to small PGNP clusters with poor local order. These clusters subsequently grow into large 3-D PGNP crystals. Detailed tomography analysis of a 3-D PGNP crystal with single particle resolution confirms the presence of defects and reduced positional order

of NPs at the surfaces and edges, suggesting rather weak cohesive energy and slow local NP diffusion. This precipitating additive approach is facile where the PGNP crystal formation depends on polymeric additive loading, solvent evaporation rate, PGNP size and nucleation sites. As an example, a patterned substrate is used to grow hierarchically-ordered arrays of PGNP crystals with controlled size, location and orientation. This study elucidates how to balance cohesive energy density and NP diffusivity to simultaneously favor nuclei formation energetically and kinetic growth in dilute solutions to rapidly crystalize NPs over multiple length scales. Furthermore, the amount of impurities needed to grow NP crystals (<0.1%) reminds us of the importance of fine details to interpret experimental observations in nanoscience.

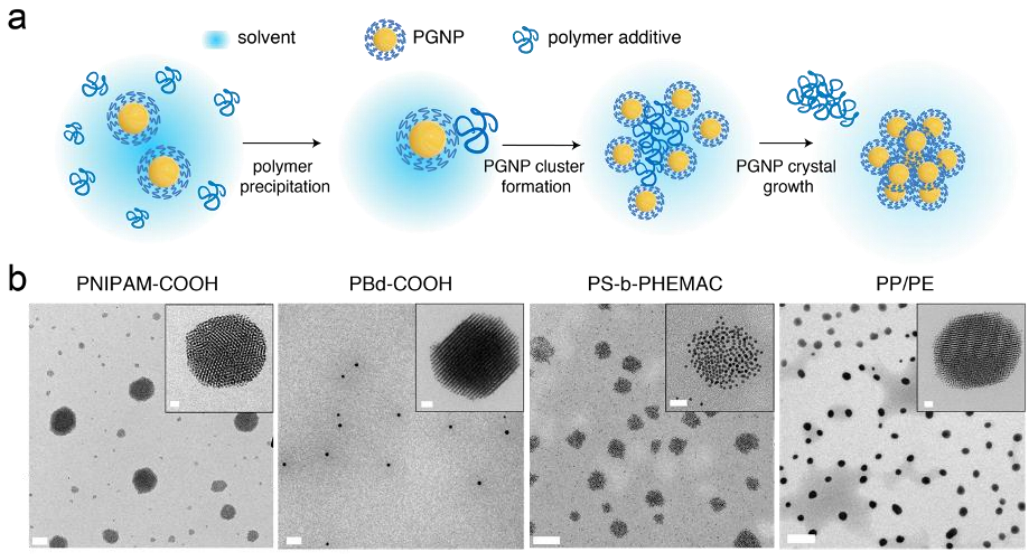

Figure 1. Polymer precipitation induced PGNP crystallization in solution during solvent evaporation. a) Schematic of polymer precipitant-induced PGNP crystallization: the added polymers precipitate onto PGNP surfaces to form small PGNP clusters that grow into crystals. b) TEM images of PGNP assemblies of Au-PS NPs with various polymer precipitants.

2. Hierarchical NP crystals with atomic registry

Extensive work has been done showing that NPs can behave as artificial atoms, and as such, form superlattices with different crystal structures and packing densities[1–2]. However, though ordered superlattices present a relatively high degree of long-range positional order, the relative crystallographic orientation of the nanocrystals with respect to each other tends to be random. In this work, we show that orientational alignment can be achieved by synthesizing low-symmetry faceted NPs, shown in Figure 2a (inset). The 2D superlattices were self-assembled at liquid-air interfaces which allows the NPs to freely orient and align facet-to-facet during the early stages of the self-assembly. As the packing density increases, we found that the NPs lock-in their alignment with their first neighbor and become frustrated when other NPs come in proximity; thus, forcing them to shift their orientations. This frustrated crystallization resulted in a phase referred to as orientational glass by which only distinct orientations were possible. The wide-angle Selected-Area Electron Diffraction (SAED) in Figure 2b shows distinct spots in the lattice planes. A typical randomly oriented nanocrystals in a 2D superlattice form rings in the wide-angle SAED as shown in Figure 2c.

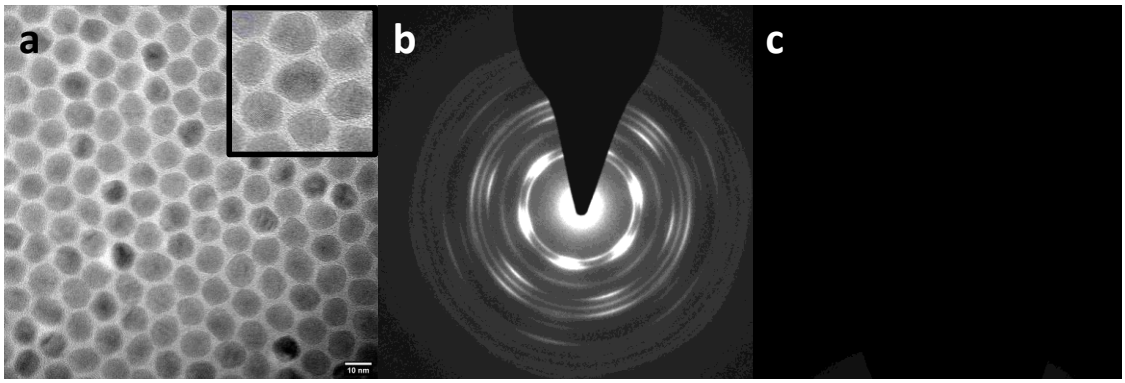

Figure 2. a) TEM image of self-assembled QD NP superlattice (inset. high-resolution TEM). Wide angle Selected-Area Electron Diffraction (SAED) pattern of b) oriented NPs showing clear preferential crystallographic alignment, c) randomly oriented NPs showing a typical ring pattern.

Future Plans

Our findings provide new systems for investigations of new NP crystal phases and their mechanism of formation. Further understanding of the NP crystallization behavior will bring us closer to the full potential of NP-based materials. Future plans include the following aims:

1. Using nano-FTIR to elucidate the polymer-induced NP crystallization mechanism.

   Combing several control experiments and energy considerations, the process of polymer-induced NP crystallization has been proposed. However, experimentally validating the mechanism requires advanced techniques with the ability to perform in-situ chemical characterization to understand the influence of polymer on NP surface. Using a new methodology based on Fourier transform infrared nanospectroscopy (nano-FTIR)[3], the studies of the molecular structure of NP-polymer interfaces with nanoscale spatial resolution will be enabled. Additionally, the monitoring of local polymer-included NP nucleation and crystallization can be realized in order to provide a comprehensive understanding of NP-polymer interactions.

2. Further exploration of the key effects of different NP parameters towards a full understanding of NP crystallization behavior.

   The ability to modulate the position, orientation, and interparticle spacing of NPs, as well as the symmetry of the assembled structures, is of great interest for applications in electronics, photonics, and magnetics. In order to achieve the full potential of NP-based applications, further understanding of the NP crystallization behavior is required. Effects of different parameters such as polymer chemistry, ligand grafting density and NP sizes will be further explored.

3. Constructing functionally useful binary superlattices with structural engineerability.

   Recent advances in NP assembly suggest that far broader structural engineerability of superlattices, as is required for tuning collective properties and for building a theoretical framework, is possible. Polymeric ligands have been used beneficially to expand the

structural diversity of NP superlattices[4]. Here, the use of polymeric ligands for building binary NP superlattices with tunable symmetries and interparticle distances will be further explored. Construction of complex, ordered, and functionally useful mesoscopic and macroscopic materials will be enabled using binary NP systems. For example, using optically active NP combinations will allow the study of the energy and electron transfer[5-6], providing insights into the effect of orientation and ordering on improving the transfer rate.

References

1. Redl, F.X., Cho, K.S., Murray, C.B. and O'Brien, S. Three-dimensional binary superlattices of magnetic nanocrystals and semiconductor quantum dots. Nature, 423(6943), 968-971 (2003).
2. Nykypanchuk, D., Maye, M. M., van der Lelie, D. & Gang, O. DNA-guided crystallization of colloidal nanoparticles. Nature 451, 549–552 (2008).
3. Lu, Y.H., Larson, J.M., Baskin, A., Zhao, X., Ashby, P.D., Prendergast, D., Bechtel, H.A., Kostecki, R. and Salmeron, M. Infrared nanospectroscopy at the graphene–electrolyte interface. Nano letters, 19(8), 5388-5393 (2019).
4. Ye, X., Zhu, C., Ercius, P., Raja, S.N., He, B., Jones, M.R., Hauwiller, M.R., Liu, Y., Xu, T. and Alivisatos, A.P., Structural diversity in binary superlattices self-assembled from polymer-grafted nanocrystals. Nat. Commun. 6, 10052 (2015).
5. Rainò, G. et al. Superfluorescence from lead halide perovskite quantum dot superlattices. Nature 563, 671–675 (2018).
6. Cherniukh, I., Rainò, G., Stöferle, T., Burian, M., Travesset, A., Naumenko, D., Amenitsch, H., Erni, R., Mahrt, R.F., Bodnarchuk, M.I. and Kovalenko, M.V. Perovskite-type superlattices from lead halide perovskite nanocubes. Nature, 593, 535-542 (2021).

Publications

Qian, Y., Da Silva, A., Yu, E., Anderson, C.L., Liu, Y., Theis, W., Ercius, P. and Xu, T. Crystallization of nanoparticles induced by precipitation of trace polymeric additives. Nature communications, 12(1),1-8 (2021).

Kinetically Controlled Synthesis of Metastable Nitride Materials

Andriy Zakutayev, National Renewable Energy Laboratory

Program Scope

The objective of this program is to understand selective synthesis of new metastable yet long-lived nitride materials with desired structure and useful properties. This program aims to answer the following scientific question: "*how to synthesize metastable materials by surpassing kinetic energy barriers under non-equilibrium conditions*?". The hypothesis is that metastable ternary nitrides can be obtained by a kinetically controlled synthesis approach (**Fig.1a**)—through intermediate energy states that are structurally or compositionally related to the metastable product. The approach consists of two kinetically controlled synthesis methods: 1) cation-exchange reactions controlled by composition; and 2) crystallization from atomically dispersed precursors controlled by structure. The most important expected outcome of this program is a fundamental understanding of non-equilibrium kinetically controlled synthesis pathways for nitrides and other inorganic materials chemistries. In addition, this program is expected to discover new nitride materials through precise control of composition and structure, which could impact energy-relevant applications including more efficient light-emitting diodes, better superconducting qubits, energy-efficient data storage, and new magnetic materials.

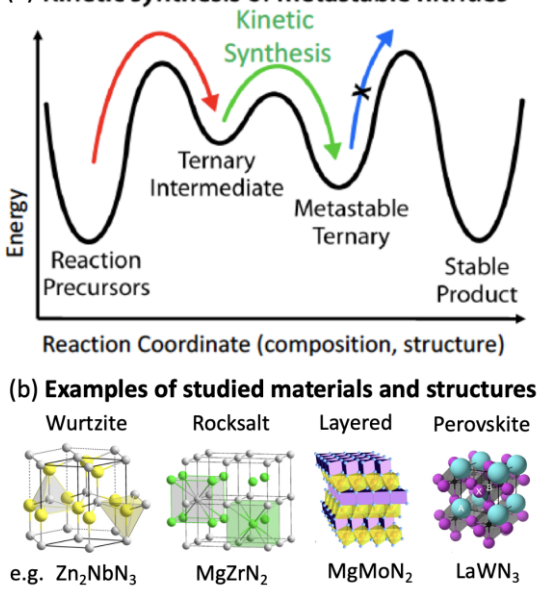

Fig.1 Program scope: (a) kinetically controlled synthesis of metastable nitrides, using nucleation of disordered precursors and cation exchange reactions; (b) examples of materials and crystal structures synthesized in the past two years of this program.

Examples of nitride materials (**Fig.1b**) studied in the first two years of the program include wurtzite-derived structures (Zn_2NbN_3, $MgSnN_2$, $(ZnSnN_2)_{1-x}(ZnO)_{2x}$ and $Al_{1-x}Sc_xN$ alloys), rocksalt-derived structures ($MgZrN_2$, Mg_2NbN_3, ZrN), layered materials ($MgMoN_2$, $ZnZrN_2$, SbN), and perovskites (e.g. $LaWN_3$). Below we present a few examples of recent advances in each of these materials classes, highting their relevance to the topic of kinetically controlled synthesis of metastable nitride materials using crystallization from atomically dispersed precursors and cation-exchange reactions.

Recent Progress

Wurtzite structures: This program synthesized a new Zn_2NbN_3 ternary nitride semiconductor using a two-step approach that consists of room-temperature deposition and rapid thermal annealing up to 500-600ºC [1], which can be also used for other ternary nitrides. The resulting thermodynamically stable material (**Fig.2a**) has distorted wurtzite-derived crystal structure (c/a=1.55) and wide band gap (E_g=2.1 eV) typical of wurtzite ferroelectric materials. To increase the synthesis temperature, this program developed AlN protection layers that prevent side reactions of nitride thin films with the substrate and the atmosphere during nucleation from amorphous precursors [2]. These diffusion barriers and capping layers increase thermal stability of the test-case ZrN thin films up to 1200ºC (**Fig.2b**), which can be used for capturing metastable phases during crystallization, and for nitride coatings in extreme environments. In addition, this program collaborated with other projects on experimental synthesis of $MgSnN_2$ semiconductors in wurtzite and rocksalt crystal structures [11], and the perfectly short-range ordered alloy with line-compound-like properties in the $(ZnSnN_2)_{1-x}(ZnO)_{2x}$ material system [12].

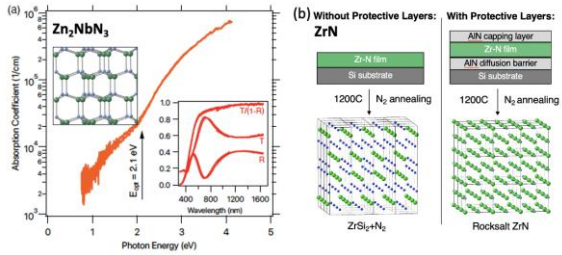

Fig.2. Wurtzite structures: (a) crystal structure and optical absorption of Zn_2NbN_3 [1], (b) XRD patterns of Zr-N films with different protection layers [2]

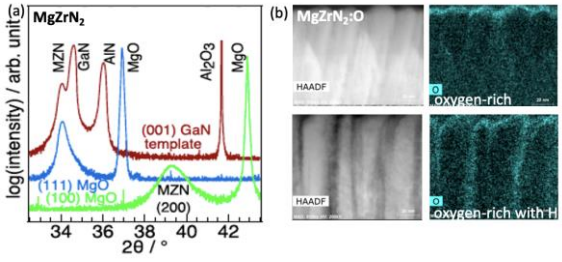

Fig.3 Rocksalt structures: (a) Epitaxial growth of $MgZrN_2$ on various crystal substrates [9], (b) Influence of O_2, H_2 on $MgZrN_2$ microstructure [10]

***Rocksalt structures*:** This program demonstrated epitaxial growth of single-crystal $MgZrN_2$ thin films on (100) and (111) MgO substrates, and (001) GaN/Al_2O_3 templates [9]. $MgZrN_2$ crystallizes in a rocksalt-derived structure with Mg/Zr disorder on cation sub-lattice despite single-crystal epitaxial character of the layers (**Fig.3a**), indicating that crystallinity is not correlated with cation ordering. To investigate the role of unintentional impurities during the synthesis, this program measured structural, optical and electrical properties of $Mg_{1+x}Zr_{1-x}N_2$ thin films synthesized by sputtering with a wide range of cation compositions in the presence of oxygen and hydrogen [10]. Surprisingly, excess oxygen improved crystallinity of $Mg_{1+x}Zr_{1-x}N_2$ thin films according to 2-3x larger XRD peak intensity, and hydrogen attracted oxygen to Mg-rich grain boundaries (**Fig.3b**) leading to reduction in electrical conductivity. In addition, this program synthesized bulk powder $MgZrN_2$ and related Mg_2NbN_3 ternary nitride products (**Fig.4a**) with $MgCl_2$ byproduct (washed away), starting from a mixed anion nitrogen source Mg_2NCl and $ZrCl_4$ or $NbCl_5$ as a precursor [3]. These experiments demonstrate a route to bulk synthesis of other ternary nitrides under relatively mild conditions (up to 800-900ºC).

Layered structures: This program synthesized several ternary nitride materials with layered 2D-like crystal structures in addition to the 3D-like wurtzites and rocksalts described above. For example, bulk powder $MgMoN_2$ with layered hexagonal crystal structure (**Fig.4a**) was synthesized by a two-step reaction, where the second higher-temperature step (800-900ºC) crystalizes the ternary product and the first lower-temperature step (300-400ºC) leads to Mg-Mo-N bond formation as indicated by calorimetry measurements [3]. In contrast to this bulk $MgMoN_2$ powder with octahedral Mg and trigonal prismatic Mo, the $MgMoN_2$ thin films without Mg and Mo cation ordering but with a similar hexagonal structure are synthesized. Thin film synthesis is achieved by a two-step process, with ambient temperature deposition of a disordered cubic rocksalt structure, and transformation to a more ordered hexagonal structure at >700ºC annealing temperature. This program also synthesized $Zn_{1+x}Zr_{1-x}N_2$ thin films with metastable layered BN-derived structure (**Fig.4b**) [4], rather than the stable 'wurtsalt' structure with alternating wurtzite and rocksalt layers predicted in collaboration with other project. This program also experimentally observed a computationally predicted layered metastable SbN transient phase using *in-situ* X-ray diffraction during rapid thermal annealing. [5]

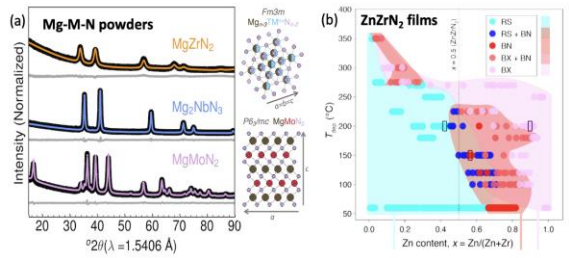

Fig.4. Layered structures: (a) XRD refinement of 3 Mg-M-N bulk powders including $MgMoN_2$ [3], (b) non-equilibrium synthesis diagram of $ZnZrN_2$ [4]

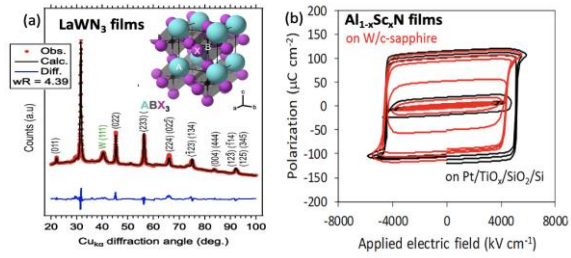

Fig.5. Perovskites and ferroelectrics: (a) XRD of the first nitride perovskite $LaWN_3$ [9], (b) polarization loops of ferroelectric metastable $Al_{1-x}Sc_xN$ alloys [10]

Perovskites and ferroelectrics: Beyond the scope of Zn-M-N and Mg-M-N materials in primary focus on this program, we used kinetically-controlled synthesis approaches developed here to synthesize several other ternary nitride materials. For example, we used crystallization from atomically dispersed precursors to synthesize polar $LaWN_3$ (**Fig.5a**) - the first oxygen-free nitride perovskite with non-centrosymmetric crystal structure and large piezoelectric response [9]. The crystallization pathway and energetics are studied by a combination of X-ray diffraction and pair distribution function at different stages of rapid thermal annealing, and by in-situ nanocalorimetry measurements as a function of synthesis temperature. These $LaWN_3$ nitride perovskite studies have been inspired by recent breakthrough reports of ferroelectric switching in metastable $Al_{1-x}Sc_xN$ nitride alloys of interest to energy-efficient non-volatile ferroelectric memory. This program, in collaboraiton with other projects, demonstrated epitaxial thin films of metastable $Al_{1-x}Sc_xN$ alloys (**Fig.5b**) with 0.4 ± 0.3 MV/cm smaller coercive field due to 0.01 ± 0.007 Å smaller c-axis lattice constant [6], and used in-situ optical emission spectrometry during synthesis to understand the importance of nucleation conditions on subsequent growth of these metastable $Al_{1-x}Sc_xN$ alloys [7].

Future Plans

In the future, this program will continue experiments aimed to understand selective synthesis of new metastable nitride materials with desired structure, transition the focus to structural control of material properties, and expand the kinetically controlled synthesis approach to other classes of solid-state inorganic materials. The activities planned for the next two years include:

- Synthesize high energy polymorphs of $ZnZrN_2$, Zn_2NbN_3, $ZnMoN_2$ by cation exchange from $MgZrN_2$, Mg_2NbN_3, $MgMoN_2$ and compare their properties to ground state structures.

- Measure structural transformation from disordered to ordered form in $MgMoN_2$ and MoN, and collaborate with theoretical groups to get atomistic insights into the transformation pathways.

- Characterize structural and stability trends as a function of cation composition in the Mg-M-N and Zn-M-N class of ternary nitride materials.

- Use multi-step kinetically-controlled synthesis approaches developed here to synthesize other families of ternary nitride materials such as perovskites and fluorites.

- Expand the range of synthesis conditions for the Mg-M-N and Zn-M-N bulk ternary nitrides, and develop new synthesis routes to RE-M-N bulk nitride perovskites and fluorites.

- Discover new nitride ferroelectric by understanding which short-range features or long-range motifs that enable ferroelectric switching in $Al_{1-x}Sc_xN$ alloys.

- Transfer kinetically controlled synthesis lessons from ternary nitride materials to other 'softer' chemistries such as phosphides or sulfides.

- Demonstrate other functionality of new ternary nitride materials, for example in quantum, photoelectrochemical, magnetic, detector, or communication applications.

In addition, this program will work to foster research community in solid state chemistry of nitride materials, by organizing a research symposium at an international conference, publishing a book chapter on nitride materials, and writing review articles about solid state chemistry of metastable nitrides.

Publications

Note: publications are listed in reverse chronological order for the first 2 years of this program

[1] Synthesis of Zn_2NbN_3 ternary nitride semiconductor with wurtzite-derived crystal structure, Zakutayev, A.* *Journal of Physics: Condensed Matter* (2021) DOI: 10.1088/1361-648X/abfab3

[2] Influence of Protection Layers on Thermal Stability of Nitride Thin Films, Zakutayev, A*. Perkins, C.L*., Physica status solidi (RRL)–Rapid Research Letters* (2021) DOI: 10.1002/pssr.202100178

[3] Two-step bulk solid-state synthesis of ternary magnesium metal nitrides, Todd, P.K., Zakutayev, A.,* *(under review) arXiv:2106.09752* (2021)

[4] The role of disorder in the synthesis of metastable ternary nitrides, Woods-Robinson, R., Stevanović, V., Lany, S., Heinselman, K., Persson, K.A., Zakutayev, A.* *(under review) arXiv:2012.12455* (2021)

[5] Synthesis of Computationally Predicted Metastable Phase of Antimony Nitride using Rapid Thermal Annealing and *in situ* X-ray Diffraction, Chen, B.-R., Lany S., Kelly, L.L., Iguchi Y., Arca, A., Perkins J.D., Yanagi Y., Toney, M. F., Schelhas, L.T., Zakutayev A.* *(under review)*

[6] Reduced coercive field in epitaxial thin film of ferroelectric wurtzite $Al_{0.7}Sc_{0.3}N$, Yazawa, K., 7rury, D., Zakutayev, A., Brennecka, G. L. *Applied Physics Letters*, *118*(16), 162903 (2021)

[7] Understanding Reproducibility of Sputter-Deposited Metastable Ferroelectric Wurtzite $Al_{0.6}Sc_{0.4}N$ Films Using In Situ Optical Emission Spectrometry, Drury, D., Yazawa, K., Mis, A., Talley, K., Zakutayev, A., Brennecka, G. L. *Physica Status Solidi (RRL)–Rapid Research Letters*, 2100043 (2021).

[9]. Synthesis of polar $LaWN_3$ - the first nitride perovskite, Talley, K.R., Perkins, C.L., Diercks, D.R., Brennecka, G.L., Zakutayev, A.*, *(under review),* arXiv:2001.00633 (2021)

[9]. Epitaxial growth of rock salt $MgZrN_2$ semiconductors on MgO and GaN, Bauers, S.R., Mangum, J., Harvey, S.P., Perkins, J.D., Gorman, B., Zakutayev, A.*, *Applied Physics Letters*, 116 102102 (2020)

[10] Influence of hydrogen and oxygen on the structure and properties of sputtered magnesium zirconium oxynitride thin films, Kim, J., Bauers, S.R., Khan, I.S., Perkins, J.D., Park, B.I., Talley, K.R., Kim, D., Zakutayev, A.*, Shin, B., *Journal of Materials Chemistry A* 8 9364 (2020)

[11]. Combinatorial synthesis of magnesium tin nitride semiconductors Greenaway, A.L., Loutris, A., Heinselman, K.N., Melamed, C.L., Schnepf, R.R., Tellekamp, M.B., Woods-Robinson, R., Sherbondy, R., Bardgett, D.J., Bauers, S.R., Zakutayev, A., Christensen S. T., Lany. S., Tamboli A. C., *Journal of the American Chemical Society* 142 8421 (2020)

[12] Perfect short-range ordered alloy with line-compound-like properties in the $ZnSnN_2$:ZnO system, Pan, J., Cordell, J., Tucker, G., Zakutayev, A., Tamboli, A., Lany S., *npj Computational Material* 6 63 (2020)

UNIVERSITY GRANT PROJECTS

Understanding Flow Cell Porous Electrodes as Active Materials for Electrochemical Transformations

Michael Aziz, Shmuel Rubinstein, Jennifer Lewis, Christopher Rycroft
Harvard John A. Paulson School of Engineering and Applied Sciences, Cambridge MA

Program Scope

The objective of this program is to understand the porous electrode of a flow battery, fuel cell, electrolyzer or desalination system, filled with flowing active fluid, as an active composite material. Currently, porous electrodes are predominantly optimized for a given application in the absence of a fundamental understanding of their structure-function relationship across a range of length scales and geometries. We view the electrolyte-filled porous electrode as analogous to human muscle tissue, which is permeated by branching capillaries that enable tissue function by transporting reactants into and products out of the organ. This analogy opens new avenues for scientific investigation, which will lead to the design of novel structures of porous materials with unprecedented functionality.

We are pursuing a hypothesis-driven research program that advances our basic understanding of flow cell porous electrodes in three directions and connects them in an iterative design cycle. (1) In the first direction, we systematically vary the microstructural features of macroscopically homogeneous porous electrodes and quantify their influence on mass and charge transport processes. (2) With this resulting insight, the second direction develops new computational and analytical models to describe the behavior of these materials across multiple length scales. (3) The third direction creates new porous electrode structures with hierarchical architectures that exhibit functionality unattainable in macroscopically homogeneous electrodes. This iterative process — structure variation, modeling and characterization — will be carried out to ultimately yield a deep mechanistic as well as phenomenological understanding of structure-function relationships in active porous matter.

Our approach takes advantage of the unique fabrication, characterization, and computation capabilities of our team. Fundamental questions are formulated and tested to probe the effects of a particular structural feature and length scale on mass and charge transport within these electrodes. Using an extrusion-based 3D printing method, known as direct ink writing, electrode structures composed of periodic mesoscale lattices are fabricated, as well as those with programmed types and strengths of heterogeneities, or hierarchies across multiple length scales. We are developing new sub-pore-scale 4D electrolyte concentration and velocity field mapping techniques using time-resolved fluorescence microscopy. Numerical solutions to multiphysics governing equations (i.e., flow, diffusion, migration, advection, electrochemical conversion, conduction) at the fiber and pore scale are generated using a new method that we have pioneered,

which permits large scale multiphysics simulations at fine spatial resolution. Precise measurements of electrochemical potential and pressure drop, as well as concentration and velocity fields, are to be used iteratively with the multiphysics simulations in a validation regimen. Informed by the results, new mesoscale models are to be developed for describing transformations in porous electrodes; for example, a reliable mesoscale description of power dissipation from viscous flow, ohmic resistance to ionic and electronic conduction, and Faradaic overpotentials based on statistical information about the microstructure. Hierarchical electrode structures are to be designed, fabricated, and characterized based on the lessons learned.

This research program will lead to a deep fundamental understanding of electrolyte-filled porous electrodes. The insights gained will enable the flow cell community to design high-performance electrodes from the bottom up, based solely on knowledge of the physical, chemical, and electrochemical properties of redox electrolytes. Ultimately, this will lead to higher efficiencies and power densities, reduced costs, and increased competitiveness of electrochemical devices that rely on electrolyte-filled porous electrodes. The development of novel hierarchical porous electrodes is likely to have broader applications as yet unexplored.

Recent Progress

Fabrication

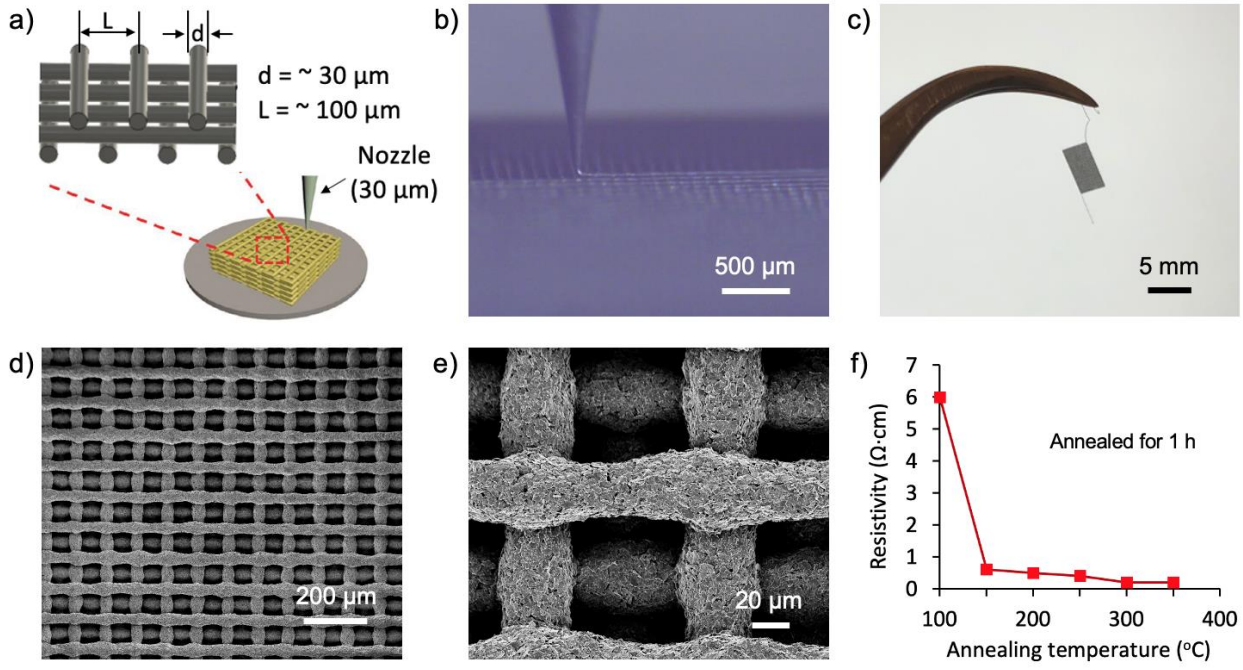

Figure 1: 3D graphene electrodes for redox flow batteries. (a) Schematic illustration of 3D electrode assembly via direct ink writing (DIW). (b) Optical image of a representative 3D graphene (GP) electrode printed by extruding a GP ink through a tapered nozzle (30 µm in diameter). (c) Optical image of the free-standing GP lattice. (d)-(e) SEM images of the free-standing GP lattices at low and high magnification, respectively. (f) Electrical resistivity measured on cast GP films annealed for 1 h at varying temperatures.

(i) 3D graphene (GP) electrodes: Direct ink writing (DIW) enables the fabrication of 3D battery electrodes with controllable porosity and distribution by engineering center-to-center filament diameter, spacing, and number of printed layers (**Fig. 1a**). First, we developed a method for producing highly concentrated graphene (GP) inks using GP particles (3 μm in diameter) as a conductive filler, thermosetting polyurethane (TPU) as a flexible and stretchable binder, and organic solvents. 3D GP electrodes were produced by extruding the GP-based ink through a 30-μm nozzle onto a glass substrate coated with a sacrificial (release) layer (**Fig. 1b**). Free-standing GP lattices (3 mm × 6 mm, 7 layers) were obtained after heat treatment at 90 ^{o}C for 12 h, followed by dissolving the sacrificial layer (**Fig. 1c**). SEM images reveal that these GP lattices contain spanning filaments (30 μm in diameter) with center-to-center spacing of ~100 μm (**Fig. 1d, e**). Electrical resistivity of cast GP films was 6 Ω·cm after annealing at 100 ^{o}C for 1 h, which decreased by ~ 30× upon increasing the annealing temperature to 400 ^{o}C (**Fig. 1f**).

(ii) 3D metal-coated graphene electrodes: The GP electrodes, when annealed to reach low enough resistance for electrochemical studies, became too brittle to be handled in electrochemical cells. To create mechanically robust 3D electrodes with low electrical resistance (~ 10 Ω), we uniformly coated the GP lattices using electroless nickel deposition followed by gold electroplating (**Fig. 2a**). Upon optimizing this two-step process, the electrical resistance of the 3D metal-coated GP lattices was reduced by five orders of magnitude compared to pure graphene lattices (**Fig. 2b-c**). These conductive lattice-based electrodes exhibited an electrical resistance as low as 5 Ω after electroless nickel plating at 65 ^{o}C for 10 min, followed by gold electroplating at 37 ^{o}C for 10 min (**Fig. 2d**). A thin gold layer (~ 2 μm thick) with grain size of ~1 μm was conformally deposited on the underlying 3D GP lattice (**Fig. 2e-f**). These 3D composite electrodes are now being used to investigate the flow behavior and electrochemical properties of redox flow cells.

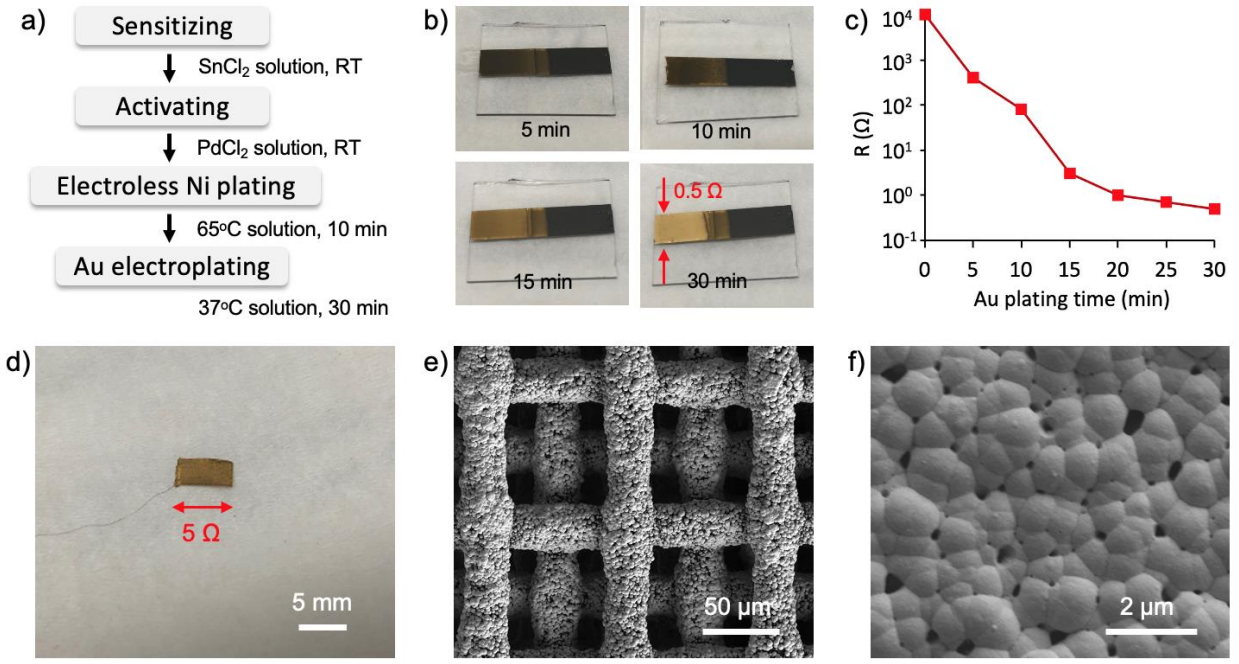

Figure 2: 3D metal-coated graphene electrodes for redox flow batteries. (a) Processing steps used to create conductive, metal-coated GP lattices. (b) Optical images and (c) electrical resistance of cast graphene films as a function of gold electroplating time. (d) Optical image of the 3D GP lattice after Au electroplating for 30 min. (e-f) SEM images of the metal-coated graphene lattices at low and high magnification, respectively.

(iii) 3D metal-coated, indium tin oxide (ITO) electrodes: To reduce the surface roughness of these 3D printed electrodes, we developed an indium thin oxide (ITO) ink composed of Sn/Pd-activated ITO nanoparticles (80 nm diameter) as a conductive filler, a thermosetting polyurethane (TPU) as a binder, and organic solvents. The ITO ink can be readily printed through 30-μm nozzles without clogging (**Fig. 3a**). The as-printed ITO electrodes exhibit an electrical resistance as high as 1 MΩ. To reduce the resistance to ~5 Ω, these 3D lattices were conformally coated via electroless nickel deposition at 65 °C for 10 min followed by gold electroplating at 37 °C for 10 min (**Fig. 3b-c**). These 3D metal-coated ITO lattices possess smoother surfaces compared to their graphene-based counterparts (**Fig. 3d-e**). The total thickness of these 3D lattices is approximately 140 μm (**Fig. 3f**). Experiments are underway to evaluate the effects of 3D metal-coated ITO electrodes on the flow behavior and electrochemical performance of redox flow batteries.

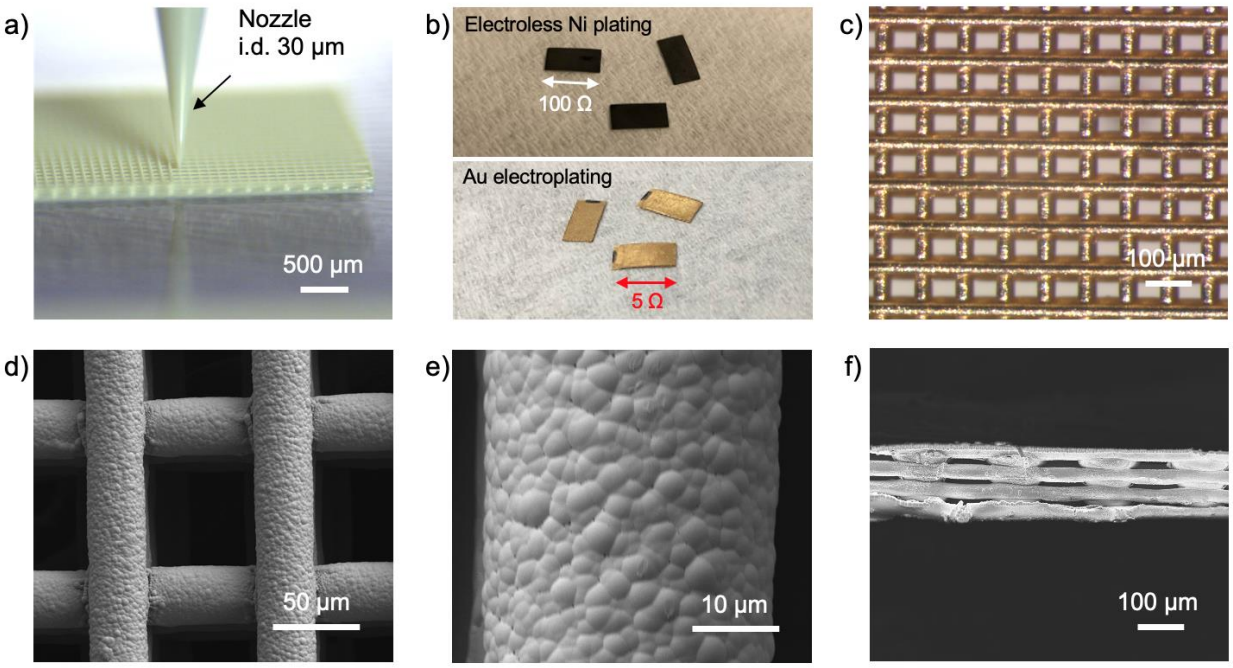

Figure 3: 3D metal-coated ITO electrodes for redox flow batteries. (a) Optical image of a representative 3D ITO electrode printed by extruding an ITO ink through a tapered nozzle (30 μm diameter). (b) Optical images of 3D ITO lattices after electroless nickel deposition (top) and gold electroplating (bottom). (c) High magnification optical image of a 3D metal-coated ITO lattice. (d-e) SEM images of a representative 3D metal-coated ITO lattice at low and high magnification, respectively. (f) SEM image of a 3D metal-coated ITO lattice (edge-on view). The SEM images in (d) and (f) reveal that these lattices contain interconnected pore channels in all three directions.

Characterization

i) 2D direct visualization of electrochemical reactions and fluid flow in operating commercial porous electrodes: We used 2D wide-field fluorescence microscopy coupled with electrochemistry to directly observe the reaction and transport of redox-active molecules within porous carbon electrodes during flow cell operation [1]. Studying several commercial porous electrodes, we observed surprisingly heterogeneous electrolyte channeling features (**Fig. 4**) at length scales an order of magnitude greater than the ~50 μm characteristic pore size, leading to spatially distinguishable advection-dominated and diffusion-dominated regions within each electrode. These results challenge the common assumption that transport in porous electrodes can be modeled by a homogenous, mean-field, Darcy-like permeability, as embodied by the Newman porous-electrode model – particularly at the length scales relevant to many electrochemical

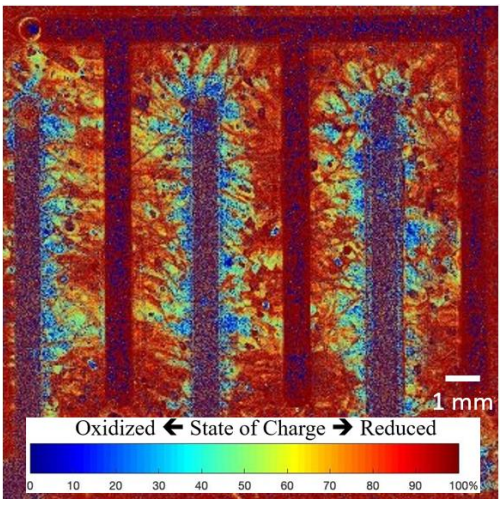

Figure 4: Steady-state reaction-flow map of AQDS reduction to H_2AQDS in a commercial electrode across the full 2-cm^2 interdigitated flow field. Electrolyte flows from inlet channels (blue, running up from manifold at bottom hidden by color scale) through porous carbon paper across ribs and exits via top manifold channels through hole in upper left.

systems such as flow batteries. This recently-published work introduces the research community to a new platform to provide highly resolved spatial and temporal insight into electrolyte reactions and transport behavior within porous electrodes.

ii) Fabrication of a miniature electrochemical cell for 3D fluorescence mapping of the SOC: we designed and built a microfluidic-based electrochemical cell (**Fig. 5a**) to accommodate and test 3D-printed electrodes with a small size (**Fig. 5b**). The channels for the electrolyte were designed and made directly on PDMS, which is UV transparent and commonly used in microfluidic devices, enabling us to image the electrode with a confocal microscope. The microfluidic-based cell provided several other benefits. Keeping the electrodes intact during cell compression and sealing was crucial because 3D printing the electrode structures is very time-consuming. Because PDMS is soft, it reduced the tendency to fracture the 3D-printed electrodes, which would adversely affect the flow hydrodynamics and electrical current distribution. Additionally, it allowed us to design to

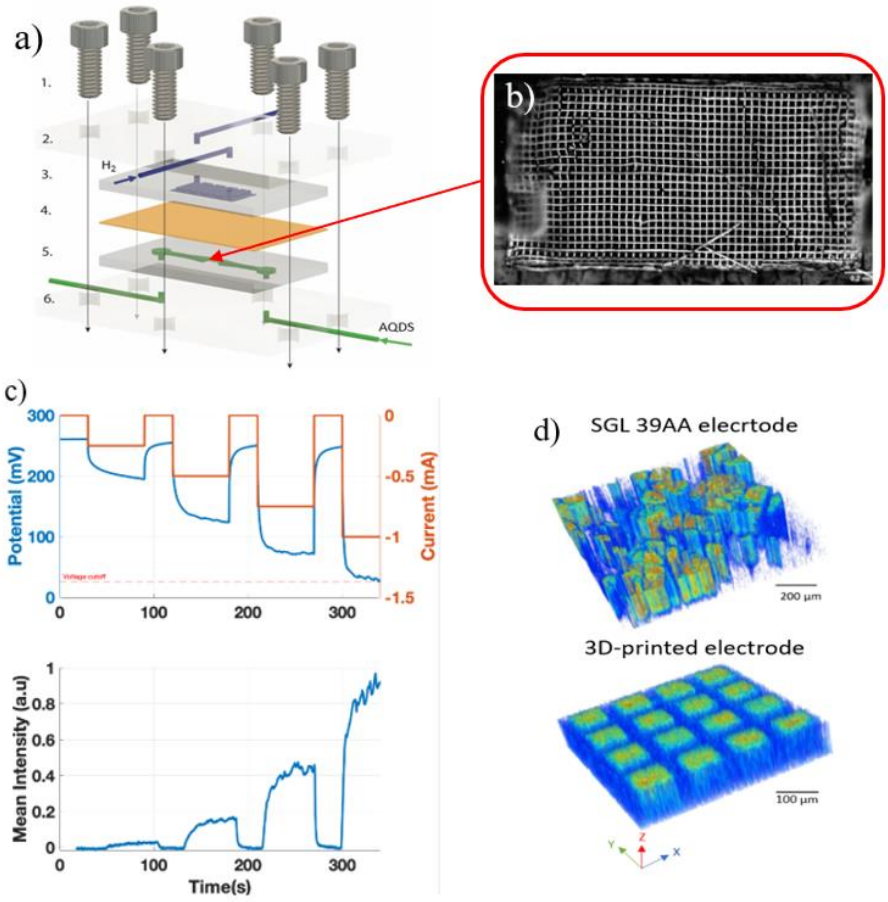

Figure 5. Schematic diagrams illustrating **(a)** Computer-aided design drawing of the electrochemical cell (numbered parts are: 1. Screws, 2. H_2 side acrylic plate, 3. PDMS with flow channel and electrode design for H_2 side, 4. membrane, 5 and 6. PDMS and acrylic parts for the AQDS side). **(b)** Wide-field microscopy snapshot of the 3D-printed electrode with a dimension of 3 mm x 6 mm x100 µm placed in the cell. **(c)** Top plot: result of a transient galvanostatic experiment at various applied currents for the 3D-printed electrode at a flow rate chosen to provide a sufficient residence time for the electrochemical reaction of AQDS. The applied current was set back to zero prior to an increase to a greater (negative) value in order to assure that the cell responded to the changes as expected. Bottom plot: simultaneous measurement of the average fluorescence intensity, which is proportional to the reduced AQDS concentration, as the electrochemical reaction proceeded. ***(d)*** 3D mapping of the steady state concentration of the reduced AQDS at a constant applied current and flow rate. Blue and red color represent the lowest and highest intensities. Top and bottom plots show the results for commercial and 3D-printed electrodes, respectively. The ion-conducting membrane is on the top surface of each electrode.

high precision the position of the electrode on PDMS with techniques including photolithography or 3D printing. The PDMS flow cell is made from a 3D printed master, enabling extremely fast design iteration and flexibility.

iii) Development of confocal in-operando fluorescence imaging over three spatial dimensions: After developing the miniature electrochemical cell, electrochemical tests with 3D-printed and commercially available SGL39AA electrodes were performed. The commercial electrode is useful for an initial assessment of the differences between a fully disordered fiber structure and the fully ordered, 3D-printed structure. Simultaneously with electrochemical measurements, the intensity of fluorescent light emitted from $AQDSH_2$, the electroactive species used for characterization purposes, was detected over time and three spatial dimensions (4D imaging) using a spinning-disk confocal microscope. The electrochemical and fluorescence signals are shown in **Fig. 5c**, allowing us to correlate features in the growth of the average fluorescence intensity with the temporal history of the current. **Fig. 5d** shows one visualization of the 3D concentration fields of the reduced form in two different electrodes at a steady-state condition. The results of **Fig. 5d** demonstrate that the 3D printed electrode offers a more uniform distribution of reduced species compared to that for the commercial electrode. The significance of this observation will be developed through quantitative analysis of the SOC distribution in the porous electrode and comparison with simulations, to be discussed next.

Modeling

i) General phenomena associated with the electrode geometry. To gain insight into the role of disorder, we initially performed a study on a simplified (2D) model system consisting of 10-micron diameter parallel cylinders arranged in different configurations, with flow normal to the cylinder axes. As shown in **Fig. 6**, structures with same porosity and surface area can give rise to vastly different flow and electrochemical behavior, underscoring the need for more sophisticated structural descriptors. Mass transport limitations (i.e. fuel starvation) are evident in configurations with higher density closer to the walls, where flow is slower. In one case (top structure), the two length scales along the flow direction allow for replenishing of the reactant in between the dense regions where reaction occurs. Substantial mixing and flow redirection is also observed in randomly placed cylinders of uniform diameter. Different operating conditions and arrangements with different porosity have also been investigated. Ongoing structural characterization of our simulated configurations will allow the identification of structure-property relationships. Similar investigations will be then performed for (more complex) 3D fiber geometries.

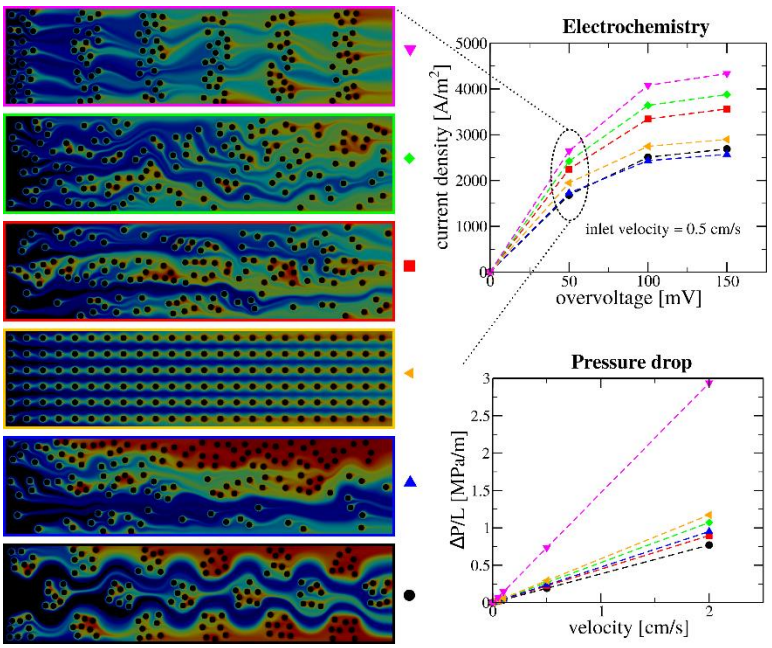

Figure 6. Left: snapshots showing the state of charge (from blue to red, from 0% to 100%) for different arrangements of the same number of parallel cylinders in a 2D simulation. The systems are confined between two walls and are under the same operating conditions. The membrane is located at the bottom, the flow is left to right, and a constant potential is applied to the solid. **Right:** Quantification of the electrochemical and flow behavior of the different configurations. Larger current is generated in the top configuration, at the cost of a larger pressure drop.

ii) Investigation of experimentally realizable lattices. The 3D-printed lattices represent a unique platform to investigate the different ways of redirecting the flow and their effect on the electrochemical performance. Several of the concepts we identified looking at the behavior of 2D disordered structures can be readily investigated by appropriately designing the lattices (**Fig. 7a**). Notably, the 3D-printed cylinders can span distances of tens of diameters, i.e. a few hundreds of microns, making the design space extremely rich. We first performed 2D simulations, investigating the effects of arranging parallel cylinders across the flow direction, which already highlighted non-trivial behavior (**Fig. 7b**). For example, we observed that removing beams (i.e. introducing vacancies) in the ordered array prevents the shadowing effect on the downstream material, which is therefore exposed to a larger amount of reactant compared to the complete array. This results in extracting more current from a structure with less surface area.

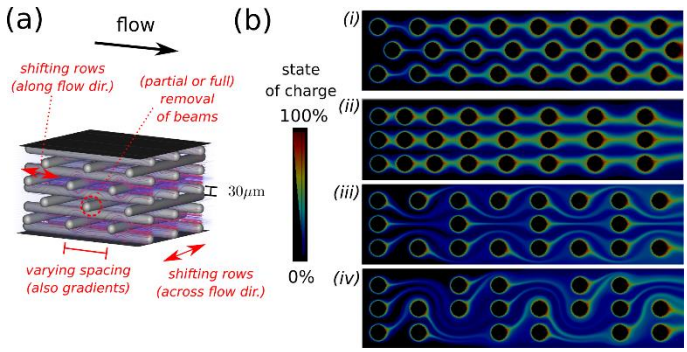

Figure 7 (a) Design space of the 3D-printed lattices. (b) Simulation snapshots showing the concentration profile when (i) one array of beam is shifted, (ii) there is a gradient in lattice spacing, (iii) vacancies are introduced in the middle of the channel, or (iv) at the boundary walls. In the last two examples, redirecting the flow prevents shadowing and allows a higher reaction rate in the downstream material. As a result, a larger current can be extracted despite a reduced surface area ("less is more").

We have now moved to 3D simulations (**Fig. 8**) to investigate how additional flow effects associated with the third dimension, and additional variations in the fibers aligned along the flow direction, can change the observed trends among structures. In this way, we are also able to better capture the impact of geometrical features peculiar to the 3D lattices (e.g. a bottom layer composed of hemispherical beams, because the structure is printed on a substrate, resulting in a symmetry-breaking of the flow and higher mass density close to the membrane wall). Synergistic collaboration with the experimental colleagues will further unveil the impact of geometry on the flow field and electrochemical performance under various operating conditions.

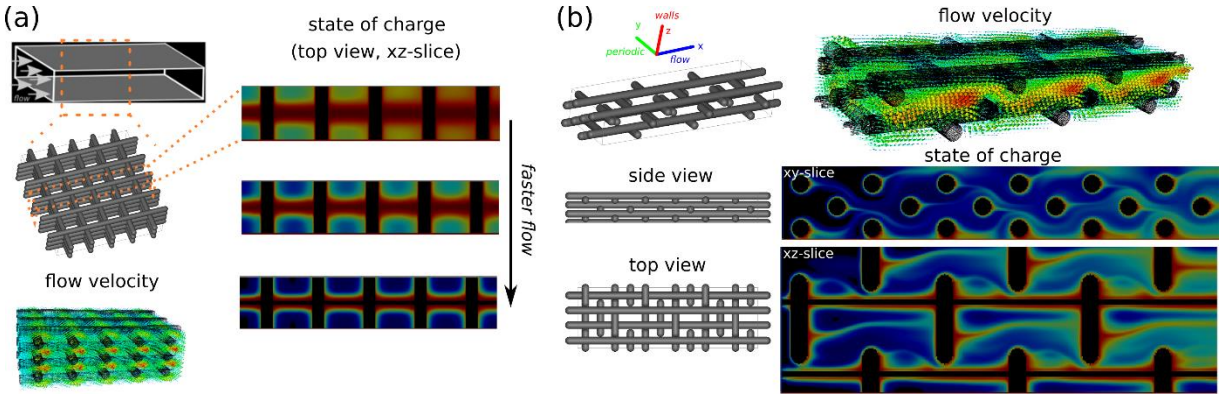

Figure 8 (a) Example of 3D simulations in similar geometries to the experimental specimens. In addition to the flow field, the concentration profile in a region of the periodic lattice is shown. When the flow is faster, the concentration profile becomes narrower, reflecting the relative increase in advective transport compared to diffusive transport. (b) More complex flow and concentration patterns can be obtained when shifting rows of cylinders (both across and along the flow direction) and partially removing (or shortening) some of the cylinders perpendicular to the flow direction.

Future Plans

Fabrication

The fabrication effort is now focused on systematically varying 3D printed electrode geometry and filament size, spacing, and surface roughness in order to understand their effects on the flow and electrochemical behavior in coordination with the other efforts.

Characterization

In the characterization effort, we plan to improve our depth resolution for determining the local concentration of fluorescing species in the Z-direction (through plane). This improvement in resolution is essential for quantitative measurements of SOC and velocity fields at scales approaching that of the fibers in three dimensions. Achieving this requires the use of microscope objectives with higher magnifications, higher numerical apertures, and a smaller depth of field. These objectives require a short working distance, whereas our current cell has a relatively thick transparent base. To resolve the scales of the fibers in three dimensions, we will design and fabricate a new electrochemical cell made of PDMS to be compatible with a very short working

distance of the microscope objective (~2.5 mm). Additionally, a confocal microscope with smaller pinholes on the spinning disk will be utilized to improve image resolution in the Z-direction. This change, however, comes at the cost of blocking more fluorescence light, diminishing the signal intensity. To cope with the challenge, elevated concentrations of the redox-active species will be investigated to reach a sufficiently strong fluorescence. Furthermore, because the 3D printed electrodes are opaque, preventing us from obtaining information behind the fibers, designs with misaligned fibers will be investigated to ameliorate the problem. Finally, in order to simultaneously evaluate hydrodynamics and electrochemistry, fluorescent tracer particles will be added to the electrolyte containing electroactive species so that we can perform Particle Imaging Velocimetry as the electrochemical reaction proceeds. These developments are expected to lead to imaging of the SOC and velocity fields with high accuracy and resolution over three spatial and one temporal dimension. In coordination with the fabrication and modeling efforts, this will permit the validation of the simulation results and, subsequently, the development of new mesoscale models for transformations in porous electrodes that rely on statistical information about the electrode structure.

Modeling

The modelling effort will move forward along the two parallel directions described above: (i) by leveraging the possibility of simulating many disordered structures in 2D, we will establish structure-property relationships that look at different structural parameters, going beyond the simple use of porosity and surface area as descriptors (e.g. looking at spatial correlations between pores). The identified trends will be subsequently tested in 3D simulations; (ii) we will work closely with the rest of the DOE-BES team by suggesting interesting structures and variations to print and comparing simulation results with results of the electrochemistry and imaging experiments.

References

[1] A.A. Wong, S.M. Rubinstein and M.J. Aziz, “Direct visualization of electrochemical reactions and heterogeneous transport within porous electrodes *in operando* by fluorescence microscopy” *Cell Reports Phys. Sci.* **2021**, 100388; https://doi.org/10.1016/j.xcrp.2021.100388

Publications

A.A. Wong, S.M. Rubinstein and M.J. Aziz, “Direct visualization of electrochemical reactions and heterogeneous transport within porous electrodes *in operando* by fluorescence microscopy” *Cell Reports Phys. Sci.* **2021**, 100388; https://doi.org/10.1016/j.xcrp.2021.100388

Bimolecular Interactions in Organic Semiconductors: Hot Charge, Hot Excitons, Efficiency Droop, and Instability

M.A. Baldo, ***Dept. of Electrical Engineering and Computer Science, MIT***
T. Van Voorhis, ***Dept. of Chemistry, MIT***

Program Scope

The poor stability of blue OLEDs is arguably the most important problem in modern organic semiconductor technologies. It is also a mortal threat to the viability of OLED-based solid state lighting. Perhaps the most serious consequence is its impact on efficiency. Indeed, if blue stability was solved, the application of state-of-the-art phosphorescent materials[1] would increase[2] the quantum efficiency for blue emission by a factor of 4, doubling the power efficiency of white OLEDs, and allowing this technology to reach the DOE target of 150lm/W.

The absence of stable blue emitters comes after more than 10 years of intensive materials development in industry. This work was remarkably successful in green and red, and the creation of an entirely new market based on organic semiconductors is testament to the power of repeated iterations of material synthesis and commercial stability tests. On the other hand, the failure of this approach in blue suggests that there may be fundamental challenges underlying the performance of blue light emitters.

Color	CIE	Efficiency (cd/A)	T95 (hours)
Red	(0.64,0.36)	30	50,000
Green	(0.31,0.63)	85	18,000
Light Blue	(0.18,0.42)	50	700

Figure 1. A comparison of commercial performance and lifetime data for phosphorescent OLEDs operating at 1000 cd/m^2. From Universal Display Corporation (2012).

Recent Progress

The relatively short lifetime of blue OLEDs has been widely regarded as a chemical degradation problem that is specific to every combination of materials. In recent work we have demonstrated that there are general physical principles that determine the stability of OLEDs, and that stability can be engineered via photonic design. Fundamentally, the degradation rate is controlled by the energy density within a device. A key component is the lifetime of triplet excited states, which is experimentally isolated and systematically varied, yielding up to a 1000-fold improvement in photostability for a 7-fold change in exciton lifetime, corresponding to a cubic dependence. The dominant role of triplet exciton

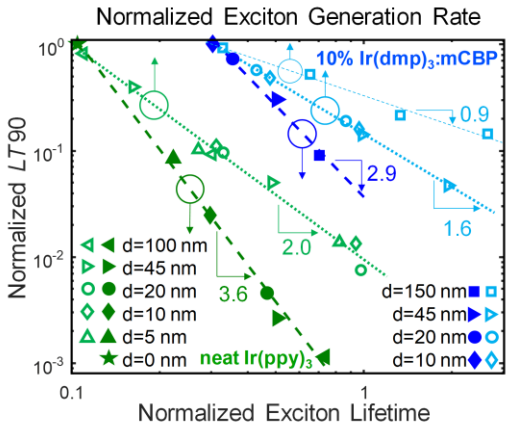

Figure 2. The stability in both green and blue systems as a function of the generation rate of triplet excitons, G, and the triplet exciton lifetime, τ. Note the strong power law dependence on exciton lifetime. Baldo, Van Voorhis, *et al.* Adv. Opt. Materials 2019.

lifetime suggests that the performance of the best OLED materials can be further improved by engineering the device structure for rapid extraction of the energy stored in triplet excitons.

As an alternative to reducing the triplet lifetime in blue phosphorescent materials, we are also considering schemes that rely on triplet-triplet annihilation, which generates one blue fluorescent excited state from two triplets with half the energy. Because the triplets in this scheme have very low energy, the stability of the device is inherently better. Indeed, commercial blue OLEDs presently use this approach.

The downside of triplet-triplet annihilation, however, is its relatively poor efficiency. The annihilation process limits the quantum yield (photons out/electrons in) to 50% at most, although the operating voltage can be correspondingly smaller. But more seriously, not all triplet annihilation events result in an emissive singlet exciton. Because the combination of two triplets has total spin 2, there is also the possibility to generate triplets and quintets in the process, both of which can cause losses.

We have studied the fundamental 'spin statistical limit' of the triplet-triplet annihilation process in order to identify schemes that might increase performance. The fundamental nature of the problem is relevant to applications beyond organic light emitting devices. Triplet fusion based photon upconversion holds promise for a wide range of applications, from photovoltaics to bioimaging.

In recent work, we have shown that the tailorability and highly porous structure of metal-organic frameworks (MOFs) can be used to minimize intertriplet exchange coupling and engineer effective spin mixing between singlet and quintet triplet-triplet pair states. We demonstrate singlet-quintet coupling in a pyrene-based MOF, NU-1000. An anomalous magnetic field effect is observed from NU-1000 corresponding to an induced resonance between singlet and quintet states that yields an increased fusion rate at room temperature under a relatively low applied magnetic field of 0.14 T. By engineering singlet-quintet resonances, the fundamental efficiency limit of triplet-triplet annihilation processes can be increased by 40% to 80%. Our results suggest that MOFs offer particular promise for engineering the spin dynamics of multi-excitonic processes and improving their upconversion performance.

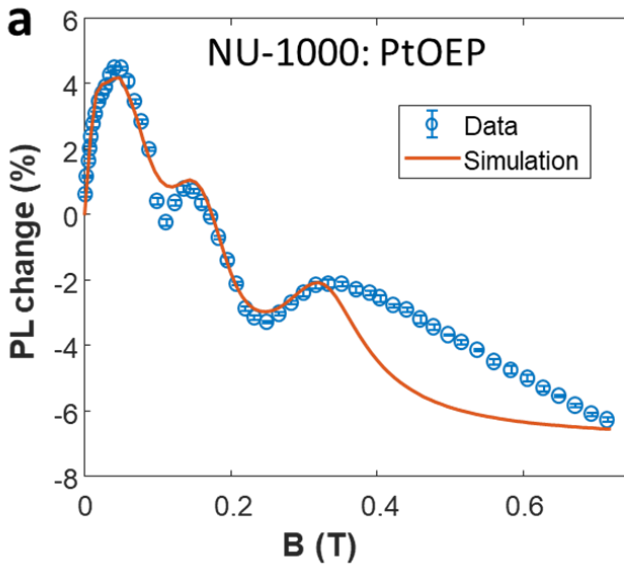

Figure 3. The anomalous magnetic field dependence of triplet-triplet annihilation in a metal organic framework demonstrates singlet-quintet resonances at room temperature under weak magnetic fields. Such resonances can be engineered to double the efficiency limit of light emission in these systems. Baldo, Van Voorhis, Dinca, *et al.* unpublished.

Future Plans

The precise structural design that is enabled by metal organic frameworks offers a promising new pathway for experimental probes of multiexciton behavior that crucially underpins the performance of soldi state lighting and solar conversion systems. For example, the two metal organic frameworks below employ the same organic ligand, but in different crystal structures.

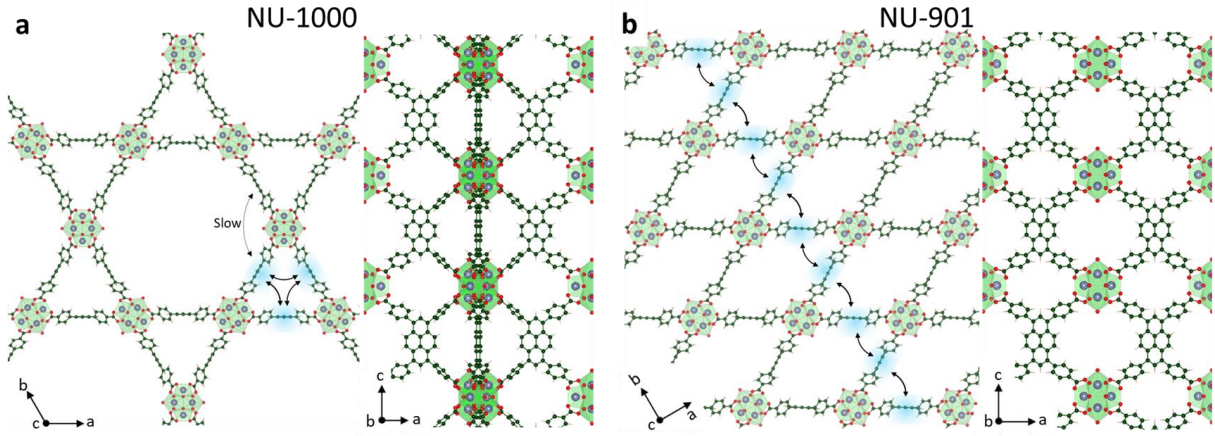

Figure 4. Chemical structure of (a) NU-1000, (b) NU-901, showing different exciton diffusion pathways enabled by the structure. Baldo, Van Voorhis, Dinca, *et al.* unpublished.

In the first, triplet excited states are confined and localized in the a-b plane. But in the second, triplets can diffuse along the b axis. The difference in structure yields dramatically different photophysical behavior, with no evidence of resonances in NU-901. We intend to further develop this approach, building on other recent work, where we have introduced a new growth technique for large single crystals of π-conjugated MOFs[3].

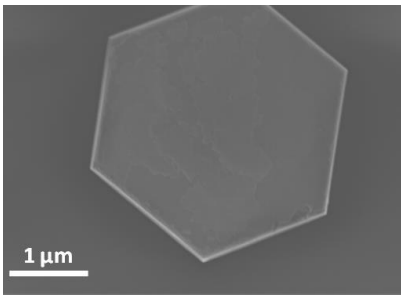

Figure 5. Single crystals of Ni-CAT-1 grown using our solution-solid growth technique. [3]

References

1. M. A. Baldo, D. F. O'Brien, Y. You, A. Shoustikov, S. Sibley, M. E. Thompson, S. R. Forrest, High efficiency phosphorescent emission from organic electroluminescent devices. *Nature* **395**, 151-154 (1998).
2. M. A. Baldo, D. F. O'Brien, M. E. Thompson, S. R. Forrest, The excitonic singlet-triplet ratio in a semiconducting organic thin film. *Physical Review B* **60**, 14422-14428 (1999).
3. Dong-Gwang Ha, Mehdi Rezaee, Yimo Han, Saima Siddiqui, Robert Day, Lilia Xie, Brian Modtland, David Muller, Jing Kong, Philip Kim, Mircea Dinca, and Marc Baldo,Large single crystals of a two-dimensional pi-conjugated metal-organic framework via biphasic solution-solid growth, *ACS Central Science*, **7**, 124, 2021.

Publications

1. Nanocrystal-Sensitzed Infrared-to-Visible Upconversion in a Microcavity under Subsolar Flux, Mengfei Wu, Ting-An Lin, Jan Tiepelt, Vladimir Bulovic, and Marc Baldo, Nano Letters, **21**, 1011, 2021.

2. Large single crystals of a two-dimensional pi-conjugated metal-organic framework via biphasic solution-solid growth, Dong-Gwang Ha, Mehdi Rezaee, Yimo Han, Saima Siddiqui, Robert Day, Lilia Xie, Brian Modtland, David Muller, Jing Kong, Philip Kim, Mircea Dinca, and Marc Baldo, ACS Central Science, **7**, 124, 2021.

3. Investigation of External Quantum Efficiency Roll-Off in OLEDs Using the Mean-Field Steady-State Kinetic Model, Alexandra McIsaac, Valerie Wellborn, Markus Einzinger, Nadav Geva, Hayley Weir, Marc Baldo, and Troy Van Voorhis, Journal of Physical Chemistry C, **124**, 14424, 2020.

4. Strategies for High-Performance Solid-State Triplet-Triplet-Annihilation-Based Photon Upconversion, Ting-An Lin, Collin Perkinson, and Marc Baldo, Advanced Materials, **32**, 1908175, 2020.

5. Toward Prediction of Nonradiative Decay Pathways in Organic Compounds II: Two Internal Conversion Channels in BODIPYs, Zhou Lin, Alexander W. Kohn, and Troy Van Voorhis. Journal of Physical Chemistry C. **124**, 3925, 2020.

6. Lock-and-Key Exciplexes for Thermally Activated Delayed Fluorescence. Constantin Voll, Georgios Markopoulos, Tony Wu, Matthew Welborn, Jens Engelhart, Sebastien Rochat, Grace Han, Graham Sazama, Ting-An Lin, Troy Van Voorhis, Marc Baldo and Timothy Swager, Organic Materials, **2**, 1, 2020.

7. Dominance of Exciton Lifetime in the Stability of Phosphorescent Dyes, Dong-Gwang Ha, Jan Tiepelt, Michael Fusella, Michael Weaver, Julie Brown, Markus Einzinger, Michelle Sherrott, Troy Van Voorhis, Nicholas Thompson, and Marc Baldo, Advanced Optical Materials, **7**, 1901048, 2019.

8. Extracting Design Princtiples for Efficient Thermally-Activated Delayed Fluorescene (TADF) from Simple Four-State Model, Piort de Silva, Changhae Kim, Tianyu Zhu, and Troy Van Voorhis, Chemistry of Materials, **31**, 6995, 2019.

9. Toward Prediction of Nonradiative Decay Pathways in Organic Compounds I: The Case of Naphthalene Quantum Yields, Alexander Kohn, Zhou Lin, and Troy Van Voorhis, **123**, 15394, 2019.

10. Unraveleing the Fate of Host Excitons in Host-Guest Phosphorescent Organic Light-Emitting Diodes, Tianyu Zhu, and Troy Van Voorhis, Journal of Physical Chemistry C, **123**, 10311, 2019.

Solid-State Chemistry of Novel Pnictides with Complex Structures

Svilen Bobev
Department of Chemistry and Biochemistry, University of Delaware, Newark DE 19716

Program Scope

Our research program is focused on the synthetic and structural work on novel materials, stepping up the research efforts in the creation of new crystalline forms of matter for energy production and conversion. The discoveries from our research are expected to be an important part in the development of new materials/technologies for thermoelectric waste heat recovery. From a more fundamental point of view, the structure-property relationships derived from our work can be used for developing a rationale for the synthesis of new compounds, as well as for tuning of properties of existing ones. The "final product" of our research, naturally, is ascertaining the connection among the synthesis, crystal structure, and properties, and by doing so, building up the predictive power of solid-state chemistry (still in its infancy compared to the other chemical disciplines), establishing new ideas of why and how Nature allows atoms to assemble and form new compounds and structures.

Recent Progress

In the last two decades, compounds from a somewhat forgotten class have emerged as superb candidate-materials for thermoelectric (*TE*) applications, the so called Zintl phases.[1–14] Without giving a full overview of the history of Zintl phases within the context of thermoelectrics, we will briefly mention here the poster child—the *p*-type material $Yb_{14}MnSb_{11}$,[1] where all of the *phonon-glass elecron-crystal* requirements seem to be met—and as a result, has become known as "*a substance with substantially higher figure of merit than any other competing compounds, braking more than a decade-long stagnation in high-temperature thermoelectric power generation*". Its discovery has been widely considered as a *"paradigm-shifting"*, and is credited for *"opening a new class of thermoelectric materials*."[5,6] This poorly metallic compound has a very complex structure, and a remarkably low thermal conductivity (Figure 1), which is retained as the PF is optimized. Following the observation of high *zT* (higher than 1.2 at 1200 K) in properly tuned $Yb_{14}MnSb_{11}$, many of its derivatives have been studied to date.[14] Several other pnictide-based systems (pnictides is a generalized term for phosphides, arsenides, antimonides and bismuthides), specifically the ones with

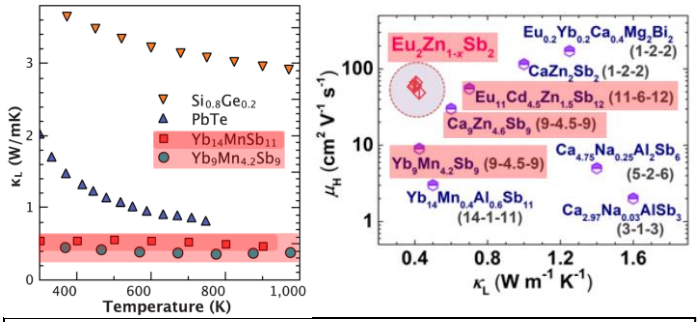

Figure 1. The exceptionally low lattice thermal conductivity of some Zintl phases. Compounds in highlights, like $Eu_2Zn_{1-x}Sb_2$, $Yb_9Mn_{4+x}Sb_9$, $Eu_{11}Zn_6Sb_{12}$, $Ca_9Zn_{4+x}Sb_9$ have been originally discovered in our laboratory.

similarly complex structures and multifaceted chemical bonding have also been found to show great promise (Figure 2). Our group, among several other teams working in this field, has published many papers on new Zintl phases, and has demonstrated that their structures can be rationally modified so that the charge- and heat-transport properties can be brought to optimal levels. This extensive prior research has established that the electronegative constituents in complex pnictides are usually bound tightly through strong covalent interactions to form polyanionic chains, layers, or networks, whereas the interactions between cations and anions are more ionic than covalent in character. This provides almost unlimited potential for alterations on the cation sites and fine-tuning of the transport properties without changing the polyanionic backbone of the structure, which is believed to contribute to the low lattice thermal conductivity.

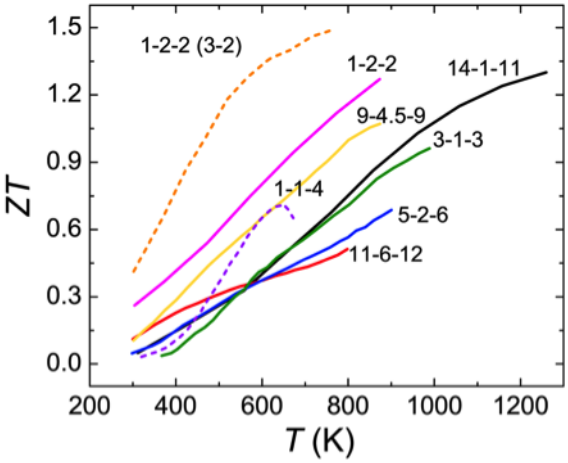

Figure 2. Figure of merit *ZT* of several types of pnictides, mostly antimonides and bismuthides that have piqued the attention of the *TE* community. The compounds are identified with their nominal stoichiometries, i.e., 11-6-12 stands for $Eu_{11}Cd_6Sb_{12}$. While the plotted *ZT* values are not from our studies, much of the ground-breaking synthetic and structural work for the given examples has origins in our laboratories.

Several compounds synthesized and structurally characterized for the first time by us, have already been shown to be susceptible to tuning of the carrier concentration. Importantly, this happens without major disruptions of the electron mobility, which is the driving force behind the ongoing, by other teams, optimizations that can lead to enhancements of the already promising *zT*.

Five years ago, we proposed to use rare-earth metals (*RE*) to modulate the structure and properties of $Ca_{14}MnSb_{11}$, a close analog of $Yb_{14}MnSb_{11}$.[1] In terms of the Zintl-Klemm concept, the $Ca_{14}MnSb_{11}$ structure can be rationalized as consisting of 14 Ca^{2+} cations, and three types of anions—the $[MnSb_4]^{10-}$ tetrahedral species, four isolated $[Sb]^{3-}$ anions and $[Sb_3]^{7-}$. It is one-electron short of the ideal number valence electrons (the $AlBi_4$-tetrahedra bear 9– charge, while $MnSb_4$ are 10–). As a result, $Ca_{14}MnSb_{11}$, as well as the "star" *TE* material $Yb_{14}MnSb_{11}$, do not have the perfect Zintl electron count, which could be the main reason why all measured $Yb_{14}MnSb_{11}$ samples show *p*-type behavior. The resulting electron deficiency in such compounds containing Mn and other divalent M^{2+} metals can be lifted by electron doping, driving the system toward semiconducting state. For example, partial substitution of Mn by Al in $Yb_{14}Mn_{1-x}Al_xSb_{11}$ leads to a decrease of the carrier concentration resulting in an enhanced *zT*. Analogous approach is the replacing of one divalent Ca^{2+} or Yb^{2+} with one trivalent RE^{3+} cation—it also provides a way for reducing the holes concentration in "14–1–11" phases. The solid solutions $Yb_{14-x}RE_xMnSb_{11}$ (*RE* = Pr, Sm; $x \approx 0.2$–0.6) have been studied in the past and shown to display electrical resistivity that is higher than that of the pristine $Yb_{14}MnSb_{11}$. An added benefit of the introduction of rare-earth metals

into this system, besides the prospects for achieving charge balance, concerns the many new opportunities to diversify the crystal chemistry; bringing f-electrons into the picture could also offer new, exciting ways to tune the "14–1–11" systems.

The approach described on the previous page proved very successful. We predicated our synthetic work on two main considerations: 1) the atoms size matches—evidently, there will be an optimal space-filling when the sizes of the "parent" and the "foreign" cations are comparable. Based on the above, we speculated that the compounds that would have the strongest "desire" to achieve charge balance might be those where early rare-earths are used, since they are the largest cations from the lanthanide family, and their ionic radii match closely the radius of Ca^{2+}.[15]

Early exploratory work in the *RE*–Ca–Mn–Sb and *RE*–Ca–Mn–Bi systems validated these suppositions. According to the formal electron count presented above, a substitution of one full Ca^{2+} cation (per formula unit) by an RE^{3+} cation should recover the electron-balanced Zintl composition. This was shown to be the case for the $Ca_{14-x}RE_xMnSb_{11}$ (*RE* = La–Nd, Sm; $x \approx 1$) series, where bulk $Ca_{13}REMnSb_{11}$ samples were prepared and demonstrated to have intrinsic semiconducting properties. Switching to Bi, the series $Ca_{14-x}RE_xMnBi_{11}$ were obtained for *RE* = La–Nd, Sm, and Gd–Ho with $x \approx 0.8$–0.6. The structural analysis showed that higher substitution levels ($x \approx 1$) can be also achieved, but increasing the nominal *RE*/Ca ratio in the reaction mixture, under the reaction conditions, leads to the inevitable formation of the unwanted side phases *RE*Bi and RE_4Bi_3.

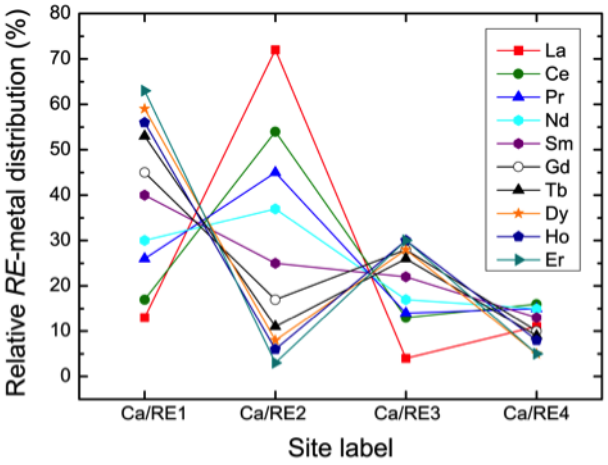

Figure 3. Relative distribution of the rare-earth metals among the four independent Ca sites in the crystal structure of $Ca_{14-x}RE_xMnBi_{11}$ ($x \approx 0.6$–0.8). Although the total rare-earth metal content is slightly lower, compared to the $Ca_{14-x}RE_xMnSb_{11}$ ($x \approx 1$) series, the trends in the occupancies are mirrored.

There are four crystallographically distinct Ca positions in the structure. All Ca atoms are six-fold coordinated by Bi (from neighboring Bi^{3-} and Bi_3^{7-} units), adopting distorted octahedral environment. The average Ca–Bi distances in $Ca_{14}MnBi_{11}$ are 3.261 Å, 3.417 Å, 3.296 Å, and 3.374 Å for Ca1, Ca2, Ca3, and Ca4, respectively. Similar to the antimonides $Ca_{14-x}RE_xMnSb_{11}$, Ca2 position displays the longest distances to the pnictogen atoms and is therefore more likely to be occupied by larger *RE* atoms when substitution is taking place. Analogously, the coordination polyhedron around Ca1 offers the smallest available volume, and its occupation must be preferred by smaller substituting atoms. The anticipated preference is fully confirmed by the relative occupation of the Ca sites by *RE* atoms in $Ca_{14-x}RE_xMnBi_{11}$ (Figure 3). The clear trend shows that the early members of the lanthanide family i.e., La through Nd, accumulate at the Ca2 site, whereas the late *RE*-metals preferably occupy the Ca1 site. The gradual decrease of the *RE* atomic size is reflected in the continuous change of the relative occupation.

How the electronic structure and physical properties of $Ca_{14}MnBi_{11}$ and the $Ca_{14-x}RE_xMnBi_{11}$ solid solutions compare is also a very interesting subject to discuss. The density of states (DOS) curves are plotted in Figure 4. As the total DOS indicates, $Ca_{13}LaMnBi_{11}$ is predicted to be a semiconductor, In accordance with the formal electron count. For the majority spins, a small gap of only 0.08 eV opens at the Fermi level. The minority-spin states show a much larger gap of about 0.6 eV at E_F. This leads to an almost half-metallic behavior, with a total gap of 0.04 eV. It is worthwhile to mention that the parent compound $Ca_{14}MnBi_{11}$ was found to display an electronic structure similar to that of a half-metallic ferromagnet. Half-metallic-like character of $Ca_{14}MnBi_{11}$ and other representatives of the "14–1–11" family was discussed as a possible origin of the colossal magnetoresistance observed in some of them. A more sophisticated treatment of electronic correlations, e.g., within the LSDA+*U* approach, and an account of the spin-orbit coupling, that may be especially important for Bi, should lead to a larger energy separation of the conduction and valence bands. Although a certain underestimation of electronic bandgaps is an inherent drawback of the density functional theory, the value of ca. 0.04 eV calculated for $Ca_{13}LaMnBi_{11}$ is close to the $Ca_{13}LaMnSb_{11}$ bandgap determined from the temperature dependence of the electrical resistivity.

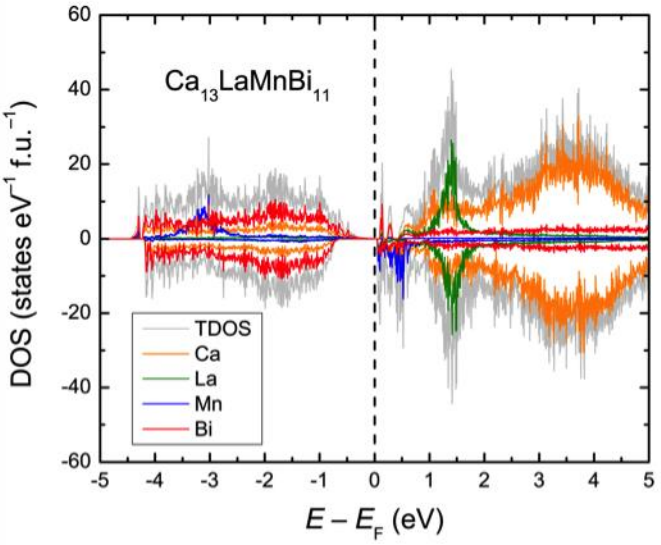

Figure 4. Electronic density of states of $Ca_{13}LaMnBi_{11}$. Energy of the Fermi level is set as a reference point at 0 eV. Positive and negative DOS denote majority and minority spin directions, respectively. For the purpose of the electronic structure calculations, we did the following: first, we considered a model where the La substitution occurs only at the Ca2 site (32*g*). The occupation factor was taken as 0.25 (in comparison with the experimental value of 0.14), yielding the idealized composition $Ca_{13}LaMnBi_{11}$. Next, we transformed the tetragonal structure with space group $I4_1/acd$ to an orthorhombic one with the space group *Iba*2, a subgroup of $I4_1/acd$, in which the original 32*g* site splits into four 8*c* sites. By considering La at one of these four sites, while keeping the remaining three ones occupied by Ca, an ordered $Ca_{13}LaMnBi_{11}$ model was derived.

Attention should be drawn to the fact that for 3 of the studied lanthanides, specifically Er, Tm, and Lu, the structural $Ca_{14-x}RE_xMnBi_{11}$ data did not follow the established trends. For *RE* = Er, only modest substitution could be attained, as evident from $Ca_{14-x}Er_xMnBi_{11}$ ($x \approx 0.2$), a composition refined from single-crystal X-ray diffraction work. For the heaviest (i.e., smallest) rare-earths Tm and Lu, structure refinements from single-crystal showed undoped $Ca_{14}MnBi_{11}$. For $Ca_{14-x}RE_xMnSb_{11}$ (*RE* = Er, Tm, Lu), *x* was close to zero as well. These findings put into the spotlight some results from the literature, where Lu-doped variants of $Yb_{14}MnSb_{11}$, prepared by SPS, had been suggested to have an improved thermoelectric performance. Structural details are missing from the cited work,[16] and detailed property data were not available to discern the

substitutional chemistry. Importantly, however, an increase in *zT* has been attributed to an *increasing* charge-carrier concentration in the $Yb_{14-x}Lu_xMnSb_{11}$ sample. If the knowledge from our systematic structural work on $Ca_{14-x}RE_xMnBi_{11}$ or $Ca_{14-x}RE_xMnSb_{11}$ were transferable to the related $Yb_{14-x}RE_xMnSb_{11}$, then, an aliovalent Yb^{2+}–Lu^{3+} substitution should contribute to a more precise charge-balance, hence, a *decrease* in the charge-carrier concentration should be expected. This discrepancy between expected crystal chemistry and experiment is further exacerbated by another study on a Tm-doped $Yb_{14}MnSb_{11}$,[17] where the presence of Tm in the samples has been confirmed based on microprobe analysis and increased magnetic moment, but the provided single-crystal X-ray diffraction data exhibited unit cell parameters almost identical to those of pristine $Yb_{14}MnSb_{11}$. Structural refinements showed insignificant difference in occupancies, angles / distances, which is also unexpected given the large difference of Yb^{2+} and Tm^{3+} radii.[15]

These uncertainties raise an important fundamental question as to what is the exact role of the late rare-earth elements Tm and Lu in the "14–1–11" structures. Aiming at answering this question and at the full understanding of the effects of the rare-earth metal substitutions, we performed a systematic investigation. The results from it point at interesting and unexpected answers, which extend existing concepts of possible coordination of late rare-earth metals in solid-state compounds and cause us to rethink the role of alumina crucibles—one of the most common reaction vessel used in the synthesis of solid-state materials.

Key finding #1. A reaction between the Ca, Lu, Mn, and Bi metals (in a nominal ratio 13:1:1:11) performed in an alumina crucible using the Pb-flux method easily yielded very nice crystals (Figure 5). The crystalline material appeared to be nearly phase-pure by lab powder X-ray diffraction (PXRD). Based on the PXRD, we anticipated it to be $Ca_{14-x}Lu_xMnBi_{11}$, but single-crystal X-ray diffraction analysis revealed two outright problems: i) the unit cell volume was *larger* than that of any of the ten known $Ca_{14-x}RE_xMnBi_{11}$ examples or pristine $Ca_{14}MnBi_{11}$; and ii) the refined occupancy of the Mn-site was *lower* than 100%. Since the crystals large and well-shaped, it was easy to select one with nice, clean and smooth surfaces and subject it to elemental microanalysis (notice that all the work had to be done in the glovebox to prevent the material from oxidizing in air). The results from this experiment were also surprising—the synthesized sample *did not contain measureable amounts of Mn*! In addition to large peaks from Ca and Bi, the EDX spectrometer also picked small signals from Lu and Al (Figure 6), and no other metals. Identification of aluminum was unexpected since Al was not an element that was used in the synthesis, but it was possible to explain the signal since the sample was mounted on a stub made of aluminum.

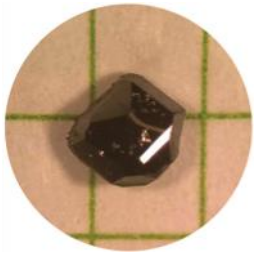

Figure 5. Optical microscope image of the grown crystals. Background is mm-sized grid.

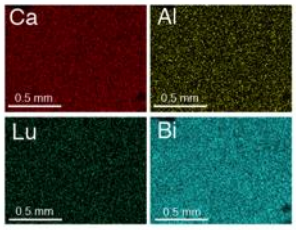

Figure 6. EDS X-ray maps showing homogeneous distribution of 4 metals.

We reasoned, however, that the origin of Al could have been the Al_2O_3 crucible and since the reaction mixture was Ca-rich and highly

reducing, alumina could have become an advertent source of Al metal. To prove or disprove this hypothesis, we ran a reaction between the Ca, Lu, and Bi (nominal ratio 13:1:11) and performed it again in an alumina crucible using the Pb-flux method. As control experiments, two other reactions were also set up: 1) between Ca, Lu, Al, and Bi (nominal ratio 13:1:1:11) and 2) between Ca, Al, and Bi (nominal ratio 14:1:11). They were carried out in the same manner as above. All three reactions afforded large single crystals, which had the *same* unit cell volumes as the crystal obtained from the experiment with Mn. Importantly, XRF and EDX analyses from each specimen showed nearly identical chemical make-up (Baranets and Bobev, JACS, ref. 18). These results unambiguously confirmed that the alumina crucibles are unsuitable for these types of reactions, suggesting that what we had synthesized previously was not $Ca_{14-x}Lu_xMnBi_{11}$ (nor $Ca_{14}MnBi_{11}$), but rather $Ca_{14}AlBi_{11}$. This discovery raises additional questions and calls for careful reconsideration of the old results, where similar synthetic approaches may have been used and serendipitous Al-contamination of the prepared samples might have gone undetected.

Key finding #2. $Ca_{14}AlBi_{11}$, $Ca_{14-x}Lu_xAlBi_{11}$ or $Ca_{14}Lu_xAl_{1-x}Bi_{11}$? From the three experiments described in the preceding paragraph, two had Lu in the elemental mixture and one did not. The sample that did not have Lu in it was characterized in a straightforward manner as the ternary compound $Ca_{14}AlBi_{11}$. The latter is a new Zintl phase from earth-abundant elements with a great potential for thermoelectric energy conversion (resistivity measurements on as-synthesized single crystalline sample show temperature dependence akin to those of heavily doped semiconductors or the bad metals). In addition to the moderately high electrical conductivity (ρ_{300} = 1.05 mΩ·cm), specimens of $Ca_{14}AlBi_{11}$ also exhibit excellent thermopower, with the Seebeck coefficient approaching 200 μV/K at 700 K. These metrics are comparable with the best state-of-the-art *p*-type Zintl thermoelectric materials, and are among the best within the known bismuthides with the same atomic arrangements. Subsequently, structure refinements brought to light something out of ordinary: the displacement parameter of the Al atom was negative; freeing the Al-site occupation factor suggested 160-180% "over-occupation". At the same time, the site occupation factors for the remaining eight positions did not deviate from unity by more than 3σ, except for Ca1, where the deviations were consistently higher than 100%, but only within 5–7σ. Several additional data collections on different crystals showed the same problem, which rules out potential crystal/data quality issues. Considering all of the above, the increased electron density can be explained as arising from a heavier element that randomly substitutes Al in the $Ca_{14}AlBi_{11}$ structure. A scenario where Al is not part of the structure, and the position is just partially occupied by heavier element can be rejected from the independent assessment of the chemical make-up. Lead was excluded, also from EDS work, which revealed no traces of Pb in the bulk, with only some residual microdroplets of lead on the surface. There are three remaining elements at play—Ca, Lu and Bi. Which one is the culprit?

The excess electron density, in most cases, exceeds the scattering factor of Ca, rendering Ca–Al substitutions improbable. Co-refining Bi and Al is possible, leading to refined $Ca_{14}Al_{1-x}Bi_{11+x}$ compositions ($x < 0.1$), which are indistinguishable by EDS. Clearly, analytical tools are not particularly helpful in this analysis, but by carefully examining all experimental findings, Bi can

be unmistakably ruled out—recall that Ca–Al–Bi experiments, carried out in an identical manner, yield $Ca_{14}AlBi_{11}$, where there is *not* "overoccupation" on the Al site.

Therefore, by deduction, the excessive electron density must be due to Lu-substitution. This notion is corroborated by EDS data, which consistently showed Lu in every measured specimen. Although the amount is at the sensitivity limits, EDS results agree well with ICP-MS data and the structural refinements. Additional proof that the rare earth metal "enters" the crystal structure was obtained by carrying out synthesis with Tm, instead of Lu. The radii of Lu^{3+} and Tm^{3+} are very close, therefore, $Ca_{14-x}Tm_{x+y}Al_{1-y}Bi_{11}$ and $Ca_{14-x}Lu_{x+y}Al_{1-y}Bi_{11}$ have nearly the same unit cell parameters. Elemental analysis confirmed Tm-level of inclusion to be similar to that of $Ca_{14-x}Lu_{x+y}Al_{1-y}Bi_{11}$. The large effective magnetic moment for free-ion Tm^{3+} (7.56 μ_B) allowed the small Tm concentration in the sample to be probed by magnetization measurements (acknowledging that $\chi_m(T)$ provides only a qualitative confirmation of the Tm-inclusion and is not a means to assess the amount of Tm). Curie-Weiss behavior is observed upon zero-field (ZFC) and field cooling (FC). Since Tm is the only element in the structure with unpaired electrons, and since there is no evidence for an impurity phase in the measured grain, the paramagnetism can only be attributed to Tm^{3+} inside. Using the formula weight of $Ca_{13.91(1)}Tm_{0.17}Al_{0.93}Bi_{11}$ from crystallographic work, the amount of contributing magnetic atoms is calculated as 0.19 Tm/f.u., in good agreement with the SCXRD refinements and the EDS.

Having unequivocally ascertained the presence of Tm and Lu in the synthesized phases, let us now focus the attention on the role of late rare earth metals in the structure. As already discussed, besides the Al site, the Ca1 site (in all cases) also had small "overoccupation" problem. This was also attributed to Tm and Lu substitution. Presence of Tm/Lu on Ca2, Ca3 and Ca4, if any, is below the limit of detection. The subtle Ca–Tm/Lu substitution is not as pronounced as it is for the early lanthanides, for example in $Ca_{14-x}RE_xMnPn_{11}$ ($x \approx 1$). It appears that replacing Ca by Tm/Lu is hindered, likely rooted in the relatively large differences in their crystal/ionic radii: Ca (1.17 Å/1.03 Å); Tm (1.02 Å /0.88 Å), and Lu (1.00 Å/0.86 Å).[15] An indirect evidence supporting this reasoning based on space-packing can be found analyzing the refined structure of the isostructural La-compound $Ca_{13.90(2)}La_{0.10}AlBi_{11}$, which was purposely prepared as a test of our hypothesis. The latter exhibits small occupational disorder on the most "spacious" Ca2 site. The suggested Ca–*RE* (*RE* = Tm, Lu, and La) admixing is consistent with the previous studies on the *RE* substitution preferences, where Gd, Tb, and Dy (smaller size) have been found to prefer the Ca1 site, whereas the early lanthanides La and Ce (larger size) always show highest affinity for the Ca2 site (Figure 3).

The very small size of Tm^{3+} and Lu^{3+} compared to the rest of the RE^{3+} is the likely reason why only these two rare-earth elements are capable of adopting tetrahedral coordination. Since all rare-earth elements have stable 3+ state, just as Al, the *RE*–Al substitutions should be isovalent and not limited by electronic factors. Yet, as it is apparent from the refinement of the $Ca_{13.90(2)}La_{0.10}AlBi_{11}$ structure, this does not happen. Instead, La^{3+} partially substitutes Ca^{2+} on an octahedral site (which is an aliovalent process, pushing the system away from the ideal Zintl electron count). To reconcile these finding, one must recall that the lowest known coordination

number for rare earth ions in solid-state compounds is CN 6. Here, for the first time, evidence is provided for the existence of Tm and Lu, coordinated by four Bi's (at the refined level, one of approx. eight to ten Al atoms is replaced by Tm and Lu). On the other side, coordination complexes of rare earth metals are known to have CN 4, 3, and even 2. In several of them, lanthanides are found coordinated to both pnictogen atoms and organic ligands. Species with *RE*–Bi bonds are rare—a commensurate example could be the dinuclear $[(C_5Me_5)_2Sm]_2$ [μ-η^2Bi_2], where each Sm is tetrahedrally coordinated by two (C_5Me_5) ligands and two Bi atoms. In all of these organometallic examples, steric hindrance might play an important role for the stabilization of such low coordination numbers, which clearly is not the case with the "bare" $TmBi_4^{9-}$ and $LuBi_4^{9-}$ tetrahedra. The very large differences between the Sm–Bi bonds in organometallic $[(C_5Me_5)_2Sm]_2[\mu\text{-}\eta^2Bi_2]$ (ca. 3.3 Å long) vs the Lu–Bi bonds (ca. 2.8 Å long) cannot be attributed to atomic sizes and point to a very different nature of the bonding.

Future Plans

As elaborated in the previous section, exploring rare-earth metal (*RE*) substitutions in the "14–1–11" Zintl phase $Ca_{14}AlBi_{11}$ led to the discovery of unprecedented chemistry, exemplified by $Ca_{14}Lu_xAl_{1-x}Bi_{11}$ (Figure 11). We are currently optimizing the reactions conditions for growth of large crystals of the new compounds (Figure 5), which appear to have electronic properties in a practically relevant range. Precise measurements of the transport properties will be possible on these large crystals. In addition, in collaboration with Prof. Prashun Gorai, we are pursing computational work on the crystal-defect chemistry. Those studies are ramping up at present, and they will continue during the next phase of this award.

The identification of inadvertent reduction of alumina (crucible material) and possible "contamination" of the $Ca_{14-x}RE_xMnBi_{11}$ samples (*e.g.*, resistivity values across the series were very different and there was no solid explanation as to why this could be the case, except that some of the samples could be "over-doped") left some open questions. We are currently synthesizing the compounds in BN, graphite and metal crucibles and are pursing concurrent structural and properties work that is ultimately expected to affect many other materials systems. The reasons for this line of thinking are based on the following hypotheses: (**i**) small Al inclusions affect the dupability of the material, and (**ii**) once the synthesis parameters are sorted out and, Al metal substituting Mn or Zn in the crystal structure can be used as an effective "tuning" parameter. Such studies are expected to continue throughout the next phase as well.

References

1. Brown, S. R.; Kauzlarich, S. M.; Gascoin, F.; Snyder, G. J. "$Yb_{14}MnSb_{11}$: New High Efficiency Thermoelectric Material for Power Generation" *Chem. Mater.* **2006,** *18,* 1873.
2. Snyder, G. J.; Toberer, E. S. "Complex Thermoelectric Materials" *Nat. Mater.* **2008**, *7*, 105.
3. Sootsman, J. R.; Chung, D. Y.; Kanatzidis M. G. "New and Old Concepts in Thermoelectric Materials" *Angew. Chem. Int. Ed.* **2009**, *48*, 8616.

4. Kauzlarich, S. M., "Chemistry, Structure, and Bonding of Zintl Phases and Ions" **1996,** VCH Publishers: New York.
5. Kauzlarich, S. M.; Brown, S. R.; Snyder, G. J. "Zintl Phases for Thermoelectric Devices" *Dalton Trans.* **2007**, *21*, 2099.
6. Toberer, E. S.; May, A. F.; Snyder, G. J. "Zintl Chemistry for Designing High Efficiency Thermoelectric Materials" *Chem. Mater*. **2010**, *22*, 624.
7. Yi, T.; Zhang, G.; Tsujii, N.; Fleurial, J.-P.; Zevalkink, A.; Snyder, G. J.; Grønbech-Jensen, N.; Kauzlarich, S. M. "Phase Characterization, Thermal Stability, High-Temperature Transport Properties, and Electronic Structure of Rare-Earth Zintl Phosphides $Eu_3M_2P_4$ (M = Ga, In)" *Inorg. Chem*. **2013**, *52*, 3787.
8. Zintl, E. "Internietallische Verbindungen" *Angew. Chem.* **1939**, *52*, 1.
9. Schäfer, H.; Eisenmann B.; Müller, W.; "Zintl Phases: Transitions Between Metallic and Ionic Bonding" *Angew. Chem., Int. Ed. Engl.* **1973**, *12*, 694.
10. Nesper, R. "Structure and Chemical Bonding in Zintl-phases Containing Li" *Prog. Solid State Chem.* **1990**, *20*, 1.
11. Kauzlarich, S. M. "A Rational Approach to Solid State Synthesis, The Zintl Concept" *Comments Inorg. Chem.*, **1990**, *10*, 75.
12. Kazem, N.; Kauzlarich, S. M. "Thermoelectric Properties of Zintl Antimonides" *Handb. Phys. Chem. Rare Earths* **2016**, *50*, 177.
13. Kauzlarich, S. M. "Zintl Phases with d-Metal" in "*Comprehensive Inorganic Chemistry II*" volume 2: Transition Elements, Lanthanides and Actinides, **2013**.
14. Zevalkink, A; Toberer, E. S.; Snyder, G. J. "Zintl Phases: Recent Developments in Thermoelectrics and Future Outlook" in "*Thermoelectric Materials and Devices*" Chapter 1, **2016**.
15. (a) Shannon, R. D.; Prewitt, C. T. "Effective Ionic Radii in Oxides and Fluorides" *Acta. Cryst.* **1969**, *B25*, 925; (b) Shannon, R. D. "Revised Effective Ionic Radii in Oxides and Fluorides" *Acta Cryst.* **1976**, *A32*, 751.
16. Yu, C.; Chen, Y.; Xie, H.; Snyder, G. J.; Fu, C.; Xu, J.; Zhao, X.; Zhu, T. "Improved Thermoelectric Properties in Lu-Doped $Yb_{14}MnSb_{11}$ Zintl Compounds" *Appl. Phys. Express* **2012**, *5*, 031801.
17. Roudebush, J. H.; Grebenkemper, J.; Hu, Y.; Kazem, N.; Abdusalyamova, M. N.; Kauzlarich, S. M. "$Yb_{14-x}Tm_xMnSb_{11}$ ($0 < x < 0.5$): Structure and Magnetic Properties" *J. Solid State Chem.* **2014**, *211*, 206.
18. Baranets, S.; Bobev, S. "Caught in Action. The Late Rare Earths Thulium and Lutetium Substituting Aluminum Atoms in the Structure of $Ca_{14}AlBi_{11}$" *J. Am. Chem. Soc.* **2021**, *143*, 65.

Publications (since 2018)

(in reverse order; *the names of the contributing undergraduate researchers are underlined*)

1. "*On the Structural Uniqueness of the $[Nb(As_5)_2]^{5-}$ Cluster in the Zintl Phase Cs_5NbAs_{10}*" Baranets, S.; Ovchinnikov, A.; Dmitrenko, O.; Bobev, S. *J. Phys. Chem.* **2021**, *in print* (invited article to the special issue *dedicated to the 70th birthday of Prof. Alexander Boldyrev*).
   doi: 10.1021/acs.jpca.1c01771
2. "*Synthesis and Structural Characterization of Orthorhombic $Cu_{3-d}Sb$ ($d \approx 0.1$) and Hexagonal $Cu_3Sb_{1-x}In_x$ ($x \approx 0.2$) Phases*" Sinclair, J.; Baranets, S.; Bobev, S. *Z. Kristallogr.* **2021**, *236*, 61 – *available online 03/03/2021*.
   doi: 10.1515/zkri-2021-0003
3. "*Ultra-low Thermal Conductivity and High Thermopower in a New Family of Zintl Antimonides $Ca_{10}MSb_9$ (M = Ga, In, Mn, and Zn) with Complex Structures and Heavy Disorder*" Ovchinnikov, A.; Chanakian, S.; Zevalkink, A.; Bobev, S. *Chem. Mater.* **2021**, *33*, 3172 – *available online 04/05/2021*.
   doi: 10.1021/acs.chemmater.0c04940
   INVITED INSIDE COVER PAGE FOR: *Chem. Mater.* **2021**, vol. 33, number 9, May 11th issue.
4. "*Single Crystal Growth and Characterization of New Zintl Phase $Ca_9Zn_{3.1}In_{0.9}Sb_9$*" Smiadak, D. M.; Baranets, S.; Rylko, M.; Marshall, M.; Calderón-Cueva, M.; Bobev, S.; Zevalkink, A. *J. Solid State Chem.* **2021**, *296*, 121947 – *available online 01/06/2021*.
   doi: 10.1016/j.jssc.2020.121947
5. "*Caught in Action. The Late Rare Earths Thulium and Lutetium Substituting Aluminum Atoms in the Structure of $Ca_{14}AlBi_{11}$*" Baranets, S.; Bobev, S. *J. Am. Chem. Soc.* **2021**, *143*, 65 – *available online 12/30/2020*.
   doi: 10.1021/jacs.0c11026
6. "*New n-type Zintl Phases for Thermoelectrics: Discovery, Structural Characterization and Band Engineering of the Compounds A_2CdP_2 (A = Sr, Ba, Eu)*" Balvanz, A.; Xu, J.; Baranets, S.; Ertekin, E.; Gorai, P.; Bobev, S. *Chem. Mater.* **2020**, *32*, 10697 – *available online 12/20/2020*.
   doi: 10.1021/acs.chemmater.0c03960
7. "*Observation of an Unexpected n-type Semiconducting Behavior in the New Ternary Zintl Phase Eu_3InAs_3*" Rajput, K.; Baranets, S.; Bobev, S. *Chem. Mater.* **2020**, *32*, 9616 – *available online 09/11/2020*.
   doi: 10.1021/acs.chemmater.0c03168
   COVER PAGE FOR: *Chem. Mater.* **2020**, vol. 32, number 22, November 24th issue
8. "*Synthesis, Structural Characterization, and Electronic Structure of the Novel Zintl phase Ba_2ZnP_2*" Balvanz, A.; Baranets, S.; Bobev, S. *Acta Cryst. C* **2020**, *76*, 869 – *available*

online 08/10/2020.
doi: 10.1107/S2053229620010827

9. "*Magnetic Mixed Valent Semimetal $EuZnSb_2$ with Dirac States in the Band Structure*" Wang, A.; Baranets, S.; Liu, Y.; Tong, X.; Stavitski, E.; Zhang, J.; Chai, Y.; Yin, W.-G.; Bobev, S.; Petrovic, C. *Phys. Rev. Research.* **2020**, *2*, 033462 – *available online 09/22/2020*.
doi: 10.1103/PhysRevResearch.2.033462
10. "*$Ca_{14}AlBi_{11}$—a New Zintl Phase from Earth-abundant Elements with a Great Potential for Thermoelectric Energy Conversion*" Baranets, S.; Bobev, S. *Mater. Today Adv.* **2020**, *7*, 100094 – *available online 08/14/2020*.
doi: 10.1016/j.mtadv.2020.100094
11. "*Synthesis and Structural Characterization of the New Zintl Phases $Ba_3Cd_2P_4$ and $Ba_2Cd_2P_3$—Two Rare Examples of n-type Semiconductors Within This Class of Materials*" Balvanz, A.; Baranets, S.; Bobev, S. *J. Solid State Chem.* **2020**, *289*, 121476 – *available online 05/28/2020*.
doi: 10.1016/j.jssc.2020.121476
12. "*On the New Oxyarsenides $Eu_5Zn_2As_5O$ and $Eu_5Cd_2As_5O$*" Darone, G. M.; Baranets, S.; Bobev, S. *Crystals.* **2020**, *10*, 475 – *available online* 06/03/2020 (invited article for the special issue on *Compounds with Polar Metallic Bonding Volume II*).
doi: 10.3390/cryst10060475
13. "*Exploration of Multi-component Vanadium and Titanium Pnictides Using Flux Growth and Conventional High-temperature Methods*" Ovchinnikov, A.; Bobev, S. *Inorg. Chem. Front.* **2020**, *7*, 909 – *available online* 01/10/2020 (invited article for the special collection – *Flux Crystal Growth: From Fundamentals to Crystal Functionality*).
doi: 10.3389/fchem.2019.00909
14. "*Bismuth as a Reactive Solvent in the Synthesis of Multicomponent Transition-metal-bearing Bismuthides*" Ovchinnikov, A.; Bobev, S. *Inorg. Chem.* **2020**, *59*, 3459 – *available online* 12/20/2019 (invited article for the ACS Inorganic Chemistry Forum *Bismuth – The Magic Element*).
doi: 10.1021/acs.inorgchem.9b02881
15. "*Synthesis and Structural Characterization of the Type-I Clathrates $K_8Al_xSn_{46-x}$ and $Rb_8Al_xSn_{46-x}$ ($x \approx 6.4–9.7$)*" Baranets, S.; Schäfer, M. C.; Bobev, S. *Acta Cryst. C* **2019**, *75*, 1535 – *available online* 10/28/2019.
doi: 10.1016/10.1107/S205322961901427X
16. "*Synthesis and Structure of $Sr_{14}Zn_{1+x}As_{11}$ and $Eu_{14}Zn_{1+x}As_{11}$ ($x \leq 0.5$). New Members of the Family of Pnictides Isotypic with $Ca_{14}AlSb_{11}$, Exhibiting a New Type of Structural Disorder*" Baranets, S.; Darone, G. M.; Bobev, S. *J. Solid State Chem.* **2019**, *280*, 120990 – *available online* 10/08/2019.
doi: 10.1016/j.jssc.2019.120990
COVER PAGE FOR: *J. Solid State Chem.* **2019**, vol. 280, December issue.

17. 199. "*Five New Ternary Indium-Arsenides Discovered. Synthesis and Structural Characterization of the Zintl Phases $Sr_3In_2As_4$, $Ba_3In_2As_4$, $Eu_3In_2As_4$, $Sr_5In_2As_6$ and $Eu_5In_2As_6$*" Childs, A.; Baranets, S.; Bobev, S. *J. Solid State Chem.* **2019**, *278*, 120889 – *available online* 07/29/2019.
doi: 10.1016/j.jssc.2019. 07.050
COVER PAGE FOR: *J. Solid State Chem.* **2019**, vol. 278, October issue.
18. "*Synthesis, Crystal Structure and Physical Properties of the Solid Solutions $Ca_{14-x}RE_xCdSb_{11}$ (RE = La–Nd, Sm, Gd–Yb, $x \approx 0.85 \pm 0.15$)*" Baranets, S.; Voss, L.; Stoyko, S.; Bobev, **S.** *J. Appl. Phys.* **2019**, *125*, 245101– *available online* 06/24/2019 (invited article for the themed issue *Advanced Thermoelectrics*).
doi: 10.1063/1.5099632
19. "*From the Ternary Phase $Ca_{14}Zn_{1+\delta}Sb_{11}$ ($\delta \approx 0.4$) to the Quaternary Solid Solutions $Ca_{14-x}RE_xZnSb_{11}$ (RE = La–Nd, Sm, Gd, $x \approx 0.9$). A Tale of Electron Doping via Rare-earth Metal Substitutions and the Concomitant Structural Transformations*" Baranets, S.; Bobev, S. *Inorg. Chem.* **2019**, *58*, 8506 – *available online* 06/17/2019.
doi: 10.1021/acs.inorgchem.9b00809
20. "*Data from the Electronic Band Structures of Several Zintl Phases with Group 15 Elements and the Transition Metals*" Ovchinnikov, A.; Bobev, S. *Data in Brief* **2019**, *22*, 446 – *available online 12/16/2018.*
doi: 10.1016/j.dib.2018.12.040
21. 193. "*Zintl Phases with Group 15 Elements and the Transition Metals: A Brief Overview of Pnictides with Diverse and Complex Structures*"
22. Ovchinnikov, A.; Bobev, S. *J. Solid State Chem.* **2019**, *270*, 346 – *available online 11/22/2018* (invited review article for the special issue *50 Years of Solid State Chemistry*).
doi: 10.1016/j.jssc.2018.11.029
23. "*Exploratory Work in the Quaternary System Ca–Eu–Cd–Sb: Synthesis, Crystal and Electronic Structures of New Zintl Solid Solutions*" Ovchinnikov, A.; Darone, G. M.; Saparov, B.; Bobev, S. *Materials* **2018**, *11*, 2146 – *available online 10/31/2018* (invited article for the themed issue *Advances in Zintl Phases*).
doi: 10.3390/ma11112146
24. "*Synthesis and Structural Characterization of $Ba_7Li_{11}Bi_{10}$ and $AE_4(Li,Tr)_7Pn_6$ (AE = Sr, Ba, Eu; Tr = Ga, In; Pn = Sb, Bi)*" Ojwang, D. O.; Bobev, S. *Inorganics* **2018**, *6*, 109 – *available online 10/06/2018*.
doi: 10.3390/inorganics6040109
25. "*Crystal Structure of the Layered Arsenide $Rb_3Cu_3As_2$*" Ovchinnikov, A.; He, H.; Bobev, S. *Acta Cryst. C* **2018**, *74*, 1715 – *available online 11/22/2018*.
doi: 10.1107/S2053229618014341
26. "*Crystal Chemistry of $RE_6Mg_xCd_{23-x}Pb$ ($0.6(1) \leq x \leq 3.2(1)$; RE = La and Ce). New Mixed-Metal Derivatives of the $RE_6Cd_{23}T$ Phases (T = group 14/15/16 element)*"

Desroches, G.; Ovchinnikov, A.; Bobev, S. *Z. Anorg. Allg. Chem.* **2018**, *644*, 1734 – *available online 09/12/2018* (special issue *dedicated to the 65th birthday of Prof. Wolfgang Bensch*).
doi: 10.1002/zaac.201800317

27. "*Synthesis, Crystal and Electronic Structures of the Titanium-rich Bismuthides $AE_3Ti_8Bi_{10}$ (AE = Sr, Ba, Eu)*" Ovchinnikov, A.; Bobev, S. *Inorg. Chem.* **2019**, *58*, 2934 – *available online 09/13/2018*.
doi: 10.1021/acs.inorgchem.8b01952
COVER PAGE FOR: *Inorg. Chem.* **2019**, vol. 58, number 5, March 4th issue.
28. "*Yet Again, New Compounds Found in Systems with Known Binary Phase Diagrams. Synthesis, Crystal and Electronic Structure of Nd_3Bi_7 and Sm_3Bi_7*" Ovchinnikov, A.; Makongo, J. P. A.; Bobev, S. *Chem. Commun.* **2018**, *54*, 7089 – *available online 06/04/2018* (themed issue *New Molecules and Materials from the f-block*).
doi: 10.1039/C8CC02563K
FEATURED ON: *http://www.ChemistryViews.org*, June 6, 2018.

New paradigms for controlling molecular and ion transport in precise, tight and reconfigurable polymer networks

Paul Braun (PI), Christopher Evans, Randy Ewoldt, Ken Schweizer, Charles Sing
Materials Research Laboratory, University of Illinois Urbana-Champaign

Program Scope. The central goal of this project is development of the fundamental science of precision synthesized, heavily crosslinked, neutral and ionic permanent and dynamic polymer networks as a new class of materials for controlling the absolute and selective transport of neutral and charged molecules of diverse size, shape and interactions. The novel fundamental science lies in understanding how the multiple tunable length and time scales characteristic of the structure and dynamics of these polymeric matrices can greatly amplify differences of the activated diffusion constant of related families of molecules and ions. We are exploring this issue via a synergistic experimental, simulation, and theoretical effort focused on how controllable physicochemical factors such as the ratio of network mesh to penetrant size, degree of network strand charge functionalization, packing differences for penetrants of variable size and shape in confined network spaces, lifetime of crosslinking junctions spanning the range from static to the dynamically re-arranging dissociative and conserved topology (vitrimer) realizations, specific attractive interactions between molecules with network strands and the dynamic crosslinking groups, and mechanical deformation, determine the absolute and relative magnitudes of molecular and ion transport. We anticipate our studies of dynamic bond polymer networks will lead to qualitatively new physical mechanisms of mass transport via tunable nanoscale dynamic fluctuations which can release the localizing constraints experienced by a penetrant in a tight network. Given the ease of large amplitude deformations of polymer networks, we are exploring the application of external stress as a new nonequilibrium pathway for strongly and selectively modifying molecule and ion diffusion via the introduction of network mesh scale anisotropies, accelerated strand relaxation, and modified dynamic crosslink lifetimes.

The body of work is organized into two complementary and tightly integrated efforts: *Selective Molecular and Ion Transport in Precise Permanent Polymer Networks* which addresses the diffusive transport of ions and molecules in neutral and ionic chemically crosslinked tight networks and coupled molecule-ion dynamics, and *Dynamic Networks for Selective Molecular Transport* based on reconfigurable tight polymer transient networks that form reversible bonds of both a dissociative (associating copolymers) and topological rearrangement (vitrimers) nature.

Recent Progress. The first 9 months of the team's efforts focused on the Topic of *Selective Molecular and Ion Transport in Precise Permanent Polymer Networks.* Two classes of permanent network systems were studied: (i) butyl acrylate polymer networks with incorporated fluorescent dyes (**Fig. 1**) (*Evans*) to investigate the effect of permanent crosslink density and temperature on the diffusion of aromatic dyes (aspect ratio ~3),

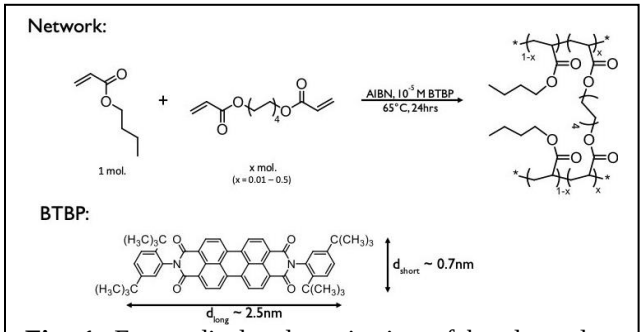

Fig. 1. Free radical polymerization of butyl acrylate networks with the incorporated fluorescent dye BTBP.

and (ii) single cation conducting copolymers designed by *Evans* and *Braun* containing anionic sidegroups, polar sidegroups to enhance cation-anion dissociation, photo-triggerable ion-binding groups, and crosslinkers to investigate effects of crosslink density and ion binding on ion mobility.

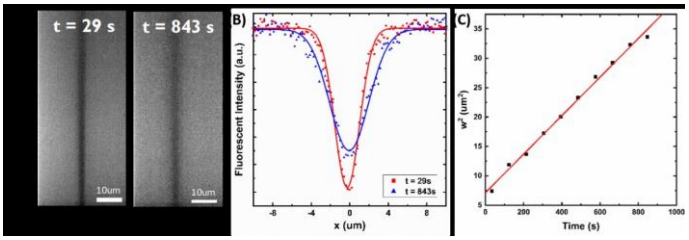

Fig. 2. Representative FRAP data for a BTBP-containing polymer network. The initial line is bleached, and over time the line becomes brighter and broader as unbleached dye diffuses into the region. The width of the Gaussian grows over time and from it a diffusion coefficient is extracted from the slope.

Dye penetrant diffusion was measured using Fluorescence Recovery After Photobleaching (FRAP) (**Fig. 2**). In the butyl acrylate network, increasing crosslink density reduces the degree of polymerization between crosslinks (N_x) resulting in a dramatic two decade decrease in the aromatic probe translational diffusion coefficient ($\mathcal{D}$) (**Fig. 3**)[1] that follows a strong exponential dependence on the ratio of the probe long axis (d_{long}) to the mesh size. At higher temperatures (T_0), the slope decreases. Crosslinking results in a significant increase in the network glass transition temperature (T_g) which strongly suppresses $\mathcal{D}$. All these observations are well predicted by the new penetrant hopping theory of *Schweizer*, and provide new insights regarding the effect of covalent crosslinks on probe diffusion important for the design and development of separation membranes. Transport in single ion conductors was also initiated with control studies where the anion and cation both diffuse, but no ion exchange step is necessary. *Braun* observed a reversible 30% change in ion conductivity in a LiCl doped polymer before and after UV light exposure which converts spiropyran to the cation-binding merocyanine form.

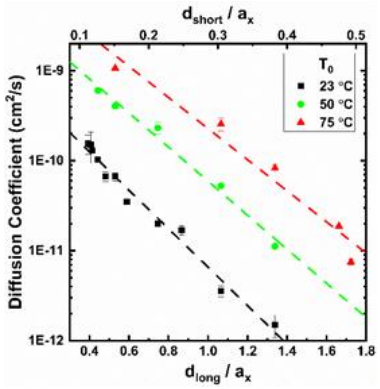

Fig. 3. Diffusion coefficients as a function of the aromatic probe molecule dimensions relative to the distance between crosslinks. The dependence is exponential with a slope that becomes weaker at higher temperatures indicating less sensitivity to the crosslinks.

Ewoldt, *Evans*, and *Braun* performed foundational mechanical measurements on ionic and neutral permanent polymer networks to understand their failure strength and the critical strains required for the emergence of nonlinearity using oscillatory strain amplitude sweeps. A stronger nonlinearity reveals that smaller strains can cause significant deviation from equilibrium, and we find differences of more than a factor of ten between the different polymer materials studied.

Schweizer employed his self-consistent cooperative hopping theory of penetrant activated dynamics to elucidate the role of temperature, matrix density, and penetrant-to-matrix particle size ratio for a spherical particle mixture model.[2] As the matrix dynamics slows and/or penetrant size grows, higher barriers emerge and the collective elasticity associated with the correlated matrix dynamic displacement that facilitates penetrant hopping becomes important, resulting in a near exponential growth (suppression) of penetrant relaxation time (diffusivity) with size ratio. Quantitative comparisons with literature experiments reveal good agreement, and testable predictions were made.[2] The theory has been tentatively extended to take

into account semiflexible chain matrices, crosslinking and molecular penetrant shape. Motivated by the above experiments of *Evans*, the diffusivity of a cylindrical-like shape penetrant in crosslinked polymer matrices was predicted, and the results shown to explain our observations.

In a complementary simulation effort, *Sing* developed a coarse grained model of permanent network structure (informed by the poly(acrylate) chemistry of *Evan*s) which takes into account stochastic crosslinking 'reactions' between randomly chosen monomers. It was shown to capture the apparent glass transition temperature as a function of crosslink density consistent with experiment (*Evans*). Relatively small spherical penetrants were then added and their dynamic mean square displacement (MSD) computed. The capability to simulate nonspherical penetrants based on Gay-Berne potentials was developed to mimic small-molecule dyes of various aspect ratios relevant to our experimental (*Evans*) and theoretical (*Schweizer*) studies.

Underpinning theoretical and simulation efforts on foundational problems germane to topic 2 (dynamic networks for selective molecular transport) have begun. *Schweizer* constructed a new model for the bond breaking time scale of attractive sticker groups in associating copolymer liquids that form transient networks and showed it provides a consistent description for diverse polymer chemistries as a function of temperature and fraction of sticky groups.[3] The development of a coarse grained simulation model of dynamic networks with reversible bonds has begun (*Sing*) that accounts for the 'swapping' of conserved dynamic bonds relevant to the planned experimental studies of vitrimers by *Evans*.

Future Plans. Moving forward, greater effort will be placed on transport studies, and less on synthetic efforts, especially the impact of deformation on penetrant transport. Preliminary FRAP experiments on a chemically crosslinked network reveal transport is accelerated perpendicular to the deformation by an order of magnitude, but modestly slowed along the direction of the load. Understanding this striking anisotropic behavior will be pursued in a coordinated experimental (*Evans, Ewoldt*), theory (*Schweizer*) and simulation (*Sing*) effort. *Braun*, *Evans*, and *Ewoldt* will also investigate the effect of strain on transport in ionic permanent networks. Initial results for a cationic network with large fluorinated mobile anions indicate that shear reduces the out of deformation plane conductivity of single ion conducting networks.

The open question of whether stress, strain, or strain rate is the most fundamental cause of mechanical and transport nonlinearities will be studied by extending the medium-amplitude oscillatory shear (MAOS) technique (*Ewoldt*) to stress-controlled forcing per a creep measurement. Step stress experiments will simultaneously measure mechanics and penetrant diffusion and connect directly with theory and simulation (*Schweizer, Sing*). We expect the results will have major implications for understanding transport under deformation.

Schweizer will systematically establish how the many experimental variables (polymer stiffness, temperature, penetrant size and shape, penetrant-polymer attractive interactions, degree of crosslinking) determine penetrant diffusion in quiescent melts and crosslinked networks, including the question of selectivity, with specific applications to our experiments (*Braun, Evans*). *Schweizer* will also construct and apply to experiments (*Evans, Ewoldt, Braun*) a predictive theory for how external stress changes penetrant diffusivity and selectivity as a function of molecular shape and size, cohesive forces, thermodynamic state, and extent of

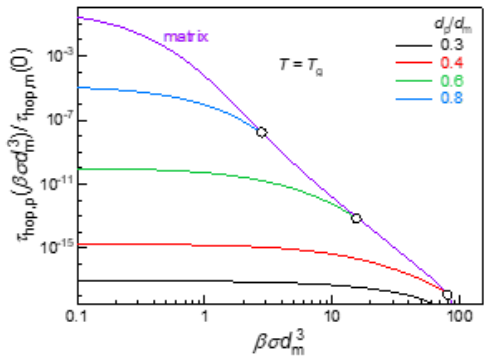

Fig 4. Penetrant hopping time (inverse diffusivity) normalized by the *quiescent* matrix structural relaxation time as a function of stress non-dimensionalized by the matrix particle diameter cubed divided by thermal energy. Penetrant-to-matrix size ratio (d_p/d_m) is varied over a wide range, with temperature fixed at the matrix T_g. The convergence of curves are indicated by the open circles and represent the onset of a "slaving regime" whence the matrix activated relaxation time fully controls the rate of penetrant transport. The curves terminate at the matrix yield stress whence penetrant and matrix dynamics are no longer thermally activated.

crosslinking. **Fig. 4** shows a preliminary result for the spherical particle mixture model which demonstrates the rich sensitivity of penetrant dynamics to stress under cold melt conditions.

Sing will employ simulation to study how large spherical penetrants are affected by crosslink density and network mesh topology at both relatively high temperatures and close to T_g. Mesh heterogeneity will be characterized by adapting pore size distribution calculation methods. A constant shear stress will be applied to change the network mesh and polymer dynamics to investigate at a detailed molecular level penetrant diffusion under deformation. These simulations will also provide valuable benchmarks to test the theories of *Schweizer*. *Sing* will also perform simulations to address these same issues for non-spherical penetrants of high experimental (*Evans, Braun, Ewoldt*) and theoretical (*Schweizer*) interest using a Gay-Berne potential as a function of crosslink density, temperature, and under a uniaxial extension.

Moving forward, the team will place greater emphasis on the study of dynamic networks. Major questions include whether labile crosslinks of transient networks can result in new modes of transport which can be exploited to achieve selective transport of larger molecules. We will pursue these questions based on rendering the (still tight) physical meshes dynamically fluctuating using chemistries that afford *dynamically exchangeable* crosslink junctions of both a dissociative (associating copolymers) and topology conserving (vitrimers) nature. The theories for penetrant transport will be extended to dissociative polymer matrices, and the development of simulation methods for dynamic networks with conserved bonds will be completed and applied. A major scientific issue is how network junction lifetime, density fluctuations triggered by bond re-arrangement, and the propensity for penetrants to preferentially segregate to such junctions, influences penetrant transport rates and selectivity. Related questions include whether and how molecules that associate via physical interactions with transient crosslinks can actively modify junction dynamics, and how or if deformation can selectively accelerate molecular transport via modification of junction lifetime and/or network strand conformation and dynamics.

References

1. G. S. Sheridan, C. M. Evans, Understanding the role of permanent crosslinks on probe diffusion in dense polymer networks, submitted to ACS Macro Letters, submitted, April 2021.

2. B. Mei, K. S. Schweizer, Activated dynamics of a dilute penetrant in glass forming liquids: decoupling, collective elasticity and correlation with matrix compressibility, *Soft Matter*, **17**, 2624 (2021).

3. A. Ghosh and K. S. Schweizer, Physical Bond Breaking in Associating Copolymer Liquids, *ACS Macro Letters*, **10**, 122 (2021).

Publications

(1) Chaudhary, G.; Bharadwaj, N. A.; Braun, P. V.; Ewoldt, R. H., Exploiting Nonlinear Elasticity for Anomalous Magnetoresponsive Stiffening, *ACS Macro Letters* **2020**, *9*, 1632-1637.

(2) Ghosh, A.; Schweizer, K. S., The role of collective elasticity on activated structural relaxation, yielding, and steady state flow in hard sphere fluids and colloidal suspensions under strong deformation, *The Journal of Chemical Physics* **2020**, *153*, 194502.

(3) Mei, B.; Dell, Z. E.; Schweizer, K. S., Microscopic Theory of Long-Time Center-of-Mass Self-Diffusion and Anomalous Transport in Ring Polymer Liquids, *Macromolecules* **2020**, *53*, 10431-10445.

(4) Ramlawi, N.; Bharadwaj, N. A.; Ewoldt, R. H., The weakly nonlinear response and nonaffine interpretation of the Johnson–Segalman/Gordon–Schowalter model, *Journal of Rheology* **2020**, *64*, 1409-1424.

(5) Chaudhary, G.; Ghosh, A.; Kang, J. G.; Braun, P. V.; Ewoldt, R.; Schweizer, K. S., Linear and Nonlinear Viscoelasticity of Concentrated Thermoresponsive Microgel Suspensions, *Journal of Colloid & Interface Science* **2021** (in press).

(6) Ghosh, A.; Schweizer, K. S., Physical Bond Breaking in Associating Copolymer Liquids, *ACS Macro Letters* **2021**, *10*, 122-128.

(7) Mei, B.; Schweizer, K. S., Activated penetrant dynamics in glass forming liquids: size effects, decoupling, slaving, collective elasticity and correlation with matrix compressibility, *Soft Matter* **2021**, *17*, 2624-2639.

(8) Wang, J.; Qu, S.; Zhang, R.; Yang, K.; Zhang, S.; Nuzzo, R. G.; Nanda, J.; Braun, P. V., High Energy Density and Stable Three-Dimensionally Structured Se-Loaded Bicontinuous Porous Carbon Battery Electrodes, *Energy Technology* **2021**, 2100175.

(9) Mei, B.; Zhou, Y.; Schweizer, K. S., Experimental test of a predicted dynamics–structure–thermodynamics connection in molecularly complex glass-forming liquids, *Proceedings of the National Academy of Sciences* **2021**, *118*, e2025341118.

(10) Sheridan, G. S.; Evans, C. M., Understanding the role of permanent crosslinks on probe diffusion in dense polymer networks, *ACS Macro Letters* (under review).

Unravelling the Mechanisms of Phase Determination in Metastable Multinary Chalcogenides

Richard L. Brutchey
Department of Chemistry, University of Southern California, Los Angeles, CA 90089, USA

Program Scope

While great strides have been made in the synthesis of colloidal inorganic nanocrystals, the vast majority of nanocrystals have been prepared in the known thermodynamic phases of their bulk material counterparts. Dimensionally confined materials, such as colloidal nanocrystals that can form without long-range solid-solid diffusion, represent a fertile testbed for the exploration of compositionally complex, multinary compounds possessing metastable structures trapped in states away from equilibrium. These metastable phases can exhibit value-added properties for energy-relevant technologies as compared to their thermodynamically preferred phases. Unfortunately, the synthesis of nanocrystals in metastable phases has generally only occurred by serendipity.

A virtually unexplored aspect of colloidal inorganic nanocrystal chemistry remains the possibility of rationally stabilizing compositions and structures on the nanoscale that do not exist at 298 K and 1 atm in the analogous bulk materials. This will lead to a paradigm shift whereby entirely new types of nanomaterials with novel properties can be synthesized, moving beyond the traditional model of simply shrinking the dimensions of known bulk phases. Using a materials chemistry approach, we are executing hypothesis-driven research to understand the mechanisms of phase determination in metastable chalcogenide nanocrystals. The results of this work will enable the predictive synthesis of energy-relevant nanocrystals in metastable phases.

Recent Progress

1. Rational preparation of new metastable polymorphs. Our key hypothesis is that the phase determination of multinary chalcogenide nanocrystals, such as $CuInSe_2$ and $AgInSe_2$, is directed by the anion sub-lattice symmetry of binary chalcogenide intermediates formed in situ. For example, we showed that the kinetics of diselenide precursor conversion are dependent upon C-Se bond dissociation energies (BDEs).[1] When employing diselenide precursors with relatively weak C–Se bonds (<60 kcal/mol), the resulting $CuInSe_2$ nanocrystals form in the thermodynamically stable chalcopyrite phase. However, precursors that possess stronger C-Se bonds (≥65 kcal/mol) alter the reaction kinetics so as to steer the reaction towards formation of a metastable wurtzite-like phase of $CuInSe_2$. This represented the first example of being able to predictably control the resulting metastable or thermodynamically preferred polymorph of a multinary chalcogenide nanocrystal using a precursor-enabled molecular programming approach.

These two polymorphs of $CuInSe_2$ form via distinct binary copper selenide intermediates. By comparing the Se^{2-} sub-lattices of these binary intermediates to those of the final $CuInSe_2$ phases, we developed a structural rationalization for phase determination in this system. The near exact match of the Se^{2-} sub-lattices between $Cu_{2-x}Se$ (a = 5.787 Å at 433 K) and $CuInSe_2$ (a = 5.792 Å at 433 K) facilitate the topotactic transformation of $Cu_{2-x}Se$ to chalcopyrite $CuInSe_2$. On the other hand, the conversion of Cu_3Se_2 to wurtzite-like $CuInSe_2$ nanocrystals can be understood by considering the similarity between the nearly hexagonal Se^{2-} sub-lattice of Cu_3Se_2 and wurtzite-like $CuInSe_2$. This knowledge allows us to prepare new polymorphs of multinary chalcogenides not found on bulk phase diagrams.

Quaternary I_2-II-IV-VI_4 ($A_2^+B^{2+}C^{4+}E_4^{2-}$) semiconductors crystallize with face-centered cubic anion sub-lattices that possess specific orderings of cations throughout tetrahedral holes in the structure. Two common I_2-II-IV-VI_4 structure types, kesterite (*e.g.*, $Cu_2ZnSnSe_4$) and stannite

(*e.g.*, $Cu_2FeSnSe_4$) differ only by the ordering of the A^+, B^{2+}, and C^{4+} cations throughout the structure. Stannite $Cu_2FeSnSe_4$ has received comparatively less attention than its kesterite $Cu_2ZnSnSe_4$ congener, despite also holding promise as an efficient solar absorber due to its favorable direct band gap, the Earth abundance of Fe (whereas Zn is a more critical element), and high absorption coefficient through the visible region. A hexagonal wurtzite-like polymorph of $Cu_2FeSnSe_4$ has not been reported nor predicted.

In designing a synthetic route to a new wurtzite-like $Cu_2FeSnSe_4$ polymorph, we chose Ph_2Se_2 as a selenium source as it preferentially nucleates the requisite nearly hexagonal Cu_3Se_2 intermediate in oleylamine that can give rise to wurtzite-like products. We combined Cu(oleate)$_2$, Ph_2Se_2 and Sn(ethylhexanoate)$_2$ in oleylamine, and then hot-injected Fe(acac)$_3$ to yield the nanocrystal product. X-ray diffraction (XRD) of the reaction aliquots reveal that the Cu_3Se_2 intermediate is indeed present prior to injection of Fe(acac)$_3$; notably, reflections uniquely assignable to Cu_3Se_2 quickly disappear prior to Fe(acac)$_3$ injection, indicating that Sn diffuses quickly into the scaffold provided by Cu_3Se_2 to create a distinct hexagonal, ternary intermediate (corroborated by elemental analysis). Hot-injection of Fe(acac)$_3$ leads to Fe incorporation into this ternary intermediate that crystallizes into a phase-pure wurtzite-like $Cu_2FeSnSe_4$ product (**Fig. 1a**). The wurtzite-like $Cu_2FeSnSe_4$ nanocrystals are stable in air at room temperature and do not to relax to the thermodynamic stannite phase after 7 months.

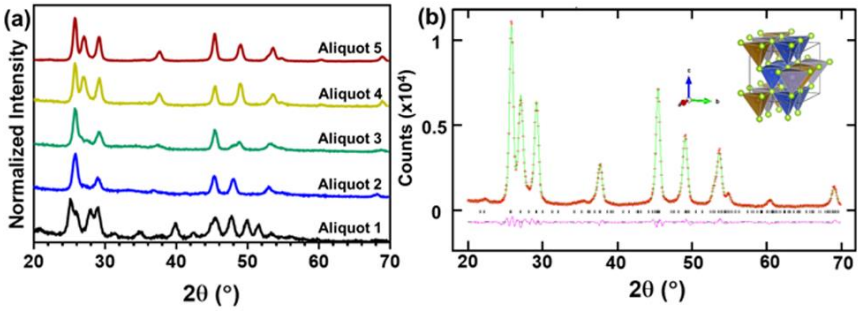

Fig. 1 (a) Powder XRD patterns of reaction aliquots taken during the synthesis of wurtzite-like $Cu_2FeSnSe_4$ nanocrystals, showing the progression from a binary Cu_3Se_2 intermediate (aliquot 1) to the final quaternary material (aliquot 5). (b) Rietveld refinement of the XRD data of aliquot 5 confirms that a cation-ordered *Pmn*2$_1$ unit cell is an appropriate structural model for this wurtzite-like polymorph (χ^2 = 3.458, w*R* = 5.75%).

Many multinary wurtzite-like phases possess ordered cation sub-lattices; indeed, quaternary compounds such as Cu_2FeSiS_4 and $Cu_2FePbSe_4$ are known to crystallize in wurtzite-like structures with the orthorhombic space group *Pmn*2$_1$.[2] We fit the XRD data to a theoretical cation-ordered structure derived from an analogous *Pmn*2$_1$ wurtzite-like structure of Cu_2FeSiS_4.[3] This refinement yielded an excellent fit, suggesting that ordering manifests in the cation sub-lattice of this polymorph (**Fig. 1b**). Symmetry considerations also support the assignment of the *Pmn*2$_1$ space group to this polymorph. The binary Cu_3Se_2 intermediate crystallizes with the $P\bar{4}2_1m$ space group. Upon incorporation of Sn and Fe, the space group symmetry is reduced, but not lost; *Pmn*2$_1$ is a non-isomorphic sub-group of $P\bar{4}2_1m$ of index 8, which confirms that there is a crystallographic symmetry relationship between the binary intermediate and the quaternary wurtzite-like product.

DFT calculations indicate that the *Pmn*2$_1$ polymorph of $Cu_2FeSnSe_4$ is dynamically stable and is slightly metastable at 9.4 meV/atom above the energy of the stannite structure of $Cu_2FeSnSe_4$. To compare the optoelectronic properties of the stannite $I\bar{4}2m$ polymorph of $Cu_2FeSnSe_4$ to the wurtzite-like *Pmn*2$_1$ polymorph, we calculated the spin-density of states (**Fig.**

2). The largest contributions to the conduction band edges originate from Se-*p* and Sn-*s* orbitals for the $I\bar{4}2m$ polymorph, while the wurtzite-like $Pmn2_1$ polymorph has a strong hybridization from Se-*s*, Se-*p*, and Sn-*s* states. Interestingly, while both polymorphs have low density of states (DOS) near the conduction band minimum (CBM), it is significantly lower for the wurtzite-like $Pmn2_1$ polymorph (**Fig. 2a**).

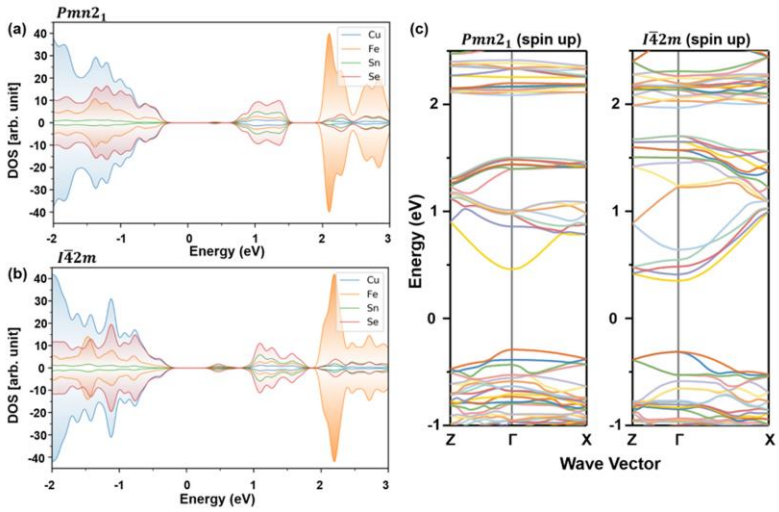

Fig. 2 Spin-density of states (DOS) calculated with the HSE06 functional for (a) the wurtzite-like $Pmn2_1$ polymorph of $Cu_2FeSnSe_4$ and (b) the stannite $I\bar{4}2m$ polymorph of $Cu_2FeSnSe_4$. (c) Band structure around the Γ point calculated with the HSE06 functional for spin-up channel.

The $Pmn2_1$ polymorph features a sharp dispersion of the CBM around the Γ point, which rationalizes the lower DOS near the CBM (**Fig. 2c**). The $Pmn2_1$ polymorph may be preferable over the $I\bar{4}2m$ polymorph in solar cell applications, since the sparse manifolds of states near the CBM in the former can increase the lifetime of hot electrons. The sharper dispersion of the CBM along the Z-Γ direction indicates the $Pmn2_1$ polymorph of $Cu_2FeSnSe_4$ has a smaller electron mass and higher electron mobility in the *z*-direction. The gap between the valence band maximum and CBM+1 for the $Pmn2_1$ polymorph is 1.15 eV, showing excellent agreement with the experiment.

2. Clarifying the crystal structure of metastable Ag_2Se nanocrystals. Ag_2Se semiconductor nanocrystals are a well-studied sub-field of colloidal quantum dots, due in large part to their highly tunable optical band gaps (from 0.2–1.5 eV).[4] As examples of Ag_2Se nanocrystals began to emerge 20 years ago, a distinct polymorph was consistently observed that did not correspond to the expected $P2_12_12_1$ orthorhombic (low temperature) or $Im\bar{3}m$ cubic (high temperature) structures of bulk Ag_2Se. This metastable polymorph was assigned to a tetragonal crystal system based on an electron diffraction study on Ag_2Se thin films by Günter and Keusch.[5] This erroneous structural assignment stuck and has been used to rationalize ensuing Ag_2Se nanocrystal properties, such as splitting of the intraband excitonic transition.[6] The metastable "tetragonal" polymorph has also been observed as a transient binary intermediate in the synthesis of metastable wurtzite-like $AgInSe_2$ nanocrystals.[7] In order to fully understand the fundamental structure-property relationships of these materials, it is crucial to precisely know their crystal structure. In the case of the metastable "tetragonal" Ag_2Se nanocrystals, however, there are no prior refinements of XRD data of these materials to the unit cell described by Günter and Keusch. Rather, the diffraction data has only been qualitatively compared to the *d*-spacings and lattice parameters reported by them.

We assessed the structure of metastable Ag_2Se nanocrystals prepared by several different synthetic methods. XRD data collected on the Ag_2Se nanocrystals are provided in **Fig. 3** and are in qualitative agreement with prior reports of this metastable phase.[4,8] A simulated XRD pattern of the theoretical "tetragonal" structure reported by Günter and Keusch is shown in red. While there are a few peaks in the XRD pattern that correspond to reflections in the simulated "tetragonal" pattern, it is clear that the "tetragonal" pattern does not account for most of the

experimentally observed reflections. Alternatively, a Rietveld refinement with a good quality-of-fit was obtained starting with the structure type of a closely related material; namely, anti-$PbCl_2$-like Ag_2S,[9] which is shown in blue. Thus, it appears that the average structure of the metastable Ag_2Se nanocrystals can be adequately described as anti-$PbCl_2$-like. PDF analysis of X-ray total scattering data confirms this structural assignment on the local scale.

The anti-$PbCl_2$-like structure is monoclinic with space group $P2_1/n$. Whereas the "tetragonal" structure of Ag_2Se is a slightly distorted face-centered cubic-lattice of Se^{2-} anions containing interstitial Ag^+ cations (**Fig. 3b**), the anti-$PbCl_2$-like structure features distorted edge-sharing $AgSe_4$ tetrahedra (**Fig. 3c**). The observation of the anti-$PbCl_2$-like structure of Ag_2S in Ag_2Se nanocrystals is consistent with reports of metal selenide nanocrystals that adopt metastable crystal structures not found in the bulk but are isostructural with known polymorphs that form in the bulk for analogous metal sulfides.[10] With the structure of this metastable polymorph now resolved, we performed the first-ever electronic structure calculations for this Ag_2Se polymorph. DFT calculations indicate that the anti-$PbCl_2$-like Ag_2Se polymorph is a dynamically stable, narrow-band gap semiconductor. The anti-$PbCl_2$-like structure of Ag_2Se is a low-lying metastable polymorph at 5-25 meV/atom above ground state. The $P2$ unit cell reported by Günter and Keusch appears far from a local minimum on the potential energy surface; significant structural rearrangements occur during geometry relaxation calculations and the relaxed structure is ~20 meV/atom higher in energy than the anti-$PbCl_2$-like phase.

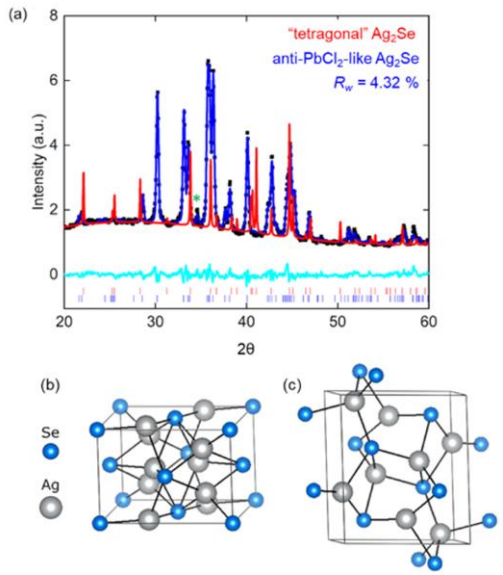

Fig. 3 (a) Rietveld refinement of the proposed anti-$PbCl_2$-like structure to the experimental powder XRD pattern of metastable Ag_2Se nanocrystals. The experimental diffraction pattern is shown with black data points, and the refined model is shown as the blue trace, with the difference pattern shown below in turquoise. The calculated powder diffraction pattern of Günter and Keusch's "tetragonal" phase is shown in red. (b) Unit cell of Günter and Keusch's "tetragonal" phase. (c) Unit cell of the proposed anti-$PbCl_2$-like polymorph of Ag_2Se.

Future Plans

The operative experimental variables that direct the symmetry of the key binary copper or silver chalcogenide intermediates are not fully known. Elucidation of the mechanism of phase determination for intermediates will be carried out in a three-part effort using a data-driven design of experiments (DoE) approach: (1) Define suspected experimental variables and their levels, (2) use a full factorial design to determine which variables are significant (or not) in phase determination, and (3) develop insight into the mechanism of phase determination by measuring the degree to which the variables interact with each other.

References

1. Tappan *Chem. Mater.* **2018**, *30*, 5704; 2. Quintero *Mater. Res. Bull.* **1999**, *34*, 2263; 3. Schäfer *Mater. Res. Bull.* **1974**, *9*, 645; 4. Sahu *J. Am. Chem. Soc.* **2011**, *133*, 6509; 5. Günter *Ultramicroscopy* **1993**, *49*, 293; 6. Son *Nano Lett.* **2020**, *20*, 4985; 7. Tappan *Chem. Mater.* **2020**, *32*, 2935; 8. Wang *Chem. Mater.* **2014**, *26*, 5647; 9. Santamaría-Pérez *Inorg. Chem.* **2012**, *51*, 5289; 10. Ng *J. Am. Chem. Soc.* **2006**, *128*, 7118.

Publications

[1] Tappan, B. A.; Chu, W.; Mecklenburg, M.; Prezhdo, O. V.; Brutchey, R. L. Discovery of a Wurtzite-like $Cu_2FeSnSe_4$ Semiconductor Nanocrystal Polymorph and Implications for Related $CuFeSe_2$ Materials. **2021**, manuscript submitted.

[2] Tappan, B. A.; Zhu, B.; Cottingham, P.; Mecklenburg, M.; Scanlon, D. O.; Brutchey, R. L. On the Crystal Structure of Colloidally Prepared Metastable Ag_2Se Nanocrystals. **2021**, manuscript submitted.

[3] Williamson, E. M.; Tappan, B. A.; Mora-Tamez, L.; Barim, G.; Brutchey, R. L. Statistical Multi-Objective Optimization of Thiospinel $CoNi_2S_4$ Nanocrystal Synthesis via Design of Experiments. *ACS Nano* **2021**, manuscript in press.

[4] Smock, S. R.; Chen, Y.; Rossini, A. J.; Brutchey, R. L. The Surface Chemistry and Structure of Colloidal Lead Halide Perovskite Nanocrystals. *Accounts of Chemical Research* **2021**, *54*, 707-718.

[5] Tappan, B. A.; Brutchey, R. L. Polymorphic Metastability in Colloidal Semiconductor Nanocrystals. *ChemNanoMat* **2020**, *6*, 1567-1588.

[6] Tappan, B. A.; Chen, K.; Lu, H.; Mallikarjun Sharada, S.; Brutchey, R. L. Synthesis and Electrocatalytic HER Studies of Carbene-Ligated $Cu_{3-x}P$ Nanocrystals. *ACS Applied Materials & Interfaces* **2020**, *12*, 16394-16401.

[7] Tappan, B. A.; Horton, M. K.; Brutchey, R. L. Ligand-Mediated Phase Control in Colloidal $AgInSe_2$ Nanocrystals. *Chemistry of Materials* **2020**, *32*, 2935-2945.

[8] Chen, Y.; Smock, S. R.`; Flintguber, A. H.; Perras, F. A.; Brutchey, R. L.; Rossini, A. J. The Surface Termination of $CsPbBr_3$ Perovskite Quantum Dots Determined by Solid-State NMR Spectroscopy. *Journal of the American Chemical Society* **2020**, *142*, 6117-6127.

[9] Smock, S. R.; Tabatabaei, K.; Williams, T. J.; Kauzlarich, S. M.; Brutchey, R. L. Surface Coordination Chemistry of Germanium Nanocrystals Synthesized by Microwave-Assisted Reduction in Oleylamine. *Nanoscale* **2020**, *12*, 2764-2772.

[10] Greaney, M. J.; Joy, J.; Combs, B. A.; Das, S.; Buckley, J. J.; Bradforth, S. E.; Brutchey, R. L. Effects of Interfacial Ligand Type on Hybrid P3HT:CdSe Quantum Dot Solar Cell Device Parameters. *Journal of Chemical Physics* **2019**, *151*, 074704.

[11] Cottingham, P.; Brutchey, R. L. Depressed Phase Transitions and Thermally Persistent Local Distortions in $CsPbBr_3$ Quantum Dots. *Chemistry of Materials* **2018**, *30*, 6711-6716.

[12] Barim, G.; Smock, S. R.; Antunez, P. D.; Glaser, D.; Brutchey, R. L. Phase Control in the Colloidal Synthesis of Well-Defined Nickel Sulfide Nanocrystals. *Nanoscale* **2018**, *10*, 16298-16306.

[13] Smock, S. R.; Williams, T. J.; Brutchey, R. L. Quantifying the Thermodynamics of Ligand Binding to $CsPbBr_3$ Quantum Dots. *Angewandte Chemie International Edition* **2018**, *57*, 11711-11715.

[14] Tappan, B. A.; Barim, G.; Kwok, J. C.; Brutchey, R. L. Utilizing Diselenide Precursors Towards the Rationally Controlled Synthesis of Metastable $CuInSe_2$ Nanocrystals. *Chemistry of Materials* **2018**, *30*, 5704-5713.

Elucidating the Link Between Alkali Metal Ions and Reaction-Transport Mechanisms in Cathode Electrodes for Alkali-ion Batteries

Assistant Prof. Ö. Özgür Çapraz,

The School of Chemical Engineering, Oklahoma State University, Stillwater, Oklahoma

Program Scope

The main objective of our study is to identify the intrinsic relationship between the role of alkali metal-ions and electrochemically-driven mechanical stability and kinetic properties of battery materials. The overall question is *"What is the role of alkali metal ions on the electrochemical and mechanical behavior of cathode electrodes?* Our guiding *hypothesis* is that intercalation of larger alkali metal-ions (Na and K) inevitably alters the coupled transport-reaction processes during battery operation in organic electrolytes, leading to intensive chemo-mechanical instabilities in cathode electrodes, resulting in rapid capacity fade. To validate the hypothesis, we experimentally characterize the reaction-transport processes and driving governing forces on instability of electrode materials in different alkali metal-ion environments by employing in situ mechanical measurements coupled with electrochemical and chemical analysis.

Recent Progress

Crystalline to Amorphous Phase Transformation in Iron Phosphate upon K intercalation: We interrogated how larger K ions deform the crystalline structure of the iron phosphate cathodes. Intercalation of large ions could cause irreversible structural deformations and amorphization in the crystalline electrodes. Design of new amorphous electrodes is another route to develop electrodes to reversibly store these ions. Lack of understanding in dynamic changes in the amorphous nanostructures during battery operation is the bottleneck for further developments. Here, we utilize in situ digital image correlation and XRD techniques to probe dynamic changes in the amorphous phase of iron phosphate during potassium intercalation (Figure 1 and 2). Interestingly, the distinct differences between the first cycle and the subsequent cycles during K ion intercalation into $FePO_4$ is observed in both strain measurements and XRD analysis. In-operando XRD analysis demonstrated the changes in the electrode structure during the first

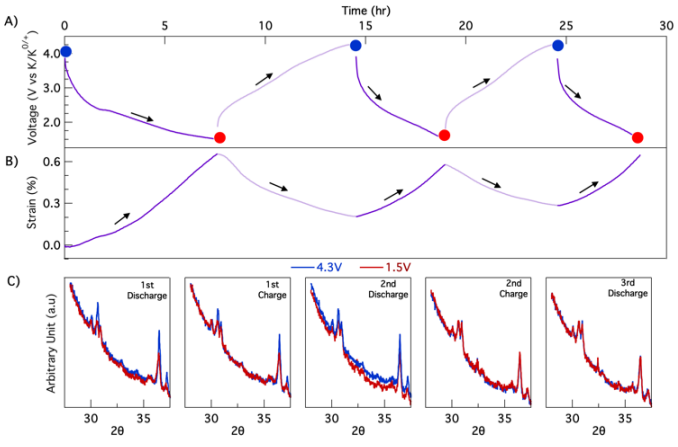

Figure 1: Discharge and Charge of Iron Phosphate Composite electrode with Potassium ions: A) Voltage and B) strain evolution in the composite electrode during potassium intercalation at C/25 rate. C) Corresponding XRD patterns at the beginning and end of each charge and discharge cycles.

cycle and in-situ strain analysis showed irreversible strain and capacity derivatives only observed during the first cycle. Beyond the first cycle, the electrode no longer undergoes any detectable changes in its crystallinity in the XRD analysis. Both evolution profile of the strain and capacity derivatives become highly reversible beyond the first cycle. Surprisingly, although in-operando XRD analysis were not able to capture any changes in the crystalline structure of the electrode during the subsequent cycles, strain derivatives analysis indicates a reversible physical change in the electrode upon K ion intercalation. The reversible strain and capacity derivatives suggest the phase transformations in the electrode structure at redox potentials of 1.9V during discharge and 2.8 V during charge cycles, respectively. Identifying the redox reactions in the amorphous phase and its associated volumetric changes upon K intercalation into amorphous phase is an important step to understand the dynamic and kinetic changes in the amorphous electrodes. We foresee that a similar approach can be utilized to study chemo-mechanics of amorphous electrodes for many different battery chemistries including Na-ion, K-ion and Zn-ion batteries. In situ probing dynamic changes in the amorphous materials during battery cycling can provide fundamental knowledge to establish a structure – mechanics- performance relationship for amorphous materials. This work is submitted for publication and the pre-print version was posted on ChemArXiv[1].

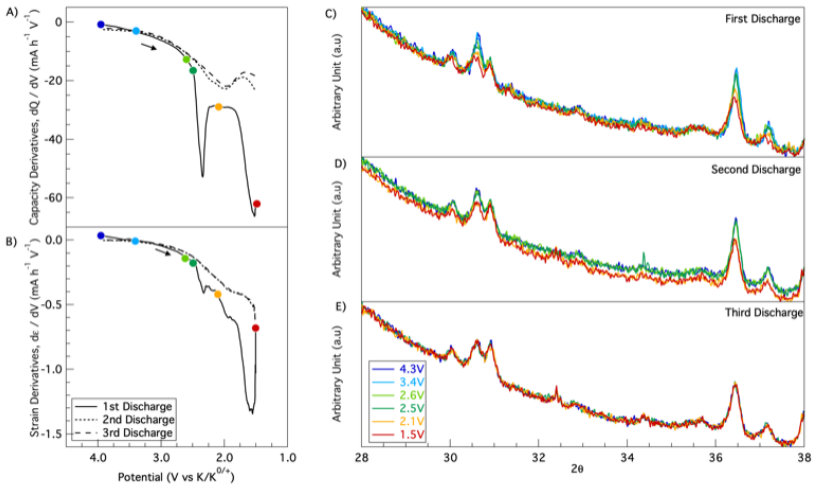

Figure 2: Structural, physical, and electrochemical response of the iron phosphate during first three discharge cycles A) capacity and B) strain derivatives with respect to voltage. C-E) Corresponding XRD patterns at selected potentials colored as shown in the figure.

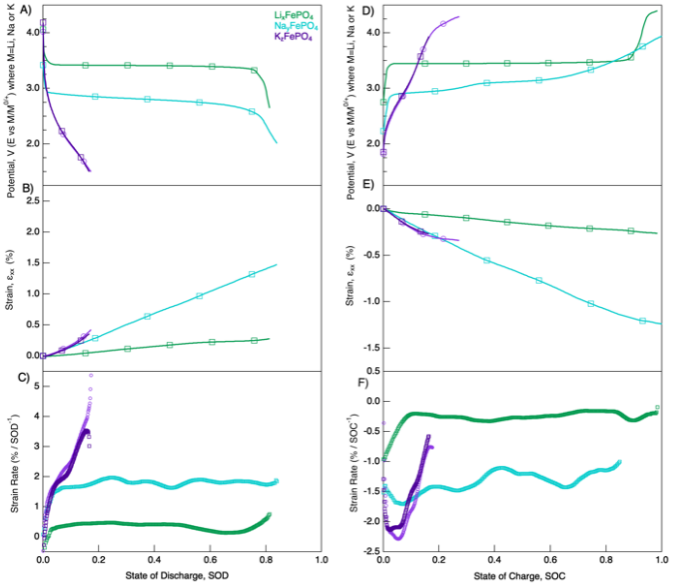

Figure 3: Potential evolution, strain generation and strain rates with respect to state of discharge (A,B, C) and charge (C, D, E) of Li (green), Na (blue) and K (purple) ions into $FePO_4$ electrode during the fourth cycle. The square and spherical symbols show when electrode is cycled either in EC:DMC or EC:PC solvents, respectively.

Impact of Alkali-ion Intercalation into Iron Phosphate: In this work, we compared the electrochemical and

mechanical response of the iron phosphate cathodes upon Li, Na and K ion intercalation by using electrochemical techniques and *in situ* digital image correlation. Iron phosphate model electrodes were prepared by electrochemical displacement technique in order to ensure identical morphology, structure, and chemistry in the pristine iron phosphate electrodes. Strain evolution during Li and Na intercalation result in more linear dependence on the state of charge / discharge (Figure 3). However, strain generation show nonlinear behavior during insertion / extraction of K ions. Interestingly, when same amount of K and Na ions are intercalated, the electrode results in almost similar expansions. However, strain rate calculations showed that K ion intercalation results in a progressive increase in the strain rate, whereas Li and Na intercalation induce nearly constant strain rates. Potential-dependent behaviors also demonstrate more sluggish redox reactions during K intercalation, compared to the Li and Na ones. This provides fundamental insights regarding to the impact of alkali ions on the redox chemistry and associated mechanical deformations. Our study quantitively analyzed the limitations of the larger alkali-ion intercalation into crystalline iron phosphate structures. The outcomes here can be transformed into other olivine-type electrode structures and similar methodology can be used to survey suitable olivine structures for reversible intercalation of larger alkali-metal ions.

The Impact of Na vs Li intercalation on Rate-Dependent Electrochemical Deformations: We also investigated how Li and Na intercalation impacts irreversible mechanical deformations in the electrode. To do that, we measured irreversible strains in the iron phosphate electrode cycled at various rates during Li or Na intercalation in electrolytes containing $LiClO_4$ or $NaClO_4$ salts, respectively. Figure 4 shows the cumulative irreversible strain generation in $LiFePO_4$ and $NaFePO_4$ electrodes. In both cases, the irreversible deformation increases dramatically in the electrodes as the scan rates increased. When both electrodes were cycled at the same rate, the deformations were greater during the Na intercalation in comparison to Li ones. For example, at the slower rate (C/25), the slope of the irreversible deformation vs time was almost 0.134 for Na whereas the slope is only about 0.039 for Li intercalation.

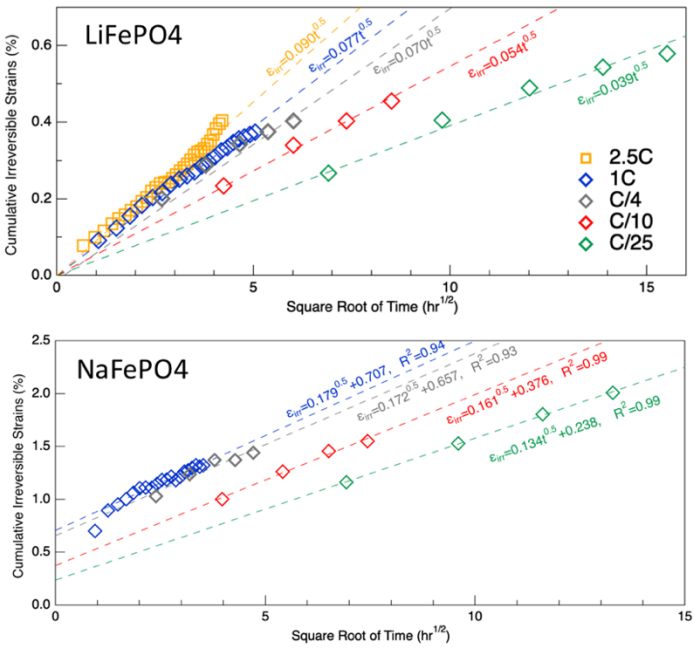

Figure 4: Cumulative irreversible strains in the composite $LiFePO_4$ and $NaFePO_4$ electrodes cycled at 2.5C (yellow), 1C (blue), C/4 (grey), C/10 (red), and C/25 (green) rates. The cumulative irreversible strains are plotted with respect to square root of cycling time. Dash lines represent the fitted data with the fitted equation.

Future Plans

Fe K-edge X-ray absorption near edge structure (XANES) will be performed at PNNL on the $FePO_4$ cathodes to determine changes in the local electronic and geometric structure during the intercalation of alkali metal ions. X-ray absorption spectroscopy provides information about the oxidation state variations of specific elements and their site symmetries. K-edge XANES spectra of cathodes will be recorded at the potentials where either distinct change in electrochemical response or strain derivatives are observed on Figure 3. Tracking the oxidation state of Fe transition metals will provide necessary information to correlate mechanical response of the cathodes with the structural changes in the material. Extended X-ray absorption fine structure (EXAFS) will be performed to investigate the variations in the local environment around the Fe in the layered oxide and the polyanionic cathodes, respectively. EXAFS will provide changes in transition metal – transition metal (e.g. Fe-Fe) and transition metal – oxygen (e.g. Mn-O) distances in the cathode structure at different state of charge / discharge. In the second year of the project, we will also perform in situ strain and stress measurements on $NaFePO_4$ cathode using $NaPF_6$, $NaClO_4$ and NaTFSI. Based on our preliminary results in the first year, we expect that $NaPF_6$ containing salt may decompose on the electrode surface. We will also perform in situ XPS study on MPF_6, $MClO_4$ and MTFSI (where M= Li or Na) on $MFePO_4$ cathode to elucidate the reactivity of electrolytes in two different alkali-ion metal compositions.

Publications

B. Ozdogru, Y. Cha, V.Murugesan, M-K Song, Ö. Çapraz. In Situ Probing Potassium-ion Intercalation-induced Amorphization in Crystalline Iron Phosphate Cathode Materials. ChemRxiv. Cambridge: Cambridge Open Engage; 2021; 10.26434/chemrxiv.14579259.v1 This content is a preprint and has not been peer-reviewed.

Looking for superconductors among tungsten-bronze-related oxides

R. J. Cava

Department of Chemistry, Princeton University

In the past, the usual way to synthesize bronzes with unusual ions in the tunnels has been to employ high pressure synthesis. This is possible to do in my lab, in an instrument that currently works to up 9 GPa and 1200 C. More straightforward, however, is an alternative synthesis method that has the chance of resulting in the fabrication of a surprisingly large range of ion-intercalated hexagonal tungsten bronzes. This would be the reaction between WO_3, WO_2 and the chlorides of the potentially tunnel-residing-metal in a temperature gradient, to create the bronzes plus a volatile oxychloride that physically leaves the bronze compound behind in the hot zone of the furnace after it transports to the cold zone. I will describe our progress in 2020 in this synthetic area. Further, a handful of ternary and quaternary niobates have been known for some time to display tetragonal tungsten bronze type structures with high dielectric constants or ferroelectric behavior (i.e. $Ba_2NaNb_{10}O_{30}$). I have been curious about whether metallic conductivity and even superconductivity can be induced through electron doping of these normally highly insulating phases for some time. I will describe our progress in 2020 in synthesizing and characterizing those materials as well.

Project Title: Polyelectrolyte-grafted Nanochannels for Enhanced Electrochemomechanical Energy Conversion

Siddhartha Das (PI) (Department of Mechanical Engineering, University of Maryland; Email: sidd@umd.edu)

Peter W. Chung (co-PI) (Department of Mechanical Engineering, University of Maryland; Email: pchung15@umd.edu)

(i) Program Scope

The overall scope of this program has been to develop a continuum as well as a Molecular Dynamics (MD) simulation framework to study the behavior of polyelectrolyte (PE) brushes grafted at a single solid surface and the walls of a nanochannel and use that understanding to probe the electrohydrodynamic transport and the resulting electrokinetic energy conversion in nanochannels grafted with such PE brushes.

(ii) Recent Progress

We developed, for quantifying the thermodynamics, electrostatics, and configurations of pH-responsive PE brushes, (1) a continuum augmented Strong Stretching Theory (SST) model that accounts for the excluded volume (EV) interactions and a more expanded form of the mass action law [see Fig. 1(a)] [1,2] and (2) a continuum augmented SST model that additionally accounts for the presence of salt of large concentrations [3]. Figs. 1(b,c) have summarized some of the key findings of these studies [1,3]. We further developed continuum models for describing the electroosmotic (EOS) [4] and the induced electrokinetic [5-7] transport in nanochannels grafted with pH-responsive PE brushes modeled using the augmented SST model [1,2]. Prior to our research, the general understanding was that the liquid transport in polymer and PE brush grafted nanochannels was invariably retarded [8,9] arising from the brushes imparting an additional drag on the fluid flow. Our results led to a paradigm shift in this understanding. We established that there is a brush-induced localization of the electric double layer (EDL) away from the nanochannel walls: this enhances the effect of the EDL-induced body force that competes with the brush-induced additional drag. For certain parameter choices, the influence of this body force became more dominant ensuring a more

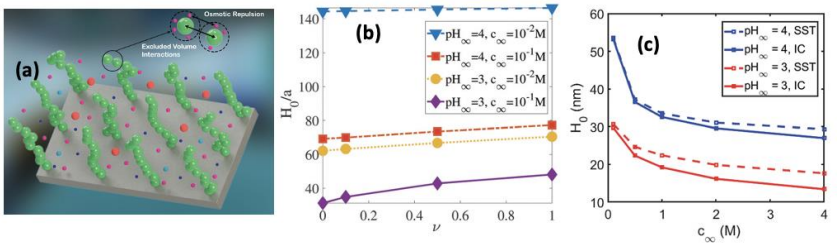

Figure 1: (a) Schematic (see Ref. 1) used to study the augmented SST model [1,2]. (b) Plot (see Ref. 1) showing the effect of excluded volume interaction parameter (ν) on the brush height (H_0) for different salt concentration and pH. The result is obtained using the model of Ref. 1. (c) Plot (see Ref. 3) quantifying the effect of the ion-ion correlation (IC) on the brush height for different pH values. The result is obtained using the model of Ref. 3.

augmented electroosmotic [4] or induced electroosmotic transport [6,7] or electrochemomechanical (electrokinetic) energy generation [5] in nanochannels grafted with PE brushes in comparison to brush-free nanochannels having the same charge as the brushes (in brush-grafted nanochannels).

In addition to the continuum models, we have also developed one of the first ever known all-atom MD simulation models for probing the behavior of PE brushes and the microstructure of the PE brushes (i.e., the behavior and the properties of the brush-supported counterions and water molecules) [see Fig. 2(a)] [10]. We studied the poly-acrylic acid (PAA) PE brushes screened by Na^+ counterions and water was modeled explicitly. The PE brush height obtained from the simulations was found to obey the scaling prediction for the brush height for the non-linear osmotic brush regime [see Fig. 2(b)]. More importantly, we discovered a WISE (Water-in-Salt-Electrolyte)-like behavior [11] of the counterions condensed on the PE brushes. We found that the water in the solvation shell of the brush-supported counterions (Na^+) got replaced by the functional groups (COO^-) of the PE brushes [see Figs. 2(c,d)]. The resulting weight and volume of this Na^+-COO^- "salt" could outweigh the weight and volume of water [see Fig. 2(e)], triggering a WISE-like behavior. Also, the large confinement effect and the electrostatic and dipole interactions ensured a significant reduction in the mobility (quantified by very small MSD or mean square displacement values) of the brush-supported Na^+ ions and water molecules inside the brush layer [see Figs. 2(f) and 2(g)]. In another all-atom MD simulation study [12], we explored the effect of charge fraction or finite degree of ionization (f) of the PAA PE brushes (f=0 and f=1 represented the cases of uncharged and fully ionized or fully charged PAA brushes) in determining the brush height, WISE-like behavior of the brush-supported Na^+ ions, and the mobility of the brush-supported Na^+ ions and water molecules. In the third all-atom MD simulation study [13], we explored the role of the large confinement triggered by the densely grafted PE brush layer in altering the water-water and water-PE hydrogen bond (HB) strength. The results confirmed a significant reduction in the strength of the water-water and water-PE HB strength with an increase in PE brush grafting density. Physically, this is

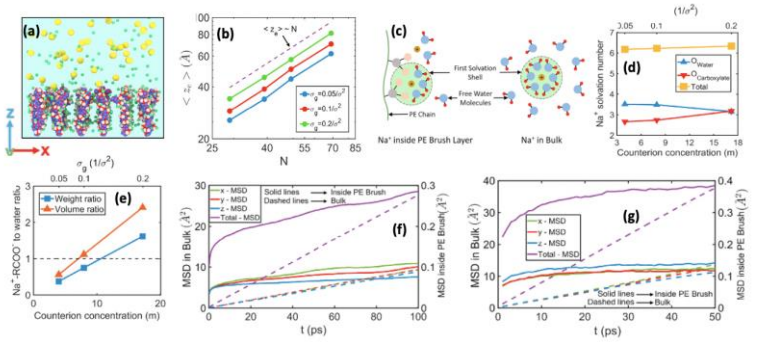

Figure 2: (a) MD simulation snapshot showing the set up for the all-atom MD simulation of the PE brushes. (b) Simulation results for PE brush height as functions of the grafting density (σ_g) and polymer size (N). The dotted line gives the scaling prediction for the brush height in the non-linear osmotic brush regime. (c) Schematic showing the onset of the WISE-like behavior, where the water (O_{water}) of the solvation shell of the PE-bound counterions are replaced by the PE functional groups ($O_{carboxylate}$) to form the Na^+-$RCOO^-$ "salt". (d) Result confirming this replacement. (e) Confirmation of the onset of "WISE"-state as the Na^+-$RCOO^-$ "salt" outweighs water by weight and volume. MSD plots confirming the reduced mobility of (f) brush-trapped counterions and (g) brush-trapped water molecules. All figures taken from Ref. 10.

explained by a breakdown of the water ring structure, confirmed by the presence of a larger number of smaller rings (or rings with lesser number of water molecules) within the brush layer. Finally, we also used all-atom MD simulations to probe the behavior of PAA brushes in the presence of multivalent screening counterions [14]. We identified that unlike the current notion [15], bridging interactions triggered by the counterions are not the sole function of the counterion valence. Rather the bridging interactions depended on the fraction of counterions (of a given type) that get physically condensed on the PE backbone as well as the size of the counterion solvation shell. As a consequence, there is not only a significant reduction of the PE brush height in presence of certain multivalent screening counterions, but might also have ushered in scenarios where the brush height reduction for certain monovalent counterions was larger than certain divalent and trivalent counterions.

We also explored the atomistic behavior of the nanoconfined Na^+-ion-screened PAA PE brush layers in presence of added NaCl salt [16]. We further studied the atomistic EOS transport in such PE-brush-grafted nanochannels in presence of an applied axial electric field [16] [see Fig. 3(a)]. It was found that for zero and low electric field strengths, there is a most remarkable overscreening (OS) effect, where there are a greater number of Na^+ counterions within the negatively charged PAA PE brush layer than needed to screen the brush layer charge. This ensured a net positive charge of the brush layer and excess Cl^- coions (in presence of the added NaCl salt) in the brush-free bulk [Figs. 3(b,c)]. However, an increase in the electric field strength lowers the brush height, ensuring that the OS-causing excess counterions are driven out of the PE brush layer and hence the OS effect ceases to exist and the number of Na^+ and Cl^- ions became similar in the bulk [see Fig. 3(d)]. Under such circumstances, in presence of electric field of low to intermediate strengths (E=0.1, 0.5 V/nm) (i.e., the conditions for which the OS effect ensures an excess of coions in the brush-free bulk), we observe a coion-dominated EOS transport, i.e., the EOS flow occurs in the direction of the motion of coions (from right to left) [Fig. 3(e)]. This is aided by the fact that at such electric field strengths the mobility of Cl^- ion is more than that of the Na^+ ion [Fig. 3(f)]. However, for larger

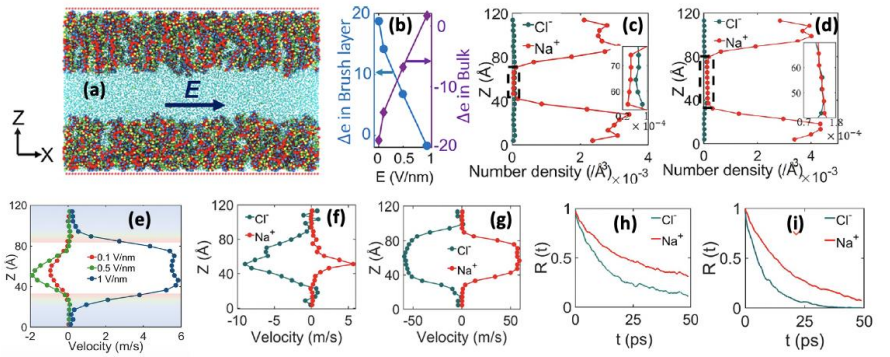

Figure 3: (a) MD simulation snapshot showing the nanoconfined PE brushes. (b-d) Results confirming the onset of OS effect at smaller electric field: hence there is a net positive charge inside the brush layer and negative charge outside the brush layer [see (b)] for smaller electric fields. This is also confirmed by a larger coion (Cl^- ion) concentration in the bulk for smaller electric fields [compare (c and d)]. (e) EOS flow profile for different E. Ion velocities for (f) small (E=0.1 V/nm) and (g) large (E=1 V/nm) electric fields. Water residence time correlation function for different ions for (h) small (E=0.1 V/nm) and (i) large (E=1 V/nm) electric fields. All results are taken from Ref. 16.

electric field strengths, both coion and counterion numbers in the brush-free bulk are similar [see Fig. 3(d)], as are their mobilities [Fig. 3(g)]. However, water residence time correlation function is always larger for the Na^+ ions than Cl^- ions [Figs. 3(h,i)]: this effect, which ensures that water stays longer within the solvation shell of the Na+ ion than Cl- ion becomes the key driver at larger electric field strengths (E=1.0 V/nm) ensuring a counterion-motion-driven EOS transport (i.e., an EOS transport occurring in the direction of motion of Na+ ions, i.e., from left to right) [Fig. 3(f)]. This result also confirms an electric field strength driven reversal in the direction of the EOS flow field.

(iii) Future Plans

This proposal will end on November 30, 2021. Until that time, we shall explore the following issues: (1) the effect of transverse electric field on the properties of brushes and the brush-supported counterions and water molecules, and (2) the pressure-driven transport and electrokinetic energy generation in PE-brush-grafted nanochannels (significant progress has already been made on this problem).

(iv) References

1. Sachar, H. S., Sivasankar, V. S., and Das, S., *Soft Matter*, **2019**, *15*, 559–574.
2. Sachar, H. S., Sivasankar, V. S., Etha, S. A., Chen, G., and Das, S., *Electrophoresis*, **2020**, *41*, 554-561.
3. Etha, S. A., Sivasankar, V. S., Sachar, H. S., and Das, S., *Phys. Chem. Chem. Phys.*, **2020**, *22*, 13536-13553.
4. Sivasankar, V. S., Etha, S. A Sachar, H. S., and Das, S., *Phys. Rev. E*, **2020**, *102*, 013103.
5. Sachar, H. S., Sivasankar, V. S., and Das, S., *Soft Matter*, **2019**, *15*, 5973–5986.
6. Sivasankar, V. S., Etha, S. A Sachar, H. S., and Das, S., *Phys. Fluid.*, **2020**, *32*, 042003.
7. Sivasankar, V. S., Etha, S. A., Sachar, H. S., and Das, S., *J. Fluid Mech.* **2021**, *917*, A31.
8. Zuo, Y., Wang, G., Yu, Y., Zuo, C., Liu, Z., Hu, D., and Wang, Y., *Microfluid. Nanofluid.*, **2014**, *17*, 923.
9. Chen, G., and Das, S., *J. Appl. Phys.*, **2015**, *117*, 185304.
10. Sachar, H. S. Pial, T. H., Desai. P.R., Etha, S. A., Wang, Y., and Das. S., *Matter*, **2020**, *2*, 1509–1521.
11. Suo, L., Borodin, O., Gao, T., Olguin, M., Ho, J., Fan, X., Luo, C., Wang, C., and Xu, K., *Science*, **2015**, *350*, 938–943.
12. Sachar, H. S., Pial, T. H., Chava, B. S., and Das, S., *Soft Matter*, **2020**, *16*, 7808–7822.
13. Sachar, H. S., Chava, B. S., Pial, T. H., and Das, S., *Macromolecules*, **2021**, *54*, 2011–2021.
14. Pial, T. H., Sachar, H. S., and Das, S., *Macromolecules*, **2021**, *54*, 4154–4163.
15. Yu, J., Jackson, N. E., Xu, X., Brettmann, B. K., Ruths, M., de Pablo, J. J., and Tirrell, M., *Sci. Adv.*, **2017**, *3*, eaao1497.
16. Pial, T. H., Sachar, H. S., Desai, P. R., and Das, S., *ACS Nano*, **2021**, *15*, 6507–6516.

(v) Publications

1. Harnoor Singh Sachar, Bhargav Sai Chava, Turash Haque Pial, and Siddhartha Das, "All-Atom Molecular Dynamics Simulations of the Temperature Response of Densely Grafted Polyelectrolyte Brushes", *Macromolecules*, 2021 (Accepted for Publication). (**Publication type: Journal Article**)
2. Turash Haque Pial, Harnoor Singh Sachar, and Siddhartha Das, "Quantification of Mono- and Multivalent Counterion-Mediated Bridging in Polyelectrolyte Brushes", *Macromolecules*, Volume 54, 4154, 2021. (**Publication type: Journal Article**)
3. Vishal Sankar Sivasankar, Sai Ankit Etha, Harnoor Singh Sachar, and Siddhartha Das, "Thermo-osmotic transport in nanochannels grafted with pH-responsive polyelectrolyte brushes modelled using augmented strong stretching theory", *Journal of Fluid Mechanics*, Volume 917, A31, 2021. (**Publication type: Journal Article**)
4. Harnoor Singh Sachar, "ATOMISTIC AND THEORETICAL DESCRIPTION OF LIQUID FLOWS IN POLYELECTROLYTE-BRUSHGRAFTED NANOCHANNELS", University of Maryland, 04/15/2021. (**Publication type: Ph.D. Dissertation**)
5. Turash Haque Pial, Harnoor Singh Sachar, Parth Rakesh Desai, and Siddhartha Das, "Overscreening, Co-Ion-Dominated Electroosmosis, and Electric Field Strength Mediated Flow Reversal in Polyelectrolyte Brush Functionalized Nanochannels", *ACS Nano*, Volume 15, 6507, 2021. (**Publication type: Journal Article**)
6. Harnoor Singh Sachar, Bhargav Sai Chava, Turash Haque Pial, and Siddhartha Das, "Hydrogen Bonding and Its Effect on the Orientational Dynamics of Water Molecules inside Polyelectrolyte Brush-Induced Soft and Active Nanoconfinement", *Macromolecules*, Volume 54, 2011, 2021. (**Publication type: Journal Article**)
7. Vishal Sankar Sivasankar, "ELECTROKINETIC TRANSPORT IN NANOCHANNELS GRAFTED WITH BACKBONE CHARGED POLYELECTROLYTE BRUSHES", University of Maryland, 08/09/2020. (**Publication type: M.S. Thesis**)
8. Harnoor Singh Sachar, Turash Haque Pial, Bhargav Sai Chava, and Siddhartha Das, "All-atom molecular dynamics simulations of weak polyionic brushes: influence of charge density on the properties of polyelectrolyte chains, brush-supported counterions, and water molecules", *Soft Matter*, Volume 16, 7808, 2020. (**Publication type: Journal Article**)
9. Vishal Sankar Sivasankar, Sai Ankit Etha, Harnoor Singh Sachar, and Siddhartha Das, "Theoretical study on the massively augmented electro-osmotic water transport in polyelectrolyte brush functionalized nanoslits", *Physical Review E*, Volume 102, 013103, 2020. (**Publication type: Journal Article**)
10. Harnoor Singh Sachar, Turash Haque Pial, Parth Rakesh Desai, Sai Ankit Etha, Yanbin Wang, Peter W. Chung, and Siddhartha Das, "Densely Grafted Polyelectrolyte Brushes Trigger ''Water-in-Salt''-like Scenarios and Ultraconfinement Effect", *Matter*, Volume 2, 1509, 2020. (**Publication type: Journal Article**)
11. Sai Ankit Etha, Vishal Sankar Sivasankar, Harnoor Singh Sachar, and Siddhartha Das, "Strong stretching theory for pH-responsive polyelectrolyte brushes in large salt

concentrations", *Physical Chemistry Chemical Physics*, Volume 22, 13536, 2020. (**Publication type: Journal Article**)

12. Vishal Sankar Sivasankar, Sai Ankit Etha, Harnoor Singh Sachar, and Siddhartha Das, "Ionic diffusioosmotic transport in nanochannels grafted with pH-responsive polyelectrolyte brushes modeled using augmented strong stretching theory", *Physics of Fluids*, Volume 32, 042003, 2020. (**Publication type: Journal Article**)
13. Harnoor Singh Sachar, Vishal Sankar Sivasankar, Sai Ankit Etha, Guang Chen, and Siddhartha Das, "Ionic current in nanochannels grafted with pH-responsive polyelectrolyte brushes modeled using augmented strong stretching theory", *Electrophoresis*, Volume 41, 554, 2019. (**Publication type: Journal Article**)
14. Harnoor Singh Sachar, Vishal Sankar Sivasankar, and Siddhartha Das, "Electrokinetic energy conversion in nanochannels grafted with pH-responsive polyelectrolyte brushes modelled using augmented strong stretching theory ", *Soft Matter*, Volume 15, 5973, 2019. (**Publication type: Journal Article**)
15. Harnoor Singh Sachar, Vishal Sankar Sivasankar, and Siddhartha Das, " Revisiting the strong stretching theory for pHresponsive polyelectrolyte brushes: effects of consideration of excluded volume interactions and an expanded form of the mass action law ", *Soft Matter*, Volume 15, 559, 2018. (**Publication type: Journal Article**)

Design of Next Generation Thermoelectrics

DOE-BES Grant No: DE-SC0014520

Vinayak P. Dravid (PI), Mercouri Kanatzidis & Christopher Wolverton
Northwestern University, Evanston, IL 60208

Project Scope: Almost 2/3rd of the energy produced annually around the globe is wasted, primarily in the form of heat loss. Thermoelectricity provides an opportunity to recapture at least a portion of this wasted energy by reversibly converting temperature gradients into electricity through the Seebeck effect[1, 2]. Advancing thermoelectric materials and their performance require unveiling the fundamental science governing the unique and complex interplay between lattice vibrations (phonons) and charge carriers; all mediated by the complex mosaic of the materials microstructure.

The thermoelectric figure-of-merit, ZT, is commonly referred parameter for evaluating the effectiveness of thermoelectrics. This dimensionless figure of merit ZT is defined by $(\sigma \cdot S^2/\kappa)T$, where σ is the electrical conductivity, S is the Seebeck coefficient, κ the thermal conductivity, and T the absolute temperature. This value is directly related to the efficiency of thermoelectric devices, and therefore thermoelectric devices are optimized through increasing the power factor ($\sigma \cdot S^2$) or decreasing the total thermal conductivity (κ) or both. Yet, the contraindicating behavior of thermoelectric properties has until recently stagnated the growth of the overall efficiency[2, 3]. This BES project has, therefore, focused on methodologies for decoupling these material properties through a variety of innovative approaches, invoking multipronged approach to study the origin of the complex thermoelectric material parameters.

In the past, our collaborative efforts have resulted in unprecedented reduction in lattice thermal conductivity through all-scale architecturing[4, 5]. In recent period, we have focused on investigating the role of point defects on the reduction of lattice thermal conductivity, such as discordant alloying. However as thermal conductivity approaches its lower (amorphous) limit, the importance of dopants and defects in the alteration of electronic properties has proven to be of growing interest. We argue that to continue to push the limits of thermoelectric performance, development of innovative strategies to enhance the power factor are needed. Subsequently our group has been at the vanguard of understanding the fundamental factors governing the power factor.

We leverage a synergistic combination of targeted experimental undertaking and data driven strategies to discover new ideal thermoelectric materials candidates as well as optimize power factor and reduce thermal conductivity in well-known thermoelectric systems. Several key scientific challenges governing this synergistic and collaborative approach include; a) insights into the collective mechanisms of charge and phonon transport across the atomic, nano- and mesoscale levels, b) understanding microstructural evolution of thermoelectric material systems, and c) potential integration of all the ZT-enhancing mechanisms simultaneously and synergistically into a single material system.

We have also been investigating power factor parameters and strategies such as: valence band convergence, minimizing band offset between multiple phases, and increasing the number of bands contributing to the transport. In addition, we search for new candidate materials with intrinsically favorable properties by leveraging data-driven approaches to design and discover new thermoelectric chemistries, explore new chalcogenide and oxide single-phase systems with potential for high-performance thermoelectrics with chemical and thermal stability at high temperature.

The past year progress included tangible advances along all fronts; with peer reviewed publications comprising multiple members of the project team in high-impact journals and other relevant metrics for evaluation of progress. Some examples of these advances are outlined below.

Recent Progress: The full account of our accomplishments during the project period are listed as archival publications. Some of the representative examples of our combined experiment-theory approach to probe the intricate interplay between thermal conductivity and charge transport are outlined below.

One part of our work has primarily focused exploring discordant alloying atoms in lead chalcogenides. To start we chose the PbSe-x%HgSe system because the lattice of PbSe is cubic rocksalt-type with Pb^{2+} in the octahedral coordination. In contrast, HgSe adopts the zincblende-type structure (cubic, tetrahedral coordination).[6] In the literature the Hg^{2+} ion is found overwhelmingly in tetrahedral coordination and in some cases in trigonal planar and even linear coordination but almost never in octahedral coordination. Therefore, the Pb2+ sites are strongly unfavorable for Hg^{2+} and would cause it to locally distort.

We describe the off-centered Hg atoms as 'discordant', since their intrinsic chemical character is out of harmony with the coordination requirements of the surrounding crystal host matrix. Using ^{199}Hg and ^{77}Se NMR, we found evidence for an asymmetric coordination environment of Hg^{2+} in the PbSe-HgSe alloy (in collaboration, at the National High Magnetic Field Laboratory), which is also supported by DFT calculations. The discordant Hg atoms not only play a role in suppressing thermal conductivity, but causes the energy offset between the L-band and lower lying Σ-band ($\Delta E_{L\text{-}\Sigma}$) to decrease significantly from 0.28 eV (in pure PbSe) to 0.16 eV in PbSe-x%HgSe, which consequently delivers a large boost to the thermopower,[2,7,8,9] which then provides a boost to the power factor ~20 $\mu W \cdot cm^{-1} \cdot K^{-2}$ which was a new record. The $Pb_{0.98-x}Na_{0.02}$-*x*%HgSe system thus outperforms any other p-type PbSe system and delivers a record high *ZT* of 1.7. We then investigated a smaller discordant atom with entirely different chemistry, specifically Ge^{2+}, which presents a stereochemically active lone pair of valence electrons. It presents off-centering in a growing number of materials, including PbSe-12%GeSe.[10] The Ge^{2+} is exemplary in being discordant because of a strong tendency to stereochemically express its $4s^2$ lone pair of electrons and distort local coordination. The role of Ge^{2+} in the rock-salt structures of PbQ is not fully understood, but it seems to be extraordinary given the very large effects on thermal transport as we found in the PbSe-GeSe system.

We have also investigated high performing SnTe–$NaSbTe_2$ and SnTe–$NaBiTe_2$ systems facilitated by cation vacancies and lattice softening. We found that unlike in most SnTe–based materials where high vacancy concentrations degrade the performance, the enhanced number of vacancies in $NaSn_mSbTe_{m+2}$ is critical to obtaining high *ZT*. The rationale for this unusual finding is twofold. First, both $NaSbTe_2$ and $NaBiTe_2$ decrease the band gap of SnTe, making the compounds more prone to detrimental bipolar diffusion than pure SnTe. In $NaSn_mSbTe_{m+2}$, however, the elevated hole concentration acts against this and suppresses bipolar diffusion.[11, 12] On the other hand, $NaBiTe_2$ does not substantially alter the carrier concentration, leaving $NaSn_mBiTe_{m+2}$ vulnerable to bipolar diffusion at high $NaBiTe_2$ fraction (m>4). Second, the vacancies facilitate low lattice thermal conductivity and are a particularly strong form of point defect scattering[13-15] predicting that $NaSn_mSbTe_{m+2}$ also have stronger phonon scattering.

The speed of sound is approximately equal to the acoustic phonon group velocity v_g at low wavevector, and because κ_{lat} scales as v_g[16] at relevant temperatures,[17] suppressing v_s can dramatically lower the lattice thermal conductivity.[18, 19] Our investigation reveals a linear reduction of v_s with increasing fraction of $NaSbTe_2$, falling ~6% from ~2150 to 2030 $m \cdot s^{-1}$. the trends in n_H and v_s indicate that the reduction in sound velocity/Debye temperature is correlated to the enhanced number of Sn vacancies in this system. In principle, the softening may come from the vacancies themselves or from impact of the higher carrier density on the interatomic force constants. The joint effects of decreased sound velocity and enhanced phonon-vacancy scattering reduce the lattice thermal conductivities of $NaSn_mSbTe_{m+2}$ beyond what would be anticipated by only alloy scattering. Considering the chemical similarity of $NaSn_mSbTe_{m+2}$ and $NaSn_mBiTe_{m+2}$, this work highlighted the importance of intrinsic defects, such as atomic vacancies, in determining a material's thermoelectric performance.

Another of our key contribution over the current funding period is the development of advanced lattice dynamics methods for simulating lattice thermal conductivity of crystalline compounds with strong anharmonicity using fully first-principles density functional theory calculations. Our theoretical framework involves state-of-the-art approaches to construct various levels of theories that explicitly account for anharmonicity up to quartic terms, with the capability of calculating anharmonic phonon renormalization from self-consistent phonon (SCPH) theory and both three- (3ph) and four-phonon (4ph) scattering, as well as thermal transport channels beyond the conventional phonon gas model. It is worth noting that our approach represents significant advancements over the currently widely used methods relying on the harmonic description of phonon dispersion and a three-phonon picture for phonon lifetimes. Using such an

improved approach, we have markedly extended the understanding of lattice thermal conductivity in thermoelectrics.

Ongoing and Future Research: The ongoing and future plans will continue to pursue strategies for understanding the origins of Seebeck effect towards power factor enhancement, to further explore novel mechanisms for thermal conductivity reduction, and in search for new anisotropic materials with ultralow intrinsic lattice thermal conductivity. Embedded in all this is to understand the structural, chemical and electronic structural parameters that control doping behavior in these materials as well as phonon scattering.

Our ongoing research has also raised key scientific questions that require deeper fundamental understanding of microstructure-transport relationship mediated by innovative materials design, novel characterization and computational insights. In this renewal, we focus on addressing the following three fundamental underpinnings, towards the design of next generation thermoelectrics:

1) **Understanding and Controlling the Effects of Discordant Atoms in Host Semiconductor lattices:** We hypothesize that discordant off-centered atoms can lower phonon velocities and introduce additional phonon scattering modes as well as favorably alter the electronic properties of semiconductors. We plan to investigate discordant atoms doped in rock salt matrix, diamond-derived structures and determine their effects on thermal transport behaviors. We also propose to investigate discordant atoms beyond the solubility and study the coupling effects from both the off-centering atoms in the matrix and the incipient nanostructures that may allow us to control the phonon behaviors.
2) **Ultralow Thermal Conductivity in Diamondoid Lattices**: We will probe prospects for ultralow thermal conductivity in diamondoid lattices in general. We hypothesize that a collection of suitably selected discordant atoms would lead to variety of nucleation/growth processes as well as generation of nanostructured microstructure. We further hypothesize that the isostructural phases will nucleate as endotaxial coherent nanostructures that may be beneficial to charge transport while inhibiting phonon propagation in the strained interfaces. Thus, we will seek deeper insights into nucleation and growth of second phase inside a tetrahedral, narrow bandgap, semiconducting matrix (e.g. CdTe analogs).
3) **Understanding High Configurational Entropy and Transport in Narrow-gap Semiconductors:** We will investigate high entropy alloys of semiconductors which distinguish them from ordinary doping to allow us study the synergy of the band structure and microstructure engineering. Here, we propose a systematic synthesis, structural, theoretical, and thermoelectric study of multi-principal-element-alloyed chalcogenides. To understand the special phonon transport, electron transport and how it derives from the special high entropy compositions, we will focus on the effects of the entropy of mixing at the atomic level. We expect this approach will help us understand how to achieve ultralow lattice thermal conductivity reaching lower values than previously possible e.g. <0.2 W/mK near the amorphous limit.

Collectively, the proposed research will help unravel important scientific concepts: i) chemical and structural effects controlling off-centering (i.e., discordant) in solute atoms, and their influence on phonon scattering and carrier mobility; ii) origin of intrinsically low thermal conductivity, and iii) role and origin of multiple electronic bands near the Fermi energy in semiconductors for high power factors.

….References and bibliography continued on next page …

References:

1. DOE, U., Quadrennial Technology Review: An Assessment of Energy Technologies and Research Opportunities. *no. September* **2015**, 1-505.
2. Snyder, G. J.; Toberer, E. S., Complex thermoelectric materials. *Nat Mater* **2008,** *7* (2), 105-14.
3. Zeier, W. G.; Zevalkink, A.; Gibbs, Z. M.; Hautier, G.; Kanatzidis, M. G.; Snyder, G. J., Thinking like a chemist: intuition in thermoelectric materials. *Angewandte Chemie International Edition* **2016,** *55* (24), 6826-6841.
4. Zhao, L.-D.; Dravid, V. P.; Kanatzidis, M. G., The panoscopic approach to high performance thermoelectrics. *Energy & Environmental Science* **2014,** *7* (1), 251-268.
5. Biswas, K.; He, J.; Blum, I. D.; Wu, C. I.; Hogan, T. P.; Seidman, D. N.; Dravid, V. P.; Kanatzidis, M. G., High-performance bulk thermoelectrics with all-scale hierarchical architectures. *Nature* **2012,** *489* (7416), 414-8.
6. Hodges, J. M.; Hao, S. Q.; Grovogui, J. A.; Zhang, X. M.; Bailey, T. P.; Li, X.; Gan, Z. H.; Hu, Y. Y.; Uher, C.; Dravid, V. P.; Wolverton, C.; Kanatzidis, M. G., Chemical Insights into PbSe-x%HgSe: High Power Factor and Improved Thermoelectric Performance by Alloying with Discordant Atoms. *J Am Chem Soc* **2018,** *140* (51), 18115-18123.
7. Bell, J. F., 3rd; Maki, J. N.; Mehall, G. L.; Ravine, M. A.; Caplinger, M. A.; Bailey, Z. J.; Brylow, S.; Schaffner, J. A.; Kinch, K. M.; Madsen, M. B.; Winhold, A.; Hayes, A. G.; Corlies, P.; Tate, C.; Barrington, M.; Cisneros, E.; Jensen, E.; Paris, K.; Crawford, K.; Rojas, C.; Mehall, L.; Joseph, J.; Proton, J. B.; Cluff, N.; Deen, R. G.; Betts, B.; Cloutis, E.; Coates, A. J.; Colaprete, A.; Edgett, K. S.; Ehlmann, B. L.; Fagents, S.; Grotzinger, J. P.; Hardgrove, C.; Herkenhoff, K. E.; Horgan, B.; Jaumann, R.; Johnson, J. R.; Lemmon, M.; Paar, G.; Caballo-Perucha, M.; Gupta, S.; Traxler, C.; Preusker, F.; Rice, M. S.; Robinson, M. S.; Schmitz, N.; Sullivan, R.; Wolff, M. J., The Mars 2020 Perseverance Rover Mast Camera Zoom (Mastcam-Z) Multispectral, Stereoscopic Imaging Investigation. *Space Sci Rev* **2021,** *217* (1), 24.
8. Liu, W. S.; Jie, Q.; Kim, H. S.; Ren, Z. F., Current progress and future challenges in thermoelectric power generation: From materials to devices. *Acta Mater* **2015,** *87*, 357-376.
9. Bharti, M.; Singh, A.; Samanta, S.; Aswal, D. K., Conductive polymers for thermoelectric power generation. *Prog Mater Sci* **2018,** *93*, 270-310.
10. Kober, M., Holistic Development of Thermoelectric Generators for Automotive Applications. *J Electron Mater* **2020,** *49* (5), 2910-2919.
11. O'Shaughnessy, S. M.; Deasy, M. J.; Doyle, J. V.; Robinson, A. J., Field trial testing of an electricity-producing portable biomass cooking stove in rural Malawi. *Energy Sustain Dev* **2014,** *20*, 1-10.
12. Pacheco, N.; Brito, F. P.; Vieira, R.; Martins, J.; Barbosa, H.; Goncalves, L. M., Compact automotive thermoelectric generator with embedded heat pipes for thermal control. *Energy* **2020,** *197*.
13. Deng, Y. D.; Zhang, Y.; Su, C. Q., Modular Analysis of Automobile Exhaust Thermoelectric Power Generation System. *J Electron Mater* **2015,** *44* (6), 1491-1497.
14. He, W.; Zhang, G.; Zhang, X. X.; Ji, J.; Li, G. Q.; Zhao, X. D., Recent development and application of thermoelectric generator and cooler. *Appl Energ* **2015,** *143*, 1-25.
15. Gude, V. G., Membrane desalination of ballast water using thermoelectric energy from waste heat. *J Mar Eng Technol* **2020**.
16. Bai, Y.; Jantunen, H.; Juuti, J., Energy Harvesting Research: The Road from Single Source to Multisource. *Adv Mater* **2018**, e1707271.
17. Ezzitouni, S.; Fernandez-Yanez, P.; Sanchez, L.; Armas, O., Global energy balance in a diesel engine with a thermoelectric generator. *Appl Energ* **2020,** *269*.
18. Jaziri, N.; Boughamoura, A.; Muller, J.; Mezghani, B.; Tounsi, F.; Ismail, M., A comprehensive review of Thermoelectric Generators: Technologies and common applications. *Energy Rep* **2020,** *6*, 264-287.
19. Zoui, M. A.; Bentouba, S.; Stocholm, J. G.; Bourouis, M., A Review on Thermoelectric Generators: Progress and Applications. *Energies* **2020,** *13* (14).

Publications resulting from work supported by the DOE grant over the previous two years

Appeared in 2019:

1. Anand, S.; Wood, M.; Xia, Y.; Wolverton, C.; Snyder, G. J., Double Half-Heuslers. Joule 2019, 3 (5), 1226-1238.
2. Chen, D.; Hao, S. Q.; Zhou, G. J.; Deng, C. K.; Liu, Q. L.; Ma, S. L.; Wolverton, C.; Zhao, J.; Xia, Z. G., Lead-Free Broadband Orange-Emitting Zero-Dimensional Hybrid (PMA)(3)InBr6 with Direct Band Gap. Inorg. Chem. 2019, 58 (22), 15602-15609.
3. Doak, J. W.; Hao, S. Q.; Kirklin, S.; Wolverton, C., Computational prediction of nanostructured alloys with enhanced thermoelectric properties. Phys. Rev. Mater. 2019, 3 (10), 8.
4. Hao, S. Q.; Dravid, V. P.; Kanatzidis, M. G.; Wolverton, C., Computational strategies for design and discovery of nanostructured thermoelectrics. npj Comput. Mater. 2019, 5, 10.
5. Hao, S. Q.; He, J. G.; Dravid, V. P.; Kanatzidis, M. G.; Wolverton, C., Dimensionally driven crossover from semimetal to direct semiconductor in layered SbAs. Phys. Rev. Mater. 2019, 3 (10), 6.
6. Hao, S. Q.; Ward, L.; Luo, Z. Z.; Ozolins, V.; Dravid, V. P.; Kanatzidis, M. G.; Wolverton, C., Design Strategy for High-Performance Thermoelectric Materials: The Prediction of Electron-Doped KZrCuSe3. Chem. Mat. 2019, 31 (8), 3018-3024.
7. He, J. G.; Xia, Y.; Naghavi, S. S.; Ozolins, V.; Wolverton, C., Designing chemical analogs to PbTe with intrinsic high band degeneracy and low lattice thermal conductivity. Nat. Commun. 2019, 10, 8.
8. Hua, X.; Hegde, V. I.; Wolverton, C., Phase Stability and Ordering in Rock Salt-Based Thermoelectrics: NaSbX2, AgSbX2, and Their Alloys with PbX and SnX (X = S, Se, Te). Chem. Mat. 2019, 31 (22), 9445-9452.
9. Isaacs, E. B.; Wolverton, C., Electronic Structure and Phase Stability of Yb-Filled CoSb3 Skutterudite Thermoelectrics from First-Principles. Chem. Mat. 2019, 31 (16), 6154-6162.
10. Isaacs, E. B.; Wolverton, C., Remarkable thermoelectric performance in BaPdS2 via pudding-mold band structure, band convergence, and ultralow lattice thermal conductivity. Phys. Rev. Mater. 2019, 3 (1), 6.
11. Khoury, J. F.; Rettie, A. J. E.; Khan, M. A.; Ghimire, N. J.; Robredo, I.; Pfluger, J. E.; Pal, K.; Wolverton, C.; Bergara, A.; Jiang, J. S.; Schoop, L. M.; Vergniory, M. G.; Mitchell, J. F.; Chung, D. Y.; Kanatzidis, M. G., A New Three-Dimensional Subsulfide Ir2In8S with Dirac Semimetal Behavior. J Am Chem Soc 2019, 141 (48), 19130-19137.
12. Lee, Y. K.; Luo, Z.; Cho, S. P.; Kanatzidis, M. G.; Chung, I., Surface Oxide Removal for Polycrystalline SnSe Reveals Near-Single-Crystal Thermoelectric Performance. Joule 2019, 3 (3), 719-731.
13. Li, J. P.; Zhou, Y. M.; Hao, S. Q.; Zhang, T. Y.; Wolverton, C.; Zhao, J.; Zhao, L. D., Thermoelectric Material SnPb2Bi2S6: The L-4,L-4 Member of Lillianite Homologous Series with Low Lattice Thermal Conductivity. Inorg. Chem. 2019, 58 (2), 1339-1348.
14. Luo, Y. B.; Cai, S. T.; Hua, X.; Chen, H. J.; Liang, Q. H.; Du, C. F.; Zheng, Y.; Shen, J. H.; Xu, J. W.; Wolverton, C.; Dravid, V. P.; Yan, Q. Y.; Kanatzidis, M. G., High Thermoelectric Performance in Polycrystalline SnSe Via Dual-Doping with Ag/Na and Nanostructuring With Ag8SnSe6. Adv. Energy Mater. 2019, 9 (2), 8.
15. Luo, Z. Z.; Cai, S. T.; Hao, S. Q.; Bailey, T. P.; Hu, X. B.; Hanus, R.; Ma, R. C.; Tan, G. J.; Chica, D. G.; Snyder, G. J.; Uher, C.; Wolverton, C.; Dravid, V. P.; Yan, Q. Y.; Kanatzidis, M. G., Ultralow Thermal Conductivity and High-Temperature Thermoelectric Performance in n-Type K2.5Bi8.5Se14. Chem. Mat. 2019, 31 (15), 5943-5952.
16. Luo, Z. Z.; Cai, S. T.; Hao, S. Q.; Bailey, T. P.; Su, X. L.; Spanopoulos, I.; Hadar, I.; Tan, G. J.; Luo, Y. B.; Xu, J. W.; Uher, C.; Wolverton, C.; Dravid, V. P.; Yan, Q. Y.; Kanatzidist, M. G., High Figure of Merit in Gallium-Doped Nanostructured n-Type PbTe-xGeTe with Midgap States. J Am Chem Soc 2019, 141 (40), 16169-16177.
17. Luo, Z. Z.; Hao, S. Q.; Cai, S. T.; Bailey, T. P.; Tan, G. J.; Luo, Y. B.; Spanopoulos, I.; Uher, C.; Wolverton, C.; Dravid, V. P.; Yan, Q. Y.; Kanatzidis, M. G., Enhancement of Thermoelectric

Performance for n-Type PbS through Synergy of Gap State and Fermi Level Pinning. J Am Chem Soc 2019, 141 (15), 6403-6412.
18. Nie, G.; Li, W. J.; Guo, J. Q.; Yamamoto, A.; Kimura, K.; Zhang, X. M.; Isaacs, E. B.; Dravid, V.; Wolverton, C.; Kanatzidis, M. G.; Priya, S., High performance thermoelectric module through isotype bulk heterojunction engineering of skutterudite materials. Nano Energy 2019, 66, 10.
19. Slade, T. J.; Bailey, T. P.; Grovogui, J. A.; Hua, X.; Zhang, X. M.; Kuo, J. J.; Hadar, I.; Snyder, G. J.; Wolverton, C.; Dravid, V. P.; Uher, C.; Kanatzidis, M. G., High Thermoelectric Performance in PbSe-NaSbSe2 Alloys from Valence Band Convergence and Low Thermal Conductivity. Adv. Energy Mater. 2019, 9 (30), 12.
20. Su, X. L.; Zhao, N.; Hao, S. Q.; Stoumpos, C. C.; Liu, M. Y.; Chen, H. J.; Xie, H. Y.; Zhang, Q. J.; Wolverton, C.; Tang, X. F.; Kanatzidis, M. G., High Thermoelectric Performance in the Wide Band-Gap AgGa1-xTe2 Compounds: Directional Negative Thermal Expansion and Intrinsically Low Thermal Conductivity. Adv Funct Mater 2019, 29 (6), 9.
21. Tan, G. J.; Hao, S. Q.; Cai, S. T.; Bailey, T. P.; Luo, Z. Z.; Hadar, I.; Uher, C.; Dravid, V. P.; Wolverton, C.; Kanatzidis, M. G., All-Scale Hierarchically Structured p-Type PbSe Alloys with High Thermoelectric Performance Enabled by Improved Band Degeneracy. J Am Chem Soc 2019, 141 (10), 4480-4486.
22. Tan, G. J.; Ohta, M.; Kanatzidis, M. G., Thermoelectric power generation: from new materials to devices. Philos. Trans. R. Soc. A-Math. Phys. Eng. Sci. 2019, 377 (2152), 28.
23. Tan, G. J.; Zhang, X. M.; Hao, S. Q.; Chi, H.; Bailey, T. P.; Su, X. L.; Uher, C.; Dravid, V. P.; Wolverton, C.; Kanatzidis, M. G., Enhanced Density-of-States Effective Mass and Strained Endotaxial Nanostructures in Sb-Doped Pb0.97Cd0.03 Te Thermoelectric Alloys. ACS Appl. Mater. Interfaces 2019, 11 (9), 9197-9204.
24. Xiao, Y.; Wu, H. J.; Wang, D. Y.; Niu, C. L.; Pei, Y. L.; Zhang, Y.; Spanopoulos, I.; Witting, I. T.; Li, X.; Pennycook, S. J.; Snyder, G. J.; Kanatzidis, M. G.; Zhao, L. D., Amphoteric Indium Enables Carrier Engineering to Enhance the Power Factor and Thermoelectric Performance in n-Type AgnPb100InnTe100+2n (LIST). Adv. Energy Mater. 2019, 9 (17), 11.
25. Xie, H. Y.; Su, X. L.; Hao, S. Q.; Zhang, C.; Zhang, Z. K.; Liu, W.; Yan, Y. G.; Wolverton, C.; Tang, X. F.; Kanatzidis, M. G., Large Thermal Conductivity Drops in the Diamondoid Lattice of CuFeS2 by Discordant Atom Doping. J Am Chem Soc 2019, 141 (47), 18900-18909.
26. Xie, H. Y.; Su, X. L.; Zhang, X. M.; Hao, S. Q.; Bailey, T. P.; Stoumpos, C. C.; Douvalis, A. P.; Hu, X. B.; Wolverton, C.; Dravid, V. P.; Uher, C.; Tang, X. F.; Kanatzidis, M. G., Origin of Intrinsically Low Thermal Conductivity in Talnakhite Cu17.6Fe17.6S32 Thermoelectric Material: Correlations between Lattice Dynamics and Thermal Transport. J Am Chem Soc 2019, 141 (27), 10905-10914.
27. Zhao, J.; Hao, S. Q.; Islam, S. M.; Chen, H. J.; Tan, G. J.; Ma, S. L.; Wolverton, C.; Kanatzidis, M. G., Six Quaternary Chalcogenides of the Pavonite Homologous Series with Ultralow Lattice Thermal Conductivity. Chem. Mat. 2019, 31 (9), 3430-3439.
Appeared in 2020:
28. Cai, S. T.; Hao, S. Q.; Luo, Y. B.; Su, X. L.; Luo, Z. Z.; Hu, X. B.; Wolverton, C.; Dravid, V. P.; Kanatzidis, M. G., Ultralow Thermal Conductivity and Thermoelectric Properties of Rb2Bi8Se13. Chem. Mat. 2020, 32 (8), 3561-3569.
29. Cai, S. T.; Hao, S. Q.; Luo, Z. Z.; Li, X.; Hadar, I.; Bailey, T.; Hu, X. B.; Uher, C.; Hu, Y. Y.; Wolverton, C.; Dravid, V. P.; Kanatzidis, M. G., Discordant nature of Cd in PbSe: off-centering and core-shell nanoscale CdSe precipitates lead to high thermoelectric performance. Energy Environ. Sci. 2020, 13 (1), 200-211.
30. Chen, D.; Dai, F. L.; Hao, S. Q.; Zhou, G. J.; Liu, Q. L.; Wolverton, C.; Zhao, J.; Xia, Z. G., Crystal structure and luminescence properties of lead-free metal halides (C6H5CH2NH3)(3)MBr6 (M = Bi and Sb). Journal of Materials Chemistry C 2020, 8 (22), 7322-7329.

31. Hodges, J. M.; Xia, Y.; Malliakas, C. D.; Slade, T. J.; Wolverton, C.; Kanatzidis, M. G., Mixed-Valent Copper Chalcogenides: Tuning Structures and Electronic Properties Using Multiple Anions. Chem. Mat. 2020, 32 (23), 10146-10154.
32. Isaacs, E. B.; Lu, G. M.; Wolverton, C., Inverse Design of Ultralow Lattice Thermal Conductivity Materials via Materials Database Screening of Lone Pair Cation Coordination Environment. J. Phys. Chem. Lett. 2020, 11 (14), 5577-5583.
33. Khoury, J. F.; He, J. G.; Pfluger, J. E.; Hadar, I.; Balasubramanian, M.; Stoumpos, C. C.; Zu, R.; Gopalan, V.; Wolverton, C.; Kanatzidis, M. G., Ir6In32S21, a polar, metal-rich semiconducting subchalcogenide. Chemical Science 2020, 11 (3), 870-878.
34. Kuo, J. J.; Wood, M.; Slade, T. J.; Kanatzidis, M. G.; Snyder, G. J., Systematic over-estimation of lattice thermal conductivity in materials with electrically-resistive grain boundaries. Energy Environ. Sci. 2020, 13 (4), 1250-1258.
35. Lin, Y.; Wood, M.; Imasato, K.; Kuo, J. J. H.; Lam, D.; Mortazavi, A. N.; Slade, T. J.; Hodge, S. A.; Xi, K.; Kanatzidis, M. G.; Clarke, D. R.; Hersam, M. C.; Snyder, G. J., Expression of interfacial Seebeck coefficient through grain boundary engineering with multi-layer graphene nanoplatelets. Energy Environ. Sci. 2020, 13 (11), 4114-4121.
36. Luo, Y. B.; Cai, S. T.; Hao, S. Q.; Pielnhofer, F.; Hadar, I.; Luo, Z. Z.; Xu, J. W.; Wolverton, C.; Dravid, V. P.; Pfitzner, A.; Yan, Q. Y.; Kanatzidis, M. G., High-Performance Thermoelectrics from Cellular Nanostructured Sb2Si2Te6. Joule 2020, 4 (1), 159-175.
37. Luo, Y. B.; Hao, S. Q.; Cai, S. T.; Slade, T. J.; Luo, Z. Z.; Dravid, V. P.; Wolverton, C.; Yan, Q. Y.; Kanatzidis, M. G., High Thermoelectric Performance in the New Cubic Semiconductor AgSnSbSe3 by High-Entropy Engineering. J Am Chem Soc 2020, 142 (35), 15187-15198.
38. Murthy, A. A.; Stanev, T. K.; dos Reis, R.; Hao, S. Q.; Wolverton, C.; Stern, N. P.; Dravid, V. P., Direct Visualization of Electric-Field-Induced Structural Dynamics in Monolayer Transition Metal Dichalcogenides. Acs Nano 2020, 14 (2), 1569-1576.
39. Pal, K.; Hua, X.; Xia, Y.; Wolverton, C., Unraveling the Structure-Valence-Property Relationships in AMM'Q(3) Chalcogenides with Promising Thermoelectric Performance. ACS Appl. Energ. Mater. 2020, 3 (3), 2110-2119.
40. Slade, T. J.; Grovogui, J. A.; Kuo, J. J.; Anand, S.; Bailey, T. P.; Wood, M.; Uher, C.; Snyder, G. J.; Dravid, V. P.; Kanatzidis, M. G., Understanding the thermally activated charge transport in NaPb(m)SbQ(m+2) (Q = S, Se, Te) thermoelectrics: weak dielectric screening leads to grain boundary dominated charge carrier scattering. Energy Environ. Sci. 2020, 13 (5), 1509-1518.
41. Slade, T. J.; Pal, K.; Grovogui, J. A.; Bailey, T. P.; Male, J.; Khoury, J. F.; Zhou, X. Q.; Chung, D. Y.; Snyder, G. J.; Uher, C.; Dravid, V. P.; Wolverton, C.; Kanatzidis, M. G., Contrasting SnTe-NaSbTe2 and SnTe-NaBiTe2 Thermoelectric Alloys: High Performance Facilitated by Increased Cation Vacancies and Lattice Softening. J Am Chem Soc 2020, 142 (28), 12524-12535.
42. Witting, I. T.; Grovogui, J. A.; Dravid, V. P.; Snyder, G. J., Thermoelectric transport enhancement of Te-rich bismuth antimony telluride (Bi0.5Sb1.5Te3+x) through controlled porosity. J. Materiomics 2020, 6 (3), 532-544.
43. Xia, Y.; Hegde, V. I.; Pal, K.; Hua, X.; Gaines, D.; Patel, S.; He, J. G.; Aykol, M.; Wolverton, C., High-Throughput Study of Lattice Thermal Conductivity in Binary Rocksalt and Zinc Blende Compounds Including Higher-Order Anharmonicity. Physical Review X 2020, 10 (4), 21.
44. Xia, Y.; Ozolins, V.; Wolverton, C., Microscopic Mechanisms of Glasslike Lattice Thermal Transport in Cubic Cu12Sb4S13 Tetrahedrites. Phys. Rev. Lett. 2020, 125 (8), 7.
45. Xia, Y.; Pal, K.; He, J. G.; Ozolins, V.; Wolverton, C., Particlelike Phonon Propagation Dominates Ultralow Lattice Thermal Conductivity in Crystalline Tl3VSe4. Phys. Rev. Lett. 2020, 124 (6), 7.
46. Xie, H. Y.; Hao, S. Q.; Bao, J. K.; Slade, T. J.; Snyder, G. J.; Wolverton, C.; Kanatzidis, M. G., All-Inorganic Halide Perovskites as Potential Thermoelectric Materials: Dynamic Cation off-Centering Induces Ultralow Thermal Conductivity. J Am Chem Soc 2020, 142 (20), 9553-9563.

47. Xie, H. Y.; Hao, S. Q.; Cai, S. T.; Bailey, T. P.; Uher, C.; Wolverton, C.; Dravid, V. P.; Kanatzidis, M. G., Ultralow thermal conductivity in diamondoid lattices: high thermoelectric performance in chalcopyrite Cu0.8+yAg0.2In1-yTe2. Energy Environ. Sci. 2020, 13 (10), 3693-3705.
48. Xie, H. Y.; Su, X. L.; Bailey, T. P.; Zhang, C.; Liu, W.; Uher, C.; Tang, X. F.; Kanatzidis, M. G., Anomalously Large Seebeck Coefficient of CuFeS2 Derives from Large Asymmetry in the Energy Dependence of Carrier Relaxation Time. Chem. Mat. 2020, 32 (6), 2639-2646.
49. Xie, H. Y.; Su, X. L.; Hao, S. Q.; Wolverton, C.; Uher, C.; Tang, X. F.; Kanatzidis, M. G., Quasilinear dispersion in electronic band structure and high Seebeck coefficient in CuFeS2-based thermoelectric materials. Phys. Rev. Mater. 2020, 4 (2), 7.
50. Yang, D. W.; Su, X. L.; Li, J.; Bai, H.; Wang, S. Y.; Li, Z.; Tang, H.; Tang, K. C.; Luo, T. T.; Yan, Y. G.; Wu, J. S.; Yang, J. H.; Zhang, Q. J.; Uher, C.; Kanatzidis, M. G.; Tang, X. F., Blocking Ion Migration Stabilizes the High Thermoelectric Performance in Cu2Se Composites. Adv. Mater. 2020, 32 (40), 10.
Appeared in 2021:
51. Luo, Z. Z.; Cai, S. T.; Hao, S. Q.; Bailey, T. P.; Spanopoulos, I.; Luo, Y. B.; Xu, J. W.; Uher, C.; Wolverton, C.; Dravid, V. P.; Yan, Q. Y.; Kanatzidis, M. G., Strong Valence Band Convergence to Enhance Thermoelectric Performance in PbSe with Two Chemically Independent Controls. Angew. Chem.-Int. Edit. 2021, 60 (1), 268-273.
52. Pal, K.; Xia, Y.; Wolverton, C., Microscopic mechanism of unusual lattice thermal transport in TlInTe2. npj Comput. Mater. 2021, 7 (1), 8.
53. Sarkar, S.; Hua, X.; Hao, S. Q.; Zhang, X. M.; Bailey, T. P.; Slade, T. J.; Yasaei, P.; Korkosz, R. J.; Tan, G. J.; Uher, C.; Dravid, V. P.; Wolverton, C.; Kanatzidis, M. G., Dissociation of GaSb in n-Type PbTe: off-Centered Gallium Atom and Weak Electron-Phonon Coupling Provide High Thermoelectric Performance. Chem. Mat. 2021, 33 (5), 1842-1851.

Modulating Phase Separation and Constituent Density Profiles in Nanostructured Polymer Electrolytes – Joint Experiment and Theory Effort in Tunable Hierarchical Assembly

Thomas H. Epps, III; University of Delaware

Lisa M. Hall; The Ohio State University

Program Scope

In this joint experimental and computational effort, we design, synthesize, and characterize new block polymer (BP)-based electrolyte systems. Generally, polymer electrolytes are sought for their improved mechanical and electrochemical stability versus liquid electrolytes, and BP materials are of special interest due to their ability to microphase separate and provide both ion-conducting pathways and a mechanically robust behavior. However, improved conductivity and ability to control ion composition profiles and ion transport through these materials are needed to enhance overall performance. *The overarching objective of this project is to enhance lithium-ion transport by leveraging an increased understanding of hierarchical assembly and ion segregation in these systems.* Specifically, by systematically controlling chain composition profile and local chemical interactions within copolymer electrolytes, one can understand how to independently optimize phase separation and nanoscale structure, while also decoupling cation and anion motion.

Recent Progress

As background, earlier work by Epps and Hall groups has often focused on the effects of tapered chain composition profiles, ion content, and chain architecture on microphase structure of BP-based materials; for the tapered BPs (TBPs), a linear gradient midblock is present between pure blocks on either end of the polymer chain. In one joint effort, the interfacial profiles of non-tapered, normal-tapered, and inverse-tapered poly(styrene-*b*-isoprene)-based BPs were compared, with quantitative agreement in segment density distributions obtained from X-ray reflectometry (XRR) and fluids density functional theory (fDFT).[1] Additionally, we (Epps/Hall) probed the interfacial profiles in polystyrene-*b*-(*oligo*-oxyethylene methacrylate) (PS-POEM) BPs of linear and cyclic architectures with varying levels of salt doping. The domain spacing and interfacial widths were measured with XRR and compared to molecular dynamics (MD) results. We semi-quantitatively captured the major trends and showed the interplay between chain architecture and effective segregation strength ($\chi_{eff}N$, in which χ_{eff} is the effective Flory interaction parameter after salt addition, and N is the chain length) – especially critical for ion-doped polymer systems.[2]

<u>*Recent Experimental Advances*</u> – We recently reported a quantitative analysis of the lithium salt and polymer distributions in lithium salt-doped PS-POEM thin films.[3] Analysis of neutron reflectometry (NR) data indicated that all salt-doped BP specimens exhibited salt distributions that were directly proportional with the local POEM concentration, a conclusion supported by the lack of even-order Bragg peaks that would result from scattering from salt-rich (centrally-localized) layers.[3] Then, we used strong-segregation theory to extract both χ_{eff} and the POEM statistical segment lengths as a function of salt concentration from XRR data. The segregation strength

increased at low salt concentrations before plateauing at higher concentrations, while the statistical segment length increased linearly.[3]

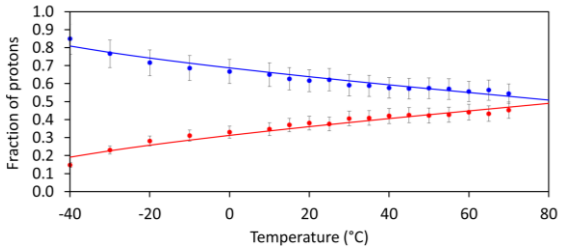

Figure 1: Fraction of mobile (red) and immobile (blue) protons in neat PS-POEM as a function of temperature. Lines are model calculations on the basis of local segmental mixing throughout the domain from XRR results, and data points are results from ^{1}H SS NMR measurements.

The knowledge of ion and monomer segment distributions provides insight into how the local composition may relate to ion and polymer mobilities. In neat PS-POEM systems, glass transition temperatures (T_gs) were estimated as a function of position in the domain on the basis of local S/OEM composition data from XRR. This analysis enabled the prediction of the fraction of mobile monomer segments as a function of temperature. These predictions were supported by proton solid state nuclear magnetic resonance (^{1}H SS NMR) spectroscopy measurements, which directly probed the fractions of mobile and immobile protons in the PS-POEM sample (Figure 1). The agreement between these results suggested that polymer mobility primarily depends on the local segmental composition.

In further work, PS-POEM was blended with POEM homopolymers of varying molecular weights (MWs).[4] The incorporation of a higher MW homopolymer additive promoted a 'dry brush-like' distribution of homopolymer and greater lithium salt concentrations in the more mobile homopolymer-rich region, raising ionic conductivity in comparison to the 'wet brush-like' (lower MW homopolymer additive) and unblended systems. XRR and NR data indicated that there was a higher salt concentration in the homopolymer-rich regions in the 'dry brush' blend than in the 'wet brush' blend. Also, using ^{7}Li SS NMR spectroscopy, we found a Li^{+} mobility transition temperature ($T_{Li\ mobility}$) that was a function of blend type.[4] Interestingly, the ionic conductivity of the blended BPs was highest in the 'dry brush' systems even though they had higher T_gs (Figure 2),[4] suggesting that homopolymer-rich pathways formed in these systems had a greater impact on conductivity than the larger Li^{+} mobility in the lower MW composite blends.

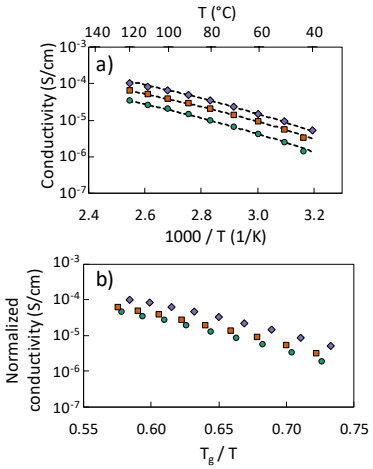

Figure 2: Ionic conductivity as a function of 1000/T, and b) ionic conductivity normalized by the volume fraction of total POEM as a function of T_g/T, for unblended (green circles), wet brush (orange squares), and dry brush (purple diamonds) samples.[4]

We also characterized a new self-doped diblock terpolymer electrolyte, in which one block was a high modulus material, and the other block was comprised of high ion-conductivity and self-doped monomer segments. This self-doped BP reduced counterion motion (relative to salt-doped BPs). It was found that the molecular weight, counterion, and ion concentration played different roles in the electrolyte performance; the molecular weight dominated the self-assembly behavior, whereas the counterion and ion concentration were primarily responsible for the T_g and conductivity. Overall, this effort presents an efficient synthetic strategy and modular platform toward the efficient generation of higher-performance polymer electrolytes.

Recent Modeling Advances – A critical feature of coarse-grained models of BP electrolytes is the treatment of ion solvation effects. The model employed in the Hall group recently is based on a standard bead-spring form with added Coulomb interactions between ions and solvation interactions of the form S/r^4 that capture the effects of Born solvation energy. For simplicity, we calculate ion-ion interactions in a uniform dielectric background representing the higher dielectric microphase. We recently showed that such a model can capture the experimentally observed behavior that increasing MW tends to increase rather than decrease ion conductivity in salt-doped BPs (in contrast to salt-doped homopolymers), as well as the decreasing trend in ion diffusion with ion concentration.[5]

We also recently advanced analysis techniques to efficiently and accurately calculate true conductivity given that calculations of true ion conduction from equilibrium simulations (rather than predicting conductivity from the diffusion constants alone) are prone to statistical error.[6] We calculated conductivity and diffusion in a single nonequilibrium simulation as shown in Figure 3 to efficiently and accurately assess conductivity and the degree of uncorrelated ion motion.[7] We used this method to determine the cation mobility and transference number for salt-doped homopolymer systems of a variety of ion sizes.[8] This work validated that our model reproduced the ratio of anion to cation diffusion constants observed in poly(ethylene oxide) doped with lithium bis(trifluoromethanesulfonyl)imide (LiTFSI) and closely matched the nonmonotonic experimental trend in conductivity as a function of ion concentration.[8] Further work analyzing self-doped (single-ion) systems *via* the same methods is ongoing. Additionally, motivated by experimental advances noted above, we are studying systems with short and long chain homopolymer additives to analyze the local ion content, local ion mobility, and resulting overall conductivity.

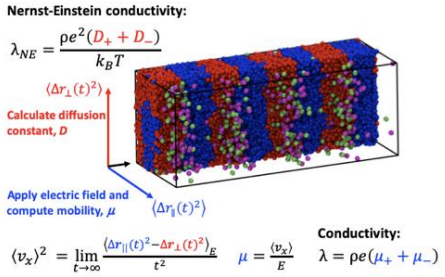

Figure 3: Schematic of protocol to calculate conductivity in lamellar sample; mobility under an electric field of both cations and anions is calculated and related to true total conductivity, while diffusion is calculated in the other perpendicular direction using the equations shown. The ratio of true conductivity to Nernst-Einstein conductivity, the degree of uncorrelated ion motion or inverse Haven ratio, is also calculated. Snapshot shows BP monomers (blue, red) cut away from half of the domain to show ions (purple, green).

Recent Advances in Experiment and Modeling Integration – Close comparison of experimental and modeling results across a series of systems with the same chemical units but various chain composition profiles allows for a robust determination and validation of modeling parameters. In ongoing work, XRR measurements of lithium trifluoromethanesulfonate (Li triflate)-doped PS-POEM TBPs and coarse-grained MD simulations of analogous systems are being compared to elucidate the structural origins of their ionic conductivity. The simulation model was refined by increasing the Lennard-Jones (LJ) interaction strength of the hard block monomers to increase their T_g. Ion interaction parameters were successfully adjusted from prior work to accurately match experimental data across sequence type and ion concentration. The monomer and ion content in close proximity to the domain interface was quantified in both experiments and simulations, with excellent agreement (Figure 4). Electrolytes with low $T_{g,POEM}$ exhibited higher ionic conductivities

and *vice versa*, and the normalization of the temperature (T) by $T_{g,POEM}$ resulted in all of the ionic conductivities collapsing onto a single master curve.

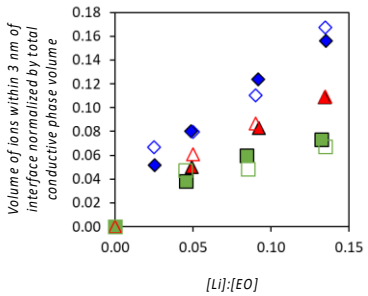

Figure 4: The volume of ions within 3 nm of interface normalized by total conductive phase volume was plotted as a function of salt concentration for non- (green squares), normal- (red triangles), and inverse-tapered (blue diamonds) samples. Filled and hollow symbols represent experimental and simulation results, respectively.

Future Plans

Our recent work established (*i*) that local ion and monomer concentrations near the interface closely relate to polymer mobility and ion conductivity and (*ii*) that these features can be precisely captured by simulations. Ongoing work is detailing the relationships between local segmental motion and ion mobility in nanostructured BP domains, as a function of domain size and relative distance from domain interfaces. These efforts will be facilitated by selective labeling of copolymer segments with fluorescent tags, SS NMR spectroscopy, and statistical analysis of local monomer and ion motion in simulations. BP-based systems with homopolymer additives are an excellent platform for applying this knowledge, gaining further understanding, and ultimately optimizing ion transport in BP-based electrolytes. Finally, we plan to explore a number of advanced chemistries in future work, including systems with controlled distributions of high and moderate dielectric constant monomer segments, sustainable bio-based polymeric systems, and systems with alternative cations. We expect this work will yield further enhancements of local and overall ion transport and provide insight on how the knowledge gained from the many years of development of standard lithium-ion-conducting diblock-based electrolyte systems can be applied to new materials systems.

References

1. Luo, M.; Brown, J. R.; Remy, R. A.; Scott, D. M.; Mackay, M. E.; Hall, L. M.; Epps, T. H., III, *Macromolecules* **2016,** *49* (14), 5213-5222.
2. Gartner, T. E., III; Kubo, T.; Seo, Y.; Tansky, M.; Hall, L. M.; Sumerlin, B. S.; Epps, T. H., III, *Macromolecules* **2017,** *50* (18), 7169-7176.
3. Gartner, T. E., III; Morris, M. A.; Shelton, C. K.; Dura, J. A.; Epps, T. H., III, *Macromolecules* **2018,** *51* (5), 1917-1926.
4. Morris, M. A.; Sung, S. H.; Ketkar, P. M.; Dura, J. A.; Nieuwendaal, R. C.; Epps, T. H., III, *Macromolecules* **2019,** *52* (24), 9682-9692.
5. Seo, Y.; Shen, K.-H.; Brown, J. R.; Hall, L. M., *Journal of the American Chemical Society* **2019,** *141* (46), 18455-18466.
6. Wheatle, B. K.; Fuentes, E. F.; Lynd, N. A.; Ganesan, V., *ACS Macro Letters* **2019,** *8* (8), 888-892.
7. Shen, K.-H.; Hall, L. M., *Macromolecules* **2020,** *53* (10), 3655-3668.
8. Shen, K.-H.; Hall, L. M., *Macromolecules* **2020,** *53* (22), 10086-10096.

Publications

1. Shen, K.-H.; Brown, J. R.; Hall, L. M. “Diffusion in Lamellae, Cylinders, and Double Gyroid Block Copolymer Nanostructures” *ACS Macro Letters* 7, 1092–1098 (2018) https://doi.org/10.1021/acsmacrolett.8b00506

2. Gartner, T. E., III; Morris, M. A.; Shelton, C. K.; Dura, J. A.; Epps, T. H., III “Quantifying Lithium Salt and Polymer Density Distributions in Nanostructured Ion-Conducting Block Polymers” *Macromolecules* 51, 1917-1926 (2018) https://doi.org/10.1021/acs.macromol.7b02600

3. (patent) Holmberg, L.; Nicastro, K. H.; Wang, S.; Shuai, L.; Saha, B.; Morris, M. A.; Vlachos, D. G.; Epps, T. H., III “Bio-based Polymer Electrolytes from Raw Lignocellulosic Biomass” US20190144590A1, Published 01/09/2019

4. Seo, Y.; Shen, K.-H.; Brown, J. R.; Hall, L. M. “Role of Solvation on Diffusion of Ions in Diblock Copolymers: Understanding the Molecular Weight Effect through Modeling” *Journal of the American Chemical Society* 141, 18455–18466 (2019) https://doi.org/10.1021/jacs.9b07227

5. Ketkar, P. M.; Shen, K.; Hall, L. M.; Epps, T. H., III “Charging toward improved lithium-ion polymer electrolytes: exploiting synergistic experimental and computational approaches to facilitate materials design” *Molecular Systems Design & Engineering* 4, 223-238 (2019) [invited review] https://doi.org/10.1039/C8ME00105G

6. Shen, K.-H.; Hall, L. M. “Ion Conductivity and Correlations in Model Salt-Doped Polymers: Effects of Interaction Strength and Concentration” *Macromolecules* 53, 3655–3668 (2020) https://doi.org/10.1021/acs.macromol.0c00216

7. Morris, M. A.; Sung, S. H.; Ketkar, P. M.; Dura, J. A.; Nieuwendaal, R. C.; Epps, T. H., III “Enhanced Conductivity via Homopolymer-Rich Pathways in Block Polymer Blended Electrolytes” *Macromolecules* 52, 9682-9692 (2019) https://doi.org/10.1021/acs.macromol.9b01879

8. Shen, K.-H.; Hall, L. M. “Effects of Ion Size and Dielectric Constant on Ion Transport and Transference Number in Polymer Electrolytes” *Macromolecules* 53, 10086–10096 (2020) https://doi.org/10.1021/acs.macromol.0c02161

9. Shen, K.-H.; Fan, M.; Hall, L. M. “Molecular Dynamics Simulations of Ion-Containing Polymers Using Generic Coarse-Grained Models” *Macromolecules* 54, 2031–2052, (2021) [invited perspective, ACS Editor’s Choice article] https://dx.doi.org/10.1021/acs.macromol.0c02557

10. (in review) Ketkar, P. M.; Shen, K.; Fan, M.; Hall, L. M.; Epps, T. H., III "Quantifying the effects of monomer segment distributions on ion transport in tapered block polymer electrolytes" *Macromolecules* 2021

11. (in preparation) Ketkar, P. M.; Epps, T. H., III "Nanostructured polymer electrolytes to enhance ion transport and processibility in lithium-ion batteries" *Accounts of Chemical Research* 2021 [invited]

Pore Space Engineering and Functionalization in Porous Metal-Organic Framework Materials

PI: Pingyun Feng
Department of Chemistry, Materials Science and Engineering Program,
University of California, Riverside, CA 92521

Program Scope

The overall research goal is to develop innovative and transformative synthetic concepts and paradigms to create new crystalline porous materials (**CPM**) with unprecedented architectural design and chemical features. The multimodular framework compositions, as well as independent scalability on pore width and height, allows for intrinsic component diversity and geometric tunability. These CPMs have the potential to provide a materials basis for a wide range of high-performance sorption-based applications such as fuel storage (e.g., H_2, CH_4, C_2H_2), gas separation (e.g., C_2H_2/CO_2, C_2H_4/C_2H_6, C_3H_6/C_3H_8), and gas capture or sequestration (e.g., H_2O vapor, CO_2, NH_3). The project integrates chemical and solvothermal synthesis, crystal structure and topology analysis, with various property studies (e.g., thermal, hydrothermal and chemical stability). Sorption properties of various gases on these new materials are systematically evaluated to establish composition-structure-property correlations that are further utilized to refine synthetic strategy to optimize materials for efficient energy-related applications. The specific aims are:

a. To design synthetic strategies for architectural pore space engineering including pore space partition to create domains of pore space with pore size commensurate with the size of guest molecules to achieve high uptake capacity, high guest selectivity, and low-cost adsorbent regeneration.
b. To design synthetic strategies that permit methodological introduction of functional active sites onto porous frameworks as well as within the pore space. To control types and density of host-guest binding sites.
c. To design synthetic strategies to create novel heterometallic systems. To achieve high materials stability and high-performing gas sorption properties.
d. To characterize crystal structures. Crystal structure analysis determines compositional and structural features that correlate with desired properties. It can reveal previously unseen compositional and structural patterns that may lead to new or improved design strategies and better materials.
e. To characterize thermal and chemical stability, and gas sorption properties. To explore applications of the new materials in energy related applications.

Recent Progress

The following summarizes select important contributions in the past three years.

1. Pore-Space Partition and Optimization for Propane-Selective High-Performance Propane/Propylene Separation

The development of effective propane (C_3H_8)-selective adsorbents for the purification of propylene (C_3H_6) from C_3H_8/C_3H_6 mixture is a promising alternative to replace the energy intensive cryogenic distillation. However, few materials possess the dual desirable features of propane selectivity and high uptake capacity. In this work, by independently scaling the pore width and height (**Figure 1**), we have synthesized a family of pore-space-partitioned crystalline porous materials (CPM) with remarkable C_3H_8 uptake capacity (up to 10.9 mmol/g) and the

highly desirable, yet uncommon C_3H_8 selectivity (up to 1.54 at 0.1 bar and 1.44 at 1bar). The selectivity-capacity synergy endows these materials with record-performing C_3H_8/C_3H_6 separation potential (i.e., C_3H_6 recovered from the mixture). Moreover, these CPMs exhibit outstanding properties including high stability, low regeneration energy, and multimodular chemical and geometrical tunability within the same isoreticular framework. The high C_3H_8/C_3H_6 separation performance was further confirmed by the breakthrough experiments. This work will be published in ACS Appl. Mater. Interfaces (publication list #1).

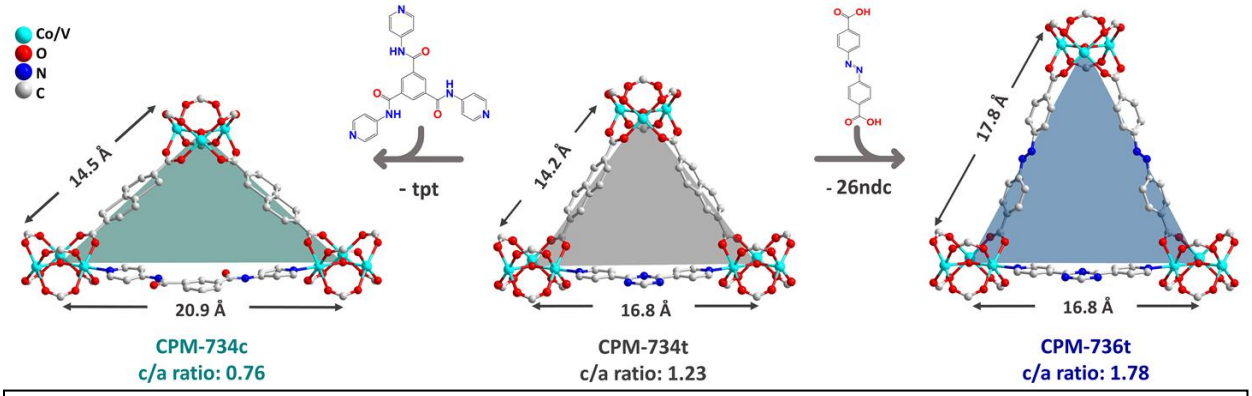

Figure 1. An illustration of compositional and geometrical design of pore geometry and functionality. CPM-734t at the middle is made of tpt and 2,6-ndc in the heterometallic Co-V composition. All three components are tunable. This design strategy is used here to develop materials with high adsorption capacity for propane and also unusual reverse selectivity for propane over propene. **tpt** = 2,4,6-tri(4-pyridinyl)-1,3,5-triazine, **2,6-ndc** = 2,6-naphthalenedicarboxylic acid. The c/a ratio is based on hexagonal unit cells.

2. A New Strategy for Constructing Pore Space Partitioned MOFs with Open Metal Sites

Introducing pore-partitioning agents into hexagonal channels of MIL-88 type structures (denoted as the *acs* topology) can endow materials with high tunability in gas sorption. In this work, the new strategy is based on insertion of in situ synthesized V-shaped 4, 4'-dipyridylsulfide (**dps**) ligands. With this strategy, one third of open metal sites in the parent *acs* net are retained in the *pacs* MOFs (**pacs** = partitioned acs) and two thirds are used for pore partition. The newly synthesized Co_2V-pacs MOFs exhibit near or record-high uptake capacities for CO_2, C_2H_2, C_2H_4, and C_2H_6. For example, the storage capacity of C_2H_2 reaches 234 cm^3/g (298 K) and 330 cm^3/g (273K) at 1 bar for CPM-733-dps (the Co_2V-BDC form, BDC=1,4-benzenedicarboxylate), the higher than all forms of MOF-74 and all other pacs members. Such high capacity is accomplished with a low C_2H_2 affinity. Furthermore, the materials are highly stable and exhibit no loss of C_2H_2 adsorption capacity after at least five adsorption–desorption cycles. The work is published in *Angew. Chem. Int. Ed.* 2020, 59, 19027 (publication list #5).

3. Tunable Metal-Organic Frameworks from 8-Connected Trimers for High-Capacity Gas Uptake

Metal trimers are well known in MOFs but are commonly seen as 6- or 9-connected units. The new 8-connected trimers presented in this work are highly unusual. In this work, we revealed a viable construction strategy called angle bending modulation that is effective for creating a prototypical MOF-type based on novel 8-connected $M_3(OH)(OOCR)_5(Py\text{-}R)_3$ trimers, M = Zn, Co, Fe). As a proof of concept, we have synthesized six members in this family using three types of ligands for the formation of frameworks denoted as CPM-80, -81, and -82. These materials do not possess open-metal sites, which contribute to their excellent gas uptake capacity for various hydrocarbon gas molecules and inverse C_2H_6/C_2H_4 selectivity. A member of this family, CPM-

81-Co made from 2,5-furandicarboxylate and isonicotinate, features selectivity for ethane over ethylene (1.80) with high uptake capacity for both ethane (123 cm^3/g) and ethylene (113 cm^3/g) at 298 K and 1 bar. The work is published in *Small* 2020, 2003167 (publication list #6).

4. Design of High-Performance Materials through Integration of Methodologies from Metal-Organic Frameworks and Covalent-Organic Frameworks

Pore space partition has been proven as a versatile design strategy for constructing crystalline porous materials (CPM) with much enhanced chemical stability and gas sorption properties. In this work, we have integrated COF-1 chemistry, also known as self-condensation of boronic acids, with MOF chemistry to develop a novel pore-partition method, leading to the synthesis of a new family of pore-partitioned materials. During the reaction, a new pore-partitioning ligand, trimer of pyridine-4-boronic acid, is formed as **tpb** (2,4,6-tri(4-pyridinyl)-1,3,5-boroxine). The simultaneous construction of two totally different reactions, self-condensation of boronic acid into trimers and metal-dicarboxylate coordination assembly (also into trimers) (**Figure 2**), requires all components to work cooperatively. It is worth noting that tpb was previously not known to exist in the literature.

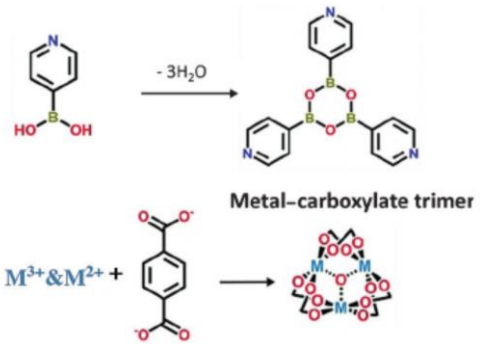

Figure 2. A new boroxine molecule (tpb) has been designed from trimerization of pyridine-4-boronic acid. The new boroxine molecule crosslinks metal trimers into a pore-partitioned material with high gas sorption performance.

These newly synthesized materials were studied for gas adsorption properties. Gas uptakes for N_2, CO_2, CH_4, C_2H_2, C_2H_4, C_2H_6, and NH_3 were measured. It is notable that gas uptakes in these tpb-pacs materials are dramatically enhanced compared to non-partitioned acs materials. At 1 bar and 273 K, the CO_2 uptakes range from 3.96 to 6.32 mmol/g in tpb-pacs, which is better than the best-performing gas sorbent in non-partitioned Mg_2V-MIL-88 (4.25 mmol/g). The C_2H_2 uptake of new materials synthesized can be tuned from 5.61 mmol/g for CPM-100c-InCo to 10.45 mmol/g for CPM-100a-FeMg at 1 bar and 273 K by using different framework compositions. Under the same condition, the C_2H_2 uptake of CPM-100a-FeMg is nearly twice that of non-partitioned Mg_2V-MIL-88 (5.25mmol/g at 273 K and 3.28 mmol/g at 298 K). This significant gas sorption enhancement is attributed to the pore-partitioning agent tpb, which increases the robustness of the framework as well as the number of binding sites.

The presence of Lewis acid sites (boron) in CPM-100 materials makes it especially interesting to study their sorption properties for ammonia. For NH_3, at 1 bar and 298 K, the NH_3 uptake can be tuned from 7.85 mmol/g to 12.56 mmol/g by changing dicarboxylates and from 11.66 mmol/g to 13.01 mmol/g by changing metal ions. There is no obvious adsorption loss after 4 cycles. The NH_3 packing density in CPM-100b and CPM-100c (0.598 g/cm^3 and 0.597 g/cm^3) is comparable to the top performing materials. The work is published in *Angew. Chem. Int. Ed.* 2019, 58, 6316 (publication list #13).

5. Pore-Space-Partition-Enabled Exceptional Ethane Uptake and Ethane-Selective Ethane-Ethylene Separation

The separation of ethane from ethylene is a vital process in chemical industry and is also energy-intensive. **[1]** This study led to the synthetic design of a family of pore-space-partitioned

crystalline porous materials (CPM) that exhibit high C_2H_6 uptake capacity, endowing them with near-record C_2H_6/C_2H_4 separation potential (i.e., C_2H_4 recovered from the mixture). The ethane uptake capacity as high as 166.8 cm^3/g at 1 atm and 298 K, more than twice that of Peroxo-MOF-74-Fe (74.3 cm^3/g), has been achieved even though the isosteric heat of adsorption (21.9-30.4 kJ/mol) of these new materials is as low as 1/3 of that for Peroxo-MOF-74-Fe (66.8 kJ/mol). [2] Also, these new materials exhibit outstanding properties including high thermal (> 450 °C) stability and aqueous stability, low adsorbent-regeneration energy, and practically infinite chemical and geometrical tunability within the same isoreticular framework. The work is published in *J. Am. Chem. Soc.* 2020, 142, 2222. (publication list #8)

Future Plans

The PI will focus on the proposed goals and will further develop innovative and transformative materials design strategies. At the same time, The PI will systematically investigate the applications of new materials developed in the PI's lab for applications in gas separation and catalysis including electrocatalysis. The major advances accomplished in this reporting period have revealed additional opportunities and challenges that will be addressed.

The pacs platform developed by the PI's group has been shown to be a highly successful and extraordinarily versatile platform and has also been adopted broadly by worldwide researchers for creating high-performance materials. The pore-space partition agent on this platform contributes dramatically to the stability and gas sorption properties of the resulting materials. At the beginning of the pacs-platform development by the PI's group in 2015, tpt was simply visualized as being encapsulated within the channels of the acs-type framework to partition the pore-space and to increase the density of guest binding sites (usually more than doubling). Over the past several years and through many synthetic studies including those presented in this abstract, it has become clear that there is a strong synergistic effect and bi-directional control between the framework formation and pore-partition ligands. In the future work, the PI will develop a set of systematic and inter-correlated synthetic strategies to design high-performance gas sorption materials in a bi-directional manner. Some highlights of the planned work are:

- the creation and development of new pore-space partitioning methods through chemical design of novel functional pore-partition agents such as angular ligands and ligands with tunable core structures and charge properties.
- the integration and synergy between various synthetic methodologies and an increased focus on the stability of materials under extreme conditions (e.g., low or high pH, high-temperature hydrothermal conditions), for example, by using negatively charged N-donor ligands in place of carboxylate-based ligands.
- the development of new platforms with rich and tunable compositions and structural features that can lead to a large family of new high-performance materials.
- the systematic study of gas sorption properties of the new materials to establish composition-structure-property correlation that can be used to guide the optimization of the materials design process.

References

1. Sholl, D.; Lively, R. Seven chemical separations to change the world. *Nature* **2016**, *532*, 435.
2. Li, L.; Lin, R.; Krishna, R.; Li, H.; Xiang, S.; Wu, H.; Li, J.; Zhou, W.; Chen, B. Ethane/ethylene separation in a metal-organic framework with iron-peroxo sites. *Science* **2018**, *362*, 443.

Publications supported by DOE-BES under award no. DE-SC0010596 in the last three years

1. Hong, A. N.; Yang, H.; Li, T.; Wang, Y.; Wang, Y-X; Jia, X.; Zhou, A.; Kusumoputro, E.; Li, J.; Bu, X.; Feng, P., Pore-Space Partition and Optimization for Propane-Selective High-Performance Propane/Propylene Separation. ACS Appl. Mater. Interfaces 2021, invited contribution, in revision.
2. Li, S.; Gao, Y.; Li, N.; Ge, L.; Bu, X.; Feng, P., Transition metal-based bimetallic MOFs and MOF-derived catalysts for electrochemical oxygen evolution reaction. Energy Environ. Sci. 2021, 14, 1897.
3. Xiao, Y.; Yang, H.; Bu, X.; Feng, P., ZIF-8 Derived Carbon Materials with Multifunctional Selective Adsorption Abilities. Carbon 2021, 176, 421.
4. Hong, A. N.; Yang, H.; Bu, X.; Feng, P., Roles of Alkali Metals and Ionic Networks in Directing the Formation of Anionic Metal-Organic Frameworks. Cryst. Growth Des. 2020, 20, 6668-6686.
5. Wang, Y.; Jia, X.; Yang, H.; Wang, Y.; Chen, X.; Hong, A.; Li, J.; Bu, X. Feng, P., A New Strategy for Constructing Pore Space Partitioned MOFs with High Uptake Capacity for C2 Hydrocarbons and CO2. Angew. Chem. Int. Ed. 2020, 59, 19027-19030.
6. Lei, X.; Yang, H.; Wang, YX.; Wang, Y.; Chen, X.; Xiao, Y.; Bu, X.; Feng, P., Tunable Metal-Organic Frameworks Based on 8-Connected Metal Trimers for High Ethane Uptake. Small 2020, 2003167.
7. Xia, Z.; Li, F.; Xu, L.; Feng, P., A stable and highly selective metalloporphyrin based framework for the catalytic oxidation of cyclohexene. Dalton Trans. 2020, 49, 11157-11162.
8. Yang, H.; Wang, Y.; Krishna, R.; Jia, X.; Wang, Y.; Hong, A. H.; Dang, C.; Castillo, H. E.; Bu, X.; Feng, P., Pore-Space-Partition-Enabled Exceptional Ethane Uptake and Ethane-Selective Ethane-Ethylene Separation. J. Am. Chem. Soc. 2020, 142, 2222.
9. Zheng, M.; Wang, Y.; Feng, P., Bifunctional Heterometallic Metal-Organic Frameworks for Solvent-Free Heterogeneous Cascade Catalysis. Catalysts 2020, 10, 309.
10. Wang, Y.; Chen, X.; Zhai, Q.; Guo, J.; Feng, P. Ultraporous nitrogen-rich carbon nanosheets derived from the synergy of eutectic liquid and zeolitic imidazolate for energy applications . J. Power Sources 2019, 434, 126678.
11. Tian, S.; Xu, S.; Liu, J.; He, C.; Xiong, Y.; Feng, P. Highly efficient removal of both cationic and anionic dyes from wastewater with a water-stable and eco-friendly Fe-MOF via host-guest encapsulation. J. Cleaner Production. 2019, 117767.
12. Xiao, Y.; Hong, A. N.; Hu, D.; Wang, Y.; Bu, X.; Feng, P., Solvent-free Synthesis of Zeolitic Imidazolate Frameworks and the Catalytic Properties of Their Carbon Materials. Chem. Eur. J. 2019, 25, 16358-16365.
13. Wang, Y.; Zhao, X.; Yang, H.; Bu, X.; Wang, Y.; Jia, J.; Li, J.; Feng, P. A Tale of Two Trimers from Two Different Worlds: A COF-Inspired Synthetic Strategy for Pore-Space Partition of MOFs . Angew. Chem. Int. Ed. 2019, 58, 6316-6320.

Fundamental Studies of Soiling and Cementation of PV Cover Glass Materials: Addressing Reliability with Advanced X-ray Scattering/Spectroscopy and First Principles Modeling

Robert A. Fleming, Arkansas State University

Program Scope

Accumulation of soils and other particulate matter on the front cover glass of solar photovoltaic (PV) modules results in transmission losses that detrimentally affect the power output of PV installations. The conventional solution to this problem is manual abrasive scrubbing of modules, which entails significant water usage and manpower. To further combat this issue, there is a concerted effort within the PV industry to develop anti-soiling (AS) coatings to mitigate power losses due to soiling of PV modules, which can exceed 35% in some cases [1]. However, relatively little is known about the fundamental physical and chemical mechanisms that enable anti-soiling behavior.

In this project, a combination of advanced X-ray analysis tools and first principles computational modeling is employed to understand the physical and chemical interactions between environmental soils and PV cover glass materials. The major goals are: 1) Accelerated soiling and cementation studies of PV cover glass materials, utilizing a custom-built soiling chamber to uniformly introduce particulate contaminant species to coverglass material samples, with cementation reactions initiated under applied heat and humidity. The resulting change in optical transmittance, surface morphology, surface chemistry, and surface wettability is then characterized as a function of contaminant species, which includes standardized particulates corresponding to diverse geographic regions; 2) synchrotron-based X-ray scattering and spectroscopy characterization at the Stanford Synchrotron Radiation Lightsource (SSRL). Small Angle X-ray Scattering (SAXS) is used to probe the morphological evolution of material surfaces in response to soiling/cementation, with scattering resolution on the nanoscale. Changes in surface chemistry are characterized using near-edge X-ray absorption fine structure (NEXAFS) spectroscopy, which is sensitive to changes in local chemical bonding; and 3) first principles computational spectroscopy modeling in partnership with the Quantum Simulations Group at Lawrence Livermore National Lab. To help interpret the chemical shifts observed in the experimental NEXAFS spectra, first principles computational X-ray absorption modeling is utilized to produce calculated X-ray absorption spectra corresponding to silica surfaces with various functional surface terminating groups. Using this computational spectroscopy framework, the calculated X-ray spectra can be compared to the experimental results to identify changes in surface chemistry that correspond to specific peak shifts.

Together, this combined experimental/computational study will support a more fundamental understanding of soiling and cementation reactions in PV coverglass materials and will contribute to the design of novel advanced materials to support the rapidly growing US solar industry.

Recent Progress

A custom-built chamber for accelerated soiling studies of PV coverglass materials has been designed, fabricated, and characterized. The chamber sample stage can be configured with a variable angle of incidence to mimic common tilt angles in the northern hemisphere and has integrated heating and cooling capabilities via an array of Peltier elements and a chiller loop, with a measured heating/cooling rate of 7.4 ± 4.0 °C/min and -1.2 ± 0.2 °C/min, respectively. The chamber also features *in situ* humidity control for simulated dew cycling.

Accelerated soiling/cementation tests have been performed on bare glass using 8 standardized test contaminants. These test contaminants are primarily silica-based, and formulated to represent the dust compositions of diverse geographic regions such as the American Southwest, the Middle East, Western China, and the Kanto region of Japan. After dust deposition, cementation is initiated by successive temperature/humidity cycling. Several test contaminant species display a marked increase in adhesion after dew cycling, verifying that cementation has occurred. Water contact angle (WCA) measurements further show that the cemented dust layer transitions to a high-energy, superhydrophilic state, suggesting a change in surface energy, as shown in Fig. 1.

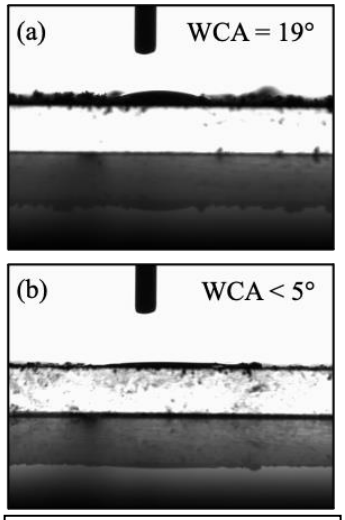

Fig. 1: WCA images of dust wettability before (a) and after (b) dew cycling.

On the computational modeling side, molecular dynamics models of amorphous silica have been constructed to serve as the baseline simulation domain for the computational spectroscopy simulations. Using the LAMMPS code [2], an α-quartz crystal composed of 5,048 atoms was constructed, and a Si-O Tersoff bond-order potential was used to model all interatomic interactions [3]. After equilibrating at 300 K under NVT (canonical ensemble) dynamics, melting was initiated by raising the model temperature to 7000 K at a rate of 33.5 K/ps with a 1 fs timestep. To produce an amorphous silica, the model was then quenched at a rate of 5 K/ps back to a temperature of 300 K. Finally, the structure was relaxed under NPT (isothermal-isobaric) dynamics at a temperature of 300 K and zero pressure to a final configuration.

The formation of an amorphous structure is confirmed via the radial distribution function (RDF), which shows an expected Si-Si and O-O bond broadening after the melt-quench procedure. The amorphous solid was then cleaved in half to produce a silica surface. This results

in under-coordinated surface oxygen atoms, as shown in Fig. 2, which will be passivated with appropriate functional groups in the X-ray absorption simulations.

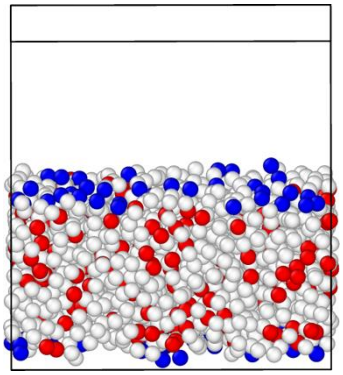

Fig. 2: Atomistic snapshot of O atoms in a-SiO_2 slab. The blue atoms on the top surface are undercoordinated.

Future Plans

Moving forward, samples subjected to accelerated soiling/cementation studies will be characterized by SAXS and NEXAFS at SSRL. For SAXS measurements, changes in the intensity/location of the primary scattering signal corresponds to changes in surface morphology and film porosity that can be used to distinguish interaction mechanisms as a function of contaminant particle size, coverglass film structure, and surface functionality (such as wettability). Since both glass and common PV coverglass materials are silica-based, the spectrum of the oxygen *K*-edge band will be investigated. Chemical shifts that are observed in the fine structure splitting of the oxygen absorption edge correspond to changes in the local oxygen bonding environment, as shown in Fig. 3. This change in surface chemistry, which is typically not observable with conventional XPS, should provide insight into the fundamental chemical interaction mechanisms that occur due to soiling and cementation.

The chemical shifts observed in the experimental NEXAFS spectra are not easily interpreted. Since the ultimate goal is to quantify the detailed surface chemistry changes that come about as a result of soiling/cementation reactions, first principles computational X-ray absorption modeling is an invaluable tool for interpreting the experimental NEXAFS spectra. Using the slabs of a-SiO_2 produced via melt-quench dynamics as the base simulation domain, *ab initio* molecular dynamics (AIMD) simulations will be performed with various functional surface terminating groups (hydroxyls, methyls, fluoromethyls, siloxanes, etc.) to derive equilibrium structures for these surface terminations. Finally, a computational spectroscopy calculation based on density functional theory (DFT) will utilized to simulate the corresponding NEXAFS signal that corresponds to each oxygen bonding environment, which can be compared to the experimental spectra to identify changes in surface chemistry that correspond to specific peak shifts.

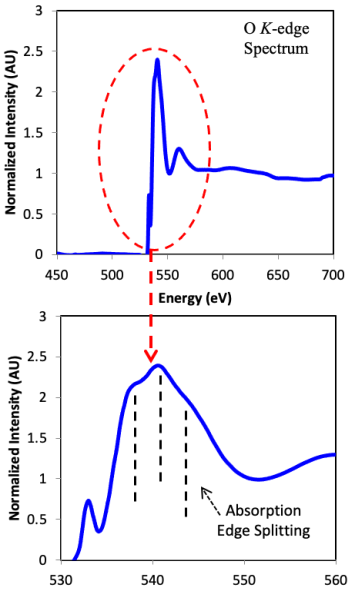

Fig. 3: NEXAFS spectra of the O *K*-edge band in silica.

References

[1] M.R. Maghami *et al*., (2016), "Power loss due to soiling on solar panel: A review,"

Renewable and Sustainable Energy Review, 59, 1307-1316, DOI: 10.1016/j.rser.2016.01.044.

[2] Plimpton, S., (1995), "Fast Parallel Algorithms for Short-Range Molecular Dynamics," *Journal of Computational Physics*, 517, 1-19.

[3] S. Munetoh, et al., (2007), "Interatomic potential for Si-O systems using Tersoff parameterization", *Computational Materials Science*, 39(2), 334-339.

Publications

1. Adawi, M. and Fleming, R.A., "Development of an Instrumented Soiling Chamber for Evaluating Solar PV Coatings," *2021 NREL Virtual Photovoltaic Reliability Workshop,* February 22-26, 2021.

Intermetallic Reactivity: From Frustrated Bonding to Mechanisms for Intergrowth and Modular Functionality in Metals and Alloys

Daniel C. Fredrickson, Department of Chemistry, University of Wisconsin-Madison

Program Scope

Intermetallic phases exhibit an immense diversity in their compositions, crystal structures, and properties, creating both a rich palette of potential materials and severe challenges for design efforts. When facing the question of structure prediction for designing new compounds, one generally begins with the component elements in a certain ratio and asks what crystal structure will provide the most stable arrangement. This approach is in-line with the synthetic procedures used for the preparation of intermetallic phases, as elemental metals are the most common starting materials. However, the geometrical arrangements encountered in these compounds hint that an alternative view may be productive. In many of the most complex intermetallic structures, fragments or blocks derivable from simpler compounds with nearby compositions can be discerned[1] suggesting that structurally-related parent phases may make better reference points for their stability (Figure 1). This project focuses on developing principles underlying this process of building complicated modular intermetallic phases from simpler precursor phases. The scope of this work includes three main objectives: (1) the determination of mechanisms driving the stability of intermetallic intergrowth structures, with a particular focus on the ways interfaces between regions with distinct structural or compositional features can be favorable; (2) the synthesis and characterization of new intermetallic phases that illustrate such mechanisms; and (3) the examination of properties and functionalities that can emerge from the modular arrangements present in the compounds studied.

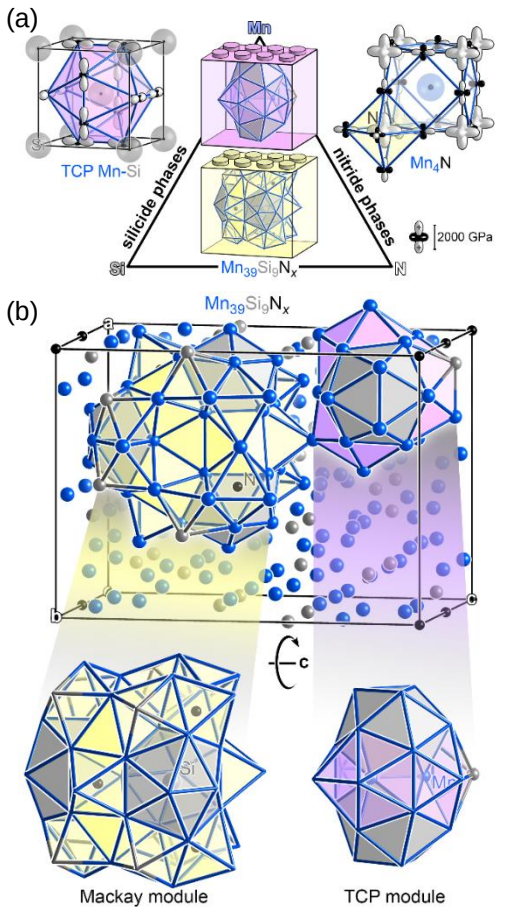

Figure 1. The modular character of $Mn_{39}Si_9N_x$ (x = 0.84), a compound elucidated under this project. (a) The complementary chemical pressure schemes of its parent structures. (b) The full crystal structure, highlighting its Mn-Si (gray and purple) and Mn-N (yellow) domains.

Recent Progress

The Intermetallic Reactivity Database. To support the development of models and guidelines for the stability of intermetallic intergrowth phases, we built the infrastructure for an online database of theoretically derived properties of solid state structures that can be visualized and correlated with the tendency of the compounds to participate in the building of more complex structures. In this database, DFT-Chemical Pressure schemes, electronic density of states distributions, and charge distributions are being collected for intermetallics to allow for the assessment of the atomic packing issues, electronic instabilities, and opportunities for topological charge stabilization that may motivate or guide the geometries of intergrowth structures. With this information, intermetallic intergrowths can be categorized by according to the types of reactivities predicted for the parent structures. By focusing on semi-quantitative descriptors of chemical stability and reactivity, this resource complements the computational data stored in such repositories as the Materials Project[2] and the Open Quantum Materials Database.[3]

Theoretical tools for examining modular structures. We have adapted the reversed approximation Molecular Orbital (raMO) method[4] to exploring this issue of how structural relationships between parent structures and intergrowths relate to similarities in their electronic structures. In the raMO approach, local MO diagrams are reconstructed from the full occupied wavefunctions of a material to test hypotheses about bonding. The resulting localized functions reveal the degree to which the hypothesized electronic features exist in a compound and the ways they interact with their broader context. To broaden the applicability of this method, we developed an implementation that directly analyzes the planewave-based wavefunctions of DFT calculation, rather than relying on a Hückel model, as in the original formulation. The DFT-raMO technique has allowed us to explain a surprising discrepancy between the seemingly electron-precise bonding scheme of the compound Mn_2Hg_5[5] and the experimental observation that it exhibits antiferromagnetic order.[6] Here, raMO analysis reveals that the antiferromagnetic order arises from the emergence of diradical character in the Mn-Mn π interactions (Figure 2), which widens the electronic pseudogap already present in non-spin-polarized results.[5] Overall, this picture illustrates how covalent magnetism can create local moments in seemingly closed-shell intermetallics.

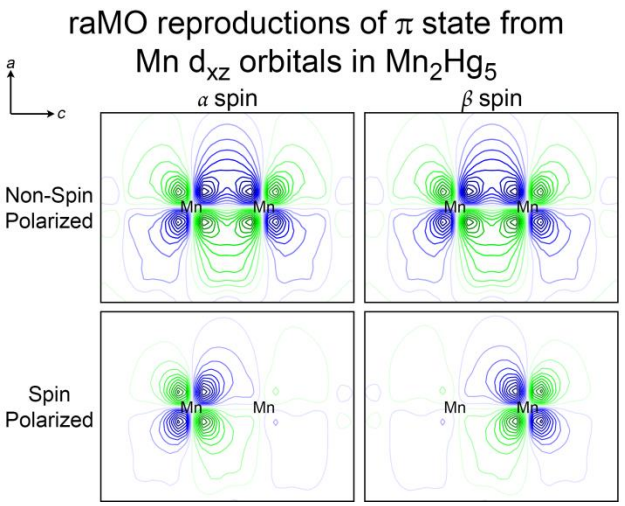

Figure 2. Diradical character in the π-bonding along the Mn chains in Mn_2Hg_5, revealed by the DFT-raMO method.

With the original DFT-calibrated Hückel implementation of the raMO method, we also discovered that the Ca_2Cu and CaCu structures are highly modular.[7] The structures are build from FCC or HCP fragments they contain and Cu zigzag chains, each of which have

well-defined and consistent electron counts according to their raMO functions. This modularity helps explain the low energy differences calculated for CaCu polymorphs based on the FeB and CrB types.

The intermetallic subnitride $Mn_{39}Si_9N_x$ (x = 0.84). We have completed our analysis of a new intermetallic subnitride illustrating the phenomenon of epitaxial stabilization.[8] $Mn_{39}Si_9N_x$ was synthesized simply by annealing mixtures of Mn and Si powders in evacuated fused silica tubes back-filled with nitrogen gas. As can be anticipated from the complementary CP schemes of Mn-rich silicide phases and the nitride Mn_4N (Figure 1a), the $Mn_{39}Si_9N_x$ structure is built from Mn-Si and Mn-N domains that closely associate with each other (Figure 1b). The Mn-Si regions are based on tetrahedral close packings similar to Mn-rich silicides. The Mn-N component, on the other hand, consists of a network of face-sharing Mn_6 octahedra, some filled with N atoms, that wrap around the Mn-Si domains. The ease with which this phase forms can be correlated with the high solubility of N in elemental Mn, which provides a facile way for N to enter into the reaction. We anticipate that it will be possible to prepare similar subnitrides in other systems combining analogous CP features and high N solubility, such as M-Si-N systems where M is a mid-row transition metal.

The modular structure of $Ca_3Cu_{7.8}Al_{26.2}$. Another experimental focal point during this project has been the crystal structure of $Ca_3Cu_{7.8}Al_{26.2}$ (Figure 3).[9] The structure of this phase can be interpreted in terms of building blocks derived from the nearby $CaAl_4$ and $CuAl_2$ phases, which assemble into a primitive cubic framework whose voids are occupied by Al_{13} cuboctahedra. Using theoretical calculations, we found that this intergrowth of between $CaAl_4$ and $CuAl_2$ (in a hypothetical fluorite polymorph) is supported not only by geometrical epitaxy, but also by a matching in the atomic charge distributions at the interfaces. In addition, the attraction between the Ca-Al and Cu-Al domains can be connected to the (1) affinity of Cu atom for certain Al sites of the $CaAl_4$ structure (driven by atomic-packing and electronegativity), and (2) the infeasibility of Cu simply substituting for Al atoms in $CaAl_4$ due to the overly-long Ca-Cu distances that would result.

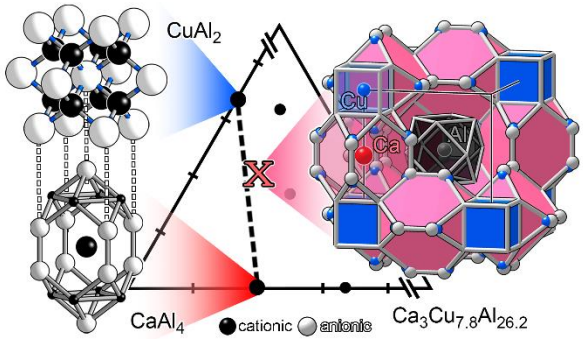

Figure 3. The structure of $Ca_3Cu_{7.8}Al_{26.2}$, and its construction (at the conceptual level) from an epitaxial relationship between $BaAl_4$-type $CaAl_4$ and a hypothetical fluorite-type polymorph of $CuAl_2$. For $CaAl_4$ and $CuAl_2$, theoretically calculated atomic charge distributions are plotted with white (anionic) and black (cationic) spheres.

Future Plans

Our immediate plans for future research include the renewed synthetic and crystallographic pursuit of intermetallic intergrowth structures that was interrupted by the COVID-19 pandemic. In particular, our synthesis of $Mn_{39}Si_9N_x$ has offered a strategy to discover other subnitrides, and

we have encountered a new intermetallic suboxide. In addition, an ongoing activity will be populating the Intermetallic Reactivity Database with new entries, and correlating the data collected with the results of our experiments and the existence of intergrowth structures in the literature. We are also in the process of examining how frameworks of face-sharing octahedra, as in $Mn_{39}Si_9N_x$, can serve as buffer regions that offer to relief of atomic packing issues in systems involving icosahedra and tricapped trigonal prisms (two units that are notoriously difficult to pack). Short term goals here are to devise guidelines for the design of systems in which the incorporation of these buffer regions is favorable, and to realize new examples experimentally.

References

(1) Harris, N. A.; Hadler, A. B.; Fredrickson, D. C. In Search of Chemical Frustration in the Ca-Cu-Cd System: Chemical Pressure Relief in the Crystal Structures of Ca_5Cu_2Cd and $Ca_2Cu_2Cd_9$. *Z. Anorg. Allg. Chem.* **2011**, *637*, 1961-1974.

(2) Jain, A.; Ong, S. P.; Hautier, G.; Chen, W.; Richards, W. D.; Dacek, S.; Cholia, S.; Gunter, D.; Skinner, D.; Ceder, G.; Persson, K. A. Commentary: The Materials Project: A materials genome approach to accelerating materials innovation. *APL Mater.* **2013**, *1*, 011002.

(3) Kirklin, S.; Saal, J. E.; Meredig, B.; Thompson, A.; Doak, J. W.; Aykol, M.; Rühl, S.; Wolverton, C. The Open Quantum Materials Database (OQMD): assessing the accuracy of DFT formation energies. *npj Comput. Mater.* **2015**, *1*, 15010.

(4) Yannello, V. J.; Kilduff, B. J.; Fredrickson, D. C. Isolobal Analogies in Intermetallics: The Reversed Approximation MO Approach and Applications to $CrGa_4$- and Ir_3Ge_7-Type Phases. *Inorg. Chem.* **2014**, *53*, 2730-2741.

(5) Yannello, V. J.; Lu, E.; Fredrickson, D. C. At the Limits of Isolobal Bonding: π-Based Covalent Magnetism in Mn_2Hg_5. *Inorg. Chem.* **2020**, *59*, 12304-12313.

(6) Legrand, E. The magnetic structure of Mn_2Hg_5. *Phys. Status Solidi* **1973**, *15*, K37-K39.

(7) Park, S.-W.; Hosono, H.; Fredrickson, D. C. Cation Clustering in Intermetallics: The Modular Bonding Schemes of CaCu and Ca_2Cu. *Inorg. Chem.* **2019**, *58*, 10313-10322.

(8) Peterson, G. G. C.; Berns, V. M.; Fredrickson, D. C. $Mn_{39}Si_9N_x$: Epitaxial Stabilization as a Pathway to the Formation of Intermetallic Nitrides. *J. Am. Chem. Soc.* **2020**, *142*, 8575-8579.

(9) Peterson, G. G. C.; Geisler, E. E.; Fredrickson, D. C. Intermetallic Reactivity: $Ca_3Cu_{7.8}Al_{26.2}$ and the Role of Electronegativity in the Stabilization of Modular Structures. *Inorg. Chem.* **2020**, *59*, 5018-5029.

Publications

(1) Park, S.-W.; Hosono, H.; Fredrickson, D. C. Cation Clustering in Intermetallics: The Modular Bonding Schemes of CaCu and Ca_2Cu. *Inorg. Chem.* **2019**, *58*, 10313-10322.

(2) Peterson, G. G. C.; Berns, V. M.; Fredrickson, D. C. $Mn_{39}Si_9N_x$: Epitaxial Stabilization as a Pathway to the Formation of Intermetallic Nitrides. *J. Am. Chem. Soc.* **2020**, *142*, 8575-8579.

(3) Peterson, G. G. C.; Geisler, E. E.; Fredrickson, D. C. Intermetallic Reactivity: $Ca_3Cu_{7.8}Al_{26.2}$ and the Role of Electronegativity in the Stabilization of Modular Structures. *Inorg. Chem.* **2020**, *59*, 5018-5029.

(4) Yannello, V. J.; Lu, E.; Fredrickson, D. C. At the Limits of Isolobal Bonding: π-Based Covalent Magnetism in Mn_2Hg_5. *Inorg. Chem.* **2020**, *59*, 12304-12313.

Permanent Magnets Featuring Heavy Main Group Elements for Magnetic Anisotropy

Danna Freedman | Massachusetts Institute of Technology

Program Scope

Permanent magnets are the functional component of the electric motors and generators that are ubiquitous in energy generation. Creating the next generation of magnets would improve energy generation across all classes of fuel sources – from wind to fossil fuels. Our goal is to develop fundamentally new magnets that generate higher magnetic flux per volume while retaining the properties conferred by rare-earth elements incorporated into current technologies. We hypothesize that by engendering a covalent interaction between two elements, we can access a new regime of magnetic materials where the two components of a magnetic moment—spin and orbital angular momentum—come from two separate atoms to form a complete magnetic moment (**Figure 1**).

Previously we harnessed high-pressure to discover two new materials which feature the desired combination of spin and orbital angular momentum. The first material, $FeBi_2$, enables the study of an unprecedented solid-state metal-metal bonding interaction. The second, $MnBi_2$ is the second member of the Mn–Bi system, the first of which is a fantastic permanent magnet. Together these chemically simple but magnetically rich materials provide an elegant platform for elucidating fundamental design principals of magnetic anisotropy while inspiring the synthesis of new magnetic materials.

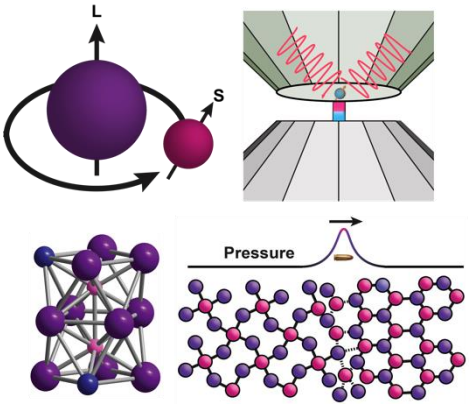

Figure 1: Our approach to new magnetic materials entails combing the orbital angular momentum (*L*) of heavy elements with the spin angular momentum (*S*) of paramagnetic transition metals. We made progress isolating newly discovered high-pressure phases via chemical substitution (bottom left), characterizing magnetic phases *in situ* with quantum sensors (top right), and began studying the kinetics of these high-pressure transformations via shockwave experiments (bottom right).

Within the most recent project period, we focused on incorporating phase stability calculations into our reactions – phase stability calculations enable us to identify metastable materials that reside at local minima. We are targeting these phases through high pressure reactions and more exotic techniques such as dynamic compression or shock wave synthesis. In parallel we are incorporating *in situ* measurements into our solid-state reactions. By introducing *in situ* probes we can both identify metastable materials at their point of formation to glean kinetic insight and study their magnetic properties as they are transformed by pressure. Within solid-state chemistry, the inherent black box nature of reactions stymies progress in targeting phases that have specific properties. Unlike solution phase chemistry where *in situ* monitoring is common place, traditionally solid-state reactions occur within literal black boxes. Creating a window into these reactions to probe structure and properties *in situ* enables us to rationally target synthetic phases. Critically, we are fusing our

lab's knowledge of quantum sensing with high pressure synthesis, taking defects in the diamonds we use for synthesis and using those defects to probe the magnetic properties of our newly created materials.

Recent Progress

Objective 1: *In situ* physical property measurements at high pressures. The use of diamond anvil cells (DACs) as transparent high-pressure reactors allows for characterization of materials by the entirety of the electromagnetic spectrum. In parallel to such approaches, we recently turned to the quantum technology of anionic nitrogen centers (NV centers) in diamond as *in situ* probes of properties for magnets and superconductors. By exploiting the fragility of the superposition state engendered by the nitrogen vacancy pair defect to local magnetic or electronic changes, NV doped diamonds host tremendous promise as quantum sensors that may be incorporated into DACs. In orthogonal DOE funded research, our group develops molecular analogues to these centers. This project brings our expertise in quantum sensing to bear on high pressure synthesis. Integration of this cutting-edge approach combines immense *spatial* and *directional* resolution with exquisite quantum sensitivity to allow for *in situ* high-pressure magnetometry. The directional resolution can be translated into a measurement of magnetic coercivity, and the temperature control enables discrete temperature measurements.

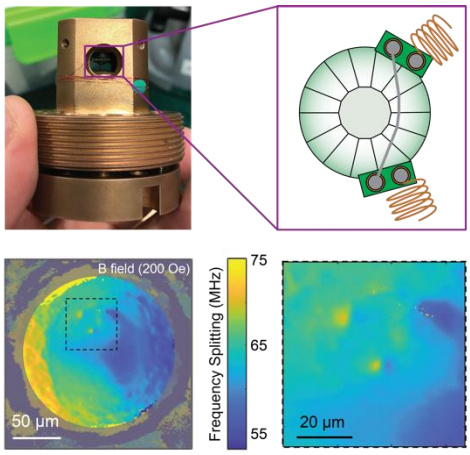

Figure 2: A non-magnetic DAC loaded with a wired diamond doped with NV centers (top) was used in the preparation of $FeBi_2$ under high-pressure conditions. ODMR spectroscopy revealed the magnetic response across the entire diamond culet (bottom left), including the presence of magnetic dipoles (bottom right) where the $FeBi_2$ is spatially located in the sample.

To probe the magnetism of $FeBi_2$ in a DAC, the first step is to perform the control experiments and study Fe metal and Bi metal in a DAC. Fortuitously, the Yao group at UC Berkeley reported a proof-of-concept system detecting the suppression of magnetism in Fe with applied pressure. We reached out to the Yao group to expand this capability and we are currently collaborating with them on this study. We designed and implemented an experimental set-up that is compatible with high-pressure synthetic conditions. Optically detected magnetic resonance spectroscopy (ODMR) revealed the magnetic dipoles of the $FeBi_2$ demonstrating that indeed it is a room temperature magnet (**Figure 2**). Variable temperature and variable field studies used to determine the figures of merit of the $FeBi_2$ phase are ongoing. In the future we anticipate being able to execute these measurements in-house.

In parallel we are pursuing conventional magnetometry experiments to elucidate the magnetic properties of $MnBi_2$. As a bulk approach requires high-purity samples in yields approaching 100%, we first explored whole-cell resistive heating measurements in set-ups compatible with X-ray

diffraction. We demonstrated uniform full cell reactivity on cylindrical sample spaces 250 microns in diameter. This readily translates to our recently purchased commercial magnetometry cell, which we calibrated on our magnetometer. We also developed protocols for constructing wired DACs that are readily integrated with our newly acquired properties measurement system. Together, these capabilities will allow for materials characterization without ever removing pressure, yielding a wealth of information on the underlying pressure-dependent magnetic and electronic properties of $MnBi_2$ as well as new systems of interest (**Figure 3**).

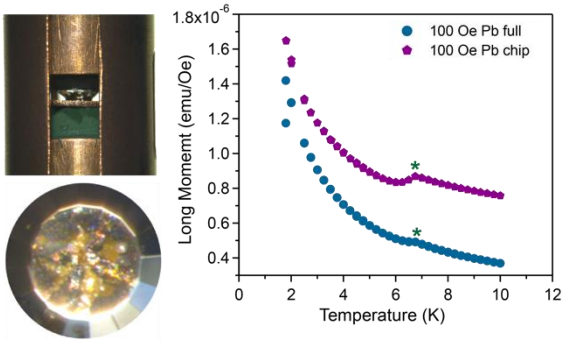

Figure 3: A non-magnetic DAC (top left) compatible with commercial magnetometers, was calibrated using the superconducting transition of elemental lead (right). We also developed capabilities to wire the diamond sample space (bottom left), which will allow for future charge transport measurements.

Note, due to the pandemic and closure of DOE National User Facilities, we concentrated on bringing new characterization capabilities to our lab. Once national lab facilities return to on-site access, we will resume our synchrotron-based studies. To begin, we have been allocated shifts at the Advanced Photon Source, Sector 4 to assess the magnetic structure of $MnBi_2$ using X-ray Magnetic Circular Dichroism techniques.

Objective 2: Discovery of new magnetic candidate materials. To support our synthetic efforts, we implemented a high-throughput computational technique which rapidly maps out the thermodynamic landscape of chemical systems of interest. *Ab Initio* Random Structure Searching (AIRSS) plots trends in stability with synthetic conditions such as pressure, temperature, and composition, shattering the otherwise black box of solid-state reactivity. Each one of these optimizations identifies a local minimum in energy within a chemical space and thus a potentially metastable synthetic candidate. We have used AIRSS on a wide range of chemical systems to simultaneously enable rapid feedback on synthetic hypotheses and gain a deeper understanding of their thermodynamic landscape.

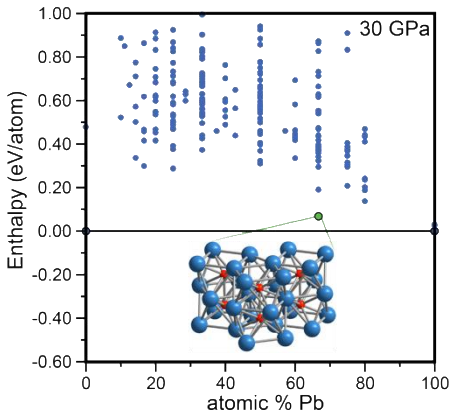

Figure 4: Plot of the enthalpy of Fe–Pb phases versus composition showing that $FePb_2$ is a promising metastable structure.

Continuing our pursuit of new transition metal-heavy main group magnetic materials, we explored the Fe–Pb system. The large earth abundance of Pb and its similar inherent spin-orbit coupling to Bi recommends it as an ideal contributor of orbital angular momentum in magnetic phases. Akin to the Fe–Bi system, Fe and Pb exhibit immiscibility up to very high temperatures at ambient pressure. Thus, we performed AIRSS calculations at analogous conditions under which $FeBi_2$ forms (**Figure 4**). Notably, $FePb_2$, isostructural to $FeBi_2$, has the lowest enthalpy of all the

structures calculated at 30 GPa. In fact, the calculated enthalpy of formation for this phase at 30 GPa is 66 meV/formula unit, which is 217 meV/formula unit less than at ambient pressure, demonstrating the tendency of this structure to stabilize with increasing pressure and recommending it for even higher-pressure experiments. Work is ongoing to synthesize new phases in this system and other systems with promising magnetic character aided by the AIRSS approach. Note, this approach is also critical to identifying target phases for shockwave synthesis.

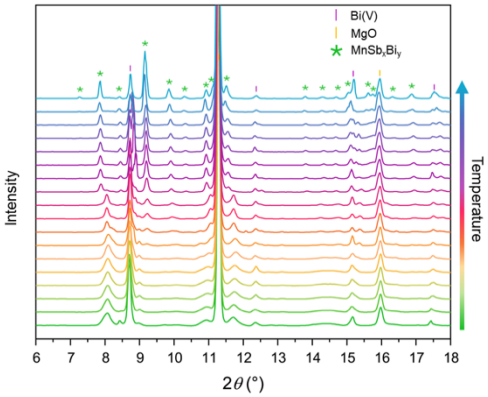

Figure 5: Powder X-ray diffraction patterns collected during laser heating of MnSb and Bi at 9 GPa. During the reaction, new peaks grew in (green), while Bi(V) peaks (purple) decreased in intensity, suggesting the formation of a new ternary phase.

An important parallel direction is the pursuit of synthetic approaches that enable ambient pressure recovery of promising magnetic high-pressure phases. We hypothesize that incorporating Sb will allow us to access the optimal size ratio between the M and Bi/Sb sites to maintain and stabilize Sb-doped MBi_2 to ambient pressure. Toward this end, we found novel reactivity between MnSb and Bi, forming a new ternary phase (**Figure 5**) whose structure and properties we are in the process of investigating.

Future Plans

Quantum sensing may enable *in situ* measurements of solid-state materials thereby allowing us to precisely target functional materials. We are pursuing generalizing this technique beyond a few proof-of-concept experiments performed by others. Leveraging quantum sensing technology with high-pressure expertise will allow for rapid screening of more complicated high-pressure materials – and might serve as a screen for desired products of ternary reactions. In addition, as has been noted by others, high pressure magnetometry is an excellent way to determine whether a superconductor has been formed at high pressure.

Through shockwave experiments at DOE national facilities, we aim to study structures with millisecond time resolution to gain insight into structure formation dynamics at high-pressure. As $MnBi_2$ readily forms upon compression with low temperature annealing, this is an ideal material for these investigations. Further the structural relationship between MnBi and $MnBi_2$ offers a unique opportunity to investigate the dynamics of phase transformations with pressure. We have submitted a beamline proposal to perform these experiments at the Advanced Photon Source and are awaiting the results of its review. Such studies will propel the field of solid-state chemistry toward a mechanistic understanding of structure formation, enabling the rational designing of new magnetic materials.

References

Walsh, J. P. S.; Clarke, S. M.; Meng, Y.; Jacobsen, S. D.; Freedman, D. E. Discovery of $FeBi_2$. *ACS Cent. Sci.* **2016**, *2*, 867–871.

Bayliss, S. L.; Laorenza, D. W.; Mintun, P. J.; Kovos, B.D.; Freedman, D.E.; Awschalom, D. D. Optically Addressable Molecular Spins for Quantum Information Processing *Science,* **2020**, *370,* 1309-1312.

Hsieh, S.; Bhattacharyya, P.; Zu, C.; Mittiga, T.; Smart, T.J.; Machado, F.; Kobrin, B.; Höh, T. O.; Rui, N. Z.; Kamrani, M.; Chatterjee, S.; Choi, S.; Zaletel, M.; Struzhkin, V. V.; Moore, J. E.; Levitas, V. I.; Jeanloz, R.; Yao, N. Y. Imaging Stress and Magnetism at High Pressures Using a Nanoscale Quantum Sensor. *Science*, **2019**, *366,* 1349-1354.

Altman, A. B.; Tamerius, A. D.; Koocher, N. Z.; Meng, Y.; Pickard, C.; Walsh, J. P. S.; Rondinelli, J. M.; Jacobsen, S. D.; Freedman, D. E. Computationally Directed Discovery of $MoBi_2$. *J. Am. Chem. Soc.* **2021**, *143,* 214-222.

Publications

Walsh, J. P. S.; Clarke, S. M.; Puggioni, D.; Tamerius, A. D.; Meng, Y.; Rondinelli, J. M.; Jacobsen, S. D.; Freedman, D. E. $MnBi_2$: A Metastable High-Pressure Phase in the Mn–Bi System. *Chem. Mater.* **2019**, *31*, 3083-3088.

Compositional Control of Fundamental Electronic and Magnetic Properties of Ordered Layered Multielemental MXenes

PI: Yury Gogotsi (Drexel University)
Co-PIs: Steven May (Drexel University)
Babak Anasori (Drexel University)[*]

Program Scope

Two-dimensional (2D) materials have attracted much attention owing to their potential to host functional properties that differ markedly from their bulk counterparts. In 2011, a large family of 2D transition metal carbides and nitrides (Ti_3C_2, Ti_2C, V_2C, Mo_2C, etc.), so called MXenes, was discovered at Drexel University. These 2D solids host a unique combination of physical attributes including metallic conductivity, hydrophilicity, and ability to intercalate a host of ions and small organic molecules, that in turn lead to outstanding performance in energy storage, harvesting, electrocatalysis, sensing, communication devices and electromagnetic interference (EMI) shielding. More than 30 different stoichiometric MXenes and more than 20 solid solutions have been reported and the properties of numerous other MXenes have been theoretically studied.[1]

This project focused on the synthesis and characterization of double-M (where M is a transition metal) MXenes with the aim of the understanding how this flexibility of the M-site chemistry impacts their electronic, magnetic, and optical properties. We hypothesized that the different arrangement of transitions metal atoms, surface terminations (denoted T_x), and intercalated species can be used to control the properties of the ordered multi-element MXenes. Synthesis efforts have targeted stabilizing new multi-elemental MXenes, where the transition metal chemistry is systematically varied in both the surface and sub-surface layers. Using these multi-M MXenes, we investigated how the electronic and magnetic properties depend on the surface groups, intercalants, and the composition and ordering of the M-site atoms.

Recent Progress

Electronic contributions of surface and sub-surface M-site atoms: With earlier work on the project highlighting the important role of surface terminations on electrical conductivity and work functions,[2, 3] we aimed to understand the length scales associated with electronic interactions between the T_x surface groups and electronic bands derived from transition metals. Using soft X-ray absorption spectroscopy carried out at Brookhaven National Laboratory and Lawrence Berkeley National Laboratory, we have distinguished the electronic contributions of the surface and sub-surface M-sites in ordered multi-element MXenes revealing that surface groups disproportionately impact band derived from surface M-sites.[4] This work exploited the different M-site locations of Ti atoms in different MXenes (**Figure 1a**) to understand the T_x-M interactions. The Ti *L*-edge spectral features are significantly modified upon conversion from the MAX parent

[*] Current affiliation: Indiana University Purdue University – Indianapolis (IUPUI)

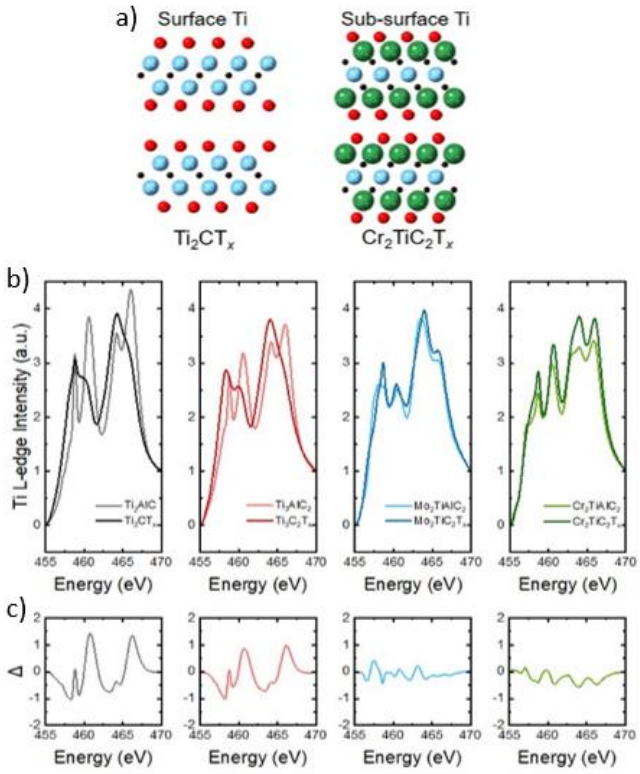

Figure 1. (a) Schematics of Ti_2CT_x and $Cr_2TiC_2T_x$ MXenes illustrating the difference in surface versus sub-surface position of the Ti atoms (represented by blue spheres); T_x atoms are represented by red spheres. (b) Ti *L*-edge X-ray absorption spectra of Ti_2CT_x, $Ti_3C_2T_x$, $Mo_2TiC_2T_x$, and $Cr_2TiC_2T_x$ compared to their respective MAX phase precursors, Ti_2AlC, Ti_3AlC_2, Mo_2TiAlC_2, and Cr_2TiAlC_2. (c) The difference between the MAX spectra and the MXene spectra. $Cr_2TiC_2T_x$ MXenes illustrating the difference in surface versus sub-surface position of the Ti atoms (represented by blue spheres); T_x atoms are represented by red spheres.

phase in MXenes with Ti in the surface sites (**Figure 1b,c**). In contrast, the Ti spectra from the ordered double-M MXenes are very similar to that of their parent MAX phases, indicating that the bands derived from the sub-surface Ti atoms are not strongly modified by the surface termination. This result is consistent with our interpretation that the sub-surface Ti atoms have much weaker interactions with the T_x groups than surface Ti, which suggests that the surface groups have limited impact on the sub-surface M-sites. In all cases, *d*-electron count per Ti atom, obtained from the branching ratio of the absorption spectra, decreases upon conversion of MAX to MXenes. Additionally, elementally resolved partial density of states calculations were used to further support our interpretation of the X-ray absorption spectra and confirm the trends in the Ti *d* electron count obtained from the branching ratios. These results indicate that the electronic implications of the T_x groups are largely accommodated within the surface-most M-site layers and have more limited impact on sub-surface M-site atoms. With these new insights, we proposed a general design strategy to stabilize surface invariant properties in ordered double-M MXenes, wherein the interior M-site atoms are selected to host the desired electronic, magnetic, and topological functionalities.

Magnetic interactions between M-sites: In a detailed study of $Cr_2TiC_2T_x$, we provided the first direct experimental evidence of a magnetic transition within a MXene material.[5] Previous theoretical work predicted that $Cr_2TiC_2T_x$ could host an antiferromagnetic ground state in the case of a uniform -F or -OH surface termination.[6] Motivated by previous ground state antiferromagnetism predictions on uniform -F or -OH surface terminated $Cr_2TiC_2T_x$, we produced atomically thin flakes of $Cr_2TiC_2T_x$ and characterized their magnetic properties through a combination of dc magnetometry, ac susceptibility and magnetotransport experiments. As shown in **Figure 2a**, $Cr_2TiC_2T_x$ exhibits a clear bifurcation between zero-field-cooled (ZFC) and field-

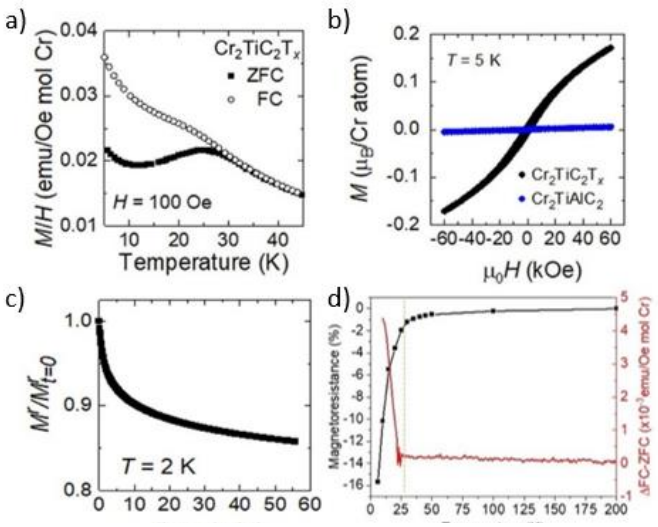

Figure 2. (a) Zero-field-cooled (filled squares) and field-cooled (empty circles) magnetization from 5–45 K of $Cr_2TiC_2T_x$ MXene. (b) Field-dependent magnetization of $Cr_2TiC_2T_x$ MXene (black) and Cr_2TiAlC_2 MAX phase (blue) measured at 5 K. (c) Time-dependent magnetization measured after cooling $Cr_2TiC_2T_x$ MXene from 300 K to 2 K in 60 kOe external field. (d) A comparison between magnetoresistance magnitude of magnetoresistance (left axis, H = 70 kOe) and the difference between the field-cooled and zero-field-cooled magnetization (right axis).

cooled (FC) curves between 25-40 K, which is evidence of a magnetic transition as such behavior is inconsistent with paramagnetism. At low temperature, nonlinearity in the magnetization as a function of field is visible (**Figure 2b**), which is not observed in the Cr_2TiAlC_2 MAX phase. Furthermore, the in-phase component of the ac susceptibility has a slight frequency dependence and a time-dependent decay of the remanent magnetization suggesting a spin freezing transition to a glassy state (**Figure 2c**). The inhomogeneous nature of the surface species inherent to these MXenes likely inhibits long-range magnetic order, resulting in the observed glassy state. Moreover, additional magnetic disorder could arise from the flake-to-flake coupling of the randomly oriented flakes inevitably present in the samples studied. Further confirmation of a magnetic transition was obtained through temperature dependent resistivity and magnetoresistance measurements. A significant increase in magnetoresistance that is negative, linear, and non-saturating up to 90 kOe was found below the magnetic transition temperature (T_f), coincide with the divergence of the ZFC-FC magnetization (**Figure 2d**), which is attributed to a reduction of spin-dependent scattering as the field aligns the moments. Additionally, angular-dependent longitudinal magnetoresistance shows a clear difference between that measured above and below T_f. Finally, in temperature dependent resistivity measurements, we find an inflection point in the reduced activation energy at around 25-30 K, further indicating a coupling between electronic properties and Cr-hosted magnetic interactions of this MXene.

Physical properties of multi-M solid solution MXenes. Besides the ordered double-M MXenes, the synthesis of multi-M solid-solutions offers another route for tuning properties. Three interrelated binary solid-solution MXene systems were synthesized and characterized, based on Ti, Nb, and/or V at the M-site in the M_2XT_x structure (**Figure 3a**).[7] All three MXene systems ($Ti_{2-y}Nb_yCT_x$, $Ti_{2-y}V_yCT_x$, and $V_{2-y}Nb_yCT_x$) show complete solubility and random distribution of metal elements in the M-site sublattice. The temperature-dependent resistivity (**Figure 3b,c**) increases with the increasing Nb concentration in both $Ti_{2-y}Nb_yCT_x$ and $V_{2-y}Nb_yCT_x$ from 10-300 K. For the $Ti_{2-y}V_yCT_x$ system, all resistivity values are within the same order of magnitude, while a slight increase in ρ coincides with increased V concentration. To better understand the role of M-site composition on the electronic structure of these MXenes, soft XAS was collected at room temperature. For Ti and V, the relative *d*-electron count per atom was obtained from the $L_{2,3}$ branching ratio. Comparing $Ti_{2-y}V_yCT_x$ and $Ti_{2-y}Nb_yCT_x$, we find a clear M-site chemistry dependence to the branching ratio, indicating that the Ti band filling is influenced by its M-site counterpart. Comparing the Ti branching ratio in both Ti-containing MXenes, the Ti atoms in $Ti_{2-y}V_yCT_x$ have higher electron

count compared to $Ti_{2-y}Nb_yCT_x$, as shown in **Figure 3d**. The difference in Ti electron count in the two MXene systems is also found in the Ti *d*-orbital-derived DOSs obtained from DFT calculations of unterminated MXenes. The normalized fraction of occupied states within the valence band, also shown in **Figure 3d** (brown circles), indicates that the Ti bands in $Ti_{2-y}V_yC$ have larger fraction of occupied states than the equivalent bands in $Ti_{2-y}Nb_yC$. Based on the combined electronic transport, XAS and DFT results, we conclude that the electronic behavior of the solid-solution systems is impacted by the M-site metal composition.

Future Plans

In the remaining period of the project, we aim to further understand the contribution of intrinsic and extrinsic properties on macroscopic electrical conductivity in MXenes. These efforts include understanding the role of flake size and interlayer spacing on conductivity, decoupling the electronic concentration and the mobility contribution, and analyzing the correlations among the optical properties, the dielectric constants, and the electronic properties. We are utilizing scanning probe measurements to reveal spatial inhomogeneities in properties such as work functions and conductivity. Synthetic efforts are aimed at stabilizing uniform surface terminations on multi-M MXenes.

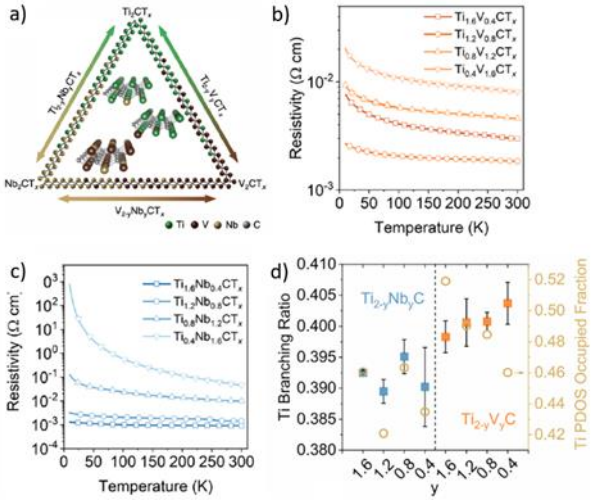

Figure 3. (a) The compositional triangle of $Ti_{2-y}Nb_yCT_x$, $Ti_{2-y}V_yCT_x$, and $V_{2-y}Nb_yCT_x$, showing the continuous solid solutions of M_2C-type MXenes studied in this project. Temperature dependence of resistivity for (b) $Ti_{2-y}V_yCT_x$ and (c) $Ti_{2-y}Nb_yCT_x$ MXene films. (d) Ti branching ratios of $Ti_{2-y}Nb_yC$ and $Ti_{2-y}V_yC$ obtained from X-ray absorption spectra; it shows the correspondence with the Ti *d*-orbital-derived PDOS occupied fractions.

References

1. VahidMohammadi, A.; Rosen, J.; Gogotsi, Y., *Science* **2021,** *372* (6547), eabf1581.
2. Hart, J. L.; Hantanasirisakul, K.; Lang, A. C.; Anasori, B.; Pinto, D.; Pivak, Y.; van Omme, J. T.; May, S. J.; Gogotsi, Y.; Taheri, M. L., *Nat. Commun.* **2019,** *10* (1), 522.
3. Schultz, T.; Frey, N. C.; Hantanasirisakul, K.; Park, S.; May, S. J.; Shenoy, V. B.; Gogotsi, Y.; Koch, N., *Chem. Mater.* **2019,** *31* (17), 6590-6597.
4. Yang, Y.; Hantanasirisakul, K.; Frey, N. C.; Anasori, B.; Green, R. J.; Rogge, P. C.; Waluyo, I.; Hunt, A.; Shafer, P.; Arenholz, E.; Shenoy, V. B.; Gogotsi, Y.; May, S. J., *2D Mater.* **2020,** *7* (2), 025015.
5. Hantanasirisakul, K.; Anasori, B.; Nemsak, S.; Hart, J. L.; Wu, J.; Yang, Y.; Chopdekar, R. V.; Shafer, P.; May, A. F.; Moon, E. J.; Zhou, J.; Zhang, Q.; Taheri, M. L.; May, S. J.; Gogotsi, Y., *Nanoscale Horizons* **2020,** *5* (12), 1557-1565.
6. Yang, J.; Zhou, X.; Luo, X.; Zhang, S.; Chen, L., *Appl. Phys. Lett.* **2016,** *109* (20), 203109.
7. Han, M. K.; Shuck, C. E.; Rakhmanov, R.; Parchment, D.; Anasori, B.; Koo, C. M.; Friedman, G.; Gogotsi, Y., *ACS Nano* **2020,** *14* (4), 5008-5016.

Publications

1. N. C. Frey, H. Kumar, B. Anasori, Y. Gogotsi, V. B. Shenoy. Tuning noncollinear spin structure and anisotropy in ferromagnetic nitride MXenes. *ACS Nano*, **2018**, *12*, 6319.

2. K. Hantanasirisakul, Y. Gogotsi, Electronic and optical properties of 2D transition metal carbides and nitrides (MXenes). *Adv. Mater.* **2018**, *30*, 1804779.

3. A. L. Bennett-Jackson, M. Falmbigl, K. Hantanasirisakul, Z. Gu, D. Imbrenda, A. V. Plokhikh, A. Will-Cole, C. Hatter, L. Wu, B. Anasori, Y. Gogotsi, J. E. Spanier. Van der Waals Epitaxy of Highly (111)-oriented $BaTiO_3$ on MXene. *Nanoscale*, **2019**, *11*, 622.

4. J. L. Hart, K. Hantanasirisakul, A. C. Lang, B. Anasori, D. Pinto, Y. Pivak, J. T. van Omme, S. J. May, Y. Gogotsi, M. L. Taheri. Control of MXenes' Electronic Properties Through Termination and Intercalation. *Nat. Commun.*, **2019**, *10*, 522.

5. N. Frey, A. Bandyopadhyay, H. Kumar, B. Anasori, Y. Gogotsi, V. B. Shenoy. Surface-Engineered MXenes: Electric Field Control of Magnetism and Enhanced Magnetic Anisotropy. *ACS Nano*, **2019**, *13*, 2831.

6. C. Zhang, L. McKeon, M. P. Kremer, S.-H. Park, O. Ronan, A. Seral-Ascaso, S. Barwich, C. Ó. Coileáin, N. McEvoy, H. C. Nerl, B. Anasori, J. N. Coleman, Y. Gogotsi, V. Nicolosi. Additive-free MXene Inks and Direct Printing of Micro-supercapacitors. *Nat. Commun.*, **2019**, *10*, 1795.

7. K. Hantanasirisakul, M. Alhabeb, A. Lipatov, K. Maleski, B. Anasori, P. Salles, C. Ieosakulrat, P. Pakawatpanurut, A. Sinitskii, S. J. May, Y. Gogotsi. Effects of Synthesis and Processing on Optoelectronic Properties of Titanium Carbonitride MXene. *Chem. Mater.*, **2019**, *31*, 2941.

8. X. Xiao, P. Urbankowski, K. Hantanasirisakul, Y. Yang, S. Sasaki, L. Yang, C. Chen, H. Wang, L. Miao, S. H. Tolbert, S. J. L. Billinge, H. D. Abruña, S. J. May, Y. Gogotsi. Scalable Synthesis of Ultrathin Mn_3N_2 Exhibiting Room-Temperature Antiferromagnetism. *Adv. Funct. Mater.*, **2019**, *1809001*.

9. Y. Gogotsi, B. Anasori. The Rise of MXenes. *ACS Nano*, **2019**, *13*, 8491.

10. T. Schultz, N. C. Frey, K. Hantanasirisakul, S. Park, S. J. May, V. B. Shenoy, Y. Gogotsi, N. Koch. Surface Termination Dependent Work Function and Electronic Properties of $Ti_3C_2T_x$ MXene. *Chem. Mater.*, **2019**, *17*, 6590.

11. J. D. Cain, A. Azizi, K. Maleski, B. Anasori, E. C. Glazer, P. Y. Kim, Y. Gogotsi, B. A. Helms, T. P. Russell, A. Zettl. Sculpting Liquids with 2D Materials: The Assembly of MXene Sheets at Liquid–Liquid Interfaces, *ACS Nano*, **2019**, *13*, 12385.

12. G. Deysher, C. E. Shuck, K. Hantanasirisakul, N. C. Frey, A. C. Foucher, K. Maleski, A. Sarycheva. V. B. Shenoy, E. A. Stach, B. Anasori, Y. Gogotsi. Synthesis of Mo_4ValC_4 MAX Phase and Two-Dimensional Mo_4VC_4 MXene with Five Atomic Layers of Transition Metals. *ACS Nano*, **2020**, *14*, 204.

13. A. Lipatov, M. Alhabeb, H. Lu, S. Zhao, M. J. Loes, N. S. Vorobeva, Y. Dall'Agnese, Y. Gao, A. Gruverman, Y. Gogotsi, A. Sinitskii. Electrical and Elastic Properties of Individual Single-Layer $Nb_4C_3T_x$ MXene Flakes. *Adv. Electron. Mater.*, **2020**, *6*, 1901382.

14. Y. Yang, K. Hantanasirisakul, N. Frey, B. Anasori, R. Green, P. Rogge, I. Waluyo, A. Hunt, P. Shafer, E. Arenholz, V. B. Shenoy, Y. Gogotsi, S. J. May. Distinguishing Electronic Contributions of Surface and Sub-surface Transition Metal Atoms in Ti-based MXenes. *2D Mater.*, **2020**, *7*, 025015.

15. H. Riazi, M. Anayee, K. Hantanasirisakul, A. A. Shamsabadi, B. Anasori, Y. Gogotsi, M. Soroush. Surface Modification of a MXene by an Aminosilane Coupling Agent. *Adv. Mater. Interfaces.*, **2020**, 1902008.

16. A. Iqbal, F. Shahzad, K. Hantanasirisakul, M. Kim, J. Kwon, J. Hong, H. Kim, D. Kim, Y. Gogotsi, C. M. Koo. Anomalous Absorption of Electromagnetic Waves by 2D Transition Metal Carbonitride Ti_3CNT_x (MXene). *Science*, **2020**, *369*, 446.

17. G. Valurouthu, K. Maleski, N. Kurra, M. Han, K. Hantanasirisakul, A. Sarycheva, Y. Gogotsi. Tunable Electrochromic Behavior in Titanium-based MXenes. *Nanoscale*, **2020**, *12*, 14204.

18. M. Han, K. Maleski, C. E. Shuck, Y. Yang, J. T. Glazar, A. C. Foucher, K. Hantanasirisakul, A. Sarycheva, N. C. Frey, S. J. May, V. B. Shenoy, E. A. Stach, Y. Gogotsi. Tailoring Electronic and Optical Properties of MXenes through Forming Solid Solutions. *J. Am. Chem. Soc.*, **2020**, *142*, 19110-19118.

19. K. Hantanasirisakul, B. Anasori, S. Nemsak, J. L. Hart, J. Wu, Y. Yang, R. V. Chopdekar, P. Shafer, A. F. May, E. J. Moon, J. Zhou, Q. Zhang, M. L. Taheri, S. J. May, Y. Gogotsi. Evidence of Magnetic Transition in Atomically Thin $Cr_2TiC_2T_x$ MXene. *Nanoscale Horiz.*, **2020**, *5*, 1557–1565.

20. J. L. Hart, K. Hantansirisakul, A. C. Lang, Y. Y. Li, F. Mehmood, R. Pachter, A. I. Frenkel, Y. Gogotsi, M. L. Taheri, Multimodal spectroscopic study of surface termination evolution in $Cr_2TiC_2T_x$ MXene. *Adv. Mater. Interfaces* **2021**, *8*, 2001789.

21. W. Jindata, K. Hantansirisakul, T. Eknapakul, J. D. Denlinger, S. Sangphet, S. Chaiyachad, C. Jaisuk, A. Rasritat, T. Sawasdee, H. Nakajima, A. Rattanachata, I. Fongkaew, S. Limpijumnong, Y. Gogotsi, W. Meevasana. Spectroscopic signature of negative electronic compressibility from the Ti core-level of titanium carbonitride MXene. *Appl. Phys. Rev*. **2021**, *8*, 021401.

Materials and Interfacial Chemistry for Sustainable Sodium-based Batteries

John B. Goodenough and Arumugam Manthiram
Texas Materials Institute, University of Texas at Austin, Austin, TX 78712

Program Scope

The objective of this project is to develop a firm, in-depth understanding of the materials and interfacial chemistry for sustainable sodium-based batteries. Sodium-based batteries have great potential as next generation batteries due to their use of abundant, low-cost materials. However, sodium-based batteries are still in their infancy with numerous challenges to tackle, and a basic science investigation of the materials and interfacial chemistry is critical to make them viable. This project focuses on the investigation of structural, chemical, surface, and interfacial aspects of the cell components, including cathodes, anodes, electrolytes, and the interfaces associated with them. With this goal, our focus for the last two years has been on a range of new sodium-based electrode and electrolyte materials: cobalt-free layered oxide cathodes, rationally designed solid electrolytes, special electrolytes for sodium-sulfur batteries, and organosulfur cathodes.

Recent Progress

1. Sodium Cells with Layered Oxide Cathodes

Layered oxide cathodes are at the forefront for sodium-ion batteries due to their similarities with lithium-based layered oxides.[1] However, most sodium-based layered oxides suffer from poor cycle life compared to their lithium counterparts. We have carried out a rigorous investigation of the effects of extended high-voltage cycling on a promising O3 type $Na(Ni_{0.3}Fe_{0.4}Mn_{0.3})O_2$ (NFM343) material. By analyzing the extended cycling performance in conjunction with advanced characterization methodologies, an irreversible high-voltage (OP2) phase transition above 4.0 V (**Figure 1**) was found to cause Fe^{3+} migration to the sodium plane and rapid capacity fade during the initial stages of cycling. After the disappearance of the OP2 phase or in cells cycled below 4 V (*i.e.*, without the OP2 phase formation), electrolyte decomposition and surface reactivity were recognized as the main sources of capacity fade.[2]

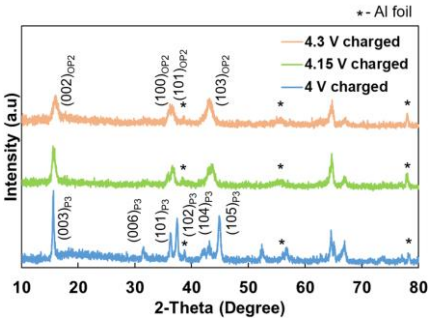

Figure 1. (a) *Ex-situ* XRD of fully charged NFM343 at C/5 rate, followed by a constant voltage step for 8 h.

In addition to aggressive surface reactivity with the electrolyte, most sodium layered oxides also suffer from poor surface stability in ambient air. To mitigate the surface instability, we have pursued a facile sodium phosphate coating on the surface of NFM343. By comparing different coating methods and phosphate contents, we found that a 1 wt.% phosphate coating forms a

uniform, thin layer on NFM343 surface. In contrast to the lithium layered oxides, in which the phosphate groups react with the residual LiOH and Li_2CO_3 on the cathode surface to form a lithium phosphate coating, sodium ions are pulled from the bulk of the sodium layered oxide NFM343 to form sodium phosphate. Despite the differences in the mechanism, the protective coating layer significantly improved the cycle life **(Figure 2)** of the Na/NFM343 cells and the stability of NFM343 in humid air.

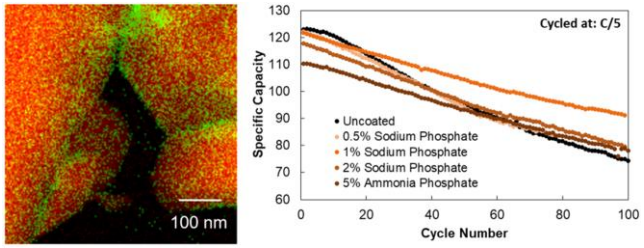

Figure 2. (a) TEM-EDS image of phosphate coating (green for phosphorous) on NFM (orange for nickel). (b) Cycling performances of Na/NFM343 cells with 0%, 0.5%, 1%, 2%, and 5% phosphate coating on NFM343 cathodes.

Unlike lithium layered oxides, sodium layered oxides adopt several possible structures, and many of them suffer from Na^+-ion ordering and transition-metal layer gliding, which lead to multiple plateaus in their voltage profiles and poor cycling stability. We have developed an O′3-layered $Na_3Ni_{1.5}TeO_6$ ($Na_{5/6}[Na_{1/6}Ni_{3/6}Te_{2/6}]O_2$) (**Figure 3a**), which displays an unusual phenomenon. The vacancies in the sodium layer assist in a quick gliding of the transition-metal slabs when the material is charged, shifting the O′3-layer to a P′3-layer stacking and resulting in a single plateau associated with the $Ni^{2+}/^{3+}$ redox couple (**Figure 3a**). This cathode shows good capacity retention (**Figure 3b**) and rate capability as high as 2C. The structural nuances of this material can serve as a guide for designing high-capacity, durable sodium layered oxides.[3]

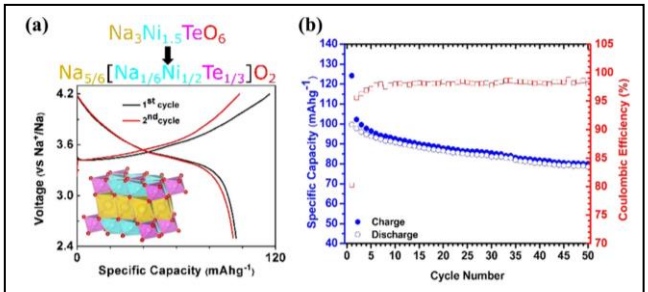

Figure 3. (a) Charge-discharge profiles at a C/20 rate of O′3-layered $Na_3Ni_{1.5}TeO_6$; yellow: NaO_6 octahedra; cyan: $[Na_{1/4}Ni_{3/4}]O_6$ octahedra; light purple: TeO_6 octahedra. (b) Cyclability and coulombic efficiency of $Na_3Ni_{1.5}TeO_6$.

To further improve the cycling stability of layered $Na_3Ni_{1.5}TeO_6$, while also enabling a sodium-metal anode and improving the safety, we have developed a quasi-solid-state electrolyte composed of an ionic liquid (IL) integrated with a metal organic framework (MOF). The MOF matrix was designed rationally based on a UIO (Universitetet i Oslo) architecture (UIO-66), but with a sodium sulfonic ($-SO_3Na$) group grafted within the structure (**Figure 4a**). A high Na^+-ion conductivity of 3.6×10^{-4} S cm^{-1} was facilitated in IL-MOF

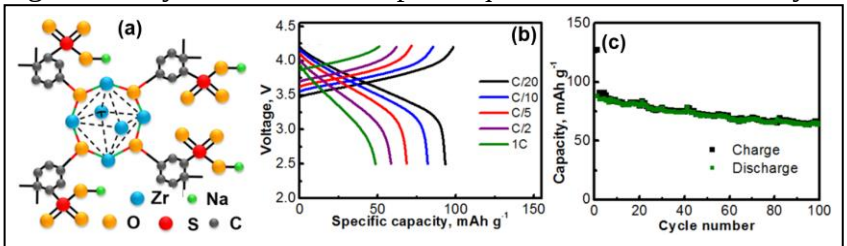

Figure 4. (a) Structural schematic of the UIOSNa (UIO-66 with $-SO_3Na$ functional groups grafted). (b) Charge-discharge profiles at various rates and (c) cyclability at C/10 rate of the Na ‖ IL-UIOSNa ‖ $Na_3Ni_{1.5}TeO_6$ cells.

due to both the laden Na-IL (sodium bis(trifluoromethylsulfonyl)imide (NaTFSI) in 1-n-butyl-1-methylpyrrolidinium bis(trifluoromethylsulfonyl) imide (Bmpyr-TFSI)) and the grafted -SO_3Na functional group. The IL laden MOF not only suppressed sodium dendrites, but also formed a favorable interface between the electrodes and electrolyte with fast ion transport. The solid-state cell assembled with the IL-MOF electrolyte showed good cyclability, as seen in **Figure 4b** and **c**.[4]

2. Sodium Cells with Sulfur Cathodes:

The concerns associated with mining and cost of transition metals have created much interest in sulfur as it is abundant and offers an order of magnitude higher capacity than the oxide cathodes. Pairing sulfur with a sodium anode is one of the best sustainable technologies we can think of. However, room-temperature Na-S batteries are faced with two critical challenges: polysulfide shuttle and Na dendrite formation. Li-S and Na-S systems share these same challenges, so the Li-S chemistry serves as a useful model system for understanding the chemistry of alkali-metal polysulfides. We studied the effects of tellurium (Te) substitution in polysulfides and its influence on Li-metal anode cycling efficiency. To explore this, an anode-free coin cell configuration with Li_2S cathode and an Ni-foil current collector without any free Li metal was employed. As the lithium inventory is limited in this cell configuration, it reliably reveals the effect of polysulfide chemistry on Li-metal cycling.[5] With Te, the lithium polysulfides (Li_2S_y) generated during cell operation react to form $Li_2Te_xS_y$, which migrates to the anode and forms lithium thiotellurate (Li_2TeS_3) as a robust SEI, preventing further reduction of lithium polysulfides or the electrolyte. This dramatically improves the cycling efficiency of Li-metal anode, resulting in a 7-fold improvement in the cycle life of anode-free cells. Such a strategy is useful to mitigate the Na-metal cycling inefficiencies in Na-S batteries.[6]

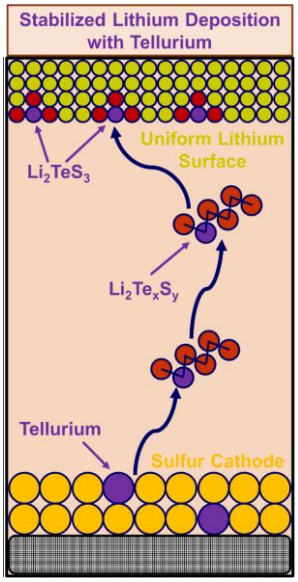

Figure 5. Mechanism of Li-anode stabilization.

We have also investigated a new type of electrolyte for the simultaneous inhibition of sodium dendrite formation and polysulfide migration. A concentrated solution of 1,2-dimethoxyethane (DME) and sodium bis(fluorosulfonyl)imide (NaFSI) forms a unique solvation structure. The solvated species is then diluted with an "inert" solvent. The "inert" diluent has little effect on the solvation structure of cation−anion aggregates that exist in the concentrated electrolyte, leading to a localized high concentration electrolyte (LHCE). Compared to a high-concentration electrolyte, LHCE can significantly lower the sodium salt concentration, reduce the viscosity, increase the conductivity,

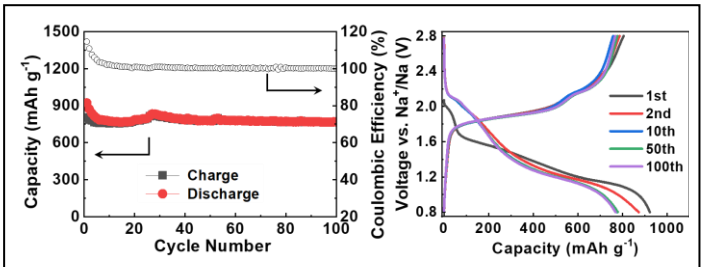

Figure 6. (a) Cyclability and (b) charge/discharge curves at C/10 rate of a Na-S cell with LHCE electrolyte.

and improve the wettability of the electrolyte. The donor ability of the DME molecule diminishes upon complexing with Na^+ and consequently the ability of LHCE to dissolve sodium polysulfides (Na_2S_m, $m \geq 4$) decreases with a decrease in the molar ratio of DME. Also, the $[FSI]^-$ anion is a weak Lewis-base. As a result, Na_2S_m is poorly solvated in the solvate ionic liquid (LHCE). More importantly, the sulfur reaction pathway transitions from a dissolution–precipitation process to a quasi-solid-state conversion process, prohibiting polysulfide shuttle. The resulting Na-S cells with the LHCE electrolyte show stable cycling over 100 cycles (**Figure 6**).

Future Plans

We plan to continue focusing on the stabilization of interfaces and cycle life of Na-ion cells with oxide cathodes. As sodium layered oxides suffer from poor surface stability in ambient air and during cycling, one approach is to reduce the surface area through morphological manipulation. Large, single-crystal particles have shown promise with lithium layered oxides by reducing the total surface area and improving the cyclability. Single-crystal morphology has yet to be explored for sodium layered oxides, so we intend to employ single-crystal synthesis techniques to improve the overall material stability and gain a deeper understanding of the crystallite formation process of sodium layered oxides. We are already in the process of successfully synthesizing single-crystal $Na(Ni_{0.3}Fe_{0.4}Mn_{0.3})O_2$ with a molten-salt synthesis method, as shown in **Figure 7**.

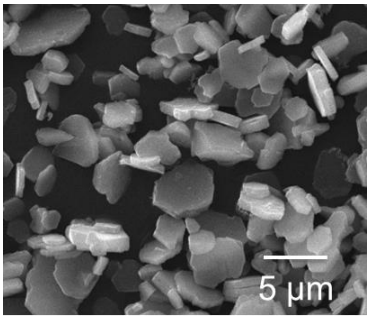

Figure 7. SEM image of a single-crystal sodium layered oxide material.

Owing to the similarities of Li and Na alkali-metal polysulfide chemistry, we hope to elucidate the effect of Te substitution in sodium polysulfides. LHCE-based electrolytes offer a stable cycling of the sulfur cathode when paired with a Na-metal anode. Therefore, the LHCE and the Te additive could be coupled to understand the dynamics of Na-metal cycling with Te-substituted polytellurosulfides. On another front, the presented LHCE electrolyte is the first iteration of such an electrolyte. The effects of varying the salt and diluent will also be studied. Additives that can further stabilize Na-anode cycling will be explored and mechanistically studied.

References

1. Darga, J.; Lamb, J.; Manthiram, A. *Energy Technol.* **2020**, *8*, 2000723.
2. Lamb, J.; Stokes, L.; Manthiram, A. *Chem. Mater.* **2020**, *32*, 7389–7396.
3. Grundish, N.; Seymour, I.; Li, Y.; Sand, J.B.; Henkelman, G.; Delmas, C.; Goodenough, J. *Chem. Mater.* **2020** 32, 10035-10044.
4. Yu, X.; Grundish, N.; Goodenough, J.; Manthiram, A. ACS *Appl. Mater. Interfaces* **2021,** 13, 24662-24669.
5. Nanda, S.; Manthiram, A. *Adv. Energy Mater.* **2021**, 11, 2003293.
6. Nanda, S.; Bhargav, A.; Manthiram, A. *Joule* **2020**, 4, 1121-1135.

Publications

1. H. Wang, Y. Jiang, and A. Manthiram, "Long Cycle Life, Low Self-discharge Sodium-selenium Batteries with High Selenium Loading and Suppressed Polyselenide Shuttling," *Advanced Energy Materials* **8**, 1701953 (1-8) (2018).
2. X. Yu, M. Broyer, G. Hwang, and A. Manthiram, "Room-temperature Aluminum-sulfur Batteries with a Lithium-ion-mediated Ionic Liquid Electrolyte," *Chem* **4**, 586-598 (2018).
3. X. Yu, S. Feng, M. Boyer, M. Lee, R. Ferrier, N. Lynd, G. Hwang, G. Wang, S. Swinnea, and A. Manthiram, "Controlling the Polysulfide Diffusion in Lithium-Sulfur Batteries with a Polymer Membrane with Intrinsic Nanoporosity," *Materials Today Energy* **7**, 98-104 (2018).
4. X. Yu and A. Manthiram, "Electrode-Electrolyte Interfaces in Lithium-based Batteries," *Energy and Environmental Science* **11**, 527-543 (2018).
5. M. Gross and A. Manthiram, "A Rechargeable Zinc-Aqueous Polysulfide Battery with a Mediator-ion Solid Electrolyte," *ACS Applied Materials and Interfaces* **10**, 10612-10617 (2018).
6. X. Yu and A. Manthiram, "Electrochemical Energy Storage with an Aqueous Zinc-Quinone Chemistry Enabled by a Mediator-ion Solid Electrolyte," *ACS Applied Energy Materials* **1**, 273-277 (2018).
7. X. Yu and A. Manthiram, "Electrochemical Energy Storage with an Aqueous Quinone-Air Chemistry," *ACS Applied Energy Materials* **1**, 2424-2428 (2018).
8. L.G. Xue, H.C. Gao, Y.T. Li, and J. B. Goodenough, "Cathode Dependence of Liquid-Alloy Na-K Anodes," *Journal of the American Chemical Society* **140**, 3292-3298 (2018).
9. H. C. Gao, L. G. Xue, S. Xin, and J. B. Goodenough, "A High-Energy-Density Potassium Battery with a Polymer-Gel Electrolyte and a Polyaniline Cathode," *Angewandte Chemie International Edition* **57**, 5449-5453 (2018).
10. H. C. Gao, S. Xin, L. G. Xue, and J. B. Goodenough, "Stabilizing a High-Energy-Density Rechargeable Sodium Battery with a Solid Electrolyte," *Chem* **4**, 833-834 (2018).
11. H. Xu, S. Wang, and A. Manthiram, "Hybrid Lithium–sulfur Batteries with an Advanced Gel Cathode and Stabilized Lithium-metal Anode," *Advanced Energy Materials* **8**, 1800813 (2018).
12. J. He, Y. Chen, and A. Manthiram, "MOF-derived Cobalt Sulfide Grown on 3D Graphene Foam as an Efficient Sulfur Host for Long-life Lithium-Sulfur Batteries," *iScience* **29**, 36-43 (2018).
13. Y. You, S. Xin, W. Li, P.-F. Wang, Y.-G. Guo, and A. Manthiram, "Insights into the Improved High-voltage Performance of Li-incorporated Layered Oxide Cathodes for Sodium-ion Batteries," *Chem* **4**, 2124-2139 (2018).
14. G. Gnana kumar, S.-H. Chung, T. Raj kumar, and A. Manthiram, "A 3D Graphene-CNT-Ni Hierarchical Architecture as a Polysulfide trap for Lithium-Sulfur Batteries," *ACS Applied Materials & Interfaces* **10**, 20627-20634 (2018).
15. X. Yu and A. Manthiram, "A Strategically Managed Rechargeable Battery System with a Neutral Methyl Viologen Anolyte and an Acidic Air-Cathode Enabled by a Mediator-ion Solid Electrolyte," *Sustainable Energy & Fuel* **2**¸1452-1457 (2018).
16. N. Grundish, C.D. Amos, and J.B. Goodenough, "Characterization of $LiAlCl_4 \cdot xSO_2$ Inorganic Liquid Li^+ Electrolyte" *Journal of the Electrochemical Society* **9**, A1694-A1696 (2018).

17. J. He, Y. Chen, and A. Manthiram, "Vertical Co_9S_8 Hollow Nanowall Arrays Grown on Celgard Separator as a Multifunctional Polysulfide Barrier for High-performance Li-S Batteries," *Energy and Environmental Science* **11**, 2560-2568 (2018).
18. R. Pipes, A. Bhargav, and A. Manthiram, "Nanostructured Anatase Titania as a Cathode Catalyst for Li-CO_2 Batteries," *ACS Applied Materials and Interfaces* **10**, 37119-37124 (2018).
19. H. Gao, L. D. Seymour, S. Xin, L. Xue, G. Henkelman, and J. B. Goodenough, "$Na_3MnZr(PO_4)_3$: A High-Voltage Cathode for Sodium Batteries," *Journal of the American Chemical Society*, **140**, 51, 18192-18199 (2018).
20. X. Yu and A. Manthiram, "A Reversible Nonaqueous Room-temperature Potassium-sulfur Chemistry for Electrochemical Energy Storage," *Energy Storage Materials*, **15**, 368-373 (2018).
21. R. Yu, S.-H. Chung, C.-H. Chen, and A. Manthiram, "A Core-shell Cathode Substrate for Developing High-loading, High-performance Lithium-sulfur Batteries," *Journal of Materials Chemistry A* **6**, 24841-24847 (2018).
22. M. Gross and A. Manthiram, "An Aqueous Polysulfide-Air Battery with a Mediator-ion Solid Electrolyte and a Copper Sulfide Catalyst for Polysulfide Redox," *ACS Applied Energy Materials* **1**, 7230–7236 (2018).
23. M. Gross and A. Manthiram, "Development of Low-cost Sodium-Aqueous Polysulfide Hybrid Batteries" *Energy Storage Materials* **19**, 346-351 (2019).
24. R. M. Pipes, A. Bhargav, and A. Manthiram, "Phenyl Disulfide Additive for Solution-mediated Carbon Dioxide Utilization in Li-CO_2 Batteries," *Advanced Energy Materials* **9**, 1900453 (2019).
25. J. He, Y. Chen, and A. Manthiram, "Metal Sulfide-decorated Carbon Sponge as a Highly Efficient Electrocatalyst and Absorbant for Polysulfide in High-loading Li_2S Batteries," *Advanced Energy Materials* **9**, 1900584 (2019).
26. M. Gross and A. Manthiram "Long–Life Polysulfide–Polyhalide Batteries with a Mediator-ion Solid Electrolyte," *ACS Applied Energy Materials* **2**, 3445-3451 (2019).
27. S.-H. Chung and A. Manthiram, "Current Status and Future Prospects of Metal-Sulfur Batteries," *Advanced Materials* **31**, 1901125 (2019).
28. Y. You, B. Song, K. A. Jarvis, A. Huq, and A. Manthiram, "Insights into the Improved Chemical Stability against Water of LiF-incorporated Layered Oxide Cathodes for Sodium-ion Batteries," *ACS Materials Letters* **1**, 89-95 (2019).
29. J. He, A. Bhargav, and A. Manthiram, "Three-Dimensional Fe_3O_4/N-Graphene Sponge as an Efficient Organosulfide Host for High-Performance Lithium-Organosulfur Batteries," *Energy Storage Materials* **23**, 88-94 (2019).
30. X. Yu, L. Xue, J. B. Goodenough, and A. Manthiram, "A High-Performance All-solid-state Sodium-ion Battery with a Poly(ethylene oxide) – $Na_3Zr_2Si_2PO_{12}$ Composite Electrolyte," *ACS Materials Letters* **1**, 132-138 (2019).
31. S.-H. Chung and A. Manthiram, "A Li_2S-TiS_2-Electrolyte Composite for Stable Li_2S-based Lithium-Sulfur Batteries," *Advanced Energy Materials* **9**, 1901397: 1 - 9 (2019).
32. B. Heligman, K. J. Kreder III, and A. Manthiram, "Zn-Sn Interdigitated Eutectic Alloy Anodes with High-Volumetric Capacity for Lithium-ion Batteries," *Joule* **3**, 1051-1063 (2019).
33. X. Yu and A. Manthiram, "Sodium-sulfur (Na-S) Batteries with a Polymer-coated NASICON-type Sodium-ion Solid Electrolyte," *Matter* **1**, 439-451 (2019).

34. J. He and A. Manthiram, "A Review on the Status and Challenges of Electrocatalysts in Lithium-Sulfur Batteries," *Energy Storage Materials* **20**, 55-70 (2019).
35. X. Yu, H. Wu, J. H. Koo, and A. Manthiram, "Tailoring the Pore Size of a Polypropylene Separator with a Polymer having Intrinsic Nanoporosity for Suppressing the Polysulfide Shuttle in Lithium-Sulfur Batteries," *Advanced Energy Materials* **10**, 1902872 (2019).
36. R. Pipes, J. He, A. Bhargav and A. Manthiram, "Efficient Li-CO_2 Batteries with Molybdenum Disulfide Nanosheets on Carbon Nanotubes as a Catalyst," *ACS Applied Energy Materials* **2**, 8685-8694 (2019).
37. J. He and A. Manthiram, "Long-life, High-rate Lithium-sulfur Cells with a Carbon-free VN Host as an Efficient Polysulfide Adsorbent and Lithium Dendrite Inhibitor," *Advanced Energy Materials* **10**, 1903241 (2020).
38. R. Yu, S.-H. Chung, C.-H. Chen, and A. Manthiram, "An Ant-nest-like Cathode Substrate for Lithium-sulfur Batteries with Practical Cell Fabrication Parameters," *Energy Storage Materials* **18**, 491-499 (2019).
39. N. S. Grundish, I. D. Seymour, G. Henkelman, and J. B. Goodenough, "Electrochemical Properties of Three $Li_2Ni_2TeO_6$ Structural Polymorphs," *Chemistry of Materials* **31**, 9379-9388 (2019).
40. S.-H. Ahn and A. Manthiram, "Hierarchical Tri-functional Electrocatalysts Derived from Bimetallic-imidazolate Framework for Overall Water Splitting and Rechargeable Zinc-air Batteries," *Journal of Materials Chemistry A* **7**, 8641-8652 (2019).
41. X. Yu, M. Boyer, G. S. Hwang, and A. Manthiram, "Toward a Reversible Calcium-Sulfur Battery with a Lithium-ion Mediation Approach," *Advanced Energy Materials* **9**, 1803794 (2019).
42. Bhargav, J. He, A. Gupta, and A. Manthiram, "Lithium-Sulfur Batteries: Attaining the Critical Metrics," *Joule* **4,** 285-291 (2020).
43. X. Yu, J. Li, and A. Manthiram, "Rational Design of a Laminated Copolymer/Polymer-ceramic Composite Electrolyte for High-voltage All-solid-state Lithium Batteries," *ACS Materials Letters* **2**, 317-324 (2020).
44. L. Luo, J. Li, H. Yaghoobnejad Asl, and A. Manthiram, "*In-situ* Assembled VS_4 as a Polysulfide Mediator for High-loading Lithium-sulfur Batteries," *ACS Energy Letters* **5**, 1177-1185 (2020).
45. X. Yu and A. Manthiram, "A Long-cycle-life All-solid-state Lithium Battery with a Ceramic-polymer Composite Electrolyte," *ACS Applied Energy Materials* **3**, 2916-2924 (2020).
46. A. Manthiram, "A Reflection on Lithium-ion Battery Cathode Chemistry," *Nature Communications **11***, 1550 (2020).
47. S. Nanda, A. Bhargav, and A. Manthiram, "Anode-free, Lean-electrolyte Lithium-sulfur Batteries Enabled by Tellurium-stabilized Lithium Deposition," *Joule* **4,** 1-15 (2020).
48. J. He, Y. Chen, H. Yaghoobnejad Asl, and A. Manthiram, "1T'-ReS_2 Nanosheets *in-situ* Grown on Carbon Nanotubes as a Highly Efficient Polysulfide Electrocatalyst for Li-S Batteries," *Advanced Energy Materials* **10**, 2001017: 1-9 (2020).
49. L. Luo and A. Manthiram, "An Artificial Protective Coating towards Dendrite-free Lithium-metal Anodes for Lithium-sulfur Batteries," *Energy Technology* **8**, 2000348: 1-6 (2020).
50. P. Chiochan, X. Yu, M. Sawangphruk, and A. Manthiram, "A Metal Organic Framework (MOF)-derived Solid Electrolyte for Lithium-Sulfur Batteries," *Advanced Energy Materials* **10**, 2001285: 1-11 (2020).

51. R. Pipes, J. He, A. Bhargav, and A. Manthiram, "Freestanding Vanadium Nitride Nanowire Membrane as an Efficient, Carbon-Free Gas Diffusion Cathode for Li-CO_2 Batteries," *Energy Storage Materials* **31**, 95-104 (2020).
52. H. Shin, M. Baek, A. Gupta, K. Char, A. Manthiram, J. W. Choi, "Recent Progress in High Donor Electrolytes for Lithium-Sulfur Batteries," *Advanced Energy Materials* **10**, 2001456: 1-21 (2020).
53. A. Bhargav and A. Manthiram, "Xanthogen Polysulfides as a New Class of Electrode Material for Rechargeable Batteries," *Advanced Energy Materials* **10**, 2001658: 1-10 (2020).
54. Y. Ding, X. Guo, Y. Qian, H. Gao, D. Weber, L. Zhang, J. Goodenough, and G. Yu, "In situ formation of Liquid Metals via Galvanic Replacement Reaction to Build Dendrite-free Alkali ion Batteries," *Angewandte Chemie* **59**, 12170-12177 (2020).
55. S. Agarwal, X. Yu, and A. Manthiram, "A Pair of Metal Organic Framework (MOF)-derived Oxygen Reduction Reaction (ORR) and Oxygen Evolution Reaction (OER) Catalysts for Zinc-air Batteries," *Materials Today Energy* **16**, 100405 (2020).
56. X. Yu, L. Xue, J. B. Goodenough, and A. Manthiram, "Ambient-temperature All-solid-state Sodium Batteries with a Laminated Composite Electrolyte," *Advanced Functional Materials* **11**, 200244: 1-10 (2020).
57. J. Lamb, L. Stokes, and A. Manthiram, "Delineating the Capacity Fading Mechanisms of $Na(Ni_{0.3}Fe_{0.4}Mn_{0.3})O_2$ at Higher Operating Voltages in Sodium-ion Cells," *Chemistry of Materials* **32**, 7389–7396 (2020).
58. X. Yu and A. Manthiram, "A Progress Report on Metal− Sulfur Batteries," *Advanced Functional Materials* **30**, 2004084: 1-27 (2020).
59. J. He, A. Bhargav, and A. Manthiram, "Molybdenum Boride as an Efficient Catalyst for Polysulfide Redox to Enable High-Energy-Density Lithium-Sulfur Batteries," *Advanced Materials* **32**, 2004741: 1-7 (2020).
60. X. Yu and A. Manthiram, "Recent Advances in Lithium – Carbon Dioxide Batteries," *Small Structures* **1**, 2000027: 1-23 (2020).
61. J. Lamb and A. Manthiram, "Synthesis Control of Layered Oxide Cathodes for Sodium-ion Batteries: A Necessary Step Towards Practicality*," Chemistry of Materials* **32**, 8431-8441 (2020).
62. X. Yu, and A. Manthiram, "A Review of Composite Polymer-ceramic Electrolytes for Lithium Batteries," *Energy Storage Materials* **34**, 282-300 (2020).
63. J. He and A. Manthiram, "3D CoSe@C Aerogel as a Host for Dendrite-free Lithium-metal Anode and Efficient Sulfur Cathode in Li–S Full Cells," *Advanced Energy Materials* **10**, 2002654:1-9 (2020).
64. J. Darga, J. Lamb, and A. Manthiram, "Industrialization of Layered Oxide Cathodes for Lithium-ion and Sodium-ion Batteries: A Comparative Perspective," *Energy Technology* **8,** 2000723: 1-13 (2020).
65. F. Zou and A. Manthiram, "A Review of the Design of Advanced Binders for High-performance Batteries," *Advanced Energy Materials* **10**, 2002508: 1-28 (2020).
66. X. Yu, L. Xue, J. B. Goodenough, and A. Manthiram, "All-solid-state Sodium Batteries with a Polyethylene Glycol Diacrylate (PEGDA) - $Na_3Zr_2Si_2PO_{12}$ Composite Electrolyte," *Advanced Energy & Sustainability Research,* **2**, 2000061: 1-9 (2020).
67. H. Yaghoobnejad Asl and A. Manthiram, "Proton-induced Disproportionation of Jahn-Teller-active Transition-metal Ions in Oxides due to Electronically-driven Lattice Instability," *Journal of the American Chemical Society* **142**, 21122-21130 (2020).

68. N. S. Grundish, I. D. Seymour, Y. Li, J.-B. Sand, G. Henkelman, C. Delmas, and J. B. Goodenough, "Structural and Electrochemical Consequences of Sodium in the Transition-Metal Layer of O′3-$Na_3Ni_{1.5}TeO_6$", *Chemistry of Materials* **32**, 10035−10044 (2020).
69. Q. Zhou, B. Xu, P.-H. Chien, Y. Li, B. Huang, N. Wu, H. Xu, N. S. Grundish, Y.-Y. Hu, and J. B. Goodenough, "NASICON $Li_{1.2}Mg_{0.1}Zr_{1.9}(PO_4)_3$ Solid Electrolyte for an All-Solid-State Li-Metal Battery", *Small Methods* **4**, 2000764 (2020).
70. X. Yu, W. A. Yu, and A. Manthiram, "Advances and Prospects of High-voltage Spinel Cathodes for Lithium-based Batteries," *Small Methods* **5**, 2001196 (2021).
71. S. Nanda and A. Manthiram, "Delineating the Lithium-electrolyte Interfacial Chemistry and the Dynamics of Lithium Deposition in Lithium-sulfur Batteries," *Advanced Energy Materials* **11**, 2003293: 1-13 (2021).
72. X. Yu and A. Manthiram, "Sustainable Battery Materials for Next Generation Electrical Energy Storage," *Advanced Energy & Sustainability Research* **2**, 2000102 (2021).
73. Y. Tang, Y. Huang, L. Luo, D. Fan, Y. Lu, and A. Manthiram, "Self-supported MoO_2/MoS_2 Nano-sheets Embedded in a Carbon Cloth as a Binder-free Substrate for High-energy Lithium-sulfur Batteries," *Electrochimica Acta* **367**, 137482-137490 (2021).
74. J. He, A. Bhargav, and A. Manthiram, "High-Energy-Density, Long-Life Lithium-Sulfur Batteries with Practically Necessary Parameters Enabled by Low-Cost Fe-Ni Nanoalloy Catalysts," *ACS Nano* **15**, 8583-8591 (2021).
75. X. Yu, N. S. Grundish, J. B. Goodenough, and A. Manthiram, "Ionic Liquid (IL) Laden Metal Organic Framework (IL-MOF) Electrolyte for Solid-state Sodium Batteries," *ACS Applied Materials & Interfaces* **13**, 24662−24669 (2021).

Articles Submitted

76. J. He and A. Manthiram, "In-situ Grown 1T'-$MoTe_2$ Nanosheets on Carbon Nanotubes as an Efficient Electrocatalyst and Lithium Regulator for Stable Lithium-sulfur Full Cells," *Advanced Materials* (submitted).
77. X. Yu, Y. Liu, J. B. Goodenough, and A. Manthiram, "A Rationally Designed PEGDA - LLZTO Composite Electrolyte for Solid-state Lithium Batteries," *ACS Applied Materials & Interfaces* (submitted).
78. R. Fang, B. Xu, N. S. Grundish, Y. Xia, Y. Li, Y. Liu, N. Wu, and J. B. Goodenough, "Impacts of Li_2S_6 additive on the electrochemical performance of a PEO-based composite electrolyte for all-solid-state lithium-metal batteries at 40 ^oC," *Angewandte Chemie* (submitted).
79. X. Yu and A. Manthiram, "A High-voltage Sodium – Methylphenothiazine (MPT) Nonaqueous Hybrid Flow Battery Enabled with a Sodium-ion Solid Electrolyte," *Materials Today Energy* (submitted).
80. J. Lamb and A. Manthiram, "Surface-modified $Na(Ni_{0.3}Fe_{0.4}Mn_{0.3})O_2$ cathodes with Enhanced Cycle Life and Air Stability for Sodium-ion Batteries," *ACS Applied Materials and Interfaces* (submitted).

Surface ligand effects on energetics, charge transfer, and stability at interfaces between metal halide perovskites and organic semiconductors

Kenneth R. Graham, University of Kentucky

Program Scope

Metal halide perovskites, HPs, are a promising class of inexpensive solution processable semiconductors for optoelectronic devices. The surface chemistry of HPs exerts a major influence over their optical and electronic properties, stability, and performance in an optoelectronic devices. The importance of HP surface chemistry is now widely recognized and surface passivation is regularly employed in creating high-efficiency photovoltaic (PV) devices with improved stability.[1] This research program is focused on the surface chemistry of HPs and the interfaces between HPs and organic semiconductors, which are critical interfaces found within most HP containing optoelectronic devices. The project is broken down into the following four objectives: 1) quantify ligand binding strength as a function of ligand binding group and perovskite composition, 2) determine how the ligand structure influences photoluminescence properties, energetics, and charge transfer processes, 3) identify how the surface ligand structure influences HP stability, and 4) develop combinations of extended π-conjugated and non-conjugated ligands to manipulate energetics, charge transfer, and stability at perovskite-organic interfaces. Much of the research takes advantage of the photoelectron spectroscopy capabilities developed in the Graham laboratory specifically for investigating more damage prone materials, which include x-ray, ultraviolet, and inverse photoelectron spectroscopy (XPS, UPS, and IPES, respectively). The program is currently in its fourth year, out of five, and the focus for the remaining 14 months will be on objectives 3 and 4, which focus on stability of HPs upon surface ligand treatment and the use of extended π-conjugated ligands.

Recent Progress

A large series of ligands have been applied to Pb-based and Sn-based HP thin films and Pb-based HP nanocrystals throughout the first four years of this research program. We have found that there is not a one-size fits all ligand passivation approach. For example, the reactivities of nanocrystals and thin films to different ligand binding groups can vary significantly and each class of ligands has their advantages and disadvantages. Furthermore, we have contributed to the understanding that treatment of HPs with surface ligands is often more complicated than for other classes of materials, as many surface ligands can penetrate the HP and create new material phases where the 3D structure is split into 2D or pseudo-2D phases.

The series of ligands depicted in Figure 1a, where both the ligand binding group and ligand tail are varied, were applied to methylammonium lead iodide ($MAPbI_3$) thin films. Here, using angle dependent XPS measurements combined with modeling we quantified the extent of ligand surface coverage and qualitatively probed whether the ligands are confined to the film

surface or penetrate into the $MAPbI_3$ film. The XPS data shows that phosphonic acid, carboxylic acid, and ammonium containing ligands all reproducibly bind to the $MAPbI_3$ surface with a surface coverage that is readily detectable with XPS. Thiols serve to passivate defect states, as evidenced by increased photoluminescence intensity, but no thiol binding is detectable with XPS. Through comparing photoelectron intensities to models of surface ligand adsorption we calculate near complete surface coverage for OPA and high surface coverage for the carboxylic acid containing derivatives. These XPS measurements also show that PPA and the ammonium containing ligands in Figure 1a penetrate into the $MAPbI_3$ films to varying extents and result in the formation of pseudo-2D phases.

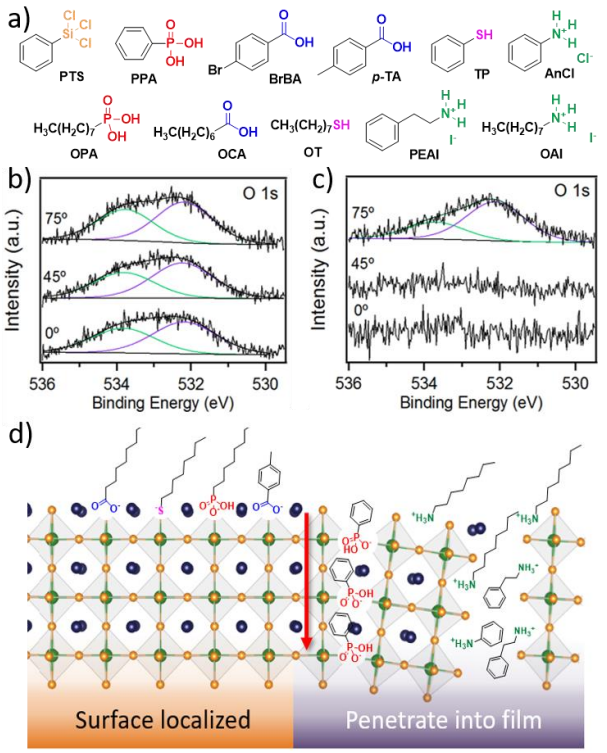

Figure 1. Surface ligands applied to $MAPbI_3$ (a), angle dependent XPS spectra for PPA (b) and OPA (c) on $MAPbI_3$, and a schematic showing ligand surface localization vs. penetration (d).

$MAPbI_3$ is one of the less stable HPs and displays a relatively low activation energy for ion diffusion.[2] An investigation of more stable HP compositions, including $Cs_{0.15}FA_{0.85}PbI_3$, $Cs_{0.15}FA_{0.85}PbBr_3$, and K doped $Cs_{0.15}FA_{0.85}PbI_3$ (FA: formamidinium), and five selected ligands OAI, AnI, PEAI, OPA, and PPA show that there is minimal difference in ligand penetration and ligand binding with perovskite composition across this series. Similarly, these results are consistent with $MAPbI_3$, indicating that the family of organic lead halide perovskites all show similar reactivities with ammonium and phosphonic acid functionalized surface ligands.

Ligand penetration can have a large influence on interfacial energetics, charge transfer, and the performance of optoelectronic devices; thus, it is important to understand the variables that influence ligand penetration. The impact of the ligand tail group structure with ammonium binding groups was investigated as a function of extent of fluorination, maximum cross-sectional area of the ligand, and ligand tail length. We find that the best means to reduce or eliminate ammonium ligand penetration is to increase the maximum cross-sectional area beyond what can be accommodated into a 2D perovskite structure, such as with 3,5 di-tert-butylanilinium iodide. Furthermore, ligands with larger cross-sectional areas, including those that do penetrate $MAPbI_3$ and result in formation of pseudo-2D phases, are found to result in the largest stability improvements to $MAPbI_3$.

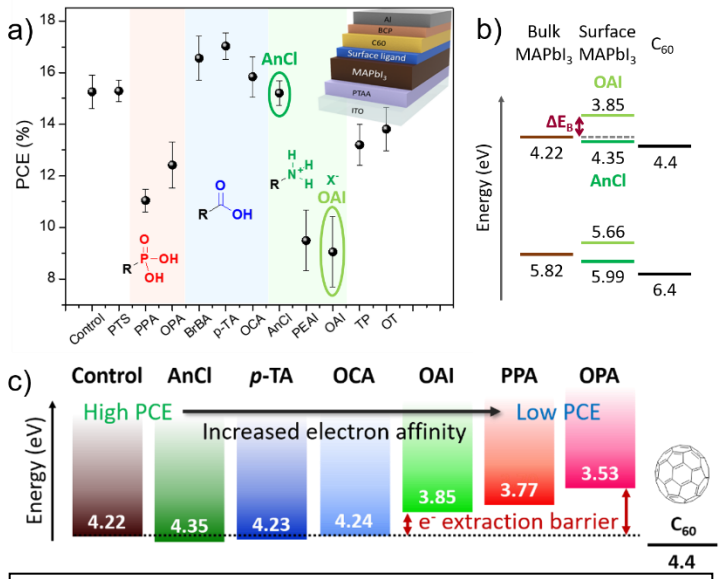

Figure 2. Power conversion efficiency (PCE) of *p-i-n* PV cells as a function of the surface ligand applied (a), energetic schematic at the electron-extracting interface (b), and a comparison of the electron affinity of the various ligand treated $MAPbI_3$ films showing the correlation with PCE (c).

Surface ligand treatment has a large impact on the PV performance, as shown in Figure 2a. Here, phosphonic acids result in decreased PV performance, carboxylic acids increase the PV performance, and ammonium ligands show mixed results. Using UPS and IPES to characterize the energetics, we find that the primary influence of the surface ligand on PV performance is in how the ligand impacts the surface energetics. When the surface ligand introduces a barrier to charge extraction (Figure 2b and c), as would be the case when the electron affinity decreases in the *p-i-n* architecture devices investigated here, the power conversion efficiency is sharply reduced. Improvements in PV performance occur when the surface ligand both passivates defect states and creates a favorable energy landscape for charge extraction.

The impact of surface energetics on charge transfer and PV performance translates over to 2D/3D device architectures, where a pseudo-2D phase is formed on a 3D HP, and extended π-conjugated surface ligands. Through a collaboration with the Sargent group (University of Toronto) we determined that the performance of 2D/3D perovskite PV devices is highly dependent on the dimensionality of the 2D phase, i.e., the thickness of the inorganic sheets, and the transport energetics of the 2D surface phase. Here, the 2D phase should not introduce a barrier to charge extraction. For extended π-conjugated surface

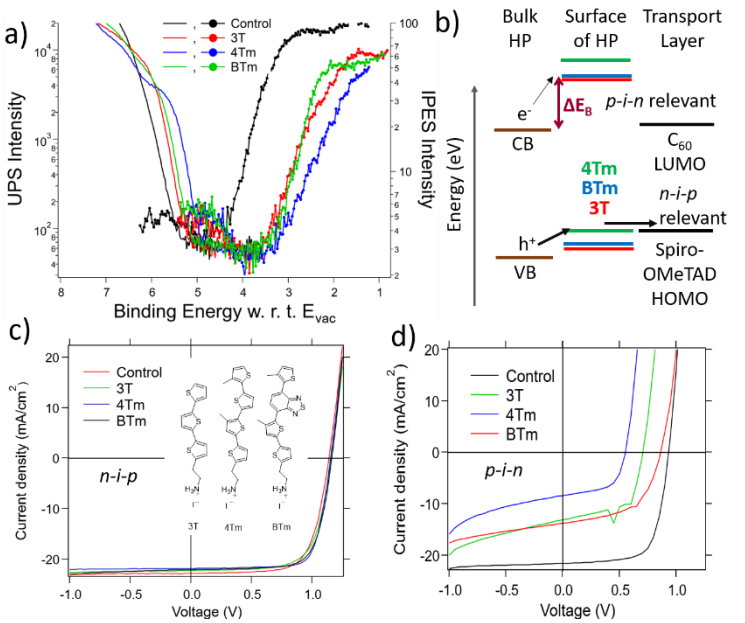

Figure 3. Combined UPS and IPES spectra of HP films treated with extended π-conjugated surface ligands (a), resulting interfacial energetics (b), and PV performance for *n-i-p* (c) and *p-i-n* (d) devices.

ligands we worked with the Dou group (Purdue University) to show that the transport energetics of the π-conjugated surface ligands play a critical role in charge extraction and PV performance. As Figure 3 shows, the π-conjugated surface ligands result in significant changes to surface energetics. This surface phase presents a barrier to charge extraction in the *p-i-n* device architecture, but not in the *n-i-p* architecture. As a result, PV devices with the *n-i-p* architecture show high performance whereas the *p-i-n* devices show poor performance.

In the area of Sn-based perovskites we have characterized the complete interfacial energy landscape at the formamidinium tin iodide ($FASnI_3$)/C_{60} interface both with and without surface ligands. One major finding of this work is that iodide diffusion from $FASnI_3$ into C_{60} occurs and results in *n*-type doping of C_{60}. Surface ligands can be used to reduce iodide diffusion and improve $FASnI_3$ stability, such as through the use of a fluorinated ammonium ligand.

Metal halide perovskite nanocrystals were a major part of the first three objectives of this work and resulted in three publications. Several ligands and ligand combinations were identified to stabilize HP nanocrystals and passivate defect states; however, application of these same ligands to thin films does not result in the same enhancements. The difference in ligand impact on nanocrystals and thin films is attributed to the significantly different surface chemistries of the as-synthesized materials, with the nanocrystals consisting of much more reactive Pb-halide rich surfaces with weakly coordinating ligands that are easily displaced.

Future Plans

The remaining work will focus primarily on extended π-conjugated ligands and stability, with an increased focus on the stability of Sn-based HPs. We will synthesize extended π-conjugated ligands with targeted energetic variations to determine how surface ligand energetics impact charge-transfer processes and stability. These extended π-conjugated ligands will be combined with smaller ligands of varying dipole moments to provide additional control over interfacial energetics, aid in defect state passivation, and increase stability. It is well known that Sn-based HPs are much less stable than their Pb-based counterparts and in the final year of this project we will determine the extent to which surface ligands can be used to enhance the stability of Sn-based HPs. This investigation will include how the surface ligand binding and tail groups can be used to impede iodide diffusion out of the HP and how the surface ligand structure influences degradation reactions upon exposure to water vapor and oxygen.

References

(1) Su, T. Sen; Eickemeyer, F. T.; Hope, M. A.; Jahanbakhshi, F.; Mladenović, M.; Li, J.; Zhou, Z.; Mishra, A.; Yum, J. H.; Ren, D.; *et al.* Crown Ether Modulation Enables over 23% Efficient Formamidinium-Based Perovskite Solar Cells. *J. Am. Chem. Soc.* **2020**, *142*, 19980–19991.

(2) Tan, S.; Yavuz, I.; De Marco, N.; Huang, T.; Lee, S. J.; Choi, C. S.; Wang, M.; Nuryyeva, S.; Wang, R.; Zhao, Y.; *et al.* Steric Impediment of Ion Migration Contributes to Improved Operational Stability of Perovskite Solar Cells. *Adv. Mater.* **2020**, *32*, 1906995.

Publications

1. Xia, P.; Davies, D. W.; Patel, B. B.; Qin, M.; Liang, Z.; Graham, K. R.; Diao, Y.; Tang, M. L. *Nanoscale.* **2020**, *12*, 11174-11181. "Spin-coated fluorinated PbS QD superlattice thin films with high hole mobility"

2. Uddin, M. A.; Glover, J. D.; Park, S. M.; Pham, J. T.; Graham, K. R. *Chem. Mater.* **2020**, *32*, 5217-5225. "Growth of Highly Stable and Luminescent $CsPbX_3$ (X = Cl, Br, and I) Nanoplates via Ligand Mediated Anion Exchange of $CsPbCl_3$ Nanocubes with AlX_3"

3. Park, S. M.; Abtahi, A.; Boehm, A. M.; Graham, K. R. *ACS Energy Lett*. **2020**, *5*, 799-806. "Surface Ligands for Methylammonium Lead Iodide Films: Surface Coverage, Energetics, and Photovoltaic Performance"

4. Boehm, A. B.; Liu, T.; Park, S. M.; Abtahi, A.; Graham, K. R. *ACS Appl. Mater. Interfaces* **2020,** 12, 5209-5218. "Influence of Surface Ligands on Energetics at FASnI3/C60 Interfaces and Their Impact on Photovoltaic Performance"

5. Yurash, B.; Cao, D. X.; Brus, V. V.; Leifert, D.; Wang, M.; Dixon, A.; Seifrid, M.; Mansour, A. E.; Lungwitz, D.; Liu, T.; Santiago, P. J.; Graham, K. R.; Koch, N.; Bazan, G. C.; Nguyen, T.-Q. *Nature Mater.* **2019**, *18*, 1327-1334. "Towards understanding the doping mechanism of organic semiconductors by Lewis acids"

6. Uddin, M. A.; Mobley, J. K.; Masud, A. A.; Liu, T.; Calabro, R. L.; Kim, D.-Y.; Richards, C. I.; Graham, K. R. *J. Phys. Chem. C* **2019**, *123*, 18103-18112. "Mechanistic Exploration of Dodecanethiol-Treated Colloidal CsPbBr3 Nanocrystals with Photoluminescence Quantum Yields Reaching Near 100%"

7. Huang, Z.; Xu, A.; Mahboub, M.; Liang, Z.; Jaimes, P.; Xia, P.; Graham, K. R.; Tang, M. L.; Lian, T. *J. Am. Chem. Soc.* **2019**, *141*, 9769-9772. "Enhanced Near-Infrared-to-Visible Upconversion by Synthetic Control of PbS Nanocrystal Triplet Photosensitizers"

8. Uddin, M. A.; Calabro, R. L.; Kim, D.-Y.; Graham, K. R. *Nanoscale*, **2018**, *10*, 16919-16927. "Halide Exchange and Surface Modification of Metal Halide Perovskite Nanocrystals with Alkyltrichlorosilanes"

9. Park, S. M.; Mazza, S. M.; Liang, Z.; Abtahi, A.; Boehm, A. M.; Parkin, S. R.; Anthony, J. E.; Graham, K. R. *ACS Appl. Mater. Interfaces*, **2018**, *10* (18), 15548-15557. "Processing Dependent Influence of the Hole Transport Layer Ionization Energy on Methylammonium Lead Iodide Perovskite Photovoltaics"

Shaping Symmetry and Molding Morphology of Triply-Periodic Network Assemblies via Molecular Design of Block Copolymers

Gregory M. Grason and E. Bryan Coughlin, Polymer Science and Engineering, University of Massachusetts, Amherst

Edwin L. Thomas, Materials Science and Engineering, Texas A & M University

Program Scope

This project integrates theory, synthesis and advance characterization approaches to uncover and advance "molecular design rules" for block copolymer (BCP) assemblies of triply-periodic network (TPN) phases. The double-gyroid (DG) network morphology has been a prime target of "bottom up" approaches to nanostructured, hybrid materials, and yet, the ability to manipulate the ultimate morphology of TPN assemblies beyond the narrow composition window provided by diblock DG networks has advanced relatively little since its discovery. This project seeks the fundamental knowledge needed for: i) tailorable molecular design that targets and achieves equilibrium assembly of TPN symmetries beyond canonical DG phases; and ii) unprecedented control over the intra-unit cell compositions of stable TPN (i.e. arbitrary ratios of channel/inter-channel domain volumes) as well as control of network node functionality. Organized under this overarching goal are the following collaborative efforts, including advancing theoretical principles of molecule-to-morphology design of TPN; novel characterization and metrology of sub-domain morphological features of TPN assemblies; and synthetic approaches to create precisely defined and labeled BCP architectures for direct imaging of key nanofeatures in novel morphologies.

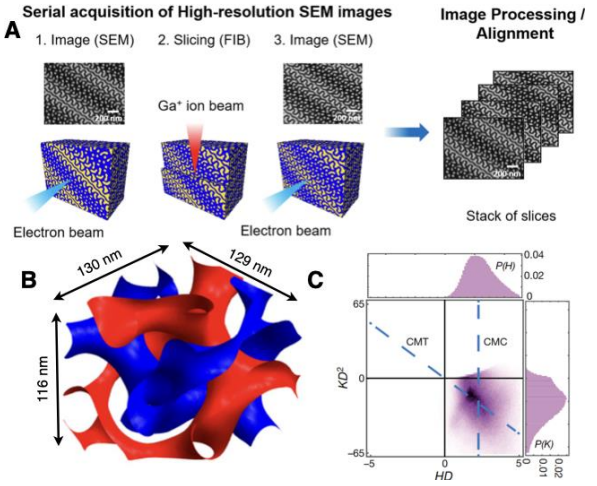

Fig. 1(A) Schematic of SVSEM measurement of BCP morphology. (B) High-resolution 3D reconstruction of IMDS shapes of PS-PDMS gyroid, from SVSEM. (C) shows measured mean and Gaussian curvature distribution of IMDS.

Recent Progress

Quantitative and multiscale measurement of complex BCP domains. We adopted slice and view scanning electron microscopy (SVSEM) tomography to study well-ordered DG and double diamond (DD) polymer networks for the first time, both at the supra-unit cell level and sub-unit cell level[P1]. Most critically, our work exploited the unique capability of SVSEM to access ultra-large volumes of coherent soft crystalline order. As shown in Fig. 1, SVSEM analyses of large volumes of triply-periodic structure are essential for 3D Fourier diffraction (without loss of phase information), unambiguous information in all spatial directions, and 3D high-resolution

reconstruction of subdomain morphologic. Unlike TEM tomography, SVSEM tomography provides significantly arbitrarily large dimensions reconstruction in all three spatial directions, enabling high-resolution and statistically meaningful analysis of the morphologies at an unprecedented level of detail. Analysis of the sub-unit cell morphology of the polystyrene-*block*-poly(dimethyl siloxane) (PS-*b*-PDMS) gyroid, focuses on the shape of the inter-material dividing surface (IMDS) and the distribution of the subdomain thicknesses. While the resolution of the raw SVSEM tomogram is limited by the ~ 3 nm size of image voxels, the intra-grain coherence over large volumes facilitates analysis of an "average" unit-cell at high resolution accomplished through Fourier averaging the raw SVSEM data via application of a 3D Bragg-filter. Precise measurement of the mean (*H*) and Gaussian (*K*) curvature distributions contrasts with existing heuristic models of constant mean curvature (CMC) or constant mean thickness (CMT) IMDS shape[R1,R2]. More crucially, this analysis revealed that experimental DG crystals are distorted from the predicted cubic symmetry by a previously unrecognized, facilitated by a novel coupling between distortion of the supradomain periodicity and non-affine symmetry breaking at the subunit cell level.

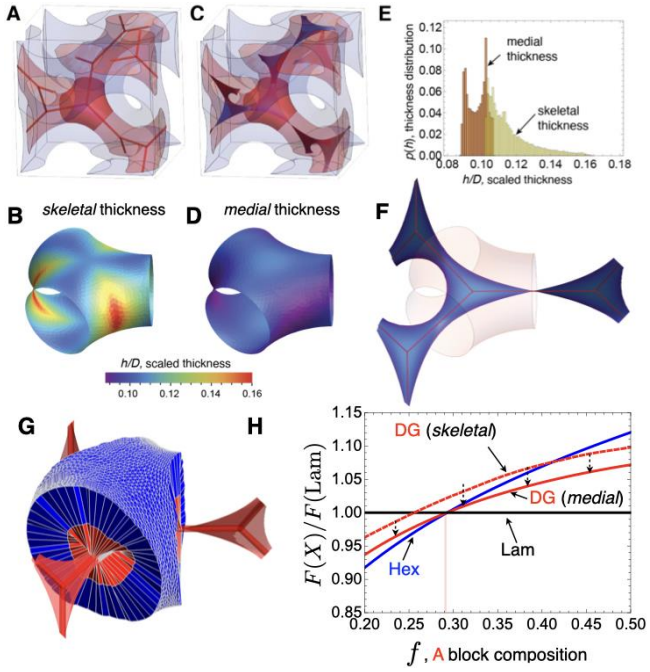

Fig. 2 (A-E) Comparison between skeletal thickness and medial thickness of minority blocks of DG, with (F) showing the anatomy of the inner medial "web". (G) shows a medial SST tessellation of the network node of DG (minority = red/matrix = blue), with the corresponding predictions for free energies for linear AB diblocks in (H).

Medial metrics of subdomain morphology. The unprecedented range of scales and high-fidelity captured by SVSEM tomography now makes closed-loop theory and experimental study of the detailed shapes of BCP domains possible, but also raises challenges to define metrics of subdomain morphology that push beyond coarse descriptions based on domain spacing, topology and space group. We have developed a novel and fully general approach to characterize the "thickness" of arbitrary BCP domains based on the medial surfaces (MS) of the IMDS[P4]. Medial surface analysis originated in the field of computational geometry. While it was previously proposed as a metric of the inhomogeneity of lyotropic sponge phases[R3], our approach is the first to analyze the MS for TPN phases of BCP, and more importantly, to critically confront the theoretical distributions with the experimentally measured distributions based on high fidelity measurement of the IMDS. We applied the medial analysis to DG domains, to address the critical puzzle about how the minority blocks extend into the "middle" of the tubular domain as well as how the majority blocks extend outwards from the IMDS (Fig. 2). Notably, this analysis revises a standard picture for packing frustration in TPN phases[R4], which assumes that minority block

chains must extend 1D skeletal graphs of the network. Instead, we find the MS of the minority block forms twisted web-like surfaces, suggesting that minority blocks "spread out" over a 2D surface that greatly lowers their extension, representing a far lower average thickness and corresponding lower free energy. Medial analysis for the tubular PDMS domains in the DG formed in Fig. 1, suggest mean thickness falls substantially (more than 15%) below the skeletal estimate, a result that has key implications for thermodynamics. Finally, we shown that medial analysis generalizes to all domain types without additional assumptions, and developed computational algorithms for medial thickness characterization based on both computational (SCFT) and experimental (SVSEM) data of complex BCP domains, from networks to complex sphere phases.

Medial SST and the strong segregation stability of DG. Our new insights based on MS analysis connect with a long-standing puzzle for BCP theory namely, is the DG phase an equilibrium phase in the strong segregation limit (i.e. $\chi N \to \infty$)? One on hand, seminal strong segregation theory (SST) predictions concluded that no window of stable TPN phase exists between lamella and hexagonal cylinders for diblock melts[R5,R6]. This would seemingly confirm the "pinch off" suggested from the early SCFT calculations although more recent advances in SCFT calculations[R7] (not to mention experiments) that push to much higher χN show that, nevertheless, equilibrium DG persists to, at least, very high degrees of segregation. We have developed a novel approach to SST based on the medial geometry of BCP domains (see Fig. 2G), which critically incorporates the degrees of freedom associated with "spreading" of termini of the web-like surfaces in TPN, allowing for space filling packings *at a drastically lower entropic penalty for chain stretching.* Fig. 2H shows that medial packing reduces the overall free energy of DG formation by more than 3% over the previous best calculation based on the "skeletal" packing assumption. While seemingly small, this margin is sufficient to bring the free energy of DG just below its competitors in a narrow composition window between hexagonal packed cylinders and lamella, and the window of DG stability slightly widens (and shifts to higher tubular domain thickness) with increasing elastic asymmetry (e.g. conformational or architectural) between the blocks. Our results resolve the long-standing discrepancy between SST and SCFT at high χN with regard to the stability of bicontinuous phases and lays the groundwork to extend the medial SST to understand the connection between molecular features to complex morphologies, well beyond the simplest case of linear AB diblocks and the DG phases.

Single molecule insertion approaches to architectural control of BCP. Novel approaches that combine radical polymerization in conjunction with single-molecule insertion (SMI) have led to considerable recent progress for sequentially and architectural-defined polymers[R7]. We have developed and demonstrated a new SMI approach based on pentafluoro phenyl ester maleimide (PFPMI) at the polymer chain-ends[P3]. This methodology was extended to the synthesis of discrete PMMA-*b*-PS-*g*-PEO block polymer architectures which lie along the unexplored and newly defied continuum between a 3-arm star and A-B-C linear triblock polymer, Fig. 3. For the beginning of the continuum, the synthesis of a 3-arm star was performed by RAFT polymerization to prepare a

PMMA homopolymer. Performing the SMI with the PFPMI molecule at the chain-end of PMMA, followed by chain-extension using styrene, leads to the synthesis of PMMA-PFPMI-PS diblock polymers with an active grafting site at the junction of the two blocks. Utilizing the *grafting to* approach, an amine-terminated PEO was grafted to the diblock polymer, generating the 3-arm star architecture. Likewise, for the synthesis of the linear end of the continuum, a controlled radical polymerization of MMA followed by styrene leads to the synthesis of PMMA-*b*-PS, subsequent SMI of the PFPMI molecule at the active chain-end yields PMMA-*b*-PS-PFPMI. Grafting of amine-terminated PEO generates the linear triblock architecture PMMA-*b*-PS-*g*-PEO. Morphological studies using small-angle X-ray scattering and conventional and energy-filtered transmission electron microscopy reveal the transition between lamellae, perforated lamellae, and cylindrical morphologies with systematic variation in the graft position, a trend attributed to the topological frustration and the associated repulsion between the three blocks. This work demonstrates the versatility of the SMI technique which can be used to synthesize a wide variety of polymer architectures by adjusting the location of the SMI on the polymer backbone.

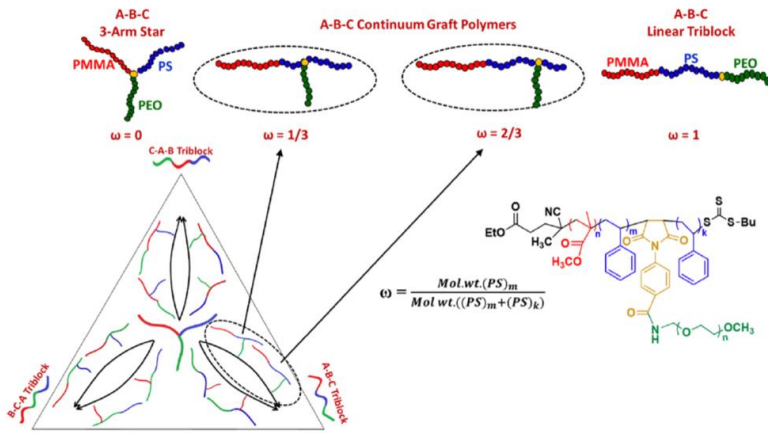

Fig. 3 Schematic of SMI preparative path to architectural continuum between ABC miktoarm stars and ABC linear triblocks.

Future Plans

Future efforts will address-the following objectives aimed at advancing the control of multi-scale morphologies of complex BCP networks through molecular design and processing:

- Extend the medial SST approach to understand subdomain packing and thermodynamics of stability of complex phases beyond DG (e.g. perforated layer morphologies, double diamond, primitive, and novel network "alloy" phases, with mixed node functionality[R8]).
- Test new concepts of for tailoring sensitivity of BCP structure to targeted subdomain packing via synthesis, characterization and theory of "mixed graft length" stars.
- Advance cryo-SVSEM approach to capture and characterize "mesoatomic" morphologies and kinetic pathways of precursors to DG (and other TPN) during solvent evaporation.
- Experimentally characterize subdomain morphologies of complex BCP crystals beyond the IMDS (e.g. terminal boundaries and areal density) via 3D SVSEM reconstruction analysis of labeled BCP chemistries using SMI for installation at precise locations of siloxane labels.

References

R1) Thomas, E. L., Anderson, D. M., Henkee, C. S., and Hoffman, D. "Periodic Area-Minimizing Surfaces in Block Copolymers" *Nature* 334, no. 6183 (1988): 598–601. doi:10.1038/334598a0.

R2) Jinnai, H., Nishikawa, Y., Spontak, R. J., Smith, S. D., Agard, D. A., and Hashimoto, T. "Direct Measurement of Interfacial Curvature Distributions in a Bicontinuous Block Copolymer Morphology" *Physical Review Letters* 84, no. 3 (2000): 518–521. doi:10.1103/PhysRevLett.84.518.

R3) Schröder, G. E., Ramsden, S. J., Christy, A. G., and Hyde, S. T. "Medial Surfaces of Hyperbolic Structures" *European Physical Journal B* (2003): doi:10.1140/epjb/e2003-00308-y.

R4) Matsen, M. W. and Bates, F. S. "Origins of Complex Self-Assembly in Block Copolymers" *Macromolecules* 29, no. 23 (1996): 7641–7644. doi:10.1021/ma960744q.

R5) Olmsted, P. D. and Milner, S. T. "Strong Segregation Theory of Bicontinuous Phases in Block Copolymers" 9297, no. 98 (1998): 4011–4022.

R6) Likhtman, A. E. and Semenov, A. N. "Theory of Microphase Separation in Block Copolymer/Homopolymer Mixtures" *Macromolecules* 30, no. 23 (1997): 7273–7278.

R7) Cochran, E. W., Garcia-Cervera, C. J., and Fredrickson, G. H. "Stability of the Gyroid Phase in Diblock Copolymers at Strong Segregation" *Macromolecules* (2006): doi:10.1021/ma0527707.

R7) Matyjaszewski, K. "Architecturally Complex Polymers with Controlled Heterogeneity" *Science* 333, no. 6046 (2011): 1104–1105. doi:10.1126/science.1209660.

R8) Bonneau, C. and O'Keeffe, M. "High-Symmetry Embeddings of Interpenetrating Periodic Nets. Essential Rings and Patterns of Catenation" *Acta Crystallographica Section A: Foundations of Crystallography* 71, no. 1 (2015): 82–91. doi:10.1107/S2053273314019950**.**

Publications

P1) X. Feng, C. J. Burke, M. Zhuo, H. Guo, K. Yang, A. Reddy, I. Prasad, R.-M. Ho, A. Avgeropoulos, G. M. **Grason**, and E. L. **Thomas**, "Seeing the Mesoatomic Distortions in Soft Matter Crystals", *Nature* **575**, 175 (2019), DOI: 10.1038/s41586-019-1706-1

P2) A. Reddy and G. M. **Grason**, "Supramolecular Assembly: A Cornerstone of Complex Crystals", *Nature Chemistry* **11**, 865 (2019), DOI: 10.1038/s41557-019-0333-7

P3) R. Gupta, M. Misra, W. Zhang, A. Mukhtyar, S. P. Gido, A. Ribbe, F. A. Escobedo and E. B. **Coughlin**, "Topological Frustration as a New Parameter to Tune Morphology Revealed through Exploring the Continuum between A-B-C 3-Arm Star and Linear Triblock Polymers", *Macromolecules* **54**, 4401 (2021), DOI: 10.1021/acs.macromol.1c00277

P4) A. Reddy, X. Feng, E. L. **Thomas** and G. M. **Grason**, "Block copolymers beneath the surface: measuring and modeling complex morphology at the sub-domain scale", under review in *Macromolecules* (2021).

P5) A. Reddy, M Dimitriyev and G. M. **Grason**, "Medial packing and elastic asymmetry stabilizes the double gyroid in strongly segregated block copolymers", to be submitted (2021).

P6) M. Dimitriyev and G. M. **Grason**, "End-zone exclusion for molten polymer brushes of arbitrary shape", to be submitted (2021).

P7) X. Feng, M. Dimitrivev, G.M. **Grason** and E. L. **Thomas**, "Creating and Characterizing Nearly Cubic Double Diamond Networks," to be submitted (2021).

Self-assembly of cocontinuous nanostructured copolymer templates with compositional and architectural dispersity

PI: Ryan C. Hayward

Department of Chemical and Biological Engineering, University of Colorado Boulder

Program Scope

This project aims to better understand and exploit the formation of cocontinuous nanostructures within blocky copolymer architectures containing architectural and compositional dispersity. Materials in which two (or more) disparate microphases with nanometer-scale domains simultaneously percolate in three dimensions offer promise in contexts including electrodes, catalysts, water purification, and stiff but tough materials. We seek to understand of how varying types and degrees of randomness in blocky copolymer architectures promote the formation of disordered cocontinuous nanostructures. By subsequently degrading or extracting one of the components, interconnected porous samples can be obtained, which can be used to template a variety of functional nanostructured materials.

Recent Progress

We have made recent progress on understanding the behavior of two specific architectures: linear multiblock copolymers and randomly crosslinked copolymer networks. In the former case, we have prepared multiblock copolymers with dispersity in effective block length and number by joining telechelic acrylate end-functionalized polystyrene (PS) and poly(lactic acid) (PLA) chains with dithiol linkers using thiol-Michael chemistry. This approach yields blocky polymers of random sequence and with high length dispersity. As summarized in Figure 1A, we developed a phase diagram in terms of the PLA content (weight fraction, w_{PLA}) and the degree of immiscibility χN. Interestingly, at low incompatibility, close to the critical value for microphase separation, the cocontinuous window is rather wide, spanning 0.25 in w_{PLA}. However, at larger χN, ordered phases form over a larger range, reducing the cocontinuous window to only 0.10 in w_{PLA}. A key advantage of this approach is that the polymer remain solution processable after linking, thus enabling the formation of thin membranes (Figure 1B). In the latter case, we

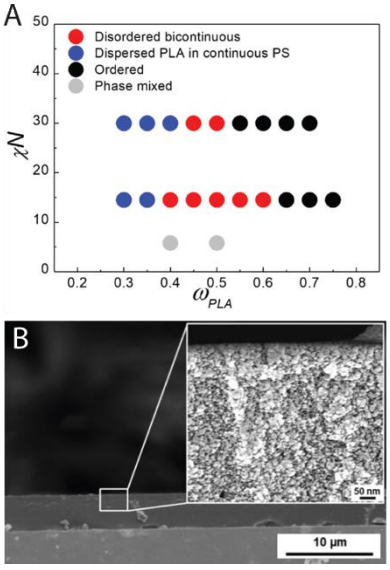

Figure 1. (A) Phase diagram for PS-PLA linear multiblock polymers and (B) cross-sectional SEM of porous thin film.

have prepared linear copolymers of PS and poly(2-vinyl pyridine), each containing a small fraction of allyl methacrylate comonomers containing pendent allyl functionalities that can be subsequently crosslinked by thiol-ene reactions with multi-functional thiol linkers. Compared to our previous work on randomly *end*-linked copolymer networks, this approach facilitates network formation, since the precursor polymers do not need to be prepared with well-controlled end groups. We have found that this approach is similarly effective at promoting formation of disordered cocontinuous nanostructures as randomly end-linking.

In addition, we have made recent progress on using these approaches to prepare functional nanostructured and nanoporous materials. In one example, we have studied the use of polysulfone (PSU) strands in place of PS, and formed both randomly end-linked copolymer networks and linear multi-block copolymers. Since PSU is formed by a step-growth polymerization, it is straightforward to achieve telechelic linear homopolymers end-capped with desired functional groups that can subsequently be linked together with difunctional or multifunctional linkers. We have found that PSU-PLA systems are similarly effective as PS-PLA systems at forming disordered cocontinuous nanostructures, but with greatly improved mechanical toughness thanks to the properties of the engineering polymer PSU. This enables the formation of interconnected nanoporous membranes with sufficient mechanical toughness for subsequent characterization in filtration applications.

Future Plans

In the future, we plan to extend our study of randomly-linked copolymers to star-like architectures to further elucidate the importance of dispersity in strand lengths vs. preferred curvature of junctions. In addition, we will further demonstrate the utility of this platform for assembly and templating of functional materials including nanoporous carbon and high surface area heterojunctions of polymerized ionic liquids.

Publications

D. Zeng, R. Gupta, E.B. Coughlin, R.C. Hayward, "Assembly of Disordered Cocontinuous Morphologies by Multiblock Copolymers with Random Block Sequence and Length Dispersity", *ACS Applied Polymer Materials*, **2**, 3282-3290 (2020). DOI: 10.1021/acsapm.0c00428

H. Kim, N. Hight-Huf, J.-H. Kang, P. Bisnoff, S. Sundararajan, T. Thompson, M. Barnes, R.C. Hayward, T. Emrick "Polymer Zwitterions for Stabilization of $CsPbBr_3$ Perovskite Nanoparticle and Nanocomposite Films", *Angewandte Chemie International Edition*, **59**, 10802-10806 (2020). DOI: 10.1002/anie.201916492

D. Zeng, R.C. Hayward, "Effects of Randomly End-Linked Copolymer Network Parameters on the Formation of Disordered Cocontinuous Phases", *Macromolecules*, **52**, 2642–2650 (2019). DOI: 10.1021/acs.macromol.9b00050

D.E. Acevedo-Cartagena, J. Zhu, M. Kocun, S.S. Nonnenmann, R.C. Hayward, “Tuning metastability of poly(3-hexyl thiophene) solutions to enable in situ atomic force microscopy imaging of surface nucleation”, *Macromolecules*, **52**, 7756-7761 (2019). DOI: 10.1021/acs.macromol.9b01547

H. Kim, S. So, A. Ribbe, Y., W. Hu, V.V. Duzhko, R.C. Hayward, T. Emrick, "Functional Polymers for Stabilizing CsPbBr3 Perovskite Nanoparticles", *Chemical Communications*, **55**, 1833-1836 (2019). DOI: 10.1039/C8CC09343A

K. Heo, C. Miesch, J.-H. Na, T. Emrick, R.C. Hayward, “Assembly of P3HT/CdSe nanowire networks in an insulating polymer host”, *Soft Matter*, **14**, 5327 - 5332 (2018). DOI: 10.1039/C8SM01001C

Predictive coarse-grained modeling of morphologies in polymer nanocomposites with specific and directional intermolecular interactions

Arthi Jayaraman, Dept. of Chemical and Biomolecular Engineering & Dept. of Materials Science and Engineering, University of Delaware, Newark

Program Scope

The overarching goal of the project is to develop predictive coarse-grained (CG) models for investigating structure and dynamics in soft materials with chemistries that have specific and directional molecular interactions. The successful development of qualitatively, and in some cases quantitatively, accurate coarse-grained models is enabled by synergistic feedback from experiments via synthesis and structural characterization of these materials using x-ray scattering, neutron scattering and microscopy. Although past computational studies have been tremendously useful in understanding molecular phenomena and guiding synthesis of new macromolecular soft materials for a wide variety of applications, the inability to capture small scale specific and directional interactions alongside macromolecular length and time scales represents a key limitation of most studies to date. Our work in this project addresses this next grand challenge in computational materials chemistry, i.e., to be able to model the anisotropic, directional, and specific interactions that govern the behavior of many macromolecular soft matter systems of interest, thus, greatly expanding the predictive potential of simulations.

Recent Progress

The past work described in 3-year publication list at the end of this abstract was focused on development of *new coarse-grained models* [Publication #1, 3, 5, and 6] that capture hydrogen bonding in polymeric systems and their use in molecular simulations and PRISM theory to study *structure and thermodynamics in polymer nanocomposites* [Publication #1, 7, and 8] *and solutions* [3 and 5]. Recent progress and ongoing work are described below:

► **Impact of Composition and Placement of Hydrogen Bonding Groups along Polymer Chains on Blend Phase Behavior: Coarse-Grained Molecular Dynamics (MD) Simulation Study.** We use molecular dynamics (MD) simulations to study polymer blends comprised of two polymer chemistries, one polymer containing hydrogen bonding (H-bonding) acceptor groups and the other containing H-bonding donor groups. Using a previously developed coarse-grained (CG) model [Publication #1] capable of representing both, the attractive directional interactions between H-bonding acceptor and donor groups as well as the unfavorable isotropic polymer-polymer interactions, we

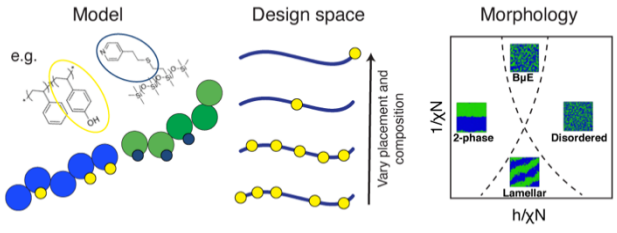

Figure 1: Connecting the composition and placement of Hydrogen bonding groups along polymer chains to the observed blend morphology

predict the morphology (i.e., two-phase, ordered/lamellar, disordered, and bicontinuous microemulsion or BμE) in symmetric blends of these polymer chemistries at varied composition (i.e., fraction of monomers containing hydrogen bonding groups along the polymer chain) and placement of hydrogen bonding groups along polymer chains. We validate our CGMD approach to describe phase behavior in H-bonding polymer blends by comparing our simulation phase diagrams to past theoretical phase diagram of Fredrickson and co-workers for end-associating polymer chains at varying H-bonding and polymer segregation strengths ($h/\chi N$ and $1/\chi N$). Simulation results show that with increasing H-bonding strength, end-associating blends with short chain lengths transition from two-phase to BμE and finally to disordered microphase morphologies, while those with longer chain lengths at similar polymer segregation strengths transition from two-phase to ordered lamellar phases. The simulated phase diagram in $1/\chi N$ vs. $1/\chi N$ space agrees with past theoretical phase diagram for end-associating polymer chains.

Next, we study polymer blends with center placement of a single H-bonding group in each polymer chain and random and regular placement of multiple H-bonding groups per polymer chain. With increasing H-bonding strength, regardless of number and placement of H-bonding groups, the fraction of associated H-bonding groups increases with the system transitioning from unassociated polymers to a mixture of associated copolymers and unassociated polymers and finally a melt of fully associated supramolecular copolymers. At intermediate strengths of H-bonding, we observe BμE morphologies in all systems with end, center, random, and regular placement of H-bonding group(s). At high strengths of H-bonding attraction, the blend morphology is disordered with microphase domain sizes being largest for the center case, followed by the end case and then regular and random placement cases. We demonstrate that these trends in disordered domain sizes for blends with varying composition and placement of hydrogen groups are linked to the supramolecular copolymer architecture formed upon association of the two homopolymer chemistries at high strengths of H-bonding. The center placement case forms miktoarm star copolymers which show smaller domain sizes compared to diblock copolymers formed in the end placement case at the same molecular weight, while the random and regular cases form non-linear copolymer architectures with dispersity in arm length and branching leading to larger domain sizes. Overall, our work establishes design rules for incorporating H-bonding functional groups along polymer chains to create blends with precisely tuned morphology and disordered domain sizes.

Publications in preparation: ● **A. Kulshreshtha**, R. Hayward, **A. Jayaraman*,** Coarse-Grained Modeling and Simulation Study of Structure and Phase Behavior in Blends of Homopolymers with Hydrogen Bonding (to be submitted July 2021); ● **A. Kulshreshtha**, J. Ju, R. Hayward*, **A. Jayaraman*,** Effect of Composition and Placement of Hydrogen Bonding Groups along Polymer Chains on the Formation and Stability of Bicontinuous Microemulsions in Polymer Blends. (in preparation) ● **A. Kulshreshtha**, **A. Jayaraman*,** Machine Learning Guided Closures for Polymer Reference Interaction Site Model (PRISM) Theory Studies of Macromolecules with Directional Interactions. (in preparation)

► **Coarse-Grained Molecular Dynamics (MD) Simulations of Hydrogen-bonding Induced Ordering among Polysulfamide Chemistries.** N,N′-disubstituted sulfamides, have been synthesized [Ref. **1**] and found use in a wide variety of applications ranging from catalysis to medicinal chemistry. Despite their promising properties including high thermal stability, tunable glass transition temperature, and potential to be recycled back to constitutive monomers via hydrolysis, polysulfamides are still not as commonly used as polyureas in many applications. This is due to insufficient fundamental understanding of how polysulfamides behave in solutions and blends with other materials, partly due to difficulties in synthesis, until recently via SuFEx click chemistry [Ref. 1], and partly due to lack of molecular models that can be used to simulate these materials. The latter limitation has motivated our recent computational work to address this knowledge gap in collaboration with Prof. Q. Michaudel at Texas A&M, whose group synthesizes these macromolecules.

Inspired by past coarse-grained (CG) models [Publication #1, 3, 5, and 6] developed in our group within this DOE project, we have created a new coarse-grained model (Figure 2) for various polysulfamides synthesized by Q. Michaudel and coworkers at Texas A&M. Donors (-NH) and acceptors (-S=O) are embedded in the sulfamide CG bead and together they are modeled as rigid body. The groups on either side of the sulfamide bead are modeled with CG beads whose sizes are scaled roughly by atomistic diameters of corresponding chemistries. As shown in Figure 2, for modelling diphenylmethane group (left side chain in this example) we use a bulky CG bead and stiff angle potential; for aliphatic chains (right side chain in this example) we use a small CG bead and flexible chains. We are using these CG models and molecular dynamics simulations to correlate the choice of the two groups on either side of the sulfamide group in the repeating unit of the chain, specifically the two groups' flexibilityand bulkiness, to the extent of crystallinity observed in experiments. So far, we have found that the bulkiness rather than the flexiblity of the groups on either side of the sulfamide chemistry seems to be the determining factor of the hydrogen bonding propensity (in our simulation) and crystallinity (in their experimental findings). Bulky groups hinder hydrogen bond formation and lead to lower crystallinity.

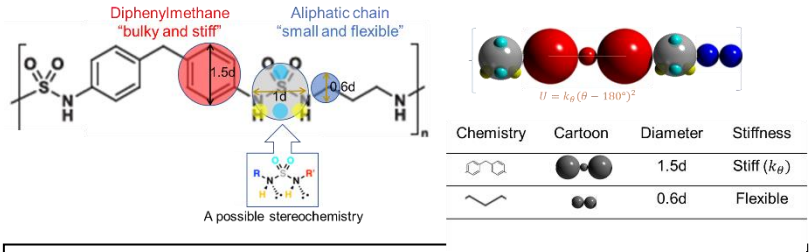

Figure 2: Coarse-grained models for polysulfamide chemistries to enable molecular simulations of assembly of polysulfamide chains.

Publications in preparation: ● **Z. Wu,** J. W. Wu, Q. Michaudel*, **A. Jayaraman*,** Hydrogen bonding induced assembly of polysulfamides in solution: coarse-grained simulations and experiments (in preparation)

Future Plans

In the last 6 months of this project, the two graduate students supported on this grant, A. Kulshreshtha and Z. Wu, and PI Jayaraman will complete work on the four publications in preparation. Two out of the four papers are joint experiment - simulation papers, one with collaborator Prof. Quentin Michaudel in Texas A&M on polysulfamides and another with sub-awardee of this DOE grant Prof. Ryan Hayward at Univ. of Colorado Boulder. For both papers, we still need some results from experiments to create the feedback loop with the simulations and any additional simulation results post-improvements to the CG models made based on the feedback look.

References

1. R. W. Kulow, J. W. Wu, C. Kim, and Q. Michaudel, Synthesis of unsymmetrical sulfamides and polysulfamides via SuFEx click chemistry, *Chem. Sci.***,** 2020,**11**, 7807-7812

Publications 3-year list of publications supported by DOE-BES.

(* denotes corresponding author, # denotes equal contributions, † denotes undergraduate researcher**)**

1. A. Kulshreshtha, K.J. Modica†, A. Jayaraman*, Impact of Hydrogen Bonding Interactions on Graft−Matrix Wetting and Structure in Polymer Nanocomposites, *Macromolecules*, 52 (7), 2725-2735 (2019)
2. T. E. Gartner, III, A. Jayaraman*, Modeling and Simulations of Polymers: A Roadmap, an invited perspective article for *Macromolecules*, 52 (3), 755–786 (2019) *Invited Front Cover Art. Now listed in the Top 10 Most Read Articles in Macromolecules*
3. D. J. Beltran-Villegas, D. Intriago†, K. Kim, N. Behaptu, J. D. Londono, A. Jayaraman*, Coarse- grained molecular dynamics simulations of α-1,3-glucan, *Soft Matter*, 15, 4669-4681 (2019)
4. A. Jayaraman*, Modeling and simulation of macromolecules with hydrogen bonds: Challenges, successes and opportunities, an invited viewpoint in *ACS Macro Letters* 9, 656–665, (2020)
5. U. Kapoor[#], A, Kulshreshtha[#], A. Jayaraman*, Development of Coarse-Grained Models for Poly(4-vinylphenol) and Poly(2 vinylpyridine): Polymer Chemistries with Hydrogen Bonding, *Polymers,*12, 2764 (2020).
6. Z. Wu, D. Beltran-Villegas, A. Jayaraman*, Development of a new coarse-grained model to simulate assembly of cellulose chains due to hydrogen bonding, *Journal of Chemical Theory and Computation* 16, 7, 4599–4614 (2020)
7. A. Kulshreshtha, A. Jayaraman*, Dispersion and Aggregation of Polymer Grafted Particles in Polymer Nanocomposites Driven by the Hardness and Size of the Grafted Layer Tuned by Attractive Graft-Matrix Interactions, *Macromolecules*, 53 (4), 1302-1313 (2020)
8. S. M. Maguire, N. M. Krook, A. Kulshreshtha, C. R. Bilchak, R. B., A-M. Pana, P. Rannou, M. Maréchal, K. Ohno, A. Jayaraman*, R, J. Composto*, Interfacial Compatibilization in Ternary Polymer Nanocomposites: Comparing Theory and Experiments, *Macromolecules*, 54, 2, 797-811(2020)

9. A. Jayaraman*, A. Kulshreshtha, P. Taylor, A. Prhashanna, Coarse-Grained Modeling and Simulations of Thermoresponsive Biopolymers and Polymer Nanocomposites with Specific and Directional Interactions, in: Maginn E.J., Errington J. (eds) *Foundations of Molecular Modeling andSimulation, Molecular Modeling and Simulation (Applications and Perspectives). Springer*, Singapore, 37-74 (2021)

Fundamental Studies of Charge Transfer in Nanoscale Heterostructures of Earth-Abundant Semiconductors for Solar Energy Conversion

Song Jin, John C. Wright, and Robert J. Hamers (contact PI email: jin@chem.wisc.edu)
Department of Chemistry, University of Wisconsin-Madison, Madison, Wisconsin 53706

Program Scope

Hybrid metal halide perovskites are inexpensive semiconductor materials promising for high performance solar cells and light emitting diodes (LEDs) because they are easy to make and tolerant of defects. The interactions between the organic and inorganic components in hybrid perovskites result in "polarons", which gives them unique physical properties that are very different from conventional semiconductor materials and creates more complexity for understanding the physical processes at heterojunctions of halide perovskites. A fundamental understanding of the factors controlling the carrier transfer mechanisms in heterostructures of halide perovskites is crucial for guiding the synthetic strategies to improve properties and energy device applications. To address these challenges, our collaborative team synergistically combines complementary expertise in synthesis of new materials and nanoscale heterostructures (Jin) with the development of new ultrafast spectroscopies (Wright) and scanning probe microscopy (Hamers) designed to probe complex heterostructures at the single quantum state level.

Recent Progress

In the current project period, we have made significant progress in the materials chemistry, spectroscopic studies and physical properties of two families of materials and their heterostructures: lead halide perovskites and layered metal chalcogenide (MX_2). We have developed new methods for synthesizing nanostructures of halide perovskites including two-dimensional (2D) layered perovskites and using them to create novel heterostructures. We have also developed fully coherent multidimensional spectroscopy (CMDS) methods for characterizing semiconductor materials and their nanoscale heterostructures. Some highlights include:

Distinct Carrier Transfer Properties Across Heterostructures of 2D/3D Perovskites

Two-dimensional-on-three-dimensional (2D/3D) halide perovskite heterostructures have been extensively utilized in optoelectronic devices. However, the labile nature of halide perovskites makes it difficult to form such heterostructures with well-defined compositions, orientations, and interfaces, which inhibits understanding of the carrier transfer properties across these heterostructures. We have developed solution growth of both horizontally and vertically aligned 2D perovskite $(PEA)_2PbBr_4$ (PEA = phenylethylammonium) microplates onto 3D $CsPbBr_3$ single crystal thin films (Fig. 1), with well-defined heterojunctions. Time-resolved photoluminescence (TRPL) transients of the heterostructures exhibit the monomolecular and bimolecular dynamics expected from exciton annihilation, dissociation, and recombination, as well as evidence for carrier transfer in these heterostructures. Two kinetic models based on Type-I and Type-II band alignments at the interface are applied to reveal a shift in balance between carrier transfer and recombination (Fig. 1): Type-I band alignment better describes the behaviors

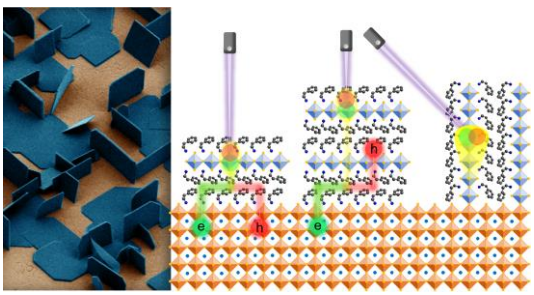

Fig. 1. Horizontally and vertically aligned heterostructures of 2D $(PEA)_2PbBr_4$/3D $CsPbBr_3$ perovskites and different carrier transfer mechanisms.

of heterostructures with thin 2D perovskite microplates but Type-II band alignment better describes those with thick 2D microplates (>150 nm). TRPL of vertically aligned 2D microplates is dominated by directly excite d PL and is independent of the height above the 3D film. Electrical measurements reveal current rectification behaviors in both heterostructures with vertical heterostructures showing better electrical transport. This work provides insights on the charge transfer mechanisms in these 2D/3D perovskite heterostructures and guidelines for designing better optoelectronic devices, but also leaves many unsettled questions for further study.

Deterministic Fabrication of Arbitrary Vertical Heterostructures of RP Halide Perovskites

We have further developed methods for creating large-area vertical or lateral heterostructures of Ruddlesden−Popper (RP) perovskites with the goal of precisely controlling the compositions and the stacking sequence of each layer. We first developed a new solution growth for synthesizing large nanosheets of a variety of phase-pure 2D RP lead halide perovskites (30+) with different LA and A cations with lateral dimensions of up to a few hundred micrometers and thicknesses of down to a monolayer. We have further developed the soft contact transfer methods to sequential transfers and physically stacking of different nanosheets to create vertical heterostructures in a deterministic fashion (see examples in Fig. 2). The self-assembled bilayer of LA cations can act as natural diffusion barrier and prevent halide migration across the adjacent perovskite layers, maintaining stable and atomically sharp junctions. These advances enabled the deterministic fabrication of arbitrary vertical heterostructures and multi-heterostructures of different RP perovskites with unprecedented structural degrees of freedom that define the electronic structures of the heterojunctions (Fig. 2). This work also shows that rationally designed novel heterostructures exhibit interesting interlayer properties, such as efficient interlayer energy transfer and reduction of photoluminescence line width. These RP perovskite heterostructures will enable the exploration of carrier transfer dynamics and novel exciton physics in the next project cycle. For example, we have further made suitably designed heterostructures with presumed Type II band alignment and preliminarily observed the evidence for interlayer excitons.

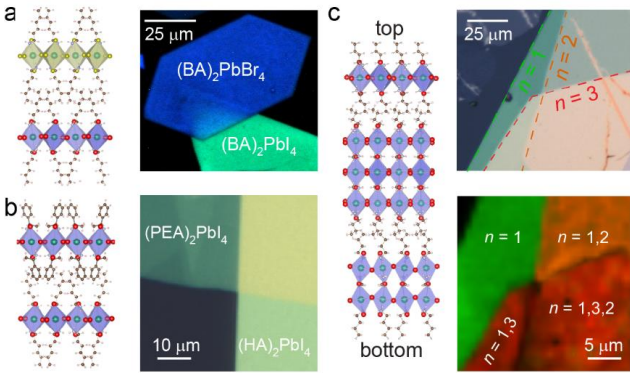

Fig. 2. Various novel vertical heterostructures (a,b) and multiheterostructures (c) of 2D RP perovskites we fabricated.

Lateral Heterostructures of RP Halide Perovskites Formed via Anion Exchange

We have synthesized lateral heterostructures of RP halide perovskites via halide anion exchange. The halide miscibility in RP perovskites decreases with perovskite layer thickness (n), enabling the formation of sharp halide lateral heterostructures from n = 1 and 2 RP lead iodide microplates via anion exchange with hydrogen bromide (HBr) vapor. In contrast, RP perovskites with $n \geq 3$ form more diffuse lateral heterojunctions, more similar to those in 3D perovskites. The anion exchange behaviors show a strong dependence on the spacer and A-site cations in the RP perovskites. These new insights, and kinetic studies of the exchange reactions, enable the preparation of lateral heterostructures from various n = 2 RP perovskites that are show to be more stable against anion interdiffusion and degradation for potential optoelectronic device applications.

Super-twisted Spirals of MX_2 Materials enabled by Growth on non-Euclidean Surfaces

Tuning the twist angles between 2D materials results in the formation of moiré patterns and the manipulation of electronic states, which have led to novel quantum phenomena in 2D materials, including unconventional superconductivity, moiré excitons, and tunable Mott insulators. Such twisted structures of layered materials have so far been fabricated by elaborate mechanical stacking of different layers in a one-off and low throughput fashion. We have developed a novel method to rationally produce twisted MX_2 spiral structures with consistent twisting alignment between successive MX_2 layers (Fig. 3). This is enabled by a general model describing the growth of layered materials with screw dislocation spirals on non-Euclidean surfaces, which leads to the rational realization of continuously twisted layered superstructures. We experimentally demonstrated the growth of twisted spirals of WS_2 and WSe_2 draped over nanoparticles near their centers. Microscopic structural analysis shows that the twist of the crystal lattice is consistent with the geometric twist of the layers, leading to moiré superlattices between the atomic layers.

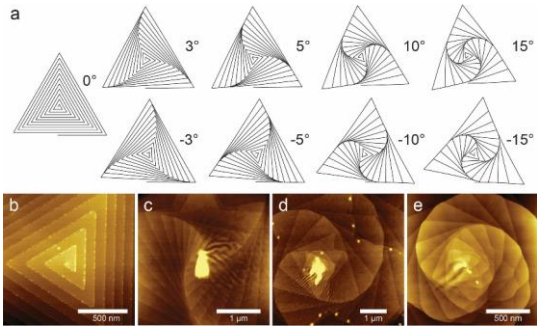

Fig. 3. Super-twisted spirals of MX2 materials due to non-Euclidean Surfaces.

Dynamics of 2D RP Perovskite Charge Carrier with Steady-State Carrier Control

Our previous work developed a new TRPL approach to study and quantitatively characterize the charge carrier dynamics of a 3D hybrid perovskite by creating and controling a steady-state concentration of excited carriers and considering a complete model of carrier kinetics, in the form of rate equations. We recently developed a new modeling approach that controls the steady state carrier concentration by the pulse repetition rate to study a series of RP perovskite $(PEA)_2(CH_3NH_3)_{n-1}Pb_nI_{3n+1}$ (PEA = phenethylammonium, *n* = 1, 2, 3, 4, and infinity) single crystals where the PL is dominated by excitonic recombination. Transient excitation created variations of the total photoexcited carrier density over the timescale of the measurement (10^5 – 10^8 cm^{-2} $layer^{-1}$), allowing us to probe the carrier dynamics at both exciton-dominated (at high density) and free-carrier-dominated (at low density) regimes, as expected from the Saha equilibrium. Thus, despite only measuring excitonic emission, we can analyze the dynamic and steady-state dynamics of the TRPL transients while also resolving the free carrier dynamics. We obtained an Arrhenius-like relationship between the exciton dissociation rate constant and the exciton binding energy (determined by the quantum well thickness, n) for all values of n as well as the dependence of the exciton annihilation and the electron-hole recombination rate constants. Moreover, we examined the influence of excitation power and trap filling on the observed value of each parameter. We developed a computational framework called KinetiKit for fitting time-resolved data, which will serve as a general framework for understanding the mechanisms of carrier dynamics. We have also developed a multidimensional harmonic generation method to eliminate the complications from multiphoton PL to accurately determine the second harmonic generation (SHG) of RP perovskites.

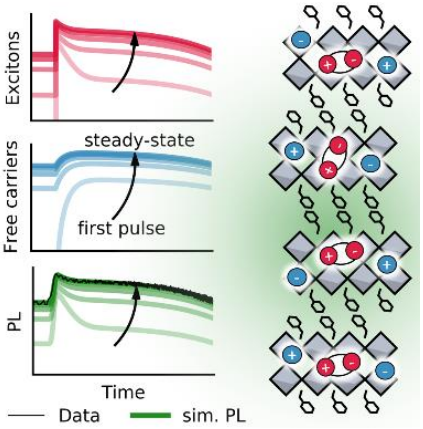

Fig. 4. Systematic TRPL and kinetic modeling studies of 2D RP perovskites with different n value to differentiate the excitonic vs. free-carrier photophysics.

Development of New Spectroscopic Methods and Investigations of New Materials.

The primary goal for our fully coherent ultrafast spectroscopy program is the development of methods that can characterize complex nanostructures. Current ultrafast methods work well for simple material systems but fail when the materials become more complex because they lack the spectral resolution required to probe interactions between multiple parts of a complex nanostructure. We have developed Triple Sum Frequency (TSF) fully coherent spectroscopy to entangle multiple quantum states and isolate the interactions between states. Even more importantly, TSF provides an instantaneous snapshot in time of the quantum states and their coupling to each other that is free from any relaxation effects. This capability is the result of the quantum Zeno effect where the coherence of the quantum states is maintained by the electromagnetic field driving the sample. Fig. 5 shows a pump-fully coherent probe spectroscopy for a WS_2/MoS_2 lateral heterostructure and its ability to resolve both the coherent and population relaxation dynamics. Note the differences in the spectral line shapes at the bottom and how they depend on the delay times. There are important quantum mechanical interference effects between the excitons that control the line shapes.

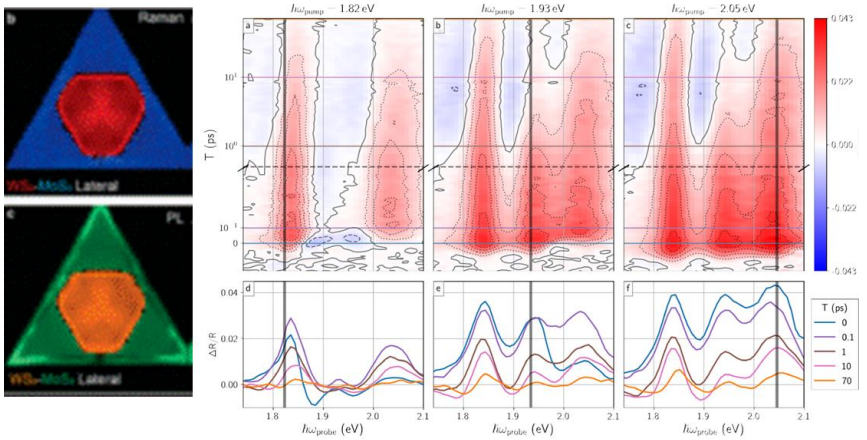

Fig. 5. Confocal Raman and PL image of the monolayer WS_2-MoS_2 lateral heterostructures. Pump-TSF probe spectra of a WS_2/MoS_2 lateral heterostructure showing dynamics of MoS_2 A and B excitons and WS_2 A exciton. 1a) coherent evolution of MoS_2 A exciton. Note absence of WS_2 exciton. 1b) Emergence of WS_2 A exciton while being coherently driven. 1c) Population dynamics as the WS_2 A exciton relative to MoS_2.

Future Plans

We will continue to synthesize heterostructures of 2D perovskites and spectroscopically study them to not only understand carrier transfer across heterojunctions but also the fundamental polaron mechanisms underlying the unique physical properties of hybrid perovskites. We will directly synthesize or stack arbitrary 2D perovskite layers and create several novel types of high quality heterostructures of 2D or 2D/3D halide perovskites with well-defined interfaces. A wide range of structural characterization and conventional time-resolved spectroscopic methods will be employed to correlate the properties of these heterostructures with their structures. We will further develop new CDMS methods that take advantage of quantum mechanical effects to spectrally, temporally, and spatially resolve the electronic and vibrational states and the coupling between them in heterostructures of halide perovskites at specific instants in time, toward the goal of fully understanding the complex charge transfer mechanisms in various model heterostructures of halide perovskites. The fundamental insights provided by this project promises to accelerate the creation of new and rationally designed heterostructures of halide perovskites with optimized properties for energy applications. It also promises to highlight how the new ultrafast spectroscopic technology can provide the same guidance to the global materials research community.

References (see the next section)

Three Year List of Publications Supported by BES:

1. Roy, C. R.; Pan, D.; Wang, Y.; Hautzinger, M. P.; Zhao, Y.; Wright, J. C.; Zhu, Z.; Jin, S.: Anion Exchange of Ruddlesden–Popper Lead Halide Perovskites Produces Stable Lateral Heterostructures. *J. Am. Chem. Soc.* **2021**, *143*, 5212-5221. DOI: 10.1021/jacs.1c01573.
2. Kuo, M.-Y.; Spitha, N.; Hautzinger, M. P.; Hsieh, P.-L.; Li, J.; Pan, D.; Zhao, Y.; Chen, L.-J.; Huang, M. H.; Jin, S.; Hsu, Y.-J.; Wright, J. C.: Distinct Carrier Transport Properties Across Horizontally vs Vertically Oriented Heterostructures of 2D/3D Perovskites. *J. Am. Chem. Soc.* **2021**, *143*, 4969-4978. DOI: 10.1021/jacs.0c10000.
3. Pan, D.; Fu, Y.; Spitha, N.; Zhao, Y.; Roy, C. R.; Morrow, D. J.; Kohler, D. D.; Wright, J. C.; Jin, S.: Deterministic fabrication of arbitrary vertical heterostructures of two-dimensional Ruddlesden–Popper halide perovskites. *Nat. Nanotech.* **2021**, *16*, 159-165. DOI: 10.1038/s41565-020-00802-2.
4. Zhao, Y.; Zhang, C.; Kohler, D.D.; Scheeler, J. M.; Wright, J.C.; Voyles, P. M.; Jin, S., Supertwisted spirals of layered materials enabled by growth on non-Euclidean surfaces. *Science* **2020**, *370*, 442-445. DOI: 10.1126/science.abc4284.
5. Morrow, D. J.; Kohler, D. D.; Zhao, Y.; Scheeler, J. M.; Jin, S.; Wright, J. C., Quantum interference between the optical Stark effect and resonant harmonic generation in WS_2. *Phys. Rev. B* **2020,** *102*, 161401. DOI: 10.1103/PhysRevB.102.161401.
6. Morrow, D. J.; Hautzinger, M. P.; Lafayette, D. P.; Scheeler, J. M.; Dang, L.; Leng, M.; Kohler, D. D.; Wheaton, A. M.; Fu, Y.; Guzei, I. A.; Tang, J.; Jin, S.; Wright, J. C., Disentangling Second Harmonic Generation from Multiphoton Photoluminescence in Halide Perovskites using Multidimensional Harmonic Generation. *The Journal of Physical Chemistry Letters* **2020,** *11*, 6551-6559. DOI: 10.1021/acs.jpclett.0c01720.
7. Spitha, N.; Kohler, D. D.; Hautzinger, M. P.; Li, J.; Jin, S.; Wright, J. C., Discerning Between Exciton and Free-Carrier Behaviors in Ruddlesden-Popper Perovskite Quantum Wells through Kinetic Modeling of Photoluminescence Dynamics. *The Journal of Physical Chemistry C* **2020**, *124*, 17430–17439. DOI: 10.1021/acs.jpcc.0c06345.
8. Hautzinger, M. P.; Pan, D.; Pigg, A. K.; Fu, Y.; Morrow, D. J.; Leng, M.; Kuo, M.-Y.; Spitha, N.; Lafayette, D. P.; Kohler, D. D.; Wright, J. C.; Jin, S., Band Edge Tuning of Two-Dimensional Ruddlesden–Popper Perovskites by A Cation Size Revealed through Nanoplates. *ACS Energy Letters* **2020,** *5*, 1430-1437. DOI: 10.1021/acsenergylett.0c00450.
9. Zhao, Y.; Jin, S., Controllable Water Vapor Assisted Chemical Vapor Transport Synthesis of WS_2-MoS_2 Heterostructure. *ACS Materials Letters* **2020**, *2*, 42-48. DOI: 10.1021/acsmaterialslett.9b00415.
10. Morrow, D. J.; Kohler, D. D.; Zhao, Y.; Jin, S.; Wright, J. C., Triple sum frequency pump-probe spectroscopy of transition metal dichalcogenides. *Physical Review B* **2019**, *100*, 235303. DOI: 10.1103/PhysRevB.100.235303.
11. Fu, Y.; Hautzinger, M. P.; Luo, Z.; Wang, F.; Pan, D.; Aristov, M. M.; Guzei, I. A.; Pan, A.; Zhu, X.; Jin, S., Incorporating Large a Cations into Lead Iodide Perovskite Cages: Relaxed Goldschmidt Tolerance Factor and Impact on Exciton–Phonon Interaction. *ACS Central Science* **2019**, *5*, 1377-1386. DOI: 10.1021/acscentsci.9b00367.
12. Chen, J.; Luo, Z.; Fu, Y.; Wang, X.; Czech, K. J.; Shen, S.; Guo, L.; Wright, J. C.; Pan, A.; Jin, S., Tin(IV)-Tolerant Vapor-Phase Growth and Photophysical Properties of Aligned

Cesium Tin Halide Perovskite ($CsSnX_3$; X = Br, I) Nanowires. *ACS Energy Letters* **2019**, *4*, 1045-1052. DOI: 10.1021/acsenergylett.9b00543.

13. Fu, Y.; Zhu, H.; Chen, J.; Hautzinger, M. P.; Zhu, X. Y.; Jin, S., Metal Halide Perovskite Nanostructures for Optoelectronic Applications and the Study of Physical Properties. *Nature Reviews Materials* **2019**, *4*, 169-188. DOI: 10.1038/s41578-019-0080-9.
14. Shearer, M. J.; Li, W.; Foster, J. G.; Stolt, M. J.; Hamers, R. J.; Jin, S., Removing Defects in WSe_2 Via Surface Oxidation and Etching to Improve Solar Conversion Performance. *ACS Energy Letters* **2019,** *4*, 102-109. DOI: 10.1021/acsenergylett.8b01922.
15. Fu, Y.; Zheng, W.; Wang, X.; Hautzinger, M. P.; Pan, D.; Dang, L.; Wright, J. C.; Pan, A.; Jin, S., Multicolor Heterostructures of Two-Dimensional Layered Halide Perovskites That Show Interlayer Energy Transfer. *J. Am. Chem. Soc.* **2018,** *140*, 15675-15683. DOI: 10.1021/jacs.8b07843.

The following are minor collaborative papers that acknowledged support from this project:

16. Wang, T.; Fu, Y.; Jin, L.; Deng, S.; Pan, D.; Dong, L.; Jin, S.; Huang, L., Phenethylammonium Functionalization Enhances Near-Surface Carrier Diffusion in Hybrid Perovskites. *J. Am. Chem. Soc.* **2020**, *142*, 16254–16264. DOI: 10.1021/jacs.0c04377.
17. Guo, S.; Zhao, Y.; Bu, K.; Fu, Y.; Luo, H.; Chen, M.; Hautzinger, M. P.; Wang, Y.; Jin, S.; Yang, W.; Lü, X., Pressure-Suppressed Carrier Trapping Leads to Enhanced Emission in Two-Dimensional Perovskite $(HA)_2(GA)Pb_2I_7$. *Angew. Chem. Int. Ed.* **2020,** *59*, (n/a). DOI: 10.1002/anie.202001635.
18. Song, K.; Liu, L.; Zhang, D.; Hautzinger, M. P.; Jin, S.; Han, Y.: Atomic-Resolution Imaging of Halide Perovskites Using Electron Microscopy. *Adv. Energy Mater.* **2020**, *10*, 1904006. DOI: 10.1002/aenm.201904006.
19. McClintock, L.; Xiao, R.; Hou, Y.; Gibson, C.; Travaglini, H. C.; Abramovitch, D.; Tan, L. Z.; Senger, R. T.; Fu, Y.; Jin, S.; Yu, D.: Temperature and Gate Dependence of Carrier Diffusion in Single Crystal Methylammonium Lead Iodide Perovskite Microstructures. *J. Phys. Chem. Lett.* **2020**, *11*, 1000-1006. DOI: 10.1021/acs.jpclett.9b03643.

Electroactive Subunits in Insulating Polymer Heterostructures

Howard E. Katz, Daniel H. Reich, Arthur E. Bragg, and Tim Mueller, Departments of Materials Science and Engineering, Physics and Astronomy, and Chemistry, Johns Hopkins University, 3400 North Charles Street, Baltimore, Maryland 21117

Program Scope

The current program builds on results obtained from static charge storage experiments on blended and attached small electroactive molecules in organic transistor gate dielectric polymers based on polystyrene backbones. The key innovation in the present work is to design and investigate electroactive organic crystallites, rather than individual molecules, as the charge-storing subunits. The crystallites show broad electronic capabilities, e.g. polarizability, memory effects and transport capabilities, and can be deployed in more intricate self-assembled morphologies. The key project tasks are synthesis, heterostructure formation, x-ray scattering, spectroscopy, and multiscale electronic characterization within different device architectures for enhancements in energy storage, utilization, and conversion based on organic materials.

Recent Progress

Highly dilute small molecule phenylenediamine donors. We incorporated two strong phenylenediamine electron donors, N,N'-diphenyl-N,N'-di-p-tolylbenzene-1,4-diamine (MPDA, **1**) and 4-anilinotriphenylamine (PATPA, **2**) (Figure 1), into polystyrene (PS) gate dielectrics in

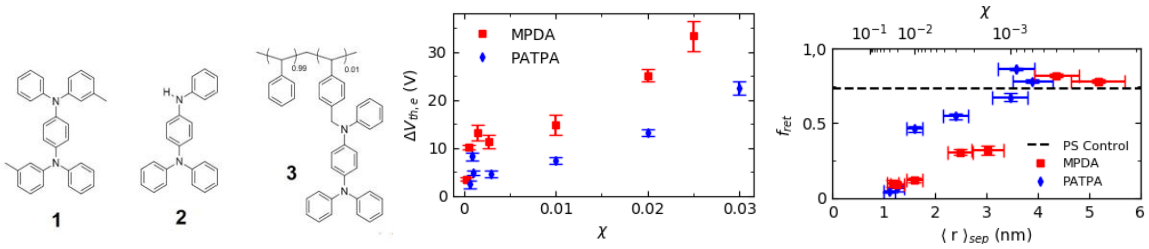

Figure 1. Phenylenediamines MPDA (**1**), PATPA (**2**), and tethered PATPA (**3**); plots of excess threshold voltage shift $\Delta V_{th,e}$ vs. mole fraction of additive χ for OFETs with PATPA and MPDA blend dielectrics, above that of co-fabricated devices with pure PS dielectrics, and fraction f_{ret} of post-charge threshold voltage shift retained at the end of characterization plotted against the average molecule separation $\langle r \rangle_{sep}$.

pentacene transistors. We found that the effect of these molecules on transistor characteristics after static charging extended to additive mole fractions as low as 3 x 10^{-4}. At the lowest mole fractions, there was a stable enhancement to the charge stored in the system. On the other hand, there was an inverse relationship between the amount of charge that could be stored, assessed from the threshold voltage shift (ΔV_{th}) of the transistors, and the stability of the shifts at larger mole fractions near 10^{-2}, where inter-additive molecule distances became comparable to their

size (~1 nm) and hopping transport becomes possible, suggesting that suggest that the average intermolecular separation is a key determinant of charge storage stability in blended dielectrics.

Highly branched, nearly interconnected phenylenediamine donors. We synthesized a much larger, highly branched electron donating phenylenediamine oligomer **4**, as well as a polymethoxylated triphenylamine donor **5**, and attached them to 2% of the monomer units in PS gate dielectrics (Figure 2). This appeared to be the maximum combination of molecular charge stabilizing activity and side chain concentration that still allowed gate dielectric function. We determined the effect of modifying the highly branched oligomer by mixing coordinating, electron-donating ZnO nanoparticles and attaching an electron withdrawing tricyanovinyl group by reaction with tetracyanoethylene (TCNE) as verified using visible and near-infrared

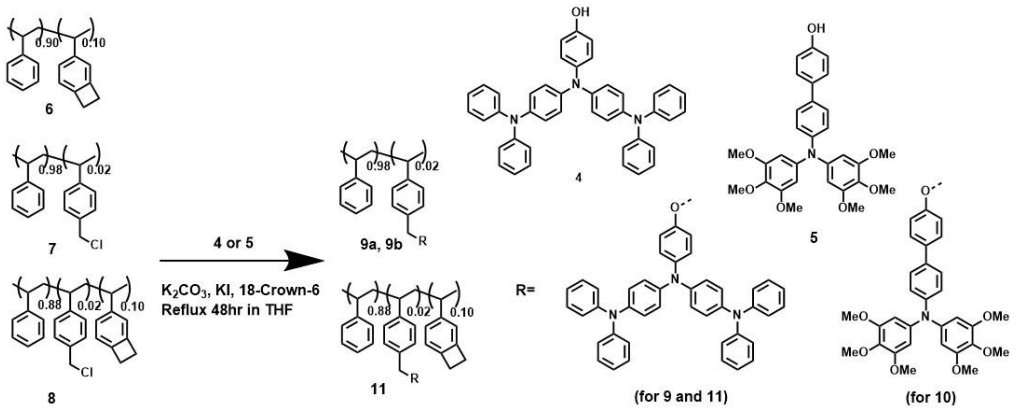

Figure 2. Synthetic chemistry and intermediates for highly branched phenylenediamine donors.

spectroscopy. We used three architectures: with substituted PS as a single layer dielectric (barely functional as a gate, insignificant charge storage), on top of a crosslinked PS layer but in contact with the pentacene (bilayers), and sandwiched between two PS layers in trilayers (Figure 3). Particularly large bias stress effects and ΔV_{th}, larger than the hexamethoxy and previously studied dimethoxy analogs, were observed in the second case and the effects increased with the increasing electron donating properties of the modified side chains. The highest ΔV_{th} was consistent with most of the side chains stabilizing trapped charge. Trilayer devices showed decreased charge storage capability compared to previous work in which we used less donating side chains but in higher concentrations. The ZnO and TCNE modifications resulted in slightly more and less negative ΔV_{th}, respectively. A trend of

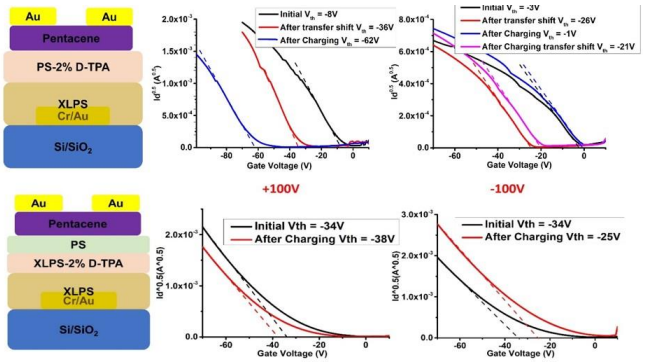

Figure 3. Device structures and representative transfer curves. Top: bilayer showing transfer curve affected by bias stress followed by additional ΔV_{th} from charging. Bottom: trilayer showing transfer curves before and after charging.

increased negative ΔV_{th} with increasing electron donating ability was observed among the differently modified side chain-substituted polymers, verifying the side chain controlling of ΔV_{th} and indicating that charge storage was directly associated with the attached molecules.

Conjugated small molecule crystallites. We hypothesize that charge storage by conjugated molecule crystallites in dielectrics will be distinct from that of small, nonaggregating molecules, and will lead to percolated charge transport at high enough crystallite number density. We began by studying α-quaterthiophene (α-4T) in PS. α-4T is marginally soluble in PS and in solvents for PS, and thus readily precipitates after spincoating and thermal annealing. Crystallites in PS are observed by laser optical and scanning electron microscopy, and are identified compositionally by energy-dispersive x-ray analysis showing sulfur, and by x-ray diffraction peaks matching α-4T. Figure 4 illustrates α-4T crystallite formation in PS.

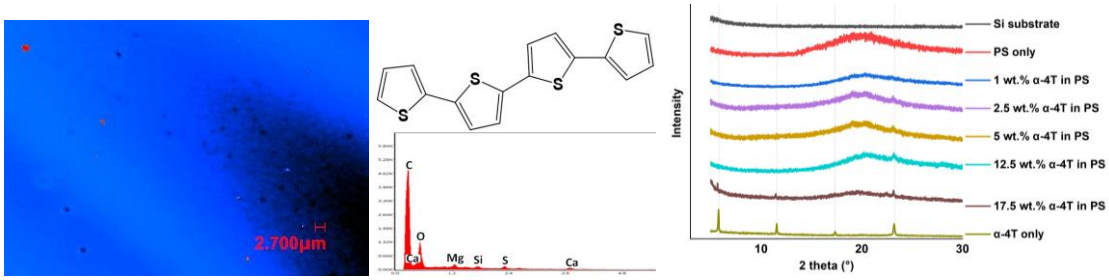

Figure 4. Crystallites (~1 µm), α-4T structure, sulfur peak in EDX of crystallite (red), and powder x-ray peaks.

Crystallite-PS composites with >5 wt. % α4T display measurable concentration-dependent conductance that increases further with oxidizing vapor doping. Lower concentrations, ~1%, show charge storage in pentacene transistors where two spin-coated composite layers serve as gate dielectric. When charged in the accumulation mode, the transistors show stabilization against bias stress. Depletion mode charging shows stepwise

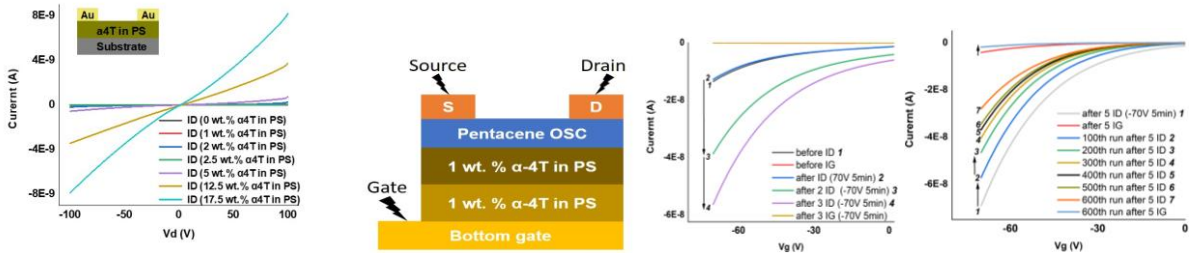

Figure 5. Two-terminal conductance vs α4T concentration, transistor configuration with 1% α4T in gate dielectric, and bias stress stabilization (1→2) and stepwise transistor current increases (2→3 and 3→4) and decreases (far right transfer curves, 1→2→…7).

output current increases that can be reversed in stages (neuromorphic-like behavior) (Figure 5). A preliminary scanning Kelvin probe characterization of the crystallites shows localized positive charge coincident with crystallite locations.

Density functional theory (DFT) calculations were performed on 5-hexyl-α4T to model α4T as an aggregated polymer side chain. Increasing aggregation number (cluster sizes) from 1-4 resulted in decreased ionization energy (increased hole stability) of about 0.8 eV in vacuum and PS surroundings. Aggregation did not significantly affect electron affinity. This is in contrast to an electron-accepting pyromellitic diimide (PyDI) derivative, the 2-molecule aggregate showing slightly increased electron affinity compared to the monomer (Figure 6).

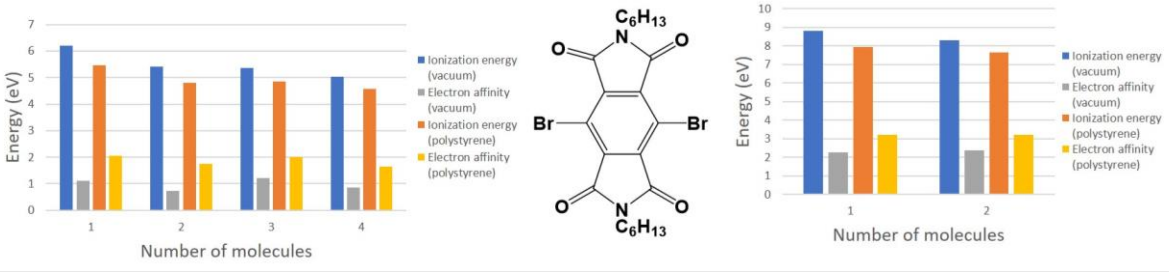

Figure 6. Result of DFT calculations on α4T aggregates (left) and PyDI monomer(M.L.Yeh) and dimer (right).

Polystyrene copolymers promoting crystallites. For greater morphology control, we are synthesizing diblock styrene copolymers in which aggregates of defined size and spacing will form. One block, containing highly conjugated and barely soluble side chains, is expected to phase separate and cause side chain aggregation. The first such side chain, anthracenamine, has been attached (Figure 7). For an initial n-type copolymer, chemistry for C_{60} attachment to PS is available from prior work(O.Alley).

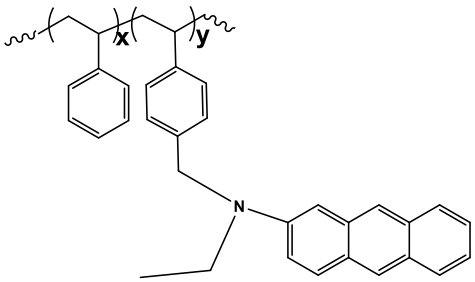

Figure 7. Anthracenamine side chain.

Future Plans

More electroactive and n-type molecules will be grown in and attached to polymers. Theoretical calculations of conjugated molecule solubility (related to crystallizability) in polymers will be carried out. The materials will be studied in additional configurations such as capacitors, memristors, and diodes. Connections to energy storage, information storage, and lighting will be pursued. More detailed morphology studies will be performed using x-ray reflectivity. Spectroscopic signatures of charged aggregates will be determined. Seebeck characterization of percolated aggregates will be done to determine carrier energy level distributions.

References

Earlier relevant papers supported under this program Alley, O.J.; et al. Macromolecules 49, 3478-3489 2016 (heterostructures, C_{60} attachemnt) and Yeh, M.L. et al., J. Mat. Chem. C, 3, 3029-3037 2015 (PyDI derivatives).

Publications Supported by This Program, Past Three Years. Department of Energy, Office of Science, Office of Basic Energy Sciences, Materials Research Program, grant number DE-FG02-07ER46465.

Ireland, R.M.; Wu, L.; Salehi, M.; Oh, S.; Armitage, N.P.; Katz, H.E.
"Nonvolatile Solid-State Charged-Polymer Gating of Topological Insulators into the Topological Insulating Regime" Physical Review Applied 9, 044003
https://doi.org/10.1103/PhysRevApplied.9.044003 2018

Zhang, Q.; Kale, T.; Plunkett, E.; Shi, W.; Kirby, B.K.; Reich, D.H.; Katz, H.E. "Highly Contrasting Static Charging and Bias Stress Effects in Pentacene Transistors with Polystyrene Heterostructures Incorporating Oxidizable N,N'-bis(4-Methoxyphenyl)aniline Side Chains as Gate Dielectrics" Macromolecules 51 6011-6020 10.1021/acs.macromol.8b00596 2018

Plunkett, E; Kale, T.S.; Zhang, Q.; Katz, H.E.; Reich, D.H.
"Effects of trifluoromethyl substituents on interfacial and bulk polarization of polystyrene gate dielectrics" Applied Physics Letters 114 023301 https://doi.org/10.1063/1.5080951 2019

Li, H.; Plunkett, E.; Cai, Z.; Qiu, B.; Wei, T.; Chen, H.; Thon, S.M.; Reich, D.H.; Chen, L.; Katz; H.E. "Dopant-Dependent Increase in Seebeck Coefficient and Electrical Conductivity in Blended Polymers with Offset Carrier Energies" Advanced Electronic Materials 5 1800618 https://doi.org/10.1002/aelm.201800618 2019

Jang, H.; Wagner, J.; Li, H.; Zhang, Q.; Mukhopadhyaya, T.; Katz, H.E.
"Analytical Platform to Characterize Dopant Solution Concentrations, Charge Carrier Densities in Films and Interfaces, and Physical Diffusion in Polymers Utilizing Remote Field-Effect Transistors" Journal of the American Chemical Society 141 4861-4869 10.1021/jacs.8b13026 2019

Zhang, Q.; Barrett, B.; Bragg, A.E.; Katz, H.E. "Static Polystyrene Gate Charge-Density Modulation of Dinaphthothienothiophene with Tetrafluorotetracyano quino dimethane Layer Doping: Evidence from Conductivity and Seebeck Coefficient Measurements and Correlations" ACS Applied Electronic Materials 1 2708-2715 10.1021/acsaelm.9b00747 2019

Barrett, B.; Saund, S.S.; Dziatko, R.A.; Clark-Winters, T.L.; Katz, H.E.; Bragg, A.E.
"Spectroscopic studies of charge-transfer character and photoresponses of F_4TCNQ-based donor-acceptor complexes" Journal of Physical Chemistry C 124 9191-9202
10.1021/acs.jpcc.0c01372 2020

Han, J.; Fan, H.; Zhang, Q.; Katz, H.E.; Hu, Q.; Russell, T.P. "Dichlorinated Dithienylethene-Based Copolymers for Air-Stable n-Type Conductivity and Thermoelectricity" Advanced Functional Materials 31 2005901 10.1002/adfm.202005901 2020

Plunkett, E.C.; Zhang, Q.; Katz, H.E.; Reich, D.H.
“Charge Trapping in Polymer Electrets with Highly Dilute Blended Aryl-amine Donors”
ACS Applied Electronic Materials 3, 1656-1662 10.1021/acsaelm.0c01116 2021

Multi-length Scale Synthesis of Silicon Materials

Rebekka S. Klausen, PI, Johns Hopkins University, Baltimore, MD, 21218

Program Scope

Hierarchical materials are forms of matter with defined levels of organization at multiple length scales. Hierarchical materials are also a unique approach to harnessing complex functionality across multiple length scales, allowing the emergence of unique properties not accessible from the individual components. While nature has perfected the multi-length scale synthesis and assembly of biological macromolecules such as proteins and nucleic acids, control of energy-relevant synthetic inorganic and organic hierarchical materials remains an enormous challenge for energy science.

This project describes strategies enabling the design and preparation of silicon-based hybrid materials across multiple length scales. Silicon is a transformative energy-relevant material and the technical and cultural revolutions arising from silicon microelectronics and silicon solar cells cannot be understated. Critical energy-relevant semiconductor properties such as light absorption and emission, electron transport, and stability are length-dependent. The preparation of well-defined hierarchical silicon materials is largely unexplored.

Recent Progress

Polymers based on main group elements find application as solution-processable precursors to ceramics (polymer-derived ceramics, PDCs). To understand microstructure-dependent polycyclosilane pyrolysis, three distinct polymer architectures **P1-3** were synthesized (Figure 1). Linear **P1** and cyclic **P2** were synthesized under a prior DOE award (DE-SC0013906), while **P3** is a new linear polymer of 1,3Si_6.

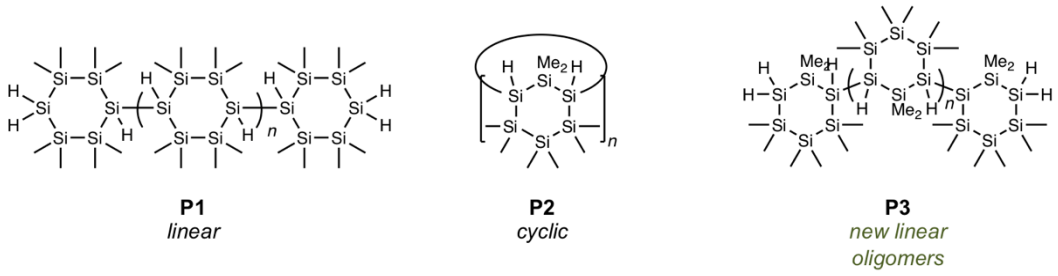

Figure 1. Linear and cyclic polymers of the cyclosilane building blocks **1,3Si$_6$** and **1,4Si$_6$**.

The thermal decomposition of **P1-3** was studied by thermogravimetric analysis (TGA, Figure 2). TGA curves of derivative weight change reveal two main phases of weight loss when samples are heated from 40 to 600 ˚C in argon flow. When temperature increased to 500 °C, about 50% weight loss is observed in all three samples. Then, the weight became constant above 550 ˚C. A black solid residue remained in the sample pan after the TGA measurement. These

observations are consistent with ceramization, although the ceramic will be characterized in future studies.

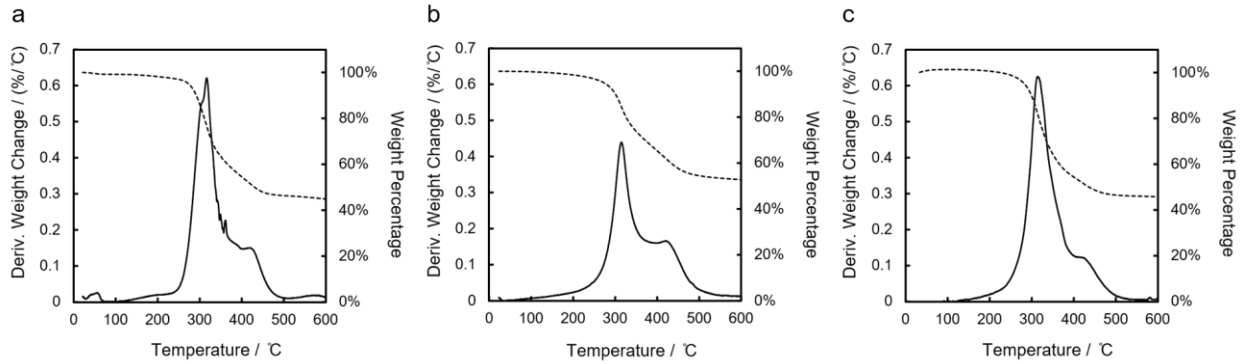

Figure 2. Thermogravimetric analysis of P1-3 shows lower mass loss in cyclic P2.

Some differences between the polymer systems were also apparent between 200 to 400 °C. **P1** and **P3** both showed similar derivative weight change in this region, with a peak value greater than 0.6, while for **P2** the peak value was lower than 0.5. Both linear polymers lost approximately 45% of their weight in this phase, while only 33% for cyclic **P2**. This indicates that linear **P1** and **P3** decomposed more rapidly than **P2** in this temperature range.

Computational studies indicated that the Si–Si bond between cyclosilane repeat units is the weakest bond in polycyclosilanes. These data suggest that the Si-Si bonds between monomers homolyse first in polycyclosilane thermolysis. Small, volatile silanes generated from homolysis near an end group in linear P1 and P3 would result in a significant weight decrease, which is consistent with the major weight loss observed between 200 to 400 ˚C in TGA measurements. In cyclic P2, without end groups, fewer volatile products may be formed as at least two Si–Si bond rupture events would be required to form a volatile byproduct. This may account for the slower mass loss observed in **P2** relative to **P1** and **P3**.

P1-3 were also studied by differential scanning calorimetry (DSC). Only the cyclic polymer P2 was found to exhibit a glass transition temperature at 108 °C. No phase transitions were apparent for **P1** and **P3** in the range 60 to 200 °C, below the decomposition temperature. These results are rationalized in terms of the known differences between cyclic and linear polymers: the lack of mobile end groups in cyclic polymers results in less reptation and elevated glass transition temperatures relative to linear systems.

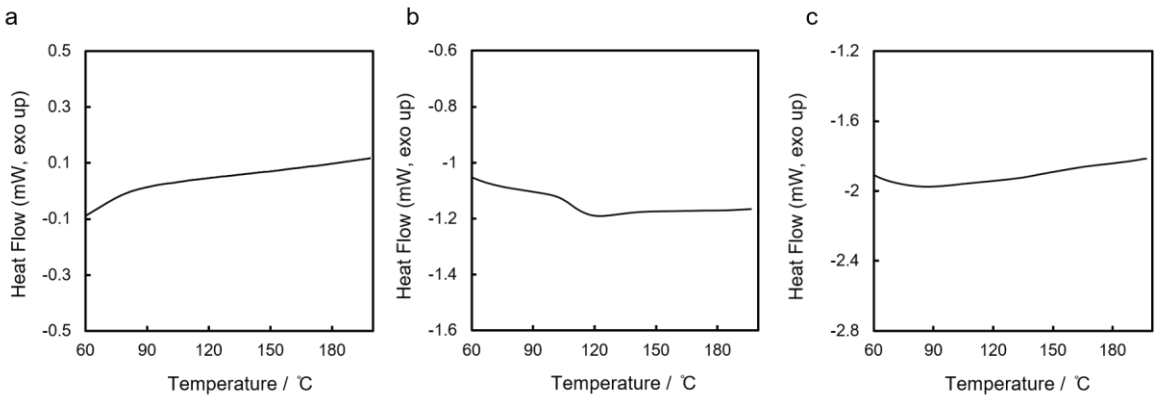

Figure 3. DSC curves for P1-3: only cyclic P2 exhibits a glass transition.

A significant challenge in the bottom-up synthesis of hierarchical materials is structure determination: can the hypothesized long-range order and structural regularity be conclusively determined? To address this challenge in silane materials, we reported a model system for determining relative configuration by NMR spectroscopy. This characterization tool will be particularly impactful in the context of materials that are semicrystalline or amorphous.

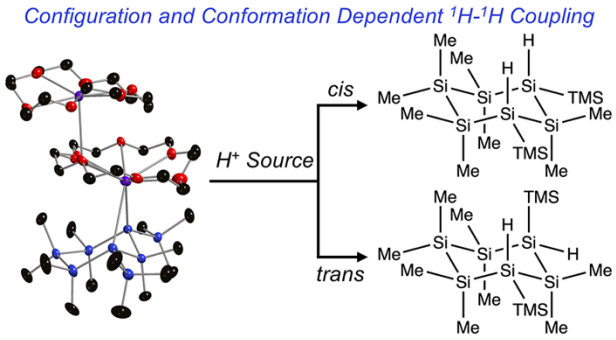

Figure 4. Stereoselective synthesis of either diastereomer of a mixed hydro- and methyl-substituted cyclosilane.

In this study, we stereoselectively synthesized both diastereomers of mixed methyl- and hydro-substituted cyclosilane possessing cis/trans relative configuration (Figure 5). Each diastereomer of 1 possessed distinct symmetry elements (*cis*-**1**: C_s-symmetric; *trans*-**1**: C2-symmetric). Cyclosilane **1** exhibited configuration- and conformation-dependent long-range proton–proton coupling. Extensive NMR spectroscopic characterization, including one-dimensional ^{1}H NMR and ^{29}Si DEPT and INEPT+ spectra and two-dimensional ^{1}H–^{29}Si and ^{1}H–^{1}H correlated spectroscopy (HSQC, HMBC, COSY). On the basis of these experiments, molecular connectivity consistent with four-bond ^{1}H–^{1}H coupling was confirmed. A "W-conformation" seen in the cis diastereomer is optimal for long-range coupling and allows for the cis and trans isomers to be distinguished by ^{1}H NMR.

Future Plans

Future work focuses on the synthesis of hybrid materials containing both cyclosilane and organic moieties, with a particular focus on catalytic methods affording high structural precision.

Supporting these efforts are additional studies on new cyclosilane building blocks and polymers, such as copolymers.

Publications Supported by This Award

1. Ferguson, J. T.; Jiang, Q.; Marro, E. A.; Siegler, M. A.; Klausen, R. S. Long-range Coupling in Cyclic Silanes, *Dalton Trans*., **2020**, *49*, 14951-14961.

2. Jiang, Q.; Klausen, R. S. Effect of Polycyclosilane Microstructure on Thermal Properties, *Polymer Chemistry*, **2021**, Advance Article, doi.org/10.1039/D1PY00383F

Crystal Growth and Quantum Phases of Frustrated Rare Earth Oxides

Joseph W. Kolis, Department of Chemistry, Clemson University,
Kate Ross, Department of Physics, Colorado State University

Program Scope

This project is a collaborative effort between Joseph Kolis in the Department of Chemistry at Clemson University and Kate Ross in the Department of Physics at Colorado State University. The goal is to grow high quality crystals containing three-dimensional trigonal symmetry, having magnetic ions with effective spin values of ½ within the lattice. The physical and magnetic properties of these materials are studied in detail using cryomagnetic and neutron scattering methods. Ideally, these materials will be subject to strong spin frustration with massively degenerate low temperature states. Frustrated geometries such as the ones we study here, combined with low spins, are ripe for emergent nonclassical behaviors such as quantum spin liquids. Most previous work on such effects has focused on 1-D systems like sawtooth chains, and 2-D layers like Kagome lattices. Work on 3-D systems is much more limited. This project targets two general classes of 3-D solids with trigonal symmetry, namely the pyrochlores and the cubic double perovskites.

Pyrochlores display considerable potential for emergent quantum behavior, particularly $RE_2B_2O_7$, where RE is a magnetic rare earth ion with S_{eff} =1/2, like Yb, Er or Pr, and B is a nonmagnetic tetravalent ion like Ti, Sn, or Ge. This is a potentially very rich class of materials with considerable experimental and theoretical background. The cubic double perovskites $A_2BB'O_6$ with rock salt B/B' site ordering are not well unexplored experimentally, but some early theoretical work is extremely promising. Some examples like Ba_2RESbO_6 are predicted to host strong Kitaev exchange which leads to unusual many-body quantum phenomena. There are two significant practical limitations to these investigations. One is the tendency to form atomic disorder over the A and B sites both in the pyrochlores and perovskites. The other problem is the formation of oxide defects in the lattice due to "stuffing", redox changes, or other related effects. Both issues can occur to a significant degree and cause problems in identifying new quantum behavior. We think we can overcome these problems using the precision synthesis methodology in the Kolis lab. This will provide samples with well-ordered sites and minimal lattice defects, which enable the Ross lab to perform low temperature magnetic and inelastic neutron scattering (INS) studies to begin to identify new emergent quantum phenomena such as quantum spin liquid behavior caused by spin frustration at low temperatures.

The Kolis lab employs a hydrothermal technology to grow refractory oxide materials at the relatively low temperatures of 600-750˚C in high pressure aqueous fluids. These relatively low temperatures and sealed reactor conditions lead to well-ordered A/B sites and relatively few lattice defects. In many cases large high-quality single crystals can also be grown as opposed to just powders. The single crystals are particularly useful for oriented studies in applied magnetic fields or for single crystal INS measurements, again including in external magnetic fields in some cases. The Ross lab is well equipped to perform cryogenic physical property measurements ($\geq$ 50mK) including heat capacity measurements, magnetic profiling, and heat capacity measurements in an

applied magnetic field. In addition, Ross has extensive experience performing detailed INS measurements including studies in ultra-low temperatures and applied magnetic fields at user facilities such as Oak Ridge National Laboratory's Spallation Neutron Source and High Flux Isotope Reactor. Finally, Ross has a rich network of theoretical collaborators to help interpret and clarify results. This collaborative approach is an excellent route to the designed preparation of new quantum materials.

Recent Progress

Our initial approach focused on the $RE_2B_2O_7$ pyrochlores where RE = Er, Yb and B = Sn, Ge). These types of materials already showed considerable promise as potential emergent quantum phases but were also somewhat hindered by the factors described above. We were fortunate to be able to prepare single crystals of $Er_2Ge_2O_7$ and $Yb_2Ge_2O_7$ in the desired cubic phase. It is ordinarily difficult to access these germanates in the cubic phase as the smaller Ge ion tends to stabilize a lower symmetry tetragonal phase and extremely high pressures are normally required to stabilize the cubic phase. Using suitable hydrothermal conditions (ca.700˚C/200MPa in 10M CsOH) we were able to grow well ordered high quality single crystals of the cubic phases for detailed INS and magnetic studies. We were able to apply these conditions to the corresponding tin analogs and found that all the lanthanide pyrochlores can be grown as large high quality single crystals in the cubic phase. To our knowledge this is the only tetravalent B ion than allows all the rare earth analogs to form. Detailed work with neutron, magnetic and heat capacity measurements $Er_2Sn_2O_7$ and $Yb_2Sn_2O_7$ were undertaken for direct comparison with the germanate analogs (see below). A particularly interesting system is $Ce_2Sn_2O_7$ since it is theoretically predicted to display unique dipole-octupole QSL behavior. Like many Ce^{3+} compounds it presents a number of synthetic challenges, but we recently optimized a hydrothermal approach that allows scaleup of pure crystals. (Fig. 1) We performed some detailed X-ray diffraction experiments to indicate the purity and site ordering of the material. Since Ce is a weak neutron scatterer, we had to prepare a fairly large quantity of very pure material for neutron scattering. These experiments are now underway.

We recently turned our attention to the ordered double perovskites $A_2BB'O_6$. In the rock salt ordered phase the cubic symmetry is retained along the corresponding 3-D trigonal symmetry. We prepared single crystals of Rb_2NaYbF_6 and Ba_2ErSbO_6 and demonstrated that they are cubic with complete B/B' site ordering. In the case of Rb_2NaYbF_6 however, we were unable to observe any magnetic coupling even down to 50mK, the lowest possible measuring temperature for our instruments. This is attributed to the long through-space coupling distances (≥7Å) between the weakly coupling rare earth ions. In an attempt to increase the coupling constant between the magnetic centers in these double perovskites we synthesized large single crystals of Ba_2CoWO_6. We demonstrated that the large single crystals are again cubic and well site ordered. Magnetic measurements are underway on these materials. Initial magnetic studies indicate that these compounds order at 17K despite having interaction distances similar to those in Rb_2NaYbF_6, showing that these S_{eff} = ½ Co^{2+} ions may display coupling magnitudes suitable for experimental observation of frustration and other quantum magnetic behavior in the double perovskites. Synthetic and magnetic work on these systems is continuing.

The results to date obtained from Ross' group on crystals grown in the Kolis lab include: 1) an INS study of spin waves in $Yb_2Ge_2O_7$, which enabled the quantitative determination of interactions

between quantum spins on the Yb ions and thereby provided an explanation for the strange magnetic behavior seen across multiple Yb pyrochlores, 2) observation of "reentrance" in the magnetic field vs. temperature phase diagram of $Er_2Sn_2O_7$, which can be explained via a new mechanism of reentrance, (Fig. 2) and 3) an unusually clear example of the existence of pseudo-spins with no magnetic moment in certain directions, resulting from a neutron diffraction experiment on the triangular lattice material $K_3ErV_2O_8$.

Future Plans

Our most immediate plans include heat capacity measurements and detailed neutron scattering investigation of $Ce_2Sn_2O_7$. At present we are performing neutron scattering experiments on a powder sample. The next step will be experiments in an applied magnetic field. If warranted, future neutron scattering experiments will employ oriented single crystals. Subsequent work may involve other Ce^{3+} pyrochlores such as $Ce_2Zr_2O_7$ and $Ces_2Hf_2O_7$. Other S_{eff} = ½ pyrochlores may be targeted such as $Yb_2Pt_2O_7$. The double perovskites also show a great deal of early promise, especially those containing the S_{eff} = ½ Co^{2+} ion. They show an appropriate degree of through space magnetic coupling across the double perovskite distance to suggest further investigation.

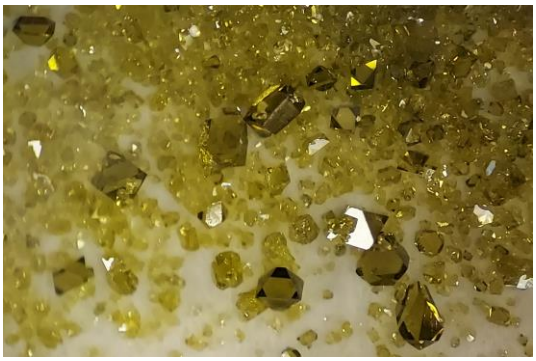

Figure 1. Crystals of $Ce_2Sn_2O_7$ (1-2mm)

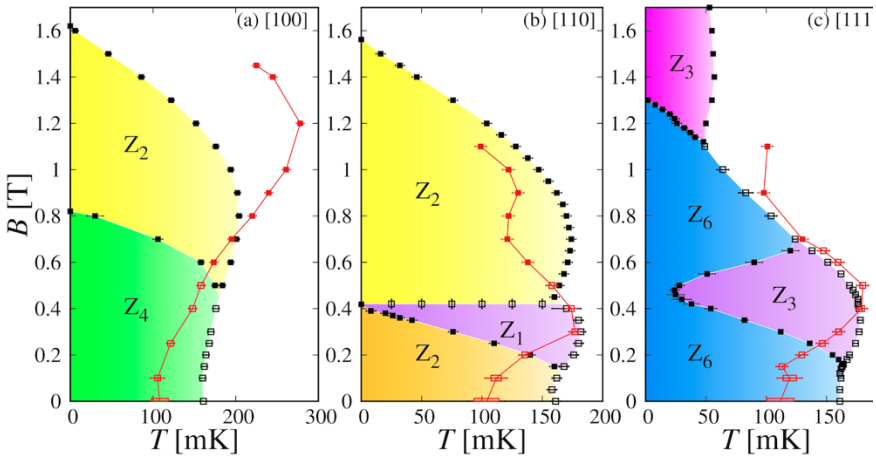

Figure 2. B-T phase diagrams of $Er_2Sn_2O_7$ in the (a) [100], (b) [110] and (c) [111] field directions, comparing experimental data with sharp and smooth heat-capacity peaks

Publications from this work

"High Temperature Hydrothermal Synthesis of Inorganic Compounds" Kolis, J. W.; McMillen, C. D. Comprehensive Inorganic Chemistry **2021** submitted.

"Understanding Reentrance in Frustrated Magnets: The Case of $Er_2Sn_2O_7$ Pyrochlore" Yahne, D.R.; Pereira, Jaubert, L. C. D. Sanjeewa, L. D.; Powell, M.; Kolis, J. W. Xu, G.; Gingras, M. J. P.; Ross, K. A. Phys. Rev. Lett. **2021** in revision. arXiv preprint arXiv:2101.08361. 2021 Jan 20.

"Thermochemistry of Rare Earth Oxyhydroxides, REOOH (RE =Eu-Lu)" S. Yang, M. Powell, J.W. Kolis, A. Navrotsky J. Solid State Chem. **2020**, 287,121344 doi.org/10.1016/j.jssc2020.121344.

"Unravelling competing microscopic interactions at a phase boundary: a single crystal study of the metastable antiferromagnetic pyrochlore $Yb_2Ge_2O_7$" Sarkis, C. L.; Rau, J. G.; Sanjeewa, L. D.; Powell, M.; Kolis, J. W.; Marbey, J.; Hill, S.; Rodriguez-Rivera, J. A,; Nair, H. A.; Gingras, M. J. P.; Ross, K. A. Phys Rev. B. **2020** 102, 134418. 10.1103/PhysRevB.102.134418

"Pseudo-Spin Versus Magnetic Dipole Moment Ordering in the Isosceles Triangular Lattice Material $K_3Er(VO_4)_2$" D. R. Yahne, L. D. Sanjeewa, A. S. Sefat, B. Stadleman J. W. Kolis, S. Calder, K. A. Ross* Phys Rev B **2020** 102, 104423 DOI: 10.1103/PhysRevB.102.104423.

"Quantification of local-Ising magnetism rare-earth pyrogermanates $Er_2Ge_2O_7$ and $Yb_2Ge_2O_7$" D. M. Pajerowski, K. M. Taddei, L. Sanjeewa, A. T. Savici, M. B. Stone, J. W. Kolis Phys. Rev. B **2020** 101, 014420. 10.1103/PhysRevB.101.014420

C.L. Sarkis Ph.D. Dissertation Colorado State University *Frustration Driven Emergent Phenomena in Quantum and Classical Magnets* (March 2021)

Novel 2D Materials and Structures via Janus Manipulation

Jing Kong, Massachusetts Institute of Technology

Program Scope

This project aims at developing a variety of novel 2D materials and structures via our Janus manipulation technique, in the following three areas: (1) synthesis of Janus TMDs such as MoSSe, WSSe, WSTe, etc and investigate their intriguing properties; (2) development of heterostructures (vertical or lateral) based on Janus TMDs to enable a wide range of energy related applications; (3) novel synthetic route and materials discovery, including developing novel synthetic route for existing 2D materials, or synthesizing novel 2D materials that has been theoretically speculated but have not been obtained up to now.

Recent Progress

Under the support of this project, during the past two and half years, we have made the following progress:

1. At the time of starting this project, we discovered that our Janus conversion can be carried out at room temperature. During the past couple of years, we have greatly utilized this fact and developed a variety of novel structures that have never been realized before (please see section 2 with details). In addition, through our collaborations with Prof. Ting Cao's group in U. of Washington, we have obtained understanding why this process can occur, basically the reaction path is steered in a way that only very small barriers are involved, this is in contrast to typical methods[1,2] when the metal-chalcogen bond is broken first by high temperature or other means, as illustrated in Figure 1 (our method is labeled at RT-ALS: room-temperature atomic layer substitution). This could inspire the formation of other novel structures.

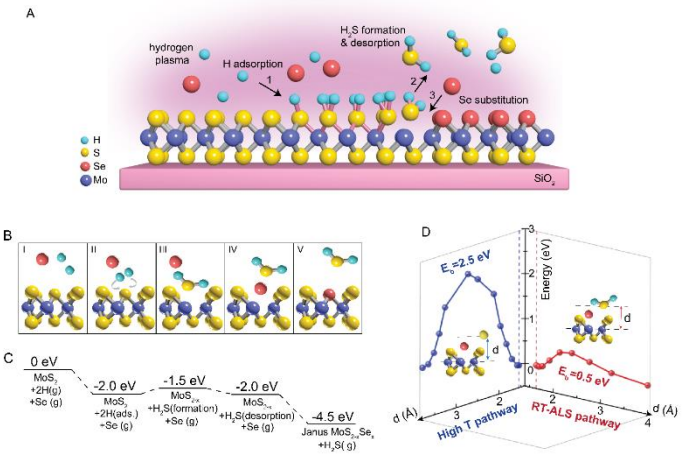

Figure 1. (A) Schematic illustration of our Janus conversion process. (B) Schematics of the five key reaction steps (cartons from left to right): before H adsorption, 2 H adsorption and diffusion to the same S, formation of H_2S, desorption of H_2S, and Se occupation of the S vacancy. (C) Free energy of each steps in (B), relative to that of the first step. (D) Comparison of activation energy barrier between our method (red) and the conventional high-temperature substitution (blue). In RT-ALS process, the largest energy barrier occurs at a critical distance where H_2S starts to form. In the high-temperature pathway, the largest energy barrier corresponds to when S and Se are both disconnect with Mo.

2. Because we were able to carry out the Janus conversion at room temperature, we can combine lithography patterning and flip transfer technique to obtain programmable in-plane patterns with different out-of-plane crystal symmetry and electric polarization (as shown in

Figure 2). This enables us to obtain a completely new class of monolayer lateral heterostructures and multi-heterostructures with dipole/non-dipole structures, and the vertical dipole can be either pointing up or pointing down the 2D plane. Unusual physical properties and unprecedented functionality could be possible on such a platform, ranging from nonlinear optics, electronic band engineering, nanoscale origami, to electrochemical catalysis, all of which can be modulated by different electrostatic forces (currently we are trying to set up different collaborations to explore their properties)

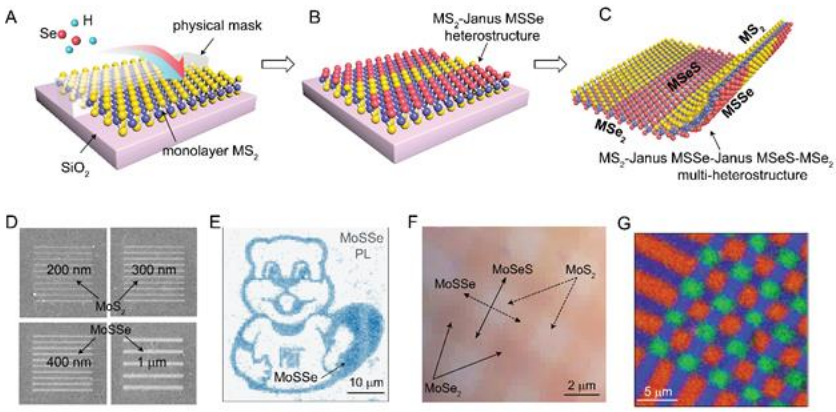

Figure 2. (A-C) Schematic illustration of novel structures enabled by combining lithography and flip-transfer with our Janus conversion (D) SEM images of monolayer Janus MoSSe-MoS_2 stripe patterns with different widths. (E) Spatially resolved PL mapping for a MIT mascot "Tim the beaver" pattern (Janus MoSSe) on a monolayer MoS_2 canvas (F) Optical microscope image of monolayer multi-junction composed with MoS_2-Janus MoSSe-Janus MoSeS-$MoSe_2$. (G) Spatially resolved Raman mapping for A_{1g} mode intensity of monolayer multi-heterostructures based on MoS2-Janus MoSSe-Janus MoSeS-MoSe2. The red area represents MoS_2 region, the blue one represents Janus region and the green one represents $MoSe_2$ region. and the conventional high-temperature substitution (blue).

3. Up to now, we have successfully carried out the following conversions: (1) from 2H MoS_2 to 2H MoSSe, then to 2H $MoSe_2$; (2) from 2H $MoSe_2$ to 2H MoSeS, then to 2H MoS_2; (3) from 2H WS_2 to WSSe, then to WSe_2; (4) from 2H WSe_2 to WSeS, then to WS_2; in addition to the **2H** TMD monolayer, we have also investigated the conversion (5) from **1T'** MoS_2 to 1T' MoSSe, these indicate the universality of our method. We have been having challenges to obtain MoSTe starting from MoS_2, but in the coming year we are planning to using monolayer 2H and 1T' $MoTe_2$ as starting material for this investigation (please see future plans).

4. In terms of characterization of these Janus TMD materials, we have carried out collaborations with Prof. Shengxi Huang's group at PennState University regarding how the vertical dipole and strain in the Janus TMD affect the interlayer interaction between Janus TMD layer and normal TMD layer. We have found out that these features strongly enhance the vdW interlayer coupling by as much as 13.2% when forming MoSSe/MoS_2 heterostructure as compared to the pristine MoS_2 counterparts. For this work we used noncontact ultralow-frequency Raman spectroscopy for the characterization. We also worked with Prof. Efthimios Kaxiras' group at Harvard University to carried out theoretical understanding on this

phenonmenon. Based on our linear chain model and density functional theory calculations, the enhancement is confirmed and the origins could be understood as charge redistribution in Janus MoSSe and reduced interlayer distance. These results uncover the potential of tuning interlayer coupling strength through Janus heterostacking. Our manuscript has been published in JACS.

5. We have carried out collaborations with Prof. Ju Li's group on the theoretical prediction that monolayer Janus TMDs in the 1T' phase possess colossal nonlinear photoconductivity owing to their topological band mixing, strong inversion symmetry breaking, and small electronic bandgap. 1T' Janus TMDs have inverted bandgaps on the order of 10 meV and are exceptionally responsive to light in the terahertz (THz) range. The shift current conductivity can be as large as 2300 nm μA V^{-2}, equivalent to a photo-responsivity of 2800 mA/W. The circular current (CC) conductivity of 1T' Janus TMDs is as large as$\sim 10^4$ nm μA V^{-2}. This manuscript has been published in npj Computational Materials.

6. During the course of this project, Dr. Yunfan Guo and Dr. Nannan Mao (who are supported by this project) have also carried out collaborations within our own group or outside our group. Even though these progresses are not in the direction of Janus materials, they are important progresses in the field acknowledging the support of this project.

Future Plans

In the coming year, and also the following few years, we are planning to carry out the following investigations:

1. The incorporation of Se atoms into MoS_2 structure causes a strain in the lattice. Researchers have proposed to utilize the strain to form interesting Origami and Kirigami structures. However, the strain in the Janus structure has not been well studied yet due to the limitation of obtaining the samples. We are planning to work with Prof. Yimo Han's group at Rice University to use STEM to characterize the strain in MoSSe and also at the interface between lateral heterostructures of MoS_2 and MoSSe.
2. The intrinsic properties of the Janus TMDs have not been thoroughly explored. We are planning to collaborate with Prof. Xiaodong Xu's group at University of Washington to study the properties of MoSSe and WSSe, their excitons, exciton binding energies, etc.
3. Previously interesting single photon emission (SPE) behaviors were found in WSe_2 monolayers [3, 4]. Researchers have also identified that by straining the TMD lattice, SPE can be controllably introduced [5]. Since intrinsic strains were introduced into the WSSe lattice, we are planning to investigate SPEs in these WSSe structures.
4. In our collaboration with Prof. Ju Li's group, we have identified the fascinating properties of 1T' MoSTe. Up to now, we had limited success for the conversion of MoS_2 to MoSTe, possibly due to the weaker bonding between Mo and Te compared to Mo with S. In the coming year we are planning to using 1T' $MoTe_2$ as a starting material, to obtain 1T' MoSTe.

References

[1] Jing Zhang, Shuai Jia, Iskandar Kholmanov, Liang Dong, Dequan Er, Weibing Chen, Hua Guo, Zehua Jin, Vivek B. Shenoy, Li Shi, and Jun Lou, "Janus Monolayer Transition-Metal Dichalcogenides". *ACS Nano* **11**, 8192-8198 (2017).

[2]Yu-Chuan Lin, Chenze Liu, Yiling Yu, Eva Zarkadoula, Mina Yoon, Alexander A. Puretzky, Liangbo Liang, Xiangru Kong, Yiyi Gu, Alex Strasser, Harry M. Meyer III, Matthias Lorenz, Matthew F. Chisholm, Ilia N. Ivanov, Christopher M. Rouleau, Gerd Duscher, Kai Xiao, and David B. Geohegan, "Low Energy Implantation into Transition-Metal Dichalcogenide Monolayers to Form Janus Structures". *ACS Nano* **14**, 3896-3906 (2020)

[3] M. Koperski, K. Nogajewski, A. Arora, V. Cherkez, P. Mallet, J.-Y. Veuillen, J. Marcus, P. Kossacki & M. Potemski, "Single photon emitters in exfoliated WSe_2 structures", Nature Nanotech 10, 503–506 (2015)

[4] Yu-Ming He, Genevieve Clark, John R. Schaibley, Yu He, Ming-Cheng Chen, Yu-Jia Wei, Xing Ding, Qiang Zhang, Wang Yao, Xiaodong Xu, Chao-Yang Lu & Jian-Wei Pan, "Single quantum emitters in monolayer semiconductors", Nature Nanotech 10, 497–502 (2015)

[5] Carmen Palacios-Berraquero, Dhiren M. Kara, Alejandro R.-P. Montblanch, Matteo Barbone, Pawel Latawiec, Duhee Yoon, Anna K. Ott, Marko Loncar, Andrea C. Ferrari & Mete Atatüre, "Large-scale quantum-emitter arrays in atomically thin semiconductors", Nat Commun 8, 15093 (2017).

Publications

List of publications SUPPORTED BY BES:

1. Yunfan Guo, Yuxuan Lin, Kaichen Xie, Biao Yuan, Jiadi Zhu, Pin-Chun Shen, Ang-Yu Lu, Cong Su, Enzheng Shi, Kunyan Zhang, Zhengyang Cai, Jihoon Park, Qingqing Ji, Jiangtao Wang, Xiaochuan Dai, Xuezeng Tian, Shengxi Huang, Letian Dou, Ju Li, Yi Yu, Juan-Carlos Idrobo, Ting Cao, Tomás Palacios, Jing Kong, "Designing Artificial Two-Dimensional Landscapes via Room-Temperature Atomic-Layer Substitution", arXiv preprint arXiv:2011.07690 (manuscript under review at PNAS)
2. Haowei Xu, Hua Wang, Jian Zhou, Yunfan Guo, Jing Kong, Ju Li, "Colossal switchable photocurrents in topological Janus transition metal dichalcogenides", npj Computational Materials, 7, 1-9 (2021)
3. Kunyan Zhang, Yunfan Guo, Daniel Larson, Ziyan Zhu, Shiang Fang, Efthimios Kaxiras, Jing Kong, Shengxi Huang, "Tailoring interlayer coupling and charge transfer by Janus transition metal dichalcogenide", submitted to ACS Nano.
4. Kunyan Zhang, Yunfan Guo, Qingqing Ji, Ang-Yu Lu, Cong Su, Hua Wang, Alexander A Puretzky, David B Geohegan, Xiaofeng Qian, Shiang Fang, Efthimios Kaxiras, Jing Kong, Shengxi Huang, "Enhancement of van der Waals interlayer coupling through polar Janus MoSSe", JACS, 142, 17499-17507 (2020)
5. Qingqing Ji, Cong Su, Nannan Mao, Xuezeng Tian, Juan-Carlos Idrobo, Jianwei Miao, William A Tisdale, Alex Zettl, Ju Li, Jing Kong, "Revealing the Brønsted-Evans-Polanyi Relation in Halide-Activated Fast MoS2 Growth Towards Millimeter-Sized 2D Crystals", arXiv preprint arXiv:2103.07031 (manuscript under review at Science Advances)
6. Pin-Chun Shen, Cong Su, Yuxuan Lin, Ang-Sheng Chou, Chao-Ching Cheng, Ji-Hoon Park, Ming-Hui Chiu, Ang-Yu Lu, Hao-Ling Tang, Mohammad Mahdi Tavakoli, Gregory Pitner, Xiang Ji, Zhengyang Cai, Nannan Mao, Jiangtao Wang, Vincent Tung, Ju Li, Jeffrey Bokor, Alex Zettl, Chih-I Wu, Tomás Palacios, Lain-Jong Li, Jing Kong, "Ultralow contact resistance between semimetal and monolayer semiconductors", Nature, 593, 211-217 (2021)
7. Zhiren Zheng, Qiong Ma, Zhen Bi, Sergio de la Barrera, Ming-Hao Liu, Nannan Mao, Yang Zhang, Natasha Kiper, Kenji Watanabe, Takashi Taniguchi, Jing Kong, William A Tisdale, Ray Ashoori, Nuh Gedik, Liang Fu, Su-Yang Xu, Pablo Jarillo-Herrero, "Unconventional ferroelectricity in moiré heterostructures", Nature, 588, 71-76 (2020)

Unraveling the links between molecular structure, microstructure, delocalization and charge transport in new high-performance semiconducting polymers

Christine K. Luscombe, University of Washington; Alberto Salleo, Stanford University; Frank C. Spano, Temple University

Program Scope

π-Conjugated polymers have received significant research attention for use in a number of applications including organic light emitting diodes (OLEDs), organic photovoltaics (OPVs), and more recently in the area of bioelectronics. All these applications rely on an important intrinsic property of the semiconductor: its ability to transport charge efficiently. In this award, the Salleo (characterization), Spano (theory), and Luscombe (synthesis) groups are working together to understand in greater detail how short-range vs. long-range order affects charge transport in these polymers. As a starting point of this work, we are focusing on donor-acceptor copolymers that have high charge mobilities but one where the polymer is known to have a level of crystallinity (i.e. have long range order, specifically diflourobenzothiadiazole (F2BT) and diketopyrrolopyrrole (DPP)-based polymers) and be highly disordered (i.e. have short range order, specifically, indacenothiophene (IDT)-based polymers).

Recent Progress

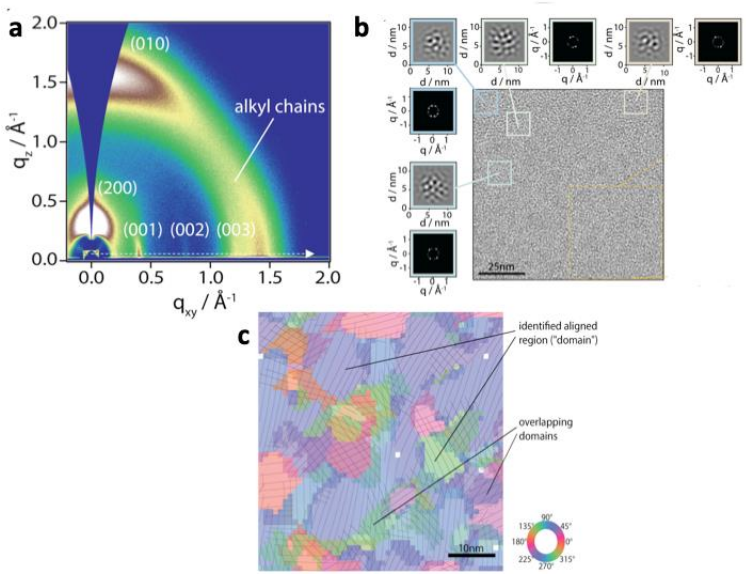

Figure 1: GIWAXS pattern of IDT-BT showing a backbone peak (001) on the q_z=0 axis and lamellar (200) and p-stacking (010) peaks on the q_{xy}=0 axis (a). HRTEM image showing examples of windows where the Fourier transforms are calculated and the backbone peaks in those windows (b). Reconstructed microstructure with aligned nanocrystalline domains (c).

The *Salleo* group has used spectroscopic and microstructural characterization techniques, coupled with the *Spano* group analysis on materials made by the *Luscombe* group[1] in order to elucidate how molecular conformation and microstructure couple in governing charge delocalization and transport. As far as materials system, we focused on indacenodithiophene-co-benzothiadiazole (IDT-BT) for several reasons: (1) it is a co-polymer allowing us to test the D-A extension of the theory by *Spano*; (2) it has been proven to have exceptional charge transport characteristics conventionally attributed to low energetic disorder; (3) it has a disordered microstructure with weak and broad X-ray diffraction peaks. As a result, this material is interesting as it presents a paradox whereby structural disorder is not coupled to energetic disorder and typically ensuing poor charge transport.[2] Furthermore, structural disorder makes it challenging to characterize allowing us to refine our methods. For structural characterization we used a combination of cryo-high-

resolution TEM (HRTEM) and synchrotron-based x-ray diffraction.[3] Cryo capabilities are needed to avoid beam damage and sample wandering, nevertheless correction algorithms were developed specifically to eliminate sample wandering, which would create an alignment artifact in the images, creating the illusion that the polymer is more aligned than it is in reality.

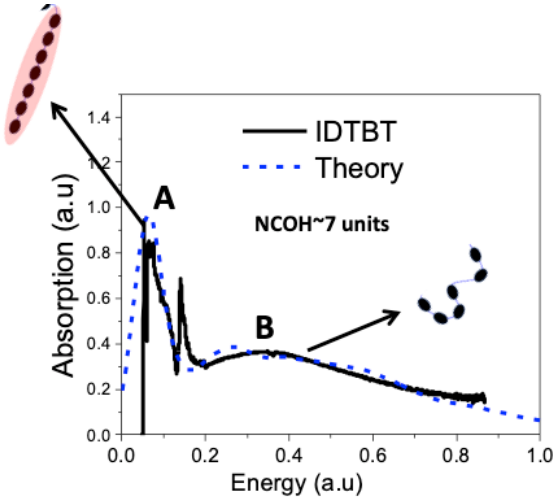

Figure 2: CMS spectrum of an IDT-BT film showing a high-intensity, low-energy A peak due to highly delocalized charges and a low-intensity, high-energy B peak due to charges localized in disordered regions of the polymer.

While this polymer is often described as quasi-amorphous, a sharp diffraction peak attributed to periodicity along the backbone direction is visible at q~0.4Å^{-1} with a coherence length of approximately 9 D-A repeat units (Fig. 1a). Such long coherence length is due to the relative high rigidity of the polymer. In addition to the backbone peak, the X-ray diffraction pattern displays both a broad π-stacking peak and a sharper lamellar peak along the q_{xy}=0 axis. The texture of the polymer appears thus a mix of edge-on and face-on polymer, not allowing us to exclude that π-stacking and interchain delocalization might play a role in in-plane transport processes. In order to characterize the material by HRTEM, we set the defocus to maximize the contrast transfer function at the backbone spatial frequency. HRTEM micrographs were sectioned into smaller windows to calculate local Fourier transforms that allow us to map the backbone direction everywhere in the field of view (Fig. 1b). This method reveals that the microstructure of IDT-BT is far from being quasi amorphous, as medium-range order with domain sizes on the order of ~20 nm, where the polymer backbones are approximately parallel to each other, is clearly visible (Fig. 1c). The rigidity and planarity of the backbone enable this microstructure while the side-chains prevent the formation of a truly semicrystalline microstructure (i.e. order in more than one crystallographic direction) due to steric hindrance. Because the only diffracting direction is along the backbone, we are unable to tell whether there is π-stacking in those nanocrystalline domains, which may allow 2D delocalization of the charges.

The *Salleo* group used charge-modulation spectroscopy (CMS) to char acterize the mid-IR (500 cm^{-1} to 3,000 cm^{-1}) absorption of polarons and the *Spano* group model for copolymers to gain more insight into their delocalization (Fig. 2). The spectrum is characterized by a sharp "A" low-energy peak (<600 cm^{-1}) and a broader, higher energy "B" peak (~3000 cm^{-1}). According to the model, these peaks strongly suggest that charges are located on a single chain. Thus we conclude that even if π-stacking occurs, it is inconsequential from the standpoint of transport. Furthermore, the A peak can be attributed to polarons strongly delocalized into ~7 repeat units while the B peak corresponds to polarons delocalized over a smaller distance of ~4 repeat units. Thus, we find that in IDT-BT the polarons have an "ordered" and a "disordered" signature, suggesting two different site populations in the polymer. Preliminary experiments indicate that the ordered signature can be entirely suppressed by replacing the benzothiadiazole monomer with benzopyrrolodione (IDT-BPD), which induces conformational torsion along the backbone of the polymer. Thus, we demonstrate that the combination of designer polymers, advanced

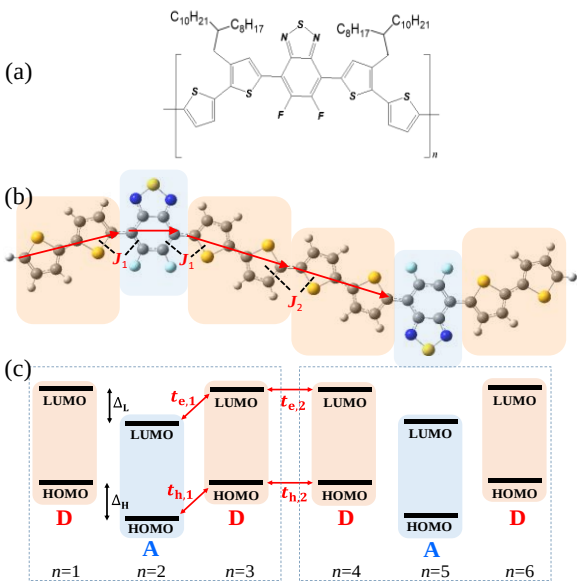

Figure 3 a) Molecular structure of PCE11. b) Minimized geometry showing fragment transition dipole moments (red arrows) and nearest-neighbor Coulombic couplings, J_1 and J_2. c) Fragment HOMO and LUMO levels for a $(DAD)_N$ chain.

multi-modal characterization and theory is a powerful way to understand how materials properties at multiple scales, from molecular to mesoscale, affect charge transport.

In order to the advance the theory, the *Spano* group have focused attention on the photophysics of neutral (i.e. undoped) donor-acceptor copolymers containing donor-acceptor-donor (DAD) repeat units. These include polymers such as PCE11,[4] having bithiophene donors and difluorbenzothiadiazole acceptors, as shown in Figure 1. A vibronic exciton model based on the Frenkel-CT Holstein Hamiltonian was developed to account for the UV-Vis absorption spectral features of $(DAD)_N$ oligomers and polymers.[5] Single chains were found to behave just like J-aggregates due to the head-to-tail orientation of the interacting transition dipole moments corresponding to donor and acceptor fragments (Figure 3b), as well as the in-phase relationship between the electron and hole transfer integrals connecting neighboring donor and acceptor HOMO and LUMO orbitals shown in Figure 3c. The J-behavior is evidenced by an increased red-shift in the low-energy absorption band along with a heightened A_1/A_2 peak ratio, where A_1 and A_2 are the oscillator strengths of the first two vibronic peaks in the progression sourced by the symmetric quinoidal-aromatic vibration.[6] Figure 4 shows a comparison between theory and experiment.[5]

We further investigated π-stacks of $(DAD)_N$ oligomers.[7] Within such stacks J-aggregate-promoting *intra*c hain interactions compete with H-aggregate-promoting *inter*chain interactions. The latter includes 1) Coulombic coupling, which arises from "side-by-side" fragment transition dipole moments and 2) intermolecular charge transfer (ICT), which is enhanced in geometries with substantial overlap between donors on one chain and acceptors on a neighboring chain. Interchain Coulomb interactions result in an attenuated A_1/A_2 vibronic peak ratio, similar to what has been established in H-aggregates of homopolymers like P3HT.[8,9] An attenuated A_1/A_2 ratio is also caused by H-promoting ICT when the electron and hole transfer integrals are out-of-phase. In this case, the A_1 peak is also significantly red-shifted, as shown in Figure 5, in contrast to the blue-shift characteristic of conventional Kasha H-aggregates. With slight modifications, the ratio formula derived previously

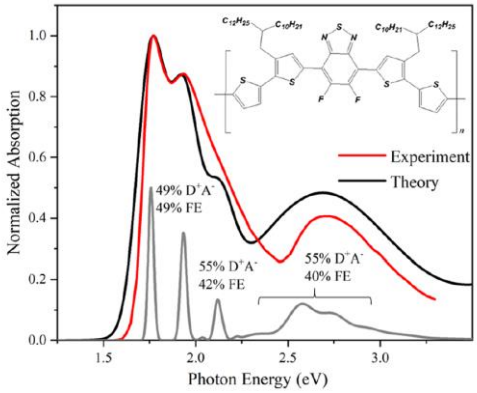

Figure 4 Absorption spectrum of PffBT4-2DT (red) in dichlorobenzene at 25°C from ref. 3 along with our simulation (black). The gray curve is the same simulation, but with all line widths reduced by a factor of five and intensity by a factor of two. CT (D^+A^-)-and Frenkel-exciton (D*, A*) admixtures are also indicated.

for P3HT aggregates[9] was shown to apply to $(DAD)_N$ aggregates as well, allowing one to determine the effective free-exciton interchain coupling from A_1/A_2. Applications were made to polymers based on 2T-DPP-2T and 2T-BT-2T repeat units, where the importance of the admixture of the excited acceptor state in the lowest energy band was emphasized.

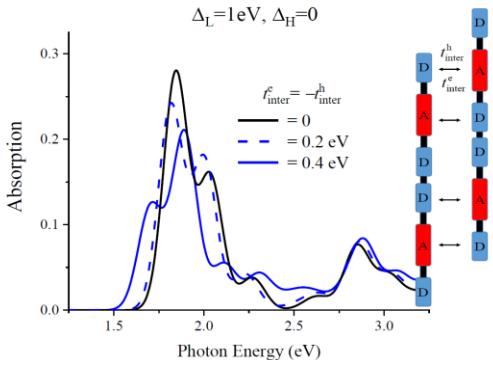

Figure 5 Calculated absorption spectrum of a $(DAD)_2$ dimer. Only ICT-mediated coupling is included with the interchain electron and hole transfer integrals taken to be out of phase.

Future Plans

In the next funding period we will work to extend the IDT-BT work by studying IDT-BPD in more detail as well as random copolymers of these two polymers made by the *Luscombe* groups. These co-polymers will allow us to tune the amount of backbone disorder, which will in turn allow us to determine how it affects the microstructure, as studied by HRTEM, as well as charge delocalization as studied by CMS. These model materials will allow us to map out the effect of torsion and chain rigidity. Furthermore, we will continue developing CMS, and in particular a step-scan variant of it, which will allow us to study the spectrum as a function of charge density. We will apply the vibronic exciton model to understand the photophysics of polymers such as IDT-BT which have very similar UV-Vis spectra to PCE11 shown in Figure 3. The goal here is to look for signatures of extended intrachain exciton coherence in IDT-BT, which is believed to account for the high mobilities despite significant interchain disorder.[10] In conjunction with these studies we will refine the polaron model to describe the mid-IR line shape. We are also working on models to describe bipolarons and trions, with particular emphasis on spectral signatures which distinguish polarons, bipolarons and trions. These studies combined will elucidate whether there really are two distinct populations of sites, as suggested by the CMS spectra, as well as how they are separated energetically in the density-of-states.

Finally, the *Salleo* group will start a study of the DPP-based polymers described by *Spano* and synthesized by *Luscombe*, and in particular, we will control the degree of aggregation by using different solvents and characterize the films structurally (mainly by synchrotron-based X-ray scattering) in order to correlate degree of aggregation to spectral features predicted by the model.

References

[1] Sommerville, P. J. W.; Li, Y.; Dong, B. X.; Zhang, Y.; Onorato, J. W.; Tatum, W. K.; Balzer, A. H.; Stingelin, N. S.; Patel, S. N.; Nealey, P. F.; Luscombe, C. K. "Elucidating the Influence of Side-Chain Circular Distribution on the Crack Onset Strain and Hole Mobility of Near-Amorphous Indacenodithiophene Copolymers" Macromolecules, 53, 7511-7518 (2020).

[2] Venkateshvaran, D.; Nikolka, M.; Sadhanala, A.; Lemaur, V.; Zelazny, M.; Kepa, M.; Hurhangee, M.; Kronemeijer, A. J.; Pecunia, V.; Nasrallah, I.; Romanov, I.; Broch, K.; McCulloch, I.; Emin, D.; Olivier, Y.; Cornil, J.; Beljonne, D.; Sirringhaus, H. Approaching

Disorder-Free Transport in High-Mobility Conjugated Polymers. Nature 515 (7527), 384–388 (2014).

[3] C. Cendra, et al., Unraveling the unconventional order of a high-mobility indacenodithiophene-benzothiadiazole copolymer, Nano Letters (in revision).

[4] Y. Liu, J. Zhao, Z. Li, C. Mu, W. Ma, H. Hu, K. Jiang, H. Lin, H. Ade and H. Yan, Aggregation and morphology control enables multiple cases of high-efficiency polymer solar cells, Nat. Commun. 5 (1), 5293 (2014).

[5] M. B. Qarai, X. Chang and F. C. Spano, Vibronic exciton model for low bandgap donor-acceptor polymers, Journal of Chemical Physics 153 (24), 16 (2020).

[6] V. Dantanarayana, J. Fuzell, D. Nai, I. E. Jacobs, H. Yan, R. Faller, D. Larsen and A. J. Moule, Put Your Backbone into It: Excited-State Structural Relaxation of PffBT4T-2DT Conducting Polymer in Solution, J. Phys. Chem. C 122 (12), 7020-7026 (2018).

[7] X. Chang, M. Balooch Qarai and F.C. Spano, HJ-Aggregates of Donor-Acceptor-DonorOligomers and Polymers, J. Chem. Phys. (in press).

[8] F. C. Spano and C. Silva, H- and J-Aggregate Behavior in Polymeric Semiconductors, Ann. Rev. Phys. Chem. 65, 477-500 (2014).

[9] F. C. Spano, Modeling disorder in polymer aggregates: The optical spectroscopy of regioregular poly(3-hexylthiophene) thin films, J. Chem. Phys. 122, 234701 (2005).

[10] X. Zhang, H. Bronstein, A. J. Kronemeijer, J. Smith, Y. Kim, R. J. Kline, L. J. Richter, T. D. Anthopoulos, H. Sirringhaus, K. Song, M. Heeney, W. Zhang, I. McCulloch and D. M. DeLongchamp, Molecular origin of high field-effect mobility in an indacenodithiophene–benzothiadiazole copolymer, Nat. Commun. 4 (1), 2238 (2013).

Publications

Sommerville, P. J. W.; Li, Y.; Dong, B. X.; Zhang, Y.; Onorato, J. W.; Tatum, W. K.; Balzer, A. H.; Stingelin, N. S.; Patel, S. N.; Nealey, P. F.; Luscombe, C. K. "Elucidating the Influence of Side-Chain Circular Distribution on the Crack Onset Strain and Hole Mobility of Near-Amorphous Indacenodithiophene Copolymers" Macromolecules, 53, 7511-7518 (2020).

Gu, K.; Onorato, J. W.; Luscombe, C. K.; Loo, Y.-L. "The Role of Tie Chains on the Mechano-Electrical Properties of Semiconducting Polymer Films" Adv. Electron. Mater., 6, 1901070 (2020).

M. Balooch Qarai, Xin Chang and F.C. Spano, Vibronic Exciton Model for Low Band-gap Donor-Acceptor Polymers, J. Chem Phys. **153**, 244901 (2020).

Huang, Y.; Cohen, T. A.; Sommerville, P. J. W.; Luscombe, C. K. "Green syntheses of stable and efficient organic dyes for organic hybrid light-emitting diodes" J. Mater. Chem. C, Advance Article (2021).

Xin Chang , M. Balooch Qarai and F.C. Spano, HJ-Aggregates of Donor-Acceptor-Donor Oligomers and Polymers, J. Chem. Phys. (in press).

Diffusion and Kinetics in Organic Radical Polymers

Jodie L. Lutkenhaus, Texas A&M University

Program Scope

Organic radical polymers are rapidly growing in interest due to their unusual electronic nature and their wide breadth of potential applications.[1] This is exemplified by the intense interest in organic radical batteries, which offer fast charging, high power, and excellent rate capability. Because it is an organic material, radical polymers can be potentially derived from biomass or other natural resources, and its availability is more secure than other electrode materials that are comprised of rare or toxic metals. The current major challenges for organic radical batteries are a lack of a quantitative understanding of electron and ion transport, addressing swelling effects arising from favorable polymer-solvent interactions, and the development of polymer batteries using degradable materials. Accordingly, there is a need to develop a fundamental understanding of the diffusion and kinetics of the redox reaction for organic radical polymers. This proposed experimental project will uncover how electron and ion transport influence the kinetics of the redox reaction, and how these connect to battery performance. The main focuses of the project so far are to investigate internal electron transfer in conjugated radical polymers, determine the ion-solvent coupled transport that occurs during the redox of organic radical polymers, and finally, develop a degradable battery that utilizes degradable organic radical polymers. The knowledge gained from these projects will highlight the important design criteria for next generation polymer-based batteries.

Recent Progress

To understand that nature of electron transfer in conjugated radical polymers (CRPs), a series of polythiophenes loaded with 0, 25, or 100% nitroxide radicals (2,2,6,6-tetramethyl-1 piperidinyloxy [TEMPO], denoted as P3HT-TEMPO-X where X is the TEMPO functionalization) were examined.[2] One might expect that capacity or electron transfer might improve due to the conjugated backbone, but this study revealed that the performance is in fact reduced. P3HT-TEMPO-100 exhibits a charge-discharge profile similar to PTMA (the polymer analog containing a non-conjugated backbone in place of P3HT). P3HT-TEMPO-25 shows hybrid

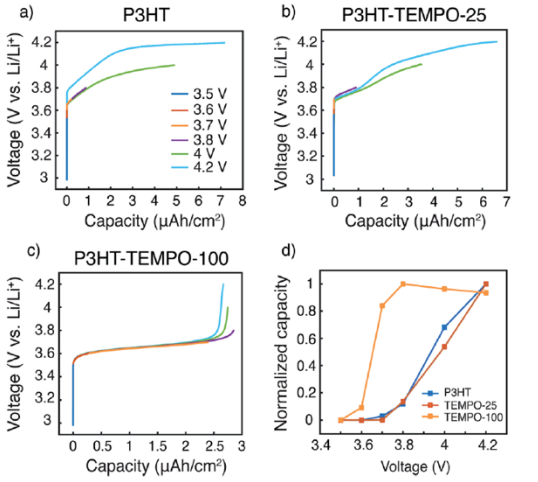

Figure 1. Galvanic charging to various potential cutoffs for (a) P3HT-TEMPO-25, and (b) P3HT-TEMPO-100. Normalized specific capacities of (c) P3HT-TEMPO-25 and (d) P3HT-TEMPO-100.

behavior. To isolate the contributions of the nitroxide group and the polythiophene backbone, the TEMPO-loaded CRPs were charged to various potential cutoffs and the charging capacity was calculated (**Figure 1**). P3HT-TEMPO-25 does not show a clear nitroxide radical plateau during charging, and the capacity contribution from the nitroxide radical was negligible. For P3HT-TEMPO-100, there is a clear nitroxide radical plateau around 3.6-3.7 V dominating the charge storage process, comprising about 85% of the total charging capacity. The polythiophene backbone only contributes to about 15% of the total capacity from 3.7 V to 4.2 V. Electrochemical quartz crystal microbalance with dissipation monitoring (EQCM-D) was used to measure the *in situ* mass change occurring during charging and discharging; it was found that about one solvent molecule transferred per anion. Taken together, these results confirm that internal charge transfer occurs due to the different redox potentials of the TEMPO radical group and the P3HT backbone. Further, these findings confirm the underlying reasons for these CRP's generally low conductivity and capacity. On the other hand, the feature of internal charge transfer might be leveraged to mitigate voltage excursions when used as an electrode additive.

Polymer-based batteries can be made "greener" by moving to aqueous-based electrolytes, but the design features for polymer-electrolyte pairs is not clear. A series of TEMPO-substituted non-conjugated polymers with varying polymer-water interactions were explored by changing the polymer chain and linker group, **Figure 2a**.[3] *In situ* EQCM-D was employed to observe the simultaneous mass change of each polymer electrode during cycling. By quantifying the redox kinetics and real-time mass and charge transfer of these polymers in water-based, metal free electrolyte (0.5 M $TEABF_4$), a universal design strategy for polymer-based metal-free aqueous batteries was demonstrated. Namely, the polymer should have favorable

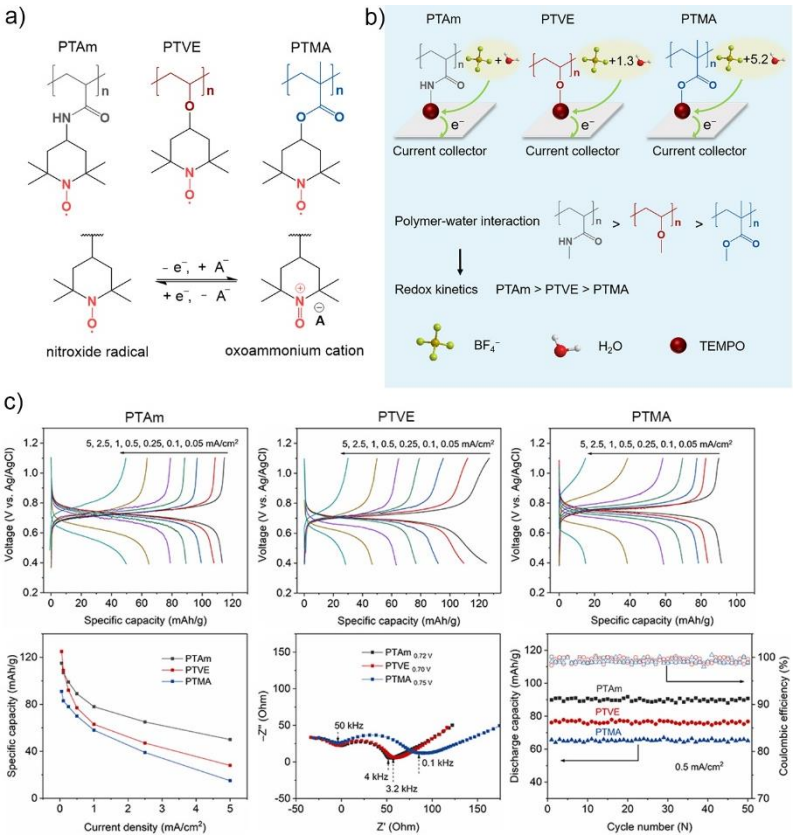

Figure 2. a) Molecular structure and redox mechanism of PTAm, PTVE and PTMA. b) Schematic diagram of doping mechanism with different degrees of water participation and their relationship between polymer-water interaction and kinetics. c) Electrochemical properties comparation of PTAm, PTVE and PTMA electrodes in 1 M $TEABF_4/H_2O$ electrolyte.

interactions with water, but not so favorable as to lead to dissolution. The degree of water participation, the effect on charge storage behavior with mass transport, and the apparent molecular weight profile of the transferred species were correlated to the polymer-water affinity using solubility parameters, **Figure 2b**. Specifically, improved polymer-water interactions manifest in accelerated kinetics, which promote capacity retention at higher discharge rates. The most hydrophilic polymer, poly(2,2,6,6-tetramethylpiperidinyloxy-4-yl acrylamide) (PTAm), yielded a capacity of 115 mAh/g, or 97% of its theoretical value, at 0.05 mA/cm^2. At 5 mA/cm^2, the PTAm capacity remained relatively high at 50 mAh/g, whereas comparable polymer capacities were much lower, **Figure 2c**. Similarly, PTAm (the most hydrophilic polymer) swelled the most with water (3.1 vol%), which favorably led to reduced water transfer with the anion during cycling (only one water molecule per anion). This marks the first time that mixed water-ion transfer in radical polymers has been studied in such detail. By doing so, it is revealed that polymer-solvent interactions are key drivers in electrochemical performance for non-conjugated radical polymers.

Previous work investigating fully polymeric-based batteries have utilized chemistries that were designed without end-of-life considerations.[1,4,5] By accounting for end-of-life degradation, Lutkenhaus and Wooley developed novel redox-active polypeptides, with degradable backbones and linker groups.[6] The redox activity and backbone stability were confirmed using electrochemical methods and were utilized to produce a fully-polypeptide based metal-free battery.[6] This marks the first report of a polypeptide-based battery that degrades on command. Specifically, α-Helix polypeptides poly(g-propargyl-l-glutamate)-g-TEMPO or biTEMPO polypeptide and poly((6-iodo)-l-glutamate)-g-methyl viologen or viologen polypeptide, for short, were investigated. Wooley's synthetic efforts were separately funded through her lab (NSF DMR-1507429), and the Lutkenhaus lab's electrochemical characterization was supported by this present DOE grant. **Figure 3** shows the redox reactions associated with the "all polypeptide" metal-free battery with composite polypeptide electrodes. The assembled battery exhibited two redox peaks at $E_{1/2}$ = 3.64 V and 2.52 V, as seen in both **Figure 3a**

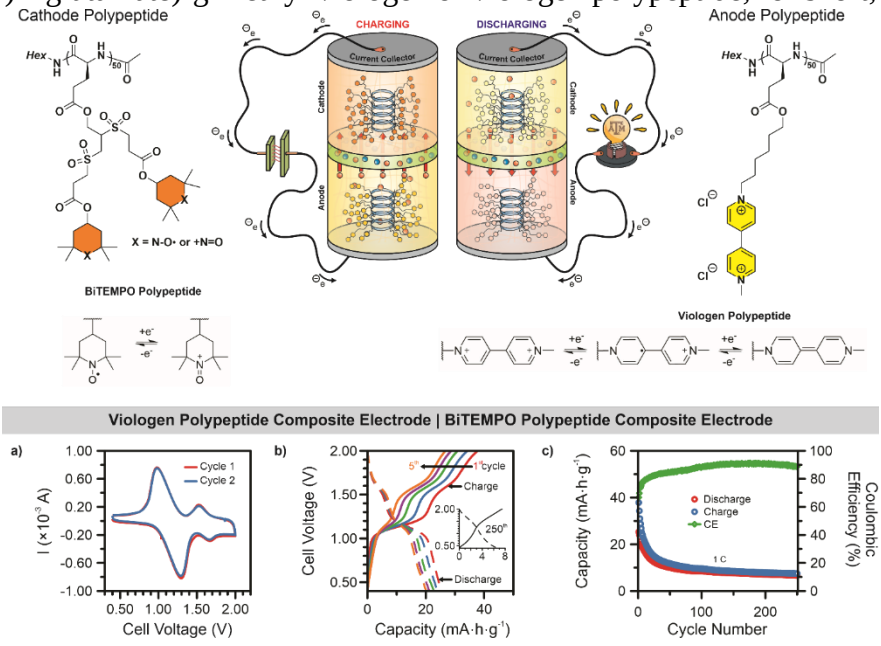

Figure 3. Redox-active polypeptides are used to create an all-polypeptide battery. a) CV, b) charge-discharge, and c) cycling stability for a full battery with a biTEMPO composite cathode and viologen composite cathode as thin films on ITO-coated glass.

and **b**. The initial capacity was 37.8 $mA \cdot h \cdot g^{-1}$ which faded to 7.5 $mA \cdot h \cdot g^{-1}$ after 250 cycles charge-discharge cycles at 1 C (**Figure 3c**). The main source of capacity fade was dissolution of polypeptides into the liquid electrolyte, as seen by the low Coulombic efficiency and steep early capacity fade. The cyclic voltammograms and charge-discharge curves indicate that the redox activity of the groups is retained even in this α-helix conformation and the lack of additional peaks confirm the stability of the degradable functionalities.

Future Plans

Future plans will be to investigate the role of ion type on the redox process and diffusion control of the polymer-based aqueous dual-ion batteries. To study the effect of ion type, ions have been selected that have varying hydration energy and charge density. These ions will be used for *in* situ EQCM-D studies of PTAm and poly(benzimidazobenzophenanthroline) with the hopes of developing aqueous electrolytes that enhance coupled ion-electron transport. Additionally, a series of viologen-based polypeptides will be used to consider how the helical backbone of the polypeptides modulates the diffusion coupled electron transfer in organic radical polymers.

References

1. Muench, S. *et al.* Polymer-Based Organic Batteries. *Chemical Reviews* **116**, 9438-9484 (2016).
2. Wang, S. *et al.* Quantifying internal charge transfer and mixed ion-electron transfer in conjugated radical polymers. *Chemical Science* **11**, 9962-9970 (2020).
3. Ma, T., Easley, A. D., Wang, S., Flouda, P. & Lutkenhaus, J. L. Mixed electron-ion-water transfer in macromolecular radicals for metal-free aqueous batteries. *Cell Reports Physical Science* **2**, 100414 (2021).
4. Suga, T., Sugita, S., Ohshiro, H., Oyaizu, K. & Nishide, H. p- and n-Type Bipolar Redox-Active Radical Polymer: Toward Totally Organic Polymer-Based Rechargeable Devices with Variable Configuration. *Advanced Materials* **23**, 751-754 (2011).
5. Wild, A., Strumpf, M., Häupler, B., Hager, M. D. & Schubert, U. S. All-Organic Battery Composed of Thianthrene- and TCAQ-Based Polymers. *Advanced Energy Materials* **7**, 1601415 (2017).
6. Nguyen, T. P. *et al.* Polypeptide organic radical batteries. *Nature* **593**, 61-66 (2021).

Publications

- Nguyen, T. P., Easley, A. D., Kang, N., Khan, S., Lim, S.-M., Rezenom, Y. H., Wang, S.; Tran, D. K., Fan, J., Letteri, R. A., He, X., Su, L., Yu, C.-H., Lutkenhaus, J. L., Wooley, K. L. Polypeptide Organic Radical Batteries. *Nature* **2021**, 593, 61-66
- Ma, T., Easley, A.D., Wang, S., Flouda, P., & Lutkenhaus, J.L., Mixed electron-ion-water transfer in macromolecular radicals for metal-free aqueous batteries. *Cell Reports Physical Science* **2021**, 2 (5), 100414
- Easley, A.D., Vukin, L.M., Howard, D.L., Pena, J.L., & Lutkenhaus, J.L., Nitroxide Radical Polymer–Solvent Interactions and Solubility Parameter Determination. *Macromolecules* **2020**, 53 (18), 7997–8008
- Wang, S., Easley, A.D., Thakur, R.M., Ma, T., Yun, J., Zhang, Y., Ober, C.K., & Lutkenhaus, J.L., Quantifying Internal Charge Transfer and Mixed Ionic-Electronic Transfer in Conjugated Radical Polymers. *Chemical Science* **2020**, 11, 9962-9970
- Wang, S., Easley, A.D., & Lutkenhaus, J.L., 100th Anniversary of Macromolecular Science Viewpoint: Fundamentals for the Future of Macromolecular Nitroxide Radicals. *ACS Macro Letters* **2020**, 9 (3), 358-370
- Wang, S., Park, A.M.G., Flouda, P., Easley, A.D., Li, F., Ma, T., Fuchs, G.D., & Lutkenhaus, J.L., Solution-processable thermally crosslinked organic radical polymer battery cathodes. *ChemSusChem* **2020**, 13, 2371
- Wang, S., Li, F., Easley, A.D., & Lutkenhaus, J.L., Real-time insight into the doping mechanism of redox-active organic radical polymers. *Nature Materials* **2019**, 18, 69-75
- Li, F., Wang, S., Zhang, Y., & Lutkenhaus, J.L., Electrochemical Energy Storage in Poly(dithieno[3,2-b:2′,3′-d]pyrrole) Bearing Pendant Nitroxide Radicals. *Chemistry of Materials* **2018**, 30 (15), 5169-5174
- Lutkenhaus, J.L., A radical advance for conducting polymers. *Science* **2018**, 359 (6382), 1334-1335

Converting Metal–Organic Liquids into Microporous Glasses via Non-Equilibrium Syntheses

Jarad A. Mason, Department of Chemistry and Chemical Biology, Harvard University

Program Scope

Glasses are critical to many of the technologies that support our modern lifestyle, and new types of glassy materials will play an important role in addressing a wide range of global challenges. Despite their importance, the compositional and structural diversity of glasses that have been designed, synthesized, and studied to date pales in comparison to other classes of materials. The realization of new types of glasses is complicated by the intrinsic non-equilibrium nature of all glass phases. This project seeks to apply coordination chemistry principles to direct the formation of metal–organic framework glasses by quenching equilibrium molten phases. These materials will serve as a platform for manipulating glass structure across multiple length scales and establishing new structure-property relationships. Moreover, these materials will provide access to longer-range structural ordering than observed in conventional inorganic glasses—given the increased length of organic bridging ligands—and to glass phases with accessible microporosity. Currently, there are extremely few examples of extended (one-, two-, or three-dimensional) coordination solids that undergo melting transitions to form stable liquid phases. As such, we have first worked to establish generalizable strategies to design new classes of melt-quenched metal–organic glasses by manipulating non-equilibrium synthesis pathways. These design principles will be applied to expand the library of metal–organic frameworks with accessible glass phases, to better understand non-equilibrium synthesis pathways, and to establish robust structural-property relationships.

Recent Progress

This project aims to explore how the structure and composition of metal–organic glasses can be controlled in a predictable fashion by cooling liquid phases of extended coordination networks under non-equilibrium conditions. Towards this end, our laboratory has developed generalizable thermodynamic strategies to promote reversible, low-temperature melting transitions and successfully discovered several new series of two- and three-dimensional metal–bis(acetamide) frameworks that undergo melting transitions to form stable liquid phases at record low temperatures. The low melting temperatures of these compounds are the result of weak coordination bonds, conformationally flexible bridging ligands, and weak electrostatic interactions between spatially separated cations and anions, which collectively reduce the enthalpy and increase the entropy of fusion.

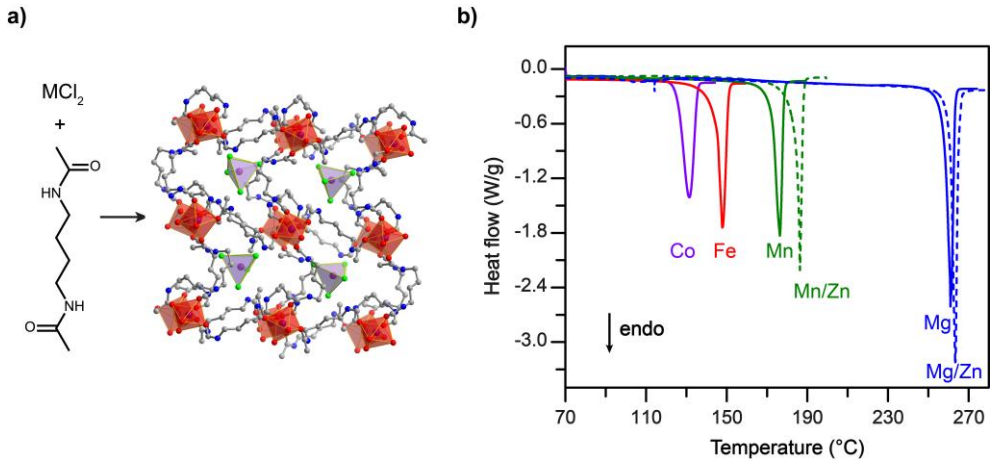

Figure 1. (a) Crystal structure of $M(bba)_3[M'Cl_4]$. Purple, red, gray, blue, green spheres represent M, O, C, N, and Cl atoms, respectively; H atoms have been omitted for clarity. (b) Representative differential scanning calorimetry (DSC) heating traces of the isostructural series of $M(bba)_3[M'Cl_4]$ compounds illustrating a wide range of melting temperatures.

During the last reporting period, we designed and synthesized the series of three-dimensional networks $M(bba)_3[M'Cl_4]$ (bba = *N, N'*-1,4-butylenebisacetamide; M = Mn, Fe, Co; M = Mn, M′ = Zn; M = Mg, M′ = Co, Zn), which undergo reversible melting transitions from 124 to 260 °C (Figure 1). All frameworks form stable liquid phases, many of which can be quenched to form metal–organic glasses. The amorphous nature of the glassy state is confirmed by PXRD, with samples prepared either by recollecting powders from DSC pan or melt quenching inside capillaries. Bulk, cm-sized glass films with uniform thickness were also successfully prepared by a melt-press method (Figure 2). Interestingly, shortening the polymethylene bridge in bis(acetamide) ligands leads to an increase in T_g to above 298 K, allowing us to obtain stable glasses at ambient temperature (Figure 3). This is consistent with shorter ligands with limited flexibility restricting structural relaxation in the supercooled liquids, therefore promoting glass formation at higher temperatures.

We further characterized the liquid structure of the lowest melting 3-D network, $Co(bba)_3[CoCl_4]$, with both extended X-ray fine structure (EXAFS) and pair distribution function (PDF) analysis. The EXAFS spectrum of molten $Co(bba)_3[CoCl_4]$ could be well-modeled with half of the Co centers in the melt coordinated to 4 Cl atoms—consistent with the persistence of $[CoCl_4]^{2-}$ anions in the melt—and half of the Co centers coordinated to 4.8(7) O atoms of bba ligands (Figure 4a). The average coordination number of 4.8(7) is well above the bond percolation threshold of 2.4 for a three-dimensional aperiodic network, indicating that metal–ligand coordination is persistent in the melt to provide extended connectivity spanning the entire liquid. PDF analysis, conducted in collaboration with the Billinge Group at Columbia, also reveals sharp, well-retained local-range features, consistent with limited changes to coordination environment around Co centers upon melting. Beyond the local coordination environment, the PDF of molten $Co(bba)_3[CoCl_4]$ contains oscillations at $r > 20$ Å that provide evidence of extended-range

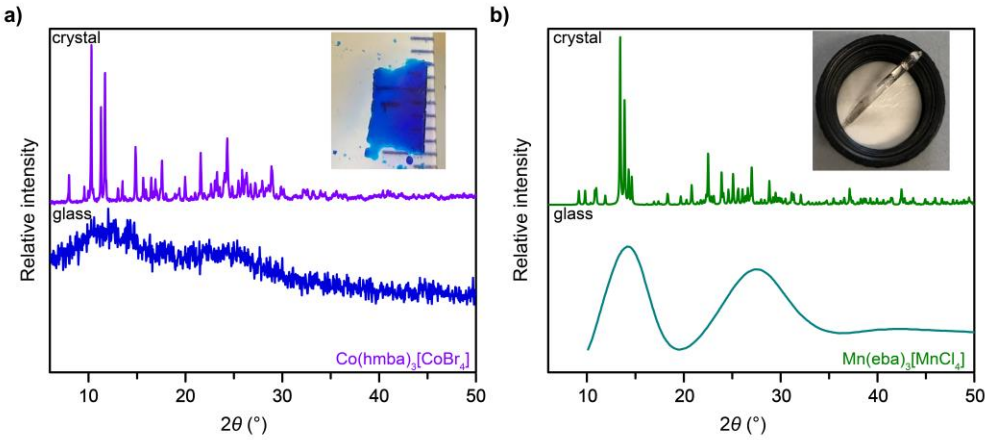

Figure 2. (a) Powder X-ray diffraction patterns of crystalline and glassy phases of $Co(hmba)_3[CoBr_4]$. Diffraction pattern of the glass was measured on powders recollected from a bulk melt-quenched sample. Inset: An example of an even-thickness, cm-sized, transparent melt-pressed glass film. (b) Powder X-ray diffraction patterns of crystalline and glassy phases of $Mn(eba)_3[MnCl_4]$. Diffraction pattern of the glass was collected on samples directly melt-quenched inside a capillary. Inset: An example of transparent glassy sample inside a capillary.

structural correlations (Figure 4b). This represents, to the best of our knowledge, the first evidence of extended-range order in the liquid phase of a metal–organic framework.

Combined viscosity and variable ramp-rate DSC measurements allow the dynamics of metal–organic liquids to be probed. A strong correlation is found between high molten phase viscosity and facile glass formation, consistent with high viscosity reducing recrystallization kinetics and slowing down relaxation dynamics. As supercooled liquids approach the glass transition, viscosity increases significantly, and we are able to study dynamics in this region by fitting higher temperature viscosity data with theoretical models or deriving fragility index (*m*, defined as the change in viscosity at $T \rightarrow T_g$) via evaluating the scan-rate dependence of T_g with DSC.

With improved control over non-equilibrium synthesis and a broader diversity of structural composition, metal–organic glasses will have highly tunable properties—such as free volume, mechanical, optical, and thermal properties—and provide access to new functions. To begin understanding free volume in metal–organic glasses, we have measured the density of the glass phase of $Co(hmba)_3[CoBr_4]$ through He pycnometry. The measured density of the glass phase, 1.49 g/cm^3, is 6% lower than the density of its crystalline state (1.58 g/cm^3). This result

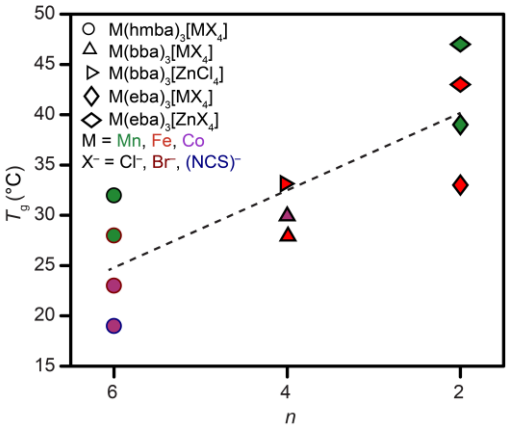

Figure 3. Correlation between increased glass transition temperature (T_g) and decreased polymethylene chain length (*n*). The dotted line is included as a visual guide.

indicates that glass transitions in metal–organic frameworks can lead to increased free volume, similar to conventional glass formers, and we are working to understand the distribution and accessibility of such free volume.

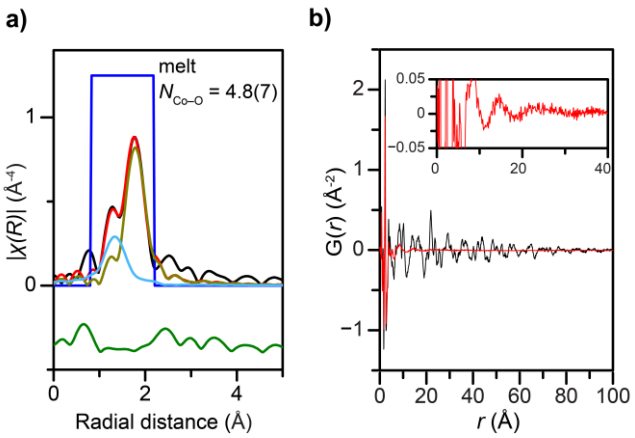

Figure 4. (a) Extended x-ray fine structure of $Co(bba)_3[CoCl_4]$ in the liquid phase above the melting temperature. (b) Pair distribution functions of $Co(bba)_3[CoCl_4]$ in the crystalline solid phase just below the melting temperature (black) and in the liquid phase above the melting temperature (red).

Future Plans

Towards further enhancing the diversity of metal–organic liquids, we will be working to implement new ligand design strategies, such as varying the length and rigidity of bis(acetamide) ligands, covalently attaching anionic groups to eliminate space-filling uncoordinated anions, and exploring additional weakly coordinating functional groups (such as sulfonates and nitriles) to vary the binding mode. In addition, given the non-equilibrium nature of the glass transition, the structure and dynamics of metal–organic glasses will also be impacted by the conditions under which they are formed. As such, we will explore how different non-equilibrium synthesis parameters impact glass formation.

To further probe structure and dynamics of molten and supercooled metal–organic liquids, we will perform EXAFS and PDF measurements with variable temperature programs in order to probe changes in liquid and glass structure in response to different quenching conditions. On the dynamics front, inelastic neutron scattering (INS) experiments, which resolve both the energy and momentum of neutrons after they are scattered by a sample, can provide information about dynamics occurring on timescales ranging from 10^{-14} s to 10^{-8} s, such as molecular vibrations, rotations, and diffusion.

Given their unique connectivity, bonding modes and bonding strengths compared to common inorganic and polymer glass formers, metal–organic glasses are expected to have distinct stiffness, hardness, and failure modes. To directly investigate mechanical properties, we will characterize metal–organic glasses with nanoindentation experiments. Finally, glass transitions followed by reversible cold crystallization and a detectable property change across the glass and crystalline states are of interest for phase-change memory and data storage, as well as certain nanoswitches. As such, we aim to better understand reversible glass–crystal transitions with tunable glass transition temperature and crystallization kinetics in our systems, as well as to measure optical and thermal properties across the glass-crystalline transitions.

Publications

Liu, M.; McGillicuddy, R. D.; Vuong, H.; Tao, S.; Slavney, A. H.; Gonzalez, M. I.; Billinge, S. J. l.; Mason, J. A. Network-Forming Liquids from Metal–Bis(acetamide) Frameworks with Low Melting Temperatures. *J. Am. Chem. Soc.* **2021**, *143*, 2801–2811.

Dynamic Properties of Nanostructured Porous Materials

Principal Investigator: Adam J. Matzger; Co-Investigator: Antek G. Wong-Foy
Department of Chemistry and the Macromolecular Science and Engineering Program
University of Michigan, Ann Arbor, MI 48109-1055

Program Scope

The overarching goal for this project is to develop an enhanced understanding of dynamic phenomena in metal-organic frameworks (MOFs) and to harness this knowledge to explain and optimize MOF creation and behavior. The work is guided by the assumption that MOFs can only be viable sorbents for large-scale gas storage and separations tasks if there is a path to produce them from readily available feedstocks using processes that are not energy intensive. From a materials synthesis standpoint, there is an emphasis on using simple and scalable approaches that rely on fundamental reactivity considerations yet can yield materials with high levels of function. The process of material activation is one aspect of these studies that we have been continuously engaged in; more recent studies exploit the dynamics of reagent diffusion and reactivity to create MOFs with hierarchical structure.

Recent Progress

1. Reagent reactivity and solvent choice determine metal–organic framework microstructure during postsynthetic modification

Postsynthetic modification (PSM) is one of the primary methods used to install new functionality into metal–organic frameworks (MOFs) due to the diversity of functional groups it can incorporate as well as its ability to alter the physical and chemical properties of the resultant MOF.[1] PSM is accomplished by placing an already assembled MOF into a solution containing a reagent which will react with the linker and produce the desired MOF. This method for adding chemical diversity to MOFs is widely used, but the effects of its use on framework microstructure were not well understood. MOF microstructure is expected to affect guest interactions within the MOF and impact MOF applications. Another commonly used postsynthetic method, postsynthetic exchange, has already been demonstrated by our group to result in core–shell microstructures in multiple MOF systems.[2] Additionally, the design of MOFs with sophisticated microstructures is an active area of research, and the development of higher order forms is seen as a means to obtain materials with advanced functionality in fields such as chromatography, chemical sensing, and catalysis.

To investigate the microstructure of MOFs after PSM, a method has been developed using scanning electron microscopy (SEM) in conjunction with energy-dispersive X-ray spectroscopy (EDS) to detect the spatial distribution of chlorine-tagged substituents added to the MOF. PSM experiments were performed using chloroacetyl isocyanate and 2-chloroethyl isocyanate to react with 2-aminoterepthalate linkers in IRMOF-3 (Figure 1a). These isocyanates were chosen due to

their differences in reactivity which we expected would give rise to different microstructures. Additionally, isocyanates were chosen because they do not produce side products which can become trapped within the MOF and complicate SEM-EDS analysis. PSM was also performed in either toluene or chloroform to probe the effect of changing solvent polarity on the resultant MOF microstructure. Time points for the PSM reactions at room temperature were taken at 3, 6, 9, and 24 hours to monitor the progression of new substituent addition over time. Regardless of whether chloroform or toluene is used, SEM-EDS mapping of the sectioned crystal shows that, during PSM with chloroacetyl isocyanate, a core–shell microstructure is produced (Figure 1b), while PSM with 2-chloroethyl isocyanate produces a more uniformly distributed microstructure (Figure 1c).

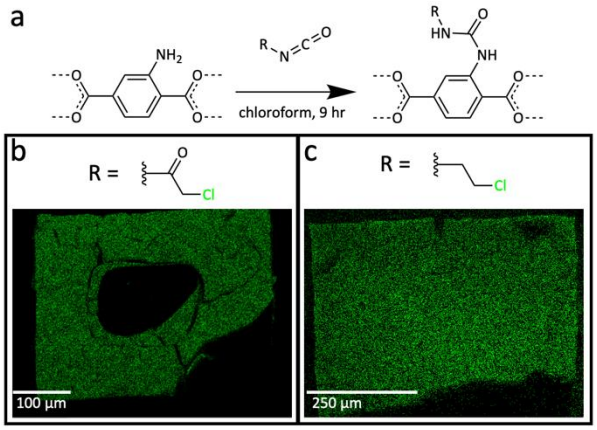

Figure 1. a) PSM scheme. b) Characteristic EDS mapping data for PSM of IRMOF-3 with chloroacetyl isocyanate and c) chloroethyl isocyanate. Chlorine is marked green for EDS mapping data.

The effect of solvent choice on microstructure was investigated using 4-bromophenyl isocyanate as a reagent having intermediate reactivity to 2-chloroethyl isocyanate and chloroacetyl isocyanate. The hypothesis was that increased polarity of the solvent would result in increased core–shell character after PSM by stabilizing the polar transition state leading to functionalization. PSM was performed under dry conditions in toluene, chloroform, and a mixture of the two. SEM-EDS linescans show that PSM of 4-bromophenyl isocyanate in toluene results in a uniform distribution of new functionality (Figure 2a) whereas PSM in chloroform shows microstructure with increased core–shell character (Figure 2b). PSM in the 1:1 mixture of toluene and chloroform displays increased core–shell character relative to toluene and reduced overall reactivity compared to chloroform (Figure 2c). Additional experiments wherein a 1:5 ratio of anhydrous DMF to toluene was used show that adding anhydrous DMF to toluene increases the core–shell character of the resultant MOF while suppressing core functionalization (Figure 2d). Collectively, the above results support the hypothesis that altering the solvent used for PSM is a viable method to influence the resultant microstructure of the functionalized MOF, which is best viewed as a sliding scale between uniform distribution and core–shell.

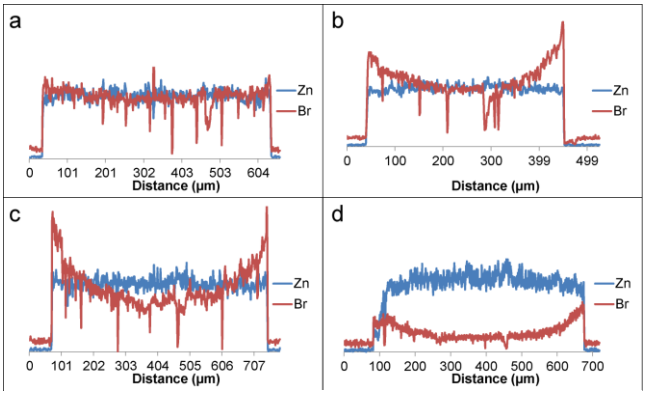

Figure 2. SEM-EDS linescan of IRMOF-3 cross sections after PSM with 4-bromophenyl isocyanate in a) toluene, b) chloroform, c) a 1:1 mixture of toluene and chloroform, and d) a 1:5 mixture of DMF and toluene.

To demonstrate the utility of understanding the dynamics of PSM, a one-pot core–shell MOF was generated through PSM with a mixture of chloroacetyl isocyanate and 4-bromophenyl isocyanate

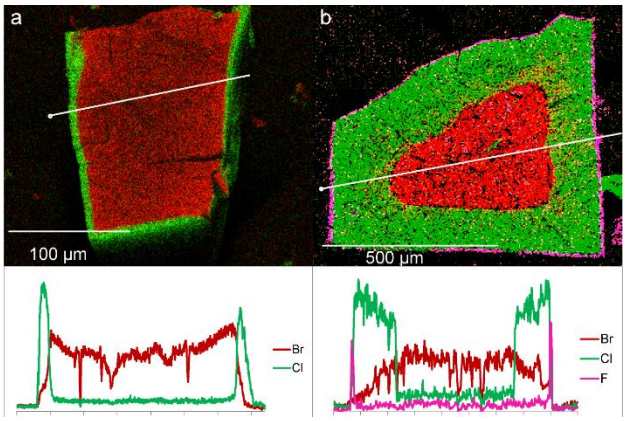

Figure 3. SEM-EDS maps and linescans of cross sections of IRMOF-3 after PSM with a) chloroacetyl isocyanate and bromophenyl isocyanate (core–shell) and b) trifluoroacetyl isocyanate, chloroacetyl isocyanate, and 4-bromophenyl isocyanate (Matryoshka).

(Figure 3a). The result is dramatic, because the demarcation between the chloroacetyl isocyanate-functionalized zone (shell) and the 4-bromophenyl isocyanate-functionalized zone (core) is sharp. Using stepwise functionalization, a triple functionalized MOF was generated in two PSM steps, forming a Matryoshka microstructure MOF (Figure 3b). With these results, it has been shown that controlling the degree and spatial distribution of functionalization by adjusting the reagent reactivity and the solvent used can increase MOF complexity and open the door for complex applications in sequential catalysis, chromatography, and chemical sensing.

2. Resolvation-induced MOF collapse

MOF activation involves the removal of solvent and other guests from MOF pores by a set of "activation" conditions tailored to their specific solvent compatibilities and structural stabilities. Improperly performed, MOF activation has well-documented destructive potential. When MOFs are used in liquid phase applications, particularly in the area of catalysis, they are often activated according to best practices, but subsequently submerged in high surface tension solvents. From a practical standpoint, it is important to understand the limits of these materials in this use condition. As an example, if structural reorganization were to occur during resolvation of a catalytically active framework, it could compromise the access of reactants to the catalytic centers leading to lower apparent activity than would be observed with pristine materials. Similar concerns are present when applying MOFs in liquid phase adsorption applications such as fuel desulfurization and wastewater cleanup.

The destructive potential of MOF resolvation was assessed across a range of model systems, including highly stable UiO-66, intermediate stability IRMOF-3 and UMCM-9, and fragile FJI-1. Samples were characterized before and after resolvation and reactivation using two-dimensional powder X-ray diffraction (2D-PXRD), which shows changes in sample crystallinity and mosaicity, and surface area analysis, which gives information about the ability of the framework to accommodate molecular guests. While UiO-66 was found to be insensitive to resolvation with all solvents tested, the other frameworks showed sensitivity to resolvation, particularly when using high surface tension solvents such as *N*,*N*-dimethylformamide (DMF) and dimethylsulfoxide. No functional differences were noted between samples degraded due to resolvation and those subject to activation-induced MOF collapse, suggesting that the same physical phenomena are responsible for both processes.

To mitigate the effects of MOF resolvation, an approach termed reverse solvent exchange (RSE) was developed (Figure 4). RSE involves resolvation with a low surface tension solvent followed by exchange into the desired higher surface tension solvent, and is a much less destructive route than direct resolvation with high surface tension solvents. For example, while resolvation of activated UMCM-9 with DMF leads to a 78% decrease in accessible sample surface area, resolvation with hexane followed by solvent exchange into DMF causes only a 14% decrease in surface area. This substantial retention of surface area is associated with greater sample crystallinity, as confirmed by 2D-PXRD.

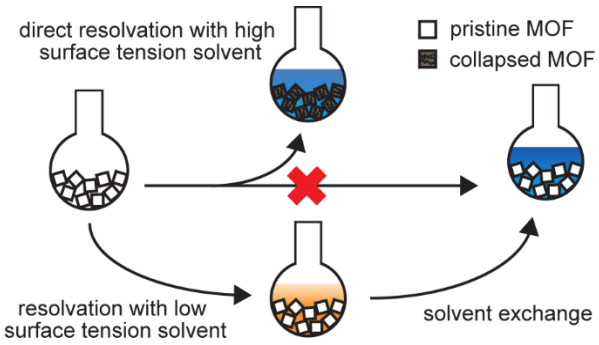

Figure 4. Schematic representations of direct resolvation and stepwise "reverse solvent exchange" resolvation.

This stepwise approach to resolvation was successful even for the most fragile framework tested, FJI-1. When FJI-1 is activated, best-in-class approaches such as activation from perfluorohexane or supercritical CO_2 must be taken, or the framework will collapse. Even activation from hexane gives a product with negligible crystallinity and nearly zero accessible surface area. When the MOF is activated according to best practices, direct resolvation with DMF gives a 66% decrease in surface area whereas resolvation with hexane leads to less than a 1% loss in surface area. This compatibility with hexane resolvation allows RSE resolvation with DMF to occur with negligible loss in sample surface area.

This research informs best practices for MOF handling in applications involving catalysis, environmental remediation/pollutant capture, separations, and chemical sensing. While optimized procedures should be developed on a system-by-system basis, this work provides a rationally implementable protocol from which to begin this optimization. Paying attention to the role of resolvation offers the distinct benefit of ensuring MOF function is maximized for a given material in a particular solvent system and that performance results are not convoluted by solvation-induced framework damage.

Future Plans

Work pertaining to the activation of MOFs containing coordinatively unsaturated metal sites is accelerating. With postsynthetic modification studies finished, we are turning attention to testing function as well as phase selection by seeding.

References

1. Cohen, S. M., "The Postsynthetic Renaissance in Porous Solids" J. Am. Chem. Soc. 2017, 139, 2855-2863.

2. Boissonnault, J. A.; Wong-Foy, A. G.; Matzger, A. J., "Core–Shell Structures Arise Naturally During Ligand Exchange in Metal–Organic Frameworks" J. Am. Chem. Soc., 2017, 139, 14841-14844.

Publications

Damron, J. T.; Ma, J. Kurz, R.; Saalwaechter, K,; Matzger, A. J.; Ramamoorthy, A., "The Influence of Chemical Modification on Linker Rotational Dynamics in Metal-Organic Frameworks." *Angew. Chem.* **2018**, *57*, 8678-8681.

Dodson, R. A..; Wong-Foy, A. G.; Matzger, A. J., "The Metal-Organic Framework Collapse Continuum: Insights from Two-Dimensional Powder X-ray Diffraction" *Chem. Mater.*, **2018**, *30*, 6559-6565.

Dodson, R. A.; Matzger, A. J., "Resolvation-Based Damage to Metal–Organic Frameworks and Approaches to Mitigation" *ACS Materials Lett.*, **2019**, *1*, 344-349.

Suresh, K.; Matzger, A. J., "Enhanced Drug Delivery by Dissolution of Amorphous Drug Encapsulated in a Water Unstable Metal-Organic Framework (MOF)" *Angew. Chem. Int. Ed.*, **2019**, *58*, 16790-16794.

Suresh K.; López-Mejías, V.; Roy, S.; Camacho, D. F.; Matzger, A. J. "Leveraging Framework Instability: A Journey from Energy Storage to Drug Delivery" *Synlett.*, **2020**, *31*, 1573-1580.

Dodson, R. A.; Kalenak, A. P.; Du Bois, D. R.; Gill-Ljunghammer, S. L.; Matzger, A. J. "*N*,*N*-Diethyl-3-methylbenzamide (DEET) acts as a metal–organic framework synthesis solvent with phase-directing capabilities" *Chem. Commun.*, **2020**, *56*, 9966-9969.

Dodson, R. A.; Kalenak, A. P.; Matzger, A. J. "Solvent Choice in Metal-Organic Framework Linker Exchange Permits Microstructural Control" *J. Am. Chem. Soc.*, **2020**, *142*, 20806-20813.

Du Bois, D. R.; Matzger, A. J. "Reagent Reactivity and Solvent Choice Determine Metal-Organic Framework Microstructure during Postsynthetic Modification" *J. Am. Chem. Soc.*, **2021**, *143*, 671-674.

Polymer Macrocycles: A novel topology to control dynamics of rubbery materials

Gregory B. McKenna, Department of Chemical Engineering, Texas Tech University

Judit E. Puskas, Department of Food, Agricultural and Biological Engineering, The Ohio State University

Julia A. Kornfield, Division of Chemistry and Chemical Engineering, California Institute of Technology

i) Program Scope

Understanding the dynamics of polymers of different topologies is an important field of study and one of the most important unanswered questions in this field is "how do circular polymers move," particularly in the melt state. The work performed here tackles this subject through a collaboration in which specialists in polymer synthesis, polymer physics and polymer rheology work together to investigate the thermophysical behavior of circular macromolecules. The project goals are to use a novel synthesis method of "green" oxidative polymerization to produce high purity macrocycles that would be highly entangled were they linear chains and to investigate their linear viscoelastic behavior as a function of molecular weight. Such measurements can provide the measure of the dynamics of circular macromolecules to sizes that correspond to linear molecule entanglement densities higher than previously obtainable with synthetic polymers and permit comparisons with the known behavior of other molecular architectures, especially that of linear chains. Chemical chain end characterization and critical edge fractionation methods are being used with the purpose of quantifying the numbers of circular and linear molecules in each sample. Nonlinear viscoelastic measurements, including extensional viscosity, are also being made.

ii) Recent Progress

a. Ring Purity from Linear Chains

It is very important to know the purity of the rings in the sense of their freedom from linear chain contamination. The present state of the problem has been complicated by two different issues. One is the contamination by the presence of linear chains in the putative ring samples and the other is the fact that even if the rings were pure, they have been limited in molecular weight to fewer than about 15 entanglement equivalents for the linear counterpart. How this affects properties and the ability to judge actual material behavior and compare it with that predicted by theory can be ascertained from the data[1-6] shown in Figures 1a and 1b. Because of the need for such understanding we have been characterizing the chains from the Reversible Radical Recombination Polymerization (R3P) using three methods. We used Liquid Chromatography at Critical Conditions (LCCC)[8,9], 800 MHz NMR for chain end analysis, and a novel chemical reaction technique devised by the CalTech group. We summarize the results

from these investigations next.

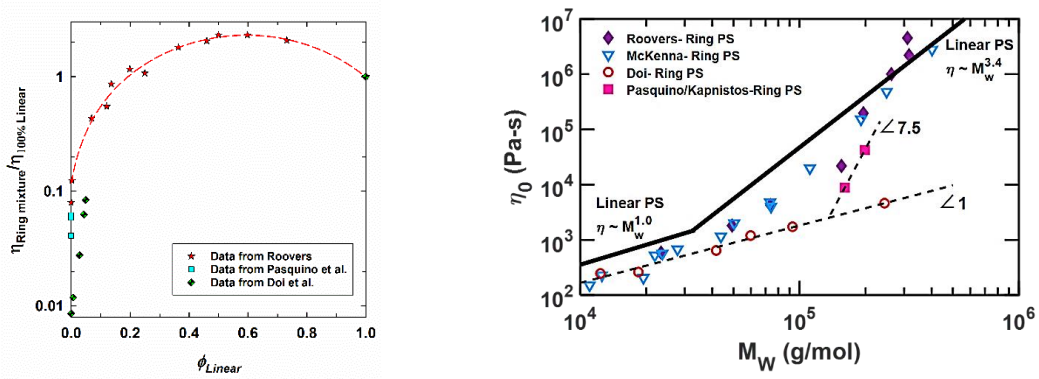

Figure 1. a) Zero shear rate viscosity of rings normalized to that of the linear counterpart showing the strong effect of linear contamination on the viscosity as well as the differences among reports from different groups. **b)** Viscosity of polystyrene rings vs. molecular weight for measurements from different groups for rings that were thought to be free of linear chains at the times of the measurements. Data from references 1-7. Figure **a**) from PI McKenna. Figure **b)** from Kong et al ref. 8.

In the LCCC work, it is important to know the sensitivity of the method to finding linear polymers, both for systems that are freshly synthesized, viz., not fractionated, and for systems that have been fractionated. In the present work, because the R3P synthesis should give high quality rings, we began our study by characterizing the sensitivity of the LCCC to detect known additions of linear chains to a cyclic counterpart. By adding a known amount of linear chain and using UV absorption measurements we were able to obtain a calibration line as shown in Figure 2 where we see that the UV absorption increases linearly with addition of the linear counterpart. Furthermore, as shown in Figure 3, we can see in the UV detection traces for the GPC output of the ring/linear mixtures that those at 0% added linear chain and 6% added linear chain are indistinguishable. These results provide an estimate of the LCCC as a means of obtaining pure rings to be limited by the detection sensitivity to about 6%. Thus, for the systems we have looked at one can say with some confidence that they have no more than 6% linear contaminant.[10] They could have less, but the LCCC method cannot distinguish better than this for the polyDODT (poly(3,6-dioxa-1,8-octanedithiol)) polymers studied here. It is also of interest that we ran LCCC on samples of ring polyDODT of M_n=366,700 g/mol, 77,800 g/mol, and 75,300 g/mol in addition to the M_n=27,400 g/mol sample just referred to and there was no evidence of linear contamination in the UV intensity vs. elution time, thus telling us that the samples are at least 94% rings.

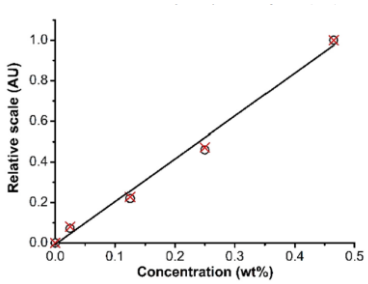

Figure 2. UV absorbance vs concentration of added linear chain for a 1300 g/mol polyDODT sample as a function of wt. concentration showing linear dependence of intensity with concentration. After reference 10.

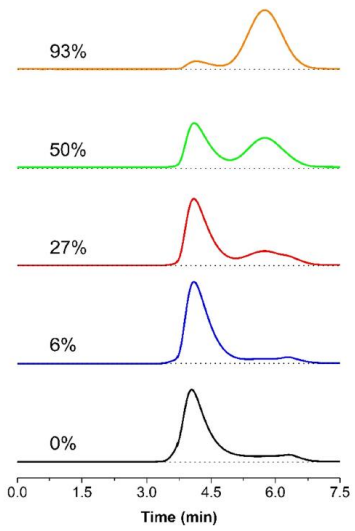

Figure 3. UV absorbance vs ekuiton time in GPC traces of mixtures of linear chain (1300 g/mol) into a 27,400 g/mol ring sample showing that the sensitivity is limited to detecting linear contamination of the rings above 6% by weight.nce of intensity with concentration. After reference 10.

In addition to the LCCC work we have also used 800 MHz NMR and found that for one sample of M_n=35,800 g/mol the linear chain limit of detection, based on signal strength of the chemical shift for the chain end was 1.5%. However, since the sensitivity scales approximately linearly with the molecular weight, the sensitivity limits of the NMR are not very good beyond about 70,000 g/mol (≈ 3%). Thus another more sensitive method is necessary.

To this end, the group at CalTech had the insight to postulate that the R3P system offers a very sensitive qualitative method to ascertain the purity of cyclic polyDODT: catalytic stability testing[11]. Even traces of linear polymer or monomer residues with thiol end groups will react with the disulfide bonds, that would be accelerated by a catalyst such as TEA. A thiolate anion in equilibrium with covalently bonded thiols is a strong nucleophile, displacing a sulfur atom of the disulfide via an S_N2 mechanism as shown in Figure 4[12]. This "shuffle" can lead to either degradation or molecular weight increase. To test this theory, first the cyclic sample that did not show color change was dissolved in THF and mixed with TEA only (sample with M_n=35,800 g/mol). After 3 days the SEC trace matched exactly that of the original trace, indicating that no degradation took place. Since TEA would deprotonate any thiols present, we concluded that the sample investigated contained no linear contaminants with thiol end groups. When the same sample was mixed with DODT monomer, after 3 days the molecular weights decreased, with substantial increase in dimer content. The largest decrease was observed when both DODT and TEA was added to the polymer. This work is on-going but the preliminary results suggest that we can detect reactivity at additions of TEA equivalent to fewer than 1% linear chain ends in the highest molecular weight samples being investigated (M_n=366,700 g/mol). This method is being deployed to further examine the quality of the samples.

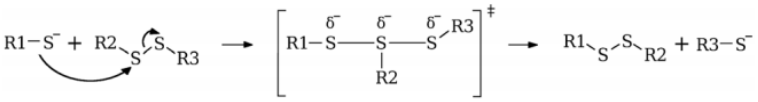

Figure 4. Scheme of Thiol-disulfide exchange. After reference 12.

b. Rheological properties

Linear rheology has been performed on samples both in the melt state and in concentrated solution[12]. The use of solutions in addition to melts was necessary to work at low entanglement densities because it is very difficult to make low molecular weight polymer by R3P synthesis. The results of the viscosity vs. entanglement number Z are shown in Figure 5 along with a

comparison for lower molecular weight cycles taken from the literature as well as the comparison with linear chain behavior. Two things are clear from these data. First, the region of low viscosity dependence on entanglement number goes to much higher Z-values than do the linear chains. Second, once "entanglement coupling" sets in, the scaling of the dependence on Z approaches a value of 6, which is significantly greater than the value of 3.4 obtained from linear chains. Since the materials of highest molecular weight, but in solution, fall on the same scaling with the melt of the lower molecular weight rings we are confident that these results represent the behavior of entangled rings and this to several hundred entanglements vs. the prior reported values of approximately 15 entanglements for the largest rings studied.

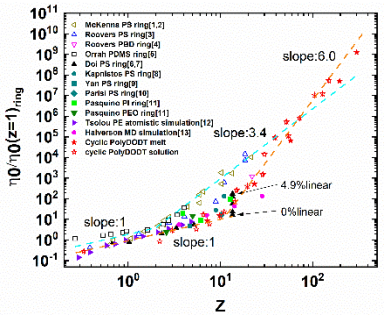

Figure 5. Reduced viscosity vs. entanglement number for rings and linear polymers from the literature compared to the results for the polyDODT samples from both melt and solution determinations. From Chen et al reference 13. Literature data from references 2-7.

iii) Future plans

The project is nearly completed but we are continuing work to establish with more certainty the quality of the ring samples. This includes further work with LCCC and catalytic stability testing. In addition, there is significant interest in these molecules as they are potentially able to reduce hysteretic loss due to, e.g., the Payne effect, in tires due to their lack of chain ends. We are pursuing work in this direction as it plays a direct role in fuel efficiency of vehicles using rubber tires.

iv) References

1. J. Roovers, Macromolecules 1988, 21 (5), 1517-1521.
2. R. Pasquino et al, ACS Macro Letters 2013, 2 (10), 874-878.
3. Y. Doi et al, Macromolecules 2015, 48 (9), 3140-3147.
4. Y. Doi et al, Rheologica Acta 2017, 56 (6), 567-581.
5. J. Roovers, Macromolecules 1985, 18 (6), 1359-1361.
6. M. Kapnistos et al, Nature Materials 2008, 7 (12), 997-1002.
7. G.B. McKenna et al, Macromolecules 1987, 20 (3), 498-512.
8. D. Kong et al, in preparation.
9. K. Molnar et al, Paper B37, Rubber Division 198th Annual Meeting, Oct. 2020 (virtual).
10. K. Molnar et al, Journal of Molecular Liquids 2021, 322, 114956,
11. K. Molnar et al, in preparation.
12. M. Putzu et al, Phys. Chem. Chem. Phys. 2018, 20 (23), 16222–16230.
13. D. Chen, et al. in preparation.

Publications

1. K. Molnar, C. A. Helfer, G. Kaszas, E. Krischa, D. Chen, G. B. McKenna, J. A. Kornfield and J. E. Puskas, " Liquid chromatography at critical conditions (LCCC): Capabilities and limitations for polymer analysis," Journal of Molecular Liquids 2021, **322**, 114956.
2. K. Molnar, C. A. Helfer, G. Kaszas, D. Chen, G. B. McKenna, J. A. Kornfield and J. E. Puskas, "Rings or Not? Analysis of Disulfide Polymers with Liquid Chromatography at Critical Conditions (LCCC)," Paper B37, Rubber Division 198th Annual Meeting, Oct. 2020 (virtual).
3. C. A. Helfer, K. Molnar, G. Kaszas, D. Chen, G. B. McKenna, J. A. Kornfield and J. E. Puskas, "Ring Polymers: Topology to control properties of elastomeric materials," Paper B36, Rubber Division 198th Annual Meeting, Oct. 2020 (virtual).
4. S. Jin and G.B. McKenna, "Effect of Nanoconfinement on Polymer Chain Dynamics," Macromolecules, 2020, **53**, 10212-10216.
5. D. Chen and G.B. McKenna, ""Deep glassy state dynamic data challenge glass models: Configurational entropy models," Journal of Non-Crystalline Solids 2021, **566**, 120871.
6. K. Molnar, H. Kim, D. Chen, C. A. Helfer, G. Kaszas, G. B. McKenna, J. A. Kornfield and J.E. Puskas, "Effect of Reaction Conditions on the Structure of Polyether Disulfide Elastomers: Synthesis of High Purity Cycles," In preparation.
7. D. Chen, C. A. Helfer, K. Molnar, H. Kim, G. Kaszas, J. A. Kornfield, J.E. Puskas, and G.B. McKenna, "Linear rheology of highly entangled cyclic polymer in melts and solutions: Extraordinarily high dependence of viscosity on number of entanglements," In preparation.

Design and Validation of Defect-Resistant Multinary Chalcogenide Semiconductors for Energy Conversion

David B. Mitzi, Duke University (Principal Investigator)
Volker Blum, Duke University (Co-Investigator)

Program Scope

The use of complex, multinary (comprising three or more elements) semiconductors has enabled high-performance energy conversion devices based on a range of different physical processes, including photovoltaic/photoelectrochemical, light emission and thermoelectric effects. However, despite increased chemical/electronic tunability, as more elements are combined into a specific material, the relationships between the crystal structure, chemistry and device-related properties become more complex. In addition to structure and chemistry, materials defects (e.g., missing atoms, atoms swapping places) play a major role in the properties of energy conversion devices and can even limit the advancement of a technology. For example, in the case of $Cu_2ZnSn(S,Se)_4$ (CZTSSe)—a heavily studied solar cell material because of non-toxic and abundant component elements—intrinsic defects limit the solar cell performance to roughly half that of commercial technologies. The goal of the current program is to assess/broaden a new class of promising multinary semiconductors based on related I_2-II-IV-X_4 and I_2-I'-V-X_4 (where I = Li, Cu, Ag; II = Sr, Ba, Pb; I' = K, Rb; IV = Si, Ge, Sn, Ti, Zr; V = P, As, Sb, Nb, V, Ta; X = S, Se, Te) stoichiometries, providing 243 possible elemental combinations (32 were reported prior to the program start). Previous research has indicated properties that strongly depend on crystal structure and that these compounds may have reduced concentrations of device-limiting defects. This project will predict novel semiconducting materials/structures within this family—using a newly proposed approach based on crystal packing consideration—and validate these predictions using computational, synthesis and characterization techniques. The program therefore targets a paradigm for designing new defect-resistant semiconductors and provides insight into the potential of these novel materials for sustainable energy conversion through 4 thrusts: (1) structure rationalization/prediction, (2) compositional tuning, (3) alloying, and (4) defect exploration.

Recent Progress

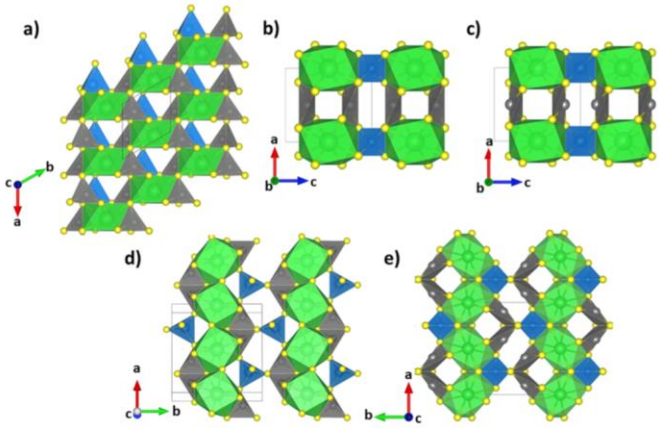

Fig. 1. Selected crystallographic views of (a) Cu_2BaSnS_4 ($P3_1$), (b) Ag_2BaGeS_4 (I-42m), (c) $Ag_2BaSnSe_4$ (I222), (d) $Cu_2BaSnSe_4$ (Ama2), and (e) Ag_2PbGeS_4 (Ama2†) to illustrate connectivity of M−X polyhedra. Atom/polyhedra colors are I: gray, II: green, IV: blue, X: yellow. (From Ref. 1)

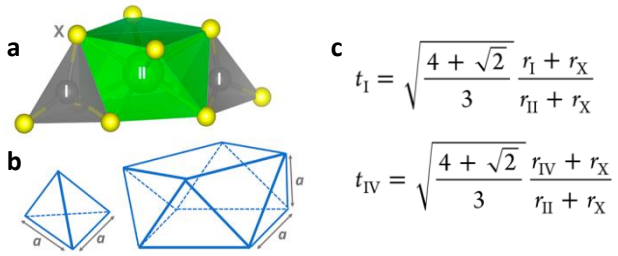

Fig. 2. [I-X_4][II-X_8][I-X_4] face-sharing unit common to $P3_1$ and *Ama*2 structures (taken from $Cu_2BaSnSe_4$ unit cell), (b) dimensions of idealized regular tetrahedron and uniform square antiprism, and (c) derived dimensionless tolerance factors, describing the agreement with bond distance ratios in idealized polyhedra, where t_I and t_{IV} are the tolerance factors for the I and IV atoms and r_I, r_{II}, r_{IV}, and r_X are the ionic radii of the associated atoms. (From Ref. 1)

Examination of known I_2-II-IV-X_4 materials reveals that there are five related crystal structure types in which these compounds generally crystallize (***Fig. 1***)—$P3_1$, *Ama*2, *I*-42*m*, *I*222, and *Ama*2† († indicates a distinct crystal structure from the conventional *Ama*2 structure). Further analysis of these structures reveals similar connectivity of the metal-chalcogen (M-X) polyhedra. Using the specific bonding relationships of the M-X polyhedra in the $P3_1$ / *Ama*2 structures (***Fig. 2***) we developed a mathematical relationship describing how well the polyhedra of a specific compound fit into this motif based upon the metal and chalcogen ionic radii and the dimensions of the idealized M-X polyhedra.[1] The dimensionless tolerance factors, labeled t_I and t_{IV}, can be plotted for the known I_2-II-IV-X_4 compounds, revealing distinct phase regions for each of the crystal structures, especially when employing experimental bond lengths in place of Shannon radii[2] (***Fig. 3***). This tolerance factor map has formed a basis for our program to identify targeted semiconductors, with initial successfully synthesized and characterized new family members including Cu_2PbGeS_4 ($P3_1$), Cu_2SrSiS_4 ($P3_1$), Ag_2SrSiS_4 (*I*-42*m*), Ag_2SrGeS_4 (*I*-42*m*) and Ag_2BaSiS_4 (*I*-42*m*), further providing support for the model.[1,3] From successfully synthesized powders of the new semiconductors, we determined bandgaps of 1.55 eV (Cu_2PbGeS_4), 3.4 eV (Cu_2SrSiS_4), 2.08 eV (Ag_2SrSiS_4), 1.73 eV (Ag_2SrGeS_4) and 2.2 eV (Ag_2BaSiS_4), in qualitative agreement with density functional theory (DFT) calculations (***Fig. 4***), which also resolved the indirect nature of the bandgaps.[1,3] Notably, the tolerance factor approach is not able to predict the stability of these compounds relative to prospective binary/ternary decomposition products (i.e., as seen for Cu_2PbSnS_4, which could not be synthesized), pointing to a direction for future study.

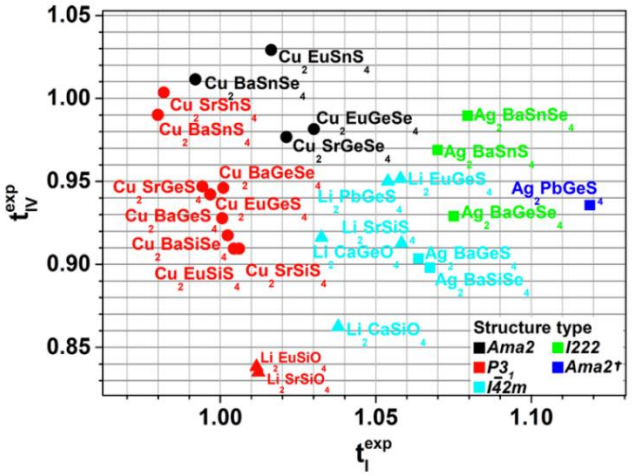

Fig. 3. Tolerance factors of reported I_2-II-IV-X_4 compounds calculated using experimental bond lengths derived from single crystal structures (I = Ag: squares; Cu: circles; Li: triangles). Colors represent different structure types, as noted in the legend. Cu_2EuSnS_4 has been reported in both $P3_1$ and *Ama*2 space groups. (From Ref. 1)

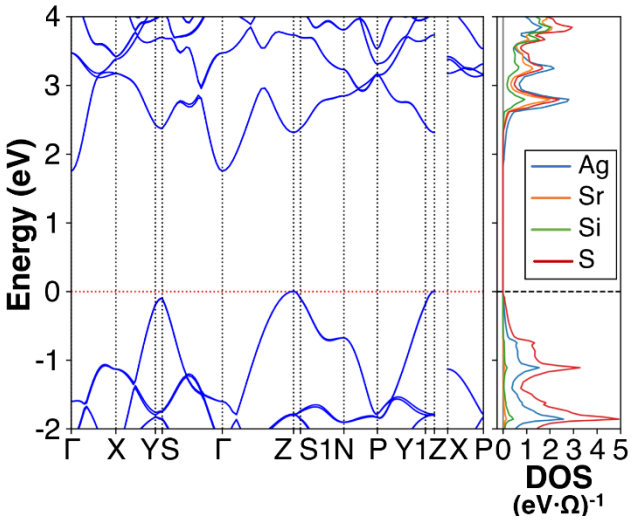

Fig. 4. Example of band structure and partial density of states (DOS) calculations for new multinary chalcogenide semiconductors, here shown for Ag_2SrSiS_4, which also has interesting non-linear optical properties. Ω is the unit cell volume used in the HSE06 calculations, which include spin-orbit coupling. (From Ref. 3)

Another important direction for the program involves the study of defects in particularly interesting members from the I_2-II-IV-X_4 family. $Cu_2BaSn(S,Se)_4$ (CBTSSe) offers a tunable quasi-direct band gap to values as low as 1.55 eV though varying S:Se ratio.[4] Using solution-deposited stoichiometric CBTSSe films with band gap of 1.59 eV ($x \approx 3$), temperature- and excitation-dependent photoluminescence studies reveal a dominant defect emission at ~1.5 eV and a second deep defect feature at 1.15 eV.[5] From time-resolved terahertz measurements, we find a charge carrier (electron and hole sum) mobility of ~140 cm^2 /Vs (***Fig. 5***)—i.e., comparable to values in CZTSSe—as well as a two-component minority carrier lifetime. A longer-lived lifetime component (~2 ns) arises from bulk recombination. However, strong recombination at the (bare) surface leads to a ~50 ps lifetime, inferior to state-of-the-art CZTSSe absorbers. This recombination issue may worsen for CBTSSe/CdS interfaces, due to a cliff-like band alignment with 0.6 eV band offset, as revealed by ultraviolet photoemission spectroscopy. A low number of charge carriers within the absorber further contributes to a high series resistance. Overall, the study shows that, while CBTSSe offers reduced overall defect density, leading to reduced band tailing, a significant deep defect concentration, coupled with low electron affinity and carrier density pose challenges for current-generation PV device design. CBTSSe surfaces appear to be Cu deficient from XPS study, possibly connecting to the noted surface recombination and relating to formation of a newly identified $Cu_2Ba_3Sn_2(S,Se)_8$ phase, found to be stable under S deficient conditions at elevated temperature.[6]

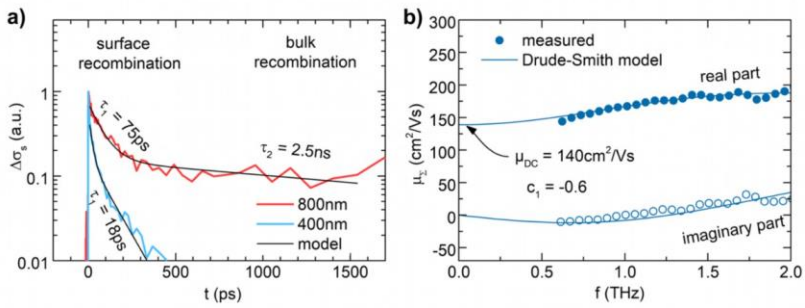

Fig. 5. a) Transient photoinduced sheet conductivity $\Delta\sigma_s$ of CBTSSe film after exciting at 400 and 800 nm. Fast-initial decay is attributed to surface recombination and the long component sets a lower limit for the bulk lifetime. b) Sum of electron/hole mobility μ_Σ measured at terahertz frequencies and fitted by the Drude-Smith model, reflecting the DC-mobility and pointing to partial carrier localization. (From Ref. 5)

Future Plans

The program will continue to probe the broad applicability of the tolerance factor approach among newly considered I_2-II-IV-X_4 and I_2-I'-V-X_4 chalcogenides, as well as associated properties of these materials. Examples of particular

interest include bandgap control in $Ag_2NH_4AsS_4$ (I_2-I'-V-X_4) analogs and understanding how the I_2-II_3-IV_2-X_8 phases[6] interface with the I_2-II-IV-X_4 systems in terms of stability. Computational studies on optical property changes due to rare-earth element doping in chalcogenide semiconductors will be pursued. It is known that dopants such as Ce, Pr, Tm, Gd, Nd, Yb, Eu can be used in light-emitting semiconductor devices. Further, some of the impacts of these dopants on optical properties have been experimentally studied—e.g., Eu can provide broad band emission peaking in the NIR (near-infrared) region.[7] However, the impacts of these dopants on I_2-II-IV-X_4 materials are not broadly understood. In addition, for particular systems, the program will continue to explore detailed defect properties—e.g., comparing $Cu_2BaGe(S,Se)_4$ (CBGSSe) with CBTSSe. An underlying hypothesis for the program is that atomic size and coordination preference can be used to control defect formation in multinary chalcogenide systems—e.g., given the large size difference between Ba and Cu/Sn, we might expect CBTSSe to have less antisite disorder relative to CZTS. The interest in CBGSSe lies in the fact that Ge and Cu are also of significantly different size (unlike the Cu and Sn in CBTSSe). Therefore, the CBGSSe system provides an interesting point of comparison relative to CBTSSe in terms of defect formation. Properties and selected energy device demonstrations will also be pursued for emerging multinary chalcogenide systems.

References

1. J.-P. Sun, G. C. McKeown Wessler, T. Wang, T. Zhu, V. Blum, D. B. Mitzi, "A structural tolerance factor approach to defect-resistant I_2-II-IV-VI_4 semiconductor design," *Chem. Mater.* **32**, 1636 (2020).

2. R. D. Shannon, "Revised effective ionic radii and systematic studies of interatomic distances in halides and chalcogenides," *Acta Cryst* **A32**, 751 (1976).

3. G. C. McKeown Wessler, T. Wang, J.-P. Sun, Y. Liao, M. Fischer, V. Blum, and D. B. Mitzi, "Structural, optical, and electronic properties of two new quaternary chalcogenide semiconductors: Ag_2SrSiS_4 and Ag_2SrGeS_4," *Inorg. Chem.*, submitted (2021).

4. D. Shin, B. Saparov, T. Zhu, W. P. Huhn, V. Blum, D. B. Mitzi, "$BaCu_2Sn(S,Se)_4$: Earth-abundant chalcogenides for thin-film photovoltaics," *Chem. Mater.* **28**, 4771 (2016).

5. B. Teymur, S. Levcenco, H. Hempel, E. Bergmann, J. A. Márquez, L. Choubrac, I. G. Hill, T. Unold, D. B. Mitzi, "Optoelectronic and material properties of solution-processed earth-abundant $Cu_2BaSn(S,Se)_4$ films for solar cell applications," *Nano Energy* **80**, 105556 (2021).

6. J. Marquez, J.-P. Sun, H. Stange, H. Ali, L. Choubrac, S. Schaefer, C. Hages, K. Leifer, T. Unold, D. B. Mitzi, R. Mainz, "High-temperature decomposition of Cu_2BaSnS_4 with Sn loss reveals newly identified compound $Cu_2Ba_3Sn_2S_8$, *J. Mater. Chem. A* **8**, 11346 (2020).

7. J. Qiao, G. Zhou, Y, Zhou, Q. Zhang, Z. Xia, "Divalent europium-doped near-infrared-emitting phosphor for light-emitting diodes," *Nat. Commun.* **10**, 5267 (2019).

Publications

Jon-Paul Sun, Garrett C. McKeown Wessler, Tianlin Wang, Tong Zhu, Volker Blum, David B. Mitzi, "A structural tolerance factor approach to defect-resistant I_2-II-IV-VI_4 semiconductor design," *Chem. Mater.* **32**, 1636−1649 (2020).

Jose Marquez, Jon-Paul Sun, Helena Stange, Hasan Ali, Leo Choubrac, Stefan Schaefer, Charles Hages, Klaus Leifer, Thomas Unold, David B. Mitzi, Roland Mainz, "High-temperature decomposition of Cu_2BaSnS_4 with Sn loss reveals newly identified compound $Cu_2Ba_3Sn_2S_8$, *J. Mater. Chem. A* **8**, 11346-11353 (2020).

Betul Teymur, Sergiu Levcenco, Hannes Hempel, Eric Bergmann, José A. Márquez, Leo Choubrac, Ian G. Hill, Thomas Unold, David B. Mitzi, "Optoelectronic and material properties of solution-processed earth-abundant $Cu_2BaSn(S,Se)_4$ films for solar cell applications," *Nano Energy* **80**, 105556 (2021).

Jiwoo Song, Betul Teymur, Yihao Zhou, Edgard Ngaboyamahina, David B. Mitzi, "Porous $Cu_2BaSn(S,Se)_4$ film as a photocathode using non-toxic solvent and a ball-milling approach," *ACS Appl. Energy Mater.* **4**, 81-87 (2021).

Garrett C. McKeown Wessler, Tianlin Wang, Jon-Paul Sun, Yuheng Liao, Martin Fischer, Volker Blum, and David B. Mitzi, "Structural, optical, and electronic properties of two new quaternary chalcogenide semiconductors: Ag_2SrSiS_4 and Ag_2SrGeS_4," *Inorg. Chem.*, submitted (2021).

Informed Materials Design Principles From Local Structures and Dynamics In Hybrid Inorganic-Organic Perovskite Halides [DE-SC001608]

James R Neilson
Department of Chemistry
Colorado State University

Program Scope

Hybrid inorganic-organic perovskite halides have the potential to shift the paradigm by which we use functional semiconducting materials for energy-conversion technologies, as the structure/ property relationships of hybrid perovskites follow a distinct set of rules in which the lattice and molecular dynamics play a large role. In this project, we elucidate the materials design principles behind if and how dynamic organic dipoles and disorder correlate with the paradigm-shifting electronic properties in hybrid inorganic-organic perovskite halides. The potential for transformative properties of these materials (*e.g.*, high photovoltaic energy conversion efficiencies, radiation detectors, and thermoelectrics) suggests that new materials design principles are needed to produce materials with tailored properties that will enable the next-generation of energy-relevant technologies.

Recent Progress

Anharmonicity and inorganic-organic coupling in hybrid perovskites: Vacancy-ordered *double* perovskite halides provide a crystalline framework for understanding the organic-derived interactions, as the octahedra are not covalently connected. Many attributes of the lattice dynamics suggest that the impact on functional properties results from the *anharmonic* nature of the motion [1]. While this anharmonicity can derive from the alkali [2] or main group cation sizes [3], we also observed the role of the organic cation shape and orientation. We recently discovered a low-temperature, hysteretic phase transition of $(CH(NH_2)_2)_2SnI_6$, where the hysteresis stems from organic–inorganic coupling mediated by local and spontaneous strain from the orientations of the formamidinium cations, which yield a ferroelastic phase transition (Figure 1) [4]. This discovery provides evidence of organic-inorganic coupling and the atomistic origin and impact of anharmonic lattice dynamics on the charge transport properties of hybrid perovskite halide semiconductors.

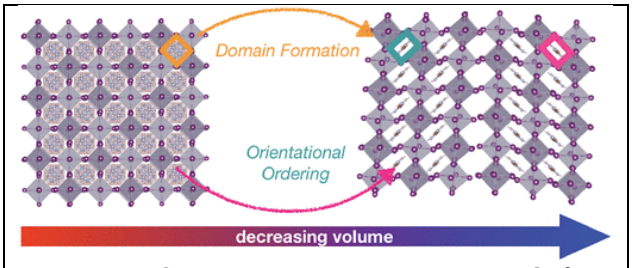

Figure 1: The spontaneous strain generated from orientations of formamidinium yields a ferroelastic phase transition [4].

Frustration and dynamics of organic cation orientations in halide perovskites: Formamidinium-based halide perovskites tend to exhibit unusual temperature-dependent trends in photoluminescence, dielectric constant, and phase behavior. These are hypothesized to originate from the $CH(NH_2)_2^+$ orientations and their dynamics. We discovered the presence of five

distinct temperature-dependent phase transitions in $CH(NH_2)_2PbBr_3$ that produce changes in the steady-state photoconductivity (Figure 2) [5]. Three of these phase transitions do not result in any detectable crystallographic changes and instead relate to the degrees of freedom of $CH(NH_2)_2^+$ orientational dynamics, as evidenced by quasielastic neutron scattering [5], as well as later confirmation by ^1H NMR and ^{14}N NMR spectroscopy [6]. The crystallographically unresolvable phase transitions resemble ferroelastic transitions with the formation of nanoscale domains. We hypothesize that these effects are mediated by the strain surrounding $CH(NH_2)_2^+$, which has a strong electrostatic quadrupolar moment that couples strongly to local electric field gradients (e.g., strain). This work demonstrates the importance of cation orientation and dynamics, domain behavior, and their interdependence in the steady-state optoelectronic properties of hybrid perovskites.

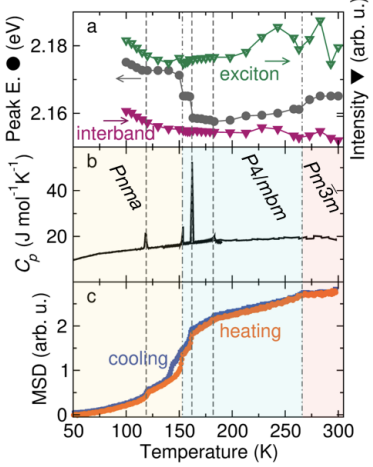

Figure 2. Temperature-dependent (a) photoconductivity, (b) heat capacity, and (c) mean squared displacement from fixed window elastic neutron scattering of $(CH(NH_2)_2)PbBr_3$ showing 5 entropy-releasing phase transitions; only the transitions at 153 K and 266 K result in a change of crystallographic symmetry (dashed-dotted lines) [5].

Building upon these results, we identified why strain and chemical substitution have been vital for understanding device performance and stability. We studied how Cs^+ substitution in place of formamidinium in $(CH(NH_2)_2)_{1-x}Cs_xPbBr_3$ suppresses four (of the five) phase transitions [6]. We proposed that *organic–organic interactions* are largely responsible the four suppressed lower-temperature phase transitions of $CH(NH_2)_2PbBr_3$. The large quadrupolar moments of formamidinium cations yield a strain field owing to electrostatic interactions with the inorganic octahedra, as positive charge density on the cation attracts the anionic sublattice and negative charge density repulses the anionic sublattice (Figure 3). This interaction creates a strong preference for the formation of a "T" shaped orientation between two cations; however, such local ordering cannot geometrically tile space in three dimensions and must therefore yield a symmetry-breaking phase transition. This symmetry breaking is also observed via the spontaneous stain generated by the shearing coalignment of formamidinium in $(CH(NH_2)_2)_2SnI_6$ (Figure 1, [4]), a material which displays no covalent connectivity between octahedra. The local compressive strain caused by Cs^+ substitution, as evidenced by synchrotron X-ray diffraction, inelastic neutron scattering, and ^{79}Br nuclear quadrupolar spectroscopy, overrides the orientation driven by the organic−organic interactions, disrupting the concerted changes at the low temperature phase transition. Yet, the local formamidinium dynamics are retained after chemical substitution, in contrast to the substitution of methylammonium-based perovskites which show orientational glass behavior [7, 8]. The retained dynamics is thought to be advantageous for a higher dielectric permittivity associated with the screening of charged point defects and myriad other behaviors that we recently reviewed (e.g.,

giant polarons, phonon bottlenecks, dynamic Rashba splitting) [9]. This provides a compelling rationalization for the primary use of formamidinium in champion devices [10].

Organic cation orientation and dynamics in layered halide perovskite derivatives: The dynamics and disorder of large "spacer" cations that drive formation of layered halide perovskite derivatives also play an important functional role. From collaborations with Prof. Wei You, we used crystallography to show how orientational degeneracy of the cations leads to poorer film formation and resulting photovoltaic efficiencies [11]. Along these lines, we have been performing quasielastic neutron scattering experiments to uncover the structure-dynamics-properties relationships that influence photoluminescence behavior in butylammonium, octanediammonium and γ-aminobutric acid based lead bromides. The cations' dynamics, which appear to correlate with their secondary structures, are largely responsible for their effective volume that subsequently influences distortions of the inorganic framework. These distortions thus correlate with the optical properties [12]. We have also used materials chemistry, crystallography, and neutron scattering to understand the interplay between the layered geometry, octahedral tilting, and small organic cation dynamics (e.g., methylammonium) in the layered, Ruddlesden-Popper derived materials [13].

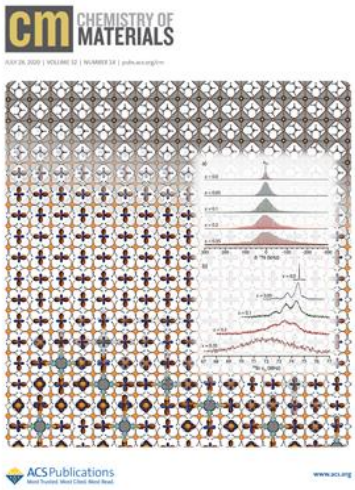

Figure 3. Illustration of the interactions between $(CH(NH_2)_2)^+$-based electrostatic quadrupoles and how cesium substitution disrupts the interactions [6].

Future Plans

Our group continues to elucidate how compositional substitution and structural modification influences the dynamics and phase behavior of hybrid perovskites, including in cases where inorganic and organic dipoles couple (e.g., Sn^{2+}). We continue to use neutron crystallography and spectroscopy to provide a molecular-level understanding of what enables and influences cation dynamics in layered crystal structures, while deriving insight into the properties that result from these dynamics.

References

1. (*a*) A. E. Maughan, A. M. Ganose, A. M. Candia, J. T. Granger, D. O. Scanlon, and J. R. Neilson, Anharmonicity and Octahedral Tilting in Defect-Ordered Hybrid Perovskites. *Chem. Mater.* (2018), 30(2), 472-483. (*b*) A. E. Maughan, A. M. Ganose, D. O. Scanlon, J. R. Neilson, Perspectives and Design Principles of Vacancy-Ordered Double Perovskite Halide Semiconductors, *Chem. Mater.*, (2019), 31(4), 1184- 1195.

2. A. E. Maughan, A. M. Ganose, M. A. Almaker, D. O. Scanlon, and J. R. Neilson, Tolerance Factor and Cooperative Tilting Effects in Vacancy-Ordered Double Perovskite Halides, *Chem. Mater.* (2018), 30(11), 3909-3919. '

3. (*a*) A. E. Maughan, A. A. Paecklar, J. R. Neilson, Bond valences and anharmonicity in vacancy-ordered double perovskite halides, *J. Mater. Chem. C.* (2018), 6, 12095-12104. (*b*) V. E. Combs, I. W. H. Oswald, J. R. Neilson, Hydrothermal Crystal Growth of Mixed Valence Cs_2SbBr_6, *Cryst. Growth & Des.*, (2019), 19, 7, 4090-4094.

4. A. E. Maughan, E. M. Mozur, A. M. Candia, J. R. Neilson, Ferroelastic Phase Transition in Formamidinium Tin(IV) Iodide Driven by Organic-Inorganic Coupling. *Inorg. Chem.* (2020), 59(19), 14399-14406.

5. E. M. Mozur, J. C. Trowbridge, A. E. Maughan, M. J. Gorman, C. M. Brown, T. R. Prisk, J. R. Neilson, Dynamical Phase Transitions and Cation Orientation Dependent Photoconductivity in $CH(NH_2)_2PbBr_3$. *ACS Materials Lett.*, (2019), 1, 2, 260-264.

6. E. M. Mozur, M. A. Hope, J. C. Trowbridge, D. M. Halat, L. L. Daemen, T. R. Prisk, C. P. Grey, J. R. Neilson, Cesium substitution Relieves Geometric Frustration in Formamidinium Hybrid Perovskites. *Chem. Mater.* (2020), 32(14), 6266-6277.

7. E. M. Mozur, A. E. Maughan, Y. Cheng, A. Huq, N. Jalarvo, L. L. Daemen, and J. R. Neilson, Orientational Glass Formation in Substituted Hybrid Perovskites. *Chem. Mater*. (2017), 29(23), 10168-10177.

8. M. Simenas, S. Balciunas, J. N. Wilson, S. Svirskas, M. Kinka, A. Garbaras, V. Kalendra, A. Gagor, D. Szewczyk, A. Sieradzki, M. Maczka, V. Samulionis, A. Walsh, R. Grigalaitas, J. Banys. Suppression of phase transitions and glass phase signatures in mixed cation halide perovskites. *Nat. Commun.* (2020) 11**,** 5103.

9. E. M. Mozur, J. R. Neilson, Cation Dynamics in Hybrid Halide Perovskites. *Ann. Rev. Mat. Res.* (2021), 51 (ASAP). https://doi.org/10.1146/annurev-matsci-080819-012808

10. J. Y. Kim, J. W. Lee, H. S. Jung, H. Shin, N. G. Park. High-Efficiency Perovskite Solar Cells. *Chem. Rev.* (2020) 120, 7867–7918.

11. (*a*) J. Hu, I. W. H. Oswald, S. Stuard, M. M. Nahid, N. Zhou, O. Williams, Z. Guo, L. Yan, H. Hu, Z. Chen, X. Xiao, Y. Lin, Z. Yang, J. Huang, A. Moran, H. Ade, J. R. Neilson, W. You, Synthetic Control over Orientational Degeneracy of Spacer Cations Enhances Solar Cell Efficiency in Two-Dimensional Perovskites. *Nat. Commun.*, (2019) 10, 1276. (*b*) J. Hu, I. W. H. Oswald, H. Hu, S. J. Stuard, M. M. Nahid, L. Yan, Z. Chen, H. Ade, J. R. Neilson, W. You, Aryl-Perfluoroaryl Interaction in Two-Dimensional Organic–Inorganic Hybrid Perovskites Boosts Stability and Photovoltaic Efficiency. *ACS Materials Lett.*, (2019) 1, 1,171-176.

12. M. D. Smith, A. Jaffe, E. R. Dohner, A. M. Lindenberg, H. I. Karunadasa. Structural origins of broadband emission from layered Pb–Br hybrid perovskites. *Chem. Sci.* (2017) 8(6), 4497-504.

13. T. Yamamoto, I. W. H. Oswald, C. Savory, T. Ohmi, A. A. Koegel, D. O. Scanlon, H. Kageyama, J. R. Neilson, Structure and optical properties of layered perovskite $(MA)_2PbI_{2-x}Br_x(SCN)_2$ ($0 \leq x < 1.6$). *Inorg. Chem.*, (2020), 59, 23, 17379-17384.

Publications

1) A. E. Maughan, A. M. Ganose, A. M. Candia, J. T. Granger, D. O. Scanlon, and J. R. Neilson, Anharmonicity and Octahedral Tilting in Defect-Ordered Hybrid Perovskites. *Chem. Mater.* (2018), 30(2), 472-483.
2) I. W. H. Oswald, A. A. Koegel, J. R. Neilson. General Synthesis Principles for Ruddlesden–Popper Hybrid Perovskite Halides from a Dynamic Equilibrium. *Chem. Mater.* (2018), 30(23), 8606-8614.
3) A. E. Maughan, A. A. Paecklar, J. R. Neilson, Bond valences and anharmonicity in vacancy-ordered double perovskite halides, *J. Mater. Chem. C.* (2018), 6, 12095-12104.
4) A. E. Maughan, A. M. Ganose, M. A. Almaker, D. O. Scanlon, and J. R. Neilson, Tolerance Factor and Cooperative Tilting Effects in Vacancy-Ordered Double Perovskite Halides, *Chem. Mater.* (2018), 30(11), 3909-3919.
5) I. W. H. Oswald, H. Ahn, J. R. Neilson, Influence of organic cation rigidity on structural templating in hybrid metal-halides. *Dalton Trans.*, (2019), 48, 16340-16349.
6) E. M. Mozur, J. C. Trowbridge, A. E. Maughan, M. J. Gorman, C. M. Brown, T. R. Prisk, J. R. Neilson, Dynamical Phase Transitions and Cation Orientation Dependent Photoconductivity in $CH(NH_2)_2PbBr_3$. *ACS Materials Lett.*, (2019), 1, 2, 260-264.
7) J. Hu, I. W. H. Oswald, H. Hu, S. J. Stuard, M. M. Nahid, L. Yan, Z. Chen, H. Ade, J. R. Neilson, W. You, Aryl-Perfluoroaryl Interaction in Two-Dimensional Organic–Inorganic Hybrid Perovskites Boosts Stability and Photovoltaic Efficiency. *ACS Materials Lett.*, (2019) 1, 1,171-176.
8) V. E. Combs, I. W. H. Oswald, J. R. Neilson, Hydrothermal Crystal Growth of Mixed Valence Cs_2SbBr_6, *Cryst. Growth & Des.*, (2019), 19, 7, 4090-4094.
9) I. W. H. Oswald, I. P. Moseley, H. Ahn, J. R. Neilson, Hybrid charge-transfer semiconductors: $(C_7H_7)SbI_4$, $(C_7H_7)BiI_4$, and their halide congeners, *Inorg. Chem.*, (2019), 58(9), 5818-5826.
10) J. Hu, I. W. H. Oswald, S. Stuard, M. M. Nahid, N. Zhou, O. Williams, Z. Guo, L. Yan, H. Hu, Z. Chen, X. Xiao, Y. Lin, Z. Yang, J. Huang, A. Moran, H. Ade, J. R. Neilson, W. You, Synthetic Control over Orientational Degeneracy of Spacer Cations Enhances Solar Cell Efficiency in Two-Dimensional Perovskites. *Nat. Commun.*, (2019) 10, 1276.
11) A. E. Maughan, A. M. Ganose, D. O. Scanlon, J. R. Neilson, Perspectives and Design Principles of Vacancy-Ordered Double Perovskite Halide Semiconductors, *Chem. Mater.*, (2019), 31(4), 1184- 1195.
12) T. Yamamoto, I. W. H. Oswald, C. Savory, T. Ohmi, A. A. Koegel, D. O. Scanlon, H. Kageyama, J. R. Neilson, Structure and optical properties of layered perovskite $(MA)_2PbI_{2-x}Br_x(SCN)_2$ ($0 \leq x < 1.6$). *Inorg. Chem.*, (2020), 59, 23, 17379-17384.
13) A. E. Maughan, E. M. Mozur, A. M. Candia, J. R. Neilson, Ferroelastic Phase Transition in Formamidinium Tin(IV) Iodide Driven by Organic-Inorganic Coupling. *Inorg. Chem.* (2020), 59(19), 14399-14406.

14) E. M. Mozur, M. A. Hope, J. C. Trowbridge, D. M. Halat, L. L. Daemen, T. R. Prisk, C. P. Grey, J. R. Neilson, Cesium substitution Relieves Geometric Frustration in Formamidinium Hybrid Perovskites. *Chem. Mater.* (2020), 32(14), 6266-6277.
15) J. R. Neilson, Organic cation dynamics in hybrid halide perovskite semiconductors. *Neutron News*, (2021), 32(1), 11-12. (*Invited perspective*)
16) E. M. Mozur, J. R. Neilson, Cation Dynamics in Hybrid Halide Perovskites. *Ann. Rev. Mat. Res.* (2021), 51 (ASAP). https://doi.org/10.1146/annurev-matsci-080819-012808

Understanding Novel Lewis Acid Doping Mechanisms in Organic Semiconductors

Thuc-Quyen Nguyen and Guillermo C. Bazan, Department of Chemistry and Biochemistry, University of California, Santa Barbara

Sergei Tretiak, Theoretical Division and Center for Integrated Nanotechnologies (CINT), Los Alamos National Laboratory

Program Scope

This program aims to understand doping mechanism in a class of conjugated polymers that contain Lewis basic atoms such as nitrogen and/or sulfur. The pyridine or sulfur moiety on the polymer provides an accessible lone-pair of electrons that can associate with the Lewis acid. Addition of the Lewis acid effectively tunes the optical gap and p-dopes the hole transport in the parent polymer, leading to increases in the free hole density and thus the charge-carrier mobility. The program integrates materials design, electronic characterization of thin films and a theoretical effort that seeks to connect bulk variables with molecular-scale interactions and thereby deliver a foundation for rational development of Lewis acid doping and significantly accelerate their applications.

Recent Progress

The ability to precisely control the equilibrium carrier concentration in traditional inorganic semiconductors is a fundamental underpinning of modern electronics. This importance provides much of the motivation behind the long-standing interest in the doped states and methods to achieve doping in organic semiconductors. *P*-doping using molecular dopants such as F_4TCNQ relies on electron transfer from the semiconductor's highest occupied molecular orbital (HOMO) to the lowest unoccupied molecular orbital (LUMO) of F_4TCNQ. This occurs by either matching the electron affinity of the dopant to the ionization energy of the organic semiconductor (*p*-doping), or by matching the ionization energy of the dopant with the electron affinity of the organic semiconductor (*n*-doping). The requirement of energy level matching thus limits the available dopants. F_4TCNQ is a strong electron acceptor with a LUMO energy of –5.2 eV, which matches well with the HOMO energy of a wide range of polymeric and molecular systems.**Error! Bookmark not defined.** Thus, much of the published work on *p*-doping organic semiconductors has centered on the use of F_4TCNQ. For solution-processed organic semiconductors this approach suffers from the differential solubilities of the dopant, the molecular anion (F_4TCNQ^-), and of the organic semiconductor; limiting the ultimate processability of the blend.[1] Furthermore, it is not possible to dope wide band gap organic semiconductors with F_4TCNQ (HOMO ~ –5.8 eV). In the past few years, a growing body of literature has indicated that $B(C_6F_5)_3$, hereafter referred to as BCF,

represents a promising new class (i.e. Lewis acids) of p-type dopant for organic semiconductors due to its excellent solubility in common organic solvents and its ability to dope organic semiconductors without the need for energy level matching.[2] However, the doping mechanism is not well understood.

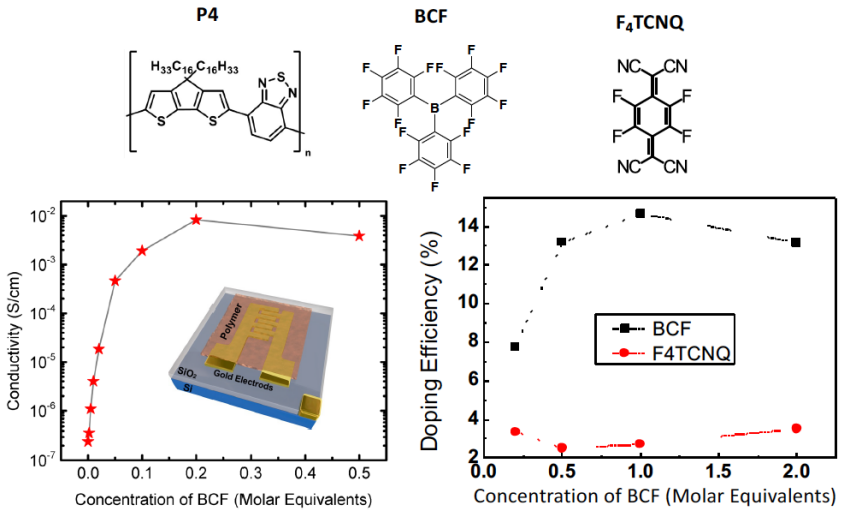

Figure 1. (Top) Chemical structures of the conjugated polymer, BCF, and F4TCNQ used in this study. (Bottom) The conductivity, the doping efficiency, and the device structure used for conductivity measurement.

The doping efficiency of BCF was found to be superior to that of F_4TCNQ, reaching a maximum of 14.6% at 0.010 molar equivalents for P4 (Figure 1). The conductivity of P4 can be improved over 4 orders of magnitude with BCF, reaching a maximum conductivity of 8 x 10^{-3} S/cm with 0.200 molar equivalents. High resolution 1D and 2D ssNMR techniques provide additional insights into the intermolecular interactions which underly the observed difference in doping efficiency between these two systems. BCF can dope the P4 host polymer with minimal disruption to the conjugated backbone stacking which is critical for charge transport in organic semiconductors. The backbone stacking between the donor and acceptor units of the polymer are greatly disrupted by the F_4TCNQ dopant which explains a much lower doping efficiency of P4 by F_4TCNQ as compared to doping using BCF-water complex.

We proposed that doping of a conjugated copolymer of 4,4-dihexadecyl-4*H*-cyclopenta[1,2-*b*:5,4-*b*′]dithiophene (CPDT) and 2,1,3-benzothiadiazole (BT)-based (P4, see Figure 1 for the chemical structure) by BCF is an example of oxidation by proton. Specifically we suggested protonation of the CPDT moieties by the strong Brønsted acid BCF(H_2O) (Step 1 in Scheme 1), followed by electron transfer from a neutral polymer chain segment to a protonated chain forming a neutral, protonated radical species [P4-H]$^{\bullet}$ and a positively charged radical species [P4]$^{\bullet+}$ (a positive polaron or a hole). ^{1}H NMR provided evidence for the feasibility of polymer protonation, while ENDOR spectroscopy was consistent with simulations of a superposition of the spectra of the two radicals.[3]

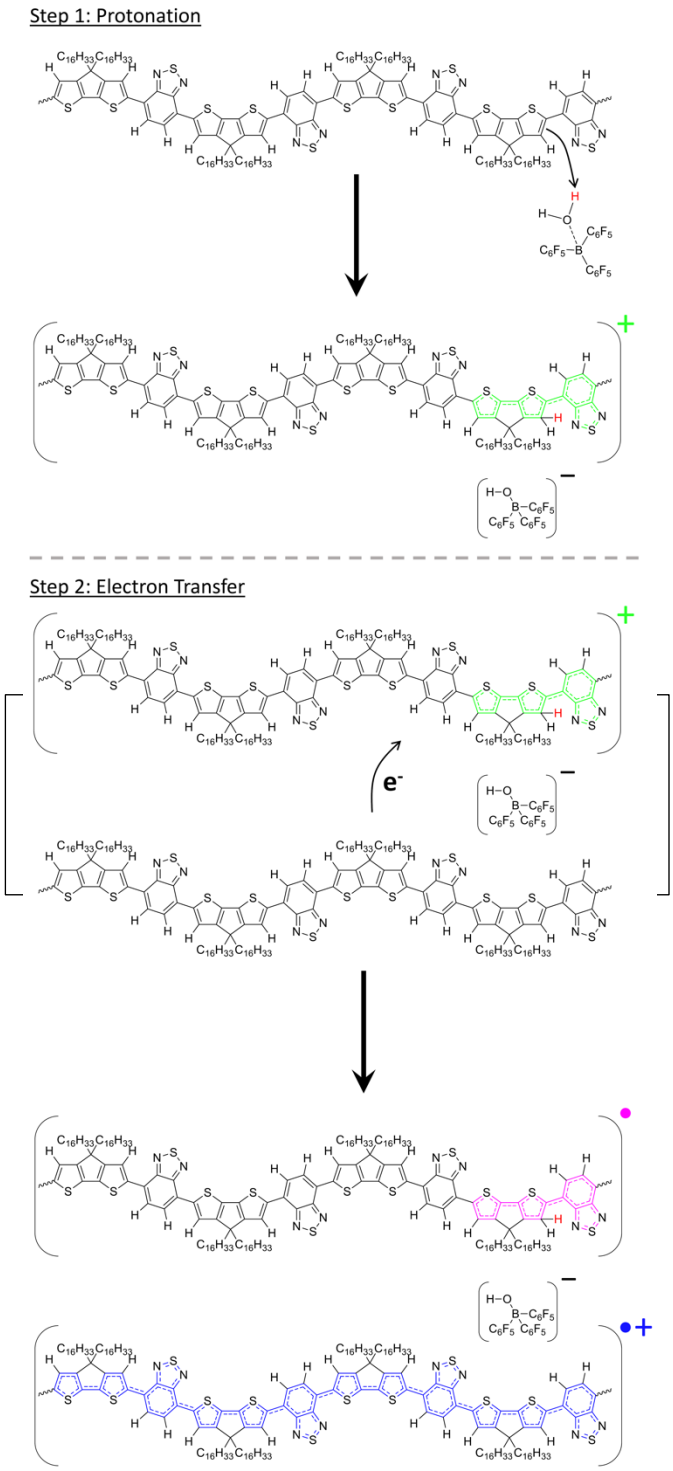

Neher and colleagues investigated doping of poly(3-hexylthiophene) (P3HT) by BCF and suggested that the overall reaction resulted in formation of H_2, rather than [P3HT-H]$^{\bullet}$, as the final hydrogen-containing side product, with one possible route for H_2 formation being reaction of two [P3HT-H]$^{\bullet}$ species (Step 3 in Figure 4).[4] DFT calculations of various scenarios from both mechanisms show highly endergonic processes (positive free energy) when considering the reaction of P4 and [BCF(OH$_2$)] to form [P4]$^{\bullet+}$ and [BCF(OH)]$^{-}$. However, if we consider the formation of a larger anion, [BCF(OH)(OH$_2$)BCF]$^{-}$ (Scheme 2), in which [BCF(OH)]$^{-}$ is hydrogen bonded to another BCF(OH$_2$) complex, DFT calculations predict that the protonation reaction (proposed by us) and the overall H_2-forming reaction (proposed by Neher) both become exergonic.[5] The formation of [BCF(OH)(OH$_2$)BCF]$^{-}$ has been observed by Doerrer and Green in their work on the oxidation of metallocenes by BCF(OH$_2$) in non-aqueous solvents (including ferrocene, which is oxidized at similar potential to P3HT), in which H_2 was also proposed to be the side product.[6] Another dinuclear anion [BCF(OH)BCF]$^{-}$ has also been formed in protonation and oxidation reactions of various organometallic complexes using BCF in the presence of small amounts of water,[7] and formation of this anion from the reaction of BCF, BCF(OH$_2$), and P4 is also calculated to be exergonic.[5] The formation of H_2 proposed in these BCF oxidations of both P3HT and metallocenes has not, however, been observed experimentally.

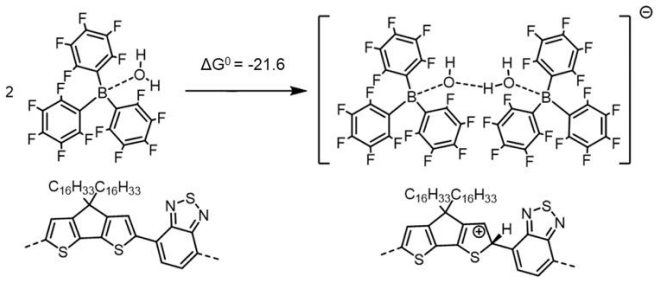

Scheme 2. Formation of the $[BCF(OH)(OH_2)BCF]^-$ anion and protonation of the neat PCPDTBT oligomer, which in this case yields a negative (exergonic) ΔG^0 = -21.6 kcal mol^{-1} (or -0.94 eV).

Future Plans

Our future plan is to gain insight into the mechanisms by which neutral polymers in non-aqueous solvents are doped by Lewis acid-water complexes (Brønsted acids). Since the doping process is not simply an electron-transfer reaction between the filled orbitals of the semiconductor molecules or polymers and the empty orbitals of the "dopants", our understanding needs to go considerably beyond consideration of the dopant electron affinity (EA) and semiconductor ionization energy (IE). We hypothesize that the driving force for p-doping is determined by the formation of delocalized stable anions to stabilize the positive polarons on the π–conjugated backbone. This, together with the release of hydrogen gas, leads to highly exergonic overall reaction.

References

[1] J. Li, G. Zhang, D. M. Holm, I. E. Jacobs, B. Yin, P. Stroeve, M. Mascal, A. J. Moule, *Chem. Mater.*, **2015**, *27*, 5765-5774.

[2] P. Zalar, C. Woellner, Z. B. Henson, Y. Zhang, M. Kuik, G. C. Bazan, T.-Q. Nguyen, *Adv. Mater.* **2014**, *26*, 724-727.

[3] B. Yurash, D. X. Cao, V. V. Brus, D. Leifert, M. Wang, A. Dixon, M. Seifrid, A. E. Mansour, D. Lungwitz, T. Liu, P. J. Santiago, K. R. Graham, N. Koch, G. C. Bazan, T.-Q. Nguyen, *Nat. Mater.* **2019**, *18*, 1327-1334.

[4] M. Arvind, C. Tait, M. Guerrini, J. Krumland, A. M. Valencia, C. Cocchi, A. E. Mansour, N. Koch, S. Barlow, S. R. Marder, J. Behrends, D. Neher, *J. Phys. Chem. B* **2020**, *124*, 7694-7708.

[5] P. S. Marqués, G. Londi, B. Yurash, T.-Q. Nguyen, S. Barlow, S. R. Marder, D. Beljonne, *Chem. Sci.* **2021**, *12*, 7012.

[6] L. Doerrer, M. L. H. Green, *J. Chem. Soc., Dalton Trans.* **1999**, 4325-4329.

[7] A. A. Danopoulos, J. R. Galsworthy, M. L. H. Green, S. Cafferkey, L. H. Doerrer, M. B. Hursthouse, *Chem. Commun.* **1998**, 2529-2530.

Publications

1) B. Yurash, D. Leifert, G. N. Manjunatha Reddy, D. Xi Cao, S. Biberger, A. Köhler, B. F. Chmelka, G. C. Bazan, T.-Q. Nguyen, "Atomic-Level Insight into the Post Synthesis Bandgap Engineering of a Lewis Basic Polymer Using the Lewis Acid Tris(pentafluorophenyl)borane, B(C6F5)3,"*Chem. Mater.* **2019**, *31*, 6715. https://doi.org/10.1021/acs.chemmater.9b01224

2) B. Yurash, D. X. Cao, V. V. Brus, D. Leifert, M. Wang, A. Dixon, M. Seifrid, A. E. Mansour, D. Lungwitz, T. Liu, P. J. Santiago, K. R. Graham, N. Koch, G. C. Bazan, T.-Q. Nguyen, "Towards Understanding the Doping Mechanism of Organic Semiconductors by Lewis Acids," Nature Materials 2019, 18, 1327–1334. doi:10.1038/s41563-019-0479-0

3) H. Phan, T. J. Kelly, E. Jarvis, A. Zhugayevych, G. C. Bazan, T.-Q. Nguyen, S. Tretiak, "Tuning Optical Properties of Conjugated Molecules by Lewis Acids: Insights from Electronic Structure Modeling," *J. Phys. Chem. Lett.* **2019**, *10*, 4632-4638.

4) D. X. Cao, D. Leifert, V. V. Brus, H. Phan, M. S. Wong, G. C. Bazan, N. Koch, T.-Q. Nguyen, "The Importance of Sulfonate to the Self-doping Mechanism of the Water-Soluble Conjugated Polyelectrolyte PCPDTBT-SO3K," *Materials Chemistry Frontiers* **2020**, *4*, 3556-3566

5) A. E. Mansour, H. Kim, S. Park, T. Schultz, D. X. Cao, T.-Q. Nguyen, W. Brütting, A. Opitz, N. Koch, "Conductive polymer work function changes due to residual water: Impact of water's temperature dependent dielectric constant," *Adv. Electronic Mater.* **2020**, *6*, 2000408.

6) G. Dufil, D. Parker, J. Y. Gerasimov, T.-Q. Nguyen, M. Berggren, E. Stavrinidou, "Enzyme-assisted in-vivo polymerisation of conjugated oligomer based conductors," *J. Mater. Chem. B* **2020**, *8*, 4221-4227.

7) P. S. Marques, G. Londib, B. Yurash, T.-Q. Nguyen, S. Barlow, S. R. Marder, and D. Beljonne, "Understanding How Lewis Acids Dope Organic Semiconductors: A "Complex" Story", *Chemical Science* **2021**, 12, 7012.

8) H. Wei, P.-A. Chen, J. Guo, Y. Liu, X. Qiu, H. Chen, Z. Zeng, T.-Q. Nguyen, Y. Hu, "Low-cost Nucleophilic Organic Bases as n-dopants for Organic Field-effect Transistors and Thermoelectric Devices,"*Adv. Funct. Mater.* **2021**, advance article. https://doi.org/10.1002/adfm.202102768

Hydrolysis, self-assembly and supramolecular assembly of early transition metal-oxo clusters: MOF nodes and aqueous reaction pathways

May Nyman, Oregon State University, Corvallis, OR 97330

Program Scope

Designing aqueous syntheses of functional metal oxide materials, oxoclusters and metal-organic frameworks (MOFs) with oxocluster nodes is an important part of a sustainable future for energy and the environment. The focus of this program is to design new materials and synthetic strategies using a metal-oxo cluster building-block approach, informed by solution-phase studies of reaction pathways. Materials include inorganic frameworks composed of metal-oxo clusters, MOFs, and metal oxide thin film coatings. In most studies, we benchmark properties of synthesized materials and study form-function relationships, in addition to studying solution-phase assembly pathways. Properties and applications include catalysis, ion exchange and metal separations.

In this meeting, time permitting, I will briefly present three ongoing studies: 1) Niobate oxoclusters and frameworks and controlling solution speciation with electrolytes; 2) New Zr/Hf^{IV} oxoclusters for cluster-based materials inspired from Zr/Hf^{IV} separations chemistry, and 3) MOFs from bismuth oxoclusters, controlling nuclearity. Recent results from these three systems are described below, preceded by more detailed introduction and motivation for each study.

Recent Progress

Niobate oxoclusters, frameworks and materials (***figure 1***)**.** Niobium (V) oxo species are technologically important, employed as base catalysts in the cluster form,[1] acid catalysts in the solid interfacial form,[2] and supercapacitors,[3] electrochromic materials[4] and piezoelectrics as thin films.[5] We have mapped the speciation of polyoxoniobates (PONb) in near neutral conditions (**figure 1a**), showing a decanuclear Nb_{10} PONb undergoes rearrangement to Nb_{24} with addition of any countercation or electrolyte or ligand that will associate with the cluster in solution.[6] These solutions can be prepared at very high concentration, near neutral pH, and they readily gel upon drying, ideal for thin film

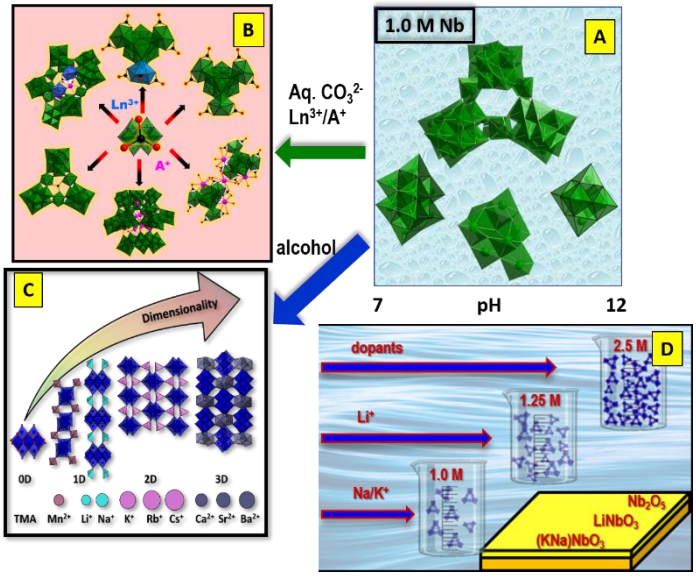

Figure 1. A) Summary of PONb solution speciation as a function of pH, **B**) Disassembly-reassembly driven by metal cations and carbonate in water, **C)** controlled dimensionality of frameworks by heterometal linking, and **D)** thin film deposition from high concentration solutions.

deposition. In recent studies, we have (1) enabled crystallization of the Nb_{24} species (and its subunits) with heterometals and ligands from solution to affirm identification of solution-phase speciation,[7,8] (2) demonstrated and compared catalytic activity (nerve agent degradation) of the pre-formed cluster to that of *in-situ* generated clusters, and (3) deposited several technologically important thin film materials from high concentration Nb_{24} solutions (**figure 1d**).[9] On the other hand, Nb_{10} in alcohol solution is stable, and shows preferential directional bonding into frameworks with heterometals, based on basicity of individual oxo-ligands within the cluster (**figure 1c**).[10] The dimensionality of the obtained frameworks depend on the charge and preferred coordination environment of the heterometal.

Zr/Hf^{IV} oxoclusters for cluster-based materials Moving one step to the left on the periodic table from Nb is very different oxocluster chemistry, featuring acidic polycations rather than basic polyanions. The $[Zr/Hf_6(OH)_4O_4]^{12+}$-oxocation is one of the most widely recognized and exploited oxocluster motifs in materials chemistry, featured in the UiO-66 MOF family (and derivatives thereof). Diversifying Zr/Hf-oxocluster chemistry as material building blocks requires disrupting and redirecting common reaction pathways. With peroxide, we have recognized new cluster motifs; an oxo-centered Zr_4-tetrahedron and a Zr_{25} wheel, both containing bridging peroxides.[11] Through studies of the solvent extraction chemistry used to separate Zr^{IV} from Hf^{IV} for nuclear energy applications (via solution studies and crystallization, see **figure 2**), we isolate oxo-centered Zr_4 and Hf_4 tetrahedral clusters ligated with thiocyanate (N-bonded), formulated $[M_4O(OH)_6(NCS)_{12}]^{4+}$, as well as a large Zr_{48} motif. The large Zr_{48} offers a plausible explanation as to how this industrially-employed separation chemistry works. We surmise the hydrolysis tendencies of Zr^{IV} are stronger than that of Hf^{IV} in the studied aqueous conditions. The tetrahedral clusters are ideal building blocks for novel oxocluster-based materials, see **Future Plans** section for strategies to implement these studies.

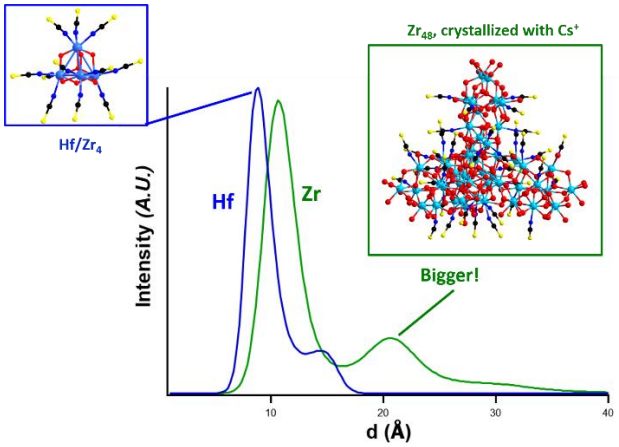

Figure 2. Size distribution analysis of small-angle X-ray scattering (SAXS) of aqueous Zr^{IV} and Hf^{IV} ammonium thiocyanate solutions, showing the difference between Hf^{IV} and Zr^{IV} aqueous speciation. Inset in the blue box is the oxo-centered tetrahedral cluster, crystallized as both Hf and Zr analogues, and also represents the highest concentration species in these solutions. Green box inset shows Zr_{48} cluster, which is also abundant exclusively in the Zr-solution. (color code: yellow spheres are sulfur, black is carbon, blue is nitrogen, red is oxygen, turquoise is metals, Hf^{IV} or Zr^{IV}).

Bismuth oxocluster MOFs Bi(III) is one of the most insoluble and inert metal oxides, and there is considerable interest in Bi-MOFs, which is only in early stages of development, in particular targeting biological applications and catalysis.[12,13] Like Zr/Hf^{IV}, Bi^{III} has strong hydrolysis tendencies, even at very low pH, and also features the ubiquitous hexamer form of UiO-66, yet the Bi_6-hexamer has only been isolated once in a MOF.[14] The Bi^{III} solution phase chemistry

is challenging to study and control due to the rapid hydrolysis reactions, in addition to the asymmetric coordination of Bi^{III}, driven by the lone pair, which has hindered Bi-MOF development.

Very recently, we have isolated a series of Bi-MOFs exploiting both disulfonate linkers and dicarboxylate linkers. These MOFs include the more common monomer, dimer, and 1d-chain Bi-node nuclearities. In addition, we have isolated several Bi_6-node MOFs, as well as the very large Bi_{38} node (**figure 3**). This series of compounds allows understanding of major parameters in controlling the node nuclearity.

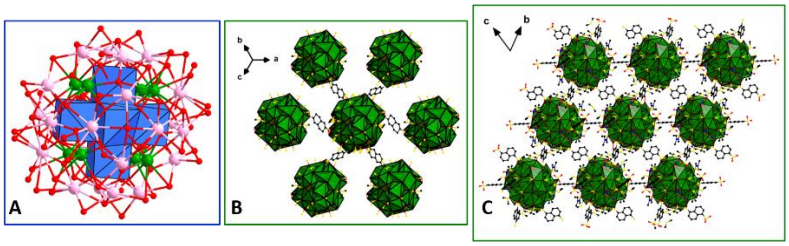

Figure 3. **Bi_{38} MOF**. **A**) Bi_{38} node represented to show how the cluster geometry is built up around the hexamer (blue, central, polyhedral representation). Pink spheres are six sets of four Bi^{III}, arranged as square faces of a cube centered by Bi_6. Green spheres are eight Bi^{III} on the corner of the same hypothetical cube. Red spheres are oxygen **B**) Bi_{38}-MOF with 2,6-napthalenedisulfonate linker. **C**) Bi_{38}-MOF with 1,5-napthalenedisulfonate linker.

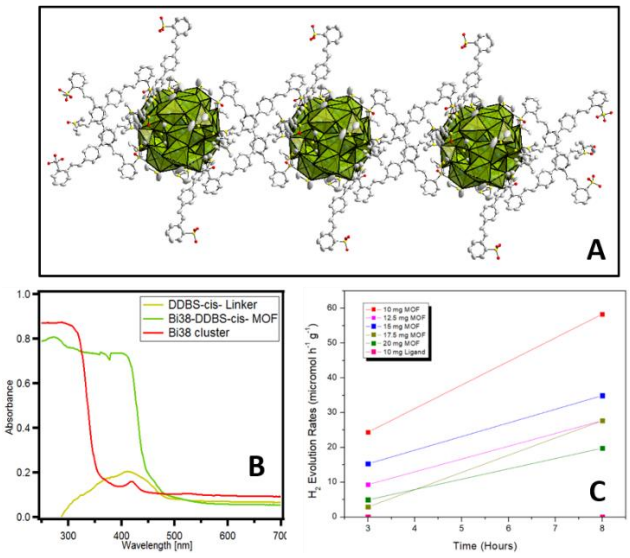

Figure 4. Bi_{38}-DDBS MOF. A) structural representation. **B**) UV-vis absorption of the Bi_{38} cluster, the DDBS linker and the Bi_{38}-DDBS MOF. **C**) H_2 evolution of different concentrations of Bi_{38}-DDBS MOF.

Specifically, the carboxylate ligands isolate smaller Bi_1 and Bi_2 nodes, while solvent is less relevant. The weaker bonding sulfonates favor the larger Bi_{38} node, in particular with DMSO solvent, while DMF and water favor the more common monomers, dimers and chains. DMSO is the only solvent that allows complete dissolution of Bi_6 and even Bi_{38} at room temperature, all other solvents require heating, and complete dissolution is never observed at room temperature. This significantly challenges our ability to study reaction pathways with in-house techniques (see more below, **Future Plans** section).

We compared photocatalytic H_2 evolution activity of various Bi_{38}-node MOFs, ligands include 1) disodium 2,2'-[biphenyl-4,4'-diyldiethene-2,1-diyl]dibenzenesulphonate (DDBS, **figure 4**), 2) 2,6-naphthalenedisulfonate (**figure 3b**) and 3) 1,5-naphthalenedisulfonate (**figure 3c**). Bi_{38}-DDBS demonstrated most efficacious H_2 evolution of the three, likely owed to the visible light absorption of the linker. The H_2 evolution reaction was observed without a co-catalyst, with visible light irradiation in the case of **Bi_{38}-DDBS**.

Future Plans

Our ultimate challenge and goal that we are continuing to pursue for the **niobate** clusters and materials is to prepare a true Nb-MOF or open framework featuring Nb-POMs with robust framework and porosity. The hurdles are many including the tendency of Nb to form anionic POMs, and identifying solution conditions that accommodate both Nb hydrolysis (for polynuclear nodes) and coordination chemistry. One future approach is the use higher-charged anionic linkers (i.e. diphosphonates and disulfonates) to balance the high Nb^{5+} charge. We are also employing additional inorganic ligands such as borate, carbonate and diphosphonate to disrupt common Nb-POM assemblies. Other approaches include combining higher-charged metal heteroatoms, Nb_{10} and linkers in conditions that do NOT undergo disassembly processes to build 3-compoment modular systems featuring this Nb-POM that undergoes selective directional bonding.

To continue the **Zr/Hf oxocluster** materials assemblies, we will combine the Hf_4 and Zr_4 tetrahedral oxoclusters (in addition to the large Zr_{48}) with soft, thiophilic metals of different charges to preferentially bind the S^{2-} of the thiocyanate group. The charge and coordination environments of the heterometals will define framework topologies. If successful, the resulting materials will represent a different type of cluster-based open framework material. Properties will be benchmarked that could include ion exchange, magnetism, luminescence and catalysis, depending on the nature of the obtained frameworks.

Studies of the **Bi-MOFs** will be continued with the major following goals. Since the DDBS linker provided the best visible light photocatalysis for the Bi_{38} family of MOFs, we endeavor to prepare Bi-monomer, Bi-dimer, Bi-polymer, and/or Bi-hexamer MOFs to compare the effect of the node on MOF stability and hole-charge separation. If possible, we would like to perform synchrotron X-ray scattering (or absorption) experiments to study Bi-speciation as a function of linker and solvent, to understand how to control this challenging solution phase chemical system.

References

1. Kinnan et al. *European Journal of Inorganic Chemistry*, 2361–2367 **2014**
2. Braga et al. *J. Catal.* **2007**, *247*(1), 68-77.
3. Augustyn et al. *Nat. Mater.* **2013**, *12* (6), 518–522.
4. Saez Cabezas et al. *Chem. Mater.* **2020**, *32* (11), 4600–4608.
5. Pham et al. *R. Soc. Open Sci.* **2019**, *6* (1) 180989.
6. Sures et al., *J Am Chem Soc*, 140 (34), pp 10803–10813, **2018.**
7. Martin et al., *Chem: Eur J*, **2019** *25*(45), pp.10580-10584
8. Amiri et al. *Angew Chem Int Ed* **2021** *60*(22), pp.12461-12466,
9. Rahman et al, **2021**, *Chemistry of Materials*, in review
10. Martin and Nyman, *Angew Chem Int. Ed*, **2021**, 60(20), 954-960
11. Sommers et al., *J Am Chem Soc* **2019,** 141 (42), 16894-16902
12. Wang et al. **2021** *Coord Chem Rev, 439*, p.213902.
13. Wang and Li. *Inorg Chemistry Frontiers*, **2020**, 8, 572-589.
14. Robison et al., *ACS Applied Bio Materials*, **2019**, *2*(3), pp.1197-1203.

Publications from last 3 years acknowledging project support (*denotes publications designed and led from this project, Ψdenotes contribution to collaborators' publications)

* **"Nb-speciation for niobate thin films from water: bigger is better"** T. Rahman, N.P. Martin, R. Elzei[b], R. Addou, G.S. Herman, M. Nyman, **2021**, *Chemistry of Materials*, in review

Ψ "**Unraveling Nanoscale Cobalt Oxide Catalysts for the Oxygen Evolution Reaction: Maximum Performance, Minimum Effort"** L. Reith, C. A. Triana, F. Pazoki, M. Amiri, M. Nyman and G.R. Patzke, **2021**, *J Am Chem Soc*, in review

* **"Deliberate construction of polyoxoniobates exploiting the carbonate ligand"** M Amiri, NP Martin, CL Feng, JK Lovio, M Nyman *Angewandte Chemie International Edition 60*(22), pp.12461-12466, **2021 https://doi.org/10.1002/ange.202017367 ***

Ψ "**Single-stranded DNA as supramolecular template for one-dimensional palladium (II) arrays."** Pérez-Romero, Antonio, Alicia Domínguez-Martín, Simona Galli, Noelia Santamaría-Díaz, Oscar Palacios, José A. Dobado, May Nyman, and Miguel A. Galindo**.** 60 (18), 10089-10094 *Angewandte Chemie International Edition* **2021 https://doi.org/10.1002/anie.202015554**

* **"Differentiating Zr/Hf^{IV} Aqueous Polyoxocation Chemistry with Peroxide Ligation"** James A. Sommers, Danielle C. Hutchison, Nicolas P. Martin, Lauren Palys, Jenn M. Amador, Douglas A. Keszler, and May Nyman, *Inorganic Chemistry*, 60 (3), 1631-1640 **2021 doi.org/10.1021/acs.inorgchem.0c03128**

* **"Directional bonding in {Nb$_{10}$} inorganic frameworks"** Nicolas P. Martin and May Nyman, *Angewandte Chemie Int. Ed*, **2021**, 60(20), 954-960 https://doi.org/10.1002/ange.202010902

Ψ **"A Molecular Intermediate in the Directed Formation of a Zeolitic Metal-Organic Framework"** Michael A. Sinnwell, Quin R.S. Miller, Lauren Palys, Dushyant Barpaga, Lili Liu, Mark E. Bowden, Yi Han,Sanjit K. Ghose, Maria L. Sushko, Herbert Todd Schaef, Wenqian Xu, May Nyman, and Praveen K. Thallapally, *Journal of the American Chemical Society*, **2020**; 142 (41), 17598-17606, https://doi.org/10.1021/jacs.0c07862

* **"Countercation-controlled nuclearity of Zr/Hf peroxo-oxalates"** Karoly Kozma, Lev N. Zakharov, and May Nyman, *Crystal Growth and Design*, **2020**, 20 (10), 6519-6527 https://doi.org/10.1021/acs.cgd.0c00713

Ψ **"Discrete Hf$_{18}$ metal-oxo cluster as a heterogeneous nanozyme for site-specific proteolysis."** Moons, Jens, Francisco de Azambuja, Jelena Mihailovic, Karoly Kozma, Katarina Smiljanic, Mehran Amiri, Tanja Cirkovic Velickovic, May Nyman, and Tatjana N. Parac-Vogt**.** *Angewandte Chemie* 132, no. 23 **2020**, 9179-9186. DOI: https://doi.org/10.1002/ange.202001036

Ψ **"Reversible M-M bonding by Alkaline Earth Metals (Mg, Ca, Sr, Ba) in Graphite Intercalation Compounds."** Xu, Wei, Karoly Kozma, Tianxiang Sha, Yi-Jen Wu, May Nyman, and Michael Lerner. *Chemistry–A European Journal* **2020**, 26, 36, 8108-8104. https://doi.org/10.1002/chem.202000504

***** **"Bismuth for Controlled Assembly/Disassembly of Transition-Metal Oxo Clusters, Defining Reaction Pathways in Inorganic Synthesis and Nature."** Mehran Amiri, Nicolas P. Martin, Omid Sadeghi, and May Nyman. *Inorganic Chemistry* 59, no. 6, **2020**: 3471-3481. DOI: https://pubs.acs.org/doi/abs/10.1021/acs.inorgchem.9b03646

***** **"Beyond Charge Balance: Counter-Cations in Polyoxometalate Chemistry."** Archismita Misra, Karoly Kozma, Carsten Streb, May Nyman. 59(2) 596-612 *Angewandte Chemie International Edition* **2020** DOI: **https://doi.org/10.1002/anie.201905600**

Ψ **Atomically-precise lanthanide-iron-oxo clusters featuring the ε-Keggin ion."**Zheng, Xiu-Ying, Ming-Hao Du, Mehran Amiri, May Nyman, Qiang Liu, Tao Liu, Xiang-Jian Kong, La-Sheng Long, and Lan-Sun Zheng. *Chemistry–A European Journal*, **2020**, 26 (6), 1388-1395 DOI: https://doi.org/10.1002/chem.201904636

***** **"Two distinct patterns of aggregation in low- and high-charge Linqvist-type Polyoxometalates define opposite solubility trends",** Mireia Segado, May Nyman and Carles Bo, *Journal of Physical Chemistry* **2019** 123 (49), 10505-10513 https://doi.org/10.1021/acs.jpcb.9b08571

***** **"Peroxide-promoted disassembly-reassembly of Zr-polyoxocations."** James A. Sommers, Nicolas P. Martin, Danielle C. Hutchison, Karoly Kozma, Douglas A. Keszler and May Nyman, *Journal of the American Chemical Society* **2019,** 141 (42), 16894-16902 https://doi.org/10.1021/jacs.9b08627

***** **"Strategic capture of the {Nb_7} polyoxometalate",** Nicolas P. Martin, Enric Petrus, Mireia Segado, Lev N. Zhakarov, Carles Bo and May Nyman, *Chemistry: A European Journal*, **2019** DOI: **https://doi.org/10.1002/chem.201902770** *25*(45), pp.10580-10584

***** **"The role of titanium-oxo clusters in sulfate production of TiO_2"** Karoly Kozma, Maoyu Wang, Pedro I. Molina, Nicolas P. Martin, Zhenxing Feng and May Nyman, *Dalton Transactions*, 48(29) pp. 11086-11093, **2019** DOI**: 10.1039/c9dt01337g**

Ψ **"Niobium uptake by $[P_8W_{48}O_{184}]^{40-}$ macrocyclic polyanion"** Alexandra A. Shmakova, Victoria V. Volchek, Vadim Yanshole, Nikolay B. Kompankov, Nicolas P. Martin, May Nyman, Pavel A. Abramov, Maxim N. Sokolov, *New Journal of Chemistry* 43, pp. 9943-9952, **2019, DOI: 10.1039/C9NJ01907C**

Ψ **"Stabilizing Reactive Fe (III) Clusters by Freeze-Dry/Solvent-Exchange To Benchmark Iron Hydrolysis Pathways."** Wei Wang, Mehran Amiri, Tao Huang, Lev N.

Zakharov, Yining Zhang, and May Nyman. ***Inorganic Chemistry*** *58*(9), pp. 5555-5560, **2019, DOI: 10.1021/acs.inorgchem.8b03446**

* **"Reaction Pathway to the inaugural open-shell transition-metal Keggin ion without organic ligation",** Wei Wang, Mehran Amiri, Karoly Kozma, Jian Lu, Lev N. Zakharov, May Nyman, *European Journal of Inorganic Chemistry*, (42), pp 4638-4642, **2018 https://onlinelibrary.wiley.com/doi/abs/10.1002/ejic.201801087**

* **"Thermochemical measurements of alkali cation association to hexatantalate**" Dylan Sures, G.P. Nagabhushana, Alex Navrotsky and May Nyman, *Molecules*, 23(10), pp 2441(6 pgs) **2018, https://www.mdpi.com/1420-3049/23/10/2441**

* **"Alkali-driven disassembly and reassembly of molecular niobium oxide in water",** Dylan Sures, Mireia Segado, Carles Bo, and May Nyman, *Journal of the American Chemical Society*, 140 (34), pp 10803–10813, **2018. DOI: DOI: 10.1021/jacs.8b05015**

Chemo-Mechanically Driven In Situ Hierarchical Structure Formation in Mixed Conductors

Nicola H. Perry, MatSE Department, University of Illinois at Urbana-Champaign

Program Scope

The overarching goal of the project is to monitor, understand, and direct structure across multiple length scales to achieve hierarchical, highly active mixed ionic/electronic conducting oxides (MIECs). MIECs enable a variety of energy and electronic applications by their dual ability to exchange oxygen with the gas phase (catalyzing electrochemical reactions) at the surface and conduct ionic and electronic species within the bulk. However, conventional MIECs are processed at high temperatures, causing coarsening and segregation of non-active cations, leading to sluggish surface exchange kinetics[i]. We are developing a new, low temperature, non-equilibrium pulsed laser deposition (PLD) method[i] that leverages MIEC chemo-mechanical coupling to create hierarchical structures with high surface reactivity and rapid mixed ionic/electronic transport. Amorphous films are fabricated by low temperature PLD and actuated into hierarchical structures by chemical contractions induced by crystallization and oxidation. The main focus is on monitoring, understanding, and controlling the emerging hierarchical structure to yield high surface area, reactive surface chemistry, and fast bulk transport behavior.

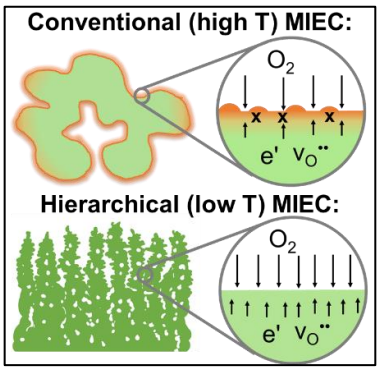

Figure 1: Motivation for low-temperature processing of MIECs

In *phase 1*, we seek to observe and understand the interplay of chemo-mechanical coupling and hierarchical structure evolution; we determine how a) local ion arrangements (amorphous vs. crystalline), b) macroscopic density and oxygen stoichiometry, c) surface composition, and d) microstructure evolve. In *phase 2*, we seek to learn how PLD growth conditions and crystallization stimuli can be tuned to tailor the resulting hierarchical structure. Here we are pursuing three approaches: a) control the magnitude of the chemo-mechanical coupling (via changing multivalent cation concentration, initial density), b) direct structure evolution by engineering initial film inhomogeneities, and c) modify crystallization conditions (thermal profile and/or local oxygen activity). In *phase 3*, we seek to measure and understand transport and surface reactivity changes during hierarchical transformation. This final task involves developing a new 2-dimensional optical transmission relaxation technique for high throughput monitoring of surface catalytic activity and applying various methods to monitor properties *in situ* during structure evolution.

Recent Progress

Our recent efforts have led to an in-depth understanding of the relationships between MIEC chemo-mechanical coupling, hierarchical structure evolution, and dramatic transformations of functional properties[1-4]. In support of this activity, we have developed an *in situ* simultaneous optical and electrical relaxation method for continuous, controlled atmosphere/temperature monitoring of defect chemistry, transport behavior, and surface exchange kinetics evolution[2,3].

Phase 1: Chemo-Mechanical Coupling and Hierarchical Structure Evolution. Our work involves studies of structural changes across many length scales during crystallization of MIECs, which has so far not been widely investigated. We hypothesized that, contrary to many other materials classes, the crystallization process in MIECs involves a compositional change via interaction with the surrounding gas atmosphere, enabling oxidation. We posited that, similar to crystalline MIECs, this oxidation would correspond to a structural contraction. Along with the expected densification caused by crystallization, this extra chemo-mechanical coupling from oxidation would contribute to the transformation of monolithic amorphous films into complex hierarchical nanostructures during crystallization. To test the hypothesis and understand the corresponding chemical/structural changes, we have been applying X-ray absorption spectroscopy, optical absorption spectroscopy, X-ray diffraction, X-ray reflectivity, scanning probe microscopy, and high resolution transmission electron microscopy with spectroscopy at various stages of the crystallization process. The prototypical MIEC composition at the center of our studies is $SrTi_{0.65}Fe_{0.35}O_{3-x}$ perovskite.

A key finding from our work is that the crystallization point is also the point of onset for "breathing" oxygen in the films: crystallization and oxygen intake from the gas phase initiate together. For $SrTi_{0.65}Fe_{0.35}O_{3-x}$, we have evidence from *ex situ* UV-vis spectroscopy scans. For this composition, our earlier work[ii] demonstrated the linear relationship of optical absorption to hole and oxygen concentrations at key wavelengths. Our *ex situ* results suggest increased hole and oxygen concentrations in the crystalline vs. amorphous films. Further evidence is from *in situ* optical transmission, and optical relaxation responses to oxygen partial pressure (pO_2) steps, during gradual annealing to induce crystallization in mixed conducting $SrTi_{0.65}Fe_{0.35}O_{3-x}$, $SrTi_{0.65}Co_{0.35}O_{3-x}$, and $Sr_2Ti_{0.65}Fe_{0.35}O_{4-x}$ films[1]. A steep optical transmission drop for each composition occurs at a point attributed to crystallization (by additional *ex situ* microscopy studies). Prior to this point, the films do not appreciably respond optically to pO_2 changes, whereas after this point extremely rapid optical responses to pO_2 steps occur. These results indicate oxygen exchange with the gas phase takes place during and after crystallization, but not before. Lastly, we have evidence from Fe K-edge XANES (fig. 2) showing an increase of average Fe valence state going from amorphous to semi-crystalline to fully crystalline films, and an increase of average Fe valence state over the first 10 minutes of a rapid anneal of an initially amorphous film in 0.21 atm O_2 at 400 °C[4]. Therefore, our hypothesis that oxidation accompanies crystallization of at least selected MIEC compositions is confirmed. This oxidation process is important for both its coupling to contractive strain, which will contribute to microstructural transformation, and its impact on point defect concentrations, which dictate functional properties of interest for energy conversion and storage.

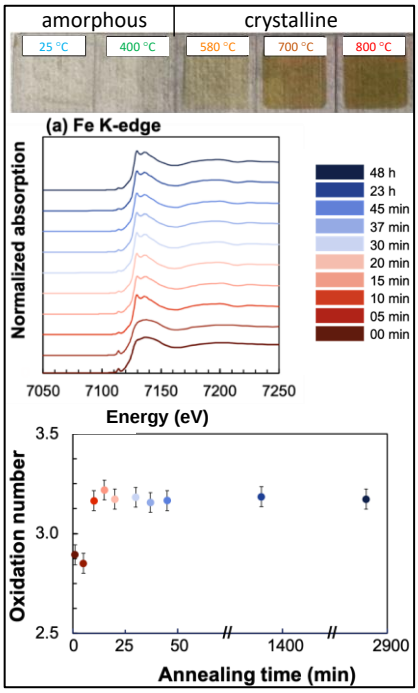

Figure 2: Optical and XAS evidence for oxidation during MIEC crystallization[1,4]

The XAS studies can further provide insight into atomic-scale structural changes that have implications for the micro-scale structural evolution. We have observed increases in Fe-O and Ti-O coordination numbers, increases in B-site (Fe/Ti) coordination unit symmetry, and increased alignment of neighboring B-site – oxygen coordination units[4] in both EXAFS and pre-edge features during crystallization, as the films become more ordered and more cubic, with complex changes in bond lengths due to the variable coordination numbers and polyhedra symmetry. Microstructural evolution during different stages of annealing at 400 °C was observed with bright- and dark-field HRTEM and local FFT and selected-area diffraction assessments of symmetry[4]. The results showed initially monolithic and homogeneous amorphous films, with appearance of nanoscopic (~4 nm) crystallites and isolated pores after 20 min (fig. 3), and larger crystallites with chains of aligned nanopores after 23 h. The appearance of a significant volume of pores is consistent with the expected solid-phase contraction induced chemically by both oxidation and crystallization. Thus the chemical strain, along with the crystallite nucleation density, informs the resulting microstructure and appearance of new surfaces. No compositional inhomogeneity of the solid phase was observed as a result of crystallization, according to high resolution EDS. Indeed, we know from depth-resolved X-ray absorption spectroscopy[1] (fig. 3) that our low-temperature-grown and in-situ-crystallized films lack appreciable segregation of the larger cation (Sr), unlike our high-temperature-grown crystalline films. X-ray diffraction further confirms single phase, randomly oriented films after crystallization.

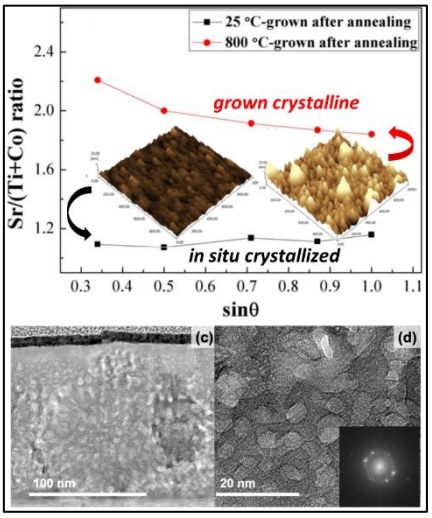

Figure 3: No Sr surface segregation[1] and nanoscopic pores in low-T MIEC[4].

Phase 3: Transformation of Functional Properties. We enabled continuous, *in situ* insights into property evolution through advanced technique development. For oxygen surface exchange coefficient (*k*) measurements, we developed capabilities for simultaneous optical transmission relaxation (OTR) and electrical conductivity relaxation (ECR) as well as simultaneous OTR with asymmetric-cell electrochemical ac impedance spectroscopy (AC-IS)[3]. We demonstrated that OTR and ECR provide excellent agreement and accurate assessment of *k*. On the other hand AC-IS results were artificially elevated and less stable, attributed to the presence of the metal current collectors and the different driving force which may change the mechanism or rate-determining step for the surface electrochemical reaction. We see therefore that OTR is advantageous as a contact-free method not requiring current collectors, while results from AC-IS, widely applied in the community, must be treated carefully. Our invited review[2] demonstrates broader use of *in situ* optical methods to determine not only interfacial kinetic parameters but also bulk diffusivities and point defect equilibria in a variety of oxide film compositions.

In situ optical and electrical measurements demonstrated orders-of-magnitude increases in k[1,3] and in-plane conductivity[3,4] (σ) of films during crystallization. In addition, the k values are

significantly higher (~2 orders of magnitude) and σ also appears higher compared to conventional fully crystalline MIECs prepared at high temperatures. We can explain the dramatic increase in σ during crystallization from the optical and XAS results: σ is the product of charge, carrier mobility, and carrier concentration. In the relatively oxidizing measurement conditions, the primary carriers are holes. We suggest that hole mobility increases, as indicated by the improved symmetry and alignment of neighboring B-site coordination units seen in XAS[4]. This alignment enables better overlap of the directional O-*2p* and Fe-*3d* orbitals which are hybridized at the top of the valence band of the crystalline material. The increase in oxygen concentration and Fe valence state observed by the shift of the Fe K absorption edge, increasing Fe coordination number, and sub-gap optical absorption increase demonstrate the increase in hole concentration. As for the increase in *k* vs. both amorphous and high-temperature-grown films, we currently understand that oxygen exchange is much faster in the hierarchical films due to several factors: increase in in-plane electronic conductivity[4], absence of appreciable Sr surface segregation, and exposure of new pristine surfaces with slight increase in surface area[1]. Our results show that *in situ* crystallization/oxidation and corresponding hierarchical actuation is beneficial for the key properties of interest: bulk electrical conductivity and surface oxygen exchange kinetics.

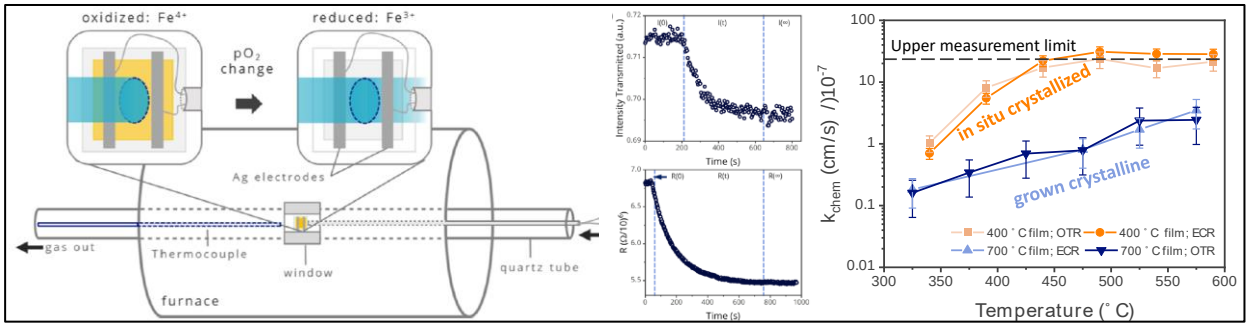

Figure 4: Simultaneous OTR/ECR setup, optical/electrical relaxation profiles, and surface exchange coefficients.[3]

Future Plans

Future work primarily revolves around phase 2, where we seek to understand how to control and tailor the resulting hierarchical microstructure by varying the growth conditions and crystallization stimuli. We hope to incorporate advanced microscopy techniques, e.g., nanobeam diffraction and custom analysis algorithms, to better quantify the resulting 3D nanostructures and strain distributions. We also plan additional studies quantifying oxygen concentration changes during crystallization by Rutherford backscattering spectrometry, valence band maximum position changes by X-ray photoelectron spectroscopy (XPS), and surface chemistry analysis with high resolution (S)TEM-EDS/EELS and XPS. In tandem, we are broadening our effort to other MIEC compositions, particularly those with different defect chemistry and crystalline transference numbers that may benefit from tailoring the oxygen content through the crystallization pathway.

References

[i] T. Chen, G.F. Harrington, K. Sasaki, and N.H. Perry, *J. Mater. Chem. A*, 5, 23006-23019 (2017).

[ii] N.H. Perry, N.H. Kim, E. Ertekin, H.L. Tuller, *Chem. Mater.*, 31 [3], 1030-1041 (2019).

Publications

1. Ting Chen, George F. Harrington, Juveria Masood, Kazunari Sasaki, and Nicola H. Perry, "Emergence of Rapid Oxygen Surface Exchange Kinetics During In Situ Crystallization of Mixed Conducting Thin Film Oxides," *ACS Appl. Mater. Interfaces* 11 [9], 9102-9116 (2019). DOI: 10.1021/acsami.8b21285
2. Haley B. Buckner and Nicola H. Perry, "In Situ Optical Absorption Studies of Point Defect Kinetics and Thermodynamics In Oxide Thin Films" *Adv. Mater. Interfaces* 6 [15], 1900496 (2019). DOI: 10.1002/admi.201900496 (Invited)
3. Emily Skiba, Ting Chen, and Nicola H. Perry, "Simultaneous Electrical, Electrochemical, and Optical Relaxation Measurements of Oxygen Surface Exchange Coefficients: $Sr(Ti,Fe)O_{3-d}$ Film Crystallization Case Study" *ACS Appl. Mater. Interfaces* 12 [43], 48614–48630 (2020). DOI: 10.1021/acsami.0c14265
4. Haley B. Buckner, Qing Ma, Joshua Simpson-Gomez, Emily Skiba, and Nicola H. Perry, "Correlating electrical conductivity and evolving multi-scale structure in perovskite $SrTi_{0.65}Fe_{0.35}O_{3-d}$ thin films during crystallization" (submitted by 7/2021)

Hierarchical Hybrid Multifunctional Materials through Interface Engineering

PI : Dr. Pierre Ferdinand Poudeu ; Department of Materials Science and Engineering, University of Michigan; ppoudeup@umich.edu

Co-PI*:* Dr. Ctirad Uher; Department of Physics, University of Michigan; cuher@umich.edu

Program Scope

The main goal of this project is to design and synthesize *stimuli-responsive hybrid multifunctional materials.* These are materials that can sense and respond to their environment. Our hypothesis is that such multifunctional materials could be realized by structurally integrating, at multiple length scales, two and more compounds that possess the desired functionalities. We have focused our investigation on bulk hybrid materials in which electronic and optical properties are strongly coupled. Such materials could be realized in bulk composite superstructures between (1) a *narrow band gap semiconductor (NBGS)* with excellent electronic properties and (2) a *wider band gap semiconductor (WBGS)* with outstanding optical properties. As model systems for the design of (1-x)NBGS/(x)WBGS multifunctional superstructures, we have selected one *NBGS (band gap E_g < 0.5 eV), Cu_2Se,* and two families of WBGS (*band gap E_g > 1.0 eV),* $CuMSe_2$ (M = Al, Ga, In). Cu_2Se is a well-studied NBGS with excellent thermoelectric properties (high electrical conductivity, large thermopower, etc.) while $CuInSe_2$ and Cu_4TiSe_4 are high performance solar absorber materials (large band gap, large absorption coefficient, etc.). Our primary objectives are to identify and control key material and growth parameters governing phase formation, microstructural evolution at various interfaces, and to understand the mechanism by which these changes of the internal structure modify the material's performance. In addition, we will explore exciting new physical and chemical phenomena that may result from the non-equilibrium at the multiscale interfaces ($Cu_2Se/CuMSe_2$) arising from the proximity of very different chemistries and structure types in bulk *(1-x)(NBGS)/(x)(WBGS)* hierarchical superstructures. Multiscale integration of the coupling between electronic and optical properties anticipated at the interfaces can lead to strong *electro-optic effects* and novel *optoelectronic* properties.

Recent Progress

We began with the investigation of *(1-x)(NBGS)/(x)(WBGS)* hierarchical composites based on four materials systems; (i)(1-x)Cu_2Se/(x)$CuGaSe_2$; (ii)(1-x)Cu_2Se/(x)$CuFeSe_2$; (iii)(1-x)Cu_2Se/(x)$CuAlSe_2$; and (iv) (1-x)Cu_2Se/(x)$CuInSe_2$. In the first three systems, we focused our attention on compositions with x<0.15, which is the range within which superior thermoelectric materials are anticipated. Within this composition range, we focused our investigation on the impact of chemical composition (choice of the WBGS composition ($CuMSe_2$), i.e., the nature of M, and the phase fraction, x values) on the microstructure of the resulting composites. We found

that the incorporation of such a small fraction of the $CuMSe_2$ phase within the narrow band gap semiconducting matrix, Cu_2Se, resulted in partial doping as well as the formation of unique microstructures depending on the chemistry (nature of M) of the inclusion phase ($CuMSe_2$). We have elucidated the atomic scale interaction between the coexisting phases (Cu_2Se and $CuMSe_2$; M = Ga, Fe, Al) and their impact on the thermoelectric properties. Results from the first three projects (M = Ga, Fe and Al) were recently published.[1-3]

For example, we demonstrated using the ***(1-x)Cu_2Se/(x)$CuGaSe_2$ (0≤x≤0.15),***[2] system an unprecedented *nanoscale engineering of c*rystal polymorphism during the synthesis. We found that the incorporation of $CuGaSe_2$ nanoseeds leads to a preferential stabilization of β-Cu_2Se at room temperature, at the expense of the thermodynamically stable α-Cu_2Se. This is attributed to the formation of low-energy coherent $CuGaSe_2$/β-Cu_2Se interfaces owing to the small lattice mismatch between β-Cu_2Se (cubic) and the *ab* plane of tetragonal $CuGaSe_2$ nanoseeds. This ability to control under ambient conditions the relative ratio between the α-Cu_2Se and β-Cu_2Se polymorphs in (x)$CuGaSe_2$/(1-x)Cu_2Se composites using $CuGaSe_2$ nanoseeds enables modulation of the functional properties. For instance, we observed a remarkable decoupling of charge and heat transport in the resulting hierarchical microstructures, which is manifested by a breakdown of the Wiedemann-Franz law.

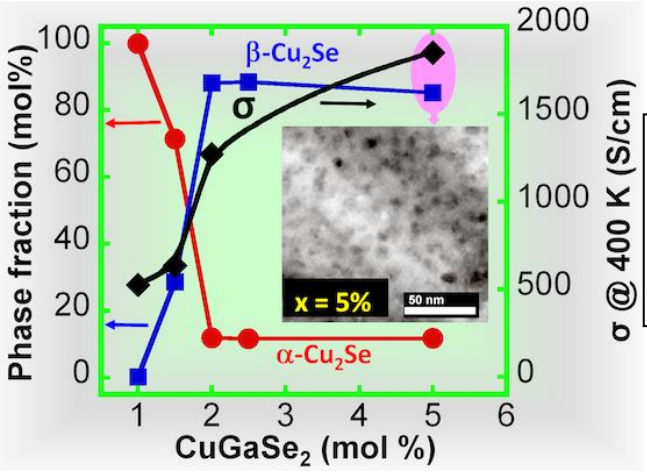

The incorporation of sub-ten nanometer $CuGaSe_2$ inclusions into Cu_2Se matrix promotes the stabilization of β-Cu_2Se at the expense of α-Cu_2Se polymorph leading to a remarkable decoupling of charge and heat transport in the synthesized of (x)$CuGaSe_2$/(1-x)Cu_2Se composites.

Adjusting the composition of the WBGS phase from $CuGaSe_2$ to $CuAlSe_2$ and $CuFeSe_2$ led to a completely different microstructures.[1, 3] For instance, we observed that the incorporation of $CuAlSe_2$ inclusions leads to the formation, near the $CuAlSe_2$/Cu_2Se interface, of a high density of Cu-deficient β-$Cu_{2-\delta}Se$ nanoparticles within the α-Cu_2Se matrix and the formation of Cu-rich $Cu_{1+y}AlSe_2$ nanoparticles with the $CuAlSe_2$ inclusions. The formation of such microstructure is facilitated by the unidirectional diffusion of Cu ions from the Cu_2Se matrix to the $CuAlSe_2$ inclusion, which serves as a "reservoir" for Cu ions diffusing away from the Cu_2Se matrix, due to their ability to accommodate a large fraction of excess metal atoms within their crystal lattice. This gives rise to a large enhancement in carrier concentration and thus electrical conductivity at elevated temperatures. Furthermore, the nanostructuring near the $CuAlSe_2$/Cu_2Se interface as well

as the extensive atomic disorder in the Cu_2Se and $CuAlSe_2$ phases significantly increase phonon scattering, leading to suppressed lattice thermal conductivity. Consequently, a significant improvement in ZT is observed for selected $Cu_2Se/CuAlSe_2$ composites. This work demonstrates the use of in-situ formed interactive secondary phases in a semiconducting matrix as an elegant alternative approach for further improvement of the performance of leading thermoelectric materials.

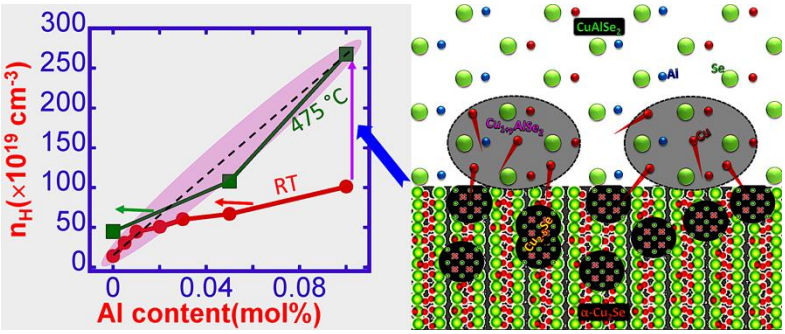

$CuAlSe_2$ precipitates extract Cu ions from a Cu_2Se matrix near the interface, giving rise to a significant temperature-dependent doping effect. The doping is correlated to the degree of penetration of Cu ions into the $CuAlSe_2$ precipitates. Full and partial penetration is observed for samples with small and large $CuAlSe_2$ inclusions, respectively, resulting in two different doping efficiencies controlled by temperature.

For $(1-x)Cu_2Se/(x)CuFeSe_2$ composites,[3] we observed uniform ultrafine dendritic structures consisting of interweaving Cu_2Se and $CuFeSe_2$ nanofibers in samples with low Fe content ($0.05 \leq x \leq 0.1$). Increasing the Fe content to $x = 0.5$ led to phase segregation into the Cu_2Se-rich region with embedded $CuFeSe_2$ fine structures interwoven with the $CuFeSe_2$-rich region containing Cu_2Se nanofibers.

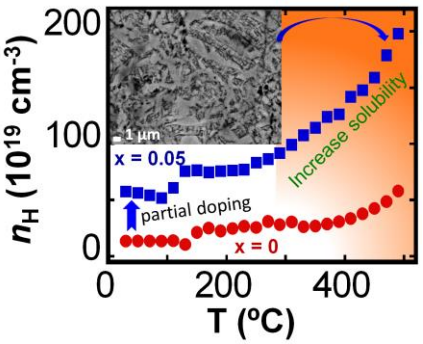

Poor solubility of Fe into Cu_2Se lattice leads to phase segregation into interwoven fine structures of Cu_2Se and $CuFeSe_2$ phases. Increase dissolution of $CuFeSe_2$ into Cu_2Se at high temperatures leads to enhanced carrier density and superior thermoelectric performance.

The formation of such an entwined dendritic structure is believed to arise from the temperature-dependent solubility of $CuFeSe_2$ in the Cu_2Se matrix. The dynamic dissolution of $CuFeSe_2$ into the Cu_2Se at high temperatures leads to temperature-dependent doping of the Cu_2Se matrix, enabling drastic enhancements of thermoelectric power factor at high temperatures. Such a strategy is expected to be a powerful tool for property modulation in thermoelectric materials.

Future Plans

Now that we have mastered a synthesis approach that was successfully applied to material systems, we will complete the synthesis of samples with compositions covering the whole range $0 \leq x \leq 1$. These samples will enable a series of systematic studies that would provide for a better understanding of the intrinsic effects of various microstructures and chemistry of the WBGS phase on the functional behavior of the synthesized composites. In the $(1-x)Cu_2Se/(x)CuInSe_2$ system, for instance, we found that the functional behavior of various composites strongly depends on the phase ratio (x values). In an early study focused on compositions with $x \leq 0.15$, we demonstrated that the incorporation of a small fraction ($x \leq 0.05$) of $CuInSe_2$ phase within the Cu_2Se matrix leads to a large increase in the thermoelectric figure of merit, ZT~2.6 at 800 K for x = 0.01, along with enhanced chemical stability of the Cu_2Se matrix.[4] Expanding the investigation to higher CuInSe2 content (increasing x values) revealed astonishing results that could not be anticipated such as a temperature-induced reversible p-type to n-type electronic transition at a critical temperature, T_{p-n}, which in turn depends on the phase ratio (x values). Simultaneously, we found that these samples also exhibit a drastic drop in the electrical conductivity upon illumination, the so called "negative photoconductivity". The magnitude of the drop also strongly depends on the phase ratio. We will focus our attention on a thorough understanding of the underlying mechanism leading to the observed unexpected electronic behavior in various $(1-x)Cu_2Se/(x)$WBGS hierarchical bulk composites, which could pave the way for rational design of a myriad of advanced multifunctional materials with unusual properties, such as (a) quantum metamaterials with tunable temperature-induced p to n electronic transition; (b) metamaterials with strong photoelectronic coupling; (c) metamaterials with negative photoconductivity, etc. These unique properties could drastically advance applications in (i) quantum computing, and (ii) low power electronic devices including energy conversion, sensing, and detecting.

References

1. Lu, R. M.; Olvera, A.; Bailey, T. P.; Uher, C.; Poudeu, P. F. P., $CuAlSe_2$ Inclusions Trigger Dynamic Cu^+ Ion Depletion from the Cu_2Se Matrix Enabling High Thermoelectric Performance. *Acs Appl Mater Inter* **2020,** *12*, 58018−58027.
2. Lu, R. M.; Olvera, A.; Bailey, T. P.; Uher, C.; Poudeu, P. F. P., Nanoscale Engineering of Polymorphism in Cu_2Se-Based Composites. *Acs Appl Mater Inter* **2020,** *12* (28), 31601-31611.
3. Lu, R. M.; Bailey, T. P.; Uher, C.; Poudeu, P. F. P., Ultrafine Interwoven Dendritic $Cu_2Se/CuFeSe_2$ Composites with Enhanced Thermoelectric Performance. *Acs Appl Energ Mater* **2020,** *3* (9), 9133-9142.
4. Olvera, A. A.; Moroz, N. A.; Sahoo, P.; Ren, P.; Bailey, T. P.; Page, A. A.; Uher, C.; Poudeu, P. F. P., Partial indium solubility induces chemical stability and colossal thermoelectric figure of merit in Cu_2Se. *Energ Environ Sci* **2017,** *10* (7), 1668-1676.

Publications

1. Ruiming Lu, Alan Olvera, Trevor P. Bailey, Jiefei Fu, Xianli Su, Igor Veremchuk, Zhixiong Yin, Brandon Buchanan, Ctirad Uher, Xinfeng Tang, Yuri Grin, Pierre F.P. Poudeu; High carrier mobility and ultralow thermal conductivity in the synthetic layered superlattice $Sn_4Bi_{10}Se_{19}$, *Mater. Adv.* **2021**, 2, 2382.

2. Sieun Chae, Kelsey Mengle, Kyle Bushick, Jihang Lee, Nocona Sanders, Zihao Deng, Zetian Mi, P. F. P. Poudeu, H. Paik, J. T. Heron, and E. Kioupakis; Perspective: Towards the predictive discovery of ambipolarly dopable ultra-wide-band-gap semiconductors: the case of rutile GeO_2; *Appl. Phys. Lett.* **2021**, *118*, doi: 10.1063/5.0056674

3. Ruiming Lu, Alan Olvera, Trevor P. Bailey, Ctirad Uher, and Pierre F. P. Poudeu, $CuAlSe_2$ Inclusions Trigger Dynamic Cu^+ Ion Depletion from the Cu_2Se Matrix Enabling High Thermoelectric Performance, *ACS Appl. Mater. Interfaces* **2020**, 12, 58018−58027.

4. Trevor P. Bailey, Ruiming Lu, Pierre F. P. Poudeu, and Ctirad Uher, Paramagnon heat capacity in (Ti,Zr,Hf)NiFexNiSn half-Heusler composites, *Phys. Rev. B.* **2020**, 102, 224412.

5. Lamia Dawahre, Ruiming Lu, Honore Djieutedjeu, Juan Lopez, Trevor P. Bailey, Brandon Buchanan, Zhixiong Yin, Ctirad Uher, and Pierre F. P. Poudeu, Lone-Electron-Pair Micelles Strengthen Bond Anharmonicity in $MnPb_{16}Sb_{14}S_{38}$ Complex Sulfosalt Leading to Ultralow Thermal Conductivity, *ACS Appl. Mater. Interfaces* **2020**, 12, 40, 44991–44997.

6. S. Chae, K. A. Mengle, R. Lu, A. Olvera, N. Sanders, J. Lee, P. F. P. Poudeu, J. T. Heron, and E. Kioupakis; Thermal conductivity of rutile germanium dioxide, *Appl. Phys. Lett*. **2020**,117, 102106.

7. Ruiming Lu, Trevor P. Bailey, Ctirad Uher, and Pierre F. P. Poudeu, Ultrafine Interwoven Dendritic $Cu_2Se/CuFeSe_2$ Composites with Enhanced Thermoelectric Performance, *ACS Appl. Energy Mater.* **2020**, 3, 9, 9133–9142.

8. Ruiming Lu, Alan Olvera, Trevor P. Bailey, Ctirad Uher, and Pierre F. P. Poudeu**,** Nanoscale Engineering of Polymorphism in Cu_2Se-Based Composites, *ACS Appl. Mater. Interfaces* **2020**, 12, 28, 31601–31611

9. Zihao Deng, Alan Olvera, Joseph Casamento, Juan S. Lopez, Logan Williams, Ruiming Lu, Guangsha Shi, Pierre F. P. Poudeu, and Emmanouil Kioupakis, Semiconducting High-Entropy Chalcogenide Alloys with Ambi-ionic Entropy Stabilization and Ambipolar Doping, *Chem. Mater.* **2020**, 32, 14, 6070–6077. (Cover art)

10. Yiqiao Huang, Ruiming Lu, Michael Wang, Jeff Sakamoto, Pierre F.P. Poudeu Hexagonal-WO_3 nanorods encapsulated in nitrogen and sulfur co-doped reduced graphene oxide as a high-performance anode material for lithium ion batteries, *Journal of Solid State Chemistry*, **2020**, 282, 121068.

11. Honore Djieutedjeu, Juan S. Lopez, Ruiming Lu, Brandon Buchanan, Xiaoyuan Zhou, Hang Chi, Kulugammana G. S. Ranmohotti, Ctirad Uher and Pierre F. P. Poudeu, Charge disproportionation triggers bipolar doping in $FeSb_{2-x}Sn_xSe_4$ ferromagnetic semiconductors enabling temperature-induced Lifshitz transition, *J. Amer. Chem. Soc.* **2019**, 141(23), 9249 – 9261. DOI: 10.1021/jacs.9b01884

12. Juan Lopez, Honore Djieutedjeu, Brandon Buchanan, Kulugammana G. S. Ranmohotti, Alexander Page, Ctirad Uher and Pierre F. P. Poudeu, Engineering magnetic transitions in $Fe_{1-x}Sn_xBi_2Se_4$ n-type ferromagnetic semiconductors through chemical manipulation of spatial separation between magnetic centers, *Chem. Mater.* **2019**, *31*, 9, 3507-3518.

13. R. Lu, J. S. Lopez, Y. Liu, T. P. Bailey, A. A. Page, S. Wang, C. Uher, and P. F. P. Poudeu, Coherent magnetic nanoinclusions induce charge localization in half-Heusler alloys leading to high-Tc ferromagnetism and enhanced thermoelectric Performance, *J. Mater. Chem. A*, **2019**, **7**, 11095-11103. DOI: 10.1039/c9ta01156k

DE-FG02-07ER46475: Activation of Hydrogen under Ambient Conditions by Main Group Molecules.

Joshua Queen and Philip P. Power, Chemistry Department University of California, Davis California 95616.

Program Scope

The main objectives of the research are a mechanistic understanding of the reactions of main group element compounds with small molecules such as hydrogen, ammonia, ethylene, or carbon monoxide under ambient conditions. In addition, this work is undertaken with a view to developing catalysts for industrially important processes based on inexpensive elements such as aluminum or silicon. The molecules we are investigating usually feature both Lewis acidic and basic sites that activate the small molecules in a synergistic manner.

Recent Progress

:$AlAr^{iPr8}$ (Figure 1), an aluminum(I) alanediyl (Ar^{iPr8} = C_6H -(C_6H_2-2,4,6-i-Pr_3)$_2$-3,5-i-Pr_2)$_2$) with the first instance of a one coordinate aluminum atom, reacts with H_2 and ethylene to form Al(III) products at room temperature and 1 atmosphere pressure (see Scheme).[1] The aryldiiodide starting material was synthesized beginning with the alane-trimethylamine complex H_3AlNMe_3.
The reaction with ethylene gives two products, one of which has been isolated and is the formal (2+2+2) addition product with $Ar^{iPr8}AlAlAr^{iPr8}$ (bottom right).
A second product identified in the ^1H NMR of the reaction mixture is the (1+2+2) addition product with $AlAr^{iPr8}$ (bottom left).

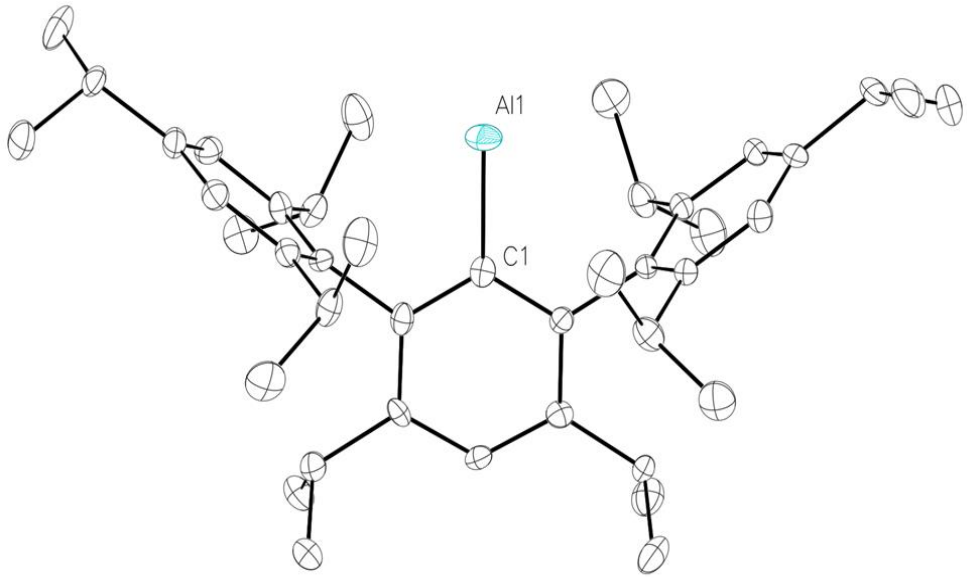

Figure 1: The molecular structure of :$AlAr^{iPr8}$ (Ar^{iPr8} = C_6H-(C_6H_2-2,4,6-^{i}Pr_3)$_2$-3,5-^{i}Pr_2)$_2$), the first example of a one-coordinate aluminum atom. Thermal ellipsoids are shown at 50% probability. For clarity, hydrogen atoms are not shown.

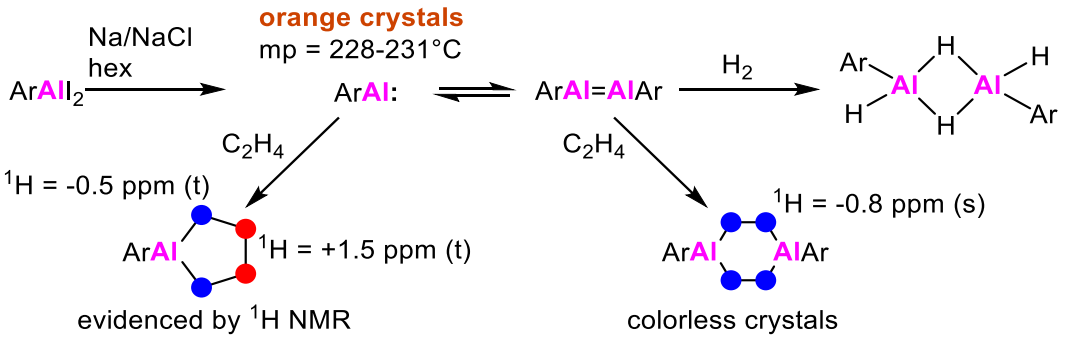

Scheme. Synthesis of :AlAr^{iPr8} (Ar^{iPr8} = C_6H-C_6H_2-(2,4,6-i-Pr_3)$_2$-3,5-i-Pr_2)$_2$)[1] and some of its reactions with small molecules under ambient conditions.

Future Plans

The study described above represents the initial stage of a focus on low-valent aluminum (the most abundant metal in the earth's crust) compounds as possible catalysts for the activation of important small molecules under ambient conditions. The most immediate objectives of our future plans are the synthesis of a range of open-shell aluminum(I) species and a detailed investigation of their reactions with both saturated and unsaturated small molecules.

References

1.Queen, J. D.; Lehmann, A.; Fettinger, J. C.; Tuononen, H. M.; Power, P. P. *J. Am. Chem. Soc.* **2020**, *142*, 20554—20559. https://doi.org/10.1021/jacs.0c10222

Publications

Queen, J.; Lehmann, A.; Fettinger, J.C.; Tuononen, H.M.; Power, P.P. The Monomeric Alanediyl :AlAr^{iPr8} (Ar^{iPr8}= C_6H-2,6-(C_6H_2-2,4,6-i-Pr_3)$_2$-3,5-i-Pr_2); An Organoaluminum(I) Compound with a One-co-ordinate Aluminum Atom. *Journal of the American Chemical Society* **2020,** *142,* 20554-20559**.** https://doi.org/10.1021/jacs.0c10222

T.-Y. Lai, L. Tao, R. D. Britt, and P. P. Power. Reversible Sn-Sn Triple Bond Dissociation in a Distannyne. *Journal of the American Chemical Society* **2019,** *141*, 12527-12530. DOI: 10.1021/jacs. 9b06845
https://doi.org/10.1021/jacs.9b06845

K. L. Gullett, T.-Y. Lai, C.-Y. Chen, J. C. Fettinger, and P. P. Power. Reversible Binding of Ethylene and Propylene by Germylenes. *Organometallics* **2019,** 38, 1425-1428. DOI: 10.1021/acs.organomet.9b100109
https://doi.org/10.1021/acs.organomet.9b00109

T.-Y. Lai, K. L. Gullett, C.-Y. Chen, J. C. Fettinger, and P. P. Power. Reversible Complexation of Alkynes by a Germylene. *Organometallics* **2019,** *38,* 1421-1434. DOI: 10.1021/acs.organomet.9b00077
https://doi.org/10.1021/acs.organomet.9b00077

M. L. McCrea-Hendrick, M. Bursch, K. L. Gullett, L. Maurer, J. C. Fettinger, S. Grimme, and P. P. Power. Counterintuitive Interligand Angles in the Diaryls E{C_6H_3-2,6-(C_6H_2-2,4,6-Pri_3) $_2$}$_2$ (E = Ge, Sn or Pb) and Related Species: The Role of London Dispersion Forces. *Organometallics*. **2018**, *37*, 2075-2085. DOI: 10.1021/acs.organomet.8b00225 https://doi.org/10.1021/acs.organomet.8b00225

T -Y. Lai, J. C. Fettinger and P. P. Power. Facile C-H Bond Metathesis Mediated by a Stannylene. *Journal of the American Chemical Society*. **2018**, *140,* 5674-5677. DOI: 10.1021/jacs.8b01878 https://doi.org/10.1021/jacs.8b01878

S. Wang, T. J. Sherbow, L. A. Berben, and P. P. Power. Reversible Coordination of H_2 by a Distannyne. *Journal of the American Chemical Society*. **2018,** *140,* 590-593. DOI: 10.1021/jacs.7b11798
https://doi.org/10.1021/jacs.7b11798

Metal-Organic frameworks: structure, function and design via hyperpolarized NMR spectroscopy

Jeffrey Reimer (PI, University of California at Berkeley)
Alexander Pines (co-PI, University of California at Berkeley)
Carlos A. Meriles (co-PI, CUNY- City College of New York)

Program Scope: This project articulates magnetic resonance and optical spectroscopy methods to investigate the spin dynamics in condensed matter systems, with special attention to using dynamic polarization schemes to improve nuclear magnetic resonance detection sensitivity of metal organic frameworks (MOF) as well as the development and application of new MOF structures to quantum information science.

Recent Progress: Throughout our first project year, we conducted various activities connected to (i) developing the necessary infrastructure for our DNP experiments in MOFs, (ii) characterizing some candidate systems through magnetic resonance and fluorescence microscopy, and (iii) introducing new conceptual approaches to DNP. For concreteness, this presentation will center on the latter, specifically, we will describe a new protocol where nuclear spins polarize efficiently under a cycle that combines alternating thermal jumps and radio-frequency pulses connecting hybrid states with opposite nuclear and electronic spin alignment. Central to this process is the difference between the spin-lattice relaxation times of either electron spin species, transiently driving the electronic spin bath out of equilibrium after each thermal jump. Without the need for microwave excitation, this route to enhanced nuclear polarization may prove convenient, particularly if the molecule serving as the polarizing agent is designed to feature electronic level anti-crossings at high magnetic fields.

Future Plans: On the experimental front, we plan to complete the physical setups under construction and conduct initial proof-of-principle DNP experiments in MOFs featuring linkers that can be optically spin pumped. On related lines, we want to pursue experiments aimed at demonstrating microwave free DNP as proposed by us recently; we also plan to characterize the optical and spin response of candidate rare-earth ions, ideally embedded in MOF structures. On the theory front, we will continue our exploration of non-Hermitian spin dynamics in molecular complexes, this time with focus on exploiting the topological properties of these systems at an exceptional point for novel sensing applications.

Publications

"Non-Hermitian dynamics of spin chains with loss and gain", S. Bussandri, P.R. Zangara, R.H. Acosta, C.A. Meriles, *Phys. Rev. B* **103**, 214409 (2021).

"Spontaneous emission dynamics of Eu^{3+} ions coupled to hyperbolic metamaterials", G.I. López-Morales, M. Li, R.K. Yadav, J. Basu, C.A. Meriles, V.M. Menon, *Appl. Phys. Lett.*, **118**, 011106 (2021).

"Microwave-free dynamic nuclear polarization via sudden thermal jumps", C.A. Meriles, P.R. Zangara, *to be submitted*.

Thin Film Platforms to Advance Scientific Frontiers in Solid State Energy Storage
Gary Rubloff, Sang Bok Lee, Paul Albertus, Alec Talin (University of Maryland)

Program Scope

Building upon the precision structures featured in our previous NEES EFRC, this program employs thin film fabricated 3D solid state battery (SSB) architectures [1][2] to understand their behavior and scaling and to reveal local properties that enrich modeling capabilities for such structures. In investigating different architectures we explore how designs can simultaneously achieve high power, high energy, and stability, tightly coupled with multiphysics modeling and simulation to motivate the designs. Complementing this, we create and employ specially designed structures – thin film fabricated platforms - to extract parameters and scientific insights not previously accessible through conventional battery configurations, which in turn enrich our modeling capabilities.

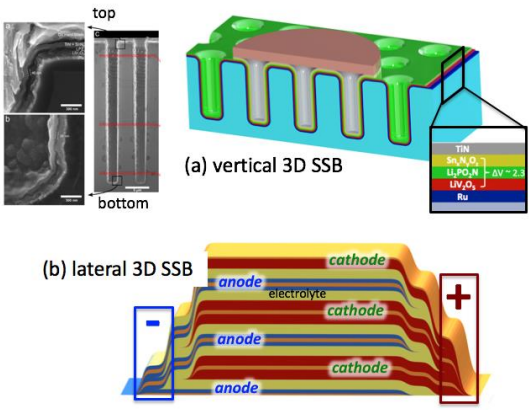

Figure 1.Exemplary 3D architectures: (a) vertical configuration built on high aspect ratio nanopore scaffold; (b) lateral multi-battery configuration sequentially patterned and assembled.

The scope of the program is reflected in its three thrust areas – architectures, mechanics, and interfaces, which together address four scientific goals. **Thrust A- architectures**, seeks to understand the mesoscale science of 3D solid state energy storage. [3][4] This includes modeling and experimental evaluation of 3D SSB architectures to achieve high power, energy, and stability. Two current examples, depicted in Figure 1, reflect contrasting synthesis strategies and power/energy benefits as well as architectural distinctions.

The benefits of thin film fabrication also drive the design of special platforms to extract ionic and electronic conductivity as a function of state of charge (SOC), as well as associated diffusion kinetics – fundamental information required to enhance modeling and simulation capabilities for energy storage. Such a platform is depicted in Figure 2, where a patterned SSB (right side) enables introduction of Li into the right end of a strip of cathode material (V_2O_5 shown) while a voltage gradient across the strip creates a gradient in SOC, from which multiple electrodes enable local EIS measurements.

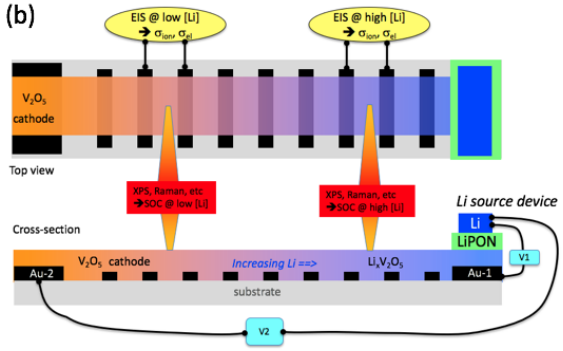

Figure 2. Lateral diffusion platform to extract ionic and electronic conductivities as a function of state-of-charge. Appropriate biasing is used to create {Li] gradients between left and right in the figure.

The coupling of mechanics with electrochemistry is the scientific focus of **Thrust B – mechanics**. Here we are developing robust models that add mechanics to the structure/electrochemistry models described above. These efforts are complemented by nanoindentation experiments on planar and

2D/3D structures to reveal the coupling and enhance modeling. We are also developing microRaman and other techniques aimed at local measurement of stress/strain, particularly in 2D/3D structures where local features are a source of inhomogeneity.

Since interface behavior can significantly affect 3D-SSB behavior, **Thrust C – interfaces** is aimed at two scientific goals. One is measurement and understanding of electrostatic (voltage) and chemical energetics near solid interfaces, particularly electrode/solid-electrolyte. This work builds directly on Talin's Kelvin probe force microscopy (KPFM) work measuring potentials across platforms made as SSB cell cross-sections, in continuing close collaboration with first-principles-informed models of Yue Qi (Brown U.) that reveal space charge regions and potential gradients. The second goal is to address interfacial reactions, particularly to understand and mitigate dendrite evolution at solid electrolyte interfaces at electrodes and at grain boundaries, using artificial grain boundary and interface platforms which can be tuned by chemical modification or interlayer introduction.

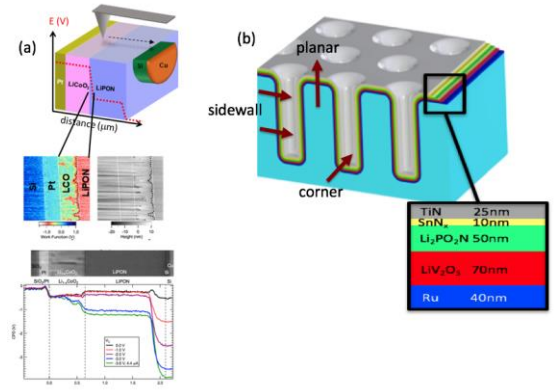

Figure 3. KPFM voltage measurements across (a) planar and (b) 3D features in SSBs.

Recent Progress

In **Thrust A – architectures** we have substantially enhanced the parameter space accessible for 3D-SSB synthesis in vertical AAO nanopores. We have developed processes for patterning AAO regions, implementing separate contacts on bottom and top of the AAO-confined SSBs, and expanding AAO nanopore diameter to ~400nm (from ~125nm) to enable a larger dynamic range of active layer thicknesses and consequent power-energy performance. We have also developed a process for sputtered $Li_xV_2O_5$ as a means to provide Li in each of the multiple SSBs synthesized on top of each other in a single process run. We are extensively using and enhancing multiphysics models to assess the electrochemical and related behavior of these architectures, from design to analysis and comparison to experiment.

We have created new thin film electrochemical platforms to assess ionic and electronic conductivities as a function of SOC (Li concentration) along the lines of the lateral gradient (LG) platform in Figure 2 and also as arrays of interdigitated electrode (IDE) test structures depicted in Figure 4. Measurements in both configurations are in progress, complemented by modeling.

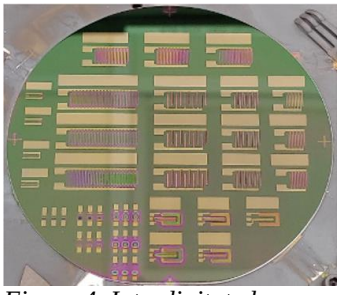

Figure 4. Interdigitated electrode (IDE) platform array

In **Thrust B – mechanics** we continue to develop and improve electrochemical models that explicitly incorporate the role of and responses to mechanical stress/strain. Comparison to experiments motivate improvements to these models. We are pursuing two experimental directions. One is nanoindentation to allow well-controlled to be imposed on planar and 3D platforms to identify mechanics-electrochemistry coupling. The other is to develop local stress/strain measurements to decode such relationships locally in 2D/3D architectures, using Raman, QD fluorescence, and DIC

methods. Anticipating significant stress/strain consequences in dense 3D-SSBs, we have begun a modeling analysis of what role a flexible interlayer might play, e.g. in the vertical AAO 3D-SSB.

In **Thrust C – interfaces** we have applied operando KPFM over cross-sections of LCO/LiPON/Si SSBs in order to map electric potential distributions across cell components and their interfaces under open circuit and varying current conditions. The largest potential drop occurs at the Si-anode/LiPON-electrolyte interface, accompanied by a smaller drop at the cathode and across the electrolyte bulk. High current cycling irreversibly increases the voltage drop at the anode interface, with corresponding increase in impedance. These results are consistent with a first-principles-informed model for ions and electrons, with neutron depth profiling (NDP) of Li concentrations through the cell, and with changes in surface height reflective of lithiation-induced volume change. KPFM mapping of the cell cross-section reveals spatial inhomogeneities in potential parallel to the planar interfaces. Revealing local potentials across the interfaces and materials in an operating SSB cell provides exceptional feedback and motivation for modeling the energy landscape that influences both electrons and ions. As indicated in Figure 3, operando mapping of 3D-SSB cross-sections, by KPFM, Raman, or other techniques, may offer unprecedented access to local properties that may be crucial to behavior of 3D electrochemical architectures.

Future Plans

A significant focus of **Thrust A – architectures** will be to complete fabrication, test and evaluation of the behavior of both the vertical and lateral 3D-SSB architectures, and in the longer run to explore other architectures. Vertical structures will benefit from the larger dynamic range of electrode thicknesses now accessible with wide AAO pores, which approach the dimensions etched Si pores previously studied. For both lateral and vertical structures we will focus on how geometry and dimensionality contribute to power and energy as well as how the 3D configurations introduce inhomogeneities degrade those metrics. Understanding the underlying mesoscale science will depend on developing methods to measure local properties (KPFM, Raman, etc.) in these 3D architectures, and very much on modeling the multiphysics of these electrochemical architectures. [5]

In complementary fashion, we will strongly emphasize the new LG and IDE platforms for evaluating local electrochemical properties, particularly ionic and electronic conductivity as a function of SOC, together with how charge/discharge dynamics and 3D architecture complicate ion diffusion kinetics. This work is intimately connected to the modeling, not only in the design of the platforms but very much in the hope that experimental results can enrich the fidelity of the models, e.g. conductivities vs SOC.

Mechanics is intrinsically crucial in electrochemical systems because of volume and material changes associated with ion transport. With our focus on high power-energy 3D-SSB designs, the mechanics and its coupling to electrochemical behavior become more complex. Accordingly, in **Thrust B – mechanics** we will continue to focus on platform designs – planar and 3D – which can yield fundamental relationships and parameters that govern the mechanics-electrochemistry coupling. We will create experimental test platforms which use both external forces (nanoindentation) and internal forces (ion transport in electrochemistry) in 3D as well as simple planar arrangements. In addition we will explore approaches to measure local stress/strain distributions during charge/discharge cycling and under external forces. Results from experiments will be formulated to enrich multiphysics models.

Future work in **Thrust C – interfaces** will build on the KPFM/NDP work and aim at understanding how electrode/electrolyte interfaces might be altered to reduce interface impedance through chemical or materials modifications in a model planar system. Complementary to other efforts aimed at local characterization, we will explore extending KPFM to measure voltage profiles across SSB layers at 3D architectural features such as edges and corners (Figure 3b). We will also investigate the design and use of platforms to use XPS/UPS to observe band-bending at buried interfaces [6] such as Li/Li_2CO_3, Li/Li_2O, and Li/LiPON. We envision to produce such interfaces by adding thin layers onto in-situ sputter-cleaned Li surfaces in UHV, using gas dosing or ALD to create ultrathin layers on the Li surfaces. Both sets of experiments will be closely tied to the theoretical predictions [7][8] of Yue Qi's group at Brown, continuing a long-standing, resonant theory-experiment collaboration.

Building on our experience in creating platforms like those in Figure 2, we will design platforms to explicitly address grain boundary diffusion and the influence of chemical modifications. With our recent ability to photolithographically pattern electrochemical materials (e.g., LiPON), we can create artificial grain boundaries as studied by Dudney [9] for Li dendrite growth. Furthermore we can produce chemical modifications or deposit additional interphase layers at the grain boundaries under ultraclean ambients.

References

[1] A. J. Pearse *et al.*, "Nanoscale Solid State Batteries Enabled by Thermal Atomic Layer Deposition of a Lithium Polyphosphazene Solid State Electrolyte," *Chem. Mater.*, vol. 29, no. 8, pp. 3740–3753, 2017.

[2] A. Pearse *et al.*, "Three-Dimensional Solid-State Lithium-Ion Batteries Fabricated by Conformal Vapor-Phase Chemistry," *ACS Nano*, vol. 12, no. 5, pp. 4286–4294, 2018.

[3] J. W. Long, B. Dunn, D. R. Rolison, and H. S. White, "Three-dimensional battery architectures," *Chem. Rev.*, vol. 104, no. 10, pp. 4463–4492, Jan. 2004.

[4] K. McKelvey, A. A. Talin, B. Dunn, and H. S. White, "Microscale 2.5D Batteries," *J. Electrochem. Soc.*, vol. 164, no. 12, pp. A2500–A2503, Aug. 2017.

[5] H.-K. Tian, A. Chakraborty, A. A. Talin, P. Eisenlohr, and Y. Qi, "Evaluation of The Electrochemo-Mechanically Induced Stress in All-Solid-State Li-Ion Batteries," *J. Electrochem. Soc.*, vol. 167, no. 9, p. 090541, 2020.

[6] A. Schwöbel, W. Jaegermann, and R. Hausbrand, "Interfacial energy level alignment and energy level diagrams for all-solid Li-ion cells: Impact of Li-ion transfer and double layer formation," *Solid State Ionics*, vol. 288, pp. 224–228, 2016.

[7] M. W. Swift, Y. Qi, M. W. Swift, and Y. Qi, "First-Principles Prediction of Potentials and Space-Charge Layers in All-Solid-State Batteries," *Phys. Rev. Lett.*, vol. 122, no. 16, p. 167701, Apr. 2019.

[8] M. W. Swift, J. W. Swift, and Y. Qi, "Modeling the electrical double layer at solid-state electrochemical interfaces," *Nat. Comput. Sci.*, vol. 1, no. March, pp. 212–220, 2021.

[9] A. S. Westover, N. J. Dudney, R. L. Sacci, and S. Kalnaus, "Deposition and Confinement of Li Metal along an Artificial Lipon-Lipon Interface," *ACS Energy Lett.*, vol. 4, no. 3, pp. 651–655, Mar. 2019.

Publications

Emily Sahadeo, Gary Rubloff, Sang Bok Lee, and Chuan-Fu Lin, "Al2O3 Thin Films on Magnesium: Assessing the Impact of an Artificial Solid Electrolyte Interphase", Frontiers in Energy Research, Volume 9, 618368, 2021.

Brandon Johnston, Hakeem Henry, Nam Kim, and Sang Bok Lee, "Mechanisms of Water-Stimulated Mg2+ Intercalation in Vanadium Oxide: Toward the Development of Hydrated Vanadium Oxide Cathodes for Mg Batteries", Frontiers in Energy Research, Volume 8, 611391, 2021.

E.A. Carmona, Y. Song, P. Albertus, M.J. Wang, and J. Sakamoto, "The Effect of Mechanical State on the Equilibrium Potential of Alkali Metal/Ceramic Single-Ion Conductor Systems", Advanced Energy Materials, in review.

Elliot J. Fuller, Evgheni Strelcov, Jamie L. Weaver, Michael W. Swift, Joshua D. Sugar, Andre Kolmakov, Nikolai Zhitenev, Jabez J, McClelland, Yue Qi, Joseph A. Dura, and A. Alec Talin, "Operando measurements of potential and Li-ion distributions across solid-state electrochemical interfaces with Kelvin probe force microscopy and neutron depth profiling", submission ready for Nat Mater.

Victoria C. Ferrari, Nam Kim, David Stewart, Sang Bok Lee and Gary Rubloff, “Electrochemically active lithium vanadium oxide made by co-sputtering as a cathode material for solid-state batteries", nearing completion for Chemistry of Materials.

Nam Kim, Keith Gregorczyk, Miles Mowbray, Jack Hayden, Marco Casareto, Gary Rubloff, Sang Bok Lee, "Impact of Anodization Currents on the Ordering of Large Pore Anodized Aluminum Oxide Templates on Si with Bottom Contact", nearing completion for J. Electrochemical Soc.

Gary W. Rubloff, Sang Bok Lee, Keith Gregorczyk, Nam Soo Kim, Alexander Kozen, David Stewart, "Structure and Architecture for Electrochemical Energy Storage (draft ~2/3 complete)", nearing completion for Chemical Reviews (INVITED).

The synthesis of metal superhydrides through extreme temperature/pressure conditions: towards room temperature superconductivity

Ashkan Salamat, Department of Physics and Astronomy, University of Nevada, Las Vegas

Program Scope

Early metal hydride studies were unable to achieve superconducting transition temperature (T_c's) above 20 K, but the discovery of superconductivity in hydrogen sulfide at 203 K changed the notion of what might be possible for phonon-mediated superconductors.[1] This has been further supported by our own report of room temperature superconductivity (RTSC) in a carbonaceous sulfur hydride.[2] The resulting paradigm shift has cemented the understanding that a hydride compound must have a large electron-phonon coupling related to the hydrogen atoms and a high density of hydrogen related states at the Fermi level to have a high T_c.[3] High hydrogen content materials that meet those two criteria can be considered as chemically pre-compressed phases relative to pure hydrogen, thus lowering the pressures necessary for metallization or high-T_c superconductivity to more experimentally feasible conditions. Therefore, the search, synthesis, and structural and physical characterization of novel metal superhydrides with high superconducting transition temperature, and an understanding of how to access metastable pathways to their recovery to ambient conditions is critical for the advancement of material science and energy transmission technology.

This new generation of high-T_c materials that have emerged and are predominantly hydrogen-rich, making their characterization and thus our understanding of them difficult in a diamond anvil cell at high pressures. We have set out to discover new materials with similar properties, but more critically to build an atomistic model of these materials to improve understanding. We are utilizing a multidisciplinary approach to develop new probes and create new materials with a theoretical component to help guide synthesis and characterize materials.

Recent Progress

The recent synthesis of yttrium superhydrides with near-ambient temperature superconductivity and our development of using a palladium catalyst to promote hydrogenation permits a wide field of possibilities and fuels the dream of loss-free transport of charge.[3] Our structural characterization of yttrium-hydrogen compounds calls for spectroscopic techniques, as X-ray diffraction studies struggle with the low X-ray scattering cross-section of hydrogen. In a recent breakthrough article on room-temperature conductivity we called for the development of new spectroscopic approaches to complement diffraction-based structural investigations.

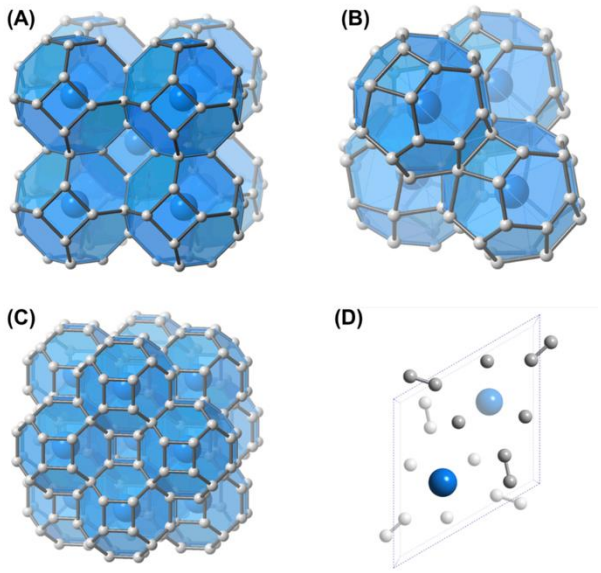

Illustrations of the (A) *Im-3m* YH_6, (B) *P6₃/mmc* YH_9, (C) *Fm-3m* YH_{10}, and (D) *P6₃/m* YH_9 yttrium superhydride structures. The blue balls are yttrium and the white/gray balls are hydrogen.

Consequently, we have developed two unique laser heating systems at the Advanced Photon Source at both a dedicated diffraction and spectroscopy beamline that will permit the synthesis of such materials, *in situ*, and to further build a more detailed structural understanding of these materials. In addition, single crystal capabilities under high pressure conditions are utilized to compliment the spectroscopic tools for solving the stoichiometry and structure of these materials.

Regarding our theory work, an inspection of the published predicted crystal structures for the recently discovered room temperature superconductor shows a favorability for low dimensionality or even molecular sub-units in the materials. Typically, these structures exhibit strong van der Waals interactions which were neglected in the original searches. We find that correctly accounting for these interactions improves the predicted properties for these materials, and that similar materials are predicted in crystal structure searches. One of the major hinderances to our theoretical efforts is the computer power required to compute a superconducting transition temperature for a material, so we have turned to machine learning to accelerate our capabilities. Our first machine learned model that incorporates a material's structural information has an out-of-sample accuracy of 95.2%, an improvement over other recently developed models.[4,5]

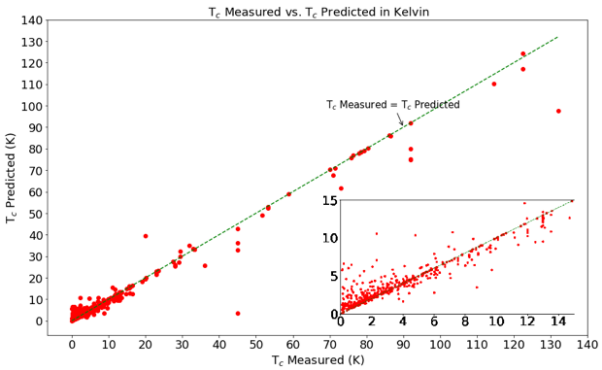

A comparison of the measured T_c for a material versus the one predicted by our machine learning model.

Future Plans

We expect to precisely determine the first-coordination shell parameters of the high-pressure sequence of superconducting metal superhydrides. These parameters, metal-H coordination number and metal–H bond distances, are of key importance for understanding the mechanism of

high temperature superconductivity. The establishment of element specific spectroscopic probes as ideal technique to directly access the hydrogen chemical shift will be an important tool in the search for future, technically applicable superconducting material and to establish chemical rules and fine tune their composition to achieve high Tc at lower pressure, eventually ambient pressure.

The theory efforts will focus on new crystal structure searches for new stoichiometries related to the carbonaceous sulfur hydride material. Additionally, we will further develop our machine learning model to improve its overall accuracy, incorporate its predicted T_c has a figure of merit in crystal structure searches, and extend it to rapidly predict other material properties related to the structure of the material. We also will reinvestigate transition metal superhydride materials to determine if previous studies' treatment of the metal's *d* and *f* electrons led to an underprediction of their superconducting properties to determine if they are worthwhile synthesis targets.

References

1. Drozdov, A. P., Eremets, M. I., Troyan, I. A., Ksenofontov, V. & Shylin, S. I. Conventional superconductivity at 203 kelvin at high pressures in the sulfur hydride system. *Nature* **525**, 73–76 (2015).

2. Snider, E. *et al.* Room-temperature superconductivity in a carbonaceous sulfur hydride. *Nature* **586**, 373–377 (2020).

3. Snider, E. *et al.* Synthesis of Yttrium Superhydride Superconductor with a Transition Temperature up to 262 K by Catalytic Hydrogenation at High Pressures. *Phys. Rev. Lett.* **126**, 117003 (2021).

4. Stanev, V. *et al.* Machine learning modeling of superconducting critical temperature. *npj Comput. Mater.* **4**, 29 (2018).

5. Konno, T. *et al.* Deep learning model for finding new superconductors. *Phys. Rev. B* **103**, 014509 (2021).

Publications

Additive-Assisted Preparation of Multinary Halides

Bayram Saparov
Assistant Professor, Chemistry & Biochemistry, University of Oklahoma (OU)

Program Scope

Solution processability of multinary halides including metal halide perovskite is one of their greatest advantages.[1] However, we still have very poor knowledge and understanding of metal halide solutions, resulting in unpredictable outcomes of solution reactions of metal halides. This project aims to prepare a series of novel multinary halides through *understanding and control* of additive-assisted solution synthesis. Examples include double perovskites $(MA)_2AgInBr_6$[2] and $(MA)_2AgBiBr_6$ (where MA = CH_3NH_3),[3] which can be only in the presence of $PbBr_2$ as an impurity additive. Through this project, we hope to study and understand the reaction pathways for solutions containing multiple metal cations and halide anions. To accomplish this ultimate goal, we have the following specific aims focused on the investigations of:

(i) the solution chemistry of homometallic halides,

(ii) solution chemistry of heterometallic halides, and

(iii) the structure-property relationships of solution-processed metal halides obtained from (i) and (ii).

Table 1. Project timeline.

	Year 1	**Year 2**	**Year 3**	**Year 4**	**Year 5**
Task 1: Solution chemistry of homometallic halides (experimental)	X	X	X		
Task 2: Solution chemistry of heterometallic halides (experimental)			X	X	X
Task 3: Computational studies of solutions chemistry of metal halides (theoretical)	X	X	X	X	X
Task 4: Crystal structures and optoelectronic properties of halide products (experimental)		X	X	X	X
Task 5: Electronic structures and excitonic properties of solid halide products (theoretical)		X	X	X	X

Recent Progress

Following our proposed project timeline (Table 1), the focus of our work in the first year of this project has been on the specific aim (i) – experimental and computational studies of solution chemistry of homometallic (i.e., containing a single B metal cation) A – B – X systems (A = Cs^+, $CH_3NH_3^+$ (MA); B = In^{3+}, Bi^{3+}, and X = Br^-, I^-). This specific aim is designed to fill the fundamental gap in the knowledge of the solution chemistry of Cu, Ag, In, Sb and Bi halides. A total of six indium and bismuth halide systems have been investigated in the first year of the project. Here, we will primarily discuss the MA – In – Br system as a representative example and as a system in which we obtained some interesting results.

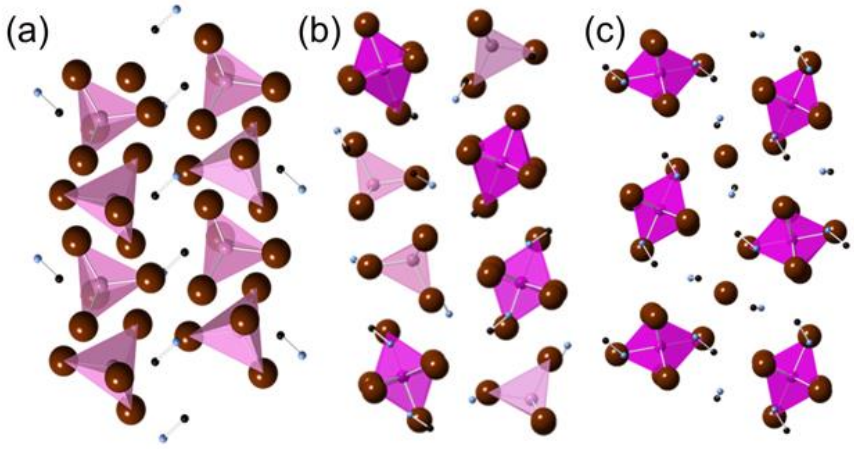

Figure 1. Polyhedral representations of the crystal structures of (a) $(MA)InBr_4$, (b) $(MA)_2InBr_5$ and (c) $(MA)_4InBr_7$.

Our results suggest that indium (In) can adopt either a tetrahedral or octahedral coordination geometries depending on the reactant loading compositions; this is in contrast to the typical behavior of most other main group metals including Bi, which tend to predominantly form structures based on octahedral $BiBr_6^{3-}$ units. Even more unusual is the fact that in some cases, indium can form both octahedral and tetrahedral building blocks within a single crystal structure. Thus, we discovered three new compounds in the ternary MA – In – Br phase diagram: $(MA)InBr_4$, $(MA)_2InBr_5$ and $(MA)_4InBr_7$ (see Figure 1). The crystal structure of $(MA)InBr_4$ is based on isolated anionic $InBr_4^-$ tetrahedra (Figure 1a). Increasing the relative bromide content leads to the formation of $(MA)_2InBr_5$, which features both octahedral and tetrahedral building blocks in its crystal structure (Figure 1b). Finally, by further increasing the Br:In ratio, we obtained in $(MA)_4InBr_7$, which contains only indium bormide octahedral building blocks (Figure 1c). These are very interesting

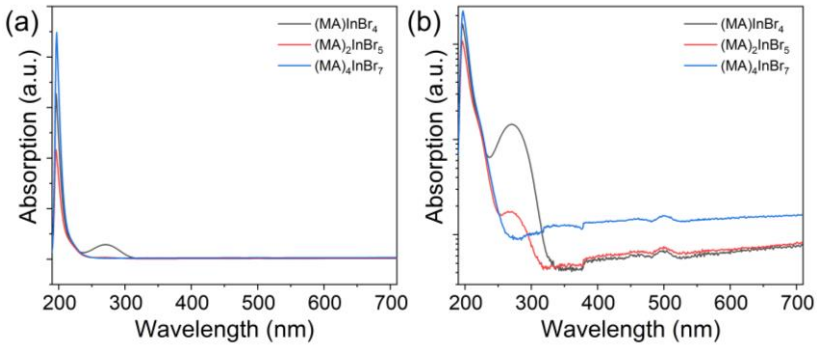

Figure 2. (a) Optical absorption spectra of $(MA)InBr_4$, $(MA)_2InBr_5$, and $(MA)_4InBr_7$. (b) A close view (i.e., logarithmic plot) of the absorption spectra to emphasize the differences in the UV region.

results, atypical for many metal halide systems, that simple changes of reactant loading ratios impact coordination polyhedra formed in the solid state.

The present project hypothesizes that the formation of solid-state products with differing structures from solution synthesis can be tied to the contents of solution. To understand our results in the MA-In-Br system, we performed a series of experimental (absorbance, photoluminescence, small angle X-ray scattering (SAXS), electrospray mass spectrometry (ESI-MS)) and computational (geometry optimization calculations and absorbance calculations) studies of MA-In-Br solutions used for the preparation of $(MA)InBr_4$, $(MA)_2InBr_5$ and $(MA)_4InBr_7$. To summarize, we see clear differences in the optical spectra of these solutions (Figures 2-3), which is indicative of the difference in the chemical contents of these solutions. For $(MA)InBr_4$ and $(MA)_2InBr_5$, we observe peaks at 275 nm attributed to tetrahedral $InBr_4^-$ anions; this assignment is consistent with our SXRD results (Figure 1a-b) and computational results (Figure 3). Note here that we have performed extensive computational work focused on elucidating optical absoprtion spectra of various indium halide species in different solvent systems (e.g., $InBr_4^-$ tetrahedra and $InBr_6^{3-}$ octahedra in methanol, water, DMF, as well as complexes in which solvent molecules are in the metal coordination spheres etc.). Similarly, we note the absence of this peak for $(MA)_4InBr_7$, again, consistent with its structure.

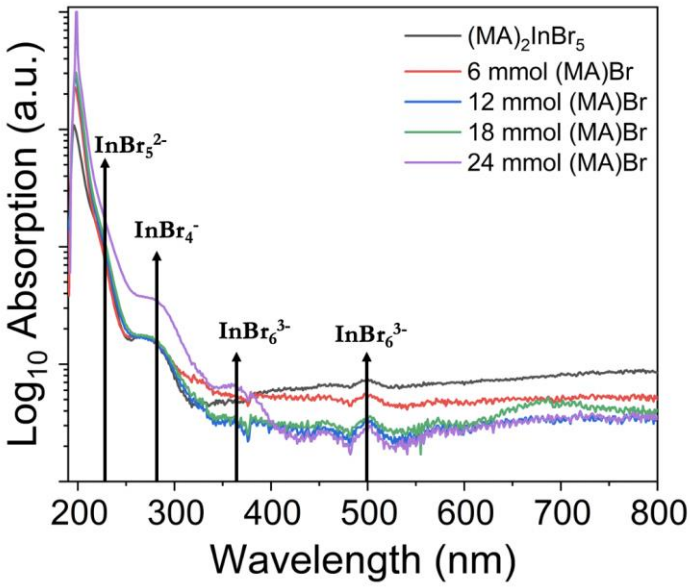

Figure 3. Evolution of optical absorption plot for $(MA)_2InBr_5$ with the addition of excess MABr. Arrows indicate DFT calculated absorption band positions for various solution species.

The $(MA)_2InBr_5$ structure is particularly interesting as it contains both octahedra and tetrahedra. Additional experiments show that upon adding excess MABr to a stoichiometric MA_2InBr_5 solution (i.e., gradually moving toward the $(MA)_4InBr_7$ composition), increase in the intensities of absorption bands at 360 and 500 nm can be seen (Figure 3); these absorption bands have been assigned to the octahedral indium bromide $InBr_6^{3-}$ based on our computational work. Our SAXS measurements (Figure 4) suggest presence of species with diameters from 4.44 to 6.7 Å. This supports the presence of nothing larger than monomeric forms, and comparison with simulated scattering data of tetrahedra and octahedra indicates partial replacement of bromide with methanol in the coordination sphere. The presence of $InBr_4^-$ tetrahedral anions and several other octahedral and tetrahedral indium bromide molecules containing solvated methanol ligands in the solution medium is further confirmed by our ESI-MS results.

Importantly, the MA-In-Br has served as a baseline to establish procedures for our experimental and computational studies. In addition to this system, we have also been studying 5 other homometallic halide systems proposed in this project, which also yielded interesting results. Our investigation results in these systems will be the focus of separate publications. We have been successful in the computational studies of homometallic halide solution systems and can now routinely assign absorption bands observed in various systems to specific chemical species in these solutions (e.g., see Figures 3-4). With these accomplishments, we are now ready to tackle more complex, heterometallic halide solutions.

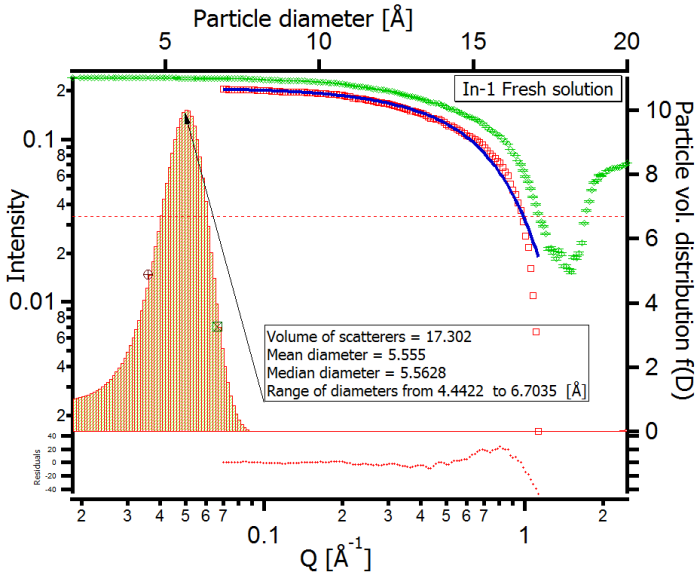

Figure 4. Particle diameter distribution data for the methanol solution of $(MA)_2InBr_5$ from small angle X-ray scattering (SAXS) measurements.

Future Plans

In the first year, our focus has been on indium and bismuth halides. Our exciting results in the MA-In-Br system will be summarized in a forthcoming publication. To complete this publication, we will measure the optoelectronic properties (Task 4) and calculate the electronic structures and excitonic properties (Task 5) of the three new compounds in the MA-In-Br system. In the next reporting period, a greater focus will be on Cu, Ag, and Sb halides.

Overall, we believe that the project is off to a good start with some very interesting results on the homometallic halide systems. Assuming our return to normalcy, we also have plans to start looking at a few heterometallic halide systems, which is originally planned for Year 3 in our project timeline. Given our interesting results in the homometallic Bi and In halide systems, however, we are eager to start investigating a few heterometallic systems a little earlier than originally planned.

References

(1) Saparov, B.; Mitzi, D. B. Organic–Inorganic Perovskites: Structural Versatility for Functional Materials Design. *Chem. Rev.* **2016,** *116*, 4558-4596.

(2) Tran, T. T.; Quintero, M. A.; Arpino, K. E.; Kelly, Z. A.; Panella, J. R.; Wang, X.; McQueen, T. M. Chemically controlled crystal growth of $(CH_3NH_3)_2AgInBr_6$. *CrystEngComm* **2018,** *20*, 5929-5934.

(3) Wei, F.; Deng, Z.; Sun, S.; Zhang, F.; Evans, D. M.; Kieslich, G.; Tominaka, S.; Carpenter, M. A.; Zhang, J.; Bristowe, P. D.; Cheetham, A. K. Synthesis and Properties of a Lead-Free Hybrid Double Perovskite: $(CH_3NH_3)_2AgBiBr_6$. *Chem. Mater.* **2017,** *29*, 1089-1094.

Publications

1. "*Charge carrier mobility of halide perovskite single crystals for ionizing radiation detection*" Zhang, Z.; **Saparov, B.*** *Appl. Phys. Lett.* **2021**, *under review*. [**Perspective Article**]

Energy Flow in Polymers with Mixed Conduction Pathways

Rachel Segalman and Michael Chabinyc - University of California, Santa Barbara

Program Scope

The simultaneous transport of ions and electrons in semiconducting polymers is essential for all electrochemical devices, ranging from fuel cells to batteries and supercapacitors to bioelectronics. However, rational design of polymeric mixed conductors is complex due to the need to maximize both ionic and electronic conduction, which exhibit different transport mechanisms across different length scales. Additionally, the degree to which these charged species interact throughout multiple length scales and the degree to which this interaction impacts device properties is unknown. Our goal in this project is to understand how ions and charge carriers interact at the molecular scale, mesoscale, and macroscale to design for maximal mixed conduction within polymeric mixed conductors and blends. Ultimately, this knowledge will provide design rules of mixed ion/electron conducting polymers and potentially lead to new applications for which mixed conductors have not been utilized.

Recent Progress

Doping of a semiconducting polymers requires a balance between steric interactions, electrostatic attraction, and structural changes. We have shown that the design of side chains controls the self-assembly and electronic structure of conjugated polymers. [10] Sidechains are also a structural constraint that can modify the position of dopants in ordered regions of these polymers.[9] The relative position of the dopant ions with respect to the charge carriers on the polymer backbones have a profound effects on doping efficacy and ultimately electrical transport. To further uncover on the role of the interaction between charge carriers and counterions, we have studied an exchange procedure to efficiently switch the counterion in doped semiconducting polymers.[3] This procedure allows us to exclusively investigate how the counterion size affects doping in absence of strong perturbations on the longer range morphology. From this study, we

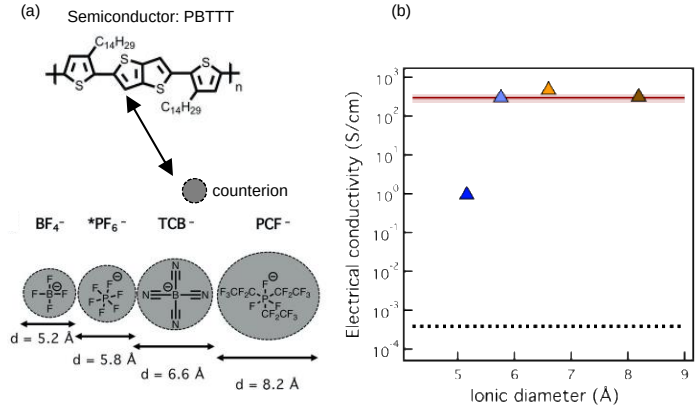

Figure 1: (a) Chemical structures of semiconducting polymer and counterions of different diameters. Larger ion size results in a larger counterion—charge-carrier distance (b) the electrical conductivity is insensitive to the local counter-ion/polaron distance. The dark blue symbol represents BF_4^-, which has a lower conductivity due to a de-doping reaction upon ion exchange.

have shown conclusively that while counterion size affects the distance between the charge carrier and the counterion, this distance does not strongly affect electrical conductivity. In particular, as shown in Figure 1, across a counterion size of 5.2 to 8.2 Å in diameter, the counter-ion distance to the charge carrier varied significantly yet there was no change to the film's electrical conductivity. It is posited that other factors dominate the electrical properties at larger length scales, such as the morphology and presence of domain boundaries. Interestingly, the temperature stability of the doped film can be drastically improved with the use of counter-ions containing less labile bonds. This platform serves as a unique way to retain the morphology of polymeric thin films while studying charge interactions at the local scale

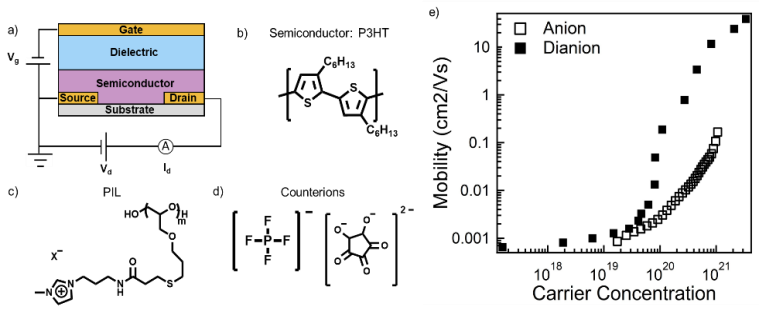

Figure 2: (a) Schematic representation of the gate electrochemical transistor structure used for transport measurements. Chemical structure of (b) the *p*-type semiconductor (P3HT), (c) the cation tethered PIL and (d) the anion and dianion counterions used to examine the role of the charge of counterions. (e) Charge carrier mobility as a function of carrier concentration for electrochemical devices gated with a polymeric ionic liquid with either an anion or a dianion.

We have found that gating semiconducting polymers with single ion conducting polymeric ionic liquid (PIL) dielectrics provides a valuable platform for probing the detailed interactions between charge carriers and counterions. The high capacitance of PILs provides the ability to precisely control the charge carrier concentrations by application of a gate bias. Using PILs as electrochemical gates, we have found that while holes induced in conjugated polymers first reside in the crystalline regions of the film, the counter-ions to these charge carriers preferentially reside in the disordered regions, verifying that a counterion need not be in the same physical domain as its associated charge carrier.[11] Additionally, because PILs are single-ion conductors, we were able to tune the spatial distribution of counterions by selectively tethering ions of positive or negative charge to the backbone of the PIL. This change in tethering will limit the counterion to reside only at the interface of the PIL and semiconducting polymer or allow penetration of the counterion into the semiconducting polymer. We found that interfacial doping, which does not require the infiltration of ions into the polymer layer, leads to a more even distribution of carriers between ordered and less ordered domains and promotes the formation of a percolated network in the film.[5] Lastly, switching the mobile ion of the PIL enables control of the amount of charge in the counter ion. In doped semiconducting polymer films, counterions cause structural and morphological perturbations, induce charge traps, and affect charge carrier molecular configuration. Changing the charge of the counterion, while keeping the volume of the ion as small as possible, minimizes the required volume fraction of counterion in the film, and thus the effect on structural order of the semiconductor. We find that implementing a dianion as the counterion can increase the electronic mobility of semiconducting polymers by over an order of

magnitude when compared to singly charged counterions of similar volume (Figure 2).[17] We posit that this large increase in carrier mobility is not only a result of the decrease in structural perturbation, but also the difference in the coulombic potential on the carrier. This represents an important insight into the effect of ion-carrier interactions on electronic transport, and it establishes a novel model system for tuning such interactions.

We have also designed mixed conducting polymer blends that have independently defined ion- and electron-conducting components utilizing the complexation phenomenon between two oppositely charged polyelectrolytes.[8, 15] This charge-mediated self-assembly result in a polymer blend that can be deposited at high concentrations (requiring minimal solvent for processing). In particular, some compositions enabled the formation of a complex coacervate of a conjugated polyelectrolyte (CPE) and a PIL (Figure 3).[15] This coacervate is a viscous fluid containing up to 50 wt% polymer, and can be readily blade-coated into solid films. Furthermore, we observed enhancement in the conjugation lengths of the CPEs upon coacervation. We postulate that the complexation process has reduced the CPE conformational disorders, leading to more delocalization of excitons along the CPE backbone. The polymer chain conformations appeared to be carried over to the solid state, as the electrical conductivity of doped solid film casted from the coacervate was twice as high as that of the doped CPE film despite the coacervate having much less conducting material per unit volume. This conductivity trend indicates faster charge carrier transport along the complexed CPE backbone, in agreement with the enhanced conjugation that was observed. This demonstrates the great potential of polyelectrolyte coacervation in processing of highly concentrated mixed conductive polymer blends, and with added enhancements to the optoelectronic properties of the electroactive component.

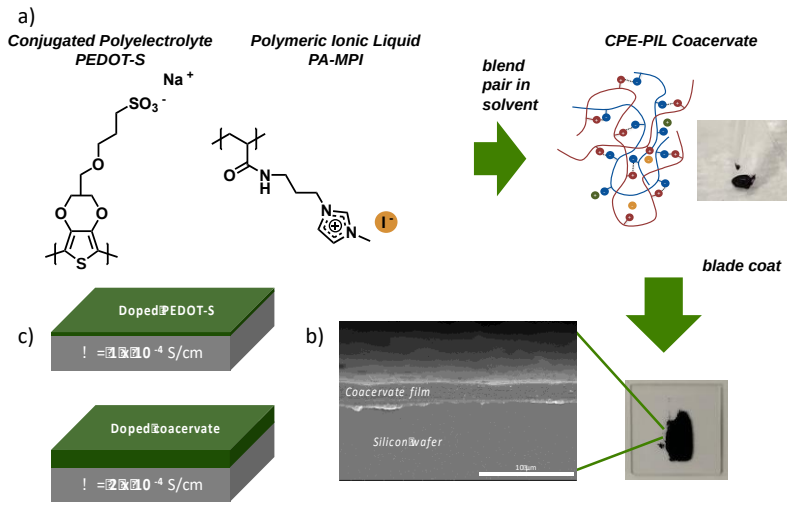

Figure 3: (a) Chemical structures of the conjugated polyelectrolyte (CPE) PEDOT-S and the polymeric ionic liquid (PIL) PA-MPI and the processing route to achieve the CPE-PIL coacervate solid film. (b) Side-view SEM image of the coacervate film upon salt and water removal. (c) Electronic conductivities of the CPE-PIL coacervate film and the neat CPE film at their optimal electrical doping states.

Future Plans

The transport of counter-ions and electrons in mixed conductors are usually coupled, with counterion transport being the rate-limiting step. However, quantifying the coupling between ionic

and electronic transport in single-component materials has yet to be done. In the next steps, we seek to understand the degree to which counterion mobility influences the electrochemical doping of semiconducting polymers. We will utilize our previously synthesized conjugated polymer ionic liquid, imidazolium substituted poly(3-alkyl thiophene), with semicrystalline ordering and appreciable mixed conductivity as the model system. *In-situ* EPR experiments will be done to monitor the degree of doping as a function of potential and frequency. Additionally, the ion self-diffusion coefficient and ionic conductivity will be measured. Collectively, these will provide quantitative insight as to the extent anion transport in the bulk semiconductor impacts doping kinetics and electronic carrier mobility.

The infiltration of ions into the solid polymer film frequently leads to the volumetric expansion within the film's ordered (and disordered) domains. We have shown that polymer crystallites impose constraints to the infiltration of ions into the doped semiconductor film at small carrier concentrations.[11] Moving forward, we seek to investigate to what extent these ordered domains limit, or permit, infiltration of dopant ions. Ultimately, this will provide fundamental insights to how the self-assembly of polymers and counterions impact doping and mixed conduction in conjugated polymers.

We have demonstrated how the electrostatic assembly of ion and electron conducting polymers could allow for formulation of concentrated polymer blends with great advantages in large-scale processing. However, the design rules for optimal performance of this system are yet to be developed due to the lack of fundamental insights into coacervation of conjugated polymer. Moving forward, we will use of a random copolymer systems where the frequency of charge-carrying moieties of the polymers can be synthetically modified. This provides an excellent synthetic handle for controlling the coacervate self-assembly via tuning the Coulombic interaction strength. By constructing a phase diagram for the coacervate that accounts for both the ion diffuseness and the spacing of charges, we will determine how coacervation thermodynamics could be controlled to access microstructure ordering within the coacervate. Combining the structure studies with transport measurement, we will gain insights on the coacervate's mixed ion-electron transport mechanism and how the structure of the coacervate could be tuned to optimize the simultaneous conduction of ions and electrons in this complex system.

Publications

Published

1. Electronic, Ionic, and Mixed Conduction in Polymeric Systems. E. M. Thomas, P. H. Nguyen, S. D. Jones, M. L. Chabinyc, R. A. Segalman. *Annu. Rev. Mater. Res.* 2021, 51 (1) DOI: 10.1146/annurev-matsci-080619-110405
2. Post-deposition Processing Influences the Relative Contributions of Electronic and Ionic Seebeck Effects in the Thermoelectric Response of Conducting Polymers. M. Sezen-

Edmonds, A. M. Glaudell, W. B. Chang, R. A. Segalman, M. L. Chabinyc, Y-L. Loo. *Journal of Physical Chemistry C* 2021 DOI: 10.1021/acs.jpcc.1c01399

3. Effects of Counter-Ion Size on Delocalization of Carriers and Stability of Doped Semiconducting Polymers. E. M. Thomas, K. A. Peterson, A. H. Balzer, D. Rawlings, N. Stingelin, R. A. Segalman, M. L. Chabinyc. *Adv. Electron. Mater.* 2020, 6 (12), 1–10. DOI: 10.1002/aelm.202000595
4. Thermoelectric Properties of Semiconducting Polymers. K. A. Peterson, E. M. Thomas, M. L. Chabinyc. *Annu. Rev. Mater. Res.* 2020, 50, 551–574. DOI: 10.1146/annurev-matsci-082219-024716
5. Controlling the doping mechanism in poly(3-hexylthiophene) thin- film transistors with polymeric ionic liquid dielectrics. D. Rawlings, E. M. Thomas, R. A. Segalman, and M. L. Chabinyc. *Chem. Mater*. 2019. 31, 21, 8820-8829. DOI: 10.1021/acs.chemmater.9b02803.
6. Absence of electrostatic rigidity in conjugated polyelectrolytes with pendant charges S. P. O. Danielsen, E. C. Davidson, G. H. Fredrickson, and R. A. Segalman. *ACS Macro Lett.,* 2019. 8, 1147-1152. DOI: 10.1021/acsmacrolett.9b00551
7. Nonaggregating Doped Polymers Based on Poly(3,4-Propylenedioxythiophene). A. Mazaheripour, E. M. Thomas, R. A. Segalman, and M. L. Chabinyc. *Macromolecules,* 2019. 52, 5, 2203-2213. DOI: 10.1021/acs.macromol.8b02389.
8. Complexation of a Conjugated Polyelectrolyte and Impact on Optoelectronic Properties. S. P. O. Danielsen, T.-Q. Nguyen, G. H. Fredrickson, R. A. Segalman. *ACS Macro Letters*, 2019, 8, 88-94. DOI: 10.1021/acsmacrolett.8b00924
9. Branched Side Chains Govern Counterion Position and Doping Mechanism in Conjugated Polythiophenes. E. M. Thomas, E. C. Davidson, R. Katsumata, R. A. Segalman, M. L. Chabinyc. *ACS Macro Lett.*, 2018, 7, 1492−1497. DOI: 10.1021/acsmacrolett.8b00778
10. Effects of Side Chain Branch Point on Self Assembly, Structure, and Electronic Properties of High Mobility Semiconducting Polymers. C. R. Bridges, M. J. Ford, E. M. Thomas, C. Gomez, G. C. Bazan, R. A. Segalman. *Macromolecules*, 2018, 51 (21), 8597-8604. DOI: 10.1021/acs.macromol.8b01906
11. X-Ray Scattering Reveals Ion-Induced Microstructural Changes During Electrochemical Gating of Poly(3-Hexylthiophene). E. M. Thomas, M. A. Brady, H. Nakayama, B. C. Popere, R. A. Segalman, M. L. Chabinyc. *Adv. Funct. Mater.*, 2018, 1803687. DOI: 10.1002/adfm.201803687
12. Tailoring the Seebeck Coefficient of PEDOT:PSS by Controlling Ion Stoichiometry in Ionic Liquid Additives. A. Mazaheripour, S. Majumdar, D. Hanemann-Rawlings, E. M. Thomas, C. McGuiness, L. d'Alencon, M. L. Chabinyc, R. A. Segalman. *Chemistry of Materials*, 2018, 30 (14), 4816-4822. DOI: 10.1021/acs.chemmater.8b02114

13. Role of Disorder Induced by Doping on the Thermoelectric Properties of Semiconducting Polymers. E. M. Thomas, B. C. Popere, H. Fang, M. L. Chabinyc, R. A. Segalman. *Chemistry of Materials* 2018 *30* (9), 2965-2972. DOI: 10.1021/acs.chemmater.8b00394

Submitted

14. Passive ion pair uptake in solid-state devices based on organic mixed ionic-electronic conductors. T. J. Quill, G. LeCroy, A. Melianas, D. Rawlings, Q. Thiburce, I. P. Maria, C. Cheng, Y. Tuchman, S. T. Keene, I. McCulloch, R. A. Segalman, M. L. Chabinyc, A. Salleo. *Advanced Functional Materials*. Submitted.
15. Aqueous Formulation of Concentrated Semiconductive Fluid Using Polyelectrolyte Coacervation. M. L. Le, D. Rawlings, S. P. O. Danielsen, R. M. Kennard, M. L. Chabinyc, R. A. Segalman. *ACS Macro Letters*. Submitted.
16. Co-addition of lithium salt and oxidative dopants provides simultaneous control over ionic and electronic conduction in conjugated polymeric ionic liquids. D. Rawlings, D. Lee, J. Kim, I. B. Magdău, G. Pace, P. Richardson, E. M. Thomas, S. P. O. Danielsen, S. Tolbert, T. F. Miller III, R. Seshadri, R. A. Segalman. *Chemistry of Materials*. Submitted
17. The effect of counterion charge on carrier transport in solid state electrochemically doped conjugated polymer films. D. Rawlings, M. L. Chabinyc, R. A. Segalman. *ACS Materials Letters.* Submitted.

Hybrid Metal Halides: Advancing Optoelectronic Materials

Ram Seshadri,[1] Michael Chabinyc,[1] and Mercouri Kanatzidis[2]

Materials Department, University of California, Santa Barbara, CA 93106

Department of Chemistry, Northwestern University, Evanston IL 60208

Program Scope Main-group halide compounds with the perovskite crystal structure, particularly hybrid organic-inorganic lead halides, have recently attracted immense attention for their remarkable optoelectronic properties, ease of preparation, and abundant constituent elements. Such compounds, of which methylammonium (MA) lead iodide ($MAPbI_3$, with MA = $CH_3NH_3^+$) has been the most extensively studied, are strong optical absorbers, display appropriate charge-carrier mobilities, exhibit long exciton diffusion lengths, and demonstrate evidence of photon recycling in photovoltaic (PV) devices, all of which gives rise to impressive photovoltaic performance. Like their well-studied oxide analogues, the halide perovskites exhibit great chemical flexibility, leading to diverse structure and function. Since the first application of hybrid lead iodides in PV devices in 2009, the scope has broadened substantially to include the pursuit of lead-free materials, bromides, and mixed halides for light emission and detection applications. However, key aspects regarding the origins of the remarkable functionality of these materials remain enigmatic. There has also been a great need for the advancement of new materials and new chemistries beyond the simple perovskites to expand this class of materials.

This project has a strong focus on the creation of new materials, as well as developing fundamental understanding of the materials science of these hybrid metal halides. Some of the questions driving the project include: How does the interaction between the organic and inorganic sublattices influence the structural transitions and lattice dynamics in halide perovskites? What is the impact of the lone pair of electrons associated with the divalent main group cation on key properties? How does halide ion migration and segregation takes place in solid-solution halide perovskites? Can the domain of known functional hybrid metal halides be expanded through the creation of novel materials? What is the nature of film growth and the impact of structural defects on electronic properties, and how does structure and chemistry influence charge carriers?

A targeted multidisciplinary approach is adopted towards understanding key questions that contribute to the high photovoltaic performance of hybrid halide materials. The insights gained from the project inform new chemical design principles for defect-tolerant semiconductors, produce new materials with enhanced stability and optimized performance, and enable materials with large, tunable bandgaps and high mobilities. The synthesis of hybrid metal halides and characterization at a fundamental level help control their diverse properties, impacting more applied aspects of these systems.

Recent Progress

Some highlights of recent work from the past years are presented below.

Tunable Broad Light Emission from 3D Hollow Bromide Perovskites through Defect Engineering: In this work, advantage was taken of the defect tolerance of hybrid halide perovskites to engineer a new family of 3D highly defective hollow bromide perovskites with general formula $(FA)_{1-x}(en)_x(Pb)_{1-0.7x}(Br)_{3-0.4x}$ (FA = formamidinium, en = ethylenediammonium, x = 0 to 0.44) [**Figure 1**]. Incorporation of en cations in the 3D perovskite structure leads to massive Pb and Br vacancies in the 3D [$PbBr_3$] framework. Pair distribution function (PDF) analysis was employed to shed light on the local structural coherence, revealing a wide distribution of Pb-Pb distances in the crystal structure, validating further that the corresponding materials are lead deficient and highly disordered. Solid state NMR studies suggested that en cations are well dispersed into the perovskite framework at en loadings less than 30 %, whereas two types of local chemical environments of en molecules are observed at en loadings greater than 30 %. By manipulating the amount of incorporated en, the optical properties of the corresponding crystals could be fine-tuned over a wide energy range both in terms of emission and absorption spectra. Above 33 % en inclusion, the hollow bromide perovskite emits strong broad light at room temperature that is directly correlated to the number of defects, increasing gradually in intensity for 42 %, and reaching a plateau at 44% en, with 1 % PLQY coupled with a lifetime of 15 ns. Considering that the only structural difference between the compounds with narrow and broad emission is the presence of another type of defect above 29 % en loading, we ascribe the formation of the self-trapped excitons (that result in white-light emission) to their presence. The corresponding material maintains its strong PL emission for at least one year in air exposure. This is the first time that strong broad light emission from a 3D hybrid halide perovskite has been observed, while its PL robustness under ambient conditions is among the highest reported for halide perovskites. This work has been published in [1].

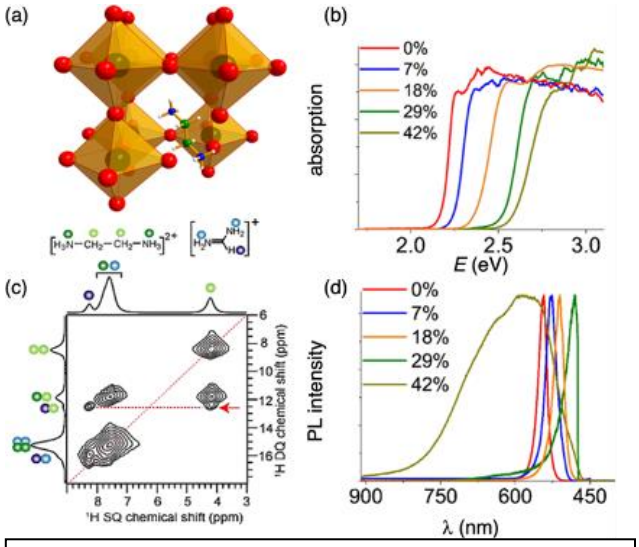

Figure 1 (a) A representation of the single crystal structure of the hollow materials. (b) Optical absorption spectra of compounds $(FA)_{1-x}(en)_x(Pb)_{1-0.7x}(Br)_{3-0.4x}$, with increasing amount of *en*. (c) Solid-state ^1H MAS NMR spectra of $FAPbBr_3$ and hollow perovskites acquired of at 18.8 T (Larmor frequency of ^1H is 850.1 MHz) and at RT with 35 kHz MAS. 2D ^1H–^1H DQ-SQ correlation NMR spectra of 41 % *en*/$FAPbBr_3$. (d) PL emission spectra of compounds $(FA)_{1-x}(en)_x(Pb)_{1-0.7x}(Br)_{3-0.4x}$, with increasing amount of *en*. Above 33% *en* loading broad light emission tunable in intensity was observed.

Ferroelastic Hysteresis in Thin Films of Methylammonium Lead Iodide: Mechanical strain can modify the structural and electronic properties of methylammonium lead iodide $MAPbI_3$. The consequences of ferroelastic hysteresis, which involves the retention of structural memory upon cycles of deformation, are reported for polycrystalline thin films of $MAPbI_3$. In this work, repeatedly bent films were examined using grazing incidence wide-angle X-ray scattering (GIWAXS) to quantitatively characterize the strains and proportions of twin domains. Approximate locations for the coercive stress and saturation on the ferroelastic stress–strain curve was identified, and changes to the stress–strain curve with cyclic strain were characterized. Notably, it was determined that an external stress source, such as thermal stress from the substrate or a roll-to-roll printing setup, must apply at least + or – 50 MPa to modify the proportions of different twins. Long-term stability testing revealed that the domain walls are highly immobile over extended periods. Nucleation of new domain walls occurs for specific mechanical strains and correlates closely with degradation. This work has been published in [2].

Chemical Control of Spin-Orbit Coupling and Charge Transfer in Vacancy-Ordered Ruthenium (IV) Halide Perovskites: In this recompeted project, the focus on functional halides, beyond optoelectronic properties, has also encompassed some magnetic properties, allowing a convergence of these optoelectronic materials with quantum materials, and in particular, an understanding of spin-orbit coupling. Vacancy-ordered double perovskites have attracted significant attention due to their chemical diversity and interesting optoelectronic properties. With a view to understanding both the optical and magnetic properties of these compounds, two series of Ru^{IV} halides have been developed: A_2RuCl_6 and A_2RuBr_6, where *A* is K, NH_4, Rb or Cs. [**Figure 2**]. It has been established that the optical properties and spin-orbit coupling (SOC) behavior can be tuned through changing the *A* cation and the halide. Within a series, the energy of the ligand-to-metal charge transfer increases as the unit cell expands with the larger *A* cation, and the band gaps are higher for the respective chlorides than for the bromides. The magnetic moments of the systems are temperature dependent due to a non-magnetic ground state with $J_{eff} = 0$ caused by SOC. Ru–*X* covalency, and consequently, the delocalization of metal d-electrons, result in systematic trends of the SOC constants due to variations in the A cation and the halide anion. This work has been published in [3].

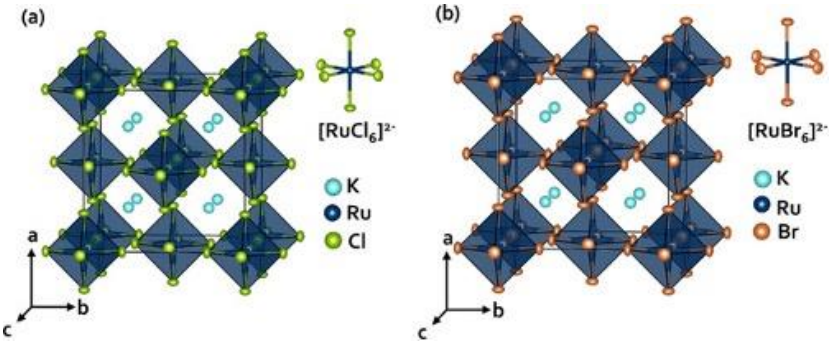

Figure 2 Single-crystal X-ray structures of (a) K_2RuCl_6 and (b) K_2RuBr_6. The atoms are shown as their thermal ellipsoids with 50 % probabilities. The ball and stick models of $[RuCl_6]^{2-}$ and $[RuBr_6]^{2-}$ octahedra are shown on the right of the respective structure.

Future Plans

Hollow perovskites: In the forthcoming year, we plan further studies on the fundamental understanding of the structure, stability, and properties of hollow perovskites including the development of new compounds. One question that is being pursued at the current time is the creation and characterization of layered perovskites (*ie*. Ruddlesden-Popper and Dion-Jacobson compounds) that are en substituted to create the cooperative vacancies that dictate structure and properties.

Thin film materials: In the forthcoming year, we will continue to expand the repertoire of preparation techniques that will allow the creation of single-phase thin films of layered materials and a development of methods to characterize them, as well as the means to properly understand the role that strain plays in developing properties such as self-trapped exciton emission. The characterization and property measurement of hollow perovskite thin films is also commencing, with plans to employ a number of different tools including cathodiluminescence and impedance spectroscopy, and time-resolved optical and electrical measurements to better understand this emerging materials class.

Perovskite-derived inorganic and hybrid transition metal halides: In the forthcoming year, we will continue expand on the range of hybrid halide materials based on cations such as Ru^{3+} and Ru^{4+} which are very interesting for their magnetism, with interesting synergies with the area of quantum materials. Layered materials with these ions have been prepared and will be better developed and understood in the coming year. Unlike Ru^{3+}, Mo^{3+} is a d^3 ion with no orbital angular momentum, and therefore provides an interesting comparison. The first Mo-containing inorganic and hybrid materials have been prepared and this is also a range of materials that will be developed. Paramagnetic NMR studies of these materials is ongoing, and magnetooptical probes of these materials are planned in the coming year.

References

[1] I. Spanopoulos, I. Hadar, W. Ke, P. Guo, E. Mozur, E. Morgan, S. Wang, D. Zheng, S. Padgaonkar, G. N. Manjunatha Reddy, E. Weiss, M. Hersam, R. Seshadri, R. Schaller, and M. Kanatzidis, Tunable broad light emission from 3D hollow bromide perovskites through defect engineering, *J. Am. Chem. Soc*. **143** (2021) 7069–7080. [DOI: 10.1021/jacs.1c01727]

[2] R. M. Kennard, C. J. Dahlman, R. A. DeCrescent, J. A. Schuller, K. Mukherjee, R. Seshadri, and M. L. Chabinyc, Ferroelastic hysteresis in thin films of methylammonium lead iodide, *Chem. Mater.* **33** (2021) 298–309. [DOI: 10.1021/acs.chemmater.0c03776]

[3] P. Vishnoi, J. L. Zuo, J. A. Cooley, L. Kautzsch, A Gómez-Torres, J. Murillo, S. Fortier, S. D. Wilson, R. Seshadri, and A. K. Cheetham, Chemical control of spin-orbit coupling and charge transfer in vacancy-ordered Ru(IV) halide perovskites, *Angew. Chem*. **60** (2021) 5184–5188. [DOI: 10.1002/anie.202013383]

Publications

1. I. Spanopoulos, I. Hadar, W. Ke, P. Guo, E. M. Mozur, E. Morgan, S. Wang, D. Zheng, S. Padgaonkar, G. N. M. Reddy, E. A. Weiss, M. C. Hersam, R. Seshadri, R. D. Schaller, and M. G. Kanatzidis, Tunable broad light emission from 3D hollow bromide perovskites through defect engineering, *J. Am. Chem. Soc*., **143**, 7069, 2021.
2. E. S. Vasileiadou, B. Wang, I. Spanopoulos, I. Hadar, A. Navrotsky, and M. G. Kanatzidis, Insight on the stability of thick layers in 2D Ruddlesden–Popper and Dion–Jacobson lead iodide perovskites, J. Am. Chem. Soc., 143, 2523, 2021.
3. H. Ryu, H. R. Byun, K. M. McCall, D. Y. Park, T. J. Kim, M. S. Jeong, M. G. Kanatzidis, and J. I. Jang, Role of the A-site cation in low-temperature optical behaviors of $APbBr_3$ (A = Cs, CH_3NH_3), *J. Am. Chem. Soc.*, **143**, 2340, 2021.
4. S. Guo, K. Bu, J. Li, Q. Hu, H. Luo, Y. He, Y. Wu, D. Zhang, Y. Zhao, W. Yang, M. G. Kanatzidis, and X. Lü, Enhanced photocurrent of all-inorganic two-dimensional perovskite $Cs_2PbI_2Cl_2$ via pressure-regulated excitonic features, *J. Am. Chem. Soc.*, **146**, 2545, 2021.
5. P. Vishnoi J. L. Zuo, J. A. Cooley, L. Kautzsch, A. Gómez-Torres, J.Murillo, S. Fortier, S. D. Wilson, R. Seshadri, A. K. Cheetham, Chemical control of spin-orbit coupling and charge transfer in vacancy-ordered ruthenium(IV) halide perovskites, *Angew. Chem.*, **60**, 5184, 2021.
6. C. J. Dahlman, R. M. Kennard, P. Paluch, N. R. Venkatesan, M. L. Chabinyc, and G. N. Manjunatha Reddy, Dynamic motion of organic spacer cations in Ruddlesden–Popper lead iodide perovskites probed by solid-state NMR spectroscopy, *Chem. Mater*., **33**, 642, 2021.
7. A. Senocrate, I. Spanopoulos, N. Zibouche, J. Maier, M. S. Islam, and M. G. Kanatzidis, Tuning ionic and electronic conductivities in the hollow perovskite {en}$MAPbI_3$, *Chem. Mater*., **33**, 719, 2021.
8. R. M. Kennard, C. J. Dahlman, R. A. DeCrescent, J. A. Schuller, K. Mukherjee, R. Seshadri, and M. L. Chabinyc, Ferroelastic hysteresis in thin films of methylammonium lead iodide, *Chem. Mater*., **33**, 298, 2020.
9. H. Ryu, D. Y. Park, K. M. McCall, H. R. Byun, Y. Lee, T. J. Kim, M. S. Jeong, J. Kim, M. G. Kanatzidis, and J. I. Jang, Static Rashba effect by surface reconstruction and photon recycling in the dynamic indirect gap of $APbBr_3$ (A = Cs, CH_3NH_3) single crystals, *J. Am. Chem. Soc.*, **142**, 21059, 2020.
10. S. Wang, E. E. Morgan, P. Vishnoi, L. Mao, S. M. L. Teicher, G. Wu, Q. Liu, A. K. Cheetham, and R. Seshadri, Tunable luminescence in hybrid Cu(I) and Ag(I) iodides, *Inorg. Chem.*, **59**, 15487, 2020.
11. C. J. Dahlman, N. R. Venkatesan, P. T. Corona, R. M. Kennard, L. Mao, N. C. Smith, J. Zhang, R. Seshadri, M. E. Helgeson, and M. L. Chabinyc, Structural evolution of layered hybrid lead iodide perovskites in colloidal dispersions, *ACS Nano*, **14**, 11294, 2020.
12. L. Mao, P. Guo, S. Wang, A. K. Cheetham, and R. Seshadri, Design principles for enhancing photoluminescence quantum yield in hybrid manganese bromides, *J. Am. Chem. Soc.*, **142**, 13582, 2020.

13. R. A. DeCrescent, X. Du, R. M. Kennard, N. R. Venkatesan, C. J. Dahlman, M. L. Chabinyc, and J. A. Schuller, Even-parity self- trapped excitons lead to magnetic dipole radiation in two-dimensional lead halide perovskites, *ACS Nano*, **14**, 8958, 2020.
14. L. Kong, G. Liu, J. Gong, L. Mao, M. Chen, Q. Hu, X. Lü, W. Yang, M. G. Kanatzidis, and H.-K Mao, Highly tunable properties in pressure-treated two-dimensional Dion–Jacobson perovskites, *Proc. Natl. Acad. Sci. USA*, **117**, 16121, 2020.
15. Y. Liu, Z. Xu, Z. Yang, Y. Zhang, J. Cui, Y. He, H. Ye, K. Zhao, H. Sun, R. Lu, M. Liu, M. G. Kanatzidis, and Shengzhong. Liu, Inch- size 0D-structured lead-free perovskite single crystals for highly sensitive stable X-ray imaging, *Matter*, **3**, 180, 2020
16. D. H. Fabini, R. Seshadri, and M. G. Kanatzidis, The underappreciated lone pair in halide perovskites underpins their unusual properties, *MRS Bulletin*, **45**, 467, 2020.
17. X. Li, Y. Fu, L. Pedesseau, P. Guo, S. Cuthriell, I. Hadar, J. Even, C. Katan, C. C. Stoumpos, R. D. Schaller, E. Harel, and M. G. Kanatzidis, Negative pressure engineering with large cage cations in 2D halide perovskites causes lattice softening, *J. Am. Chem. Soc.*, **142**, 11486, 2020.
18. P. Vishnoi, J. L. Zuo, T. A. Strom, G. Wu, S. D. Wilson, R. Seshadri, and A. K. Cheetham, Structural diversity and magnetic properties of hybrid ruthenium halide perovskites and related compounds, *Angew. Chem.*, **132**, 9059, 2020.
19. Y. Zhang, Y. Liu, Z. Xu, H. Ye, Z. Yang, J. You, M. Liu, Y. He, M. G. Kanatzidis, and S. Liu, Nucleation-controlled growth of superior lead-free perovskite $Cs_3Bi_2I_9$ single-crystals for high-performance X-ray detection, *Nature Comm.*, **11**, 2304, 2020.
20. I. Spanopoulos, I. Hadar, W. Ke, P. Guo, S. Sidhik, M. Kepenekian, J. Even, A. D. Mohite, R. D. Schaller, and M. G. Kanatzidis, Water-stable 1D hybrid tin(II) iodide emits broad light with 36% photoluminescence quantum efficiency, *J. Am. Chem. Soc.*, **142**, 9028, 2020.
21. L. Mao, P. Guo, M. Kepenekian, I. Spanopoulos, Y. He, C. Katan, J. Even, R. D. Schaller, R. Seshadri, C. C. Stoumpos, and M.G. Kanatzidis, Organic cation alloying on intralayer A and interlayer A' sites in 2D Hybrid Dion–Jacobson lead bromide perovskites $(A')(A)Pb_2Br_7$, *J. Am. Chem. Soc.*, **142**, 8342, 2020.
22. X. Li, Y. He, M. Kepenekian, P. Guo, W. Ke, J. Even, C. Katan, C.C. Stoumpos, R.D. Schaller, and M. G. Kanatzidis, Three- dimensional lead iodide perovskitoid hybrids with high X-ray photoresponse, *J. Am. Chem. Soc.*, **142**, 6625, 2020.
23. E. E. Morgan, L. Mao, S. M. L. Teicher, G. Wu, and R. Seshadri, Tunable perovskite-derived bismuth halides: $Cs_3Bi_2(Cl_{1-x}I_x)_9$, *Inorg. Chem.*, **59**, 3387, 2020.
24. H. A. Evans, Y. Wu, R. Seshadri, A. K. Cheetham, Perovskite-related ReO_3-type structures, *Nature Rev. Mater.*, **5**, 196, 2020.
25. Y. Lan, X. Tao, X. Kong, Y. He, X. Zheng, M. Sutton, M. G. Kanatzidis, H. Guo, and D. G. Cooke, Coherent charge-phonon correlations and exciton dynamics in orthorhombic $CH_3NH_3PbI_3$ measured by ultrafast multi-THz spectroscopy, *J. Chem. Phys.*, **151**, 214201, 2019.

26. L. Mao, S. M. L. Teicher, C. C. Stoumpos, R. M. Kennard, R. A. DeCrescent, G. Wu, J. A. Schuller, M. L. Chabinyc, A. K. Cheetham, and R. Seshadri, Chemical and structural diversity of hybrid layered double perovskite halides, *J. Am. Chem. Soc.*, **141**, 19099, 2019.
27. K. M. McCall, D. Friedrich, D. G. Chica, W. Cai, C. C. Stoumpos, G. C. B. Alexander, S. Deemyad, B. W. Wessels, and M. G. Kanatzidis, Perovskites with a twist: Strong In^{1+} off-centering in the mixed-valent $CsInX_3$ (X = Cl, Br), *Chem. Mater.*, **31**, 9554, 2019.
28. L. Mao, R. M. Kennard, B. Traore, W. Ke, C. Katan, J. Even, M. L. Chabinyc, C. C. Stoumpos, and M. G. Kanatzidis, Seven-layered 2D hybrid lead iodide perovskites, *Chem*, **5**, 2593, 2019.
29. N. D. Canicoba, N. Zagni, F. Liu, G. McCuistian, K. Fernando, H. Bellezza, B.Traore ´, R. Rogel, H. Tsai, L. Le Brizoual, W. Nie, J. J. Crochet, S. Tretiak, C. Katan, J. Even, M. G. Kanatzidis, B. W. Alphenaar, J.-C. Blancon, M. A. Alam, and A. D. Mohite, Halide perovskite high-k field effect transistors with dynamically reconfigurable ambipolarity, *ACS Mater. Lett.*, **1**, 633, 2019.
30. R. A. DeCrescent, N. R. Venkatesan, C. J. Dahlman, R. M. Kennard, M. L. Chabinyc, and J. A. Schuller, Optical constants and effective-medium origins of large optical anisotropies in layered hybrid organic/inorganic perovskites, *ACS Nano*, **13**, 10745, 2019.
31. N. R. Venkatesan, A. Mahdi, B. Barraza, G. Wu, M. L. Chabinyc, and R. Seshadri, Enhanced yield-mobility products in hybrid halide Ruddlesden–Popper compounds with aromatic ammonium spacers, *Dalton*, **48**, 2019.
32. S. Vegiraju, W. Ke, P. Priyanka, J.-S. Ni, Y.-C. Wu, I. Spanopoulos, S. L. Yau, T. J. Marks, M.-C. Chen, and M. G. Kanatzidis, Benzodithiophene hole-transporting materials for efficient tin-based perovskite solar cells, *Adv. Func. Mater.*, **29**, 1905393, 2019.
33. H. Nakayama Y. Zheng, J. A. Schneider, H. Wang, N. Ninomiya, T. Momose, J. Read de Alaniz, F.Wudl, and M. L. Chabinyc, Sulfur-fused perylene diimide electron transport layers allow >400 h operational lifetime of methylammonium lead iodide photovoltaics, *J. Mater. Chem. C.*, **7**, 11126, 2019.
34. S. B. Todd, D. B. Riley, A. Binai-Motlagh, C. Clegg, A. Ramachandran, S. A. March, J. M. Hoffman, I. G. Hill, C. C. Stoumpos, M. G. Kanatzidis, Z.-G. Yu, and K. C. Hall, Detection of Rashba spin splitting in 2D organic-inorganic perovskite via precessional carrier spin relaxation, *APL Materials*, **7**, 081116, 2019.
35. R. M. Kennard, C. J. Dahlman, H. Nakayama, R. A. DeCrescent, J. A. Schuller, R. Seshadri, K. Mukherjee, and M. L. Chabinyc, Phase stability and diffusion in lateral heterostructures of methyl ammonium lead halide perovskites, *ACS Appl. Mater. Interfaces*, **11**, 25313, 2019.
36. C. J. Dahlman, R. A. DeCrescent, N. R. Venkatesan, R. M. Kennard, G. Wu, M. A. Everest, J. A. Schuller, and M. L. Chabinyc, Controlling solvate intermediate growth for phase-pure organic lead iodide Ruddlesden–Popper $(C_4H_9NH_3)_2(CH_3NH_3)_{n-1}Pb_nI_{3n+1}$ perovskite thin films, *Chem. Mater.*, **31**, 5831, 2019.

37. Y. Lan, B. J. Dringoli, D. A. Valverde-Chavez, C. S. Ponseca Jr., M. Sutton, Y. He, M. G. Kanatzidis, and D. G. Cooke, Ultrafast correlated charge and lattice motion in a hybrid metal halide perovskite, *Science Adv.*, **5**, eaaw5558, 2019.
38. W. Kei, I. Spanopoulos, Q. Tu, I. Hadar, X. Li, G. S. Shekhawat, V. P. Dravid, and M. G. Kanatzidis, Ethylenediammonium-based hollow Pb/Sn perovskites with ideal band gap yield solar cells with higher efficiency and stability, *J. Am. Chem. Soc.*, **141**, 8627, 2019.
39. X. Li, H. Wang, H. Nakayama, Z. Wei, J. A. Schneider, K. Clark, W.-Y. Lai, W. Huang, J. G. Labram, J. Read de Alaniz, M. L. Chabinyc, F. Wudl, and Y. Zheng, Multi-sulfur-annulated fused perylene diimides for organic solar cells with low open-circuit voltage loss, *ACS Appl. Energy Mater*., **2**, 3805, 2019.
40. D. H. Fabini, M. Koerner, and R. Seshadri, Candidate inorganic photovoltaic materials from electronic structure-based optical absorption and charge transport proxies, *Chem. Mater*., **31**, 1561, 2019.
41. H. A. Evans, Z. Deng, I. E. Collings, Y. Wu, J. L. Andrews, K.Pilar, J. M. Tuffnell, Guang Wu, J. Wang, S. E. Dutton, Paul D. Bristowe, R.Seshadri and A. K. Cheetham, Polymorphism in $M(H_2PO_2)_3$ (M = V, Al, Ga) compounds with the perovskite- related ReO_3 structure, *Chem. Comm*., **55**, 2964, 2019.
42. P. Guo, A. Mannodi-Kanakkithodi, J. Gong, Y. Xia, C. C. Stoumpos, D. H. Cao, B. T. Diroll, J. B. Ketterson, G. P. Wiederrecht, T. Xu, M. K. Y. Chan, M. G. Kanatzidis, and R. D. Schaller, Infrared-pump electronic-probe of methylammonium lead iodide reveals electronically decoupled organic and inorganic sublattices, *Nat. Commun*, **10**, 482, 2019.

Carbon-Based Clathrates as a New Class of sp^3-Bonded Framework Materials

Timothy A. Strobel, Earth and Planets Laboratory, Carnegie Institution for Science, Washington, DC

Program Scope

This program is focused on developing novel carbon-based clathrates, which are extended guest-host materials comprised of tetrahedral carbon frameworks that trap metal atoms in polyhedral cages. Goals of the program include determining the range of possible framework types and guest/host substitutions, determining the critical parameters that dictate thermodynamic stability, and determining/optimizing physical properties. Given the large range of possible guest/host elemental substitutions, carbon-based clathrates represent a large class of light-weight, diamond-like materials with tunable electronic structures, and may thus impact a wide range of energy materials from thermoelectrics to superconductors.

Recent Progress

Following the discovery of the first carbon–boron clathrate, SrB_3C_3,[1] significant progress has been achieved in understanding new clathrate compositions and their thermodynamic stabilities and physical properties. SrB_3C_3 crystallizes in the Type-VII clathrate structure (bipartite sodalite) with one truncated octahedral cage type (Figure 1). SrB_3C_3 is synthesized at high pressures near 50 GPa, but is recoverable to ambient conditions. Divalent Sr^{2+}, which is trapped in the clathrate cages, can transfer two electrons to the sp^3 $[B_3C_3]^{3-}$ framework, and thus this clathrate is one electron short of a balanced count and is a hole conductor. A large number of different ions might also stabilize the Type-VII structure, including those with other valences. We therefore calculated the stability of MB_3C_3 clathrates, where M represents (nearly) all elements of the periodic table, and found several additional dynamically stable clathrate compositions, including the possibility for a novel ferroelectric ScB_3C_3 stabilized in a lower-symmetry structure.[2] Trivalent guests are of particular interest as they offer the possibility for a balanced electron count.

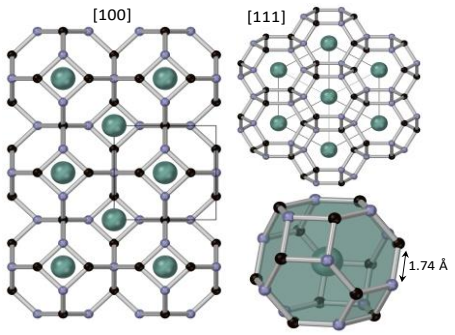

Figure 1. Type-VII carbon–boron clathrate (bipartite sodalite) structure shown along different crystallographic directions. Truncated octahedral cages formed from covalently bonded carbon (black) and boron (purple) trap metal atoms (green).

For the case of La^{3+}, we predicted that LaB_3C_3 becomes stable relative to formation elements and other binary compounds at pressures near 30 GPa, which represents a ~20 GPa reduction compared with SrB_3C_3, and is attributed to the precise electron count.[3] The Type-VII LaB_3C_3 clathrate in the bipartite sodalite structure was confirmed experimentally via high-pressure synchrotron X-ray diffraction measurements (Figure 2). Synthesis observed at 38 GPa, but not 35 GPa, places a bound on the thermodynamic stability and confirms the calculated improvement in

pressure compared with the divalent guest. Like SrB_3C_3, LaB_3C_3 is recoverable to ambient pressure while kept under an inert (dry) atmosphere. LaB_3C_3 also exhibits a large bulk modulus (B_0 = 254(9) GPa) comparable with structural armors such as boron carbide.

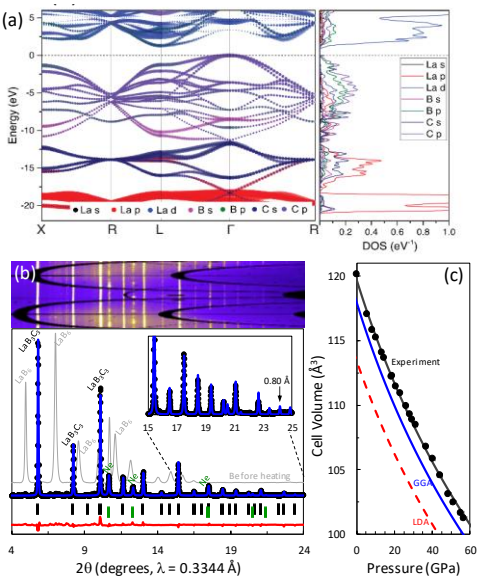

Figure 2. (a) Electronic band structure of LaB_3C_3 and density of states. (b) Synchrotron X-ray diffraction patterns before and after LaB_3C_3 synthesis with Rietveld refinement. (c) Experimental and calculated equation of state.

The additional electron in the case of LaB_3C_3 allows for formal charge balance (*i.e.*, $La^{3+}[B_3C_3]^{3-}$), which is manifested in the electronic band structure. The material possesses an indirect band gap of 1.29 eV in the Γ → L direction based on hybrid density functional theory calculations (HSE06). Additional charge transfer from guest to host is also observed in the B–C bond distances. At 0 GPa, the LaB_3C_3 lattice is slightly expanded compared with that of SrB_3C_3 where a = 4.934 Å *vs.* 4.868 Å, corresponding to B–C bond lengths of 1.74 Å and 1.72 Å, respectively. This expansion is somewhat surprising as the ionic radius of La^{3+} is expected to be smaller than that of Sr^{2+} (1.36 Å vs. 1.44 Å for 12-fold coordination),[4] and signals increased charge transfer. Indeed, Bader charge analysis reveals an average of 1.82 e^- transferred for the case of La whereas only 1.35 e^- are transferred for the case of Sr. Compared with the 2D covalent lattice found in LaB_2C_2 with B–C bond lengths ranging from 1.54–1.62 Å,[5] the significantly expanded bond length found in LaB_3C_3 reflects the change from three- to four-fold coordination of the network. The demonstration of LaB_3C_3 clathrate highlights the tunable nature of the electronic structures of carbon-based clathrates (*i.e.*, metal *vs.* semiconductor) and potential across a wide range of future applications.

As mentioned previously, SrB_3C_3 is a hole conductor and shows an appreciable density of states at the Fermi energy (Figure 3). Combined with sufficient electron–phonon coupling as expected for sp^3 clathrates,[6] SrB_3C_3 could exhibit superconductivity at high temperature. We therefore performed electron–phonon coupling calculations to investigate potential for superconductivity. The superconducting transition temperature, T_c, was estimated from the Allen-Dynes modified McMillan equation.[7] At ambient pressure, the calculated

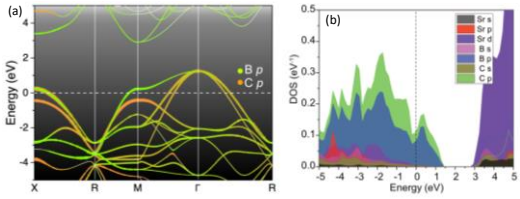

Figure 3. (a) Electronic band structure of SrB_3C_3 and (b) density of states.

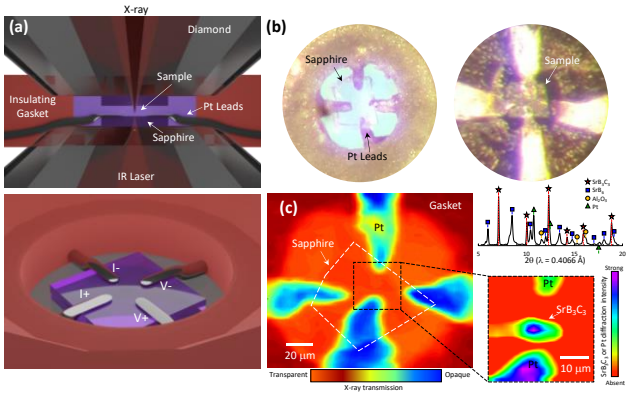

Figure 4. (a) Experimental geometry to measure electrical transport (b) Example micrographs of sample chamber. (c) Radiography and X-ray diffraction map of sample showing ~60% conversion to SrB_3C_3 between the Pt contacts.

T_c range is 27–43 K for Coulomb pseudopotential values of μ^* = 0.17–0.10, respectively. To test these predictions, we developed a novel technique for *in situ* electrical transport measurements of samples that require extreme synthesis conditions (*e.g.*, 50 GPa and >3000 K).[8] The refractory nature of B and C necessitates prolonged laser heating at very high temperatures, which is not needed in high-pressure hydride experiments that only require gentle pulsed heating at moderate temperatures <1000 K (e.g. LaH_{10}),[9] or even simple exposure to visible laser irradiation.[10] Our solution was to utilize two single crystals of sapphire (~5–10 μm thick) that rest on top of both diamond anvils and provide thermal insulation during heating from a tightly focused infrared laser. In this case, electrical leads are placed on top of one of the sapphire crystals, and we were able to synthesize SrB_3C_3 at 50 GPa and >3000 K in between the electrical probes without damaging the contacts.

After *in situ* high-pressure synthesis, the SrB_3C_3 samples were placed into an open-flow cryostat for electrical transport measurements at low temperature. Upon cooling below ~20 K, a sharp drop in the electrical resistance was observed with no detectable hysteresis upon heating, consistent with superconductivity. In addition, when the pressure was decreased, the observed resistance drop shifted to higher temperature, consistent with the calculated trend in superconductivity when μ^*=0.15 (Figure 5). The results suggest that SrB_3C_3 may be a moderately high-temperature superconductor comparable to other covalent metals like MgB_2.

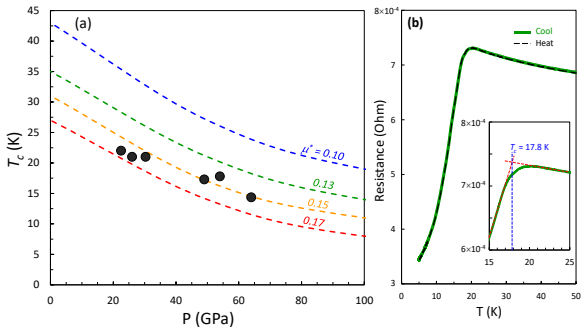

Figure 5. (a) Experimental T_c values (points) follow calculated T_c trend with μ^*=0.15 (b) Example resistance drop upon cooling/heating at 54 GPa.

Future Plans

Future research will involve continued efforts on SrB_3C_3 superconductivity, including lower-pressure and magnetic measurements. We will continue to explore the range of possible compositions in the Type-VII structure (including binary guests), optimize superconducting transitions, and establish the pressure stability range. Additional efforts will focus on new clathrate structure types with a broad range of lattice and guest substituents, and the characterization of physical properties.

References

1. Zhu, L.; Borstad, G.M.; Liu, H.; Guńka, P.A.; Guerette, M.; Dolyniuk, J.-A.; Meng, Y.; Greenberg, E.; Prakapenka, V.B.; Chaloux, B.L.; Epshteyn, A.; Cohen, R.E.; Strobel, T.A., *Sci. Adv*. 6, eaay8361 (**2020**).

2. Zhu, L.; Strobel, T.A.; Cohen, R.E., *Phys. Rev. Lett.* 125, 127601 (**2020**).

3. Strobel, T.A.; Zhu, L.; Guńka, P.A.; Borstad, G.M.; Guerette, M., *Angew. Chem. Int. Ed.* 133, 2913-2917 (**2021**).

4. Shannon, R., *Acta. Cryst. A*, 32, 751-767 (**1976**).

5. Ohoyama, K.; Kaneko, K.; Indoh, K.; Yamauchi, H.; Tobo, A.; Onodera, H.; Yamaguchi, Y., *J. Phys. Soc. Jap.* 70, 3291-3295 (**2001**).

6. Blase, X.; Bustarret, E.; Chapelier, C.; Klein, T.; Marcenat, C., *Nature Mater*. 8, 375 (**2009**).

7. P. B. Allen and R. C. Dynes, Transition Temperature of Strong-Coupled Superconductors Reanalyzed, Phys Rev B 12, 905 (1975).

8. Zhu, L.; Liu, H.; Somayazulu, M.; Meng, Y.; Guńka, P.A.; Shiell, T.B.; Kenny-Benson, C.; Hoffmann, R.; Cohen, R.E.; Strobel, T.A., *Submitted*, (**2021**).

9. Somayazulu, M.; Ahart, M.; Mishra, A.K.; Geballe, Z.M.; Baldini, M.; Meng, Y.; Struzhkin, V.V.; Hemley, R.J., *Phys. Rev. Lett.* 122, 027001 (**2019**).

10. Snider, E.; Dasenbrock-Gammon, N.; McBride, R.; Debessai, M.; Vindana, H.; Vencatasamy, K.; Lawler, K.V.; Salamat, A.; Dias, R.P., *Nature* 586, 373 (**2020**).

Publications

[1] Strobel, T.A.; Zhu, L.; Guńka, P.A.; Borstad, G.M.; Guerette, M., "A Lanthanum-Filled Carbon–Boron Clathrate," *Angew. Chem. Int. Ed.*, 133, 2913-2917 (**2021**). DOI: 10.1002/ange.202012821

[2] Zhu, L.; Liu, H.; Somayazulu, M.; Meng, Y.; Guńka, P.A.; Shiell, T.B.; Kenny-Benson, C.; Hoffmann, R.; Cohen, R.E.; Strobel, T.A., "Evidence for Superconductivity in SrB_3C_3 Clathrate," *Submitted*, (**2021**).

Understanding the Interplay between Nanostructured Electrode and Aqueous Electrolyte for Na-ion Energy Storage

Xiaowei Teng, Department of Chemical Engineering, University of New Hampshire

1 Program Scope: Rechargeable lithium-ion batteries (LIBs) based on intercalation chemistry in non-aqueous electrolytes have been widely used, while high cost and safety concerns make them less appealing for large-scale stationary storage. In a grid-connected stationary battery storage system, the cost, safety, and cycle life become more imperative than mere energy density. The usage of flammable organic electrolytes and the thermal runaway hazard of reactive electrode materials are mainly attributed to the high safety risk of LIBs. In addition, the lithium reserve depletion also raises concerns over its potential price increase. Rechargeable aqueous EES shows significant advantages over non-aqueous counterparts for the following reasons: water-based electrolytes are non-flammable and environmentally benign; besides their excellent safety, aqueous EES has low production cost by avoiding rigorous manufacturing conditions required in non-aqueous battery manufacturing. Despite the significant advantages over the safety, cost, and environmental friendliness, current aqueous EES still cannot rival the energy performance of non-aqueous LIBs, and the underlying reason is its narrow voltage window and limited storage capacity. A primary theme of PI's research is to understand the charge storage mechanisms and optimize the interaction between electrodes and electrolytes to improve the energy performance and cycle life of aqueous EES systems. The specific research goals include:

(i) enhancement of aqueous storage capacity by designing electrode materials with a sizeable interstitial framework capable of hosting a large number of ions, especially the layered transition metal oxide (TMO) materials held together by *van der Waals* forces; and by introducing site defects (e.g., anion/cation deficiency, lattice mismatch) to electrode materials. Therefore, such a modified local environment for the transition metal ions provided a lower percolation threshold for ionic transport so that alkali ions could diffuse quickly without directly contacting the transition metal framework on the atomic scale.

(ii) Expansion of aqueous storage voltage window beyond 1.23 V. Expansion of aqueous voltage window has been reported previously using a "water-in-salt" electrolyte, where alleviated water activity minimizes the contact between Li metal and water and suppresses parasitic HER, and thus allow a 3.0 V voltage window for aqueous Li-ion storage.[1] However, a high concentration (> 20 M) Li salts is required. Alternatively, the PI has been studying the formation of the hydroxylated interphase on the surface of mixed-valence metal oxides during the electrochemical cycling, which inhibits the HER/OER and thus enables a kinetically stable potential window of 2.5 V for aqueous Na-ion storage in a half-cell.

2 Recent Progress: With the research goals mentioned above, the PI has developed several electrode materials, including Mn-based TMOs with hydroxylated interphase to offer a stable voltage window of 2.5 V,[2-4] closed-packed NiO, and Mn_3O_4 nanoparticles for improved aqueous storage capacity,[5,6] crystalline MnO_2 and V_2O_5 layered structures for pseudocapacitive Na- and K-ion storage,[7,8] Co- and Ni-doped crystalline MnO_2 with defective sites;[9,10] highly disordered Na-MnO_2, V_2O_5, and NaV_3O_8 for enhanced storage capacity[3,11-14]. The above research outcomes have been supported under the previous DOE award (Early Career, 2013- 2018)[2,4,5,8,11] and current DOE grant (2018-2021)[3,9,10,12-14]. The following is the brief description of recent progress.

2.1 Controlling Electrode Local Structure for Improved Aqueous Na-ion Storage

Designing electrode materials with a large interstitial framework, including nanoporous and layered structures, is essential to enhance storage capacity. Introducing 2D and 3D porous

architectures or increasing interlayer spacing certainly improves the transport properties of charge carriers; however, it may compromise the host electrode's electrical conductivity. Consequently, conductive polymers, carbon nanotubes, and graphenes are often used as conductive additives and decrease the devices' volumetric performance due to their low densities. Alternatively, doping ions such as Ni and Co into these open-framework electrodes could increase the electrical conductivity and electrochemical performance. Furthermore, these guest ions could serve as redox-active sites for charge transfer reaction and introduce the site disorder to the electrode materials to improve the storage capacity. Under current DOE support, the PI has studied the effects of cobalt doping on the layered MnO_2 birnessite. Instead of homogeneous (Co)MnO_2 layered structure, bi-phase products formed using a co-precipitation wet-chemistry method, consisting of layered MnO_2 birnessite and $Co_xMn_{3-x}O_4$ spinel [$(Co_{0.83}Mn_{0.13}Va_{0.04})_{tetra}(Co_{0.38}Mn_{1.62})_{octa}O_{3.72}$; tetra: tetrahedral sites; octa: octahedral sites; Va: vacant site]. The electrokinetics analysis showed that the MnO_2 improved the capacitive Na-ion storage process, while $Co_xMn_{3-x}O_4$ with a predominant cation disorder due to cobalt insertion improved storage capacity.[10] The X-ray and neutron total scattering and pair distribution function (PDF) analysis showed that [CoO_4] tetrahedral sites were more disordered than [CoO_6] and [MnO_6] octahedral sites, evidenced by 4% of the structural vacancies in $Co_xMn_{3-x}O_4$ spinel phase.

Remarkably, a similar wet-chemistry approach was used to synthesize (Ni)MnO_2 layered birnessite, where Ni and Mn are homogenously mixed, under current DOE support.[9] It suggested that [NiO_6] octahedra might be stable and miscible with [MnO_6] during the room-temperature co-precipitation synthetic process. Under the same synthetic conditions, Co-O polyhedra could exist in the forms of [CoO_6] octahedra and [CoO_4] tetrahedra. This might explain why Co-Mn-O biphase (layered MnO_2 birnessite and $Co_xMn_{3-x}O_4$ spinel) formed, while single-phase (Ni)MnO_2 birnessite formed under the same synthetic condition. The resulting (Ni)MnO_2 birnessite demonstrated improved rate and cycling performance compared with MnO_2, exhibiting a discharge electrode capacity of 63 mAh/g at a current density of 0.2 A/g after 2000 galvanostatic charge and discharge cycles in full-cells. The PI used neutron total scattering and PDF analysis to confirm the framework doping of Ni-ion in the [MnO_6] intralayer region and discover that [NiO_6] had a highly disordered local structure while [MnO_6] appeared to be ordered. Due to the similar electron densities of Mn and Ni, there is little difference in X-ray scattering patterns between Ni and Mn. However, neutron coherent scattering lengths of Ni and Mn have

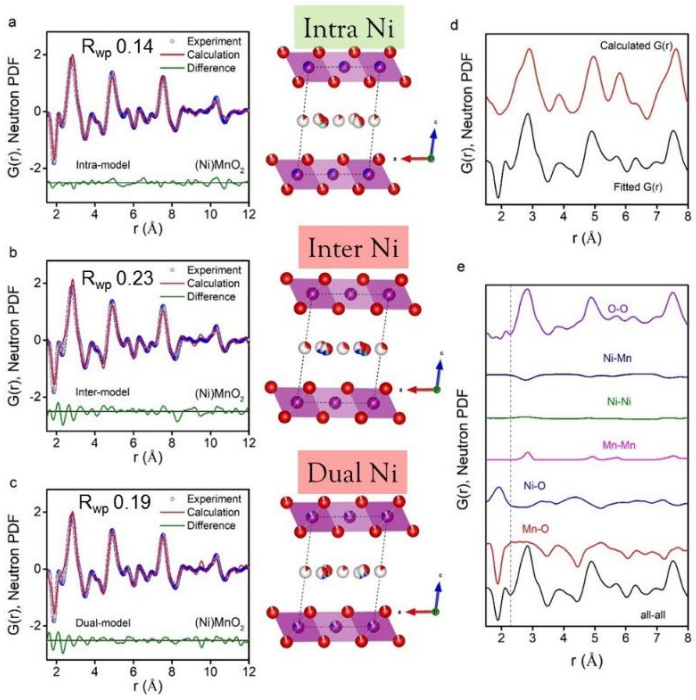

Figure 1. Neutron PDF fitting using (a) Intra-model; (b) Inter-model and (c) Dual-model. (d) the simulated PDF based on the Intra-model of $NiMnO_2$ (Purple: Mn; Blue: Ni). (e) the individual contribution from the atomic pairs to overall PDF.

distinct values and opposite signs (Ni = 10.3×10^{-15} meters; Mn = -3.73×10^{-15} meters). **Figure 1 a-c** showed the neutron PDF analyses based on three possible structure models, including intra-model (Ni-ions substituted Mn-ions in the [MnO_6] layers), inter-model (Ni-ions resided in the interlayer region), and dual-model (Ni-ions resided both intralayer and interlayer regions). The analysis results from these three models and corresponding goodness of the fittings (R_{wp}) showed that intra-model appeared the most likely structure of (Ni)MnO_2 with a best R_{wp} value of 0.137, significantly lower than those of inter-model and dual-model. Moreover, neutron PDF analysis based on the intra-model revealed that the Ni species within the framework of [(Ni/Mn)O_6] had a much higher was much isotropic atomic displacement parameter (ADP) than that of Mn,[9] indicating a much disordered [NiO_6] octahedral compared with [MnO_6]. **Figure 1d** shows the simulated pair distribution function based on the intra-model, and **Figure 1e** shows the individual atomic pair contributions to the overall atomic pair features. The results suggested that Ni-related atomic pairs possessed broader and less intensive peaks than Mn-related pairs, confirming the disordered nature of Ni sites. Electrokinetics analysis showed that Ni and Mn components were redox-active, and the disordered [NiO_6] octahedra favored *pseudocapacitive* storage mechanism and enhanced capacity and rate performance of (Ni)MnO_2 materials for aqueous Na-ion storage.

2.2 Hydroxylated interphase to expand aqueous potential window

Under previous DOE support, the PI discovered that hydroxylated interphase, formed on the surface of Mn_5O_8 ($Mn^{2+}{}_2Mn^{4+}{}_3O_8$) materials during the electrochemical cycling, inhibited the HER and OER, and enabled a stable voltage window of 2.5 V for aqueous Na-ion storage.[2,4] The PI has also discovered similar hydroxylated interphase from a highly disordered $Na_{0.27}MnO_2$ layered birnessite due to the interaction between water and Mn^{3+}.[3] This finding has been made under current DOE support. Notably, the Na-rich $Na_{0.27}MnO_2$ birnessite with a high concentration of Mn^{3+} was synthesized by a solid-state reaction between Mn_5O_8 and NaOH at high temperatures, where Na-ion diffusion into Mn_5O_8 lattice eventually converted highly crystalline layered Mn_5O_8 structure into a highly disordered birnessite-type MnO_2 layered structure, a process confirmed by *ex-situ* neutron scattering measurements. The disordered structure of $Na_{0.27}MnO_2$ was confirmed by neutron PDF analysis, as shown in **Figure 2a**. Unlike ordered Na-MnO_2 birnessite and commercial β-MnO_2, disordered $Na_{0.27}MnO_2$ showed high Tafel slopes of HER and OER, suggesting sluggish electrokinetics for gas evolution reactions (**Figure 2c**). High resistance towards HER and OER enables $Na_{0.27}MnO_2$ operated under a kinetically stable potential window of 2.5 V for aqueous Na-ion storage (**Figure 2b**).

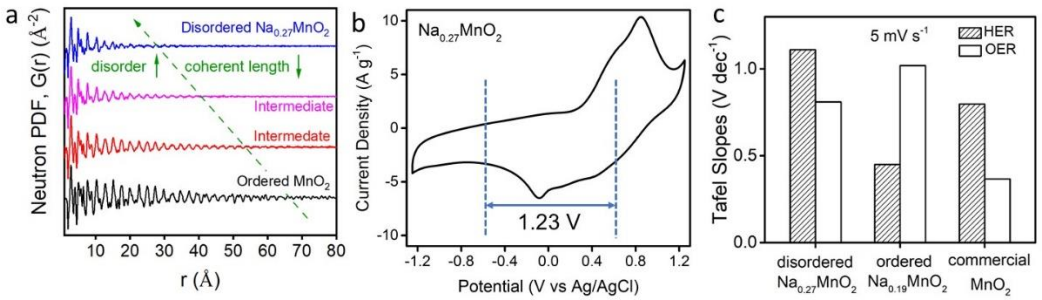

Figure 2. (a) Neutron pair distribution function (PDF) analysis of $Na_{0.27}MnO_2$, showing a disordered nature with a short coherent length (distance beyond which atomic pair interaction disappears); (b) voltammetry of $Na_{0.27}MnO_2$ in 0.1 M Na_2SO_4, showing a 2.5V-voltage window (voltage window of water at pH =7 was labeled). (c) Tafel slopes of disordered $Na_{0.27}MnO_2$, ordered Na-MnO_2, and commercial MnO_2 materials.[3]

3. Future Plans: A renewal proposal titled "*Understand and Optimize the Interplay between Electrode Materials and Electrolyte for Aqueous Energy Storage*" has been submitted to DOE-BES in Jan 2021 to understand the interplay between nanostructured metal oxides and aqueous electrolyte and to discover how such interplay contributes to the formation of the interphase and how such interphases work for aqueous energy storage.

4. Reference:

1 L. Suo *et al.*, "Water-in-salt" electrolyte enables high-voltage aqueous lithium-ion chemistries. *Science* **350**, 938-943 (2015).

2. X. Shan *et al.*, Bivalence Mn5O8 with hydroxylated interphase for high-voltage aqueous sodium-ion storage. *Nat. Commun.* **7**, 13370 (2016).

3. X. Shan *et al.*, Structural water and disordered structure promote aqueous sodium-ion energy storage in sodium-birnessite. *Nat. Commun.* **10**, 4975 (2019).

4. X. Shan, F. Guo, W. Xu, X. Teng, High purity Mn5O8 nanoparticles with a high overpotential to gas evolution reactions for high voltage aqueous sodium-ion electrochemical storage. *Front. Energy* **11**, 383-400 (2017).

5. M. P. Yeager *et al.*, Pseudocapacitive Hausmannite Nanoparticles with (101) Facets: Synthesis, Characterization, and Charge-Transfer Mechanism. *ChemSusChem* **6**, 1983-1992 (2013).

6. M. P. Yeager, D. Su, N. S. Marinkovic, X. Teng, Pseudocapacitive NiO Fine Nanoparticles for Supercapacitor Reactions. *J. Electrochem. Soc.* **159**, A1598-A1603 (2012).

7. M. Yeager *et al.*, Highly Efficient K0.15MnO2 Birnessite Nanosheets for Stable Pseudocapacitive Cathodes. *J. Phys. Chem. C* **116**, 20173-20181 (2012).

8. M. P. Yeager *et al.*, Storage of Potassium Ions in Layered Vanadium Pentoxide Nanofiber Electrodes for Aqueous Pseudocapacitors. *ChemSusChem* **6**, 2231-2235 (2013).

9. X. Shan *et al.*, Framework Doping of Ni Enhances Pseudocapacitive Na-Ion Storage of (Ni)MnO2 Layered Birnessite. *Chem. Mat.* **31**, 8774-8786 (2019).

10. X. Shan *et al.*, Biphase Cobalt-Manganese Oxide with High Capacity and Rate Performance for Aqueous Sodium-Ion Electrochemical Energy Storage. *Advanced Functional Materials* **28**, 1703266 (2018).

11. D. S. Charles *et al.*, Structural water engaged disordered vanadium oxide nanosheets for high capacity aqueous potassium-ion storage. *Nat. Commun.* **8**, (2017).

12. X. Shan *et al.*, Potentiodynamics of the Zinc and Proton Storage in Disordered Sodium Vanadate for Aqueous Zn-Ion Batteries. *ACS Appl. Mater. Interfaces* **12**, 54627-54636 (2020).

13. D. S. Charles *et al.*, Dual-stage K+ ion intercalation in V2O5-conductive polymer composites. *Journal of Materials Chemistry A*, https://doi.org/10.1039/D1TA02003J, (2021).

14. S. Kim *et al.*, High-Capacity Aqueous Storage in Vanadate Cathodes Promoted by the Zn-Ion and Proton Intercalation and Conversion–Intercalation of Vanadyl Ions. *ACS Appl. Mater. Interfaces* **13**, 25993-26000 (2021).

5. List of Publications from Current DOE Supports (DE-SC0018922)

5.1 List of Papers Published in Which Current DOE Support is Acknowledged

1). **(Back Cover)** Charles, D. S.; Guo, F.; Shan, X.; Kim, S.; Lebens-Higgins, Z. W.; Xu, W.; Su, D.; Piper, L. F. J.; Teng, X., Dual-stage K+ ion intercalation in V2O5-conductive polymer composites. *Journal of Materials Chemistry A*, **2021**; https://doi.org/10.1039/D1TA02003J

2). **(Supplementary Cover)** Kim, S.; Shan, X.; Abeykoon, M.; Kwon, G.; Olds, D.; Teng, X., High-Capacity Aqueous Storage in Vanadate Cathodes Promoted by the Zn-Ion and Proton Intercalation and Conversion–Intercalation of Vanadyl Ions. *ACS Applied Materials and Interfaces*, **2021**, 13 (22), 25993-26000.

3). **(Front Cover)** Shan, X.; Kim, S.; Abeykoon, A. M. M.; Kwon, G.; Olds, D.; Teng, X., "Potentiodynamics of the Zinc and Proton Storage in Disordered Sodium Vanadate for Aqueous Zn-Ion Batteries". *ACS Applied Materials and Interfaces*, **2020**, 12, 54627.

4) **(Supplementary Cover)** Shan, X., Guo, F., Page, K., Neuefeind, J., Ravel, B., Milinda, A.M., Kwon, G., Olds, D., Su, D., Teng, X.W. "Framework Doping of Ni Enhances Pseudocapacitive Na-Ion Storage of (Ni)MnO_2 Layered Birnessite". *Chemistry of Materials*, **2019**, 31, 8774

5). Shan, X., Guo, F., Charles, D., Lebens-Higgins, Z., Razekb, S.A., Wu, J., Xu, W., Yang, W.L., Page, K., Neuefeind, J., Mikhail Feygensone, M., Piper, L.F.J., Teng, X.W. "Structural Water and Disordered Structure Promote Aqueous Sodium-Ion Energy Storage in Sodium-Birnessite". *Nature Communications*, **2019**, 10, 4975

5.2 List of Book Chapters Published in Which Current DOE Support is Acknowledged

1) Shan, X., Teng, X.W. *Transition Metal Oxides in Aqueous Electrolytes*, Chapter in "Transition Metal Oxides for Electrochemical Energy Storage", Wiley-VCH, Weinheim, ISBN 978-3-527-34493-2; Editors: Jagjit Nanda, Veronica Augustyn, **2021**

2) Teng, X.W. *Electrode and Electrolyte Interaction in Aqueous Electrochemical Energy Storage*, Chapter in "Inorganic Battery Materials", John Wiley & Sons, Editor: Hailiang Wang, Boniface P. T., **2019**

3) Guo, F., Teng, X.W. *Enhancing pseudocapacitive process for energy storage devices: analyzing the charge transport using electro-kinetic study and numerical modeling*, Chapter in "Supercapacitors - Theoretical and Practical Solutions", Intech, New York, Editor: Lionginas Liudvinavičius, **2018**

5.3 List of Patents in Which Current DOE Support is Acknowledged

1) Teng, X.W., *Manganese oxide compositions and their use as electrodes for aqueous phase energy storage devices*, US Patent: US10468684B2, November 2019.

2) Teng, X., *Preparation of: I. Intercalative Metal Oxide/Conductive Polymer Composites as Electrode Materials for Rechargeable Batteries; II. Sodium Rich Manganese Oxide Hydrate With Capacity For Aqueous Na-ion Electrochemical Energy Storag*e, November 2018, International Application Number: PCT/US2018/060677

2D-EFICACY: Control of Metastable 2D Carbide-Chalcogenide Heterolayers: Strain and Moiré Engineering

Dr. Mauricio Terrones[a,b,c,d,e] and Dr. Susan B. Sinnott[a,b,c,e]

[a]Department of Materials Science and Engineering; [b]Center for 2-Dimensional and Layered Materials; [c]Materials Research Institute; [d]Department of Physics; and [e]Department of Chemistry, The Pennsylvania State University, University Park, PA 16802

Program Scope

Two dimensional (2D) materials are atomically thin sheets of a layered material that display properties distinct from the bulk. Graphene, a single layer of sp^2 hybridized carbon atoms, is the prototypical example of this material class. Since the discovery of graphene, interest in 2D materials has exploded, resulting in the investigation of numerous 2D systems and heterostructures for applications such as catalysis[1,2] and quantum computing.[3,4] For specific applications, performance may be improved through careful tuning of defects, heterojunctions, and other forms of interfaces. Understanding, controlling, and optimizing interfaces is crucial in 2D materials, where additional degrees of freedom originate novel interfaces, and thus material properties and functionalities are even more tunable than in conventional materials.

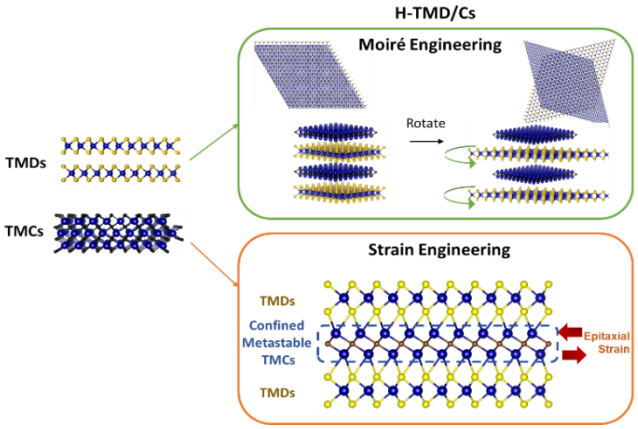

Figure 1 Schematic of strain and moiré engineering in transition metal carbide (TMC) / transition metal dichalcogenide (TMD) heterostructures.

Specifically, the weak van der Waals (vdW) coupling between layers eliminates the necessity for lattice matching between vertically stacked sheets. Moiré engineering in 2D materials is possible *via* the stacking of 2D layers with arbitrary twist angles and lattice parameters (Figure 1). As a result, new superlattices with size-tunable first Brillouin zones arise. Recent explorations of this approach include the discovery of superconductivity in twisted bilayer graphene[5] and moiré excitons in twisted transition metal dichalcogenide (TMD) heterobilayers.[6] Beyond these examples, there are many unexplored methods of engineering these interfaces, both covalent and vdW, and their interactions. In this context, strain engineering is also important, and therefore, by controlling the lattice mismatch and layer orientation, it is also possible to tune strain and moiré patterns, interlayer coupling, and the resulting physico-chemical properties. Our current research focuses on the emergent properties that arise from the integration of 2D TMDs with ultrathin transition metal carbides (TMCs), such as 2D-3D moiré lattices, enhanced superconductivity, and the stabilization of metastable TMC phases.

Recent Progress

We have realized the synthesis of enhanced superconducting MoS_2/γ'-MoC_x/γ-MoC heterostructures with a long-range moiré pattern as shown in Figure 2.[7] Our recent findings suggest that both kinetic and thermodynamic methods of engineering moiré and strained interfaces in MoC_x and MoS_2 are possible. With these results, we plan to synergistically determine the guiding principles that control the formation of layered heterostructures of stable or metastable thin TMCs and transition metal nitrides (TMNs) with TMD layers to combine interactions via moiré and strain engineering.

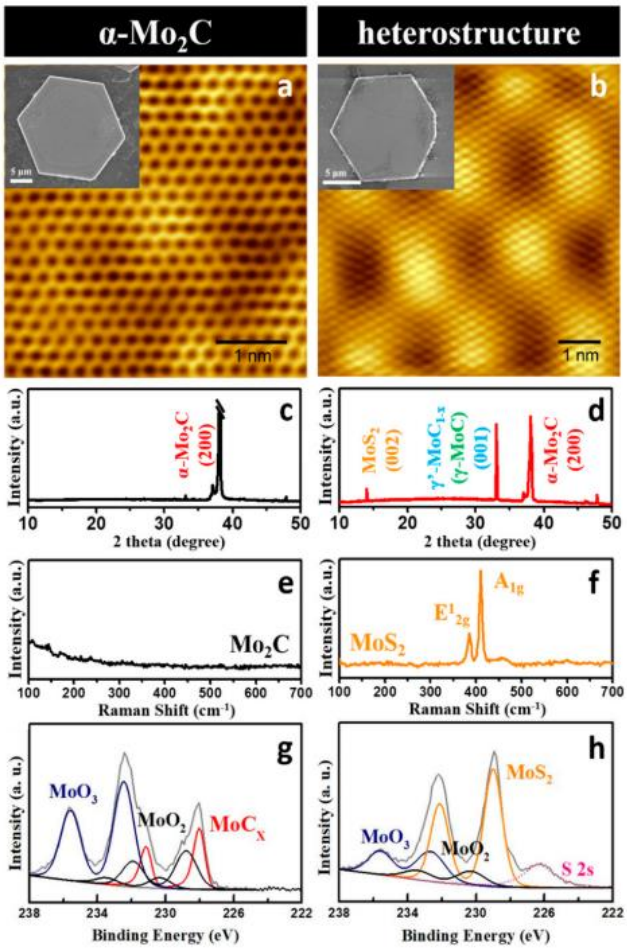

Figure 2: Characterization of α-Mo_2C and molybdenum carbide/disulfide heterostructures. (A) STM images of as-grown α-Mo_2C (insets depict SEM) and (B) a molybdenum carbide/disulfide heterostructures obtained after a 5-minute sulfurization of α-Mo_2C; (C, D) XRD patterns, (E, F) Raman spectra, and (G, H) representative XPS high resolution line scans of Mo 3d obtained from the structures depicted in (A) and (B), respectively.

The synthesized heterostructures of α-Mo_2C and γ'-MoC_x after 1-minute sulfurization exhibit superconductivity with a 70% increase in superconducting critical temperature (T_c) (6.8 K) compared to the pristine Mo_2C (4.0 K) as shown in Figure 3.[8] Typically the γ'-phase is metastable, but when confined, it stabilizes under strain induced by the sulfurization treatment. For a 5-minute sulfurization, a vertical heterostructure was formed between MoS_2 and mixed MoC_{1-x}/ MoC (γ'/γ-phase). In this case, they noted a 50% increase in T_c (6.0 K). Finally, for a 20-minute sulfurization, an MoS_2 and MoC (γ-phase) vertical heterostructure was grown. In this arrangement, superconductivity was not observed down to 1.8 K. To understand the 70% increase in T_c after 1-minute sulfurization, we performed first-principles density functional theory (DFT) calculations and propose that the large epitaxial strain and formation of a moiré lattice increases the interfacial density of states near the Fermi level. The introduction of a new γ'-MoC_x/ MoS_2 interface provides an additional handle to tune the properties of this material. This pioneering work now demonstrates the stabilization and the confinement of thin γ-MoC and metastable γ'-MoC_x, using strain and moiré engineering, and provides an emerging route to enhance the superconductivity *via* phase-transitions in thin carbide (or nitride) systems.

With the successful strain engineering in the molybdenum carbide/disulfide system, we have applied our novel approach to the tungsten carbide/disulfide system. By optimizing the experimental processing parameters for the chemical vapor deposition synthesis of α-Mo_2C, we have successfully synthesized ultrathin (<50 nm thick) single-crystal hexagonal WC flakes. Following transfer to SiO_2/Si, we sulfurized the WC and analyzed cross sections to investigate the effect of sulfur incorporation on WC. Preliminary characterization indicates that the WC-WS_2 conversion process occurs on the surface of WC as shown in Figure 4. Based on this observation, we hypothesize that the TMC-TMD conversion process depends on the type of structural defects present in the pristine TMC. The WC flakes are single-crystalline and show few defects, therefore, the TMC-TMD conversion process occurs from the edge as opposed to stacking faults observed in the α-Mo_2C flakes.

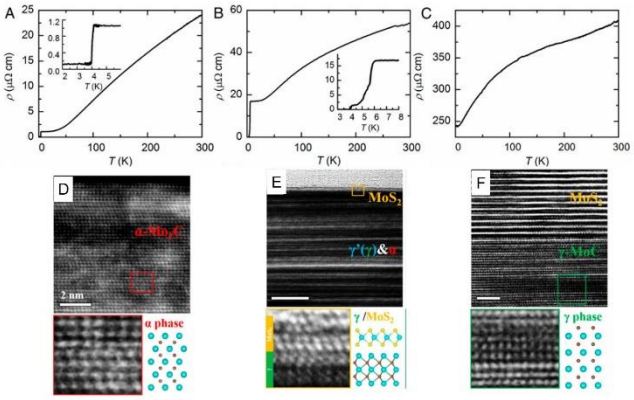

Figure 3: Superconductivity and phase evolution with increasing sulfurization time. Four-point probe resistivity versus temperature plots for (A) pristine α-Mo_2C, (B) 5 min sulfurization, and (C) 20 min sulfurization. (D) Cross-sectional HAADF-STEM images of pristine α-Mo_2C. Cross-sectional HRTEM of molybdenum carbide/disulfide vertical heterostructures formed after (E) 5 minutes and (F) 20 minutes sulfurization. Insets below (D-F) illustrate the structural phase transformation induced by sulfurization with corresponding simulated crystal structures.

Future Plans

Our immediate goal is to study the parameter space of the WC sulfurization by tuning the sulfurization temperature, time, and H_2S vapor pressure on the formation of WC/WS_2, metastable tungsten carbide phases, and emerging moiré patterns via cross-sectional S/TEM and STM. Using DFT, we also seek to understand the bonding nature of WC/WS_2 at the heterostructure interfaces. The investigation of changes to the superconducting nature of the WC/WS_2 system hinges upon the formation of metastable superconducting WC phases which we will identify in our structural characterization. In parallel, we also are tuning the synthesis of NbC and MoN using similar CVD process developed for α-Mo_2C and WC. Finally, we plan to develop a scalable TMC-TMD conversion process by cryo-milling NbC powder to induce defects that facilitate the chalcogenization of TMCs.

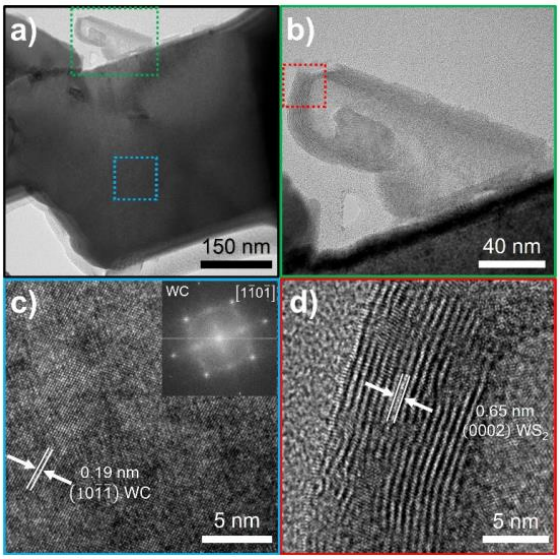

Figure 4: (a) Low and (b) medium magnification TEM images showing the structures grown on the WC surface. (c) HRTEM of single crystal WC, inset FFT corresponding to $[1\bar{1}0\bar{1}]$, and (d) multilayer WS_2.

References

1. Jaramillo, T. F.; Jørgensen, K. P.; Bonde, J.; Nielsen, J. H.; Horch, S.; Chorkendorff, I., Identification of Active Edge Sites for Electrochemical H2 Evolution from MoS2 Nanocatalysts. *Science* **2007,** *317* (5834), 100.
2. Lei, Y.; Pakhira, S.; Fujisawa, K.; Wang, X.; Iyiola, O. O.; Perea López, N.; Laura Elías, A.; Pulickal Rajukumar, L.; Zhou, C.; Kabius, B.; Alem, N.; Endo, M.; Lv, R.; Mendoza-Cortes, J. L.; Terrones, M., Low-temperature Synthesis of Heterostructures of Transition Metal Dichalcogenide Alloys (WxMo1–xS2) and Graphene with Superior Catalytic Performance for Hydrogen Evolution. *ACS Nano* **2017,** *11* (5), 5103-5112.
3. Palacios-Berraquero, C.; Barbone, M.; Kara, D. M.; Chen, X.; Goykhman, I.; Yoon, D.; Ott, A. K.; Beitner, J.; Watanabe, K.; Taniguchi, T.; Ferrari, A. C.; Atatüre, M., Atomically thin quantum light-emitting diodes. *Nature Communications* **2016,** *7* (1), 12978.
4. Moore, J. E., The birth of topological insulators. *Nature* **2010,** *464* (7286), 194-198.
5. Cao, Y.; Fatemi, V.; Fang, S.; Watanabe, K.; Taniguchi, T.; Kaxiras, E.; Jarillo-Herrero, P., Unconventional superconductivity in magic-angle graphene superlattices. *Nature* **2018,** *556* (7699), 43-50.
6. Tran, K.; Moody, G.; Wu, F.; Lu, X.; Choi, J.; Kim, K.; Rai, A.; Sanchez, D. A.; Quan, J.; Singh, A.; Embley, J.; Zepeda, A.; Campbell, M.; Autry, T.; Taniguchi, T.; Watanabe, K.; Lu, N.; Banerjee, S. K.; Silverman, K. L.; Kim, S.; Tutuc, E.; Yang, L.; MacDonald, A. H.; Li, X., Evidence for moiré excitons in van der Waals heterostructures. *Nature* **2019,** *567* (7746), 71-75.
7. Zhang, F.; Zheng, W.; Lu, Y.; Pabbi, L.; Fujisawa, K.; Elías, A. L.; Binion, A. R.; Granzier-Nakajima, T.; Zhang, T.; Lei, Y.; Lin, Z.; Hudson, E. W.; Sinnott, S. B.; Balicas, L.; Terrones, M., Superconductivity enhancement in phase-engineered molybdenum carbide/disulfide vertical heterostructures. *Proceedings of the National Academy of Sciences* **2020,** *117* (33), 19685.
8. Xu, C.; Wang, L.; Liu, Z.; Chen, L.; Guo, J.; Kang, N.; Ma, X.-L.; Cheng, H.-M.; Ren, W., Large-area high-quality 2D ultrathin Mo2C superconducting crystals. *Nature Materials* **2015,** *14* (11), 1135-1141.

Publications

1) Zhang, F.; Lu, Y.; Schulman, D.S.; Zhang, T.; Fujisawa, K.; Lin, Z.; Lei, Y.; Elías, A.L.; Das, S.; Sinnott, S.B.; Terrones, M. Carbon doping of WS2 monolayers: Bandgap reduction and p-type doping transport. Science Advances, 2019, 5, eaav5003.

2) Lu, Y.; Sinnott, S.B. Density functional theory study of epitaxially strained monolayer transition metal chalcogenides for piezoelectricity generation. ACS Applied Nano Materials, 2019, 10.1021/acsanm.9b02021.

3) Cochrane, K.A.; Lee, J.; Kastl, C.; Haber, J.B.; Zhang, T.; Kozhakhmetov, A.; Robinson, J.A.; Terrones, M.; Repp, J.; Neaton, J.B.; Weber-Bargioni, A.; Schuler, B. Vibronic response of a spin1/2 state from a carbon impurity in two-dimensional WS_2. arXiv, 2020, 2008.12196.

4) Fu Zhang, Wenkai Zheng, Yanfu Lu, Lavish Pabbi, Kazunori Fujisawa, Ana Laura Elías, Anna R. Binion, Tomotaroh Granzier-Nakajima, Tianyi Zhang, Yu Lei, Zhong Lin, Eric W. Hudson, Susan B. Sinnott, Luis Balicas, and Mauricio Terrones. Superconductivity enhancement in phase-engineered molybdenum carbide/disulfide vertical heterostructures. PNAS, 2020, pnas.2003422117.

Transforming Metal-Organic Frameworks into Polymer Hybrids and Biomimetic MetalloMOFzymes

Emmanuel Theodorakis (PI), University of California, San Diego

Program Scope

The three Specific Aims of this project are:

SA1. Development of polyMOFs. Polymers ligands, which are polymers containing metal coordinating units such as 1,4-benzenedicarboxylic acid monomers (H_2bdc), have been shown to self-assemble into a new class of polymer-MOF hybrids termed 'polyMOFs'. The scope and structural diversity of polyMOFs is in its infancy, and this aim we will seek to further explore polyMOF materials and some proof-of-concept studies for their use in molecular separations.

SA2. MOF Hybrids from Postsynthetic Polymerization. Postsynthetic polymerization (PSP) has been introduced as a strategy for combining MOF particles with polymeric binders. In this aim, a variety of PSP reactions will be explored to prepare new forms of porous MOF hybrids in the form of nylon fibers and epoxy composites.

SA3. Biomimetic 'MetalloMOFzyme' Catalysts. Biomimetic 'metalloMOFzymes' for reducing protons or carbon dioxide will be optimized upon integration into functionalized and conducting MOFs. We seek to develop highly active and robust catalysts for these important, energy relevant chemical reactions.

Recent Progress

Precise control over the dispersion and alignment of metal-organic framework (MOF) particles over a large length scale remains a distinct challenge to exploiting the various properties of these materials. In our most recent efforts, we have self-assembled MOF particles into large area monolayer membranes at the air-water interface through the grafting of polymer brushes to the particle surface. The polymer

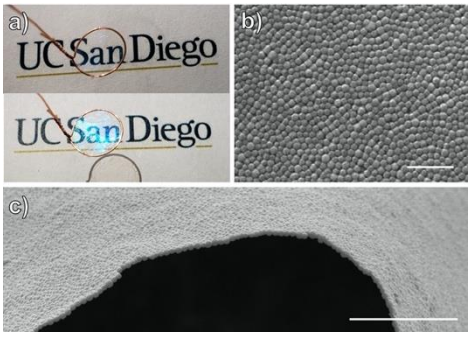

Figure: Free-standing monolayer of self-assembled UiO-66(Zr)-PMMA. (a) Images of the monolayer taken at different angles to show both clarity and iridescence. (b) SEM image of the monolayer surface showing tightly packed UiO-66(Zr)-PMMA particles. Scale bar is 2 μm. (c) SEM image of film from the side, illustrating the continuous monolayer. Scale bar

corona prevents uncontrolled particle aggregation and yields monolayers that can be transferred to other substrates and remain free-standing when suspended in air with an area of 38 mm^2. We are developing these polymer-coated MOF particles to enable simple methods that allow for control of the chemical and physical properties of the MOF materials and thin films. As shown in the list of publications from this effort, we have also made substantial progress on the development of polyMOFs, polymer-MOF hybrids made from metal-coordinating polymers, as well as other MOF-polymer hybrids (e.g., nylon-MOF composites). Overall, our work in this project has pushed the frontier in the synthesis, characterization, and understanding of MOF-polymer combined materials.

Future Plans

The future goals of this program are:

FG1. Development of polyMOFs. Polymer ligands, which are polymers containing metal coordinating units such as 1,4-benzenedicarboxylic acid monomers (H_2bdc), have been shown to self-assemble into a new class of polymer-MOF hybrids termed 'polyMOFs'. polyMOFs are unique materials that we discovered during the last program period. In this renewal, the scope and structural diversity of polyMOFs will be further explored to better understand and exploit polyMOF materials.

FG2. Self-assembly of MOF-polymer Nanoparticle Films. MOF-polymer hybrid materials have been obtained from core-shell 'corona' nanoparticles (NPs) that were developed in the prior program period. Using a MOF core and a polymer shell, self-assembled films will be prepared. This approach results in MOF-loaded films with densely packed NPs. Control over the functionalization and self-assembly of these new, ultrathin membranes will be pursued.

References

1. "Free-standing metal-organic framework (MOF) monolayers by self-assembly of polymer-grafted nanoparticles" *Chem. Sci*. **2020**, *11*, 8433-8437. DOI: 10.1039/D0SC03318A

2. "MOF-Polymer Hybrid Materials: From Simple Composites to Tailored Architectures" *Chem. Rev*. **2020**, *120*, 8267-8302. DOI: 10.1021/ACS.CHEMREV.9B00575

3. "Self-Assembly of Metal-Organic Framework (MOF) Nanoparticle Monolayers and Free-Standing Multilayers" *J. Am. Chem. Soc*. **2019**, *141*, 20000-20003. DOI: 10.1021/JACS.9B10966

4. “Defect-Free MOF-Based Mixed-Matrix Membranes Obtained by Corona Cross-Linking” *ACS Appl. Mater. Interfaces* **2019**, *11*, 13029-13037. DOI: 10.1021/ACSAMI.9B02539

Publications

1. “Structure of the Polymer Backbones in polyMOF Materials” *J. Am. Chem. Soc*. **2020**, *142*, 10863-10868. DOI: 10.1021/JACS.0C04546
2. “Free-standing metal-organic framework (MOF) monolayers by self-assembly of polymer-grafted nanoparticles” *Chem. Sci*. **2020**, *11*, 8433-8437. DOI: 10.1039/D0SC03318A
3. “Postsynthetic Modification: An Enabling Technology for the Advancement of Metal−Organic Frameworks” *ACS Cent. Sci*. **2020**, *6*, 1046-1057. DOI: 10.1021/ACSCENTSCI.0C00690
4. “MOF-Polymer Hybrid Materials: From Simple Composites to Tailored Architectures” *Chem. Rev*. **2020**, *120*, 8267-8302. DOI: 10.1021/ACS.CHEMREV.9B00575
5. “Self-Assembly of Metal-Organic Framework (MOF) Nanoparticle Monolayers and Free-Standing Multilayers” *J. Am. Chem. Soc*. **2019**, *141*, 20000-20003. DOI: 10.1021/JACS.9B10966
6. “Block co-polyMOFs: morphology control of polymer-MOF hybrid materials” *Chem. Sci*. **2019**, *10*, 1746-1753. DOI: 10.1039/C8SC04250K
7. “Defect-Free MOF-Based Mixed-Matrix Membranes Obtained by Corona Cross-Linking” *ACS Appl. Mater. Interfaces* **2019**, *11*, 13029-13037. DOI: 10.1021/ACSAMI.9B02539
8. “Nylon–MOF Composites through Postsynthetic Polymerization” *Angew. Chem. Int. Ed*. **2019**, *58*, 2336-2340. DOI: 10.1002/ANIE.201812655
9. “Polyacids as Modulators for the Synthesis of UiO-66” *Aust. J. Chem.* **2019**, *72*, 848-851. DOI: 10.1071/CH19271
10. “Electroactive Co(III) salen metal complexes and the electrophoretic deposition of their porous organic polymers onto glassy carbon” *RSC Adv*. **2018**, *8*, 24128-24142. DOI: 10.1039/C8RA04385J

11. “Development of a UiO-Type Thin Film Electrocatalysis Platform with Redox-Active Linkers” *J. Am. Chem. Soc*. **2018**, *140*, 2985-2994. DOI: 10.1021/JACS.7B13077

12. "polyMOF Formation from Kinked Polymer Ligands via ortho-Substitution" *Isr. J. Chem.* **2018**, *58*, 1123-1126. DOI: 10.1002/IJCH.201800094

13. "Supramolecular Metallopolymers: From Linear Materials to Infinite Networks" *Angew. Chem. Int. Ed*. **2018**, *57*, 14992-15001. DOI: 10.1002/ANIE.201806912

14. "The Postsynthetic Renaissance in Porous Solids" *J. Am. Chem. Soc*. **2017**, *139*, 2855-2863. DOI: 10.1021/JACS.6B11259

15. “Photocatalytic metal–organic frameworks for organic transformations” *CrystEngComm* **2017**, *19*, 4126-4136. DOI: 10.1039/C7CE00398F

16. “Isoreticular expansion of polyMOFs achieves high surface area materials” *Chem. Commun.* **2017**, *53*, 10684-10687. DOI: 10.1039/C7CC04222A

17. “Hierarchical structure and porosity in UiO-66 polyMOFs” *Chem. Commun.* **2017**, *53*, 3058-3061. DOI: 10.1039/C6CC10225E

Controlling Solid-State Conjugated Materials with Aromatic Interactions of Side Chains

Samuel W. Thomas, Tufts University, Department of Chemistry
Mu-Ping Nieh, Department of Chemical and Biological Eng., University of Connecticut
Matthew Panzer, Tufts University, Department of Chemical and Biological Eng.
Steven Wheeler, Department of Chemistry, University of Georgia

Program Scope: Over the last several decades, continuous discovery of new materials, processing techniques, and device architectures has yielded orders-of-magnitude increases in efficiency and durability organic materials in solar energy, electroluminescence, and field-effect transistors. New π-conjugated molecules and polymers propel these advances, both in more mature technologies such as bulk heterojunction solar cells, as well as more recent advances, such as thermally-activated delayed fluorescence, (TADF) aggregation-induced emission, hole-transport materials for perovskite photovoltaics, and singlet fission photovoltaics.

A critical barrier to sustained progress is that materials chemists are unable to design ensembles of molecular or polymeric materials such as in thin films or crystals.[1] This challenge, due in large part to the shallow and complex potential energy landscapes that result from many weak non-covalent interactions, extends to all of molecular science, such as drug discovery and coordination polymers. As an alternative to relying on an unpredictable and generally isotropic collection of interactions, a supramolecular engineering approach involving discrete and directional non-covalent interactions such as hydrogen or chalcogen bonding can direct solid-state structural characteristics, such as intramolecular conformation along the conjugated backbone.

The prevailing design paradigm for conjugated materials divides structure into orthogonal functional units: the conjugated "main chain," which is responsible for the optoelectronic characteristics, and the non-conjugated pendant "side chains," typically long alkyl substituents, which provide solubility.[2] Our project extends conjugated materials beyond this paradigm and enables rational design of solid-state optoelectronic properties by integrating the directional and tunable cofacial "ArF-ArH" stacking of arenes and fluoroarenes into arylene-ethynylene-based materials. Specifically, stacking of fluorinated ArF rings within side chains with more electron rich ArH arenes within the main chains twists the backbones. Using a three-ring phenylene-ethynylene (PE) molecular "test bed" that comprises a central

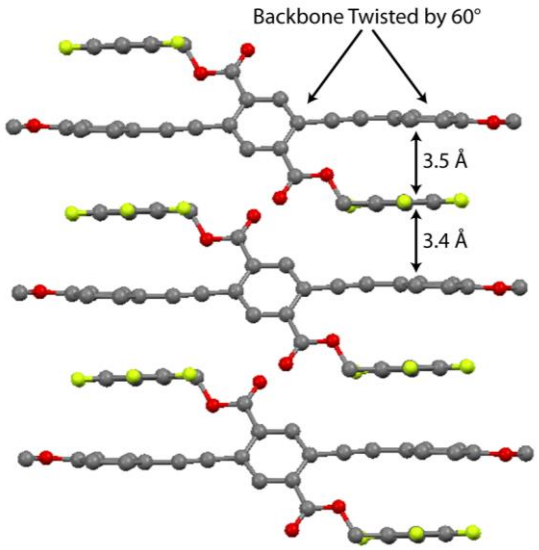

Figure 1. Crystal structure of a 3-ring phenylene-ethynylene (PE) with ArF-ArH interactions twisting PEs and preventing their aggregation.

bis(pentafluorobenzyl)terephthalate, our earlier work revealed the following:

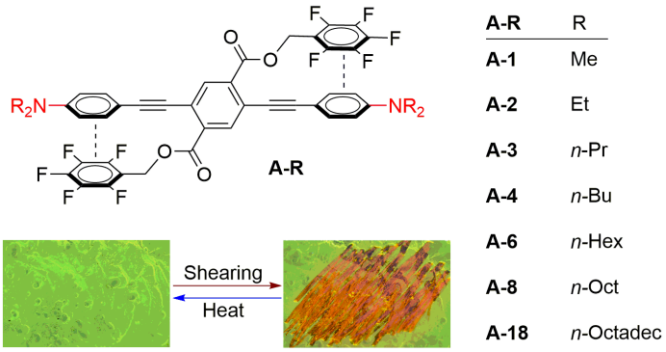

Figure 2: Example of MFC of three-ring phenylene-ethynylenes.

- Solids with these ArF-ArH interactions have solid-state optical spectra that resemble those in solution through a combination of main chain twisting and blocking of intermolecular aggregation.[3]
- Electrostatic complementarity of the ArH and ArF rings through substituent effects dictate whether ArF- ArH stacking and resultant twisting of PE backbone occurs.
- Such twisted structures are mechanofluorochromic (MFC)—mechanical shear force bathochromically shifts optical spectra reversibly due to planarization and aggregation.
- Alkyl chain lengths can dictate MFC: in one example (Fig. 2), longer alkyl chains cause recovery of hypsochromically shifted crystalline phases at lower temperatures after shearing, with those longer than butyl reverting at room temperature.

This presentation will summarize recent developments since the last BES Materials Chemistry PI meeting, which share the following themes: i) improving fundamental understanding of how chemical structure influences ArF-ArH cofacial stacking interactions and resulting solid-state optical properties, and ii) expansion of our designs into increasingly energy-relevant chemical structures and properties.

Recent Progress 1: Improved fundamental understanding of how strengths of aromatic interactions can influence solid-state functional properties using our 3-ring PE "test bed". In two papers (*Chem. Eur. J.* and *Chem. Mater.*) we uncovered examples of how seemingly insignificant changes in the structures of side chains not π-conjugated to the PE chromophore can influence solid-state packing and optical properties dramatically. Our first such discovery showed that switching the positions of H and F atoms in partially fluorinated side chains (going from 2,**4**,6-trifluorobenzyl to 2,**3**,6-trifluorobenzyl on the same π-conjugated PE chromophore red shifts solid state emission by 130 nm and also inverts the direction of MFC from *bathochromic* shifting to *hyposchromic* shifting. (Figure 3, left). X-ray crystal structures explain this difference: the 2,4,6-trifluoro derivative shows ArF-ArH interactions and twisted PE backbones, while the 2,3,6-derivative shows planar and aggregated PE backbones. Our *Chem. Mater.* full paper demonstrated consistency of these trends for related PEs with tetrafluorinated side chains (Figure 3, right), and that these trends also depend on electronic substituent effects to reinforce the importance of electrostatic complementarity in aromatic interactions.

In related work regarding how weak competing non-covalent interactions can forces can be leveraged for stimuli response behavior, Co-PIs Thomas and Nieh reported on a series of seven

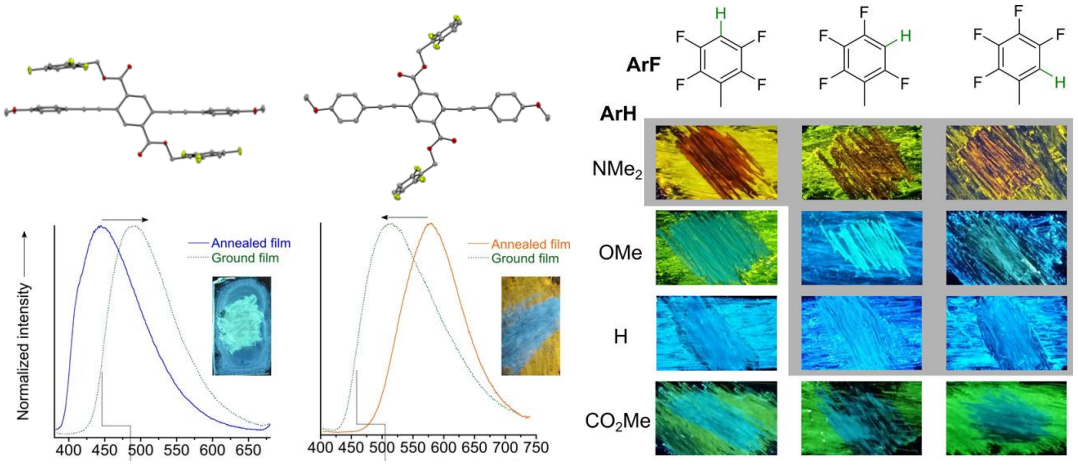

Figure 3: Dependence of solid-state emission and MFC characteristics of three-ring phenylene-ethynylenes on regiochemistry of side chains not formally conjugated to the main chain.

ester-substituted PE test-bed molecules with different alkyl chain lengths (C_1-C_{18}). These molecules, which possess comparatively weak stacking interactions due to the electron-withdrawing character of ester groups on the ArH rings, produce numerous polymorphs, including a crystal-to-crystal thermal transition of the propyl ester derivative (See Figure 4). This work, published in *J. Mater. Chem. C*, also involved acquisition of X-ray scattering data at Brookhaven National Laboratory to characterize the thermal transitions of polymorphs.

Recent Progress 2: Expanding beyond our "test bed". Beyond our three-ring test bed, we are expanding to more general structural approaches for installing intramolecular and intermolecular cofacial interactions and controlling functional properties. Our central hypothesis is that the *ortho*-pentafluorobenzyl benzoate unit is a generally applicable supramolecular synthon for introducing ArF-ArH cofacial interactions in conjugated materials and programming twisting along the chromophore backbone (Figure 4, top). Our first paper on this topic, published in *J. Mater. Chem. C*, demonstrated potential generality of this approach: six out of seven such molecules showed intramolecular ArF-ArH stacking and corresponding twisting along the conjugated backbone—one example containing a central biphenyl linkage is shown in Figure 4 (middle). Consistent with our prior work, substituent effects impact cofacial interactions, with electron-donating alkoxy groups on the ArH rings favoring a larger number of ArF-ArH interactions.

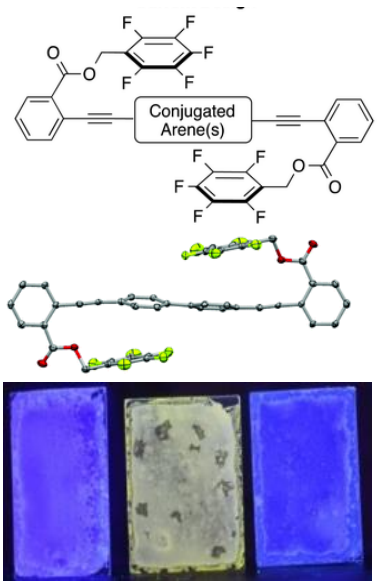

Figure 4: Crystal structure showing programmed twisting of biphenyl-linked phenylene ethynylene (middle) and solid phosphorescence of a Pt-acetylide (bottom, center) using stacking supramolecular synthon (top).

We have expanded the function of such designs to solid-state phosphors, which can be difficult to realize due to inter-chromophore aggregation and resulting quenching of long-lived excited states. Installation of the pentafluorobenzyl benzoate unit

into platinum acetylide phosphors makes phosphorescence the dominant radiative relaxation pathway as a neat solid. Analogous solids with identical conjugated backbones but different side chains showed weak fluorescence as the dominant radiative pathway (Figure 4, bottom). Crystal structures revealed ArF-ArH cofacial stacking prevents aggregation prominent in quenched analogs.

Future Directions 1: We are focusing on specific hypotheses regarding structural modifications that could have the greatest impact on modern organic optoelectronic materials. For example, two ongoing efforts involve using our test bed to test the following hypotheses: i) that the electronic characteristics of heteroaromatic ring systems such as thiophene, thienothiophene, and benzothiadiazole influence the strength of cofacial interactions and resultant solid-state assembly and optical properties, and ii) longer alkyl linkers to the ArF ring allows ArF-ArH stacking and control over optoelectronic properties. We anticipate upcoming efforts qill focus on conjugated structures with cutting-edge properties that rely on controlling intramolecular electronic coupling, such as TADF and open shell systems with relevance to quantum information science. In addition, we are working to understand an unexpected recent result that hydrostatic pressure reversibly shifts optical properties of our PE molecules in solution.

Future Directions 2: We are using modern density functional theory methods to elucidate conformational behavior, the nature of the non-covalent interactions occurring in the solid state, and the origin of observed shifts in UV-vis absorbance spectra. Current results indicate our systems exhibit six distinct classes of conformations (Figure 5), with the planar conformation 12-16 kcal/mol above the lowest-lying conformer, consistent with observed crystal structures. We will identify non-covalent contacts that preferentially stabilize the observed packing motifs and use that quantitative information to predict the favored assembly motifs and optical properties of new materials.

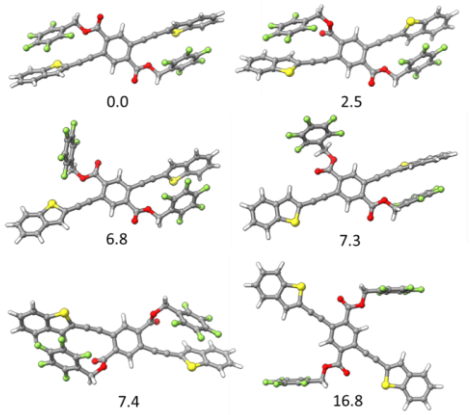

Figure 5: Calculated relative energies of conformers (kcal/mol) highlighting stabilization through ArF-ArH interactions.

1. Henson, Z. B.; Mullen, K.; Bazan, G. C., Design strategies for organic semiconductors beyond the molecular formula. *Nat. Chem.* **2012,** *4*, 699-704.
2. Mei, J. G.; Bao, Z. N. Side Chain Engineering in Solution-Processable Conjugated Polymers. *Chem. Mater.* **2014,** *26*, 604-615.
3. Pawle, R. H.; Haas, T. E.; Muller, P.; Thomas, S. W. Twisting and Piezochromism of Phenylene-Ethynylenes with Aromatic Interactions between Side Chains and Main Chains. *Chem. Sci.* **2014,** *5*, 4184-4188.
4. Sharber, S.; Baral, R. N.; Frausto, F.; Haas, T. E.; Müller, P.; Thomas, S. W. Substituent Effects that Control Conjugated Oligomer Conformation through Non-Covalent Interactions. *J. Am. Chem. Soc.* **2017**, *139*, 5164-5174.

Publications Supported by Materials Chemistry Program in Last Three Years (Since last PI Meeting)

1. Sharber, S. A.; Thomas, S. W. “Small Changes With Big Consequences: Swapping Two Atoms In Side Chains Changes Phenylene Ethynylene Packing And Fluorescence” *Chem. Eur. J.* **2018**, *24*, 16987-16991. DOI: https://doi.org/10.1002/chem.201804648

2. Mullin, W. J.; Pawle, R. H.; Sharber, S. A.; Müller, P.; Thomas, S. W. “Programmed Twisting of Phenylene-Ethynylene Linkages from Aromatic Stacking Interactions” *J. Mater Chem. C* **2019,** *7*, 1198-1207. DOI: https://doi.org/10.1039/C8TC05612A

3. Sharber, S. A. Mann, A.; Shih, K. C.; Nieh, M. P.; Mullin, W. J.; Thomas, S. W. “Directed Polymorphism and Mechanofluorochromism of Conjugated Materials through Weak Non-Covalent Control.” *J. Mater. Chem. C* **2019**, *7*, 8316–8324. DOI: https://doi.org/10.1039/C9TC01301F

4. Mullin, W. J.; Qin, H.; Mani, T.; Müller, P.; Panzer, M. J.; Thomas, S. W. “Turning On Solid-State Phosphorescence of Platinum Acetylides With Aromatic Stacking” *Chem. Commun.* **2020,** *56*, 6854–6857. DOI: https://doi.org/10.1039/D0CC02119A

5. Sharber, S. A.; Thomas, S. W. “Side Chain Regioisomers That Dictate Optical Properties and Mechanofluorochromism Through Crystal Packing” *Chem Mater* **2020,** *32*, 5785–5801. DOI: https://doi.org/10.1021/acs.chemmater.0c01676

6. Mullin, W. J.; Sharber, S. A.; Thomas, S. W. "Optimizing the Self-Assembly of Conjugated Polymers and Small Molecules Through Structurally Programmed Non-Covalent Control” *J. Polym. Sci.* **2021**, *In Press. (Invited Review Article).*

7. Sharber, S. A.; Mullin, W. J.; Thomas S. W. "Bridging the Void: Halogen Bonding and Aromatic Interactions to Program Luminescence and Electronic Properties of π-Conjugated Materials in the Solid State” *Submitted to Chem. Mater.*

8. Mullin, W. J.; Wheeler, S. E.; Thomas S.W. “Structure-dependent stacking of heteroarenes and perfluoroarenes controls conformation and aggregation of conjugated molecular solids” *Manuscript in Preparation*

Understanding and Tailoring Diffusion and Co-Adsorption Inside the Confined Pores of Metal-Organic Frameworks

Timo Thonhauser, Department of Physics, Wake Forest University
Jing Li, Department of Chemistry and Chemical Biology, Rutgers University
Kui Tan, Department of Materials Science, University of Texas at Dallas

Program Scope

The aim of this project is to develop a concise understanding of the mechanisms that control the behavior of guest molecules in pure form and mixtures inside metal organic frameworks (MOFs)—leading to design/synthesis guidelines for MOFs with desired functionality/performance—based on a closing-the-loop approach that integrates *ab initio* modeling, *in situ* spectroscopy, and synthesis. We address research questions and barriers to progress such as: How do guest molecules in gas mixtures diffuse deep into or out of the MOF and how can we unambiguously characterize that? What are the factors controlling the co-adsorption of gas mixtures in the confined pores of MOF? What role do guest molecules (pure or in mixture) play in the gate opening/closing of flexible MOFs? Our objectives are (1) to gain understanding of the gas adsorption kinetics in MOFs by uncovering diffusion mechanisms of single gases and mixtures; (2) to deepen the understanding of the equilibrium aspects of gas adsorption in MOFs by studying guest-host interactions during co-adsorption and identifying principles that govern the behavior of gas mixtures in nano-confined environments; and (3) to elucidate dynamic behaviors of flexible MOFs by studying gas adsorption and molecular trapping mechanisms of single gases and mixtures. Our closing-the-loop approach will lead to new insights into the adsorption behavior of MOFs in real-world situations where gases are mixed and will accelerate the development of MOFs with improved and tailored properties.

Recent Progress

a) Thermally Activated Adsorption in Metal–Organic Frameworks with a Temperature-Tunable Diffusion Barrier Layer [1]: Modification of the external surfaces of metal–organic frameworks offers a new level of control over their adsorption behavior. It was shown in our previous work [Nat. Comm. 2016, 7, 13871] that capping of MOFs with ethylenediamine (EDA) can effectively retain small gaseous molecules at room temperature. Our recent work reported a temperature-induced variation in the capping-layer gate-opening mechanism through a combination of *in situ* infrared characterization and *ab initio* simulations of the capping layer (see Fig. 1). An atypical acceleration and increase

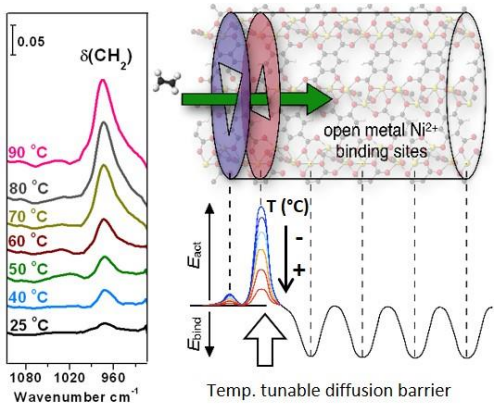

Fig. 1. Temperature-dependent IR spectra of adsorbed C_2H_4 band (left) and EDA triangular entrance to the MOF channel with a schematic energy profile (right).

in the loading of weakly adsorbed molecules upon raising the temperature above room temperature is observed. These findings show the discovery of novel temperature-dependent kinetics that goes beyond standard kinetics and suggest a new avenue for tailoring selective adsorption by thermally tuning the surface barrier. This project addresses research questions in Objective 1.

b) Porous Ti-MOF-74 Framework as a Strong-Binding Nitric Oxide Scavenger [2]: Combining novel synthesis, *in situ* IR spectroscopy, and *ab initio* modeling we show that the titanium-based porous framework Ti-MOF-74 has potential as an environmental nitric oxide (NO) scavenger, exhibiting an extraordinarily strong binding affinity and selectivity over other co-existing flue-gas components that compete with NO adsorption. The robustness upon exposure to water vapor and high flue-gas stack temperatures suggests that this material can perform well in an industrial environment. In-depth analysis of the Ti−NO bond indicates that the NO forms a strong covalent bond with the Ti. The process of this NO-bond formation involves a reaction with the OH^- capping groups of the Ti to form NO_x groups, after which the excess NO binds to the open Ti metal sites. Ti-MOF-74 thus becomes the first known porous framework that binds NO significantly stronger than water, providing novel avenues for environmental and physiological scavenging applications. This project addresses research questions in Objective 2.

c) Defect Termination in the UiO-66 Family of Metal-Organic Frameworks: The Role of Water and Modulator [3]: The defect concentration in the prototypical metal-organic framework UiO-66 can be well controlled during synthesis, leading to precisely tunable physicochemical properties for this structure. However, there has been a long-standing debate regarding the nature of the compensating species present at the defective sites. Here, we present unambiguous spectroscopic evidence that the missing-linker defect sites in an ambient environment are compensated with both carboxylate and co-adsorbed water (bound through intermolecular hydrogen bonding, see Fig. 2), which is further supported by *ab initio* calculations. In contrast to the prevailing assumption that the monocarboxylate groups (COO^-) of the modulators form bidentate bonding with two Zr^{4+} sites, COO^- is found to coordinate to an open Zr^{4+} site in an unidentate mode. The neighboring Zr^{4+} site is terminated and coordinated by a co-adsorbed H_2O, which helps stabilizing the COO^- group. This finding not only provides a new understanding of defect termination in UiO-66, but also sheds light on the origin of its enhanced physicochemical properties such as adsorption selectivity and catalytic activity. This project addresses research questions in Objective 2.

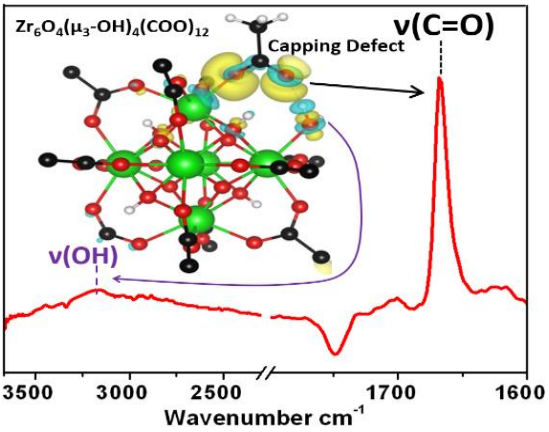

Fig. 2. Synergistic binding of acetate and co-adsorbed water on missing-linker defect site of UiO-66, as verified by their signature bands.

d) Probing and Understanding Unique Adsorption Behavior of Noble Gases in a Flexible MOF [4]: Flexible MOFs hold great promise as smart materials for specific applications such as gas capture and separation. These materials undergo interesting structural changes in response to guest molecules, which is often associated with unique adsorption behavior not possible for rigid MOFs. Understanding the dynamic behavior of flexible MOFs is crucial yet challenging as it involves weak host-guest interactions and subtle structural transformation not only at the atomic/molecular level but also in a non-steady state. We carry out an in-depth study on the adsorbate- and temperature-dependent adsorption in a flexible MOF by crystallizing atomic noble gases into its pores. $Mn(ina)_2$ (see Fig. 3) shows interesting temperature-dependent response toward noble gases. Its non-monotonic, temperature-dependent adsorption profile results in an uptake maximum at a temperature threshold, a phenomenon that is unusual. Full characterization of Xe loaded MOF structures is performed by *in situ* single crystal and synchrotron X-ray diffraction, IR spectroscopy and *ab initio* modeling. The X-ray diffraction analysis offers a detailed explanation into the dynamic structural transformation and provides a convincing rationalization of the unique adsorption behavior at the molecular scale. The guest- and temperature-dependence of the structural breathing gives rise to an intriguing reverse of Xe/Kr adsorption selectivity as a function of temperature. This project addresses research questions in Objective 3.

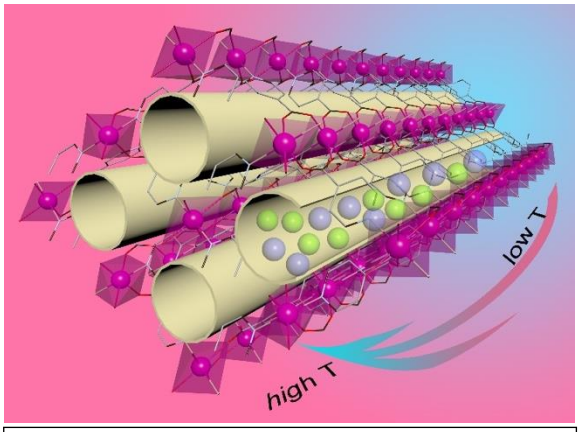

Fig. 3. Flexible MOF $Mn(ina)_2$ exhibits unique temperature- and sorbent-dependent adsorption behavior for effective separations of xenon and krypton atomic gases.

e) Effective Separation of C6 Alkane Isomers by a Flexible Zn-MOF with a Rare scu Topology [5]: Adsorption-based separation by porous solids (adsorbents) offers an energy efficient alternative for the purification of important chemicals compared to energy intensive distillations. Specifically, energy-efficient separation of linear hexane isomers from its branched counterparts is crucial to produce premium grade gasoline with high research octane number (RON). We demonstrate that a new, flexible zinc-based metal-organic framework, $[Zn_5(\mu 3\text{-}OH)_2(adtb)_2(H_2O)_5 \cdot 5DMA]$ (Zn-adtb, Figure 4) is capable of separating the C6 isomers *n*HEX, 3MP and 23DMB. The flexible MOF is constructed from a butterfly

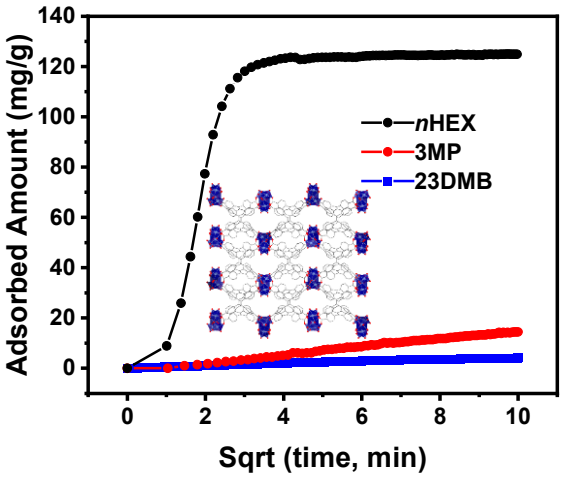

Fig. 4. Adsorption rates of *n*HEX, 3MP and 23 DMB in Zn-adtb at 30 °C. The inset shows the structure of Zn-adtb.

shaped carboxylate linker with underlying 4,8-connected *scu* topology. The adsorbate-adsorbent interactions and separation mechanism are investigated through *in situ* FTIR, solid state NMR measurements and *ab initio* modeling. These studies reveal that Zn-adtb discriminates the *n*HEX/3MP isomer pair through a kinetic separation mechanism and the *n*HEX/23DMB isomer pair through a molecular sieving mechanism. Column breakthrough measurements further confirm that the linear *n*HEX can be efficiently separated from the mono- and di-branched isomers. This project addresses research questions in Objectives 1 and 3.

Future Plans

In the near-term future, we plan to apply *in situ* spectroscopy and *ab initio* modelling to study the co-diffusion and co-adsorption mechanisms of a plethora of gas mixtures of interest to DOE including CO_2/H_2O, CO_2/C_2H_2, $C_2H_4/C_2H_2/C_2H_6$, $C_3H_4/C_3H_6/C_3H_8$ and C_6 alkane isomers in a variety of existing benchmark MOFs such as *M*FSIX and the CPM series with partitioned pore space. Our particular interest is to examine the dependence of molecular diffusivities on the co-adsorbed species and competition or cooperation behaviors among various molecules within the ultrasmall nanopores. We will continue to explore interesting and unique gas adsorption behaviors of highly flexible and robust MOF structures such as $Ca(H_2tcpb)$ and $Zn(2\text{-}cim)_2$ and ZIF derivatives with a focus on enhancing their adsorption capacity and selectivity for the separation of abovementioned important industrial chemical species in gas and/or vapor form.

References

[1] Tan, K.; Jensen, S.; Wang, H.; Feng, L.; Wei, K.; Zhou, H.-C.; Li, J.; Thonhauser, T. "Thermally Activated Adsorption in Metal-Organic Frameworks with a Temperature-Tunable Diffusion Barrier Layer", *Angew. Chem. Int. Ed.* **2020**, 59, 18468–18472.

[2] Jensen, S.; Tan, K.; Feng, L.; Li J.; Zhou, H.C.; Thonhauser, T. "Porous Ti-MOF-74 Framework as a Strong-Binding Nitric Oxide Scavenger Stephanie Jensen", *J. Am. Chem. Soc.* **2020**, 142, 16562−16568

[3] Tan, K.; Pandey, H.; Wang, H.; Velasco, E.; Wang, K.-Y.; Zhou, H.-C.; Li J.; Thonhauser, T. "Defect Termination in the UiO-66 Family of Metal−Organic Frameworks: The Role of Water and Modulator", *J. Am. Chem. Soc.* **2021**, 143, 6328−6332

[4] Wang, H.; Warren, M.; Jagiello, J.; Jensen, S.; Ghose, S.K.; Tan, K.; Yu, L.; Emge, T.J.; Thonhauser, T.; Li, J. "Crystallizing Atomic Xenon in a Flexible MOF to Probe and Understand its Temperature-Dependent Breathing Behavior and Unusual Gas Adsorption Phenomenon", *J. Am. Chem. Soc.* **2020**, 142, 20088–20097.

[5] Velasco, E.; Xian, S.K.; Wang, H.; Teat, S.J.; Olson, D.H.; Tan, K.; Ullah, S.; Popp. T.O.; Bernstein, A.; Oyekan, K.A.; Nieuwkoop, A.J.; Thonhauser, T.; Li, J. "A Flexible Zn-MOF with Rare Underlying ***scu*** Topology for Effective Separation of C6 Alkane Isomers", *ACS Appl. Mater. Interfaces* **2021**, under revision.

Publications (since the beginning of this project, 09/01/19)

[1] Zhang, G.; Tan, K.; Xian, S.; Xing, K.; Sun, H.; Hall, G.; Li, L.; Li, J. "Ultrastable Zirconium-Based Cationic Metal-Organic Frameworks for Perrhenate Removal from Wastewater", *Inorg. Chem.* **2021**. Just accepted.

[2] Tan, K.; Pandey, H.; Wang, H.; Velasco, E.; Wang, K.-Y.; Zhou, H.-C.; Li, J.; Thonhauser, T. "Defect Termination in the UiO-66 Family of Metal-Organic Frameworks: The Role of Water and Modulator", *J. Am. Chem. Soc.* **2021**, 143, 6328–6332.

[3] Velasco, E.; Osumi, Y.; Teat, S. J.; Jensen, S.; Tan, K.; Thonhauser, T.; Li, J. "Fluorescent Detection of Carbon Disulfide by a Highly Emissive and Robust Isoreticular Series of Zr-Based Luminescent Metal Organic Frameworks (LMOFs)", *Chemistry* **2021**, 3, 372–337.

[4] Hei, X.; Li, J. "All-in-one: a new approach toward robust and solution-processable copper halide hybrid semiconductors by integrating covalent, coordinate and ionic bonds in their structures", *Chem. Sci.* **2021**, 12, 3805–3817.

[5] Xian, S.; Lin, Y.; Wang, H.; Li, J. "Calcium-Based Metal-Organic Frameworks and Their Potential Applications", *Small* **2021**, 17, 2005165.

[6] Mukherjee, S.; Kumar, N.; Bezrukov, A. A.; Tan, K.; Pham, T.; Forrest, K. A.; Oyekan, K. A.; Qazvini, O. T.; Madden, D. G.; Space, B.; Zaworotko, M. J. "Amino-Functionalised Hybrid Ultramicroporous Materials that Enable Single-Step Ethylene Purification from a Ternary Mixture", *Angew. Chem. Int. Ed.* **2021**, 60, 10902–10909.

[7] Pandey, H.; Barrett, T.; Gross, M. D.; Thonhauser, T. "Adsorption properties of acetylene, ethylene and ethane in UiO-66 with linker defects and NO_2 functionalization", *Mater. Adv.* **2021**, 2, 426–433.

[8] Jensen, S.; Tan, K.; Feng, L.; Li, J.; Zhou, H.-C.; Thonhauser, T. "Porous Ti-MOF-74 Framework as a Strong-Binding Nitric Oxide Scavenger", *J. Am. Chem. Soc.* **2020**, 142, 16562–16568.

[9] Tan, K.; Jensen, S.; Wang, H.; Feng, L.; Wei, K.; Zhou, H.-C.; Li, J.; Thonhauser, T. "Thermally Activated Adsorption in Metal-Organic Frameworks with a Temperature-Tunable Diffusion Barrier Layer", *Angew. Chem. Int. Ed.* **2020**, 59, 18468–18472.

[10] Wang, H.; Warren, M.; Jagiello, J.; Jensen, S.; Ghose, S. K.; Tan, K.; Yu, L.; Emge, T. J.; Thonhauser, T.; Li, J. "Crystallizing Atomic Xenon in a Flexible MOF to Probe and Understand Its Temperature-Dependent Breathing Behavior and Unusual Gas Adsorption Phenomenon", *J. Am. Chem. Soc.* **2020**, 142, 20088–20097.

[11] Hei, X.; Liu, W.; Zhu, K.; Teat, S. J.; Jensen, S.; Li, M.; O'Carroll, D. M.; Wei, K.; Tan, K.; Cotlet, M.; Thonhauser, T.; Li, J. "Blending Ionic and Coordinate Bonds in Hybrid Semiconductor Materials: A General Approach toward Robust and Solution-Processable Covalent/Coordinate Network Structures", *J. Am. Chem. Soc.* **2020**, 142, 4242–4253.

[12] Alahakoon, S. B.; Tan, K.; Pandey, H.; Diwakara, S. D.; McCandless, G. T.; Grinffiel, D. I.; Durand-Silva, A.; Thonhauser, T.; Smaldone, R. A. "2D-Covalent Organic Frameworks with Interlayer Hydrogen Bonding Oriented through Designed Nonplanarity", *J. Am. Chem. Soc.* **2020**, 142, 12987–12994.

[13] Cure, J.; Cocq, K.; Nicollet, A.; Tan, K.; Hungria, T.; Assie-Souleille, S.; Vivies, S.; Salvagnac, L.; Quevedo-Lopez, M.; Maraval, V.; Chauvin, R.; Estève, A.; Rossi, C. "A Beehive Inspired Hydrogen Photocatalytic Device Integrating a Carbo-Benzene Triptych Material for Efficient Solar Photo-Reduction of Seawater", *Adv. Sustain. Sys.* **2020**, 4, 2000121.

[14] Li, H.-Y.; Zhao, S.-N.; Zang, S.-Q.; Li, J. "Functional metal-organic frameworks as effective sensors of gases and volatile compounds", *Chem. Soc. Rev.* **2020**, 49, 6364–6401.

[15] Li, J.; Yuan, S.; Qin, J.-S.; Huang, L.; Bose, R.; Pang, J.; Zhang, P.; Xiao, Z.; Tan, K.; Malko, A. V.; Cagin, T.; Zhou, H.-C. "Fluorescence Enhancement in the Solid State by Isolating Perylene Fluorophores in Metal-Organic Frameworks", *ACS Appl. Mater. Interfaces* **2020**, 12, 26727–26732.

[16] Lo, S.-H.; Feng, L.; Tan, K.; Huang, Z.; Yuan, S.; Wang, K.-Y.; Li, B.-H.; Liu, W.-L.; Day, G. S.; Tao, S.; Yang, C.-C.; Luo, T.-T.; Lin, C.-H.; Wang, S.-L.; Billinge, S. J. L.; Lu, K.-L.; Chabal, Y. J.; Zou, X.; Zhou, H.-C. "Rapid desolvation-triggered domino lattice rearrangement in a metal-organic framework", *Nature Chem.* **2020**, 12, 90–97.

[17] Miller, J. T.; Ren, Y.; Li, S.; Tan, K.; McCandless, G.; Jacob, C.; Wu, Z.; Chu, C.-W.; Lv, B.; Biewer, M. C.; Stefan, M. C. "Peroxide-Templated Assembly of a Trimetal Neodymium Complex Single-Molecule Magnet", *Inorg. Chem.* **2020**, 59, 10379–10383.

[18] Wang, H.; Liu, Y.; Li, J. "Designer Metal–Organic Frameworks for Size-Exclusion-Based Hydrocarbon Separations: Progress and Challenges", *Adv. Mater.* **2020**, 32, 2002603.

[19] Wu, Z.-F.; Velasco, E.; Shan, C.; Tan, K.; Zhang, Z.-Z.; Hu, Q.-Q.; Xing, K.; Huang, X.-Y.; Li, J. "Robust fluorescent calcium coordination polymers as Cu^{2+} sensors with high sensitivity and fast response", *J. Mater. Chem. C* **2020**, 8, 6820–6825.

[20] Yu, L.; Dong, X.; Gong, Q.; Acharya, S. R.; Lin, Y.; Wang, H.; Han, Y.; Thonhauser, T.; Li, J. "Splitting Mono- and Dibranched Alkane Isomers by a Robust Aluminum-Based Metal-Organic Framework Material with Optimal Pore Dimensions", *J. Am. Chem. Soc.* **2020**, 142, 6925–6929.

[21] Jensen, S.; Tan, K.; Lustig, W. P.; Kilin, D. S.; Li, J.; Chabal, Y. J.; Thonhauser, T. "Structure-Driven Photoluminescence Enhancement in a Zn-Based Metal-Organic Framework", *Chem. Mater.* **2019**, 31, 7933–7940.

[22] Wang, S.; Xhaferaj, N.; Wahiduzzaman, M.; Oyekan, K.; Li, X.; Wei, K.; Zheng, B.; Tissot, A.; Marrot, J.; Shepard, W.; Martineau-Corcos, C.; Filinchuk, Y.; Tan, K.; Maurin,

G.; Serre, C. “Engineering Structural Dynamics of Zirconium Metal–Organic Frameworks Based on Natural C4 Linkers”, *J. Am. Chem. Soc.* **2019**, 141, 17207–17216.

Using Nanoporous and Nanostructured Materials to Understand and Optimize Pseudocapacitive Charge Storage

Sarah Tolbert, University of California Los Angeles (UCLA), Departments of Chemistry & Biochemistry and Materials Science & Engineering

Program Scope

The need for improved electrochemical energy storage continues to grow in our modern society. Lithium-ion batteries are currently used for most applications because of their high energy density and reasonable cycle life, but long charging times impede some applications. Electric double layer capacitors offer faster charging times and higher power density, but at the cost of energy density. Pseudocapacitors offer an exciting alternative, combining high energy and power density through fast, faradaic near-surface redox reactions. Even higher energy densities can be realized through a process called intercalation pseudocapacitance, where fast insertion of Li^+ can occur in materials that do not undergo a discontinuous phase transition during cycling. Li^+ insertion without a phase transition can be an intrinsic materials property, or can be induced by nanoscale size or disorder. In our DOE supported work on nanostructured electrode materials, we have followed the evolution with crystallite size from bulk battery-like kinetics to pseudocapacitive behavior in a range of materials. We have also developed pseudocapacitive cathode materials to enable fast charging full cell devices.

Recent Progress

Many of the nanostructured materials described below are synthesized through template-directed methods to create porosity that allows the electrolyte to penetrate the material. Both molecular inorganic and nanocrystal precursors that are soluble in polar organic solvents can be template with micelle-forming diblock copolymers. For precursors that are soluble in aqueous solutions, charged polymer colloids, such as poly(methyl methacrylate) (PMMA) nanospheres, are ideal templates. Simple solvent evaporation, or freeze-drying ensures that the template and inorganic remain mixed during drying. Once dry, thermal or chemical removal of the template produces the final porous material.[1] Tuning the wall thickness is accomplished by varying the template size and the inorganic:template ratio. This architecture allows us to create short Li^+ diffusion distances and channels for electrolyte, while maintaining an electrically interconnected network.

Recent work has prioritized developing architectures with tunable size in addition to fast kinetics to understand the transition from battery to pseudocapacitor. We began with MoO_2, a rutile-type tunnel structure with good ionic and electrical conductivity that suffers from poor kinetics in the bulk due to a sluggish first-order phase transition. By varying the size of PMMA nanospheres and changing the ratio of polymer to inorganic precursor, we produced crystalline nanoporous MoO_2 powders with tunable pore wall thickness and porosity. SEM images of three sizes of nanoporous MoO_2 are shown in Fig. 1, along with galvanostatic cycling data for each size. Although the capacities at slow rates are similar, smaller crystal-lite sizes samples retain more capacity at higher rates (Fig. 1).

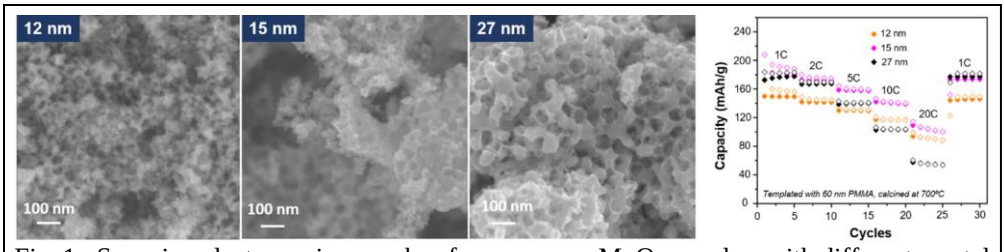

Fig. 1: Scanning electron micrographs of mesoporous MoO_2 powders with different crystal domain sizes (left) and their corresponding electrochemical cycling performance (right). Materials with large domain sizes show poorer rate capability more typical of battery materials, while nanocrystalline powders with thinner walls are capable of fast cycling.

To quantify the fraction of capacitive charge

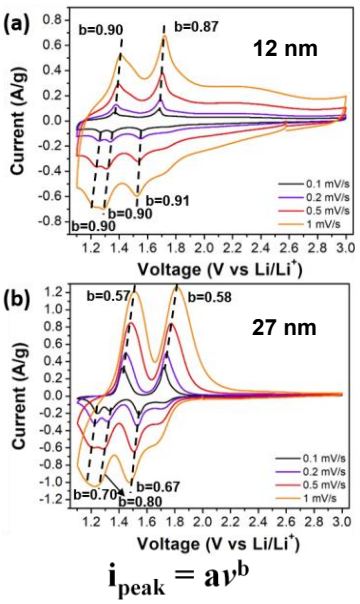

$$i_{peak} = a\nu^{b}$$

Fig. 2: Kinetics analysis using the bottom equation for two sizes of nanoporous MoO_2. Pseudo-capacitive (b~1) and battery-like (b~0.5) behavior is observed at small & large sizes, respectively.

storage compared, we turn to various sweep voltammetry methods.[2,3] For a redox reaction limited by semi-infinite diffusion, the peak current response varies with the square root of the sweep rate ($v^{1/2}$); for a capacitive process, it varies linearly with v.[4] Using the equation in Fig. 2, bottom, the exponent (b) can be easily extracted from the slope of a plot of log current vs. log sweep rate. Slopes or b-values near 0.5 correspond to pure battery-like kinetics, while a slope approaching 1 corresponds to pseudocapacitive behavior. Fig. 2 shows that the peak current for the largest and smallest sizes of nanoporous MoO_2 vary with the square root of the sweep rate and near linearly with the sweep rate, respectively, confirming that large MoO_2 is battery-like, and small MoO_2 is dominantly pseudocapacitive.

In Fig. 3, we show *operando* synchrotron XRD to probe phase transition dynamics during electrochemical cycling on nanoporous MoO_2 with three different average crystal sizes. To our surprise, we found not two, but three distinct types of phase behavior. The largest size showed bulk-like behavior: The diffraction peaks shift from MoO_2 to $LiMoO_2$ with a discontinuous phase transition (2-phase coexistence), as seen in the left panel of Fig. 3. Interestingly, the middle-sized sample (21 nm average domain size) showed the exact same beginning and ending peak positions, indicating that the same structural changes occurred in this sample, but those changes occurred via a solid-solution mechanism without a discontinuous phase transition. Decreasing the average crystallite size further appears to involve another mechanistic change, as the smallest sample showed almost no structural change. This data clearly shows the progression from two-phase coexistence to solid-solution-type phase transition behavior as crystallite size decreases, and then to a mostly suppressed phase transition as crystallite size decreases further. These results differentiate two concepts that are often convoluted in the literature (phase transition suppression *vs.* conversion from first- to second-order transition).

In addition to MoO_2, we have also examined size effects the classic van der Waals intercalation host, MoS_2. We previously showed pseudocapacitive behavior in nanocrystals of MoS_2, but size control was not possible in that system.[5] Here, nanoporous MoS_2 was synthesized from nanoporous MoO_2 similar to that shown in Fig. 1 using thermal sulfurization. By starting with different MoO_2 pore wall thicknesses, a range of MoS_2 wall thicknesses could be produced (Fig. 4a,b) with wall thickness histograms in Fig. 4c. The smallest sizes of MoS_2 displayed very fast charging behavior (Fig. 4d), with 43% capacity retention at 100C. The sloped galvanostatic traces, rather than distinct plateaus at intercalation potential, also suggest a lack of first order-phase transitions during lithiation. By contrast, large domain size materials showed much slower kinetics.

Efforts to produce new pseudocapacitive cathode materials have focused on nanoporous $LiNi_{0.80}Co_{0.15}Al_{0.05}O_2$ (NCA), which exhibits high capacity and a second-order phase transition during cycling in the bulk. The fact that first-order phase transitions are intrinsically suppressed makes NCA a promising material that could

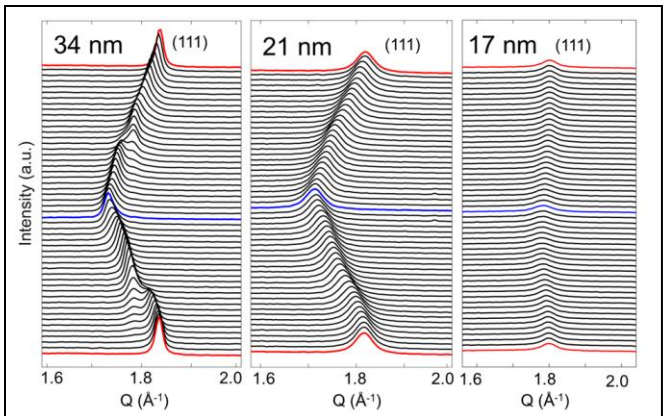

Fig. 3: *Operando* XRD on nanoporous MoO_2 with different sizes. Three types of phase-transition behavior are observed, which has not been observed before in a single system.

show pseudocapacitive behavior at sizes much larger than materials where phase transitions are suppressed by finite-size effects.[6]

Nanostructured NCA was synthesized using sol-gel methods and a colloidal PMMA template. To study the effect of size, two different calcination methods were utilized to crystallize the porous network and were compared to commercial bulk NCA, which has larger particle sizes and no nanoscale porosity (Fig. 5a). The first heating method is analogous to rapid thermal annealing (RTA), where the PMMA templated NCA precursor material was placed into a hot oven for a short amount of time (850 °C for 5 minutes). Referred to as PMMA/RTA, this sample had small particle sizes and nanoscale porosity (Fig. 5c). The NCA precursor was heated from room temperature to 800 °C over 1 hour, then held at 800 °C for 2 hours; this method is referred to as PMMA/no-RTA and resulted in medium particle sizes and nanoscale porosity (Fig. 5b).

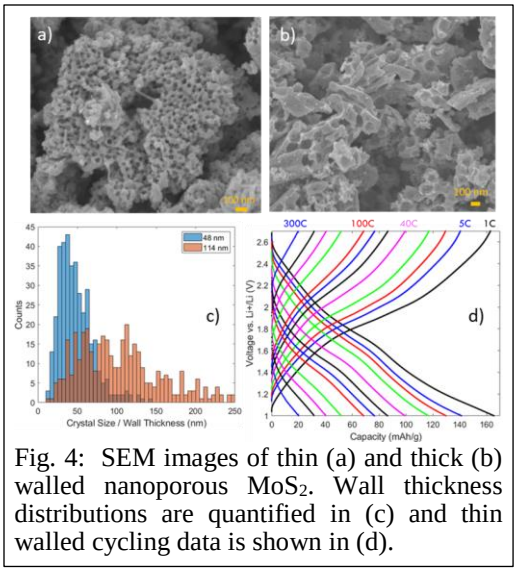

Fig. 4: SEM images of thin (a) and thick (b) walled nanoporous MoS_2. Wall thickness distributions are quantified in (c) and thin walled cycling data is shown in (d).

Two issues with NCA are cation mixing and air sensitivity. The former results from incomplete oxidation of Ni^{2+} to Ni^{3+}, and the latter from reactions with CO_2 and H_2O at the NCA surface. Although PMMA/RTA has the shortest lithium-ion diffusion lengths, the PMMA/no-RTA materials had the best capacity retention at 64C, likely due to increased surface area and incomplete Ni^{2+} oxidation during synthesis in the PMMA/RTA. To quantify pseudocapacitive behavior, electrochemical kinetic analyses were performed. The PMMA/no-RTA NCA showed pseudocapacitive characteristics with an average *b*-values of 0.94 (close to 1; Fig. 5e).

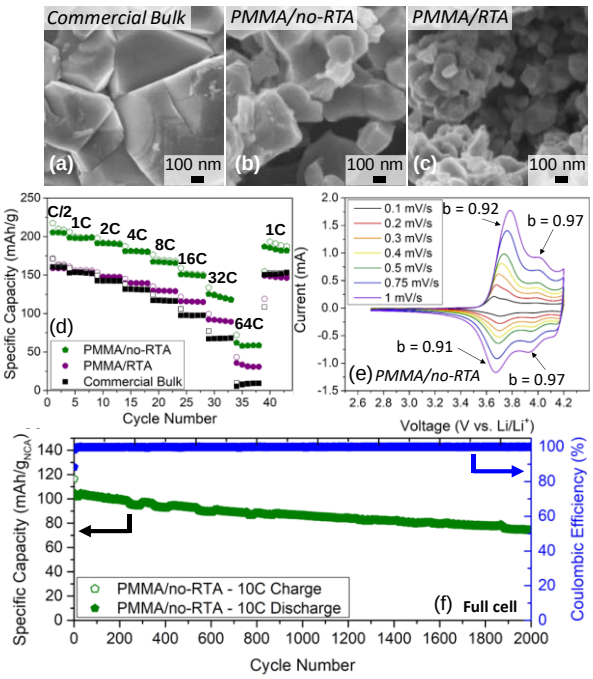

Fig. 5: (a-c) SEM images of commercial bulk, PMMA/no-RTA, & PMMA/RTA NCA. (d) Galvanostatic rate capability for the samples show in panels (a-c). (e) *b*-value analyses for PMMA/no-RTA. (c) Extended cycling for PMMA/no-RTA NCA paired with a Nb_2O_5 anode in a fast-charging full-cell.

Finally, to show the practical applicability of these materials, the PMMA/no-RTA material was paired with Nb_2O_5, a standard pseudocapacitive anode, in a fast-charging full-cell device. This full-cell was cycled 2000 times at 10C (charging/discharging in 6 minutes) with 72% capacity retention (Fig. 5f).[7]

The other cathode material we studied was a nanostructured member of a family of known fast charging battery materials – the metal phosphates. We chose to examine $LiVPO_4F$ (LVPF), which is a high voltage cathode with good reported rate capability.[8] It is usually made by solid-state methods, but under DOE support, we developed a sol-gel colloidal templating route to nanoporous LVPF that uses fluoropolymer colloids as both the template and the fluorine source. Fig. 6a shows an SEM image that demonstrates the homogeneous nanoscale porosity that we have achieved. The nanoporous LVPF shows excellent capacity retention up to 30C (Fig. 6b). One might predict that nanoporous LVPF would show suppression of standard intercalation induced phase transitions and pseudocapacitive behavior, but this is not the case. Electrochemical kinetics

studies show that lithium intercalation in LVPF is dominantly diffusion controlled with a b-value near 0.5, typical of battery materials (Fig. 6c). *Operando* diffraction show a clear first-order phase transition upon lithium extraction, with two-phase coexistence observed upon both charge and discharge (Fig. 6d). This raises the question of why nanoporous LVPF shows such fast rate capabilities and brings into question the difference between fast batteries and pseudocapacitors.

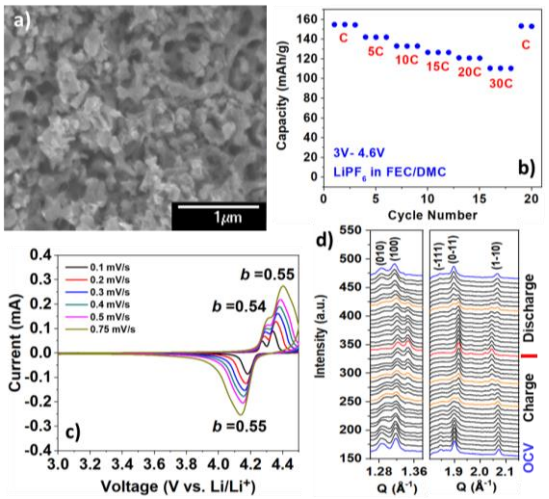

Fig. 6: (a) SEM image of nanoporous LVPF showing homogeneous nanoscale porosity and (b) galvanostatic cycling show excellent capacity retention up to 30 C. Despite this fact, the material is fundamentally a battery with a *b*-value near 0.5 (c) and multiple first order phase transitions (d, transition midpoints highlighted in orange).

Future Plans

Future work aims at clarifying our understanding of pseudocapacitive charge storage, with a focus on the relative roles of size and disorder in suppressing phase transitions and facilitating fast charging. Nanoporous materials will be synthesized with controlled size and *operando* X-ray diffraction will be used to directly follow phase transitions during (dis)charge. Electrochemical studies, including multiple sweep-rate dependent voltametric methods, galvanostatic intermittent titration testing (GITT), and electrochemical impedance, will be used to examine the signatures of pseudocapacitive charge storage. We will use temperature dependent studies to determine if phase transition suppression in nanostructured electrode materials is kinetic or thermodynamic in origin. We next consider whether the size evolution described above is general to nanostructured pseudocapacitors, and if so, which transition (1^{st}-order to 2^{nd}-order or 2^{nd}-order to transition suppression) is key to the onset of high rate charge storage. Finally, we will explore the role of structural disorder, which has been shown to suppress 1^{st}-order phase behavior in some bulk materials. A range of materials with both controlled size and controlled disorder will examined to help clarify the structural and electrochemical signatures of pseudocapacitance.

In parallel, we will expand the range of available pseudocapacitive materials. For nanoporous NCA, we work to decreasing nanoscale domain size and stabilizing the reactive NCA surfaces. Concurrently, we will explore new polymer templates for scalable materials synthesis and nanoscale versions of other high capacity/high voltage metal oxide cathodes. Finally, we will continue to examine nanoporous versions of metal phosphate cathodes like LVPF. Although Fig. 6 shows battery-like kinetics, other methods, indicate more capacitive behavior, so the system is an interesting test case for better defining fast charging pseudocapacitive behavior.

References

[1] Rauda, I. E.; Buonsanti, R.; Saldarriaga-Lopez, L. C.; Benjauthrit, K.; Schelhas, L. T.; Stefik, M.; Augustyn, V.; Ko, J.; Dunn, B.; Wiesner, U.; Milliron, D. J.; Tolbert, S. H. *ACS Nano*, **2012**, *6*, 6386.

[2] Wang, J.; Polleux, J.; Lim, J.; Dunn, B. *J. Phys. Chem. C*, **2007**, *111*, 14925.

[3] Liu, T.-C.; Pell, W.G.; Conway, B.E.; Roberson, S.L. *J. Electrochem. Soc.*, **1998**, *145*, 1882.

[4] Conway, B. E.; Birss, V.; Wojtowicz, J. *J. Power Sources*. **1997**, *66*, 1-14.

[5] Cook, J.B.; Lin, T.C.; Kim, H.S.; Siordia, A.; Dunn, B.S.; Tolbert, S.H. *ACS Nano* **2019**, *13*, 1223.

[6] Robert, R.; Bünzli, C.; Berg, E. J.; Novák, P. *Chem Mater*. **2015**, *27*, 526.

[7] Basile, V. M.; Lai, C.-H.; Choi, C. S.; Butts, D. M.; King, S. C.; Dunn, B. S.; Tolbert, S. H. Submitted.

[8] Lin, T.C.; Yan, Y.; King, S.C.; Lai, C.H.; Tolbert, S.H. *ACS Appl. Mater. Interfaces* **2020**, *12*, 33775.

Publications over the Past Three Years:

B. Lu, E. Olivera, J. Scharf, M. Chouchane, C. Fang, M. Ceja, L.E. Pangilinan, S. Zheng, A. Dawson, D. Cheng, W. Bao, O. Arcelus, A.A. Franco, X. Li, S.H. Tolbert, Y.S. Meng, "Quantitatively Designing Porous Copper Current Collectors for Lithium Metal Anodes." *ACS Appl. Energy Mater.* **XXX**, XXX-XXX (2021). DOI: 10.1021/acsaem.1c00438.

T. C. Lin, Y. Yan, S. C. King, C.-H. Lai, S. H. Tolbert, "Fast-Charging Cathodes from Polymer-Templated Mesoporous $LiVPO_4F$" *ACS Appl. Mater. Interfaces,* **12**, 33775-33784, (2020); DOI: 10.1021/acsami.0c08709.

T. C. Lin, A. Dawson, S. C. King, Y. Yan, D. S. Ashby, J. A. Mazzetti, B. S. Dunn, J. Nelson Weker, S. H. Tolbert, "Understanding Stabilization in Nanoporous Intermetallic Alloy Anodes for Li-Ion Batteries Using Operando Transmission X-ray Microscopy" *ACS Nano,* **14**, 14820–14830, (2020); DOI: 10.1021/acsnano.0c03756.

J.B. Cook, T.C. Lin, H.-S. Kim, A. Siordia, B.S. Dunn, S.H. Tolbert, "Suppression of Electrochemically Driven Phase Transitions in Nanostructured MoS_2 Pseudocapacitors Probed Using Operando X-ray Diffraction." *ACS Nano*, **13**, 1223–1231, (2019); DOI: 10.1021/acsnano.8b06381.

S. Fischer, J. Roeser, T.C. Lin, R.H. DeBlock, J. Lau, B.S. Dunn, F. Hoffmann, M. Fröba, A. Thomas, S.H. Tolbert, "A Metal-Organic Framework with Tetrahedral Aluminate Sites as a Single-Ion Li^+ Solid Electrolyte" *Angew. Chem. Int. Ed.* **130**, 16925-16929 (2018); DOI: 10.1002/anie.201808885.

E. Detsi, X. Petrissans, Y. Yan, J.B. Cook, Z.L. Deng, Y.L. Liang, B. Dunn, S.H. Tolbert, "Tuning ligament shape in dealloyed nanoporous tin and the impact of nanoscale morphology on its applications in Na-ion alloy battery anodes." *Phys. Rev. Materials* **2**, 055404 (2018); DOI: 10.1103/PhysRevMaterials.2.055404.

C.H. Lai, D.S. Ashby, T.C. Lin, J. Lau, A. Dawson, S.H. Tolbert, B.S. Dunn, "Application of Poly(3-hexylthiophene-2,5-diyl) as a Protective Coating for High Rate Cathode Materials." *Chem. Mater.* **30**, 2589–2599 (2018); DOI: 10.1021/acs.chemmater.7b05116.

Exploration of Radial Conjugation Pathways in Pi-Electron Materials

John D. Tovar, PI, Department of Chemistry, Johns Hopkins University; Ramesh Jasti, co-PI, Department of Chemistry, University of Oregon; Miklos Kertesz, co-PI, Department of Chemistry, Georgetown University

Program Scope

This project involves hypothesis-driven exploratory research on new manifestations of pi-electronic delocalization relevant to organic electronics via building onto hitherto unused structural subunits that invoke different degrees of aromaticity, conjugation, radical character and strain. Our team consists of three interrelated groups specializing in *pi-conjugated organic electronic systems with unusual properties well beyond the conventional arsenal of organic semiconductors with linear conjugation topologies present on planar pi-electron backbones*. These systems combine unusual bonding patterns, unusual curvatures, and unusual charge states in new ways that have yet to be tapped for emerging electronics applications. The synthetic and physical organic activities of Tovar and Jasti are simultaneously supported by and driven by the computational activities of Kertesz to understand molecules with novel spin systems, novel electronic delocalization and novel aromaticities. Our objectives for this research program are to (1) design and characterize new energy materials that access unusual spin states and pi-electron delocalization in curved carbon structures and (2) examine through-space delocalization as encouraged by mechanical bonding of curved components.

Recent Progress

Our team completed three foundational studies relating to the inclusion of CPP molecules into polymer structures and to the extension of advanced quantum mechanical calculations related to quinoidal architectures that will be important considerations for modulating the spin properties of oligomeric or polymeric structures based upon CPP cores.

Inclusion of radial conjugation into linear pi-conjugated pathways. The first major activity was the completion of a comparative study of [6] and [8] CPP-based conjugated small molecules and polymers alongside their terphenyl model variants.[1]

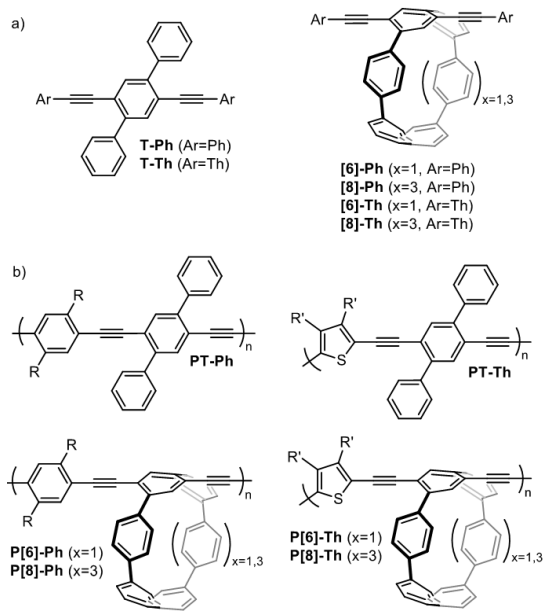

Figure 1. Library of materials prepared to study the merger of radial and linear conjugation.

We augmented the phenylene ethynylene polymers with models where the core CPP or terphenyl units were capped with two phenyl acetylene units. The library of materials thus prepared is shown in Figure 1. Quantum chemical calculations were conducted on these molecular systems and on defined oligomers to capture the extent of orbital delocalization.

Our key findings are summarized in Figure 2. The low energy UV-vis region is enhanced relative to the parent CPP core, which was initially interpreted as being due to symmetry breaking that provided further oscillator strength to the CPP HOMO-LUMO transition. However, quantum chemical calculations indicate that these broad low-energy peaks are actually superpositions of multiple closely-spaced transitions that are spread over both the CPP core and the linear conjugated elements. This is corroborated by the orbital coefficients of specific energy levels near the frontier orbitals are indeed spread over both CPP and linear conjugation pathways. This affirms one of our design motivations that merging CPP radial conjugation into linear pi-conjugation will open up new electronic states not available to the components in isolation.

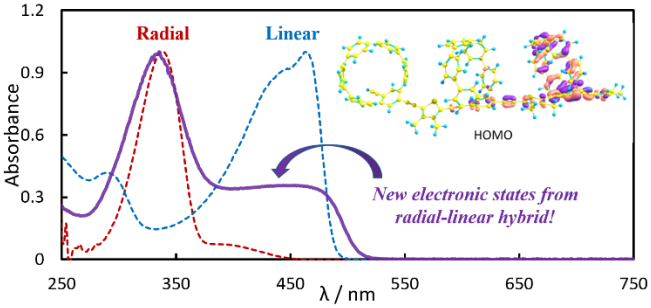

Figure 2. Spectral comparison of CPP (red dotted line) and poly arylene ethynylene (blue dotted line) to the hybrid structure (purple solid line) and a representative HOMO orbital distribution showing extended

Inclusion of radial conjugation into saturated polymer backbones. In addition to looking into the electronic contributions of CPPs in conjugated polymers, we sought to develop a method to prepare various self-assembled nanomaterials from CPPs in a controlled manner.[2] We targeted ring-opening metathesis polymerization (ROMP) as a mild method to achieve a high degree of control, and toward that end synthesized CPPs of three various sizes with a benzonorbornadiene group embedded in the nanohoop backbone (Figure 3). We found that this controlled polymerization method gives access to poly(nbCPP)s with varying molecular weights which retain the desirable characteristics of CPPs, such as solubility, size-dependent fluorescence, and host-guest interactions. Moreover, due to the living nature of this polymerization, we were able to prepare block polymers of varying sized CPPs.

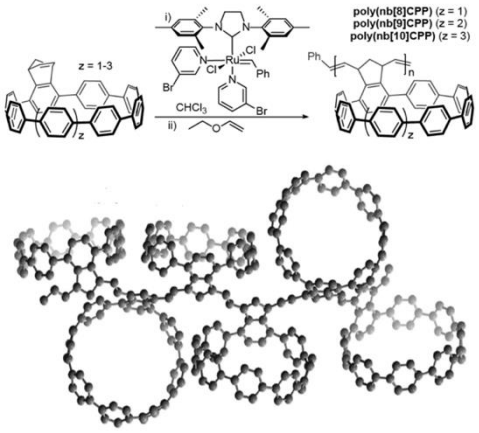

Figure 3. ROMP as a method for "living" polymerization of cycloparaphenylenes into new types of carbon nanomaterials.

All the poly-CPPs obtained via ROMP share the absorbance maximum around 340 nm found in the underivatized parent compounds (Figure 4). In terms of emission, poly[8]CPP and poly[10]CPP also maintain the characteristic fluorescence emission profiles of the respective sizes of CPPs. For the copolymers, results differed based on polymer sequence. Poly[10]CPP-*block*-

poly[8]CPP shows overlapping but clear emission peaks from both monomer types, similar to the emission profile obtained by blending samples of poly[8]CPP and poly[10]CPP. On the other hand, poly[8]CPP-*random*-[10]CPP has an emission profile which closely resembles that of [8]CPP. This unexpected emission from poly[8]CPP-*random*-[10]CPP is attributed to energy transfer between the hoop sizes, similar to what is observed in concatenated nanohoops of differing sizes. The fact that intermixing the two hoop sizes in a statistical polymer gives rise to energy transfer whereas linking [8]CPP and [10]CPP units in a block copolymer does not suggests that physical proximity is a critical factor for this effect. We further examined the fluorescence quenching of various poly-CPPs by the addition of fullerene C_{60}. We observed differential degrees of [8] and [10] CPP quenching depending on the block architecture which suggests that both sizes of hoop units are involved in the observed fluorescence quenching regardless of polymer sequence.

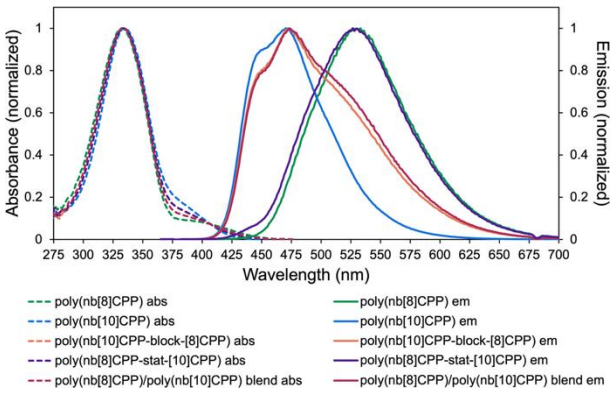

Figure 4. UV-vis and photoluminescence of poly(nb[x]CPP) homopolymers and block copolymers.

Quantum chemical exploration of quinonoid repeat units. With the purpose of engineering the band gap of conjugated polymers, we have computationally explored the space of more than two dozen heteroaromatic molecules as repeat units of potential quinonoid ground state polymers based on monomers that are synthetically accessible (Figure 5).[3] We have identified eight polymers with quinonoid ground states (Q) that are energetically more stable than their aromatic isomeric structures (A) using density functional theory. The quinonoid ground states were further characterized using inter-ring $r_{C\text{-}C}$ bond lengths. Not all, but some also possess relatively small energy gaps. Although no common trend for preference of quinonoid ground state was observed with these systems under study, polymers with 5-membered rings in their backbones tended to prefer Q ground states more than those with 6-membered rings. Diradical character, expressed as the singlet-triplet splitting and the y_0 index related to the effectively unpaired electrons, is explored as an unusual electronic structure characteristic for quinonoid-linked conjugated polymers and mixed A/Q polymers. This study provides a foundation to explore the more elaborate CPP-based quinonoidal structures. Copolymerizing the presented Q ground state systems with these A ground state CPPs will be the

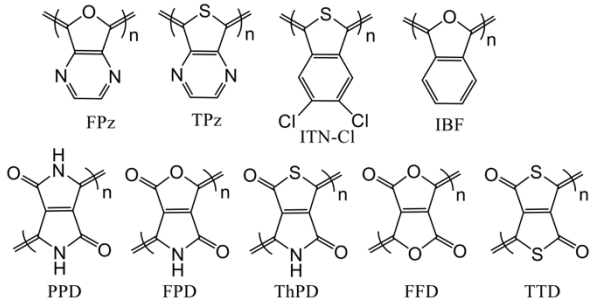

Figure 5. A selection of polymers assessed for ground-state quinonoidal preferences with the strongest quinonoidal trend found for the oligomers and polymers of TPz, IBF, FPz, PPD, and FPD.

next step with the expectation that some of these combinations will result in Q state polymers with very low band gaps and highly delocalized electronic structures.

Future Plans

Our plans for future research entail the exploration of other linear CPP polymers that might foster even more degrees of delocalization, in addition to continuing studies of so-called "disjoint" CPPs whereby ***two*** different phenyl groups of the CPP radial structure participate in the pi-extension of the linearly conjugated polymer. This "disjoint" isomer necessarily requires or invokes the full radial conjugation in order to effectively delocalize along the polymer backbone in contrast to our "linear" isomer that in principle could maintain linear delocalization without necessarily engaging the entire radial conjugation path. We will seek out block copolymers from nbCPPs, which pose exciting prospects for synthesis of organic light-emitters with tunable and perhaps even white light emission. We will explore acyclic diene metathesis (ADMET) on CPPs now that we have experience with metathesis reactions. We also expect to push further with mechanically bonded CPPs to explore through space electronic delocalization. Finally, computational work will continue to support the spectroscopic characterization of oligomers and polymers in this project by assessing preferred conformations, and predicting and analyzing optical absorption and NMR chemical shifts. Analysis of rotaxanes by computational modeling revealed preferred configurations which will be used in future design strategies.

References

1. G. M. Peters, G. Grover, R. Maust, C. Colwell, H. Bates, W. Edgell, R. Jasti, M. Kertesz, and J. D. Tovar, "Linear and radial conjugation in extended pi-electron systems," in the ***Journal of the American Chemical Society*** 2020 (142) 2293-2300. (DOI: 10.1021/jacs.9b10785)
2. R. L. Maust, P. Li, B. Shao, S. M. Zeitler, P. B. Sun, H. W. Reid, L. N. Zakharov, M. R. Golder, R. Jasti, "Controlled Polymerization of Norbornene Cycloparaphenylenes Expands Carbon Nanomaterials Design Space." in ***ACS Central Science*** 2021, Article ASAP. (DOI: 10.1021/acscentsci.1c00345)
3. G. Grover, G. M. Peters, J. D. Tovar, and M. Kertesz, "Quinonoid vs. aromatic structures of heteroconjugated polymers from oligomer calculations," in ***Physical Chemistry Chemical Physics***, 2020 (22) 11431-11439. (DOI: 10.1039/D0CP00606H)

Publications

Maust, R. L.; Li, P.; Shao, B.; Zeitler, S. M.; Sun, P. B.; Reid, H. W.; Zakharov, L. N.; Golder, M. R.; Jasti, R. "Controlled Polymerization of Norbornene Cycloparaphenylenes Expands Carbon Nanomaterials Design Space." In ***ACS Central Science*** 2021, Article ASAP. (DOI: 10.1021/acscentsci.1c00345)

G. Grover, G. M. Peters, J. D. Tovar, and M. Kertesz, "Quinonoid vs. aromatic structures of heteroconjugated polymers from oligomer calculations," in ***Physical Chemistry Chemical Physics***, 2020 (22) 11431-11439. (DOI: 10.1039/D0CP00606H)

G. M. Peters, G. Grover, R. Maust, C. Colwell, H. Bates, W. Edgell, R. Jasti, M. Kertesz, and J. D. Tovar, "Linear and radial conjugation in extended pi-electron systems," in the ***Journal of the American Chemical Society*** 2020 (142) 2293-2300. (DOI: 10.1021/jacs.9b10785)

"Polymer embodiments comprising nanohoop-containing polymer backbones and methods of making and using the same." U.S. Provisional Patent Application No. 62/907,145, filed September 27, 2019.

Expanding iClick to Link Metal Ions in Multidimensional Metallopolymers and Materials Synthesis

PI: Adam S. Veige, University of Florida

Co-PI: Kirk S. Schanze University of Texas, San Antonio

Program Scope

Metallopolymers have the potential to be next-generation materials for the energy sector, information storage, and materials synthesis. Uniquely, transition metal chemistry marries polymer science in these hybrid materials wherein the metal ion imparts new properties unimaginable for organic polymers alone. These materials can harvest light in next-generation photovoltaics or act as electrochromic components in displays by incorporating the well-defined photophysical properties of metal ions into a conductive polymer backbone. This project centers on new strategies to construct well-defined and rationally-designed metallopolymers. To achieve these goals this project takes advantage of iClick to construct new materials via cycloaddition reactions.

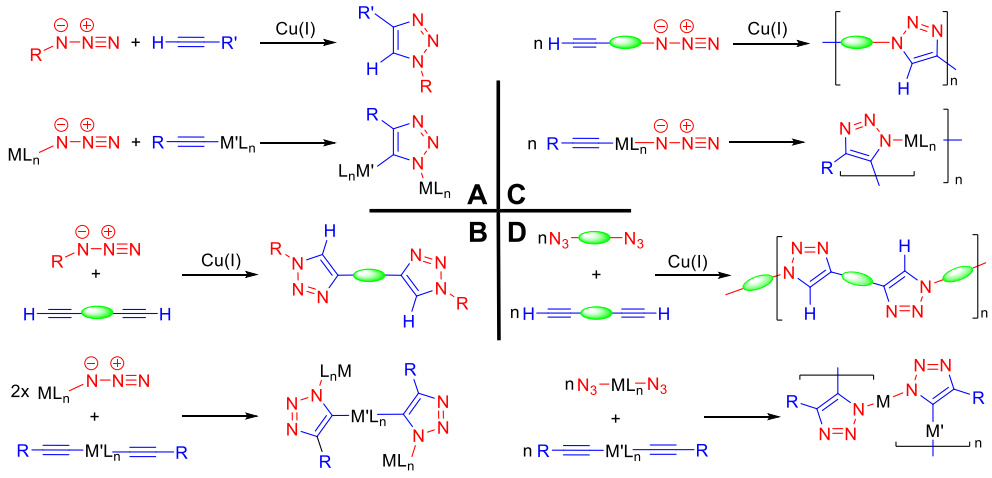

iClick reactions and their application in metallopolymer synthesis.

Recent Progress

Recent progress on the project centers on expanding iClick to other classes of reactions. Originally formulated as the reaction of a metal-azide with a metal-acetylide, the goal of the current work is to expand this functionality to include cyclooctyne reagents (Figure 2). This opens a new area of iClick involving "strain-promoted azide-alkyne cycloaddition" (SPAAC). This aspect of the project was recently accomplished, and the results submitted for publication.

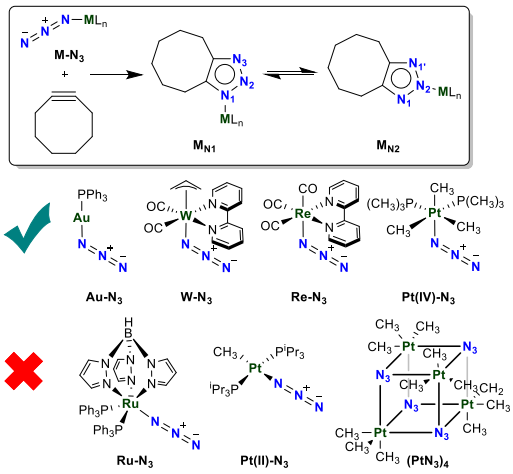

Figure 2. iClick reactions between metal-azides and cyclooctyne.

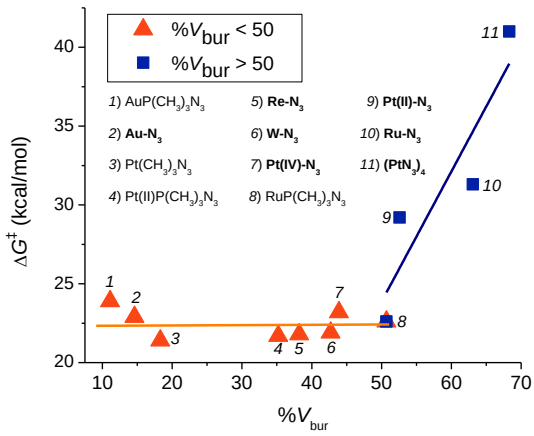

Figure 3. Plot of Calculated $\Delta G^{\ddagger}$ (kcal/mol) of SPAAC iClick vs. $\%V_{bur}$ for all structures investigated

Figure 3 summarizes the key finding that only steric factors influence the outcome of the iClick reaction and the calculated % buried volume ($\%V_{bur}$) is the sole predictor. This study establishes an approach for the rapid computational pre-screening of metal azides for reactivity with cyclooctynes. The simplicity of the single computational descriptor, i.e. a $\%V_{bur}$ less than 50% will greatly accelerate and narrow the search for metal-azides that participate in SPAAC iClick

Future Plans

After several years of elucidating the fundamental principles of iClick chemistry we are now able to exploit that chemistry in new materials applications. We plan to develop new porous material, stimuli responsive materials, and sensing materials. Each of these breakthrough materials areas relies on a fundamental principle discovered over the previous project years and we are in a unique position to exploit that knowledge. One of the applications centers on the synthesis and characterization of Pt-metallopolymers featuring NHC ligands. The goal for this work is to prepare metallopolymers of the general formula depicted in Figure 4. Initial studies have focused on small molecule additions to the Pt-acetylides and future work will center on progress to the metallopolymers.

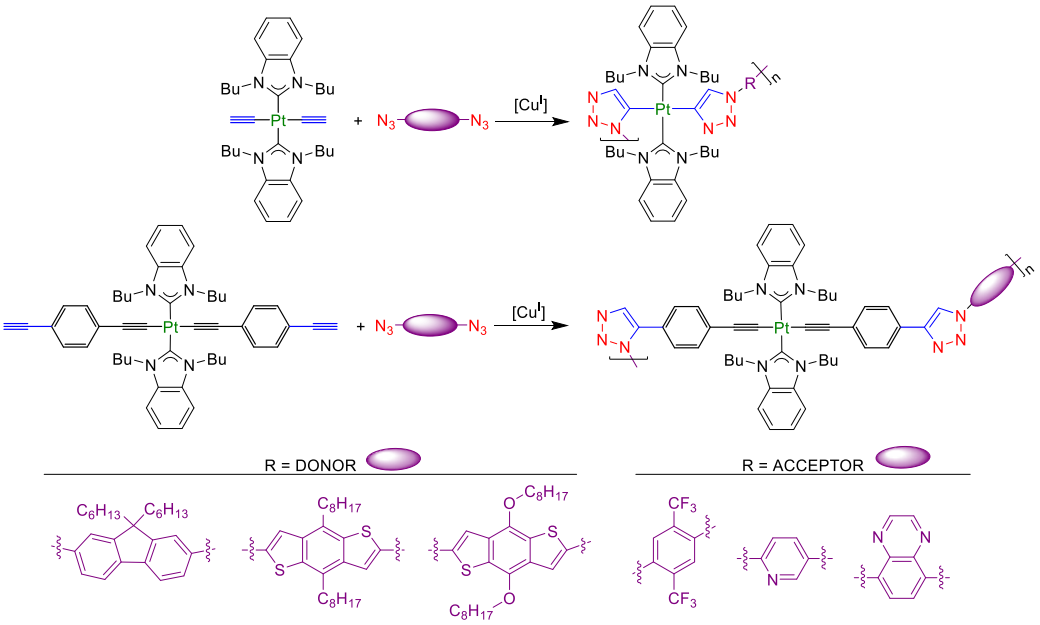

Figure 4. Proposed synthesis of in-chain conjugated Pt(II)-NHC metallopolymers via A-A/B-B step growth polymerization.

Publications

1. Shen, Y-H; Esper, A. M.; Ghiviriga, I.; Abboud, K. A.; Schanze, K. S.; Ehm, C.;* Veige, A. S.* *SPAAC iClick: Progress Towards a Bioorthogonal Reaction Incorporating Metal Ions*, *Chem. Sci*, **2021**, under revision.
2. Makal, T. A.; Veige, A. S.* Development of Inorganic Click (iClick) and Related Cycloaddition Chemistry, *Comprehensive Coordination Chemistry III*, Elsevier, **2021**, *accepted*.
3. Zeman, C. J. III; Shen, Y-H.; Heller, J. K.; Abboud, K. A.; Schanze, K. S.*; Veige, A. S.* Excited state turn-on of aurophilicity and tunability of relativistic effects in a series of digold triazolates synthesized via iClick, *J. Am. Chem. Soc.* **2020**, *142*, 8331-8341.
4. Beto, C. C.; Zeman, C. J. III; Yang, Y.; Bullock, J. D.; Holt, E. D.; Kane, A. Q.; Makal, T. A.; Yang, X.; Ghiviriga, I.; Schanze, K. S.*; Veige, A. S.* A application exploiting aurophilic interactions and iClick to produce white light emitting materials, *Inorg. Chem.* **2020**, *59*, 1893-1904.
5. Beto, C. C.; Yang, Y.; Zeman IV, C. J.; Ghiviriga, I.; Schanze, K. S.;* Veige A. S.* Cu- Catalyzed Azide-Pt-Acetylide Cycloaddition: Progress To-wards a Conjugated Metallopolymer via iClick. *Organometallics*, **2018**, *37*, 4545-4550.

Pi-Extended Porphyrins Fused with Five- and Six-Membered Rings: Synthesis, Characterization and Property Studies

Hong Wang, Professor, Department of Chemistry, University of North Texas

Francis D'Souza, Reagent Professor, Department of Chemistry, University of North Texas

Program Scope

Largely π-extended structures represent one most fascinating yet very challenging frontiers in chemistry and materials science. Incorporating both porphyrins and polycyclic aromatic hydrocarbons to obtain largely π-extended multichromophoric systems is especially attractive as the resulted largely π-extended systems are reminiscent of "nanographenes" doped with heteroatoms.[1, 2]

π-Extended porphyrins have been known for decades.[3, 4] However, due to the limited availability of synthetic methods, only the simplest symmetrical π-extended porphyrins could be obtained in low and poorly reproducible yields. The Wang group has been engaged in developing concise and versatile synthetic and functionalization methods for π-extended porphyrins. The availability of these methods has opened the door to access a large number of π-extended porphyrins with novel functionalities.[5-9] The purpose of this proposed project is threefold. First, we will develop concise and versatile synthetic methods to further extend the porphyrin π-system. Second, we will use these methods to design and access different types of PAH-fused porphyrins including extended PAH-fused, acene-fused, and cyclooctatetraene-fused π-extended porphyrins. Third, we will study the optical-, electronic-, and photophysical properties of these compounds using DFT calculations, UV-Vis/fluorescence spectroscopy, electrochemistry and spectroelectrochemistry, femto- and nanosecond transient absorption spectroscopy.

Recent Progress

We have developed several new synthetic methods to fuse different type of aromatic rings to the porphyrin periphery at the β, β-positions in the past two years. Using these methods, we have designed and prepared a number of novel π-extended porphyrin systems with fused 5- and 6-membered rings including pentacene-, pentaquinone-, acenaphtho[1,2-*b*]pentacene- and 12*H*-benzo[*f*]benzo[4,5]imidazo[2,1-*a*]isoindole-fused porphyrins.[8, 10-12] Nickel porphyrin-fused pentacenes demonstrated unusual stability. Investigation of the abnormal stability using femtosecond transient absorption technique suggested nickel porphyrin centered photo-events leading to a short-lived intermediate charge transfer state, consequently blocking the photodegradation pathways of pentacene.[10] Unsymmetrical pentacene-fused molecular systems exhibited broad and intense near-IR absorptions in the 1800-2200 nm range for both radical cation and radical anions, illustrating the exceptional ability of these pentacene-fused systems to accommodate both positive and negative charges.[11] These largely π-extended molecular systems

displayed unusual UV-Vis absorption patterns and rich redox chemistry with up to 8 observable redox states.

Figure 1. Pentacene-, acenaphtho[1,2-b]pentacenequinone - and benzoimidazoisoindole-fused porphyrins.

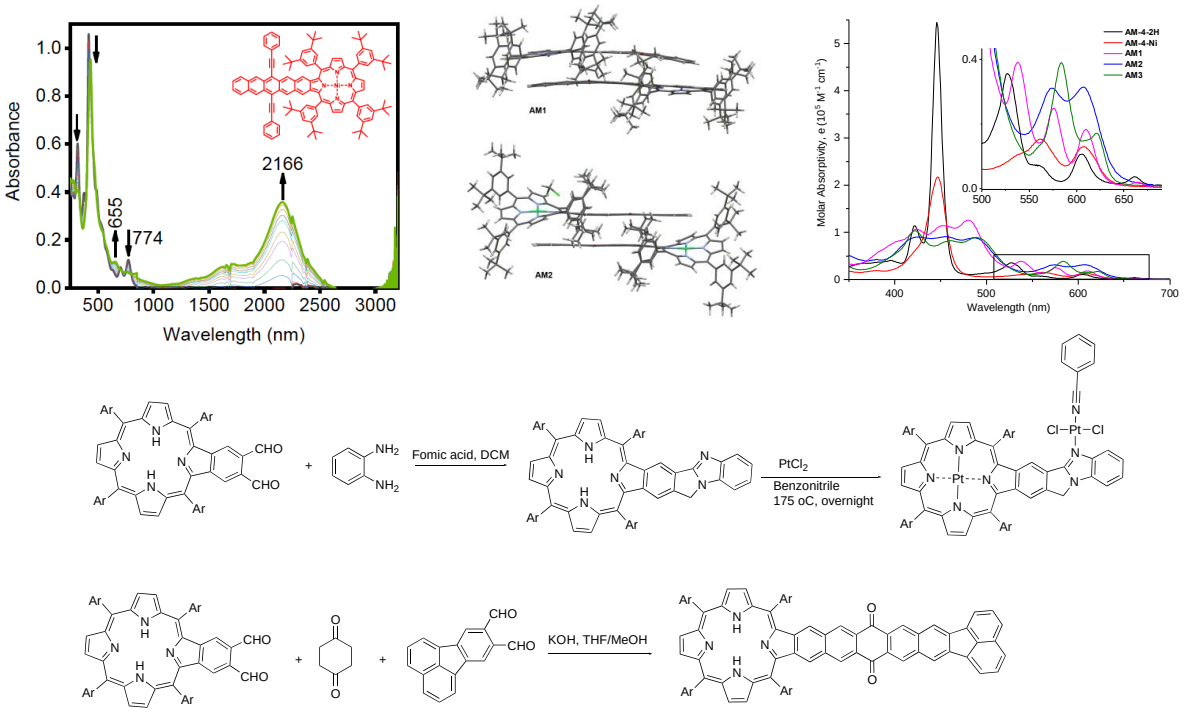

Future Plans

1. We will continue to work on methodology development to incorporate 8-member rings into the conjugated systems.
2. We will design and synthesize new cross-conjugated molecular systems incorporating larger pieces of polycyclic aromatic hydrocarbons.
3. We will study the electronic and photophysical properties of these compounds using UV-Vis spectroscopy, time-resolved and steady state fluorescence spectroscopy, transient spectroscopy, cyclic voltammetry and DFT calculations. We will establish property-structure relationships based on the shape, the topology and size of the PAHs fused to the porphyrin systems.

References

1. M. Stepien, E. Gonka, M. Zyla and N. Sprutta, *Chem Rev*, 2017, **117**, 3479-3716.
2. A. Narita, X. Y. Wang, X. Feng and K. Mullen, *Chem Soc Rev*, 2015, **44**, 6616-6643.
3. J. D. Spence and T. D. Lash, *J. Org. Chem.*, 2000, **65**, 1530-1539.

4. J. P. Lewtak and D. T. Gryko, *Chem. Commun.*, 2012, **48**, 10069-10086.

5. L. Jiang, J. T. Engle, L. Sirk, C. S. Hartley, C. J. Ziegler and H. Wang, *Org. Lett.*, 2011, **13**, 3020-3023.

6. L. Jiang, R. A. Zaenglein, J. T. Engle, C. Mittal, C. S. Hartley, C. J. Ziegler and H. Wang, *Chem Commun (Camb)*, 2012, **48**, 6927-6929.

7. S. Kumar, X. Jiang, W. Shan, R. G. W. Jinadasa, K. M. Kadish and H. Wang, *Chem Commun (Camb)*, 2018, **54**, 5303-5306.

8. L. Jiang, J. T. Engle, R. A. Zaenglein, A. Matus, C. J. Ziegler, H. Wang and M. J. Stillman, *Chem. Eur. J.*, 2014, **20**, 13865-13870.

9. S. Kumar, W. A. Webre, C. Stewart, F. D'Souza and H. Wang, *Org Lett*, 2020, **22**, 7078-7082.

10. Y. Hu, M. B. Thomas, W. A. Webre, A. Moss, R. G. W. Jinadasa, V. N. Nesterov, F. DQSouza and H. Wang, *Angew. Chem. Int. Ed.*, 2020, **59**, 20075-20082.

11. A. Moss, D. Nevonen, V. Nemykin and H. Wang, *unpublished result*.

12. A. Moss, Y. W. Jang, F. D'Souza and H. Wang, *unpublished result*.

Publications

1. Siddhartha Kumar, Whitney A. Webre, Courtney Stewart, Francis D'Souza*, Hong Wang*, "A Synthetic Approach to β-Functionalized Naphtho[2,3]porphyrins", *Org. Lett.* **2020**, 22, 18, 7078–7082.

2. Yi Hu, Michael B. Thomas, Whitney A. Webre, Austen Moss, R. G. Waruna Jinadasa, Vladimir N. Nesterov, Francis D'Souza* and Hong Wang*, "Bisporphyrin-Fused Pentacenes Exhibiting Abnormal High Stability", *Angew. Chem. Int. Ed.*, **2020**, 45 (132), 20250-20257.

3. Michael B. Thomas, Siddhartha Kumar, *Timothy Esquivel*, Hong Wang*, and Francis D'Souza*, "Excited State Electron Transfer in A2 and A2B2 Functionalized Zinc Porphyrins Carrying Rigid and Flexible β-Pyrrole π-Extended Substituents", **Invited article**, *Journal of Porphyrins Phthalocyanines*, **2020**, 24, 904-919.

4. Austen Moss, Zehua Zhou, Lin Jiang,* M. Graça H. Vicente,* Hong Wang*, Synthesis of highly water soluble tetrabenzoporphyrins and their application toward photodynamic therapy", **Invited article**, *Journal of Porphyrins Phthalocyanines*, **2020**, 24, 456-464.

5. Yi Hu, Whitney A. Webre, Michael B. Thomas, Austen Moss, *Sarah N. Hancock, Jacob Schaffner*, Francis D'Souza* and Hong Wang*, "*β*-Functionalized Push-Pull Opp-Dibenzoporphyrins as Sensitizers for Dye-Sensitized Solar Cells: The Role of the Phenylethynyl Bridge", *J. Mater. Chem. A,* **2019**, 7, 10712-10722.

6. Michael B. Thomas, Yi Hu, Karl M. Kadish,* Hong Wang,* Francis D'Souza*, "Accelerated Charge Separation and Charge Stabilization with Improved Quantum Yields upon Cation Binding to a Fused Bis Zinc Porphyrin-Quinone Donor-Acceptor Conjugate", *J. Phys. Chem. C,* **2019**, 123, 36, 22066-22073.

7. Siddhartha Kumar, Whitney Webre, *Jacob Schaffner,* Sheikh M. S. Islam, Francis D'Souza,* Hong Wang*, "A2 and A2B2 Benzoporphyrins as sensitizers for dye-sensitized solar cells", *Journal of Porphyrins and Phthalocyanines,* **2019**, 23, 599-610. **Invited article**.

8. Siddhartha Kumar, Xiaoqin Jiang, Wenqian Shan, R. G. Waruna Jinadasa, Karl M. Kadish and Hong Wang*, "*β*-*β*-Functionalized Trans-A2B2 Push-Pull Tetrabenzoporphyrins", *Chem. Commun.*, **2018**, 54, 5303-5306. **Highlighted in back Cover page**.

9. M. B. Thomas, R. G. W. Jinadasa, Y. Hu, *B. Schmitz*, H. Wang* and F. D'Souza*, "β-functionalized zinc porphyrin coordinated to C60 donor-acceptor conjugates", **Invited article**, *Can. J. Chem.*, **2018**, 96 (9), 881-889.

Understanding Interfacial Chemistry and Cation Order-Disorder in Mixed-Phase Complex Sodium Metal Oxide Cathodes for Sodium Ion Batteries

Hui (Claire) Xiong (Principal Investigator), Elton Graugnard (Co-Investigator), Micron School of Materials Science and Engineering, Boise State University

Eungje Lee, Yuzi Liu, Jeff Elam (Co-Investigators), Argonne National Laboratory

Program Scope

The major goal of this research program is to discover and understand the role of intergrown phases in the structural and electrochemical stability of layered complex sodium metal oxide (CSMO) cathode materials for sodium ion batteries (SIBs). This program focuses on testing the hypothesis that intergrown phases within complex sodium metal oxides (CSMOs) can suppress host rearrangement and enhance their structural stability and electrochemical properties. To test this hypothesis, the objectives of this program are to (1) understand the nucleation and growth of intergrown phases within CMSOs, (2) determine the chemical, electrochemical, and mechanical stability at phase interfaces within the bulk and at the electrode surface in the presence of electrolyte and upon electrochemical cycling, (3) understand the effect of intergrown phases on host rearrangement, defect evolution, and charge storage and transport, and (4) identify the fundamental charge storage and transport mechanisms of intergrown phases within mixed-phase CSMO cathode materials. Experimental work includes design and synthesis of new solid-state mixed-phase CSMOs and coatings, as well as advanced chemical, electrochemical, and structural characterizations of these materials.

Recent Progress

Despite the promise of mixed-phase CSMOs for improving electrochemical and structural properties, fundamental knowledge regarding thermodynamics, nucleation and growth of the intergrown phases, intercalation kinetics, interfacial chemistry, as well as structural stability of this class of electrode materials remain limited. This program aims to fill this knowledge gap by systematically investigating why and how intergrown phases in CSMOs can be utilized to enhance solid-state material energy, power and stability. We synthesized and investigated a series of biphasic or intergrown $Na_xLi_yTM_zO_2$ (TM: transition metals) layered compounds.

Origins of Irreversibility in Layered $NaNi_xFe_yMn_zO_2$: Layered sodium transition metal oxides Na_xTMO_2 ($x \leq 1$, TM=Ni, Fe, Mn) have received the most attention among cathode materials owing to their high capacity and close-packed structure. Binary or ternary mixtures of TMs often have a desirable balance of capacity and stability in Na_xTMO_2 that also minimizes the use of expensive or toxic elements such as Ni. Fe and Mn are abundant, and Ni provides two-electron Ni^{2+}/Ni^{4+} redox which enables high capacities. However, the influence of the TM composition and the operating potential window on the stability of the electrode has not been systematically investigated. *Understanding the evolution of the local TM bonding over many cycles is essential*

to understand the fundamental degradation mechanisms in $Na_1Fe_x(Ni_{0.5}Mn_{0.5})_{1-x}O_2$ cathode materials.

In this work, we elucidate the effects of the TM composition and potential window (2-4.0V or 2-4.3V) on the reversibility of O3-type layered $Na_1Fe_x(Ni_{0.5}Mn_{0.5})_{1-x}O_2$ (NFM) (x = 0.33, 0.5, 0.8). Galvanostatic cycling of NFM in sodium half-cells revealed that electrodes cycled at the higher operating potential window (2-4.3V) delivered larger initial capacities than the narrower window (2-4.0V), but the capacity faded more rapidly over many cycles (Fig. 1b). While all NFMs had comparable initial capacity, the samples with high content of Fe (x=0.8) demonstrated accelerated capacity fade in both potential windows. X-ray absorption spectroscopy (XAS) of pre-cycled (5th cycle) samples found that $Ni^{2+/4+}$ redox was the only significant contributor to charge compensation during the 5th cycle. $Fe^{3+/4+}$ redox is active in the first several cycles, *but on the 5th cycle Fe no longer participates in charge compensation, suggesting irreversibility of $Fe^{3+/4+}$ redox couple*. In both potential windows, XAS spectra of x=0.33 sample are highly reversible over the 5th cycle (Fig. 1c and d). When x=0.8, a significant irreversibility of $Ni^{2+/4+}$ redox is evidenced by irreversible shift in the Ni K-edge spectrum and shrinking of the Ni-O and Ni-TM distances (Fig. 1d and f). Thus, high Fe content (x=0.8) adversely affects the reversibility of Ni redox and its bonds. The effect of Fe on the Ni reversibility may be related to the irreversible oxidation of Fe^{3+} to Fe^{4+} in the first several cycles, which is inferred from the cumulative irreversible capacity over these cycles and the XAS measurements. More Fe^{4+} is formed initially at higher potentials and Fe content, to the detriment of Ni redox reversibility over further cycles. This insight on the Fe-Ni interaction provides a basis for designing methods which enhance the stability of $NaNi_xFe_yMn_zO_2$, and high-performance layered SIB cathode materials.

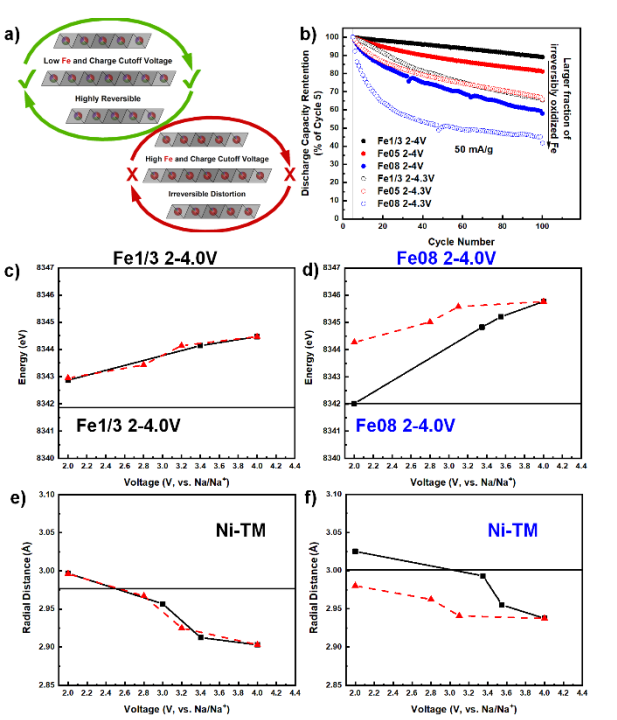

Figure 1. a) Schematic of the effects of Fe content and cutoff voltage; b) Capacity retention of NFM cathodes; c,d) First inflection point energy of Ni K-edge spectra and e,f) Ni-TM radial distance versus states of charge.

<u>*Intergrown $Na_{0.87}Li_xNi_{0.4}Fe_{0.2}Mn_{0.4}O_{2+\delta}$*</u>: Although the technology of O3-type layered cathodes for SIBs has rapidly developed, the cycling stability of such materials especially at high voltages (above 4.0 V vs. Na/Na^+) remains an issue. Phase transitions in O3-type layered cathodes play a crucial role in their charge storage properties. Particularly, the existence or reversibility of the phase transitions directly affects their stability during cycling. We prepared a series of Li-substituted layered-layered (O3/monoclinic) cathode material, $Na_{0.87}Li_xNi_{0.4}Fe_{0.2}Mn_{0.4}O_{2+\delta}$ (LS-

NFM, x = 0.0 – 0.3) to investigate phase intergrowth for enhanced sodium ion storage and cycling stability. For Li = 0 and 0.05, a single O3 type layered phase is observed. At Li 0.10 and above, two phases were present - the main O3 type phase (space group R-3m) and a secondary monoclinic phase (C2/m) assigned as $Li_xTM_yO_z$. The phase fraction of $Li_xTM_yO_z$ increases as the lithium content increases. The great structural compatibility and connectivity of the two phases are confirmed by XRD, selected area electron diffraction and high-resolution transmission electron microscopy (HR-TEM) (Fig. 2a-c). Intergrown LS-NFM electrodes exhibit enhanced rate capability and capacity retention compared to purely O3 NFM. The voltage profile of LS-NFM shows a reversible plateau above 4.0V, while the high voltage plateau of the NFM is irreversible. This suggests the enhanced structural and electrochemical stability of LS-NFM cathode is associated with the intergrowth phase that stabilized the crystal structure at high voltages.

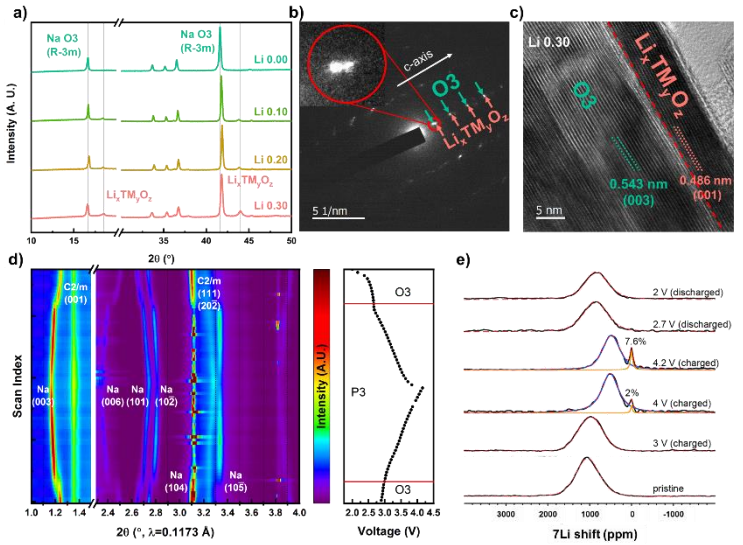

Figure 2. a) XRD of LS-NFM; b) SAED of LS-NFM; c) HR-TEM of LS-NFM; d) Operando synchrotron XRD of LS-NFM; e) ^{7}Li NMR showing the structural evolution of $Li_xTM_yO_z$ during the first charge-discharge cycle in the 2-4.2V potential window.

Operando XRD demonstrates a reversible phase transition of the O3 phase to P3, corresponding to gliding of layers during cycling (Fig. 2d) as evidenced by the increasing $d_{(003)}$ spacing and rapid decrease in the (104)/(10-5) intensity ratio. The $Li_xTM_yO_z$ phase showed shrinkage of $d_{(111)}$ and $d_{(20\text{-}2)}$ during charging to 4.2V while $d_{(001)}$ did not change indicating a contraction of the *ab*-plane. This shift was largely reversed on discharging to 2V. The result suggests that the $Li_xTM_yO_z$ phase participates in the structural evolution during cycling, which may be associated with the improvement in cycling stability. In addition, *ex situ* ^{7}Li NMR shows that the Li environment changes reversibly during cycling (Fig. 2e), corroborating the operando XRD results. Our work provides insight in the role of phase intergrowth in layered CSMOs for enhanced structural and electrochemical properties.

Role of Lithium Doping in P2-$Na_{0.67}Ni_{0.33}Mn_{0.67}O_2$: Lithium doping in layered Na_xTMO_2 has been widely shown to enhance the electrochemical properties. Due to their similar size, substitution of TMs by Li in octahedral sites is commonly assumed. Though less commonly reported, Li may occupy the prismatic sodium sites as well. *However, the influence of Li at different locations in P2-type cathodes has not been investigated previously.* We investigated the conditions which promote the placement of Li on either the octahedral TM or prismatic Na sites in P2-type $Na_{0.67}Ni_{0.33}Mn_{0.67}O_2$ (PNNMO) to evaluate the influence of Li on each site on the electrochemical

and structural properties. P2 type $Li_xNa_{0.67-y}Ni_{0.33}Mn_{0.67}O_{2+\delta}$, with different stoichiometric ratios of lithium and sodium to the TMs ($0.00 \leq x \leq 0.2$, y = 0, 0.1) were prepared. Other than the octahedral TM sites, the P2 structure has two prismatic sites in the sodium layer (Wyckoff 2b and 2d) which are partially vacant. Filling of the remaining vacancies with Li could allow for the modification of the properties of PNNMO while retaining the P2 structure. Specifically, two different Li modification strategies were demonstrated: LFN - *filling Li into both TM sites and vacancies in the prismatic Na layer by keeping the Na/TM ratio constant (y=0, x >0)*; and LSN - *stoichiometrically substituting (x=y=0.1) Na with Li to promote Li on the Na layer*. We found that although the filling of Li into the TM and Na layer of P2 (LFN) can be beneficial towards increasing capacity and stability, too much Li ($x \geq 0.2$) will destabilize the structure over many cycles. Conversely, when substituting Na with Li (*x=y=0.1*), the Li primarily occupies the Na-layer as suggested by solid state ^{7}Li NMR (Fig. 3a-b), synchrotron XAS and operando XRD characterizations (Fig. 3c). LSN showed significant enhanced cycling stability (84.6 mAh g^{-1} with >99% retention over 100 cycles) and a minor increase in specific capacity compared to the Li-free PNNMO (Fig. 3d). The enhanced structural and cycling stability in LSN is associated with higher occupancy of Li in the prismatic sites in Na layers and smaller volume change upon cycling. Our work has shown that Li at different positions (in TM layer and/or Na layer) in the P2 structure has substantially different effects on its electrochemical and structural properties.

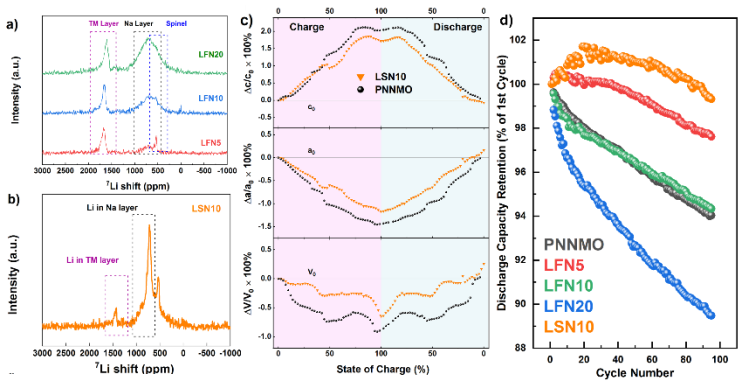

Figure 3. a,b) ^{7}Li NMR of lithium filled and lithium substituted cathodes; c) Evolution of lattice parameters and volume during first cycle for PNNMO and LSN10 extracted from operando XRD measurement; d) Capacity retention of PNNMO, LFN, and LSN samples.

Future Plans

In the future, we plan to continue our study of the discussed cathode systems and will explore the conditions related to temperature and time for nucleation and growth of intergrown phases through *in situ* TEM and *in situ* XRD, which were delayed due to the partial closure of ANL during the pandemic. Additionally, solid state NMR and neutron diffraction will help us understand the local structure of the intergrown phases. Electrochemical quartz crystal microbalance will track the activity of Li^+ and Na^+ during cycling to elucidate the evolution of the intergrown phases. We also plan to deposit NaF films through the established ALD process onto a variety of cathode materials and to evaluate the impact of the film on stability of the cathode electrolyte interface (CEI). Additionally, the NaF ALD process will be integrated with ALD processes for AlF_3 and LiF to form complex fluoride films in order to evaluate their impact on CEI and cathode performance. We will utilize established surface characterization (Raman, XPS, SECM, EC-AFM) to elucidate surface reactivities of the coated cathodes. The integration of computation models and methods will support and provide insight into the experimental results.

Publications

- Xie, Y.; Gabriel, E.; Fan, L.; Hwang, I.; Li, X.; Zhu, H.; Ren, Y.; Sun, C.; Pipkin, J.; Dustin, M.; Li, M.; Chen, Z.; Lee, E.; Xiong, H. Role of Lithium Doping in P2-$Na_{0.67}Ni_{0.33}Mn_{0.67}O_2$ for Sodium Ion Batteries. *Chem. Mater.* 2021, ASAP. https://doi.org/10.1021/acs.chemmater.1c00569

- Kuraitis, S.; Kang, D.; Mane, A. U.; Zhou, H.; Soares, J.; Elam, J. W.; Graugnard, E. Atomic Layer Deposition of Sodium Fluoride Thin Films. *J. Vac. Sci. & Tech. A* 2021, 39 (3), 032405. https://doi.org/10.1116/6.0000847 (Editor's Pick, ALD Special Topics cover art for the 2021 collection)

- Deng, C.; Gabriel, E.; Skinner, P.; Lee, S.; Barnes, P.; Ma, C.; Gim, J.; Lau, M. L.; Lee, E.; Xiong, H. Origins of Irreversibility in Layered $NaNi_xFe_yMn_zO_2$ Cathode Materials for Sodium Ion Batteries. *ACS Appl. Mater. Interfaces* 2020, 12 (46), 51397–1408. https://doi.org/10.1021/acsami.0c13850

- Deng, C.; Skinner, P.; Liu, Y.; Sun, M.; Tong, W.; Ma, C.; Lau, M. L.; Hunt, R.; Barnes, P.; Xu, J.; Xiong, H. Li-Substituted Layered Spinel Cathode Material for Sodium Ion Batteries. *Chem. Mater.* 2018, 30 (22), 8145–8154. https://doi.org/10.1021/acs.chemmater.8b02614.

BES Materials Chemistry DE-SC0018075

An Integrated Theoretical and Experimental Approach to Achieve Highly Polarizable Relaxor Ferroelectric Liquid Crystalline Polymers

PI: Lei Zhu, co-PI: Philip Taylor
Department of Macromolecular Science and Engineering, Case Western Reserve University, Cleveland, Ohio 44106, email: lxz121@case.edu

co-PI: Bin Zhao
Department of Chemistry, University of Tennessee, Knoxville, TN 37996, email: bzhao@utk.edu

Abstract for 2021 BES Materials Chemistry program PI meeting

Ferroelectric liquid crystalline polymers are functional materials for energy-related applications such as electrocaloric cooling and liquid crystalline elastomers for actuation. However, they usually exhibit a low spontaneous polarization, thus limiting the high performance. This can be attributed to the weak dipolar group used and decreased dipole density by the presence of aromatic mesogens. In this project, we aim to achieve mesogen-free ferroelectric liquid crystalline polymers, which possess a smectic C* (SmC*) type of self-assembly. To realize the SmC* packing, the main chain of the polymer is based on isotactic polyepichlorohydrin with a main-chain chiral center. In the alkyl side chains, highly dipolar sulfonyl groups (dipole moment = 4.5 D) are placed at different places: right next to and away from the main chain. Various alkyl side chains are studied; *n*-alkyl (non-chiral), chiral and racemic branched alkyl chains. It is found that the non-chiral *n*-alkyl side chains induce either crystalline or smectic A (SmA) liquid crystalline phases. Chiral branched side chains induce crystalline phases because of double chirality in both main chain and side chains. Intriguingly, racemic methyl-branched side chains can induce the SmC* liquid crystalline self-assembly. Currently, experiments are being carried out study their ferroelectric property.

DE-SC0018021: Understanding and Controlling Aggregation Processes in Mixed-Molecular Solids

Jeramy D. Zimmerman, Colorado School of Mines.

2021 Abstract

Program Scope

Over the last two decades an immense improvement in our understanding of the underlying mechanisms governing organic photovoltaics has been enabled, in large part, through understanding of morphology enabled by the development of advanced scattering techniques (e.g., X-ray and transmission electron (TEM) microscopy based). However, many materials, such as those for organic light emitting diodes (OLEDs), are difficult to probe with these techniques because of the poor contrast between different molecules and the weak chemical discrimination capabilities, making correlations to morphology difficult or unfeasible. As OLED devices are driven to the high brightness needed for display or lighting, significant losses in efficiency occur through triplet-triplet annihilation (TTA) and triplet-polaron quenching (TPQ); these mechanism are also though to be the primary mechanisms through which the molecular materials degrade. Literature models for TTA & TPQ typically assume that the emissive guest (typically 3-10 vol% doping) is randomly dispersed in the wider-gap host material. Clustering of molecules is expected to greatly increase TTA and TPQ rates due to the placement of molecules much closer together and making it easier for excited states to interact.

We have developed atom probe tomography (APT) techniques that extend its applicability to include organic molecular solids to probe materials such as OLEDs. APT combines point projection microscopy with time-of-flight mass spectrometry to provide an unparalleled nm-scale spatial resolution with concurrent mass-to-charge based chemical discrimination of <1 Da, providing. This gives the ability to probe morphologies previously unattainable and develop new structure-property relationships for solid-state blends of molecules. These mixed-molecular solids are important for a wide variety of materials, including use in devices such as OLEDs, high resolution photoresists, charge carrier doping of organic electronics, and organic photovoltaics (OPVs). This project uses primarily OLED materials to test and validate our conclusions because there are a wide variety of materials commercially available and the lessons learned will improve efficiency of OLED lighting and displays, reducing energy consumption in homes and mobile devices.

Morphology of these organic molecular materials is characterized from 100 nm-scales down to the molecular-dimer scale using APT, while TEM and atomic force microscopy (AFM) are used to probe the materials at larger scales (50 nm to 5 μm). Spatial statistics provides quantitative analysis of the APT generated point cloud data to aid in quantitative understanding of clustering. This morphology will then be correlated to physical properties of the material blends, such as the emission efficiency, transport properties, and types of energy loss mechanisms that dominate the materials (TTA & TPQ) to provide a deeper understanding of physical limitations of the materials themselves and hot to better design structures with reduced losses and degradation.

Recent Progress

In the first year of this project, we focused on refinement of atom probe tomography (APT) for molecular organic materials. We have shown that APT can be applied molecular organic systems,

where it can have a mass resolution of < 1 Da, a spatial resolution of ~0.3 nm in z and as good as ~1 nm in x-y, an analytic sensitivity of ~50 ppm, and we observe no evidence of fragmentation of molecules, making APT a very compelling technique for characterizing the morphology of small-molecule organic semiconducting systems. A paper detailing these attributes was published in Chemistry of Materials in 2019. [1]

In the second through fourth years of this project, our primary goal has been to develop structure-property relationships for these OLED materials and relate these to the morphology data. We have also found it necessary to further develop APT processes, understanding, and data analysis more than we had expected. Specifically, we have developed a developing an in-depth spatial statistics analysis framework for understanding our APT data, including a machine learning-based approach to analyze the point-patterns generated from the APT data to extract parameters such as cluster radius and concentration of a species in and out of clusters. [2] We have also developed new analysis tools to understand the APT process itself and resolution limitations that arise during this destructive analysis technique, such as fragmentation of molecules and factors contributing to aberrations in the APT data such as the field needed to field evaporate various molecules.

Correlation between morphology and photophysical properties:

Most analysis of OLEDs assumes that the distribution of light-emitting guests is random within the host material. In this work we look at the dispersion of *Tris(2-phenylpyridine)iridium (III)*, (e.g. $Ir(ppy)_3$) in a host matrix of *3,3'-Di(9H-carbazol-9-yl)-1,1'-biphenyl* (m-CBP), a prototypical guest:host system. This host has a relatively large glass transition temperature ($T_g \approx$ 97 °C), which is typically assumed to create a guest-host dispersion that is relatively stable.

Samples were created by vacuum thermal evaporation and the substrate temperature was varied (from T_{sub}=-50 °C to +50 °C) to change the extent at which molecules can diffuse on the surface before being buried and trapped in place. Devices were analyzed for a variety of properties including zero-field mobility of positive polarons (i.e., holes) in the devices, TTA, TPQ, and current-voltage-brightness analyses.

We observe that the zero-field mobility can be reduced by about two orders of magnitude when the substrate deposition temperature is reduced from 50 °C to -25 °C (see Fig. 1), in agreement with a Gaussian-disorder charge transport models.[3] This likely occurs because holes hop between $Ir(ppy)_3$ molecules and will be impacted by the orientational order between neighboring molecules.

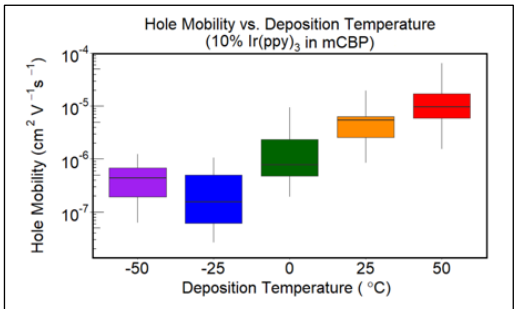

Figure 1. Zero-field mobility for films of mCBP with 10% $Ir(ppy)_3$ deposited at various substrate temperatures.

We use photoluminescence quenching experiments to observe TPA; in these experiments a laser excites the material and and 20 ns current pulses are passed through the devices to momentarily increase the polaron density in the films, leading to a momentary reduction in the luminescence brightness from TPQ. This quenching is shown in Figure 2. We see that the coldest devices show the lowest TPQ rates, which suggests that the holes and the excitons have less spatial overlap relative to layers deposited at higher temperatures.

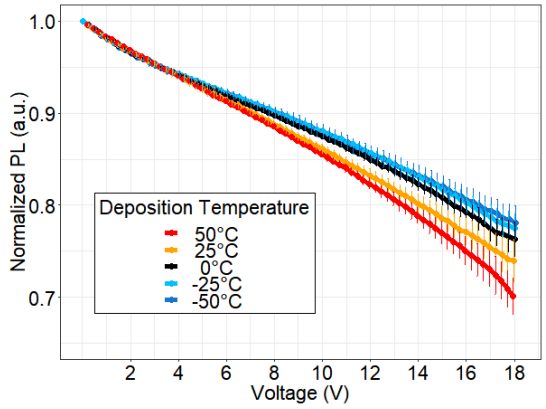

Figure 2. Photoluminesence quenching vs. applied voltage for active layers deposited between -50 °C and 50 °C showing that layers deposted at lower temperatures exhibit less TPQ.

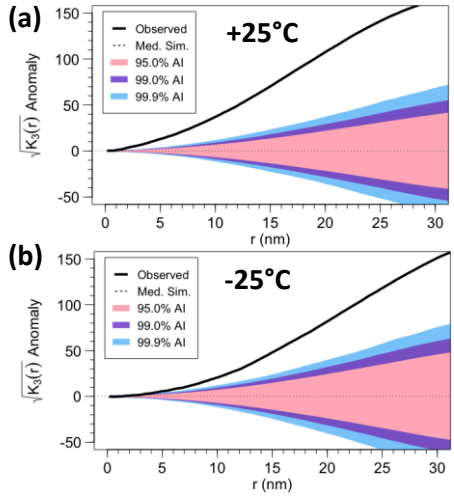

Figure 3. K-functions for mCBP with 10% $Ir(ppy)_3$, deposited at different substrate temperatures. More clustering is shown for warmer substrate temperatures.

We measure the time-resolved photoluminescence (TRPL) curves for a comparable set of films and fit the data to a single-step Förster based TTA model. In this case, we see a weak correlation between the rate constant and the deposition temperature. This is suggestive that the Förster radius for capture is large and or that there is sufficient clustering occurring in the cold-deposited film that changes in TTA are not readily observed. TEM images of films deposited at T_{sub}=+25 °C and -25 °C show that there are large clusters (10s of nm in dimension) that are sparce throughout the film and that their concentration can be reduced by reducing the substrate temperature during deposition. We have also used conductive-AFM and confirm that these clusters have a high conductivity relative to the remainder of the film.

APT data was acquired on m-CBP:$Ir(ppy)_3$ films deposited on smooth silicon tips held at a substrate temperature of T_{sub}=+25 °C and -25 °C. Films were analyzed using Ripley's K-function, as shown in Fig. 3. The K-function analysis counts the number of guest molecules within a given radius of each guest molecule normalized to the overall intensity in the sample. We use statistical relabeling of the underlying point cloud to calculate acceptance intervals (AI) for randomly dispersed morphologies. Films deposed at both temperatures show statistically significant clustering at (r<5 nm), but the extent is larger in the sample grown at a higher substrate temperature warmer sample. The large deviation outside of the envelopes at higher radii is due to small variations in the guest density at long ranges caused by either large scale clustering or variations in deposition rate throughout the layer thickness.

More detailed analysis of these APT data intended to create visual depictions of the clustering has proven difficult. We attribute this to differences in the field needed to evaporate the two different molecules in the film, which results in lateral smearing of the data (called "chromatic aberration" in the APT field). To better understand this phenomenon and select better molecule pairs, for APT analysis, we have developed a technique to better extract the evaporation field for molecules. In this we see that the evaporation field is closely correlated to molecular mass. The mass difference between m-CBP (m= 484.59 da) and $Ir(ppy)_3$ (m= 654.78da) results in significant field evaporation differences. Simulations suggest that the chromatic aberration is roughly

quadratically dependent on the evaporation field ratio. APT data better matched molecules TCP (m= 573.68 da) and $Ir(ppy)_2(acac)$ (m=599.70 da) indeed shows clustering that is visible.

Future Plans:

Using our recent findings, we have revised our plan to investigate materials with similar evaporation fields, allowing for better morphology analysis. Recent our simulations show that TRPL lifetimes and photoluminescence quantum yield for a particular material are highly dependent on the number of nearest neighbors and less susceptible to long range exciton transfer (than in the case of TTA) and may provide a better indicator of clustering in devices. Studies of guest dispersion in a number of guest:host systems with compatible evaporation fields to look for clustering and then correlate those to know efficiency metrics.

References

1. Proudian, et al., "Atom Probe Tomography of Molecular Organic Materials: Sub-Dalton Nanometer-Scale Quantification" *Chemistry of Materials* **31,** 2241-2247 (2019).
2. Galen B. Vincent, Andrew P. Proudian, and Jeramy D. Zimmerman, "Three Dimensional Cluster Analysis for Atom Probe Tomography Using Ripley's K-function and Machine Learning" Ultramicroscopy **220**, 113151 (2021).
3. H Bässler, "Charge Transport in Disordered Organic Photoconductors", Physica Status Solidi (B) 15, 15–56 (1993).

Publications supported by this DOE BES program

Papers:

1. Galen B. Vincent, Andrew P. Proudian, and Jeramy D. Zimmerman, "Three Dimensional Cluster Analysis for Atom Probe Tomography Using Ripley's K-function and Machine Learning" Ultramicroscopy **220**, 113151 (2021).
2. Andrew P. Proudian, Matthew B. Jaskot, David R. Diercks, Brian P. Gorman, and Jeramy D. Zimmerman, "Atom Probe Tomography of Molecular Organic Materials: Sub-Dalton Nanometer-Scale Quantification" *Chemistry of Materials* **31,** 2241-2247 (2019). https://doi.org/10.1021/acs.chemmater.8b04476 link to cover

Dissertations & Theses generated

3. PhD Dissertation: Matt B Jaskot "Linking morphology to electronic properties in small-molecular organic semiconductors" PhD Dissertation, Colorado School of Mines, Dec 2020. Available through Mountain Scholar: https://mountainscholar.org/handle/11124/176334
4. *PhD Dissertation*: Andrew P Proudian, "Atom Probe Tomography of Small-Molecule Organic Semiconducting Materials" PhD Dissertation, Colorado School of Mines, Dec 2019. Available through Mountain Scholar, https://mountainscholar.org/handle/11124/173992)
5. *MS Thesis*: Joseph Bales, "Solubility characteristics of luminescent materials for organic light emitting diodes" MS Dissertation, Colorado School of Mines, Jan 2020. Available through Mountain Scholar, https://mountainscholar.org/handle/11124/174059

Crystal Growth of New Complex Actinide Containing Oxides, Fluorides and Chalcogenides and the Investigation of their Optical and Magnetic Properties

Hans-Conrad zur Loye
Department of Chemistry and Biochemistry
University of South Carolina

Program Scope

Our research continues to focus on improving our understanding of actinide crystal chemistry via the synthesis and characterization of uranium and thorium oxides, fluorides, and chalcogenides. We target new synthetic approaches that build upon the existing crystal chemical knowledge of extended actinide structures to achieve the synthesis of entirely new families of actinide materials. The three classes of materials that we are investigating, oxides, fluorides, and chalcogenides, enable us to tune the actinide material's ionicity via the choice of anion that, in the case of uranium, will favor specific oxidation states as well as provide control over the expected electronic attributes of the targeted materials. Actinide fluorides have highly ionic structures and, thus, localized electrons, enabling the formation of structures exhibiting long range magnetic order. By contrast, our investigation of actinide chalcogenides enables us to probe the decrease in the overall ionicity as we transition from oxides to sulfides to selenides to tellurides, progressing to enhanced metallicity that will accompany the steady change from localized and magnetic electronic states to more delocalized and ultimately itinerant electrons. Our recently developed Boron Chalcogen Mixture (BCM) method for preparing oxygen free actinide chalcogenides is a key factor for achieving these goals, as it greatly improves the synthesis of actinide chalcogenides.

Recent Progress

Hydrothermal Crystal Growth of Fluorides:

During our previous funding period we had reported on the synthesis, crystal structures and magnetic properties of numerous uranium containing fluoride phases, including the $Na_nMU_6F_{30}$ and $Na_nMTh_6F_{30}$ series. (1) The $U_6F_{30}^{n-}$ framework can accommodate both di- and trivalent p- and d-metals, including divalent Mn^{2+}, Co^{2+}, Ni^{2+}, Cu^{2+}, Zn^{2+} and trivalent Al^{3+}, Ga^{3+}, Ti^{3+}, V^{3+}, Cr^{3+}, Fe^{3+} elements. We extended this work to the analogous thorium containing compositions, $Na_nMTh_6F_{30}$, where n = 3 when M^{III} = Al, Sc, Ti, V, Cr, Fe, Ga, or In; n = 4 when M^{II} = Mg, Mn, Co, Ni, Cu, or Zn; and n varies from 3.87 to 4.39 when the M site is partially occupied by a larger trivalent element, (In, Y), including some rare earth cations (Lu, Yb, Tm, Er, Ho, Dy). (2) In total we prepared 17 new compositions that crystallize in the trigonal space group $P\bar{3}c1$ and that are based on a framework built from vertex- and corner-sharing ThF_9 and MF_6 polyhedra. Although the framework was able to accommodate several lanthanides, our numerous attempts to obtain a lanthanide-containing compound with a full M site occupancy were unsuccessful, suggesting that the structure type reaches a certain size limit, after which only a partial site occupancy is possible.

Using the same synthetic methodology, we discovered an entirely new family of Cs containing quaternary fluorides, the $Cs_2MU_3F_{16}$ (M = Mn^{2+}, Co^{2+}, Ni^{2+}, Zn^{2+}, Mg^{2+}) series. This represents not only a new structure type, but this series is the first to exhibit long range magnetic order via coupling between a U(IV) cation and 3*d* transition metal cations in fluorides. (3) All five compounds crystallize in the centrosymmetric hexagonal $P6_3/mmc$ space group. The novel structure type consists of U(IV) sheets connected through M^{2+} cations, which creates a framework

containing channels in which the Cs atoms are located. The U(IV) fluoride sheet consists of uranium trimers connected through a μ_3-F^- anion; the trimers connect to each other by edge-sharing. Three fluoride ions from the top of one trimer and the bottom of another trimer, located above it, are coordinated to the M^{2+} cations. This creates an octahedral coordination environment for M^{2+} consisting of six fluoride ions from two sheets; building unique $(–M–U_3F_{22}–)_\infty$ pillars, which play a crucial role in the magnetism of these compounds. (Figure 1)

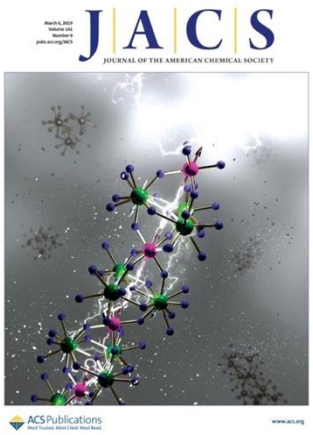

Magnetic susceptibility measurements of these phases containing Mn, Co and Ni revealed the presence of long range magnetic order, at 14 K, 4.8 K and 3.5 K, respectively. To further characterize these phases, we collected neutron diffraction data at ORNL and determined the magnetic structure, shown in Figure 1, where the total net moment of the magnetic unit cell, containing 6 spin up and 3 spin down pillars, is 15.90 μ_B for $Cs_2MnU_3F_{16}$.

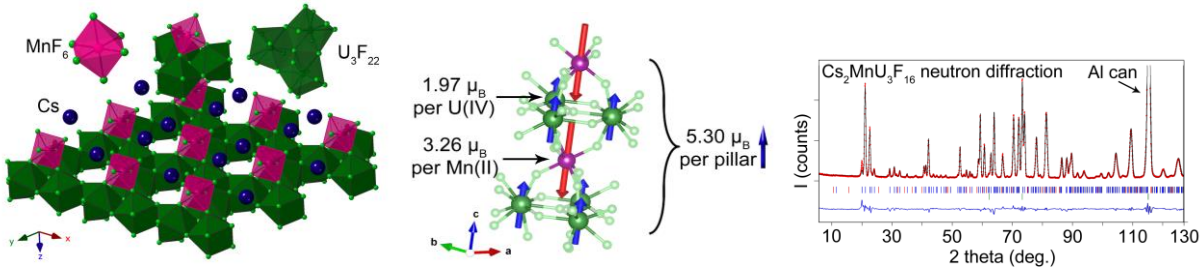

Fig. 1. (Left) $Cs_2MnU_3F_{16}$. $[U_3F_{16}]^{4-}$ sheets (green) are composed of uranium trimers, which are connected into sheets. The framework is formed by connecting the sheets through MnF_6 (pink) octahedra with cesium atoms (blue) between them. (middle) Single pillar of uranium trimers and manganese octahedra carry magnetic moments of 3×1.97 and 3.26 μ_B on them. (right) Rietveld refinement of the magnetic structure of $Cs_2MnU_3F_{16}$.

Applying the Boron-Chalcogen-Mixture (BCM) Method to Target New Chalcogenides: Actinide chalcogenides adopt diverse structure types with distinct chemical compositions and specific actinide oxidation states, which offer unique opportunities for studying 5*f* electron properties. One of the main obstacles faced when synthesizing the actinide chalcogenides are actinide oxide and oxychalcogenide impurities that often contaminate the resulting products and interfere with their property measurements. (4) Due to the high oxygen affinity of the actinides, even trace amounts of oxygen in the system will inevitably result in the formation of these impurities. Although careful oxygen exclusion from the reaction media is an intuitive and straightforward approach for avoiding oxide impurities, it is unfortunately often nearly impossible to eliminate oxide contamination present in the reagents themselves. This difficulty of needing to effectively deal with oxide or oxychalcogenide impurities in the starting materials motivated us to explore different synthetic approaches that would allow for the use of oxygen-contaminated reagents, or even oxides themselves, as the starting materials for the synthesis of oxygen free actinide chalcogenides. The ability to use binary metal oxides is especially useful when targeting products containing elements for which the simple binary metal chalcogenides are not commercially available. This is the situation for most rare earths, uranium, and thorium.

In situations where oxygen cannot be avoided in the initial reagent mixture, it is reasonable to consider the use of a highly oxophilic sacrificial component, such as boron, that would extract oxygen and subsequently leave the reaction mixture or be dissolvable in post-reaction work-up. The boron acts as an “oxygen sponge” forming highly stable B_2O_3 while leaving the sulfur to

replace oxygen. (Scheme 1) The success of the sulfurization is based on the differences between the formation energies of B_2O_3 ($\Delta_f G°$(vitreous-B_2O_3) = -1182.5 kJ/mol) and B_2S_3 ($\Delta_f G°$(vitreous-B_2S_3) = -247.6 kJ/mol), which strongly favors the formation of B_2O_3 thus leaving sulfur to react with the other reagents. (5) (6)

We applied the boron-chalcogen mixture (BCM) method to the synthesis of actinide chalcogenides from their respective oxide precursors. To demonstrate the efficacy of the BCM method, we performed the synthesis of ThS_2 and US_2 starting from ThO_2 and U_3O_8, the solid state syntheses of U*M*S_3 (*M* = Ni and Co) perovskites starting with oxide reagents to measure the magnetic properties of $UNiS_3$ for the first time, the adaptation of the BCM method to flux crystal growth and the formation of the new family of rare earth uranium sulfides, $Ln_xU_2S_5$ (Ln = Pr, Nd, Sm, Gd-Yb) containing mixed valent U(III/IV), the crystal growth of the new complex thorium thiophosphate $Rb_{1.72}Na_{0.68}I_{0.40}[Th(PS_4)_2]$ using ThO_2 as a starting reagent, and the crystal growth of the known uranium(V,VI) sulfide $Cs_6Cu_{12}U_2S_{15}$ (7) now also obtained using the BCM method's *in situ* generated polychalcogenide flux.

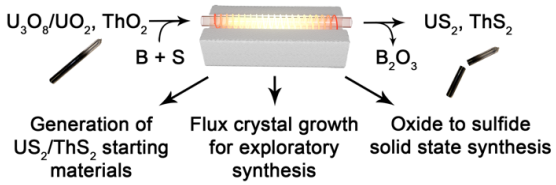

Scheme 1

Future Plans

New Chalcogenides:

The BCM method paves the way toward fast screening of chalcogenide phase space in the systems that are promising for potential magnetism. With the experience obtained from the fluoride systems, we are planning to pursue several different directions with chalcogenides by studying the magnetic interactions between U(IV) and 3*d* transition metal and rare earth metal cations, as well as the magnetism of actinides in higher oxidation states. The first approach requires application of the BCM method for solid state reactions, while exploratory crystal growth will be employed for creating new U(V) chalcogenides.

Inducing magnetic ordering in U(IV) using 3*d* transition metal and rare earth metal cations is an approach that proved useful with fluorides and that can work with chalcogenides as well. We conducted a search for structurally similar chalcogenides and identified Ba_3MnUS_6, a composition that crystallizes in a 2H hexagonal perovskite related structure type for which the main structural feature is the presence of 1D chains composed of face-sharing trigonal prisms and octahedra. The successive arrangement of the 3*d* metal cation Mn(II) and U(IV) results in magnetic exchange interactions that induce magnetic ordering in the compound. Figure 2. We will pursue the synthesis of several members of this family via the BCM method and study their magnetic properties.

We will target the preparation of diverse copper and silver actinide chalcogenides to explore our ability to control actinide oxidation states. In most of the uranium and in all neptunium and plutonium chalcogenides, the oxidation state of the actinide does not exceed +4 due to the strong reducing conditions in chalcogenide-rich reactions. However, Ibers et al. showed that rare +5 and +6 uranium oxidation states can be stabilized in chalcogenides, even when using uranium metal as a starting material. To demonstrate the applicability of the BCM method to the synthesis of high valent uranium sulfides, we applied it to the alkali copper uranium sulfide system. Using the BCM method, we already achieved an extraordinary success by nearly doubling the number of $U^{5+/6+}$ containing compounds in the A–U–Cu–S system since introducing the method one year ago. For example, rod-like crystals of $Cu_6U^{6+}S_6$ (superscript numbers denote formal oxidation states) formed in a reaction between U_3O_8, Cu, Na_2CO_3, B, and S. Low temperatures, around 600 °C, allow for stabilization of another composition, disulfide-containing $Na_5Cu_6U_2^{5.5+}S_8(S_2)_3$ with

hexagonal bipyramidal coordination of uranium atoms, a local coordination environment that has not been observed in actinide chalcogenides, but which is quite common in uranyl oxides. Along with ongoing efforts for obtaining new sulfide compounds, we demonstrated that the BCM method shows excellent results in the synthesis of selenide compounds by flux growth of the selenide analogs of the sulfide phases. (Figure 3) Furthermore, we have started a collaboration with the University of Nevada, Las Vegas to examine the applicability of the BCM method to transuranium chalcogenides, resulting in the new neptunium sulfide $NaCuNpS_3$. (Figure 3) Overall, our preliminary data provides clear evidence for the future success of this direction and strongly supports extending this work to selenides and tellurides.

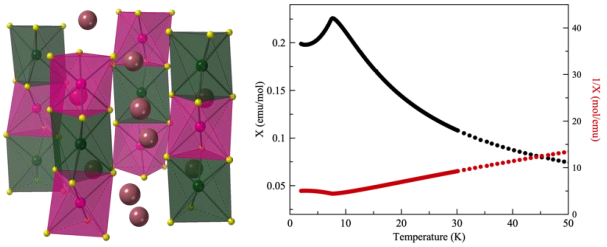

Fig 2. 2H hexagonal related perovskite, Ba_3UMnS_6, along with a plot showing its antiferromagnetic properties (right).

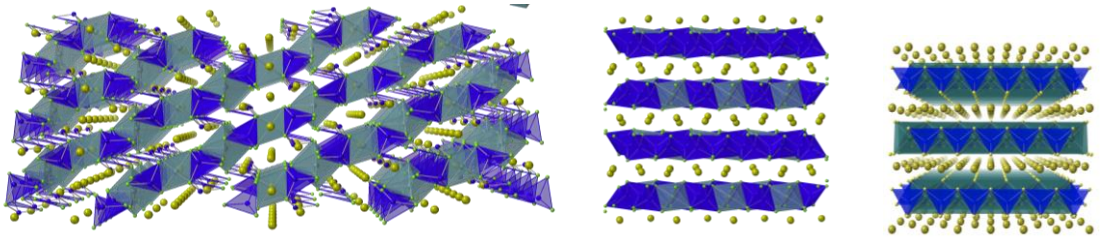

Fig. 3. (left) $Na_5Cu_6U_2Se_{14} = Na_5Cu_6U^{5.5+}{}_2Se_8(Se_2)_3$; (middle) $Na_3Cu_4U^{5+}Se_6$; (right) $NaCuNpS_3$.

References

1. Yeon, J., M. D. Smith, J. Tapp, A. Moller, and H.-C. zur Loye. "Application of a mild hydrothermal approach containing an in situ reduction step to the growth of single crystals of the quaternary U(IV)-containing fluorides $Na_4MU_6F_{30}$ (M = Mn^{2+}, Co^{2+}, Ni^{2+}, Cu^{2+}, and Zn^{2+}) crystal growth, structures, and magnetic properties", *J. Am. Chem. Soc.*, **2014**, *136*, 3955-63.
2. Klepov, V. V., G. Morrison, and H.-C. zur Loye. "$Na_nMTh_6F_{30}$ – a Large Family of Quaternary Thorium Fluorides", *Cryst. Growth Design*, **2019**, *19*, 1347-1355.
3. Klepov, V. V., K. A. Pace, S. Calder, J. B. Felder, and H.-C. zur Loye. "3d-Metal Induced Magnetic Ordering on U(IV) Atoms as a Route Toward U(IV) Magnetic Materials", *J. Am. Chem. Soc.*, **2019**, *141*, 3838-3842.
4. Mesbah, A., J. Prakash, J. C. Beard, E. A. Pozzi, M. S. Tarasenko, S. Lebegue, C. D. Malliakas, R. P. V. Duyne, and J. A. Ibers. "Positional Flexibility: Synthesis and Characterization of Six Uranium Chalcogenides Related to the 2H Hexagonal Perovskite Family", *Inorg. Chem.*, **2015**, *54*, 2851-2857.
5. Wu, L.-M., and D.-K. Seo. "New Solid-Gas Metathetical Synthesis of Binary Metal Poly-sulfides and Sulfides at Intermediate Temperatures: Utilization of Boron Sulfides", *J. Am. Chem. Soc.*, **2004**, *126*, 4676-4681.
6. Breton, L. S., V. V. Klepov, and H.-C. zur Loye. "Facile Oxide to Chalcogenide Conversion for Actinides using the Boron-Chalcogen Mixture Method", *J. Am. Chem. Soc.*, **2020**, *142*, 14365-14373.
7. Malliakas, C. D., J. Yao, D. M. Wells, M. G. Kanatzidis, J. A. Ibers. "Oxidation state of uranium in $A_6Cu_{12}U_2S_{15}$ (A = K, Rb, Cs) compounds", *Inorg. Chem.*, **2012**, *51*, 6153-6163.

Publications

Breton, L. S., Smith, M. D., zur Loye, H.-C., "Trends in Rare Earth Thiophosphate Syntheses: $Rb_3Ln(PS_4)_2$ (Ln = La, Pr, Ce), $Rb_{3-x}Na_xLn(PS_4)_2$ (Ln = Pr, Ce; x = 0.50, 0.55), and $RbEuPS_4$ Obtained by Molten Flux Crystal Growth", CrystEngComm, **2021**, submitted.

DeVore II, M. A., Villa-Aleman, E., Felder, J. B., Yeon, J., zur Loye, H.-C., Wellons, M. S., "Vibrational Spectroscopy of Uranium Tetrafluoride Hydrates", Vibrational Spectroscopy, **2021**, accepted.

Klepov, V. V., Kocevski, V., Besmann, T. M., zur Loye, H.-C., "Dimensional Reduction upon Calcium Incorporation in $Cs_{0.3}(Ca_{0.3}Ln_{0.7})PS_4$ and $Cs_{0.5}(Ca_{0.5}Ln_{0.5})PS_4$", DOI:10.1039/D0CE01524E. CrystEngComm, **2021**, *23*, 831-840.

Kutahyali Aslani, C., Breton, L. S., Klepov, V. V., zur Loye, H.-C., "A Series of $Rb_4Ln_2(P_2S_6)(PS_4)_2$ (Ln = La, Ce, Pr, Nd, Sm, Gd) Rare Earth Thiophosphates with Two Distinct Thiophosphate Units $[P^{V}S_4]^{3-}$ and $[P^{IV}{}_2S_6]^{4-}$", DOI:10.1039/D0DT03718D. Dalton Transactions, **2021**, *50*, 1683-1689.

Pace, K. A., Klepov, V. V., Berseneva, A. A., zur Loye, H.-C., "Covalency in Actinide Compounds", DOI:10.1002/chem.202004632. Chem. Eur. J., **2021**, *27*, 5835-5841.

Breton, L. S., Klepov, V. V., zur Loye, H.-C., "Facile Oxide to Chalcogenide Conversion for Actinides using the Boron-Chalcogen Mixture Method", DOI:10.1021/JACS.0C06483. J. Am. Chem. Soc., **2020**, *142*, 14365-14373.

Klepov, V. V., Berseneva, A. A., Pace, K. A., Kocesvski, V., Sun, M., Qiu, P., Wang, H., Chen, F., Besmann, T. M., zur Loye, H.-C., "$NaGaS_2$ – an Elusive Layered Compound with Dynamic Water Absorption and Wide-Ranging Ion Exchange Properties" DOI:10.1002/anie.202001203. Angew. Chem., Int. Ed., **2020**, *59*, 10836-10841.

Klepov, V. V., Pace, K. A., Breton, L. S., Kocevski, V., Besmann, T. M., zur Loye, H.-C., "Nearly Identical but not Isotypic – Influence of the Lanthanide Contraction on $Cs_2NaLn(PS_4)_2$ (Ln = La–Nd, Sm, Gd–Ho)", DOI:10.1021/acs.inorgchem.9b03200. Inorg. Chem., **2020**, *59*, 1905-1916.

Klepov, V. V., Smith, M. C., zur Loye, H.-C., "Targeted Synthesis of Uranium(IV) Thiosilicates", DOI:10.1021/acs.inorgchem.9b01307. Inorg. Chem., **2019**, *58*, 8275-8278.

Usman, M., Smith, M. D., Morrison, G., Klepov, V. V., Zhang, W., Halasyamani, P. S., zur Loye, H.-C., "Molten Alkali Halide Flux Growth of an Extensive Family of Non-Centrosymmetric Rare Earth Sulfides: Structure, Magnetic and Optical (SHG) Properties", DOI:10.1021/acs.inorgchem.9b00849. Inorg. Chem., **2019**, *58*, 8541-8550.

Usman, M., Smith, M. D., Klepov, V. V., zur Loye, H.-C., "One-Dimensional Quaternary and Penternary Alkali Rare Earth Thiophosphates Obtained via Alkali Halide Flux Crystal Growth", DOI:10.1021/acs.cgd.9b00637. Cryst. Growth Design, **2019**, *19*, 5648-5657.

Usman, M., Morrison, G., zur Loye, H.-C., "$La_2USe_3S_2$: A Serendipitously Grown Lanthanide/Actinide Chalcogenide from a Eutectic Halide Flux", DOI:10.1007/s10870-019-00780-x. J. Chem. Cryst., **2019**, *49*, 169-173.

Klepov, V. V., Breton, L., Pace, K., Kocevski, V., Besmann, T. M., zur Loye, H.-C., "Size-Driven Stability of Lanthanide Thiophosphates Grown from an Iodide Flux", DOI:10.1021/acs.inorgchem.9b00806. Inorg. Chem., **2019**, *58*, 6565-6573.

Klepov, V. V., Pace, K. A., Calder, S., Felder, J. B., zur Loye, H.-C., "3d-Metal Induced Magnetic Ordering on U(IV) Atoms as a Route Toward U(IV) Magnetic Materials", DOI:10.1021/jacs.9b00345. J. Am. Chem. Soc., **2019**, *141*, 3838-3842.

Klepov, V. V., Morrison, G., zur Loye, H.-C., "$Na_nMTh_6F_{30}$ – a Large Family of Quaternary Thorium Fluorides", DOI:10.1021/acs.cgd.8b01742. Cryst. Growth Design, **2019**, *19*, 1347-1355.

Morrison, G., Wilkins, B., Spagnuolo, N. R., Smith, M. D., zur Loye, H.-C., "Rare Earth Silicates and Germanates Crystallizing in the Wadeite and Related Structure Types",DOI:10.1016/j.jssc.2018.09.011. J. Solid State Chem., **2019**, *269*, 51-55.

Felder, J. B., Smith, M. D., zur Loye, H.-C., "Utilizing an *in situ* Reduction in the Synthesis of $BaMoOF_5$", DOI:10.1007/s10870-018-00767-0. J. Chem. Cryst., **2019**, *49*, 52-57.

Usman, M., Morrison, G., Klepov, V. V., Smith, M. D., zur Loye, H.-C., "Flux Crystal Growth, Structure, Magnetic and Optical Properties of a Family of Alkali Uranium(IV) Phosphates", DOI:10.1016/j.jssc.2018.10.033. J. Solid State Chem., **2019**, *270*, 19-26.

Tsujimoto, Y., Juillerat, C. A., Zhang, W., Fujii, K., Mastomo Yashima, M., Halasyamani, P. S., zur Loye, H.-C., "Function of Tetrahedral ZnS_3O Building Blocks in the Formation of $SrZn_2S_2O$: A Phase Matchable Polar Oxysulfide with a Large Second Harmonic Generation Response", DOI:10.1021/acs.chemmater.8b02967. Chem. Mater, **2018**, *30*, 6486-6493.

Klepov, V. V., zur Loye, H.-C., "Complex Topologies from Simple Building Blocks – Uranium(IV) Thiophosphates", DOI:10.1021/acs.inorgchem.8b01733. Inorg. Chem., **2018**, *57*, 11175-11183.

Felder, J. B., Smith, M. D., zur Loye, H.-C., "Breaking a Paradigm: Observation of Magnetic Order in the Purple U(IV) Phosphite: $U(HPO_3)_2$", DOI:10.1021/acs.inorgchem.8b00754. Inorg. Chem., **2018**, *57*, 9851–9858.

Felder, J. B., Calder, S., zur Loye, H.-C., "Retention of a Paramagnetic Ground State at Low Temperatures in a Family of Structurally Related U^{IV} Phosphates", DOI:org/10.1021/acs.inorgchem.8b01284. Inorg. Chem., **2018**, 57 9286-9295.

Usman, M., Felder, J., Morrison, G., zur Loye, H.-C., "A Family of Rare Earth Uranium Oxides, $RE_6UO_{12-\delta}$, (RE = Rare Earth). Synthesis, Structure and Magnetic Behavior", DOI:10.1016/j.jssc.2018.07.025. J. Solid State Chem., **2018**, *266*, 210-216.

Klepov, V. V., Felder, J. B., zur Loye, H.-C., “New Synthetic Strategies for the Synthesis of Ternary Uranium(IV) and Thorium(IV) Fluorides”, DOI:10.1021/acs.inorgchem.8b00570. Inorg. Chem., **2018**, *57*, 5597-5606.

AUTHOR INDEX

PARTICIPANT LIST

Name	Organization	Email
Albertus, Paul	University of Maryland	albertus@umd.edu
Aziz, Michael	Harvard University	maziz@harvard.edu
Bagchi, Kushal	University of Chicago	kbagchi@uchicago.edu
Baldo, Marc	Massachusetts Institute of Technology	baldo@mit.edu
Barcus, Kyle	University of California, San Diego	kybarcus@ucsd.edu
Bates, Christopher	University of California, Santa Barbara	cbates@ucsb.edu
Bertacche, Alessandra	Johns Hopkins University	abertac1@jhu.edu
Bhargava, Bhuvsmita	University of Maryland	bbhargav@umd.edu
Biswas, Rana	Ames Laboratory	biswasr@iastate.edu
Bobev, Svilen	University of Delaware	bobev@udel.edu
Bragg, Arthur	Johns Hopkins University	artbragg@jhu.edu
Braun, Paul	University of Illinois	pbraun@illinois.edu
Bridges, Craig	Oak Ridge National Laboratory	bridgesca@ornl.gov
Brodie, Alexander	University of Florida	brodiea@chem.ufl.edu
Brutchey, Richard	University of Southern California	brutchey@usc.edu
Çapraz, Ö. Özgür	Oklahoma State University	ocapraz@okstate.edu
Cava, Bob	Princeton University	rcava@princeton.edu
Chabinyc, Michael	University of California, Santa Barbara	mchabinyc@engineering.ucsb.edu
Chae, Sangmin	University of California, Santa Barbara	schae@ucsb.edu
Chakraborty, Jhonti	University of Florida	jchakraborty@chem.ufl.edu
Chatsirisupachai, Jirat	University of California, Santa Barbara	jirat@ucsb.edu
Chung, Duck Young	Argonne National Laboratory	dychung@anl.gov
Clayton, Tara	University of Oregon	tclayto2@uoregon.edu
Cohen, Seth	University of California, San Diego	scohen@ucsd.edu
Coughlin, Edward Bryan	University of Massachusetts, Amherst	ebc@umass.edu
Cui, Yi	SLAC/Stanford University	yicui@stanford.edu
Dadmun, Mark	Oak Ridge National Laboratory	dad@utk.edu
Das, Siddhartha	University of Maryland	sidd@umd.edu
Devlin, Kasey	Princeton University	kd4057@princeton.edu
Dimitriyev, Michael	University of Massachusetts, Amherst	mdimitriyev@mail.pse.umass.edu
Dravid, Vinayak	Northwestern University	v-dravid@northwestern.edu
D'Souza, Francis	University of North Texas	francis.dsouza@unt.edu
Duan, Xiangfeng	University of California, Los Angeles	xduan@chem.ucla.edu
Engler, Kaitlyn	University of California, Berkeley	kaitlyn.engler@berkeley.edu
Epps, Thomas	University of Delaware	thepps@udel.edu
Evans, Christopher	University of Illinois at Urbana-Champaign	cme365@illinois.edu
Ewoldt, Randy	University of Illinois at Urbana-Champaign	ewoldt@illinois.edu
Fehr, Julia	University of Oregon	jfehr@uoregon.edu
Feng, Pingyun	University of California, Riverside	pingyun.feng@ucr.edu
Feng, Xueyan	Texas A&M University	xf1@tamu.edu
Fleming, Drew	Arkansas State University	rofleming@AState.edu
Fredrickson, Glenn	University of California, Santa Barbara	ghf@mrl.ucsb.edu

Fredrickson, Daniel	University of Wisconsin-Madison	danny@chem.wisc.edu
Freedman, Danna	Massachusetts Institute of Technology	danna@mit.edu
Graham, Kenneth	University of Kentucky	kenneth.graham@uky.edu
Grason, Gregory	University of Massachusetts, Amherst	grason@mail.pse.umass.edu
Gregorczyk, Keith	University of Maryland	kgregorc@umd.edu
Grover, Girishma	Georgetown University	gg603@georgetown.edu
Gui, Xin	Princeton University	xgui@princeton.edu
Hall, Lisa	Ohio State University	hall.1004@osu.edu
Hayward, Ryan	University of Colorado, Boulder	ryan.hayward@colorado.edu
Huang, Wenyu	Ames Laboratory	whuang@ameslab.gov
Jasti, Ramesh	University of Oregon	rjasti@uoregon.edu
Jayaraman, Arthi	University of Delaware	arthij@udel.edu
Jin, Lun	Princeton University	ljin@princeton.edu
Kanatzidis, Mercouri	Argonne National Laboratory	m-kanatzidis@northwestern.edu
Katz, Howard	Johns Hopkins University	hekatz@jhu.edu
Kertesz, Miklos	Georgetown University	kertesz@georgetown.edu
Kim, Nam	University of Maryland	nsk0248@umd.edu
Klausen, Rebekka	Johns Hopkins University	Klausen@jhu.edu
Kobayashi, Takeshi	Ames Laboratory	takeshi@iastate.edu
Kolis, Joseph	Clemson University	kjoseph@clemson.edu
Kong, Jing	Massachusetts Institute of Technology	jingkong@mit.edu
Kornfield, Julia	California Institute of Technology	jak@cheme.caltech.edu
Kozen, Alexander	University of Maryland	ackozen@umd.edu
Laine, Antoine	Lawrence Berkeley National Laboratory	AntoineLaine@lbl.gov
Lawler, Keith	University of Nevada, Las Vegas	keith.lawler@unlv.edu
Lee, Eungje	Argonne National Laboratory	eungje.lee@anl.gov
Lee, Sang Bok	University of Maryland	slee@umd.edu
Li, He	Lawrence Berkeley National Laboratory	heli227@lbl.gov
Li, Jing	Rutgers University	jingli@rutgers.edu
Luong, Hoang	University of California, Santa Barbara	hoanglm@ucsb.edu
Luscombe, Christine	University of Washington	luscombe@uw.edu
Lutkenhaus, Jodie	Texas A&M University	jodie.lutkenhaus@tamu.edu
Manthiram, Arumugam	University of Texas at Austin	rmanth@mail.utexas.edu
Markowitz, Michael	U. S. Department of Energy	mike.markowitz@science.doe.gov
Mason, Jarad	Harvard University	mason@chemistry.harvard.edu
Matzger, Adam	University of Michigan	matzger@umich.edu
May, Steven	Drexel University	smay@drexel.edu
McKenna, Gregory	Texas Tech University	greg.mckenna@ttu.edu
McKeown Wessler, Garrett	Duke University	garrett.wessler@duke.edu
Meriles, Carlos	CUNY-City College of New York	cmeriles@ccny.cuny.edu
Mitzi, David	Duke University	david.mitzi@duke.edu
Nealey, Paul	Argonne National Laboratory	pnealey@anl.gov
Neilson, James	Colorado State University	james.neilson@colostate.edu

Nguyen, Tung	University of California, Santa Barbara	tung@ucsb.edu
Nguyen, Thuc-Quyen	University of California, Santa Barbara	quyen@chem.ucsb.edu
Ni, Danrui	Princeton University	danruin@princeton.edu
Nyman, May	Oregon State University	may.nyman@oregonstate.edu
Otteson, Claire	University of Oregon	cotteson@uoregon.edu
Panoy, Patchareepond	University of California, Santa Barbara	ppanoy@ucsb.edu
Perras, Frederic	Ames Laboratory	fperras@ameslab.gov
Perry, Nicola	University of Illinois at Urbana-Champaign	nhperry@illinois.edu
Peterson, Eric	Johns Hopkins University	epeter57@jhu.edu
Poudeu, Pierre Ferdinand	University of Michigan	ppoudeup@umich.edu
Powderly, Kelly	Princeton University	powderly@princeton.edu
Powell, Matthew	Clemson University	msp2@g.clemson.edu
Power, Philip	University of California, Davis	pppower@ucdavis.edu
Price, Tavis	University of Oregon	tprice@uoregon.edu
Reddy, Abhiram	University of Massachusetts, Amherst	abhiram@mail.pse.umass.edu
Reimer, Jeff	University of California, Berkeley	reimer@berkeley.edu
Ross, Kate	Colorado State University	kate.ross@colostate.edu
Rossini, Aaron	Ames Laboratory	arossini@iastate.edu
Rubloff, Gary	University of Maryland	rubloff@umd.edu
Salamat, Ashkan	University of Nevada, Las Vegas	ashkan.salamat@unlv.edu
Salmeron, Miquel	Lawrence Berkeley National Laboratory	mbsalmeron@lbl.gov
Sanchez, Regina	University of Chicago	regisanchez@uchicago.edu
Saparov, Bayram	University of Oklahoma	saparov@ou.edu
Schanze, Kirk	University of Texas at San Antonio	kirk.schanze@utsa.edu
Schweizer, Ken	University of Illinois at Urbana-Champaign	kschweiz@illinois.edu
Segalman, Rachel	University of California, Santa Barbara	segalman@ucsb.edu
Sennett, Michael	DOE/BES	michael.sennett@science.doe.gov
Seshadri, Ram	University of California, Santa Barbara	seshadri@mrl.ucsb.edu
Shan, Wenpeng	Texas A&M University	wenpengshan@tamu.edu
Shen, Yu-Hsuan	University of Florida	yuhsuan.shen@ufl.edu
Sing, Charles	University of Illinois at Urbana-Champaign	cesing@illinois.edu
Sokolov, Alexei	Oak Ridge National Laboratory	sokolovap@ornl.gov
Song, Yueming	University of Maryland	ysong722@umd.edu
Spano, Frank	Temple University	spano@temple.edu
Steinmetz, Christian	University of Massachusetts, Amherst	csteinmetz@mail.pse.umass.edu
Stewart, David	University of Maryland	steward@umd.edu
Straus, Daniel	Princeton University	dstraus@princeton.edu
Strobel, Timothy	Carnegie Institution for Science	tstrobel@carnegiescience.edu
Talin, Alec	Sandia National Laboratories	aatalin@sandia.gov
Tan, Kui	The University of Texas at Dallas	kuitan@utdallas.edu
Teng, Xiaowei	University of New Hampshire	xw.teng@unh.edu
Terrones, Mauricio	Penn State	mut11@psu.edu
Teymur, Betul	Duke University	teymurbetul@gmail.com

Thomas, Samuel	Tufts University	sam.thomas@tufts.edu
Thomas, Edwin	Texas A & M University	elt@tamu.edu
Thonhauser, Timo	Wake Forest University	thonhat@wfu.edu
Tirrell, Matthew	University of Chicago	mtirrell@uchicago.edu
Tolbert, Sarah	University of California, Los Angeles	tolbert@chem.ucla.edu
Tovar, John	Johns Hopkins University	tovar@jhu.edu
Vargo, Emma	University of California, Berkeley	evargo@berkeley.edu
Veige, Adam	University of Florida	veige@chem.ufl.edu
Vela, Javier	Ames Laboratory	vela@iastate.edu
Wakidi, Hiba	University of California, Santa Barbara	wakidi@ucsb.edu
Wang, Hong	University of North Texas	hong.wang@unt.edu
Warecki, Zoey	University of Maryland, College Park	zwarecki@umd.edu
Wolverton, Chris	Northwestern University	c-wolverton@northwestern.edu
Xiong, Claire	Boise State University	clairexiong@boisestate.edu
Xu, Ting	University of California, Berkeley	tingxu@berkeley.edu
Xu, Kaylin	Princeton University	kxxu@princeton.edu
Yang, Chen	Princeton University	cy11@princeton.edu
Yang, Peidong	University of California, Berkeley	p_yang@berkeley.edu
Zakutayev, Andriy	National Renewable Energy Laboratory	andriy.zakutayev@nrel.gov
Zhang, Teng	Drexel University	tz333@drexel.edu
Zhu, Xiaoyang	Columbia University	xyzhu@columbia.edu
Zhu, Lei	Case Western Reserve University	lxz121@case.edu
Zimmerman, Jeramy	Colorado School of Mines	jdzimmer@mines.edu
zur Loye, Hans-Conrad	University of South Carolina	zurloye@mailbox.sc.edu